Transactions of the ASME, Journal of Applied Mechanics (ISSN 0021-8936) is published bimonthly (Jan., Mar., May, July, Sept., Nov.) by The American Society of Mechanical Engineers, Three Park Avenue, New York, NY 10016. Periodicals postage paid at New York, NY and additional mailing offices. POSTMASTER: Send address changes to Transactions of the ASME, Journal of Applied Mechanics, c/o THE AMERICAN SOCIETY OF MECHANICAL ENGINEERS, 22 Law Drive, Box 2300, Fairfield, NJ 07007-2300. **CHANGES OF ADDRESS** must be received at Society headquarters seven weeks before they are to be effective. Please send old label and new address. **STATEMENT from By-Laws.** The Society shall not be responsible for statements or opinions advanced in papers or printed in its publications (B7.1, Para. 3).

Journal of Applied Mechanics

Published Bimonthly by ASME

VOLUME 75 • NUMBER 5 • SEPTEMBER 2008

GUEST EDITORIAL

RESEARCH PAPERS

SPECIAL ISSUE HONORING PROFESSOR FAZIL ERDOGAN'S CONTRIBUTIONS TO MIXED BOUNDARY VALUE PROBLEMS OF INHOMOGENEOUS AND FUNCTIONALLY GRADED MATERIALS

(Contents continued on inside back cover)

This journal is printed on acid-free paper, which exceeds the ANSI Z39.48-1992 specification for permanence of paper and library materials. ♾™
♻ 85% recycled content, including 10% post-consumer fibers.

TECHNICAL BRIEFS

The ASME Journal of Applied Mechanics is abstracted and indexed in the following:

Alloys Index, Aluminum Industry Abstracts, Applied Science & Technology Index, Ceramic Abstracts, Chemical Abstracts, Civil Engineering Abstracts, Compendex (The electronic equivalent of Engineering Index), Computer & Information Systems Abstracts, Corrosion Abstracts, Current Contents, EEA (Earthquake Engineering Abstracts Database), Electronics & Communications Abstracts Journal, Engineered Materials Abstracts, Engineering Index, Environmental Engineering Abstracts, Environmental Science and Pollution Management, Fluidex, Fuel & Energy Abstracts, GeoRef, Geotechnical Abstracts, INSPEC, International Aerospace Abstracts, Journal of Ferrocement, Materials Science Citation Index, Mechanical Engineering Abstracts, METADEX (The electronic equivalent of Metals Abstracts and Alloys Index), Metals Abstracts, Nonferrous Metals Alert, Polymers Ceramics Composites Alert, Referativnyi Zhurnal, Science Citation Index, SciSearch (Electronic equivalent of Science Citation Index), Shock and Vibration Digest, Solid State and Superconductivity Abstracts, Steels Alert, Zentralblatt MATH

Journal of Applied Mechanics

Guest Editorial

Honoring Professor Erdogan's Seminal Contributions to Mixed Boundary-Value Problems of Inhomogeneous and Functionally Graded Materials

Foreword

Professor Fazil Erdogan has influenced several generations of applied and solid mechanicians working in the area of mixed boundary-value problems of inhomogeneous media, most notably fracture and contact problems. The analytical approaches that he had developed with his students in the 1960s and 1970s for the formulation and reduction of fracture mechanics problems involving layered media to systems of singular integral equations, and the corresponding solution techniques, have motivated researchers working in this area throughout the entire world. His subsequent work on fracture mechanics problems of inhomogeneous media with smoothly varying elastic moduli has laid the foundation for applying these techniques to functionally graded materials, which played key roles in many technologically important applications (e.g., spatially tailored structures for the new generation of hypersonic aircraft, graded cementitious composites for sustainable infrastructure, high-performance graded components for automobiles, and graded microtools in mechatronics). Professor Erdogan's continuing leadership role and ceaseless contributions to the fracture and contact mechanics of this new generation of materials provide guidance and motivation for others to follow. This special issue honors Professor Erdogan in recognition of his past and continuing contributions in the area that plays a critical role in the development of engineered material systems for critical technological applications, and builds upon a minisymposium under the above title held at the recent International Conference on Multiscale and Functionally Graded Materials (M&FGM2006) on Oct. 15–18, 2006, Honolulu, HI.

The special issue is comprised of 13 invited papers containing original, previously unpublished contributions in the mechanics of inhomogeneous and functionally graded materials. The invited contributors, including Professor Erdogan who has provided with Dr. Ozturk (coauthor) the lead article summarizing the various types of singularities that may be encountered in contact and fracture mechanics, include selected authors of presentations given at the above conference. Some of these contributors are Professor Erdogan's ex-students and past or present collaborators, while others are distinguished researchers working in this topical area who did not attend the conference. Analytical, computational, experimental, and theoretical aspects of the mechanics of inhomogeneous media in the broad sense, and functionally graded materials, in particular, are covered by the 13 papers. Topics range from the fundamental aspects of crack propagation in graded materials, construction of elasticity solutions for layered anisotropic media, development of novel computational procedures, and specific problems of technological importance involving graded coatings and cover plates to micromechanics-based calculations involving periodically layered media and functionally graded particulate materials. Examination of the contributed articles reveals the need for a multipronged approach in the modeling and simulation of graded and layered materials, and the important role that locally exact analytical solutions may play in the development of new computational procedures.

Many of us who have been influenced directly or indirectly by Professor Erdogan's work hope that this will be a lasting issue in an area that continues to grow vigorously. One of the coeditors of this special issue (M.-J. P) recalls his first contact with the work of Professor Erdogan while collaborating some 25 years ago with Dr. Sailon Chatterjee at the Materials Sciences Corporation on fracture mechanics of layered anisotropic materials. "The techniques to which I was being introduced in the course of conducting research on defect criticality of composite laminates for the Naval Air Development Center were based on Professor Erdogan's now classical papers, and Sailon often telephoned *Fazil*, who he called his secret weapon, for clarification or guidance to ensure that we were on the right path. It took me a while to realize that this mysterious *Fazil* was in fact Professor Erdogan whose papers and guidance enabled us to prosper."

We are indeed grateful that we were given the opportunity to assemble this special issue in order to honor Professor Fazil Erdogan. He continues to be a source of inspiration to the mechanics community in leading the way in the area of mixed boundary-value problems in inhomogeneous and functionally graded media and also in providing selfless guidance to others.

Marek-Jerzy Pindera
University of Virginia

Glaucio H. Paulino
University of Illinois at Urbana-Champaign

M. R. Tonks
T-3, Los Alamos National Laboratory,
Los Alamos, NM, 87545;
Department of Mechanical Science and Engineering,
University of Illinois at Urbana-Champaign,
Urbana, IL 61801

A. J. Beaudoin
Department of Mechanical Science and Engineering,
University of Illinois at Urbana-Champaign,
Urbana, IL 61801

F. Schilder
Department of Mathematics,
University of Surrey,
Guildford, GU2 7XH, UK

D. A. Tortorelli
Department of Mechanical Science and Engineering,
University of Illinois at Urbana-Champaign,
Urbana, IL 61801

Investigation of Preferred Orientations in Planar Polycrystals

*More accurate manufacturing process models come from better understanding of texture evolution and preferred orientations. We investigate the texture evolution in the simplified physical framework of a planar polycrystal with two slip systems used by Prantil et al. (1993, "An Analysis of Texture and Plastic Spin for Planar Polycrystal," J. Mech. Phys. Solids, **41**(8), pp. 1357–1382). In the planar polycrystal, the crystal orientations behave in a manner similar to that of a system of coupled oscillators represented by the Kuramoto model. The crystal plasticity finite element method and the stochastic Taylor model (STM), a stochastic method for mean-field polycrystal plasticity, predict the development of a steady-state texture not shown when employing the Taylor hypothesis. From this analysis, the STM appears to be a useful homogenization method when using representative standard deviations.* [DOI: 10.1115/1.2912930]

Keywords: polycrystal plasticity, planar polycrystal, stochastic Taylor model, Kuramoto model

1 Introduction

Crystallographic textures, which evolve during manufacturing processes, are central to the anisotropic response of the processed material. These textures do not randomly evolve, but rather evolve toward certain preferred orientations determined by the crystal structure, loading, and other factors. As such, understanding the development and nature of preferred orientation is of critical importance when developing meaningful models of manufacturing processes. This is a complicated task because the driving forces behind the evolution cover multiple length scales [1]. To bridge the length scales, it is often convenient to consider the polycrystalline material as an aggregate of anisotropic mesoscale crystals.

Mean-field polycrystal plasticity models describe the aggregate response to an applied deformation by predicting the response of each crystal with a mesoscale model. These mesoscale fields are subsequently homogenized to obtain the macroscale response, including the stress in the aggregate and the evolving texture. However, a method is needed to relate the macroscale deformation to the mesoscale deformations experienced by the crystals. Several such methods appear in the literature, the most common being the fully constrained model (FCM), based on the hypothesis in Taylor [2], which asserts that the crystal deformations are equal to the macroscopic deformation. Many applications of this hypothesis validate its use [3,4]; however, it is not consistent with the physical behavior of polycrystalline materials. Several alternative methods have been proposed ranging from relaxed constraint methods in which only selected components of the macroscale and crystal deformation rate and stress are equated [5–7] to self-consistent models [8] in which each crystal is treated as a viscoplastic inclusion embedded in a homogeneous effective medium with the average properties of the other crystals. Of course, the increased accuracy of these models comes at the expense of computational complexity.

Prantil et al. [9] apply mean-field polycrystal plasticity to a simplified planar polycrystal in order to investigate texture evolution and preferred orientations. By using two slip systems to describe the plastic deformation in the planar single crystals, they develop an analytical expression defining the reorientation of a crystal throughout an imposed deformation. Using the FCM to relate deformations between the crystals and the macroscale, they find that the texture of a deformed planar polycrystal either approaches a single, preferred orientation or periodically oscillates, depending on the magnitude of the spin in the applied deformation. Kumar and Dawson [10] conduct a similar investigation on planar polycrystals but look at single crystals with two to four slip systems. As with Prantil et al. [9], they utilize the FCM. They show that as the number of slip systems increases, the number of possible texture evolution behaviors also increases, but each behavior is still either an evolution toward a single orientation or a periodic evolution. Kumar [11] show that 3D cubic polycrystals modeled with the FCM loaded under pure shear experience five stable orientations at which the texture will continue to increase in strength, but when a spin is introduced there are no stable orientations and the texture may oscillate in strength. Therefore, while crystals tend to reorient toward preferred orientations, a significant applied spin can induce periodic reorientation. The texture evolution observed in these studies may be exaggerated since the FCM overconstrains the crystals.

In this work, we investigate the development of preferred orientations using the FCM, as well as two additional methods that relax the strict equality between the macro- and mesoscale deformation rates. Our objective is to gain understanding into the dynamical nature of a preferred orientation, as well as the evolution toward this orientation. As more complex systems show similar trends to simpler idealizations, we investigate the texture evolution behavior in an idealized planar polycrystal with two slip systems. We apply the crystal plasticity finite element method (CPFEM), in which each crystal in the aggregate is represented by one or more finite elements [12–16], as well as a stochastic mean-field model [17,18] to the deformation of the planar aggregate. We begin in Secs. 2 and 3, by presenting the single crystal model for the planar polycrystal. In Sec. 4, we compare the texture trajectory to that of a system of coupled oscillators represented by the Kura-

Contributed by the Applied Mechanics Division of ASME for publication in the JOURNAL OF APPLIED MECHANICS. Manuscript received February 21, 2007; final manuscript received February 25, 2008; published online July 2, 2008. Review conducted by Antoinette Maniatty.

moto model, in turn revealing a link between the development of preferred orientations and the notion of synchronization. We compare the FCM texture evolution to that predicted from the CPFEM using an idealized microstructure in Sec. 5. In Secs. 6 and 7, we develop a stochastic method and compare the predicted behavior to the CPFEM results. Both the CPFEM and the stochastic model show the evolution toward a stable texture in the presence of macroscale spin. In both cases, this "stable" texture exhibits a dynamic character, in which component crystals continue crystallographic reorientation but the overall distribution does not change. Section 8 investigates the long-term behavior of the texture evolution and discusses the applicability of the results to planar polycrystals with more slip systems, as well as to the 3-D polycrystals.

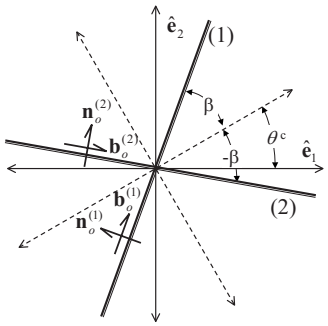

Fig. 1 Single planar crystal structure

2 General Rotation Evolution Equation

Following Kok et al. [19], we derive an expression for the evolution of the crystal lattice rotation of a crystal c as a function of the current state variables (crystal lattice rotation and "flow stress") and the current crystal velocity gradient $\mathbf{L}^c$. To simplify our analysis, we neglect elastic effects.

A material point in a crystal c identified by position vector $\mathbf{x}^c$ in the reference configuration is mapped to the location in the deformed configuration at time t identified by the position vector $\mathbf{x}_t^c$ through the motion $\mathbf{f}^c$, i.e., $\mathbf{x}_t^c = \mathbf{f}^c(\mathbf{x}^c;t)$. We define the deformation gradient as the spatial derivative, i.e., $\mathbf{F}^c = \nabla \mathbf{f}^c$ with $\mathbf{F} \in \mathrm{Lin}^+$, where Lin^+ is the set of tensors with positive determinant. As per usual, we require $\det \mathbf{F}^c > 0$ so that the mapping $\mathbf{f}^c$ at a given time t is everywhere invertible.

The material point velocity can be defined with respect to the reference configuration, giving the material velocity, or with respect to the deformed configuration, giving the spatial velocity, i.e.,

$$\dot{\mathbf{f}}^c(\mathbf{x}^c;t) = v^c(\overbrace{\mathbf{x}_t^c}^{\mathbf{f}^c(\mathbf{x}^c;t)};t).$$

Differentiating this equality with respect to the reference position $\mathbf{x}^c$ and rearranging give the expression for the spatial crystal velocity gradient

$$\mathbf{L}^c = \nabla v^c = \dot{\mathbf{F}}^c \mathbf{F}^{c-1} \tag{1}$$

The crystal deformation gradient is assumed to be the result of a plastic deformation followed by a rigid rotation, i.e.,

$$\mathbf{F}^c = \mathbf{R}^c \mathbf{F}_p^c \quad \text{with } \mathbf{R}^c \in \mathrm{Rot} \text{ and } \det \mathbf{F}_p^c = 1 \tag{2}$$

where Rot is the set of all rotations. $\mathbf{F}_p^c$ represents the plastic isochoric deformation gradient due to the motion along slip planes in the crystal lattice and $\mathbf{R}^c$ represents the crystal lattice rotation. Substituting Eq. (2) into Eq. (1), we obtain

$$\mathbf{L}^c = \dot{\mathbf{R}}^c \mathbf{R}^{cT} + \mathbf{R}^c \mathbf{L}_p^c \mathbf{R}^{cT} \tag{3}$$

where $\mathbf{L}_p^c \equiv \dot{\mathbf{F}}_p^c \mathbf{F}_p^{c-1}$ is the plastic velocity gradient. The symmetric $\mathbf{D}^c$ and skew $\mathbf{W}^c$ components of $\mathbf{L}^c$ are

$$\mathbf{D}^c = \mathbf{R}^c \mathbf{D}_p^c \mathbf{R}^{cT} \tag{4}$$

$$\mathbf{W}^c = \dot{\mathbf{R}}^c \mathbf{R}^{cT} + \mathbf{R}^c \mathbf{W}_p^c \mathbf{R}^{cT} \tag{5}$$

where $\mathbf{D}_p^c$ and $\mathbf{W}_p^c$ are the symmetric and skew components of $\mathbf{L}_p^c$, respectively. The evolution equation of the lattice rotation is obtained by solving Eq. (5) for $\dot{\mathbf{R}}^c$ giving

$$\dot{\mathbf{R}}^c = \mathbf{W}^c \mathbf{R}^c - \mathbf{R}^c \mathbf{W}_p^c \tag{6}$$

For a single crystal, the plastic velocity gradient is assumed to be given by

$$\mathbf{L}_p^c = \sum_{s=1}^{M} \dot{\gamma}^s \mathbf{S}_o^s \tag{7}$$

where, for each of the M slip systems s, $\dot{\gamma}^s$ is the shear rate, $\mathbf{S}_o^s = \mathbf{b}_o^s \otimes \mathbf{n}_o^s$ is the Schmidt tensor, and $\mathbf{b}_o^s$ and $\mathbf{n}_o^s$ are the unit vectors for the unrotated, i.e., undeformed, crystal along the slip direction and normal to the slip plane, respectively. Expressions for $\mathbf{D}_p^c$ and $\mathbf{W}_p^c$ are obtained from Eq. (7) as

$$\mathbf{D}_p^c = \sum_{s=1}^{M} \dot{\gamma}^s \mathbf{m}_0^s \tag{8}$$

$$\mathbf{W}_p^c = \sum_{s=1}^{M} \dot{\gamma}^s \mathbf{q}_o^s \tag{9}$$

with $\mathbf{m}_0^s$ and $\mathbf{q}_o^s$ being the symmetric and skew components of the Schmidt tensor, respectively.

3 Planar Aggregate Model

From Eq. (6), we derive an equation for the planar crystal aggregate motion, as shown in Prantil et al. [9]. The crystals in the aggregate have $M=2$ slip systems such that the partition of shearing among the slip systems is kinematically determined. The slip systems are portrayed in their deformed configuration in Fig. 1, where the Cartesian coordinate system is defined by the orthonormal basis vectors $(\hat{\mathbf{e}}_1, \hat{\mathbf{e}}_2, \hat{\mathbf{e}}_3)$ with $\hat{\mathbf{e}}_3$ normal to the page. Each crystal c in the aggregate experiences a rotation of the angle θ^c about $\hat{\mathbf{e}}_3$, i.e.,

$$\begin{aligned}\mathbf{R}^c = \mathbf{R}(\theta^c) = \hat{\mathbf{e}}_3 \otimes \hat{\mathbf{e}}_3 + \cos\theta^c(\hat{\mathbf{e}}_1 \otimes \hat{\mathbf{e}}_1 + \hat{\mathbf{e}}_2 \otimes \hat{\mathbf{e}}_2) \\ - \sin\theta^c(\hat{\mathbf{e}}_1 \otimes \hat{\mathbf{e}}_2 - \hat{\mathbf{e}}_2 \otimes \hat{\mathbf{e}}_1)\end{aligned} \tag{10}$$

The individual crystal deformation is due to slip over the two independent slip systems $(s=1,2)$, with

$$\begin{aligned}\mathbf{b}_o^{(1)} &= \mathbf{R}(\beta)\hat{\mathbf{e}}_1 \\ \mathbf{n}_o^{(1)} &= \mathbf{R}(\beta)\hat{\mathbf{e}}_2 \\ \mathbf{b}_o^{(2)} &= \mathbf{R}(-\beta)\hat{\mathbf{e}}_1 \\ \mathbf{n}_o^{(2)} &= \mathbf{R}(-\beta)\hat{\mathbf{e}}_2\end{aligned} \tag{11}$$

where β is known (see Fig. 1).

For general isochoric planar motions, the velocity gradient can be written as a function of three independent components, the rate of stretching Λ^c, the rate of shearing Γ^c, and the spin Ω^c,[1] i.e.,

[1]Note that these definitions are slightly different from those employed by Prantil et al. [9], in which $\dot{\Lambda}^c$ is the rate of stretching and $\dot{\Gamma}^c$ is the rate shearing.

$$\mathbf{L}^c = \Lambda^c(t)(\hat{\mathbf{e}}_1 \otimes \hat{\mathbf{e}}_1 - \hat{\mathbf{e}}_2 \otimes \hat{\mathbf{e}}_2) + \Gamma^c(t)(\hat{\mathbf{e}}_1 \otimes \hat{\mathbf{e}}_2 + \hat{\mathbf{e}}_2 \otimes \hat{\mathbf{e}}_1) + \Omega^c(t)(\hat{\mathbf{e}}_1 \otimes \hat{\mathbf{e}}_2 - \hat{\mathbf{e}}_2 \otimes \hat{\mathbf{e}}_1) \tag{12}$$

$$\mathbf{D}^c = \Lambda^c(t)(\hat{\mathbf{e}}_1 \otimes \hat{\mathbf{e}}_1 - \hat{\mathbf{e}}_2 \otimes \hat{\mathbf{e}}_2) + \Gamma^c(t)(\hat{\mathbf{e}}_1 \otimes \hat{\mathbf{e}}_2 + \hat{\mathbf{e}}_2 \otimes \hat{\mathbf{e}}_1) \tag{13}$$

$$\mathbf{W}^c = \Omega^c(t)(\hat{\mathbf{e}}_1 \otimes \hat{\mathbf{e}}_2 - \hat{\mathbf{e}}_2 \otimes \hat{\mathbf{e}}_1) \tag{14}$$

To solve for the texture evolution $\dot{\theta}^c$, we first find $\dot{\gamma}^s$ $(s=1,2)$ by substituting Eqs. (8), (10), (11), and (13) into Eq. (4) to obtain

$$\dot{\gamma}^1 = 2 \csc 4\beta(\Gamma^c \sin 2(\beta - \theta^c) - \Lambda^c \cos 2(\beta - \theta^c))$$
$$\dot{\gamma}^2 = 2 \csc 4\beta(\Gamma^c \sin 2(\beta + \theta^c) + \Lambda^c \cos 2(\beta + \theta^c)) \tag{15}$$

We then substitute Eqs. (9)–(11), (14), and (15) into Eq. (6), giving the evolution equation for the crystal orientation

$$\dot{\theta}^c = -\Omega^c + \lambda(\Gamma^c \cos 2\theta^c - \Lambda^c \sin 2\theta^c) \tag{16}$$

where

$$\lambda \equiv \sec 2\beta \tag{17}$$

To achieve an expression for the current crystal orientation θ^c whose initial orientation is θ_0^c, Eq. (16) is integrated. Assuming Γ^c, Λ^c, and Ω^c are constant, the integration gives

$$\theta^c = \tan^{-1}\left[\left(-\lambda\Lambda^c + \mathcal{F}\tanh\left[t\mathcal{F} + \tanh^{-1} \times \left[\frac{1}{\mathcal{F}}(\lambda\Lambda^c + (\lambda\Gamma^c + \Omega^c)\tan\theta_0^c)\right]\right]\right)(\Gamma^c\lambda + \Omega^c)^{-1}\right] \tag{18}$$

where $\mathcal{F} = \sqrt{\lambda^2(\Gamma^{c2} + \Lambda^{c2}) - \Omega^{c2}}$. For our subsequent analyses, we find it convenient to "invert" the above to obtain an expression for

$$\theta_0^c = \tilde{\theta}_0^c(\theta^c, \Gamma^c, \Lambda^c, \Omega^c) = -\tan^{-1}\left[\left(\lambda\Lambda^c + \mathcal{F}\tanh\left[t\mathcal{F} - \tanh^{-1} \times \left[\frac{1}{\mathcal{F}}(\lambda\Lambda^c + (\lambda\Gamma^c + \Omega^c)\tan\theta^c)\right]\right]\right)(\Gamma^c\lambda + \Omega^c)^{-1}\right] \tag{19}$$

4 Similarities to the Kuramoto Model

The orientation evolution equation, Eq. (16), bears a close resemblance to the equation governing a system of coupled oscillators described by the Kuramoto model [20] in which a collection of N coupled oscillators with phases θ_i interact through a sinusoidal coupling

$$\dot{\theta}_i = \omega_i + \frac{K}{N}\sum_{j=1}^{N} \sin(\theta_j - \theta_i), \quad i = 1, \ldots, N \tag{20}$$

where K is the coupling strength and the frequencies ω_i follow a symmetric probability density, such as a normal distribution.

In order to simplify Eq. (20), as discussed in Strogatz [21], it is convenient to introduce the complex order parameter

$$re^{i\psi} = \frac{1}{N}\sum_{j=1}^{N} e^{i\theta_j} \tag{21}$$

where the radius r measures the spread of the θ_j and ψ is the average θ_j (see Fig. 2). Kuramoto rewrote Eq. (20) through the order parameter by first multiplying both sides of Eq. (21) by $e^{-i\theta j}$ and taking the imaginary part to obtain

$$r\sin(\psi - \theta_i) = \frac{1}{N}\sum_{j=1}^{N} \sin(\theta_j - \theta_i) \tag{22}$$

Substituting Eq. (22) into Eq. (20) gives

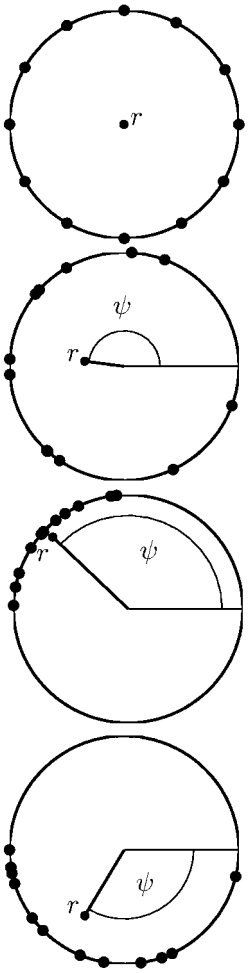

Fig. 2 Geometric representation of the order parameter, with the corresponding θ_j plotted on the unit circle

$$\dot{\theta}_i(t) = \omega_i + Kr(t)\sin(\psi(t) - \theta_i(t)), \quad i = 1, \ldots, N \tag{23}$$

As seen above, the phase of each oscillator tends toward the average phase ψ with strength proportional to the radius r. Considering steady solutions, where $r(t)$ is constant and $\psi(t)$ uniformly rotates, along with judicious choice of a rotating frame such that $\psi=0$, Eq. (23) reduces to

$$\dot{\theta}_i = \omega_i - Kr\sin\theta_i \tag{24}$$

which is essentially Eq. (16) with $\theta_i = 2\theta^c$, $\omega_i = -\Omega^c$, $Kr = \lambda\Lambda^c$, and $\Gamma^c = 0$.

The long-term response of an oscillator, i.e., $t \to \infty$, in this steady treatment of the Kuramoto model leads to two distinct types of behavior, depending on the relationship between the product of the coupling strength and spread Kr and the oscillator's natural frequency ω_i. When $Kr \geq |\omega_i|$, the coupling dominates and the oscillator approaches a stable fixed point at which it is phase locked, i.e., $\dot{\theta}_i = 0$; when $Kr < |\omega_i|$, locking cannot occur and the oscillator drifts in a nonuniform manner.

In Prantil et al. [9], the long-term response of the ODF generated using the FCM was found to depend on the relationship between λ (cf. Eq. (17)) and

$$\eta = \tilde{\eta}(\Omega^c, \Gamma^c, \Lambda^c) = \frac{|\Omega^c|}{\sqrt{\Gamma^{c^2} + \Lambda^{c^2}}} = \frac{|\Omega|}{\sqrt{\Gamma^2 + \Lambda^2}} \tag{25}$$

where Ω, Γ, and Λ are the spin, the rate of shearing, and the rate of stretching, respectively, of the applied velocity gradient $\mathbf{L}$. The

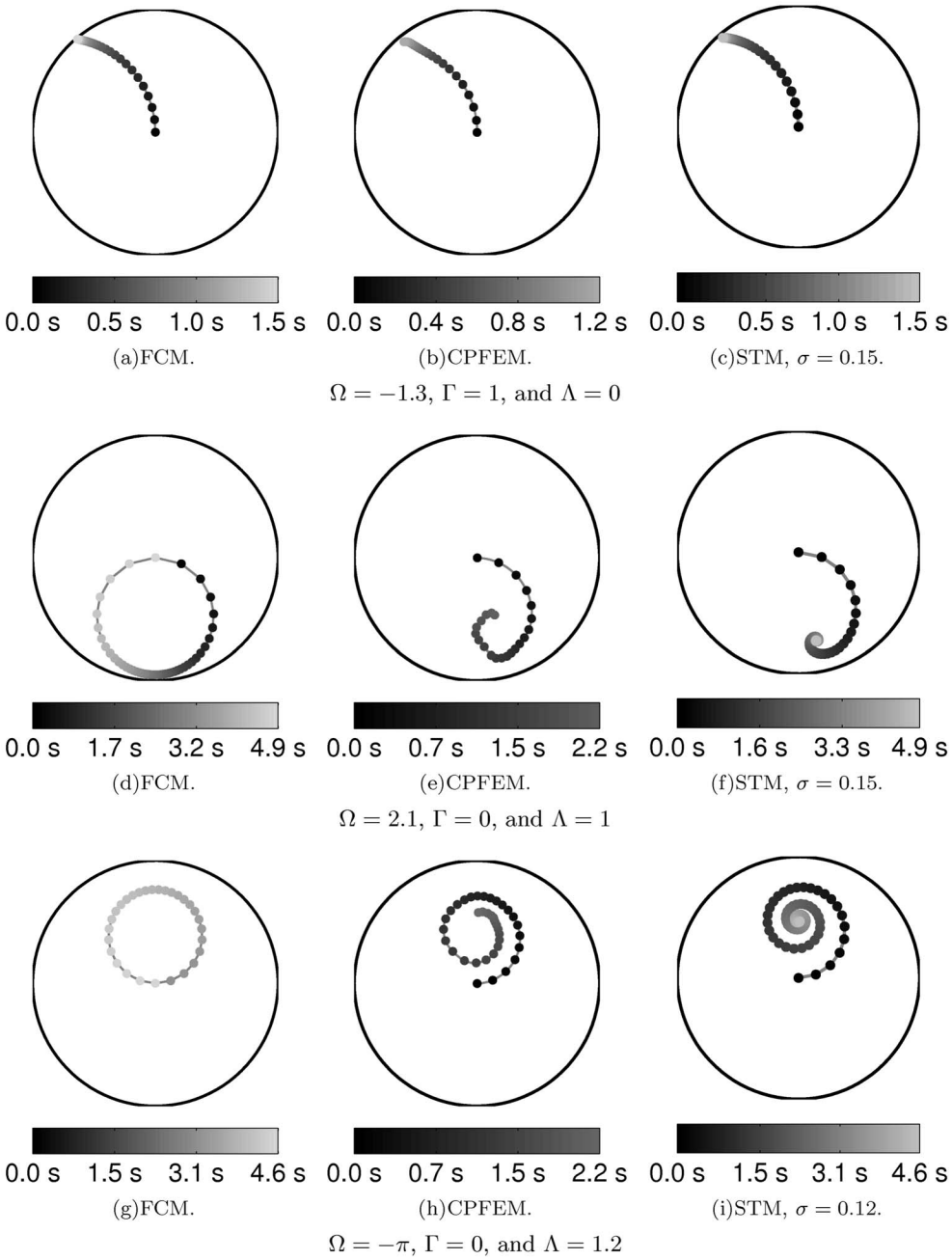

Fig. 3 The order parameter calculated from Eq. (21) with $\theta_j = 2\theta_c$ at several time instants for various loadings and simulation methods. The shading of the data points represents the corresponding time as dictated by the scale bar.

parameter λ, defined by the structure of the undeformed crystal, represents a coupling between the crystals due to their similar crystal structure, whereas η, defined by $\mathbf{L}$, represents the natural oscillation of the crystal induced by the loading. When $\lambda \geq \eta$, the internal structure dominates, causing the crystals to approach a single orientation $\theta^p = \tan^{-1}(\mathcal{F} - \lambda\Lambda)/(\lambda\Gamma + \Omega)$, i.e., in Eq. (21) $\psi \rightarrow \theta^p$ and $r \rightarrow 1$, as shown in Fig. 3(*a*). When $\lambda < \eta$, the polycrystal experiences "tumbling" behavior where the texture periodically evolves with a period of $T = \pi/\sqrt{(\Gamma^2 + \Lambda^2)(\eta^2 - \lambda^2)}$, as shown in Figs. 3(*d*) and 3(*g*). Note that the criteria for the development of a sharp texture ($\lambda \geq \eta$) and tumbling ($\lambda < \eta$) correspond, respectively, to the phase locking ($Kr \geq |\omega|$) and drifting ($Kr < |\omega|$) response of oscillators noted in the steady treatment of the Kuramoto model.

The Kuramoto model was originally developed as an abstract model to mathematically study the synchronization of a system of coupled oscillators. It was not thought to represent any known system but rather act as a tool for understanding synchronization in general terms. For this reason, the similarity between the orientation evolution equation of the planar polycrystal and the Kuramoto model is remarkable, albeit that the kinematically determined planar polycrystal is a simplification of "true" polycrystal behavior.

5 CPFEM Results

We investigate the texture evolution of the planar polycrystal using the CPFEM. The CPFEM intrinsically accounts for the crystal interactions and therefore provides a more accurate represen-

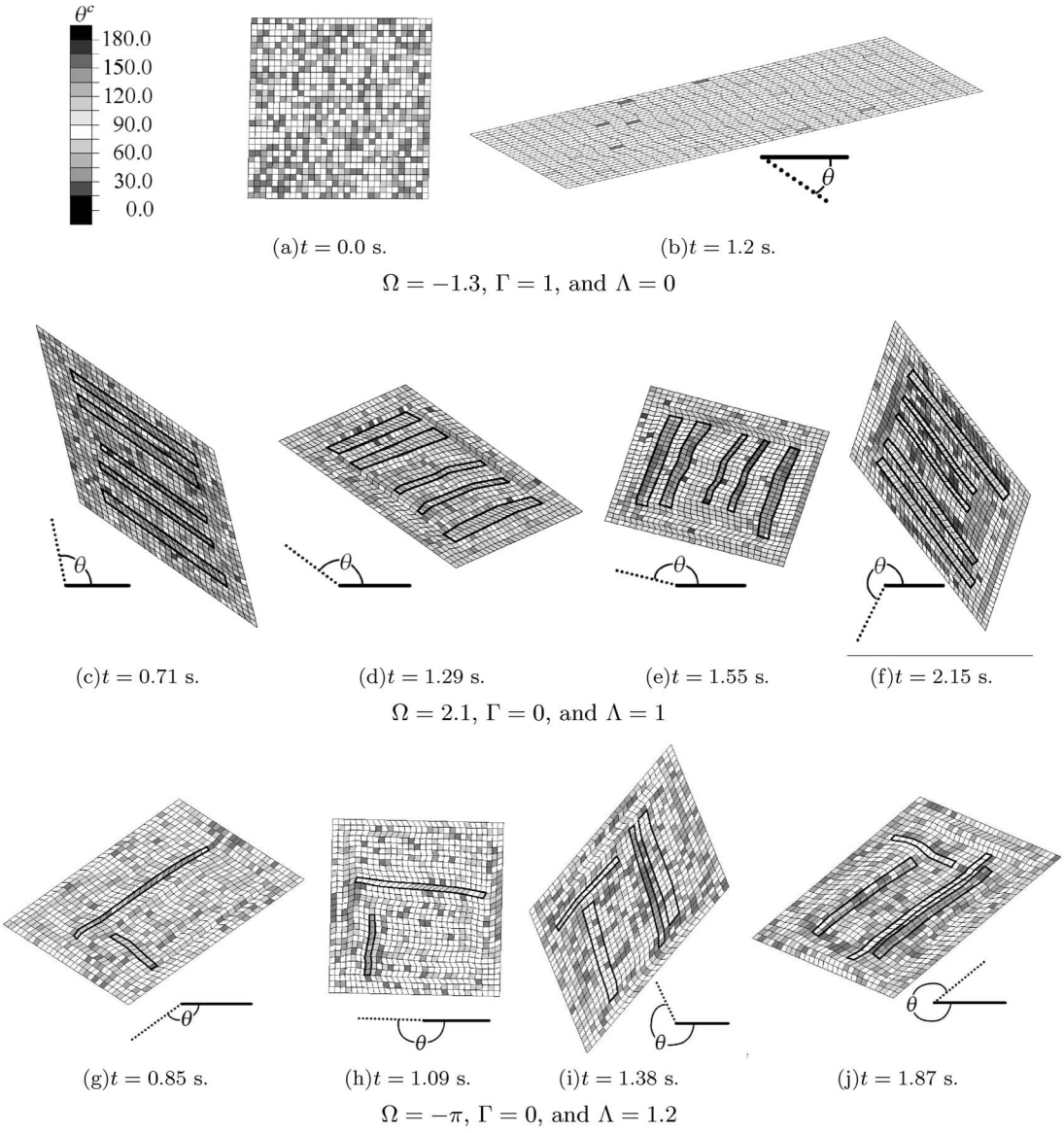

Fig. 4 The deformed mesh at the indicated times due to the indicated macrodeformation, where θ is the rigid-body rotation of the polycrstal at the time *t*. The shading of each element represents the orientation of the crystal in degrees as dictated by the legend. Elements of interest in the mesh are outlined in black.

tation of the crystal behavior, though it is also computationally expensive. In our analysis, a square polycrystal consisting of 900 crystals with a uniform initial texture distribution is deformed by a constant velocity gradient. It is modeled using 900 square elements on a 30×30 uniform grid, where each element represents one crystal. The representation of uniform crystal shape and size is unrealistic, but does provide a simplified view of the crystal behavior. The CPFEM analyses use the two slip systems described in Eq. (11) with $\beta = \pi/6$ in which the elastic constants and parameters for the crystal flow rule are taken from the Tantalum parameters presented in Bronkhorst et al. [22] with no hardening or adiabatic heating. As elastic strains are quite small, the incorporation of elasticity in these CPFEM computations does not significantly affect the texture evolution. The purely 2D planar polycrystal is numerically challenging, and therefore the CPFEM analyses are limited to lower strains than those in mean-field models.

The texture evolution predicted by the CPFEM is significantly different from that predicted by the FCM, as seen by comparing the order parameter trajectories, cf. Eq. (21), predicted by the two methods. When $\lambda \geq \eta$ (Fig. 3(*b*)), the CPFEM analysis predicts a texture that tends toward a single orientation but the crystals never completely align, i.e., $\psi \to \theta^p$ but $r \to c$, where $c < 1$, rather than $r \to 1$. When $\lambda < \eta$ (Figs. 3(*e*) and 3(*h*)), the CPFEM predicts a decaying texture oscillation. Therefore, the FCM predicts an overly sharp texture when $\lambda \geq \eta$, and a drastically different tumbling texture when $\lambda < \eta$.

The CPFEM analyses also allow us to observe the spatial distribution of the texture evolution in the polycrystal. When $\lambda \geq \eta$ (Figs. 4(*a*) and 4(*b*)), the crystals (elements) throughout the mesh evolve toward a single orientation. When $\lambda < \eta$, the mesh contains bands of crystals of similar crystallographic orientation that shear in a common direction, with bands having an alternating sense of shear. In the mesh shown in Figs. 4(*c*)–4(*f*) several of these bands are present, while in the mesh shown in Figs. 4(*g*)–4(*j*) the bands are just beginning to form (specific bands of crystals are outlined in black in the figures). It appears that decaying oscillation predicted by the CPFEM may result from transient oscillatory patterns where two groups of crystals, arranged in alternating bands, synchronize in antiphase.

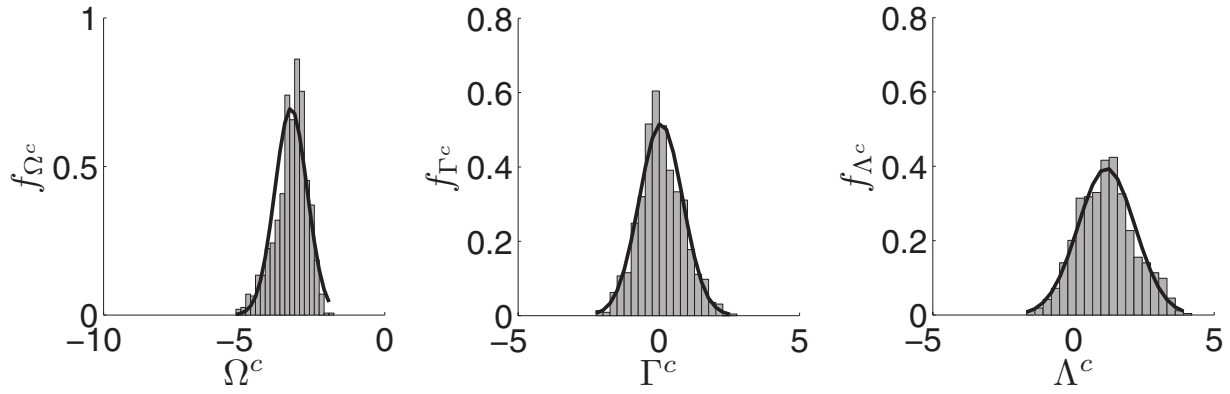

Fig. 5 f_{Λ^c}, f_{Γ^c}, and f_{Ω^c} from CPFEM with $\Omega=-\pi$, $\Gamma=0$, and $\Lambda=1.2$ at $t=2.2$ s. The bars are a histogram approximation of the PDF and the black line is a normal distribution with the measured μ and σ.

6 Stochastic Taylor Model

The CPFEM results show interesting aspects of the texture evolution. However, due to the complexity of the CPFEM, it is difficult to gain a more comprehensive view. A stochastic mean-field model provides a simple framework to describe the behavior and does not overconstrain the crystals as does the FCM. Rather than periodic oscillation, the CPFEM predicts decaying oscillation, such that the texture may approach a stable solution. The introduction of random variation into a system can lead to stability [23]; therefore, a stochastic approach adopted at the mesoscale may result in texture evolution consistent with the CPFEM results.

In Engler [24] and Ma et al. [17] CPFEM results drive the application of stochastic variations to obtain $\mathbf{L}^c$ from $\mathbf{L}$. Using the CPFEM to model 3D copper polycrystals, Sarma and Dawson [25] found that the components of the strain rate $\mathbf{D}^c$ behave as random variables following a normal distribution with mean value approximately equal to its macroscale counterpart, i.e., $\mu_{\mathbf{D}^c}=\mathbf{D}$. Furthermore, they found that stochastic behavior of the components uncorrelated and leveraged these results in a viscoplastic model with nonuniform deformation among component crystals [26]. Using this same information, Engler [24] and Ma et al. [17] modified mean-field models such that $\mathbf{D}^c$ experiences random variations in order to loosen the imposed constraints. Ma et al. [17] modified the FCM so that $\mathbf{D}^c$ follows a normal distribution with mean equal to $\mathbf{D}$ while the skew symmetric part $\mathbf{W}^c=\mathbf{W}$. This model, which we call the stochastic Taylor model (STM), gives more accurate predictions than the FCM; however, it is based on the results from a single CPFEM analysis.

For the planar polycrystal, our CPFEM results support the assumption that $\mathbf{D}^c$ follows a normal distribution with $\mu_{\mathbf{D}^c}=\mathbf{D}$ (see Fig. 5 for an example of the probability density functions f_{Λ^c} and f_{Γ^c} from CPFEM). In addition, the CPFEM results show that $\mathbf{W}^c$ follows a normal distribution (also see Fig. 5 for an example of f_{Ω^c}). Of the two parameters that define a normal distribution, the mean of $\mathbf{L}^c$ is constant but the standard deviation need not be. The CPFEM results show that the component standard deviations change with time, with σ_{Ω^c} and σ_{Γ^c} behaving in a somewhat similar manner (see Fig. 6).

The statistical description of the $\mathbf{L}^c$ taken from the CPFEM results provides guidance when applying the STM to the planar polycrystal. As discussed above, the CPFEM simulations show that both the skew and symmetric parts of $\mathbf{L}^c$ follow a normal

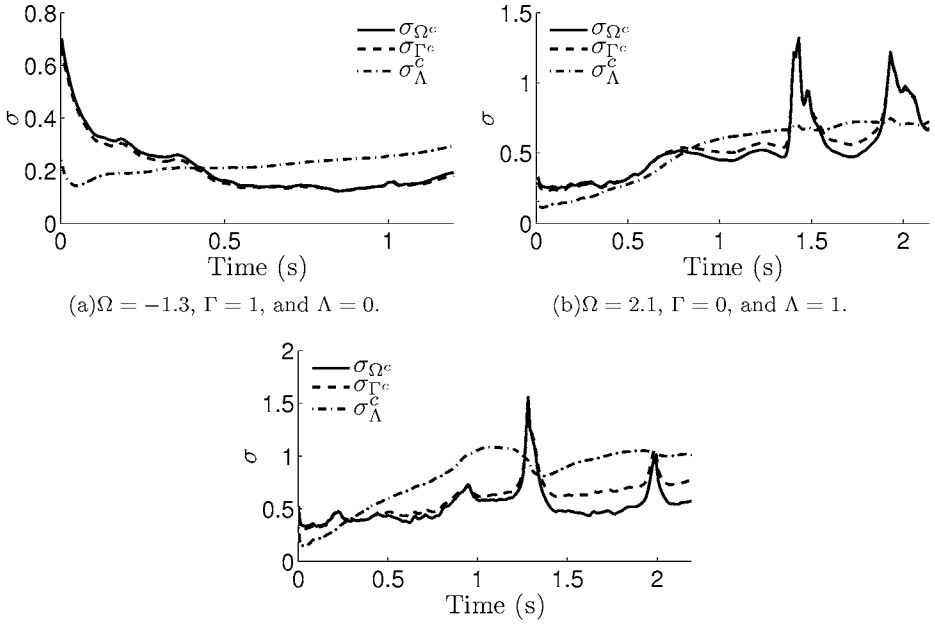

(a)$\Omega=-1.3$, $\Gamma=1$, and $\Lambda=0$.

(b)$\Omega=2.1$, $\Gamma=0$, and $\Lambda=1$.

(c)$\Omega=-\pi$, $\Gamma=0$, and $\Lambda=1.2$.

Fig. 6 The standard deviations of Ω^c, Λ^c, and Γ^c with time from CPFEM analyses

distribution, though we treat only the symmetric part as random to provide an objective statistical description. In addition, we simplify the analysis by treating the standard deviations as constant, though the CPFEM results show this assumption to be incorrect. Therefore, assuming no significant correlation, the probability density functions (PDFs) for the rate of stretching f_{Λ^c} and the rate of shearing f_{Γ^c} are assumed Gaussian, i.e.,

$$f_{\Gamma^c}(x) = \frac{e^{-(-\Gamma + x)^2/2\sigma^2}}{\sqrt{2\pi}\sigma}$$

$$f_{\Lambda^c}(y) = \frac{e^{-(-\Lambda + y)^2/2\sigma^2}}{\sqrt{2\pi}\sigma} \tag{26}$$

where the standard deviations $\sigma_{\Gamma^c} = \sigma_{\Lambda^c} = \sigma$ and Γ and Λ are obtained from $\mathbf{D}$. One limitation of this treatment is that the $\mathbf{L}^c$ are independent of the crystal orientations. STM analyses predict textures consistent with that obtained from the CPFEM analyses, as shown in Figs. 3(*c*), 3(*f*), and 3(*i*). The STM simulations, which can be performed for longer durations than the CPFEM simulations, result in the order parameter settling in a small neighborhood within the unit circle. This signifies a final texture that is either static or oscillatory with constant order parameter.

7 Orientation Distribution Function

Due to the simple nature of the FCM and the STM, expressions can be developed to describe the texture of the polycrystal at any time t. Equation (18) provides a means to find the orientation of an individual crystal; however, the texture of the entire polycrystal is characterized by the PDF of the crystal orientation, i.e., f_{Θ^c}, the orientation distribution function (ODF). Given the ODF of the undeformed polycrystal, $f_{\Theta_0^c}(\theta_0^c)$, the ODF of the deformed polycrystal is found from [27]

$$f_{\Theta^c}(\theta^c) = f_{\Theta_0^c}(\tilde{\theta}_0^c(\theta^c, \Gamma^c, \Lambda^c, \Omega^c))\left|\partial_{\theta^c}\tilde{\theta}^c{}_0(\theta^c, \Gamma^c, \Lambda^c, \Omega^c)\right| \tag{27}$$

In the above, $f_{\Theta_0^c}$ and $\mathbf{L}$ (defined by Γ, Λ, and Ω) are known; however, the $\mathbf{L}^c$ (defined by the Γ^c, Λ^c, and Ω^c) are unknown.

Using the FCM and a constant deformation, $\Gamma^c(t) = \Gamma$, $\Lambda^c(t) = \Lambda$, and $\Omega^c(t) = \Omega$, allows us to evaluate $\partial_{\theta^c}\tilde{\theta}_0^c(\theta^c, \Gamma^c, \Lambda^c, \Omega^c)$ from Eq. (19) to obtain

$$\partial_{\theta^c}\tilde{\theta}_0^c = \frac{\sec\theta^{c^2}/\cosh(t\mathcal{F} - \mathcal{W})^2}{\left(1 - \dfrac{(\lambda\Lambda + (\lambda\Gamma + \Omega)\tan\theta^c)^2}{\mathcal{F}^2}\right)\left(1 + \dfrac{(\lambda\Lambda + \mathcal{F}\tanh(t\mathcal{F} - \mathcal{W}))^2}{(\lambda\Gamma + \Omega)^2}\right)} \tag{28}$$

where

$$\mathcal{W} = \tanh^{-1}\left[\frac{1}{\mathcal{F}}(\lambda\Lambda + (\lambda\Gamma + \Omega)\tan\theta^c)\right] \tag{29}$$

For a uniform initial texture distribution, i.e., there is an equal chance of getting any orientation giving $f_{\Theta_0^c}(\theta_0^c) = 1/\pi$, the ODF becomes

$$f_{\Theta^c}(\theta^c) = \frac{\sec\theta^{c^2}/\cosh(t\mathcal{F} - \mathcal{W})^2}{\pi\left(1 - \dfrac{(\lambda\Lambda + (\lambda\Gamma + \Omega)\tan\theta^c)^2}{\mathcal{F}^2}\right)\left(1 + \dfrac{(\lambda\Lambda + \mathcal{F}\tanh(t\mathcal{F} - \mathcal{W}))^2}{(\lambda\Gamma + \Omega)^2}\right)} \tag{30}$$

Using the STM (again, for constant values of Γ, Λ, and Ω and a uniform initial texture), Eq. (18) is a function of three random variables, Γ^c, Λ^c, and θ_0^c, with known PDFs (cf. Eq. (26)) whose ODF is obtained from

$$f_{\Theta^c}(\theta^c) = \int_{-\infty}^{\infty}\int_{-\infty}^{\infty} f_{\Theta_0^c}(\tilde{\theta}_0^c(\theta^c, x, y, \Omega^c))f_{\Gamma^c}(x)f_{\Lambda^c}(y) \times \left|\partial_{\theta^c}\tilde{\theta}_0^c(\theta^c, x, y, \Omega^c)\right|dxdy \tag{31}$$

This integral is numerically evaluated, where the limits $\pm\infty$ are replaced with $\pm 10\sigma$ with $\sigma = \sigma_{\Lambda^c}, \sigma_{\Gamma^c}$, respectively.

8 STM Analysis and Discussion

The STM predicts texture evolution that more closely resembles that obtained from the CPFEM than that predicted by the FCM. As with the FCM, the behavior predicted by the STM resembles that given by the Kuramoto model. However, now the steady and oscillatory behavior is determined by the relationship between λ and $\eta^c = |\Omega^c|/\sqrt{\Gamma^{c2} + \Lambda^{c2}}$. A function of random variables, η^c has a PDF

$$f_{\eta^c}(\eta^c) = \int_{-\infty}^{\infty} f_{\Gamma^c}(\overbrace{\sqrt{\Omega^{c^2}/\eta^{c} - x^2}}^{\Gamma^c})f_{\Lambda^c}(x)\left|\partial_{\eta^c}\tilde{\Gamma}^c(\eta^c, x, \Omega^c)\right|dx \tag{32}$$

where, following the derivation of Eq. (31), we "invert" Eq. (25) to obtain an expression for Γ^c. The relationship between λ and η^c varies in each crystal, such that the behavior of the polycrystal depends on the probability that $\lambda > \eta^c$, i.e., $P(\lambda > \eta^c)$. When $P(\lambda > \eta^c)$ is high, the crystal structure dominates and the texture evolves toward a single orientation (Fig. 3(*c*)). On the other hand, when $P(\lambda > \eta^c)$ is low, the load dominates and a tumblinglike behavior is exhibited (Fig. 3(*i*)). In all other cases, an intermediate behavior is observed (Fig. 3(*f*)).

Different values of σ lead to different PDF f_{η^c} behavior and thus different values of $P(\lambda > \eta^c)$, as seen in Fig. 7. With increasing values of σ, the standard deviation of η^c, σ_{η^c}, increases and hence, more intermediate behavior is observed. Consequently, the same $\mathbf{L}$ significantly produces different ODF histories depending on the standard deviations.

An interesting aspect of the texture evolution behavior exhibited by the STM and CPFEM is that the texture evolves toward a steady ODF for any load. To understand this apparently steady texture distribution, we use the STM to model the behavior of the order parameter r over time and the shape of the steady-state ODF. The time it takes for r to reach a constant value (Fig. 8) depends on the applied load $\mathbf{L}$, through η, and on the standard deviations $\sigma = \sigma_{\Gamma^c} = \sigma_{\Lambda^c}$, i.e., increasing η/λ increases the time while increasing σ decreases the time. The shape of the steady-state ODF (Fig. 9) also depends on η and σ. As σ and η/λ increase, the standard deviation of the orientation σ_{Θ^c} increases, though the sensitivity of σ_{Θ^c} to σ decreases with increasing η/λ.

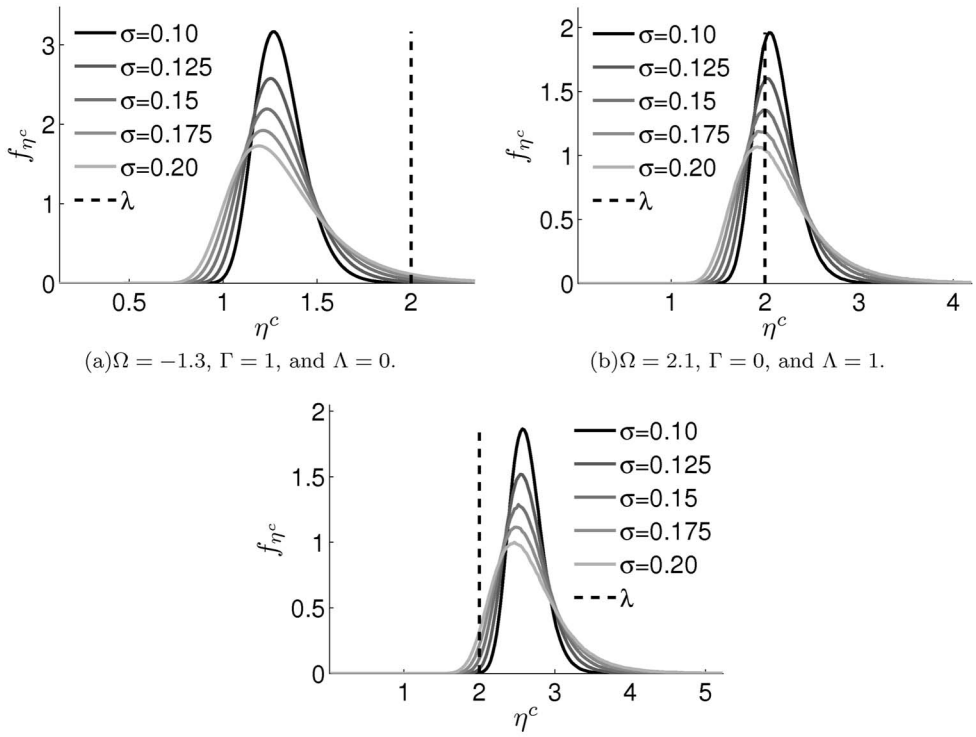

(a)$\Omega = -1.3$, $\Gamma = 1$, and $\Lambda = 0$.

(b)$\Omega = 2.1$, $\Gamma = 0$, and $\Lambda = 1$.

(c)$\Omega = -\pi$, $\Gamma = 0$, and $\Lambda = 1.2$.

Fig. 7 Relationship between the PDF of η^c and λ for several standard deviations $\sigma = \sigma_{\Gamma^c} = \sigma_{\Lambda^c}$

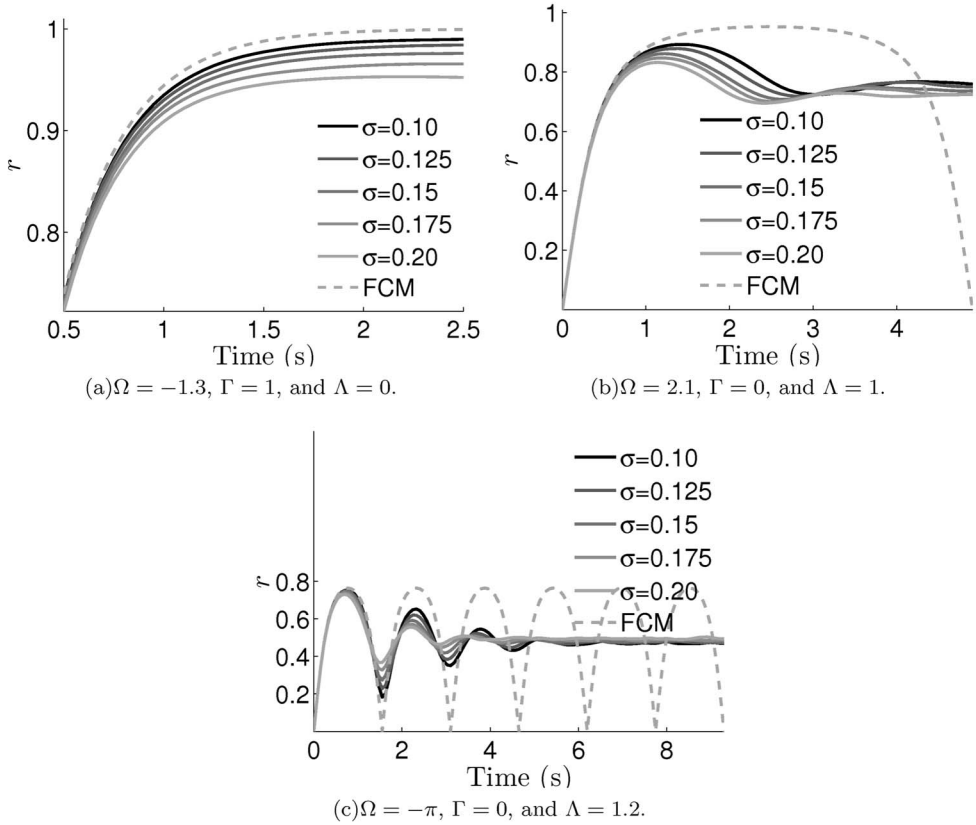

(a)$\Omega = -1.3$, $\Gamma = 1$, and $\Lambda = 0$.

(b)$\Omega = 2.1$, $\Gamma = 0$, and $\Lambda = 1$.

(c)$\Omega = -\pi$, $\Gamma = 0$, and $\Lambda = 1.2$.

Fig. 8 *r* versus time at several standard deviations $\sigma = \sigma_{\Gamma^c} = \sigma_{\Lambda^c}$

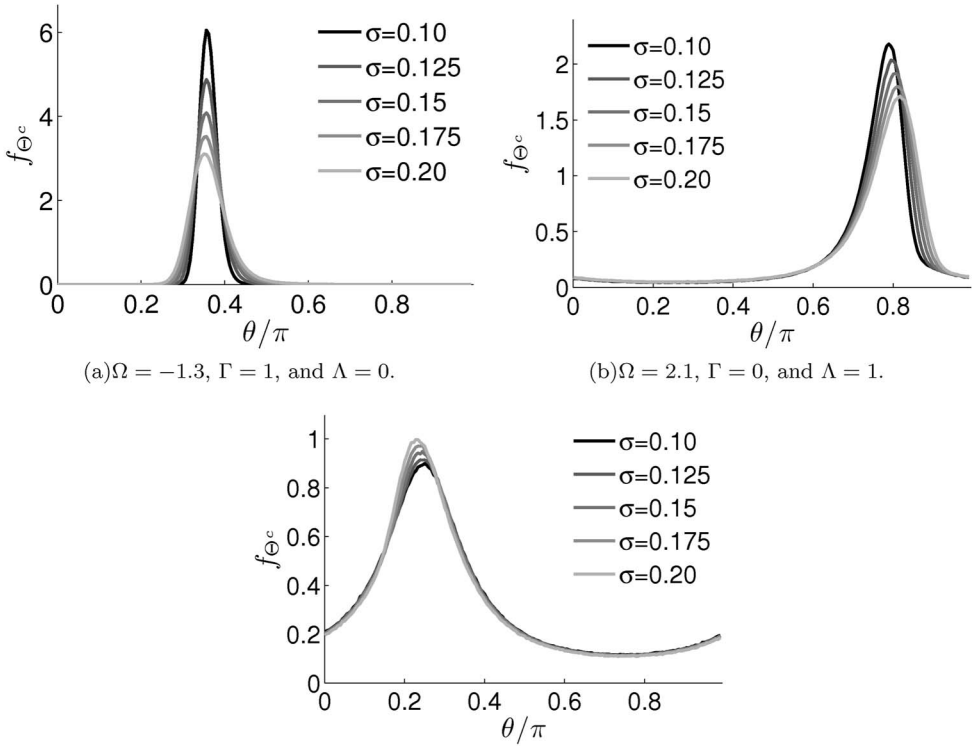

(a)$\Omega = -1.3$, $\Gamma = 1$, and $\Lambda = 0$.

(b)$\Omega = 2.1$, $\Gamma = 0$, and $\Lambda = 1$.

(c)$\Omega = -\pi$, $\Gamma = 0$, and $\Lambda = 1.2$.

Fig. 9 Steady-state ODF at several standard deviations $\sigma = \sigma_{\Gamma^c} = \sigma_{\Lambda^c}$

The CPFEM and STM predictions of the texture evolution in planar polycrystals with two slip systems are similar but distinct from the findings of Prantil et al. [9]. Whether the texture initially begins to oscillate or evolve toward preferred orientations, the ODF will eventually reach a steady-state value. The time required to reach the steady-state ODF depends on the magnitude of the imposed shear and the structure of the crystal slip systems. Once the ODF stops evolving, the crystals may still reorient in a manner such that the overall distribution does not change. Due to the similarities in the findings of Prantil et al.[9] to those of Kumar and Dawson [10] and to Kumar [11], we assume that similar behavior would occur in planar polcyrystals with more than two slip systems and 3-D polycrystals, though further research is warranted.

The STM proved to be a valuable tool in analyzing the texture evolution of the planar polycrystal. By introducing stochastic variation into the crystal strain rates, behavior similar to that shown by the CPFEM was predicted, yet the model was simple enough to allow explicit expressions to be developed to describe the texture behavior. The STM could prove to be a valuable method for mean-field polycrystal plasticity, though care must be taken to identify representative standard deviations.

9 Conclusions

The planar polycrystal plasticity treatment from Prantil et al. [9] establishes a simplified framework for observing polycrystal texture evolution, revealing that the planar texture evolution equation is similar to the Kuramoto model of a system of coupled oscillators. By simulating the texture evolution of the planar polycrystal using the CPFEM and the STM, we find that the polycrystals reach a steady-state ODF not predicted by the FCM. In the CPFEM, the steady-state ODF seems to be due to the formation of alternating bands of crystals with orientations synchronized in antiphase. The question as to whether similar behavior would result from applying the CPFEM to planar polycrystals with more slip systems and to 3-D polycrystals is a topic that warrants further study. Additionally, the STM appears to be a useful homogenization method, resulting in increased accuracy over the FCM when using representative standard deviations.

Acknowledgment

This work was supported in part by EPSRC Grant Nos. GR/R72020/01 and EP/D063906/1.

References

[1] Van Houtte, P., and Van Bael, A., 2005, "Multi-Level Versus Heirarchical Modeling of the Plastic Deformation of Polycrystalline Materials Implementation in Fe Codes," *Proceedings of the International Symposium on Plasticity*.
[2] Taylor, G. I., 1938, "Plastic Strain in Metals," J. Inst. Metals, **62**, pp. 307–324.
[3] Harren, S. V., and Asaro, R. J., 1989, "Nonuniform Deformations in Polycrystals and Aspects of the Validity of the Taylor Model," J. Mech. Phys. Solids, **37**(2), pp. 191–232.
[4] Kalidindi, S. R., Bronkhorst, C. A., and Anand, L., 1992, "Crystallographic Texture Evolution During Bulk Deformation Processing of fcc Metals," J. Mech. Phys. Solids, **40**, pp. 537–569.
[5] Honneff, H., and Mecking, H., 1982, "Analysis of the Deformation Texture at Different Rolling Conditions," *Proceedings of ICOTOM 6*, Vol. 1, pp. 347–355.
[6] Kocks, U. F., and Chandra, H., 1982, "Slip Geometry in Partially Constrained Deformation," Acta Metall., **30**, pp. 695–709.
[7] Van Houtte, P., 1982, "On the Equivalence of the Relaxed Taylor Theory and the Bishop-Hill Theory for Partially Constrained Plastic Deformation of Crystals," Mater. Sci. Eng., **55**, pp. 69–77.
[8] Lebensohn, R. A., and Tomé, C. N., 1993, "A Self-Consistent Anisotropic Approach for the Simulation of Plastic Deformation and Texture Development of Polycrystals: Application to Zirconium Alloys," Acta Metall. Mater., **41**, pp. 2611–2624.
[9] Prantil, V. C., Jenkins, J. T., and Dawson, P. R., 1993, "An Analysis of Texture and Plastic Spin for Planar Polycrystals," J. Mech. Phys. Solids, **41**(8), pp. 1357–1382.
[10] Kumar, A., and Dawson, P. R., 1996, "The Simulation of Texture Evolution with Finite Elements Over Orientation Space II. Application to Planar Crystals," Comput. Methods Appl. Mech. Eng., **130**, pp. 247–261.
[11] Kumar, A., 1996, "Polycrystal Modeling With Finite Elements Over Orientation Space," Ph.D. thesis, Cornell University.
[12] Asaro, R. J., and Needleman, A., 1985, "Texture Development and Strain

Hardening in Rate Dependent Polycrystals," Acta Metall., **33**, pp. 923–953.
[13] Mathur, K. K., and Dawson, P. R., 1989, "On Modeling the Development of Crystallographic Texture in Bulk Forming Processes," Int. J. Plast., **5**(1), pp. 67–94.
[14] Becker, R., 1991, "Analysis of Texture Evolution in Channel Die Compression–I. Effects of Grain Interaction," Acta Metall. Mater., **39**(6), pp. 1211–30.
[15] Kalidindi, S. R., Bronkhorst, C. A., and Anand, L., 1994, "On the Accuracy of the Taylor Assumption in Polycrystalline Plasticity," *Anisotropy and Localization of Plastic Deformation*, Elsevier, New York, pp. 139–142.
[16] Beaudoin, A. J., Mathur, K. K., Dawson, P. R., and Johnson, G. C., 1993, "Three-Dimensional Deformation Process Simulation With Explicit Use of Polycrystal Plasticity Models," Int. J. Plast., **9**(7), pp. 833–860.
[17] Ma, A., Roters, F., and Raabe, D., 2004, "Numerical Study of Textures and Lankford Values for fcc Polycrystals by Use of a Modified Taylor Model," Comput. Mater. Sci., **29**, pp. 353–361.
[18] Arwade, S. R., and Grigoriu, M., 2003, "Evolution of Crystallographic Orientations in Crystals Subject to Random and Deterministic Deformation," Probab. Eng. Mech., **18**, pp. 289–299.
[19] Kok, S., Beaudoin, A. J., and Tortorelli, D. A., 2002, "A Polycrystal Plasticity Model Based on the Mechanical Threshold," Int. J. Plast., **18**, pp. 715–741.
[20] Kuramoto, Y., 1984, *Chemical Oscillations, Waves, and Turbulence*, Springer, Berlin.
[21] Strogatz, S. H., 2000, "From Kuramoto to Crawford. Exploring the Onset of Synchronization in Populations of Coupled Oscillators," Physica D, **143**(1–4), pp. 1–20.
[22] Bronkhorst, C. A., Hansen, B. L., Cerreta, E. K., and Bingert, J. F., 2007, "Modeling the Microstructural Evolution of Metallic Polycrystalline Materials Under Localization Conditions," J. Mech. Phys. Solids, **55**(11), pp. 2351–2383.
[23] Mackey, M. C., Longtin, A., and Lasota, A., 1990, "Noise-Induced Global Asymptotic Stability," J. Stat. Phys., **60**(5/6), pp. 735–751.
[24] Engler, O., 2002, "A New Approach to More Realistic Rolling Texture Simulation," Adv. Eng. Mater., **4**(4), pp. 181–186.
[25] Sarma, G. B., and Dawson, P. R., 1996, "Effects of Interactions Among Crystals on the Inhomogeneous Deformations of Polycrystals," Acta Mater., **44**(5), pp. 1937–1953.
[26] Sarma, G. B., and Dawson, P. R., 1996, "Texture Predictions Using a Polycrystal Plasticity Model Incorporating Neighbor Interactions," Int. J. Plast., **12**(8), pp. 1023–1054.
[27] Rao, S. S., *Reliability-Based Design*, McGraw-Hill, New York, Chap. 5, pp. 115–138.

The Buckling of a Swollen Thin Gel Layer Bound to a Compliant Substrate

Eric Sultan
Institüt-Lorentz,
P.O. Box 9506,
2300 RA Leiden, The Netherlands

Arezki Boudaoud
Laboratoire de Physique Statistique,
UMR8550 du CNRS/ENS/Paris VI/Paris VII,
24 Rue Lhomond,
75231 Paris Cedex 05, France

Gels are used to design bilayered structures with high residual stresses. The swelling of a thin layer on a compliant substrate leads to compressive stresses. The postbuckling of this layer is investigated experimentally; the wavelengths and amplitudes of the resulting modes are measured. A simplified model with a self-avoiding rod on a Winkler foundation is in semiquantitative agreement with experiments and reproduces the observed cusplike folds. [DOI: 10.1115/1.2936922]

1 Introduction

The buckling of multilayered structures is a strong limitation in the design of sandwich panels [1]. This field has been renewed by experiments aiming at the micropatterning of surfaces through the buckling of thin films bound to compliant substrates (see, e.g., Ref. [2] for a review). For metal films vapor deposited on an elastomer [3], compressive residual stresses are generated in the film when the system is cooled, due to the mismatch in thermal expansion coefficients between the metal and the elastomer, leading to the wrinkling of the film. When the surface of elastomers is stiffened, the wrinkles may be hierarchical [4]. Recent theoretical efforts addressed nonlinear postbuckling and herringbone patterns in metal-capped elastomers [5–7]. Residual stresses are also generated in living tissues when growth occurs inhomogeneously in space [8]. Subsequent instabilities can be investigated within the framework of finite elasticity [9]. In fact, the buckling of multilayered structures was used to explain convolutions in brain development [10,11], the organization of seeds on a flower [12], or fingerprint formation [13].

Our aim is to address experimentally the postbuckling of a thin film on a compliant substrate in the case of strong residual stresses. As thermal expansion induces only small strains, we were led to use polymeric aqueous gels. They are made of a polymeric network immersed in water; they can absorb more water and swell by a length ratio of up to 10 [14]; their rate of swelling and elastic moduli can be controlled independently by tuning the chemical composition. Two main geometries were investigated experimentally in previous work (see, e.g., Ref. [15] for a review). The swelling of a gel layer bonded to a rigid substrate results in a cusped oscillating surface with a wavelength proportional to the thickness of the layer [16,17]. The swelling of a gel plate bonded at the edge to a stiff gel results in buckling with a wavelength proportional to the width of the plate [18], mimicking the wrinkling of the edge of leaves [19–21].

Here, we are concerned with a two-layered gel with a stiff swelling layer (elastic modulus E_{top}, thickness h) on top of a soft nonswelling thick substrate (modulus E_{subs}). The buckling of such a gel system was investigated theoretically in Ref. [22]. The amount of swelling determines the residual stress σ and the buckling stress σ_c and wavelength λ_c are given by the classical formulas [1],

$$\frac{\sigma_c}{E_{\text{top}}} = \frac{1}{3^{1/3}}\left(\frac{E_{\text{subs}}}{E_{\text{top}}}\right)^{2/3} \tag{1}$$

$$\frac{\lambda_c}{h} = \frac{2\pi}{3^{1/3}}\left(\frac{E_{\text{top}}}{E_{\text{subs}}}\right)^{1/3} \tag{2}$$

with a Poisson ratio $\nu = 1/2$ as gels are in general incompressible. Above threshold, the amplitude A of oscillation of the postbuckled state should be a function of the residual stress σ [5],

$$\frac{A}{h} = \sqrt{\frac{\sigma}{\sigma_c} - 1} \tag{3}$$

In the present study, we investigate experimentally postbuckled states in the case of strong residual stresses. Incidentally, the cusped oscillating shapes obtained are reminiscent of brain convolutions [10]. The article is organized as follows. We describe our experimental setup and a simplified model with a compressed self-avoiding rod bound to an elastic foundation. Then we compare and discuss the experimental and numerical results.

2 Experiments

The principle of the experiments is to first prepare the substrate layer and then pour the solution for the thin top layer. We made our gels as in Refs. [14,16–18]. A mixture of acrylamide (AA) and N,N'-methylenebisacrylamide (BISAA) is dissolved with sodium acrylate (SA) in distilled water. The polymerization is initiated by ammonium persulfate (PA) and is catalyzed with N,N,N',N'-tetramethylenediamine (TEMED) (0.3% in volume). The composition of the gels is given in Table 1. Once the mixture is completed, gelation (polymerization and solidification of the solution) occurs in a few seconds at room temperature. In order to obtain uniform layers—especially for thin layers—the solutions were cooled to slow gelation and allow the liquid to spread completely on the substrate.

The characteristics of the gel can be tuned by varying the concentrations of the components. The more concentrated (and, for a same concentration, the more concentrated in BISAA) the solution, the stiffer the gel. Likewise, the swelling ratio (the ratio between a free gel dimensions before and after swelling) can be increased by adding SA. For the purpose of the experiment, we prepared two distinct types of gel: (S) a soft and nonswelling gel; (T) a stiff and swelling gel. The swelling ratio was found by measuring the dimensions of a sample before and after swelling, while the elastic modulus was measured by hanging weights to gel samples (values in Table 1). In order to obtain a compliant substrate, we chose the highest ratio between the elastic moduli allowed by the experiment.

In preliminary experiments, we prepared a thick (3 cm) substrate made of the soft gel (S) in a Petri dish; a 1 mm thick layer of the second solution (T) was poured above. After gelation, the two layers were chemically bound to each other by the same chemical bounds as in the bulk of the gels: No delamination was

Contributed by the Applied Mechanics Division of ASME for publication in the JOURNAL OF APPLIED MECHANICS. Manuscript received January 25, 2007; final manuscript received June 12, 2007; published online July 2, 2008. Review conducted by Zhigang Suo.

Table 1 Composition and properties of the gels mainly used in the experiments. Concentrations are given in mmol L^{-1}. The swelling ratio corresponds to the length dilation factor of a gel piece after swelling, when it is free (3D) or constrained in plane strain (2D). *E* is the elastic modulus of the gel (after swelling).

	S (substrate)	T (top layer)
[AA+BISAA]	720	1202
BISAA:AA ratio	1:37.5	1:19
[SA]	0	229
Swelling ratio (3D)	1.06	1.5
Swelling ratio (2D)	1.09	1.8
E (Pa)	5.0×10^3	1.7×10^4
Poisson ratio	1/2	1/2

observed when cutting through the samples. After the preparation, water was added in the dish. It was slowly absorbed by the top layer, which started to wrinkle. The wrinkle evolution was slow and a stationary state was reached after half an hour to 1 h. A corresponding top view is shown in Fig. 1. The pattern looks like a superposition of sinusoidal modes with random directions and a wavelength of about 1 cm. The thickest (1 cm) top layers that we used would not reach a stationary state before 2–4 days. This is consistent with the fact that absorption of water by the gel is a diffusive process [14], so that the equilibration time is proportional to the square of the thickness.

In order to monitor easily the displacements of the top layer and get a better experimental control, we designed a setup to constrain plain strain. The cell was made with two glass plates with a 1 mm gap. Rubber stripes were used as spacers and delimited the bottom and sides of the cell. The glass plates were held together by clamps. The gel bilayer was prepared in the cell according to the geometry depicted in Fig. 2: a hard swelling top (T) with a thickness in the 1–6 mm range and a soft substrate (S) with a thickness of about 2.5 cm.

Absorption of water by the upper gel layer initialized swelling. In the early stages of the experiments, we observed the appearance of fold structures (usually in the center of the cell) separated by a few millimeters; the amplitude and the wavelength increase with time. Intially, only the upper part of the top layer is deformed; the deformation penetrates the top layer gradually (see Fig. 3). This is associated with the diffusion of water across the gel. Eventually, once water has penetrated across the entire gel layer, the system reaches an equilibrium state for which patterns have well-defined wavelengths and amplitudes of the order of a few millimeters (Fig. 4). The patterns seem slightly disordered but

Fig. 1 Top view after swelling of the top layer (thickness *h* =1 mm above a 3 cm thick substrate) in a dish of 10 cm diameter. The valleys are lighter than the crests. The lighting is not uniform as a dark strip was placed below to increase the contrast.

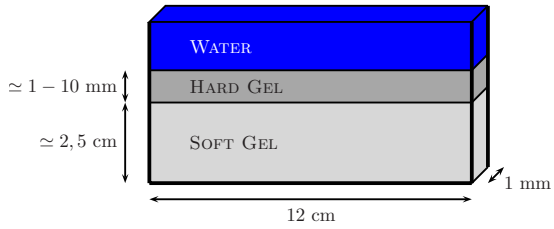

Fig. 2 Typical geometry and dimensions of the main experimental setup. Plane displacements are constrained by enclosing the whole between two glass plates with a gap of 1 mm.

this can be ascribed to the mascroscopic nature of the experiments, which makes imperfections more visible. In contrast to Ref. [4], no secondary wavelengths were observed. The surface of the gel oscillates with cusps (Fig. 4). In order to check whether the gel was damaged at these cusps, we opened the cell by taking out one glass plate (Fig. 5); it turns out that no failure occurs at the surface of the top layer.

3 Model

In order to interpret the experimental results, we generalize here the classical model of plate/rod on a Winkler foundation, remaining in the framework of linear elasticity. In the following, we will formulate the model for a rod and count the elastic energies per unit of gap of the cell, because the strains are constrained to be plane in the experiment. As we are interested in the postbuckling regime, we assume the rod to be inextensible. Indeed, for large displacements of the film, the energetical cost of stretching becomes large compared to the cost of bending [23]; therefore, stretching is avoided and the film may be assumed inextensible. Two important experimental features should be taken into account. First, there is an asymmetry between the two surfaces of the top layer. Second, cusps involve self-contact of the upper surface. As a consequence, we study a self-avoiding inextensible rod on a Winkler foundation linked to the lower surface of the rod.

More precisely, we consider an elastic rod with neutral line $\mathbf{r}(s)=x(s)\mathbf{e}_x+z(s)\mathbf{e}_z$ parametrized by the arclength $s\in(0,L)$ (Fig. 6). We define the tangential and normal unit vectors by $\mathbf{t}(s)=\mathbf{r}'(s)$, $\mathbf{n}(s)=\mathbf{t}'(s)/\|\mathbf{t}'(s)\|$ and the curvature by $\kappa(s)=\mathbf{n}(s)\cdot\mathbf{t}'(s)$. In order to take into account the finite thickness h of the gel layer, we construct its lower and upper surfaces by defining $\mathbf{r}^{\mp}(s)=\mathbf{r}(s)\mp(h/2)\mathbf{n}(s)$.

We take as a reference configuration a free rod of length L and thickness h (corresponding to the state after swelling). Then we match it to a Winkler foundation of length L_0, such that $L/L_0>1$ is the swelling ratio. To each configuration $\mathbf{r}(s)$, we associate the elastic energy

$$\mathcal{E}[\{\mathbf{r}\}]=\frac{1}{2}D\int_0^L\kappa(s)^2ds+\frac{1}{2}k\int_0^L\left(\mathbf{r}^-(s)-s\frac{L_0}{L}\mathbf{e}_x\right)^2ds-\sigma_r h(\mathbf{r}(L)-\mathbf{r}(0)-L_0\mathbf{e}_x)\cdot\mathbf{e}_x+\mathcal{H}[\mathbf{r}^+] \quad (4)$$

The first term is the bending energy with a bending stiffness $D=E_{\text{top}}h^3/9$, assuming an incompressible material. The second is the energy of the Winkler foundation where x and y displacements of the lower surface of the rod are taken into account, corresponding to the shearing and to the compression of the foundation, respectively. The reference state $\mathbf{r}^-(s)$ of the foundation has a length L_0, so that $\mathbf{r}^-(s)|_{\text{ref}}=sL_0/L\mathbf{e}_x$; the stiffness of the foundation is given by $k=4\pi/3E_{\text{subs}}/\lambda$ to be equivalent to an elastic half-space of Young's modulus E_{subs} deformed with a wavelength λ; note that in the experiment, the thickness of the substrate is larger than the observed wavelengths so that it is legitimate to consider the substrate as half-infinite. In the numerics, k was fixed and E_{subs} deduced from the value of λ. The third term contains the

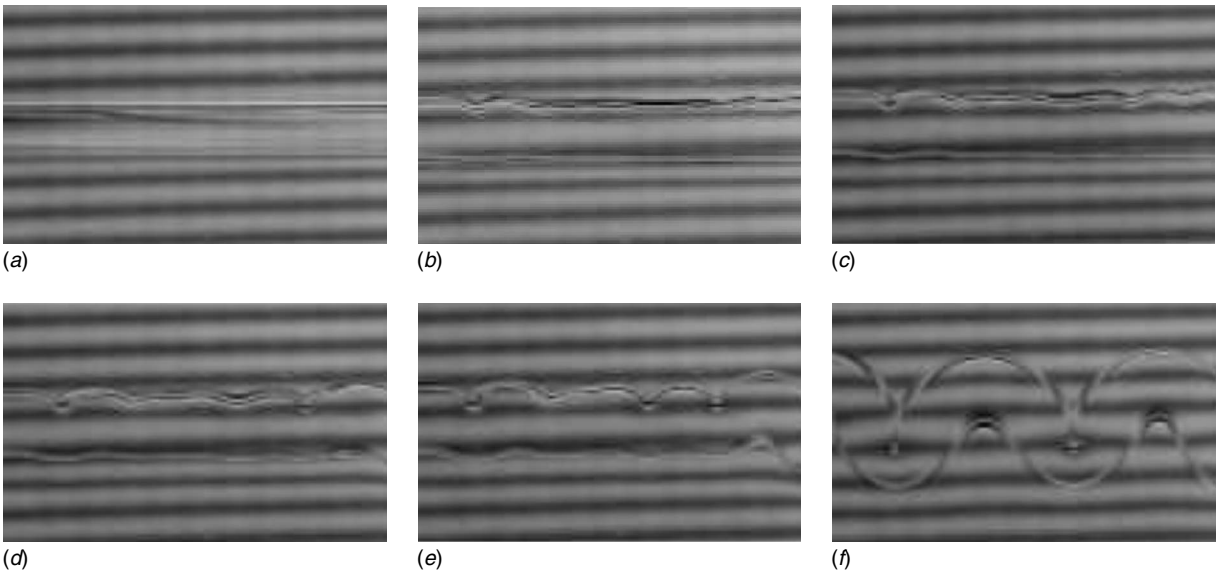

Fig. 3 The swelling process. Partial side views of the gel top layer (intial thickness 4 mm) taken at intervals of 3 h. A screen with horizontal dark lines was placed at the back to increase the contrast.

compressive stress σ_r, taken as a Lagrange multiplier, needed to achieve the projected length L_0 on the $\mathbf{e}_x$ direction. The fourth and last term is a purely geometric contribution introduced to forbid self-crossing of the upper interface. More precisely, $\mathcal{H}[\{\mathbf{r}^+\}] = +\infty$ if $\mathbf{r}^+(s) = \mathbf{r}^+(s')$ has at least one solution other then $s = s'$ and $\mathcal{H}[\{\mathbf{r}^+\}] = 0$ otherwise.

We performed the study of this rodlike model through the numerical minimization of energy (4). The rod was discretized in N parts (100–500 in practice), each of length L/N, by defining coordinates $\mathbf{r}_i = x_i\mathbf{e}_x + z_i\mathbf{e}_z$ with $x_i = (L/N)\Sigma_{j=1}^{i}\cos\theta_j$ and $z_i = (L/N)\Sigma_{j=1}^{i}\sin\theta_j$ $(i = 1, \ldots, N+1)$. Introducing the tangent $\mathbf{t}_i$ and normal $\mathbf{n}_i$ vectors to segment $(\mathbf{r}_i, \mathbf{r}_{i+1})$, the lower and upper interfaces were reconstructed by $\mathbf{r}_i^{\pm} = \frac{1}{2}(\mathbf{r}_i + \mathbf{r}_{i+1} \mp h\mathbf{n}_i)$. The energy is then a function of the θ_i. Powell's algorithm of minimization [24] allowed it to cope with the discontinuous behavior of $\mathcal{H}[\{\mathbf{r}^+\}]$. The starting configuration for the minimization was a flat rod with a small noise (of unimportant amplitude). We used either simply supported or clamped boundary conditions, which had no consequence on the results given below. Examples of minimal energy configurations are shown in Fig. 7 with values of the parameters in the experimental range. It can be seen that two experimental features are reproduced: large amplitude oscillations and self-contacting upper surface. A more quantitative comparison with the experiments is the subject of the next section, whereas the limitations of the model are discussed in the Conclusion.

Fig. 4 Side view of the gel top layer (colored with ink) after swelling. Thickness $h = 3$ mm (after swelling), wavelength $\lambda = 8.9$ mm, and amplitude $A = 5.1$ mm.

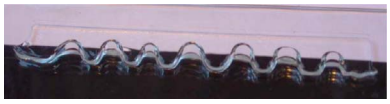

Fig. 5 View of the gel after taking out one glass plate showing that the cusps did not damage the gel. The swollen layer is oscillating out of plane due to the strong compressive residual stress.

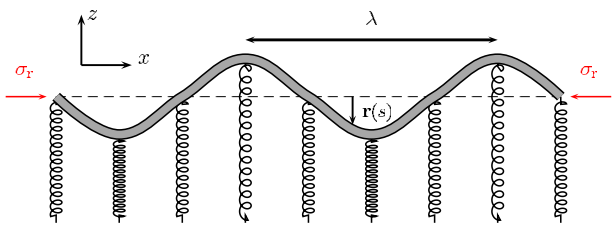

Fig. 6 Geometry of the model

4 Results

Before discussing the observations on wavelengths and amplitudes, let us estimate the residual stress induced by swelling and compare it to the buckling threshold. The swelling ratio roughly gives the residual strain $\epsilon \simeq 0.8$, which induces a residual stress $\sigma = 2/3 E_{\text{top}}\epsilon$ assuming plane strain and incompressibility of the

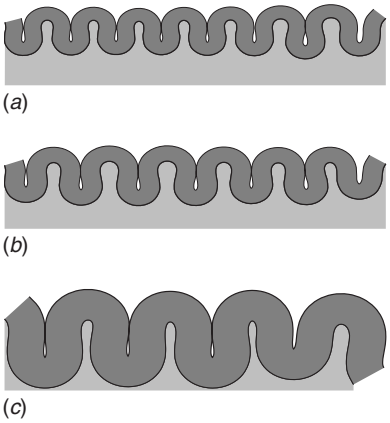

Fig. 7 Numerical equilibrium configurations for three values of the thickness h (*a*) 1.7 mm, (*b*) 2 mm, and (*c*) 4 mm. The swelling ratio of the top layer is 1.8. Its Young's modulus is $E_{\text{top}} = 4.6\ 10^4$ Pa and Young's modulus of the substrate E_{subs} is (*a*) 292 Pa, (*b*) 375 Pa, and (*c*) 585 Pas, respectively.

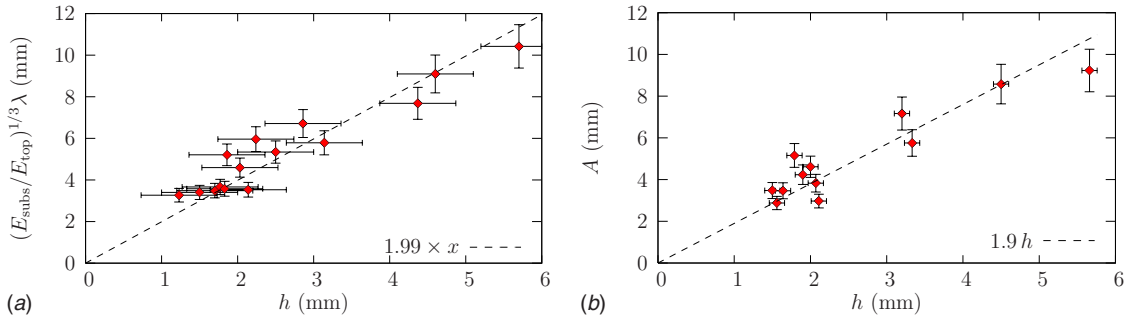

Fig. 8 Experiments: Wavelength (*a*) and amplitude (*b*) of the gel oscillations as a function of the top layer thickness. The wavelength λ was rescaled by the dimensionless coefficient $(E_{subs}/E_{top})^{1/3} \simeq 0.67$. Horizontal errorbars correspond to the (≃1 mm) measure error on the thickness *h*; vertical bars correspond to (typically 10%) fluctuations on the distance between two adjacent folds and their amplitudes.

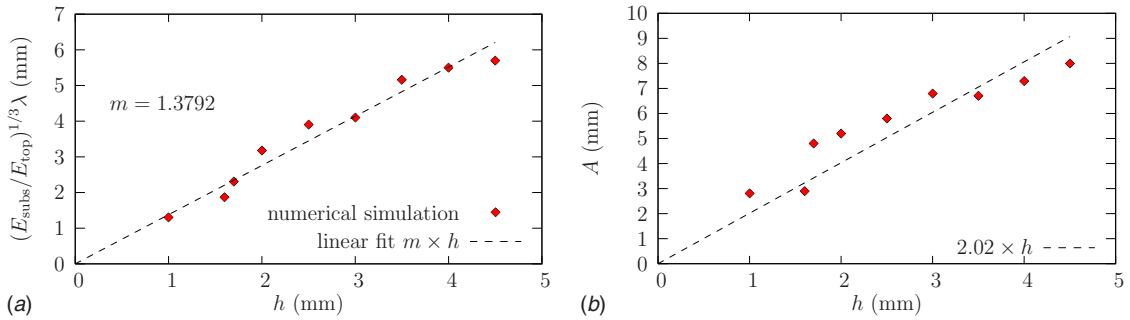

Fig. 9 Numerics: Wavelength (*a*) and amplitude (*b*) of the gel oscillations as a function of the top layer thickness. The wavelength λ was rescaled by the dimensionless coefficient $(E_{top}/E_{subs})^{1/3}$.

material. The ratio of this stress to the threshold is $\sigma/\sigma_c = 2(E_{top}/3E_{subs})^{2/3}\epsilon \simeq 2.2$, so that we expect buckling.

At constant mechanical properties (same E_{top} and E_{subs}), we measured the equilibrium wavelengths and amplitudes of oscillation. The thicknesses of the upper gel layer was in the range of 1–6 mm leading to wavelengths from 6 mm to 20 mm and amplitudes from 4 mm to 11 mm (Fig. 8). The data can be fitted by a linear dependance. We find $\lambda \simeq 2(E_{top}/E_{subs})^{1/3}h$, which is clearly below the classical value $\lambda = 4.4(E_{top}/E_{subs})^{1/3}h$ [Eq. (2)]. This last value should also hold above threshold in the small slope regime [5]. Similarly, we find $A \simeq 1.9h$ which is above the value $A = 1.1h$, given by Eq. (3).

We also modified Young's modulus of the gels as allowed by the chemical composition. Decreasing their ratio yielded only a small change in wavelengths. This can be accounted for by the weak dependence (power of 1/3) on the ratio E_{top}/E_{subs}. There seemed to be no dependence either on the thickness of the substrate or on the gap, which were, respectively, larger and smaller than the wavelength.

The classical results seem to provide the correct dependence of the wavelength and amplitude but not the prefactors. We turn now to the results of the numerical simulation of the self-avoiding rod on a Winkler foundation as introduced above. Fitting the data to a linear dependance (Fig. 9) yields $\lambda \simeq 1.4(E_{top}/E_{subs})^{1/3}h$ and $A = 2.0h$, which are much closer to experiments. In fact, accounting for large slopes tends to shorten wavelengths and increase amplitudes. Moreover, the simulations also reproduce the qualitative shapes observed in the experiments; the interface between the two gels is smooth whereas the oscillation of the free surface involves self-contacts and cusplike folds.

5 Conclusion

Using the properties of gels, we built a bilayered structure with high residual stresses. We focused on the case of a thin layer under compressive stress and a compliant substrate. The thin layer undergoes buckling with wavelengths and amplitudes that are proportional to its thickness, but with prefactors different from those of the theory of thin film buckling [1,5]. We introduced a simplified model with a self-avoiding rod on a Winkler foundation. This model relies on linear elasticity while large strains are involved and on a thin layer approximation, which is strictly valid only when its radius of curvature is larger than the thickness. Despite the shortcomings of the model, the numerical minimization of the corresponding elastic energy yielded results quantitatively closer to experiments than the classical buckling analysis, and, moreover, reproduced the cusplike folds observed in experiments.

These folds are reminiscent of the convoluted shape of the brain, which might involve mechanical instabilities [10,11]. In fact, high residual strains obtained with gels are typical of the growth of living tissues [8]. Therefore, the setup that we developed might be used to mimic living tissues. Besides, much thinner gel layers could be prepared by spin coating, which would yield an alternative way for micropatterning; using the same techniques and geometries as that introduced here, one would obtain cusped wrinkled patterns with wavelengths of the order of a few micrometers.

Acknowledgment

We thank Thierry Mora and Laurent Quartier for their experimental help. This study was partially supported by the Ministère de la Recherche-ACI Jeunes Chercheurs and by the European

Community-New and Emerging Science and Technology programs. L.P.S. is UMR 8550 of CNRS and is associated with Université Pierre et Marie Curie (Paris VI) and Université Denis Diderot (Paris VII).

References

[1] Allen, H. G., 1969, *Analysis and Design of Structural Sandwich Panels*, Pergamon, New York.

[2] Genzer, J., and Groenewold, J., 2006, "Soft Matter With Hard Skin: From Skin Wrinkles to Templating and Material Characterization," Soft Mater., **2**, pp. 310–323.

[3] Bowden, N., Brittain, S., Evans, A. G., Hutchinson, J. W., and Whitesides, G. M., 1998, "Spontaneous Formation of Ordered Structures in Thin Films of Metals Supported on an Elastomeric Polymer," Nature (London), **393**, pp. 146–149.

[4] Efimenko, K., Rackaitis, M., Manias, E., Mahadevan, L., and Vaziri, A., 2005, "Nested Self-Similar Wrinkling Patterns in Skins," Nat. Mater., **4**(4), pp. 293–297.

[5] Chen, X., and Hutchinson, J. W., 2004, "Herringbone Buckling Patterns of Compressed Thin Films on Compliant Substrates," ASME J. Appl. Mech., **71**, pp. 597–603.

[6] Mahadevan, L., and Rica, S., 2005, "Self-Organized Origami," Science, **307**, pp. 1740.

[7] Huang, Z. Y., Hong, W., and Suo, Z., 2005, "Nonlinear Analyses of Wrinkles in a Film Bonded to a Compliant Substrate," J. Mech. Phys. Solids, **53**, pp. 2101–2118.

[8] Skalak, R., Zargaryan, S., Jain, R. K., Netti, P. A., and Hoger, A., 1996, "Compatibility and the Genesis of Residual Stress by Volumetric Growth," J. Math. Biol., **34**, pp. 889–914.

[9] Ben Amar, M., and Goriely, A., 2005, "Growth and Instability in Elastic Tissues," J. Mech. Phys. Solids, **53**, pp. 2284–2319.

[10] Richman, D. P., Stewart, R. M., Hutchinson, J. W., and Caviness, V. S., Jr., 1975, "Mechanical Model of Brain Convolutional Development," Science, **189**, pp. 18–21.

[11] Toro, R., and Burnod, Y., 2005, "A Morphogenetic Model for the Development of Cortical Convolutions," Cereb. Cortex, **15**, pp. 1900–1913.

[12] Steele, C. R., 2000, "Shell Stability Related to Pattern Formation in Plants," ASME J. Appl. Mech., **67**, pp. 237–247.

[13] Kücken, M., and Newell, A. C., 2004, "A Model for Fingerprint Formation," Europhys. Lett., **68**(1), pp. 141–146.

[14] Tanaka, T., Fillmore, D., Sun, S.-T., Nishio, I., Swislow, G., and Shah, A., 1980, "Phase Transitions in Ionic Gels," Phys. Rev. Lett., **45**, pp. 1636–1639.

[15] Boudaoud, A., and Chaïeb, S., 2003, "Mechanical Phase Diagram of Shrinking Cylindrical Gels," Phys. Rev. E, **68**, p. 021801.

[16] Tanaka, T., Sun, S.-T., Hirokawa, Y., Katayama, S., Kucera, J., Hirose, Y., and Amiya, T., 1987, "Mechanical Instability of Gels at the Phase Transition," Nature (London), **325**, pp. 796–798.

[17] Tanaka, H., and Sigehuzi, T., 1994, "Surface-Pattern Evolution in a Swelling Gel Under a Geometrical Constraint: Direct Observation of Fold Structure and its Coarsening Dynamics," Phys. Rev. E, **49**, pp. R39–R42.

[18] Mora, T., and Boudaoud, A., 2006, "Buckling of Swelling Gels," Eur. Phys. J. E, **20**, pp. 119–124.

[19] Sharon, E., Roman, B., Marder, M., Shin, G.-S., and Swinney, H. L., 2002, "Buckling Cascades in Free Sheets," Nature (London), **419**, p. 579.

[20] Audoly, B., and Boudaoud, A., 2003, "Self-Similar Structures Near Boundaries in Strained Systems," Phys. Rev. Lett., **91**, p. 086105.

[21] Klein, Y., Efrati, E., and Sharon, E., 2007, "Shaping of Elastic Sheets by Prescription of Non-Euclidean Metrics," Science, **315**, pp. 1116–1120.

[22] Basu, S. K., McCormick, A. V., and Scriven, L. E., 2006, "Stress Generation by Solvent Absorption and Wrinkling of a Cross-Linked Coating Atop a Viscous or Elastic Base," Langmuir, **22**, pp. 5916–5924.

[23] Landau, L., and Lifchitz, E., 1990, "Théorie de l'élasticité," *Physique théorique (Tome 7)*. (Éditions Mir), Mir, Moscow.

[24] Press, W. H., Teukolsky, S. A., Vetterling, W. T., and Flannery, B. P., 2002, *Numerical Recipes in C*, Cambridge University Press, Cambridge, England.

Special Coordinates Associated With Recursive Forward Dynamics Algorithm for Open Loop Rigid Multibody Systems

Sangamesh R. Deepak
e-mail: sangu.09@gmail.com

Ashitava Ghosal[1]
e-mail: asitava@mecheng.iisc.ernet.in

Department of Mechanical Engineering,
Indian Institute of Science,
Bangalore 560012,
India

The recursive forward dynamics algorithm (RFDA) for a tree structured rigid multibody system has two stages. In the first stage, while going down the tree, certain equations are associated with each node. These equations are decoupled from the equations related to the node's descendants. We refer them as the equations of RFDA of the node and the current paper derives them in a new way. In the new derivation, associated with each node, we recursively obtain the coordinates, which describe the system consisting of the node and all its descendants. The special property of these coordinates is that a portion of the equations of motion with respect to these coordinates is actually the equations of RFDA associated with the node. We first show the derivation for a two noded system and then extend to a general tree structure. Two examples are used to illustrate the derivation. While the derivation conclusively shows that equations of RFDA are part of equations of motion, it most importantly gives the associated coordinates and the left out portion of the equations of motion. These are significant insights into the RFDA.
[DOI: 10.1115/1.2936923]

1 Introduction

[2]The forward dynamics of a tree structured or open loop, rigid, multibody system with n rigid bodies is efficiently done by the well known $\mathcal{O}(n)$ recursive forward dynamics algorithm (RFDA). Early contributions to this algorithm could be traced to Armstrong [1]. In Ref. [2], this algorithm has been generalized and explained using the screw theory and the concept of articulated body (AB) inertia was also introduced. The same algorithm was explained using variational equations of motion, by Bae and Haug [3]. In the work by Rodriguez [4], the algorithm was derived using the techniques similar to Kalman filtering and smoothing. Rodriguez and Kreutz-Delgado [5] used the spatial operator algebra to describe this algorithm. The concept of decoupled natural orthogonal coordinates and reverse Gaussian elimination was used to derive this algorithm by Saha [6]. Lubich et al. [7] derived the recursive algorithm using constraint equations.

As described by Bae and Haug [3], Featherstone [2], and Lubich et al. [7], the RFDA consists of two sequential stages. In the first stage, certain equations are recursively associated with each node of the tree and they are decoupled from the equations related to the descendant nodes. We refer them as the equations of RFDA of the node and the current work presents a new way to derive them. It is well known that different coordinates describing the same multibody system result in different equations of motion. The new derivation is based on recursively obtaining special coordinates for each node having the following characterization: (1) it describes the system consisting of the node and all its descendants, (2) it is consistent with all joints in the node-descendant system, and (3) most importantly, a portion of equation of motion with respect to these coordinates is the equations of RFDA for the node. Henceforth, such coordinates are referred as coordinates of RFDA. In Sec. 3.2.2, we examine that for a system as simple as a two noded planar system with a revolute joint, finding the coordinates of RFDA for the parent node is not straightforward.

In this paper, the derivation is first shown for a two noded system. For the terminal node, the coordinates of RFDA are the same as the absolute coordinates for the node. For the parent node, the coordinates of RFDA are found in two stages. In the first stage, the coordinates describing terminal node and satisfying two conditions (see Sec. 4) are found. In the second stage, using simple coordinate transformation, we obtain coordinates describing both nodes. The equation of motion in terms of the latter coordinates has a block diagonal mass matrix and the equation corresponding to one of the blocks is the equation of RFDA for the node. The originality of this paper lies in enunciating the two conditions for coordinates of the first stage and the methods used to obtain them. We later extend the derivation to a general tree structure.

This derivation conclusively shows that the equation of RFDA is actually a part of equations of motion. Most importantly, it gives the associated coordinates and the left out portion of the equations of motion. These are important insights in this cornerstone algorithm in multibody dynamics. We do not make any claims on better computer implementation.

This paper is organized as follows: In Sec. 2, we present a review of the equations of RFDA for a tree structured, rigid, multibody system. In Sec. 3, we explain the motivation for the new derivation. In Sec. 4, we present our method of obtaining equations of RFDA for a two noded tree. The details of the method are worked out in Sec. 5. Section 6 extends the method to a general tree structure. We conclude in Sec. 7.

2 Review of Equations of Recursive Forward Dynamics

Figure 1 shows the topological representation of a tree structured multibody system. Each node represents a rigid body and a line connecting two nodes represents the joint between the rigid bodies. The nodes are appropriately numbered. The joint between a node and its parent receives the same number as that of the node.

[1]Corresponding author.

[2]We have used the term coordinates to mean the quantities that *independently and completely* describe a subset or all of the rigid bodies making up a multibody system.

Contributed by the Applied Mechanics Division of ASME for publication in the JOURNAL OF APPLIED MECHANICS. Manuscript received March 12, 2007; final manuscript received April 4, 2008; published online July 2, 2008. Review conducted by N. Sri Namachchivaya.

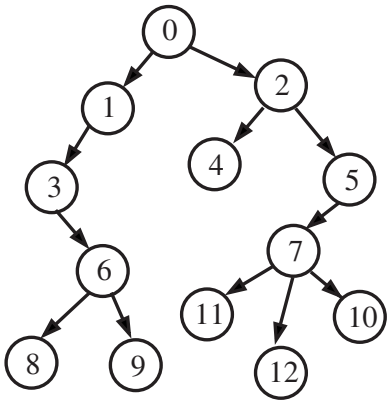

Fig. 1 A typical tree structure

If $\boldsymbol{y}$ is absolute coordinates[3] for a n-noded multibody system, then we can partition it as $\boldsymbol{y}=[\boldsymbol{y}_0^T\ \boldsymbol{y}_1^T\ \cdots\ \boldsymbol{y}_n^T]^T$, where $\boldsymbol{y}_i$ describes[4] the rigid body i.

The constraint equation due to joint j, between body j and its parent i, is represented as

$$\boldsymbol{Q}_j\dot{\boldsymbol{y}}_i+\boldsymbol{G}_j\dot{\boldsymbol{y}}_j=\boldsymbol{\nu}_j \tag{1}$$

If j is the root node, then the constraint equation has the form

$$\boldsymbol{G}_j\dot{\boldsymbol{y}}_j=\boldsymbol{\nu}_j \tag{2}$$

The differentiated form of Eq. (1) is

$$\boldsymbol{Q}_j\ddot{\boldsymbol{y}}_i+\boldsymbol{G}_j\ddot{\boldsymbol{y}}_j=\boldsymbol{\gamma}_j \tag{3}$$

where $\boldsymbol{\gamma}_j=-\dot{\boldsymbol{Q}}_j\dot{\boldsymbol{y}}_i-\dot{\boldsymbol{G}}_j\dot{\boldsymbol{y}}_j+\dot{\boldsymbol{\nu}}_j$. In Ref. [8], there is a detailed discussion on finding constraint equations in terms of absolute coordinates, for different kinds of joints.

Joint coordinates (also called relative coordinates) are also used to describe the multibody system. If $\boldsymbol{q}$ represents the joint coordinates, then it can be partitioned as $\boldsymbol{q}=[\boldsymbol{q}_0^T\ \boldsymbol{q}_1^T\ \cdots\ \boldsymbol{q}_n^T]^T$, where $\boldsymbol{q}_i$ represent the vector of joint variables of joint i. For example, if ith joint is a revolute joint, then $\boldsymbol{q}_i$ could be a one-dimensional vector containing joint angle $[\theta_i]$.

The absolute and joint coordinates are related. If body i is the parent of body j, then the relation is represented as

$$\dot{\boldsymbol{y}}_j=\boldsymbol{B}_j\dot{\boldsymbol{y}}_i+\boldsymbol{H}_j\dot{\boldsymbol{q}}_j+\boldsymbol{c}_j \tag{4}$$

One of the ways to obtain the above relation is given in Appendix A. The differentiated form of Eq. (4) is

$$\ddot{\boldsymbol{y}}_j=\boldsymbol{B}_j\ddot{\boldsymbol{y}}_i+\boldsymbol{H}_j\ddot{\boldsymbol{q}}_j+\boldsymbol{d}_j \tag{5}$$

where $\boldsymbol{d}_j=\dot{\boldsymbol{B}}_j\dot{\boldsymbol{y}}_i+\dot{\boldsymbol{H}}_j\dot{\boldsymbol{q}}_j+\dot{\boldsymbol{c}}_j$. In Ref. [3], there is a detailed discussion on finding the above equations for revolute and translational joints.

The equation of motion for the unconstrained body i in terms of absolute coordinates $\boldsymbol{y}_i$ is given by

$$\boldsymbol{M}_i\ddot{\boldsymbol{y}}_i=\boldsymbol{f}_i \tag{6}$$

The mixed differential-algebraic equation (after differentiating constraints appropriately) for the constrained tree structured multibody system has the form

$$\left\{\begin{array}{l}\boldsymbol{M}_j\ddot{\boldsymbol{y}}_j+\boldsymbol{G}_j^T\boldsymbol{\lambda}_j=\boldsymbol{f}_j-\displaystyle\sum_{k:j=\mathcal{P}(k)}\boldsymbol{Q}_k^T\boldsymbol{\lambda}_k\\ \boldsymbol{G}_j\ddot{\boldsymbol{y}}_j=\boldsymbol{\gamma}_j-\boldsymbol{Q}_j\ddot{\boldsymbol{y}}_{\mathcal{P}(j)}\end{array}\right\},\quad j=0,\ldots,n \tag{7}$$

where $\mathcal{P}(i)$ denotes parent of node i, and $k:j=\mathcal{P}(k)$ indicates all k, which has j as its parent.

Given time t, $\boldsymbol{y}$, and $\dot{\boldsymbol{y}}$, $\boldsymbol{M}_j$,$\boldsymbol{f}_j$,[5] $\boldsymbol{G}_j$, $\boldsymbol{Q}_j$, and $\boldsymbol{\gamma}_j$ could be found for $j=0,\ldots,n$. So Eq. (7) is essentially a set of linear equations in the unknowns $\ddot{\boldsymbol{y}}$ and $\boldsymbol{\lambda}$. The purpose of forward dynamics algorithm is to find $\ddot{\boldsymbol{y}}$, given t, $\boldsymbol{y}$, and $\dot{\boldsymbol{y}}$. One straightforward method to solve Eq. (7) is by using methods such as Gaussian elimination or LU decomposition. This straightforward method has $\mathcal{O}(n^3)$ complexity.

The $\mathcal{O}(n)$ recursive algorithm for forward dynamics of branched multibody system has two steps:

1. going from terminal bodies to root, forming new equations at parent nodes, along the way
2. going from root to terminal bodies, solving for $\ddot{\boldsymbol{y}}_j$ of each of the nodes j, along the way

Step 1. The new equation that is formed at a node, say j, is given by

$$\left\{\begin{array}{l}\hat{\boldsymbol{M}}_j\ddot{\boldsymbol{y}}_j+\boldsymbol{G}_j^T\boldsymbol{\lambda}_j=\hat{\boldsymbol{f}}_j\\ \boldsymbol{G}_j\ddot{\boldsymbol{y}}_j=\boldsymbol{\gamma}_j-\boldsymbol{Q}_j\ddot{\boldsymbol{y}}_{\mathcal{P}(j)}\end{array}\right\} \tag{8}$$

with the constraint part corresponding to node j remaining unchanged. In this paper, it is the first part of Eq. (8), which is referred to as the equations of RFDA for node j.

In Ref. [7], the following expression for $\hat{\boldsymbol{M}}_j$ and $\hat{\boldsymbol{f}}_j$ has been derived:

$$\hat{\boldsymbol{M}}_j=\boldsymbol{M}_j+\sum_{k:j=\mathcal{P}(k)}\boldsymbol{Q}_k^T(\boldsymbol{G}_k\hat{\boldsymbol{M}}_k^{-1}\boldsymbol{G}_k^T)^{-1}\boldsymbol{Q}_k \tag{9}$$

$$\hat{\boldsymbol{f}}_j=\boldsymbol{f}_j+\sum_{k:j=\mathcal{P}(k)}\boldsymbol{Q}_k^T(\boldsymbol{G}_k\hat{\boldsymbol{M}}_k^{-1}\boldsymbol{G}_k^T)^{-1}(\boldsymbol{\gamma}_k-\boldsymbol{G}_k\hat{\boldsymbol{M}}_k^{-1}\hat{\boldsymbol{f}}_k) \tag{10}$$

An alternate expression for $\hat{\boldsymbol{M}}_j$ and $\hat{\boldsymbol{f}}_j$ is given in Refs. [7,3,2]. The expressions are given as follows:

$$\hat{\boldsymbol{M}}_j=\boldsymbol{M}_j+\sum_{k:j=\mathcal{P}(k)}\boldsymbol{B}_k^T(\boldsymbol{I}-\hat{\boldsymbol{M}}_k\boldsymbol{H}_k(\boldsymbol{H}_k^T\hat{\boldsymbol{M}}_k\boldsymbol{H}_k)^{-1}\boldsymbol{H}_k^T)\hat{\boldsymbol{M}}_k\boldsymbol{B}_k \tag{11}$$

$$\hat{\boldsymbol{f}}_j=\boldsymbol{f}_j+\sum_{k:j=\mathcal{P}(k)}\boldsymbol{B}_k^T(\boldsymbol{I}-\hat{\boldsymbol{M}}_k\boldsymbol{H}_k(\boldsymbol{H}_k^T\hat{\boldsymbol{M}}_k\boldsymbol{H}_k)^{-1}\boldsymbol{H}_k^T)(\boldsymbol{f}_k-\hat{\boldsymbol{M}}_k\boldsymbol{d}_k) \tag{12}$$

where $\boldsymbol{B}_k$, $\boldsymbol{H}_k$, and $\boldsymbol{d}_k$ are as given in Eq. (5).

Step 2. Equation (8) could be solved for $\ddot{\boldsymbol{y}}_j$ and $\boldsymbol{\lambda}_j$ if $\ddot{\boldsymbol{y}}_{\mathcal{P}(j)}$ (corresponding to parent of j) is known. However, if $j=0$ (root), then the term $\boldsymbol{Q}_j\ddot{\boldsymbol{y}}_{\mathcal{P}(j)}$ does not exist (since root does not have a parent). So initially for $j=0$, $\ddot{\boldsymbol{y}}_j$ could be solved. Once $\ddot{\boldsymbol{y}}_0$ is known, step by step $\ddot{\boldsymbol{y}}_j$ for all the descendant nodes j could be solved. This constitutes the second stage of the recursive algorithm.

$\boldsymbol{M}_j$ is positive definite for all $j=0,\ldots,n$. The term $\Sigma_{k:j=\mathcal{P}(k)}\boldsymbol{Q}_k^T(\boldsymbol{G}_k\hat{\boldsymbol{M}}_k^{-1}\boldsymbol{G}_k^T)^{-1}\boldsymbol{Q}_k$ in Eq. (9) is positive or positive semidefinite. Thus, $\hat{\boldsymbol{M}}_j$ is also positive definite. Similar comments could be shown to hold true for $\hat{\boldsymbol{M}}_j$ in Eq. (11) also. With $\hat{\boldsymbol{M}}_j$ being positive definite for $j=0,\ldots,n$, the terms $(\boldsymbol{G}_k\hat{\boldsymbol{M}}_k^{-1}\boldsymbol{G}_k^T)^{-1}$ and $(\boldsymbol{H}_k^T\hat{\boldsymbol{M}}_k\boldsymbol{H}_k)^{-1}$ are defined only if $\boldsymbol{G}_k$ is full row rank and $\boldsymbol{H}_k$ is full column rank. We assume that $\boldsymbol{G}_k$ is full row rank. This assumption also ensures that $\boldsymbol{H}_k$ is of full column rank (see Eqs. (A3) and

[3]The symbol $\boldsymbol{y}$ actually represents coordinates stacked in the form of a *vector*.

[4]The coordinates could be pseudocoordinates. So $\dot{\boldsymbol{y}}_i$ could be familiar translational and angular velocities, while $\boldsymbol{y}_i$ itself is symbolic.

[5]There may be problems where $\boldsymbol{f}_j$ may depend linearly or nonlinearly on $\boldsymbol{\lambda}$. Those situations arise when dry friction is modeled into the equations. We will not consider such cases here.

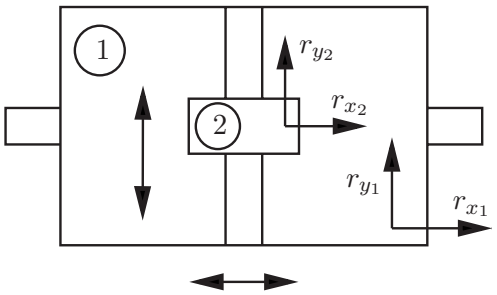

Fig. 2 A simple example given in Ref. [2]

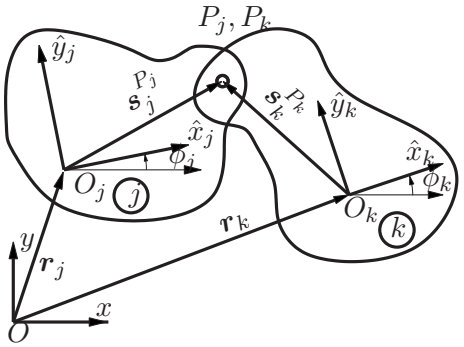

Fig. 3 Two planar rigid bodies with a revolute joint at point $P_j = P_k$

(A4)). Further, the assumption $\boldsymbol{G}_k$ being full row rank for $k=0,\ldots,n$ would render constraint Jacobian in the overall system equation (7) to be of full row rank and the existence and uniqueness of $\ddot{\mathbf{y}}$ and $\boldsymbol{\lambda}$ as solution to Eq. (7) follow from constrained dynamic existence theorem [8].

In this paper, we present a new approach to derive equations of RFDA. Our approach involves finding new coordinates with special properties. This is described next.

3 Motivation

In this section, we consider a two noded multibody system described in Ref. [2] and, using intuition, give coordinates of RFDA for it. We also consider a two noded planar multibody system with a revolute joint and realize that finding coordinates of RFDA is not straightforward. Finding coordinates of RFDA for a general multibody system has been the motivation for the new derivation given in Sec. 4.

3.1 Featherstone's Example. This system has been described in Ref. [2]. It is a planar system where Body 1 slides on the horizontal rail fixed to the base and Body 2 slides on a the vertical rail fixed to Body 1 (see Fig. 2).

3.1.1 Absolute Coordinate: Equations of Recursive Algorithm. Since the two bodies can only translate, we take absolute coordinates to be $\boldsymbol{y}=[\boldsymbol{y}_1^T\ \boldsymbol{y}_2^T]^T$, where $\boldsymbol{y}_1=[r_{x_1}\ r_{y_1}]^T$ and $\boldsymbol{y}_2=[r_{x_2}\ r_{y_2}]^T$. The two constraints on this coordinate are $r_{y_1}=0$ and $r_{x_2}-r_{x_1}=0$. The mixed differential-algebraic equation for the system has the following form:

$$\text{Node 1: } \begin{bmatrix} m_1 & 0 \\ 0 & m_1 \end{bmatrix}\begin{bmatrix} \ddot{r}_{x_1} \\ \ddot{r}_{y_1} \end{bmatrix} + \begin{bmatrix} 0 \\ 1 \end{bmatrix}\lambda_1 = \begin{bmatrix} f_{x_1} \\ f_{y_1} \end{bmatrix} - \begin{bmatrix} -1 \\ 0 \end{bmatrix}\lambda_2 \tag{13a}$$

$$\begin{bmatrix} 0 & 1 \end{bmatrix}\begin{bmatrix} \ddot{r}_{x_1} \\ \ddot{r}_{y_1} \end{bmatrix} = [0] \tag{13b}$$

$$\text{Node 2: } \begin{bmatrix} m_2 & 0 \\ 0 & m_2 \end{bmatrix}\begin{bmatrix} \ddot{r}_{x_2} \\ \ddot{r}_{y_2} \end{bmatrix} + \begin{bmatrix} 1 \\ 0 \end{bmatrix}\lambda_2 = \begin{bmatrix} f_{x_2} \\ f_{y_2} \end{bmatrix} \tag{14a}$$

$$\begin{bmatrix} 1 & 0 \end{bmatrix}\begin{bmatrix} \ddot{r}_{x_2} \\ \ddot{r}_{y_2} \end{bmatrix} = [0] - \begin{bmatrix} -1 & 0 \end{bmatrix}\begin{bmatrix} \ddot{r}_{x_1} \\ \ddot{r}_{y_1} \end{bmatrix} \tag{14b}$$

The equation of RFDA associated with Node 1 is the first part of Eq. (8). Using Eqs. (9) and (10) to calculate $\hat{\boldsymbol{M}}_1$ and $\hat{\boldsymbol{f}}_1$, we get

$$\begin{bmatrix} m_1+m_2 & 0 \\ 0 & m_1 \end{bmatrix}\begin{bmatrix} \ddot{r}_{x_1} \\ \ddot{r}_{y_1} \end{bmatrix} + \begin{bmatrix} 0 \\ 1 \end{bmatrix}\lambda_1 = \begin{bmatrix} f_{x_1}+f_{x_2} \\ f_{y_1} \end{bmatrix} \tag{15}$$

3.1.2 Coordinates of RFDA. We form a new coordinate by retaining the absolute coordinate of Body 1 and replacing the absolute coordinate of Body 2 with the joint variable r_{y_2}. The new coordinate $\bar{\boldsymbol{y}}=[r_{x_1}\ r_{y_1}\ r_{y_2}]^T$ is related to the absolute coordinate $\mathbf{y}$, by the following relation:

$$\begin{bmatrix} \dot{r}_{x_1} \\ \dot{r}_{y_1} \\ \dot{r}_{x_2} \\ \dot{r}_{y_2} \end{bmatrix} = \begin{bmatrix} 1 & 0 & 0 \\ 0 & 1 & 0 \\ 1 & 0 & 0 \\ 0 & 0 & 1 \end{bmatrix}\begin{bmatrix} \dot{r}_{x_1} \\ \dot{r}_{y_1} \\ \dot{r}_{y_2} \end{bmatrix} \tag{16}$$

The constraint for the new coordinate is $\dot{r}_{y_1}=0$. The equation of motion in terms of the new coordinate is

$$\left[\begin{array}{cc|c} m_1+m_2 & 0 & 0 \\ 0 & m_1 & 0 \\ \hline 0 & 0 & m_2 \end{array}\right]\begin{bmatrix} \ddot{r}_{x_1} \\ \ddot{r}_{y_1} \\ \ddot{r}_{y_2} \end{bmatrix} + \begin{bmatrix} 0 \\ 1 \\ 0 \end{bmatrix}\lambda_1 = \begin{bmatrix} f_{x_1}+f_{x_2} \\ f_{y_1} \\ f_{y_2} \end{bmatrix} \tag{17}$$

We notice that the mass matrix in the above equation of motion is block diagonal. Further, by comparing Eq. (17) with Eq. (15), we see that the equation corresponding to the first block is the same as the equation of RFDA. Thus, the coordinates $\bar{\boldsymbol{y}}$, defined in Eq. (16), are the coordinates of RFDA for the node.

In the next subsection, we seek coordinates of RFDA for a two noded planar system with a revolute joint.

3.2 Planar Two Rigid Body System With a Revolute Joint. Figure 3 shows two planar rigid bodies connected by a revolute joint. x-y axes, with origin O, represent global reference frame. $\hat{x}_j$-$\hat{y}_j$ axes, with origin O_j, represent local frame fixed to body j. $\mathbf{r}_j=[x_j\ y_j]^T$ is vector $\vec{OO_j}$, expressed in global coordinate. ϕ_j is angle from $\hat{x}_j$ to x. $\mathbf{s}_j'^{P_j}=[s_{j_x}'^{P_j}\ s_{j_y}'^{P_j}]^T$ represent vector $\vec{O_jP_j}$, expressed in local coordinate $\hat{x}_j$-$\hat{y}_j$. Similar conventions apply for body k also. We proceed on the same lines as the previous subsection.

3.2.1 Absolute Coordinate: Equations of Recursive Algorithm. We take absolute coordinates for the system to be $\mathbf{y}=[\mathbf{y}_j^T\ \mathbf{y}_k^T]^T$, where $\mathbf{y}_j=[x_j\ y_j\ \phi_j]^T$ and $\mathbf{y}_k=[x_k\ y_k\ \phi_k]^T$.

The constraint equation is

$$\boldsymbol{r}_k + \boldsymbol{A}(\phi_k)\boldsymbol{s}_k'^{P_k} - \boldsymbol{r}_j - \boldsymbol{A}(\phi_j)\boldsymbol{s}_j'^{P_j} = \mathbf{0} \tag{18}$$

where $\mathbf{A}(\theta)=\left[\begin{smallmatrix}\cos\theta & -\sin\theta \\ \sin\theta & \cos\theta\end{smallmatrix}\right]$.

The differential equations and constraints associated with each node are $-\{\mathbf{M}_j\ddot{\mathbf{y}}_j=\mathbf{f}_j-\mathbf{Q}_k^T\lambda_k\}$, for node j, and $\{\mathbf{M}_k\ddot{\mathbf{y}}_k+\mathbf{G}_k^T\lambda_k=\mathbf{f}_k,\ \mathbf{G}_k\ddot{\mathbf{y}}_k=\gamma_k-\mathbf{Q}_k\ddot{\mathbf{y}}_j\}$, for node k. $\mathbf{G}_k$, $\mathbf{Q}_k$, and γ_k could be evaluated using the constraint equation (18)

$$\boldsymbol{Q}_k = \begin{bmatrix} -1 & 0 & \sin\phi_j s'^{P_j}_{j_x} + \cos\phi_j s'^{P_j}_{j_y} \\ 0 & -1 & -\cos\phi_j s'^{P_j}_{j_x} + \sin\phi_j s'^{P_j}_{j_y} \end{bmatrix},$$

$$\boldsymbol{G}_k = \begin{bmatrix} 1 & 0 & -\sin\phi_k s'^{P_k}_{k_x} - \cos\phi_k s'^{P_k}_{k_y} \\ 0 & 1 & \cos\phi_k s'^{P_k}_{k_x} - \sin\phi_k s'^{P_k}_{k_y} \end{bmatrix}.$$

$$\text{Let } \boldsymbol{M}_j = \begin{bmatrix} m_j & 0 & 0 \\ 0 & m_j & 0 \\ 0 & 0 & J_j \end{bmatrix}, \quad \boldsymbol{M}_k = \begin{bmatrix} m_k & 0 & 0 \\ 0 & m_k & 0 \\ 0 & 0 & J_k \end{bmatrix},$$

$$\boldsymbol{f}_j = [f_{j_x} \quad f_{j_y} \quad \tau_j]^T, \quad \text{and} \quad \boldsymbol{f}_k = [f_{k_x} \quad f_{k_y} \quad \tau_k]^T.$$

The equation of RFDA, associated with Node 2, has the form

$$\hat{\boldsymbol{M}}_j \ddot{\mathbf{y}}_j = \hat{\boldsymbol{f}}_j \tag{19}$$

$\hat{\boldsymbol{M}}_j$ and $\hat{\boldsymbol{f}}_j$ are calculated using Eqs. (9) and (10). The explicit expression for $\hat{\boldsymbol{M}}_j(1,1)$ is given below. The rest of the elements and the elements of $\hat{\boldsymbol{f}}_j$ could be easily obtained using any symbolic math software.

$$\begin{aligned} \hat{\boldsymbol{M}}_j(1,1) = (&-2m_k^2 s'^{P_k}_{k_x} s'^{P_k}_{k_y} \sin(2\phi_k) + m_k^2 (s'^{P_k}_{k_x})^2 \cos(2\phi_k) \\ &+ m_k^2 (s'^{P_k}_{k_x})^2 + 2m_j J_k + 2m_k J_k + 2m_j m_k (s'^{P_k}_{k_x})^2 \\ &+ 2m_j m_k (s'^{P_k}_{k_y})^2 + m_k^2 (s'^{P_k}_{k_y})^2 - m_k^2 (s'^{P_k}_{k_y})^2 \cos(2\phi_k))/(2J_k \\ &+ 2m_k (s'^{P_k}_{k_y})^2 + 2m_k (s'^{P_k}_{k_x})^2) \end{aligned}$$

3.2.2 Coordinates of RFDA. We look for a coordinate having the characteristic that the equation of motion of the planar system has a block diagonal mass matrix, with equation corresponding to one block the same as Eq. (19). It is not easy to find such a coordinate. The trick of forming a new coordinate by appending absolute coordinate of parent with the joint variable does not work here. For example, consider the coordinate $\bar{\mathbf{y}} = [x_j \; y_j \; \phi_j \; \theta_k]$ where $\theta_j = \phi_k - \phi_j$ is the joint angle. This coordinate is related to the absolute coordinate by the relation

$$\begin{bmatrix} \dot{x}_j \\ \dot{y}_j \\ \dot{\phi}_j \\ \dot{x}_k \\ \dot{y}_k \\ \dot{\phi}_k \end{bmatrix} = \begin{bmatrix} \begin{bmatrix} 1 & 0 \\ 0 & 1 \\ 0 & 0 \end{bmatrix} & \begin{bmatrix} 0 \\ 0 \\ 1 \end{bmatrix} & \begin{bmatrix} 0 \\ 0 \\ 0 \end{bmatrix} \\ \begin{bmatrix} 1 & 0 \\ 0 & 1 \end{bmatrix} & \boldsymbol{T}_{22} & \boldsymbol{T}_{23} \\ \begin{bmatrix} 0 & 0 \end{bmatrix} & 1 & 1 \end{bmatrix} \begin{bmatrix} \dot{x}_j \\ \dot{y}_j \\ \dot{\phi}_j \\ \dot{\theta}_k \end{bmatrix} \tag{20}$$

where $\mathbf{T}_{22} = \mathbf{A}(\phi_j + \pi/2)\mathbf{s}'^{P_j}_j - \mathbf{A}(\phi_j + \theta_k + \pi/2)\mathbf{s}'^{P_k}_k$ and $\mathbf{T}_{23} = -\mathbf{A}(\phi_j + \theta_k + \pi/2)\mathbf{s}'^{P_k}_k$. The new coordinate is consistent with the kth joint constraint and the equation of motion would be of the form $\bar{\bar{\boldsymbol{M}}}\,\ddot{\bar{\mathbf{y}}} = \bar{\boldsymbol{f}}$. Explicit expression for $\bar{\bar{\boldsymbol{M}}}$ and $\bar{\boldsymbol{f}}$ could be obtained using first principles such as generalized d'Alembert's principle or using Eq. (B3). Some of the elements of $\bar{\bar{\boldsymbol{M}}}$ are $\bar{\bar{\boldsymbol{M}}}(1,1) = \bar{\bar{\boldsymbol{M}}}(2,2) = m_j + m_k$ and $\bar{\bar{\boldsymbol{M}}}(1,2) = \bar{\bar{\boldsymbol{M}}}(2,1) = 0$.

It turns out that, $\bar{\bar{\boldsymbol{M}}}$ is not block diagonal and Eq. (19) cannot be seen as a part of the equation, $\bar{\bar{\boldsymbol{M}}}\,\ddot{\bar{\mathbf{y}}} = \bar{\boldsymbol{f}}$.

3.3 Motivation for New Derivation. If one were to think equations of RFDA given in Eq. (8), as a part of equations of motion, then natural questions would be on the left out part of equations of motion and the coordinates associated with equations of motion. We have seen that these questions are not straightforward to answer even for a simple two noded planar system with a revolute joint. Addressing these questions for a general multibody system has been the motivation for the new derivation of this paper. Moreover, answer to these questions gives insight into the RFDA, a cornerstone algorithm in multibody dynamics.

4 New Derivation of Equations of RFDA

In this section, the derivation is explained for a two noded tree structure. In Sec. 6, the derivation is extended to a general tree structure. The nodes of the tree are numbered as k and j. k is considered as a terminal node and j is its parent and the root node. There is joint k between nodes k and j, and joint j between root node j and global reference frame.

The equation of RFDA for terminal node k is nothing but equation of motion with respect to absolute coordinate of node k. Hence, the absolute coordinate of terminal node itself is the coordinate of RFDA for the node. The following are the steps in the derivation of equations of RFDA for node j.

Step 1: Coordinates having free and constrained partitions with block diagonal mass matrix. Find coordinates $\tilde{\mathbf{y}}_k = [\tilde{\mathbf{y}}_{k_c}^T \; \tilde{\mathbf{y}}_{k_f}^T]^T$, describing the rigid body k and satisfying the following properties.

Property 1. $\tilde{\mathbf{y}}_{k_c}$ should be fully determined by $\mathbf{y}_j$ and $\tilde{\mathbf{y}}_{k_f}$ should not be constrained in any way by parent coordinates. Equivalently, if the constraint equation due to joint k is represented in terms of $\mathbf{y}_j$ and $\tilde{\mathbf{y}}_k$ as

$$\boldsymbol{Q}_k \dot{\mathbf{y}}_j + [\tilde{\boldsymbol{G}}_{k_c} \quad \tilde{\boldsymbol{G}}_{k_f}] \begin{bmatrix} \dot{\tilde{\mathbf{y}}}_{k_c} \\ \dot{\tilde{\mathbf{y}}}_{k_f} \end{bmatrix} = \tilde{\boldsymbol{\nu}}_k \tag{21}$$

then $\tilde{\boldsymbol{G}}_{k_c}$ is a nonsingular square matrix and $\tilde{\boldsymbol{G}}_{k_f}$ is a zero matrix. As a result, the way $\mathbf{y}_j$ determines $\tilde{\mathbf{y}}_{k_c}$ is given by

$$\dot{\tilde{\mathbf{y}}}_{k_c} = \boldsymbol{S}_k \dot{\mathbf{y}}_j + \boldsymbol{a}_k \tag{22}$$

where $\mathbf{S}_k = -\tilde{\boldsymbol{G}}_{k_c}^{-1}\mathbf{Q}_k$ and $\mathbf{a}_k = \tilde{\boldsymbol{G}}_{k_c}^{-1}\tilde{\boldsymbol{\nu}}_k$.

If the coordinates satisfy the above property, then we say that it has free and constrained partitions.

Property 2. $\tilde{\mathbf{y}}_k$ describes the rigid body k and we can write the equation of motion of body k in terms of $\tilde{\mathbf{y}}_k$. The mass matrix should be block diagonal corresponding to the partitions $\tilde{\mathbf{y}}_{k_c}$ and $\tilde{\mathbf{y}}_{k_f}$. In other words, the equation of motion in terms of $\tilde{\mathbf{y}}_k$ should be of the form

$$\begin{bmatrix} \tilde{\boldsymbol{M}}_{k_c} & \boldsymbol{0} \\ \boldsymbol{0} & \tilde{\boldsymbol{M}}_{k_f} \end{bmatrix} \begin{bmatrix} \ddot{\tilde{\mathbf{y}}}_{k_c} \\ \ddot{\tilde{\mathbf{y}}}_{k_f} \end{bmatrix} + \begin{bmatrix} \tilde{\boldsymbol{G}}_{k_c}^T \\ \boldsymbol{0} \end{bmatrix} \boldsymbol{\lambda}_k = \begin{bmatrix} \tilde{\boldsymbol{f}}_{k_c} \\ \tilde{\boldsymbol{f}}_{k_f} \end{bmatrix} \tag{23}$$

Example 1. In Featherstone's example (see Fig. 2), the coordinates $\mathbf{y}_2$ describing Body 2 satisfy all the above properties. It has the partition $\mathbf{y}_2 = [[r_{x_2}] \; [r_{y_2}]]^T$, with the following features.

(1) The constraint equation for Joint 2 is of the form (see Sec. 3.1.1) $[-1 \; 0]\begin{bmatrix} \dot{r}_{x_1} \\ \dot{r}_{y_1} \end{bmatrix} + [[1] \; [0]]\begin{bmatrix} [\dot{r}_{x_2}] \\ [\dot{r}_{y_2}] \end{bmatrix} = [0]$ and $[\dot{r}_{x_2}]$ is determined by the equation $[\dot{r}_{x_2}] = [1 \; 0]\begin{bmatrix} \dot{r}_{x_1} \\ \dot{r}_{y_1} \end{bmatrix}$.

(2) The equation of motion for Body 2, with respect to $\mathbf{y}_2$, is $\begin{bmatrix} [m_2] & [0] \\ [0] & [m_2] \end{bmatrix}\begin{bmatrix} [\ddot{r}_{x_2}] \\ [\ddot{r}_{y_2}] \end{bmatrix} + \begin{bmatrix} [1] \\ [0] \end{bmatrix}\lambda_2 = \begin{bmatrix} [f_{x_2}] \\ [f_{y_2}] \end{bmatrix}$. Clearly, the mass matrix is block diagonal.

Example 2. Consider the planar system with a revolute joint shown in Fig. 3. The usual coordinates for body k, $\mathbf{y}_k = [x_k \; y_k \; \phi_k]^T$, do not have a partition that satisfies Property 1 of Step 1, even though the mass matrix is diagonal (see $\mathbf{M}_k$ in Sec. 3.2.1).

Consider another set of coordinates $\bar{\mathbf{y}}_k = [[x^{P_k} \; y^{P_k}] \; [\phi_k]]^T$, defined by the relation

$$\dot{\boldsymbol{y}}_k = \begin{bmatrix} \begin{bmatrix} 1 & 0 \\ 0 & 1 \\ 0 & 0 \end{bmatrix} & \begin{bmatrix} s'^{P_k}_{k_x} \sin\phi_k + s'^{P_k}_{k_y} \cos\phi_k \\ -s'^{P_k}_{k_x} \cos\phi_k + s'^{P_k}_{k_y} \sin\phi_k \\ 1 \end{bmatrix} \end{bmatrix} \begin{bmatrix} \begin{bmatrix} \dot{x}^{P_k} \\ \dot{y}^{P_k} \end{bmatrix} \\ [\dot{\phi}_k] \end{bmatrix} \tag{24}$$

From the definition, it should be clear that $[\dot{x}^{P_k}\ \dot{y}^{P_k}]^T$ is the velocity of pivot point P^k of body k (see Fig. 3).

The constraint equation in terms of $\bar{\boldsymbol{y}}_k$ is (using Eq. (B1))

$$\boldsymbol{Q}_k \begin{bmatrix} \dot{x}_j \\ \dot{y}_j \\ \dot{\phi}_j \end{bmatrix} + \begin{bmatrix} \begin{bmatrix} 1 & 0 \\ 0 & 1 \end{bmatrix} & \begin{bmatrix} 0 \\ 0 \end{bmatrix} \end{bmatrix} \begin{bmatrix} \begin{bmatrix} \dot{x}^{P_k} \\ \dot{y}^{P_k} \end{bmatrix} \\ [\dot{\phi}_k] \end{bmatrix} = \begin{bmatrix} 0 \\ 0 \end{bmatrix}$$

where $\mathbf{Q}_k$ is given in Sec. 3.2.1. Clearly, $\bar{\boldsymbol{y}}_k$ satisfy the first property stated above.

The mass matrix for body k in terms of $\bar{\boldsymbol{y}}_k$ is (using Eq. (B3))

$$\begin{bmatrix} \begin{bmatrix} m_k & 0 \\ 0 & m_k \end{bmatrix} & -m_k \mathbf{A}(\phi_k + \pi/2) \boldsymbol{s}'^{P_k}_k \\ -(m_k \mathbf{A}(\phi_k + \pi/2) \boldsymbol{s}'^{P_k}_k)^T & J_k + m_k^2 (|\boldsymbol{s}'^{P_k}_k|^2) \end{bmatrix} \tag{25}$$

where $\mathbf{A}(\theta)$ is described in Sec. 3.2.1. The mass matrix is not block diagonal and Property 2 is not satisfied.

Thus, even in the specific example as above, it is not straightforward to come up with coordinates satisfying both properties. In Sec. 5, we deduce coordinates satisfying both properties for a general system.

Step 2: Form new coordinates describing both nodes. Define new coordinates $[\boldsymbol{y}_j^T\ \tilde{\boldsymbol{y}}_{k_f}^T]^T$ as

$$\begin{bmatrix} \dot{\boldsymbol{y}}_j \\ \dot{\tilde{\boldsymbol{y}}}_{k_c} \\ \dot{\tilde{\boldsymbol{y}}}_{k_f} \end{bmatrix} = \begin{bmatrix} \boldsymbol{I} & \boldsymbol{0} \\ \boldsymbol{S}_k & \boldsymbol{0} \\ \boldsymbol{0} & \boldsymbol{I} \end{bmatrix} \begin{bmatrix} \dot{\boldsymbol{y}}_j \\ \dot{\tilde{\boldsymbol{y}}}_{k_f} \end{bmatrix} + \begin{bmatrix} \boldsymbol{0} \\ \boldsymbol{a}_k \\ \boldsymbol{0} \end{bmatrix} \tag{26}$$

This coordinate describes the entire system consisting of two rigid bodies with a joint between them. We later see that this is the coordinate of RFDA for node j.

Step 3: Obtain equations of motion in terms of coordinates of Step 2. For writing the constraint and equation of motion in terms of the above coordinates, we make use of Eqs. (B1) and (B2), with coordinate transformation given by Eq. (26). This requires that we know the constraint equation and equation of motion in terms of $[\dot{\boldsymbol{y}}_j^T\ \dot{\tilde{\boldsymbol{y}}}_k^T]^T = [\dot{\boldsymbol{y}}_j^T\ \dot{\tilde{\boldsymbol{y}}}_{k_c}^T\ \dot{\tilde{\boldsymbol{y}}}_{k_f}^T]^T$. These are given as follows.

$$\boldsymbol{G}_j \dot{\boldsymbol{y}}_j = \boldsymbol{\nu}_j, \quad \boldsymbol{Q}_k \dot{\boldsymbol{y}}_j + \tilde{\boldsymbol{G}}_{k_c} \dot{\tilde{\boldsymbol{y}}}_{k_c} = \tilde{\boldsymbol{\nu}}_k$$

$$\begin{bmatrix} \boldsymbol{M}_j & \boldsymbol{0} & \boldsymbol{0} \\ \boldsymbol{0} & \tilde{\boldsymbol{M}}_{k_c} & \boldsymbol{0} \\ \boldsymbol{0} & \boldsymbol{0} & \tilde{\boldsymbol{M}}_{k_f} \end{bmatrix} \begin{bmatrix} \ddot{\boldsymbol{y}}_j \\ \ddot{\tilde{\boldsymbol{y}}}_{k_c} \\ \ddot{\tilde{\boldsymbol{y}}}_{k_f} \end{bmatrix} + \begin{bmatrix} \boldsymbol{G}_j^T \\ \boldsymbol{0} \\ \boldsymbol{0} \end{bmatrix} \boldsymbol{\lambda}_j + \begin{bmatrix} \boldsymbol{Q}_k^T \\ \tilde{\boldsymbol{G}}_{k_c}^T \\ \boldsymbol{0} \end{bmatrix} \boldsymbol{\lambda}_k = \begin{bmatrix} \boldsymbol{f}_k \\ \tilde{\boldsymbol{f}}_{k_c} \\ \tilde{\boldsymbol{f}}_{k_f} \end{bmatrix}$$

The above equations are consequence of Eqs. (2), (6), (21), and (23).

After coordinate transformation through Eq. (26), the constraints (after removing redundant constraints) and equation of motion in terms of $[\boldsymbol{y}_j^T\ \dot{\tilde{\boldsymbol{y}}}_{k_f}^T]^T$ become

$$\boldsymbol{G}_j \dot{\boldsymbol{y}}_j = \boldsymbol{\nu}_j \tag{27}$$

$$\begin{bmatrix} \boldsymbol{M}_j + \boldsymbol{S}_k^T \tilde{\boldsymbol{M}}_{k_c} \boldsymbol{S}_k & \boldsymbol{0} \\ \boldsymbol{0} & \tilde{\boldsymbol{M}}_{k_f} \end{bmatrix} \begin{bmatrix} \ddot{\boldsymbol{y}}_j \\ \ddot{\tilde{\boldsymbol{y}}}_{k_f} \end{bmatrix} + \begin{bmatrix} \boldsymbol{G}_j^T \\ \boldsymbol{0} \end{bmatrix} \boldsymbol{\lambda}_j = \begin{bmatrix} \boldsymbol{f}_d \\ \tilde{\boldsymbol{f}}_{k_f} \end{bmatrix} \tag{28}$$

where $\boldsymbol{f}_d = \boldsymbol{f}_j + \boldsymbol{S}_k^T \tilde{\boldsymbol{f}}_{k_c} - \boldsymbol{S}_k^T \tilde{\boldsymbol{M}}_{k_c} (\dot{\boldsymbol{a}}_k + \dot{\boldsymbol{S}}_k \dot{\boldsymbol{y}}_j)$.

Step 4: Recognize that equation of RFDA is a part of the equations of motion. For the two noded tree structure, first of Eqs. (8) for node j (i.e., equations of RFDA) would be of form $\hat{\boldsymbol{M}}_j \ddot{\boldsymbol{y}}_j + \boldsymbol{G}_j^T \boldsymbol{\lambda}_j = \hat{\boldsymbol{f}}_j$. The rows of matrix equation (28) associated with $\boldsymbol{y}_j$, i.e.,

$$(\boldsymbol{M}_j + \boldsymbol{S}_k^T \tilde{\boldsymbol{M}}_{k_c} \boldsymbol{S}_k) \ddot{\boldsymbol{y}}_j + \boldsymbol{G}_j^T \boldsymbol{\lambda}_j = \boldsymbol{f}_j + \boldsymbol{S}_k^T \tilde{\boldsymbol{f}}_{k_c} - \boldsymbol{S}_k^T \tilde{\boldsymbol{M}}_{k_c} (\dot{\boldsymbol{a}}_k + \dot{\boldsymbol{S}}_k \dot{\boldsymbol{y}}_j) \tag{29}$$

are essentially the equations of RFDA associated with the root node of a two noded multibody system. Thus, coordinates $[\boldsymbol{y}_j^T\ \tilde{\boldsymbol{y}}_{k_f}^T]^T$, defined in Step 2, are the coordinates of RFDA for node j. Further, the only constraint on $[\boldsymbol{y}_j^T\ \tilde{\boldsymbol{y}}_{k_f}^T]^T$, given in Eq. (27), corresponds to the second of Eq. (8).

Illustration. We now illustrate Steps 2, 4 for Featherstone's example.

Step 2. Define a new coordinate $[[r_{x_1}\ r_{y_1}]\ [y_{y_2}]]^T$ by the transformation

$$\begin{bmatrix} \begin{bmatrix} \dot{r}_{x_1} \\ \dot{r}_{y_1} \end{bmatrix} \\ [\dot{r}_{x_2}] \\ [\dot{r}_{y_2}] \end{bmatrix} = \begin{bmatrix} \begin{bmatrix} 1 & 0 \\ 0 & 1 \end{bmatrix} & \begin{bmatrix} 0 \\ 0 \end{bmatrix} \\ [1\ \ 0] & [0] \\ [0\ \ 0] & [1] \end{bmatrix} \begin{bmatrix} \begin{bmatrix} \dot{r}_{x_1} \\ \dot{r}_{y_1} \end{bmatrix} \\ [\dot{r}_{y_2}] \end{bmatrix}$$

Step 3. The equation of motion in terms of the above coordinate is

$$\begin{bmatrix} \begin{bmatrix} m_1 + m_2 & 0 \\ 0 & m_1 \end{bmatrix} & \begin{bmatrix} 0 \\ 0 \end{bmatrix} \\ [0\ \ 0] & [m_2] \end{bmatrix} \begin{bmatrix} \begin{bmatrix} \ddot{r}_{x_1} \\ \ddot{r}_{y_1} \end{bmatrix} \\ [\ddot{r}_{y_2}] \end{bmatrix} + \begin{bmatrix} \begin{bmatrix} 0 \\ 1 \end{bmatrix} \\ [0] \end{bmatrix} \lambda_1 = \begin{bmatrix} \begin{bmatrix} f_{x_1} + f_{x_2} \\ f_{y_1} \end{bmatrix} \\ [f_{y_2}] \end{bmatrix} \tag{30}$$

Step 4. Indeed, the first row block of the above matrix equation is the same as the equations of RFDA obtained in Eq. (15).

Thus, given that coordinates of Step 1 would be deduced in Sec. 5, we have derived equations of RFDA in Eq. (29), based on finding coordinates of RFDA, defined in Eq. (26).

5 Finding Coordinates of Step 1

In this section, we rewrite Properties 1 and 2 of Step 1 in Sec. 4 as rigorous linear algebraic conditions and deduce the relation between $\tilde{\boldsymbol{y}}_k$ and $\boldsymbol{y}_k$ coordinates. This relation itself defines $\tilde{\boldsymbol{y}}_k$. We discuss two methods to deduce the relation.

5.1 Linear Algebraic Conditions for Coordinates of Step 1. Let $\tilde{\boldsymbol{y}}_k$ be the coordinates having the partition as $[(\tilde{\boldsymbol{y}}_{k_c})^T\ (\tilde{\boldsymbol{y}}_{k_f})^T]^T$. The coordinates be related to the existing coordinates by the following relation:

$$\dot{\boldsymbol{y}}_k = [\tilde{\boldsymbol{E}}_k \quad \tilde{\boldsymbol{D}}_k] \begin{bmatrix} \dot{\tilde{\boldsymbol{y}}}_{k_c} \\ \dot{\tilde{\boldsymbol{y}}}_{k_f} \end{bmatrix} \tag{31}$$

where $[\tilde{\boldsymbol{E}}_k\ \tilde{\boldsymbol{D}}_k]$ is a nonsingular square matrix.

The constraint equation of the joint between body k and j when written in terms of $[(\tilde{\boldsymbol{y}}_{k_c})^T\ (\tilde{\boldsymbol{y}}_{k_f})^T]^T$ takes the following form (see Eqs. (1) and (B1)):

$$\boldsymbol{Q}_k \dot{\boldsymbol{y}}_j + [\boldsymbol{G}_k \tilde{\boldsymbol{E}}_k \quad \boldsymbol{G}_k \tilde{\boldsymbol{D}}_k] \begin{bmatrix} \dot{\tilde{\boldsymbol{y}}}_{k_c} \\ \dot{\tilde{\boldsymbol{y}}}_{k_f} \end{bmatrix} = \boldsymbol{\nu}_k \tag{32}$$

The mass matrix in terms of the coordinates $[(\tilde{\boldsymbol{y}}_{k_c})^T\ (\tilde{\boldsymbol{y}}_{k_f})^T]^T$ would take the following form (see Appendix B):

$$\begin{bmatrix} \tilde{\boldsymbol{E}}_k^T \boldsymbol{M}_k \tilde{\boldsymbol{E}}_k & \tilde{\boldsymbol{E}}_k^T \boldsymbol{M}_k \tilde{\boldsymbol{D}}_k \\ \tilde{\boldsymbol{D}}_k^T \boldsymbol{M}_k \tilde{\boldsymbol{E}}_k & \tilde{\boldsymbol{D}}_k^T \boldsymbol{M}_k \tilde{\boldsymbol{D}}_k \end{bmatrix} \tag{33}$$

Let the dimension of velocity space of body k when it is unconstrained be represented by p_k (the same as the number of compo-

nents of $\dot{\boldsymbol{y}}_k$). The dimension of row space of $\boldsymbol{G}_k$ be represented by p_{k_c}. If we require $[(\dot{\tilde{\boldsymbol{y}}}_{k_c})^T\ (\dot{\tilde{\boldsymbol{y}}}_{k_f})^T]^T$ to be constrained and free partitions (Property 1 of Step 1 in Sec. 4), then the following condition should be satisfied.

Condition 1. Columns of $\tilde{\boldsymbol{D}}_k$ should be a basis for the null space of $\boldsymbol{G}_k$. In other words, Columns of $\tilde{\boldsymbol{D}}_k$ should be a basis for the orthogonal complement of column space of $\boldsymbol{G}_k^T$. This condition would render the term $\boldsymbol{G}_k\tilde{\boldsymbol{D}}_k$ in Eq. (32) to be a zero matrix. Hence, $\dot{\boldsymbol{y}}_{k_f}$ is in no way constrained by the parent coordinates. This condition also ensures that the matrix $\boldsymbol{G}_k\tilde{\boldsymbol{E}}_k$ is an invertible square matrix and hence $\dot{\boldsymbol{y}}_{k_c}$ is fully determined by the parent coordinates. The proof to show that $\boldsymbol{G}_k\tilde{\boldsymbol{E}}_k$ is an invertible square matrix is given below.

$\boldsymbol{G}_k$ is assumed to be full rank. So it has p_{k_c} rows. The null space of $\boldsymbol{G}_k$ has the dimension $p_k - p_{k_c}$ (see, for example, Ref. [9]). From the above condition, the number of columns in $\tilde{\boldsymbol{D}}_k$ is $p_k - p_{k_c}$. $[\tilde{\boldsymbol{E}}_k\ \tilde{\boldsymbol{D}}_k]$ is assumed to be a nonsingular square matrix. Hence, the number of columns in $\tilde{\boldsymbol{E}}_k$ is p_{k_c}. Thus, the matrix $\boldsymbol{G}_k\tilde{\boldsymbol{E}}_k$ is square.

To prove that $\boldsymbol{G}_k\tilde{\boldsymbol{E}}_k$ is nonsingular, it is enough to show that there is not a nonzero vector, say $\boldsymbol{v}_1$, such that $\boldsymbol{G}_k\tilde{\boldsymbol{E}}_k\boldsymbol{v}_1=\boldsymbol{0}$. Suppose there is a $\boldsymbol{v}_1$ such that $\boldsymbol{G}_k\tilde{\boldsymbol{E}}_k\boldsymbol{v}_1=\boldsymbol{0}$, $\boldsymbol{v}_1\neq\boldsymbol{0}$. The vector $\tilde{\boldsymbol{E}}_k\boldsymbol{v}_1$ is nonzero (because $\tilde{\boldsymbol{E}}_k$ is full rank matrix) and lies in the null space of $\boldsymbol{G}_k$. As per Condition 1 above, columns of $\tilde{\boldsymbol{D}}_k$ form the basis for the null space of $\boldsymbol{G}_k$. Hence, there is a unique nonzero $\boldsymbol{v}_2$ such that

$$\tilde{\boldsymbol{E}}_k\boldsymbol{v}_1=\tilde{\boldsymbol{D}}_k\boldsymbol{v}_2 \tag{34}$$

This means nonzero vector $[\boldsymbol{v}_1^T\ -\boldsymbol{v}_2^T]^T$ multiplied with nonsingular matrix $[\tilde{\boldsymbol{E}}_k\ \tilde{\boldsymbol{D}}_k]$ is zero. This is a contradiction. Hence, there cannot be a nonzero $\boldsymbol{v}_1$ such that $\boldsymbol{G}_k\tilde{\boldsymbol{E}}_k\boldsymbol{v}_1=\boldsymbol{0}$.

Additionally, if the mass matrix corresponding to the partition $[\tilde{\boldsymbol{y}}_{k_c}^T\ \tilde{\boldsymbol{y}}_{k_f}^T]$ is to be block diagonal (Property 2 of Step 1 of Sec. 4), then the following condition should also be satisfied.

Condition 2. Column space of $\boldsymbol{M}_k\tilde{\boldsymbol{E}}_k$ should lie in the orthogonal complement of column space of $\tilde{\boldsymbol{D}}_k$. This condition implies $\tilde{\boldsymbol{D}}_k^T\boldsymbol{M}_k\tilde{\boldsymbol{E}}_k=(\tilde{\boldsymbol{E}}_k^T\boldsymbol{M}_k\tilde{\boldsymbol{D}}_k)^T=\boldsymbol{0}$. Hence, the mass matrix corresponding to the coordinates $[\tilde{\boldsymbol{y}}_{k_c}^T\ \tilde{\boldsymbol{y}}_{k_f}^T]^T$ would become block diagonal (see Eq. (33)).

As seen in the example of planar-revolute system, finding the transformation

$$\dot{\boldsymbol{y}}_k=[\boldsymbol{E}_k\quad\boldsymbol{D}_k]\begin{bmatrix}\dot{\tilde{\boldsymbol{y}}}_{k_c}\\ \dot{\tilde{\boldsymbol{y}}}_{k_f}\end{bmatrix}\quad([\boldsymbol{E}_k\quad\boldsymbol{D}_k]\ \text{is nonsingular}) \tag{35}$$

which satisfy the first condition (i.e., columns of $\boldsymbol{D}_k$ being the basis for the null space of $\boldsymbol{G}_k$), is not hard. For the planar-revolute system, we extract $\boldsymbol{E}_k$ and $\boldsymbol{D}_k$ from Eq. (24), as

$$\boldsymbol{E}_k=\begin{bmatrix}1&0\\0&1\\0&0\end{bmatrix},\quad \boldsymbol{D}_k=\begin{bmatrix}s_{k_x}^{\prime P_k}s\phi_k+s_{k_y}^{\prime P_k}c\phi_k\\ -s_{k_x}^{\prime P_k}c\phi_k+s_{k_y}^{\prime P_k}s\phi_k\\ 1\end{bmatrix} \tag{36}$$

In Eq. (A3) of Appendix A, we give one general procedure of finding $\boldsymbol{E}_k$ and $\boldsymbol{D}_k$, which satisfy Condition 1. Most of the time, one could arrive at $\boldsymbol{E}$ and $\boldsymbol{D}$ by looking at the geometry of the joint. In the next two sections, given $\boldsymbol{E}_k$ and $\boldsymbol{D}_k$, we show two different ways of finding $\tilde{\boldsymbol{E}}_k$ and $\tilde{\boldsymbol{D}}_k$, which satisfy both Conditions 1 and 2.

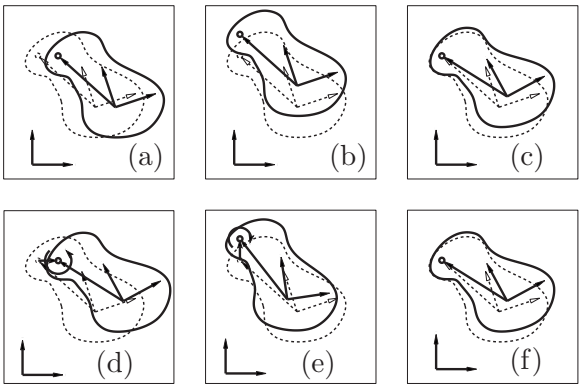

Fig. 4 Visualization of various coordinates for body *k*: (*a*), (*b*), and (*c*) indicate small changes in x^{Pk}, y^{Pk}, and ϕ_k, respectively, as a part of coordinate $\bar{\boldsymbol{y}}_k$ (see Eq. (24)); (*d*)–(*f*) indicate a small change in components of $\breve{\boldsymbol{y}}_{k_c}$ (see Eq. (39))

5.2 Two Approaches to Find $\tilde{\boldsymbol{E}}_k$ and $\tilde{\boldsymbol{D}}_k$

5.2.1 Method 1. As discussed in Eq. (35), we can find a matrix $\boldsymbol{D}_k$ whose columns are the basis for the null space of $\boldsymbol{G}_k$. As per Condition 1, we require columns of $\tilde{\boldsymbol{D}}_k$ to be also a basis for null space of $\boldsymbol{G}_k$. We may very well take $\tilde{\boldsymbol{D}}_k$ to be $\boldsymbol{D}_k$ itself. More generally, we can take $\tilde{\boldsymbol{D}}_k$ to be

$$\tilde{\boldsymbol{D}}_k=\boldsymbol{D}_k\boldsymbol{C}_f \tag{37}$$

where $\boldsymbol{C}_f$ is *any* nonsingular square matrix of size $p_{k_f}\times p_{k_f}$.

We will now find $\tilde{\boldsymbol{E}}_k$. Condition 2 requires columns of $\boldsymbol{M}_k\tilde{\boldsymbol{E}}_k$ to lie in the orthogonal complement of column space of $\tilde{\boldsymbol{D}}_k$. This orthogonal complement has dimension p_{k_c}. However, $\tilde{\boldsymbol{E}}_k$ is full column rank with p_{k_c} columns and $\boldsymbol{M}_k$ is a nonsingular matrix. Hence, columns of $\boldsymbol{M}_k\tilde{\boldsymbol{E}}_k$ have to be the basis for the orthogonal complement of the column space of $\tilde{\boldsymbol{D}}_k$. From Condition 1 (and the $\boldsymbol{G}_k$ is full row rank), columns of $\boldsymbol{G}_k^T$ are the basis for the orthogonal complement of column space of $\tilde{\boldsymbol{D}}_k$. So we may very well take $\boldsymbol{M}_k\tilde{\boldsymbol{E}}_k=\boldsymbol{G}_k^T$, or with more generality $\boldsymbol{M}_k\tilde{\boldsymbol{E}}_k=\boldsymbol{G}_k^T\boldsymbol{C}_c$ where $\boldsymbol{C}_c$ is any $p_{k_c}\times p_{k_c}$ nonsingular matrix. Hence,

$$\tilde{\boldsymbol{E}}_k=\boldsymbol{M}_k^{-1}\boldsymbol{G}_k^T\boldsymbol{C}_c \tag{38}$$

5.2.2 Method 2. In the example shown in Fig. 3, we defined coordinates $[(\bar{\boldsymbol{y}}_{k_c})^T\ (\bar{\boldsymbol{y}}_{k_f})^T]^T$ in Eq. (24), such that $(\bar{\boldsymbol{y}}_{k_c})$ is determined by $\boldsymbol{y}_j$ and $(\bar{\boldsymbol{y}}_{k_f})$ is unconstrained by $\boldsymbol{y}_j$. Figures 4(*a*)–4(*c*) show the displacement of rigid body k due to small changes in each of the components of these coordinates. For the same system, consider another set of coordinates defined by

$$\dot{\boldsymbol{y}}_k=\left[\begin{bmatrix}1\\0\\0\end{bmatrix}+\alpha\boldsymbol{t}_3\quad\begin{bmatrix}0\\1\\0\end{bmatrix}+\beta\boldsymbol{t}_3\quad\boldsymbol{t}_3\right]\begin{bmatrix}\dot{\breve{\boldsymbol{y}}}_{k_{c_1}}\\ \dot{\breve{\boldsymbol{y}}}_{k_{c_2}}\\ \dot{\breve{\boldsymbol{y}}}_{k_{f_1}}\end{bmatrix}$$

where

$$\boldsymbol{t}_3=(s_{k_x}^{\prime P_k}\sin\phi_k+s_{k_y}^{\prime P_k}\cos\phi_k,-s_{k_x}^{\prime P_k}\cos\phi_k+s_{k_y}^{\prime P_k}\sin\phi_k,\quad 1)^T \tag{39}$$

The change in the system due to infinitesimal change in $[\breve{\boldsymbol{y}}_{k_c}^T\ \breve{\boldsymbol{y}}_{k_f}^T]^T$ is shown in Figs. 4(*d*)–4(*f*) From these figures, it may be noted that $\delta\breve{y}_{k_{c_1}}$ (or δx^{P_j}) is still determined by δ_{y_j}. The point P^k

has a small displacement in x-direction if and only if there is a small change in $\breve{y}_{k_{c_1}}$. Similar arguments hold for $\breve{y}_{k_{c_2}}$. From these figures, it is also clear that $\breve{y}_{k_{f_1}}$ is still no way constrained by the parent body. (It could, however, compensate for the extra rotation due to $\boldsymbol{\delta y}_{k_c}$.) Thus, $[\breve{\mathbf{y}}_{k_c}^T \ \breve{\mathbf{y}}_{k_f}^T]^T$ defined in Eq. (39) also has the partition into constrained and free parts.

The generalization of the above concept is as follows.

If $[\bar{\mathbf{y}}_{k_c}^T \ \bar{\mathbf{y}}_{k_f}^T]^T$ is a coordinate for body k, defined by

$$\dot{\mathbf{y}}_k = [\boldsymbol{E}_k \quad \boldsymbol{D}_k] \begin{bmatrix} \dot{\bar{\mathbf{y}}}_{k_c} \\ \dot{\bar{\mathbf{y}}}_{k_f} \end{bmatrix}, \quad [\boldsymbol{E}_k \quad \boldsymbol{D}_k] \quad \text{is nonsingular} \tag{40}$$

such that $\bar{\mathbf{y}}_{k_c}$ and $\bar{\mathbf{y}}_{k_f}$ are the constrained and free partitions of $\bar{\mathbf{y}}_k$,[6] then another coordinate, say $\breve{\mathbf{y}}_k = [\breve{\mathbf{y}}_{k_c}^T \ \breve{\mathbf{y}}_{k_f}^T]^T$, defined by

$$\dot{\mathbf{y}}_k = [\boldsymbol{E}_k + \boldsymbol{D}_k \boldsymbol{A} \quad \boldsymbol{D}_k] \begin{bmatrix} \dot{\breve{\mathbf{y}}}_{k_c} \\ \dot{\breve{\mathbf{y}}}_{k_f} \end{bmatrix}, \quad \boldsymbol{A} \text{ any compatible matrix} \tag{41}$$

also has the constrained and free partitions ($\breve{\mathbf{y}}_{k_c}$ and $\breve{\mathbf{y}}_{k_c}$).

To prove the above generalization, we should show that $[\boldsymbol{E}_k + \boldsymbol{D}_k \boldsymbol{A} \ \boldsymbol{D}_k]$ is nonsingular and columns of $\boldsymbol{D}_k$ are the basis for the null space of $\boldsymbol{G}_k$ (see Condition 1 in Sec. 5.1).

Proof. $[\boldsymbol{E}_k \ \boldsymbol{D}_k]$ is a full column rank square matrix. For a column of a matrix, if we add linear combination of other columns of the matrix, then the column rank is unchanged. Hence, $[\boldsymbol{E}_k + \boldsymbol{D}_k \boldsymbol{A} \ \mathbf{D}_k]$ is a full column rank square matrix or a nonsingular matrix. Since $[\bar{\mathbf{y}}_{k_c}^T \ \bar{\mathbf{y}}_{k_f}^T]^T$ defined in Eq. (40) has partition into constrained and free parts, $\boldsymbol{D}_k$ satisfy Condition 1 given in Sec. 5.1, i.e., columns of $\boldsymbol{D}_k$ are the basis for the null space of $\boldsymbol{G}_k$.

We now show that we can find a special matrix $\widetilde{\boldsymbol{A}}_k$ such that $\widetilde{\boldsymbol{E}}_k = \boldsymbol{E}_k + \boldsymbol{D}_k \widetilde{\boldsymbol{A}}_k$ and $\widetilde{\boldsymbol{D}}_k = \boldsymbol{D}_k$, while satisfying Condition 1, also satisfy Condition 2. From Condition 2, we have

$$\widetilde{\boldsymbol{D}}_k^T \boldsymbol{M}_k \widetilde{\boldsymbol{E}}_k = \boldsymbol{D}_k^T \boldsymbol{M}_k (\boldsymbol{E}_k + \boldsymbol{D}_k \widetilde{\boldsymbol{A}}_k) = \boldsymbol{D}_k^T \boldsymbol{M}_k \boldsymbol{E}_k + (\boldsymbol{D}_k^T \boldsymbol{M}_k \boldsymbol{D}_k) \widetilde{\boldsymbol{A}}_k = \mathbf{0}$$

$\boldsymbol{D}_k$ is full column rank and $\boldsymbol{M}_k$ is positive definite. Hence, $\boldsymbol{D}_k^T \boldsymbol{M}_k \boldsymbol{D}_k$ is also positive definite and $(\boldsymbol{D}_k^T \boldsymbol{M}_k \boldsymbol{D}_k)^{-1}$ exists. So we can write

$$\widetilde{\boldsymbol{A}}_k = -(\boldsymbol{D}_k^T \boldsymbol{M}_k \boldsymbol{D}_k)^{-1} \boldsymbol{D}_k^T \boldsymbol{M}_k \boldsymbol{E}_k \tag{42}$$

$$\widetilde{\boldsymbol{E}}_k = \boldsymbol{E}_k + \boldsymbol{D}_k \widetilde{\boldsymbol{A}}_k = \boldsymbol{E}_k - \boldsymbol{D}_k (\boldsymbol{D}_k^T \boldsymbol{M}_k \boldsymbol{D}_k)^{-1} \boldsymbol{D}_k^T \boldsymbol{M}_k \boldsymbol{E}_k \tag{43}$$

$$\widetilde{\boldsymbol{D}}_k = \boldsymbol{D}_k \tag{44}$$

Thus, we have obtained $\widetilde{\boldsymbol{E}}_k$ and $\widetilde{\boldsymbol{D}}_k$ satisfying both Conditions 1 and 2. The expressions are in terms of $\boldsymbol{E}_k$ and $\boldsymbol{D}_k$ (see Eq. (35)).

To summarize, if we know coordinates $\bar{\mathbf{y}}_k = [\bar{\mathbf{y}}_{k_c}^T \ \bar{\mathbf{y}}_{k_f}^T]^T$, satisfying Property 1 of Step 1 and its relation $\dot{\mathbf{y}}_k = [\boldsymbol{E}_k \ \boldsymbol{D}_k] \begin{bmatrix} \dot{\bar{\mathbf{y}}}_{k_c} \\ \dot{\bar{\mathbf{y}}}_{k_f} \end{bmatrix}$ with $\mathbf{y}_k$, then the coordinate $\tilde{\mathbf{y}}_k = [\tilde{\mathbf{y}}_{k_c}^T \ \tilde{\mathbf{y}}_{k_f}^T]^T$ satisfying both properties of Step 1 in Sec. 4 is defined by $\dot{\mathbf{y}}_k = [\widetilde{\boldsymbol{E}}_k \ \widetilde{\boldsymbol{D}}_k] \begin{bmatrix} \dot{\tilde{\mathbf{y}}}_{k_c} \\ \dot{\tilde{\mathbf{y}}}_{k_f} \end{bmatrix}$, where $\widetilde{\boldsymbol{E}}_k$ and $\widetilde{\boldsymbol{D}}_k$ are as in Eqs. (38) and (37) or Eqs. (43) and (44). If the constraint equation corresponding to joint k and the joint variables are known, then Appendix A gives the procedure to find $\boldsymbol{E}_k$ and $\boldsymbol{D}_k$.

5.3 Simplification of Equations of RFDA to Standard Form. The coordinates $\tilde{\mathbf{y}}_k$ discussed in Step 1 are now defined as $\dot{\mathbf{y}}_k = [\widetilde{\boldsymbol{E}}_k \ \widetilde{\boldsymbol{D}}_k] \begin{bmatrix} \dot{\tilde{\mathbf{y}}}_{k_c} \\ \dot{\tilde{\mathbf{y}}}_{k_f} \end{bmatrix}$, where $\widetilde{\boldsymbol{E}}_k$ and $\widetilde{\boldsymbol{D}}_k$ are given by Eqs. (38) and (37) or Eqs. (43) and (44). $\widetilde{\boldsymbol{G}}_{k_c}$, $\widetilde{\boldsymbol{\nu}}_k$, $\boldsymbol{S}_k$, $\boldsymbol{a}_k$, $\widetilde{\boldsymbol{M}}_{k_c}$, $\widetilde{\boldsymbol{M}}_{k_f}$, $\widetilde{\boldsymbol{f}}_{k_c}$, and $\widetilde{\boldsymbol{f}}_{k_f}$, in Eqs. (21)–(23), assume the following forms: $\widetilde{\boldsymbol{G}}_{k_c} = (\boldsymbol{G}_k \widetilde{\boldsymbol{E}}_k)$, $\widetilde{\boldsymbol{\nu}}_k = \boldsymbol{\nu}_k$, $\boldsymbol{S}_k = (-(\boldsymbol{G}_k \widetilde{\boldsymbol{E}}_k)^{-1} \boldsymbol{Q}_k)$, $\boldsymbol{a}_k = (\boldsymbol{G}_k \widetilde{\boldsymbol{E}}_k)^{-1} \boldsymbol{\nu}_k$, $\widetilde{\boldsymbol{M}}_{k_c} = \widetilde{\boldsymbol{E}}_k^T \boldsymbol{M}_k \widetilde{\boldsymbol{E}}_k$, $\widetilde{\boldsymbol{M}}_{k_f} = \widetilde{\boldsymbol{D}}_k^T \boldsymbol{M}_k \widetilde{\boldsymbol{D}}_k$, $\widetilde{\boldsymbol{f}}_{k_c} = \widetilde{\boldsymbol{E}}_k^T (\boldsymbol{f}_k - \boldsymbol{M}_k (\dot{\widetilde{\boldsymbol{E}}}_k \dot{\tilde{\mathbf{y}}}_{k_c} + \widetilde{\boldsymbol{D}}_k \dot{\tilde{\mathbf{y}}}_{k_f}))$, and $\widetilde{\boldsymbol{f}}_{k_f} = \widetilde{\boldsymbol{D}}_k^T (\boldsymbol{f}_k - \boldsymbol{M}_k (\dot{\widetilde{\boldsymbol{E}}}_k \dot{\tilde{\mathbf{y}}}_{k_c} + \dot{\widetilde{\boldsymbol{D}}}_k \dot{\tilde{\mathbf{y}}}_{k_f}))$.

By substitution of the above terms in Eq. (28) and further simplification by using the expressions for $\widetilde{\boldsymbol{E}}_k$ and $\widetilde{\boldsymbol{D}}_k$ in Eqs. (38) and (37), we get

$$\begin{bmatrix} \boldsymbol{M}_j + \boldsymbol{Q}_k^T (\boldsymbol{G}_k \boldsymbol{M}_k^{-1} \boldsymbol{G}_k^T)^{-1} \boldsymbol{Q}_k & \mathbf{0} \\ \mathbf{0} & \boldsymbol{C}_f^T \boldsymbol{D}_k^T \boldsymbol{M}_k \boldsymbol{D}_k \boldsymbol{C}_f \end{bmatrix} \begin{bmatrix} \ddot{\mathbf{y}}_j \\ \ddot{\tilde{\mathbf{y}}}_{k_f} \end{bmatrix} + \begin{bmatrix} \boldsymbol{G}_j^T \\ \mathbf{0} \end{bmatrix} \boldsymbol{\lambda}_j = \begin{bmatrix} \boldsymbol{f}_j + \boldsymbol{Q}_k^T (\boldsymbol{G}_k \boldsymbol{M}_k^{-1} \boldsymbol{G}_k^T)^{-1} (\boldsymbol{\gamma}_k - \boldsymbol{G}_k \boldsymbol{M}_k^{-1} \boldsymbol{f}_k) \\ \boldsymbol{C}_f^T \boldsymbol{D}_k^T (\boldsymbol{f}_k - \boldsymbol{M}_k (\dot{\widetilde{\boldsymbol{E}}}_k \dot{\tilde{\mathbf{y}}}_{k_c} + \dot{\widetilde{\boldsymbol{D}}}_k \dot{\tilde{\mathbf{y}}}_{k_f})) \end{bmatrix} \tag{45}$$

In Eq. (C2) of Appendix C.2, we show that $\boldsymbol{Q}_k^T (\boldsymbol{G}_k \widetilde{\boldsymbol{E}}_k)^{-T} \widetilde{\boldsymbol{E}}_k^T \boldsymbol{M}_k (\dot{\widetilde{\boldsymbol{E}}}_k \dot{\tilde{\mathbf{y}}}_{k_c} + \dot{\widetilde{\boldsymbol{D}}}_k \dot{\tilde{\mathbf{y}}}_{k_f} + \widetilde{\boldsymbol{E}}_k (\boldsymbol{S}_k \dot{\mathbf{y}}_j + \dot{\boldsymbol{a}}_k)) = \boldsymbol{Q}_k^T (\boldsymbol{G}_k \boldsymbol{M}_k^{-1} \boldsymbol{G}_k^T)^{-1} \boldsymbol{\gamma}$. The rest of the simplifications in Eq. (45) is straightforward.

In Eqs. (43) and (44), we had obtained alternate expression for $\widetilde{\boldsymbol{E}}_k$ and $\widetilde{\boldsymbol{D}}_k$, in terms of $\boldsymbol{E}_k$ and $\boldsymbol{D}_k$ of Eq. (35). In Appendix A, one way to obtain $\boldsymbol{E}_k$ and $\boldsymbol{D}_k$ is given (see Eq. (A3)), along with its relation with $\boldsymbol{B}_k$, $\boldsymbol{H}_k$, and $\boldsymbol{c}_k$ (see Eq. (A4). Using Eqs. (43), (44), (A3), and (A4), we get yet another simplification as

$$\begin{bmatrix} \boldsymbol{M}_j + \boldsymbol{B}_k^T (\boldsymbol{I} - \boldsymbol{M}_k \boldsymbol{H}_k (\boldsymbol{H}_k^T \boldsymbol{M}_k \boldsymbol{H}_k)^{-1} \boldsymbol{H}_k^T) \boldsymbol{M}_k \boldsymbol{B}_k & \mathbf{0} \\ \mathbf{0} & \boldsymbol{D}_k^T \boldsymbol{M}_k \boldsymbol{D}_k \end{bmatrix} \begin{bmatrix} \ddot{\mathbf{y}}_j \\ \ddot{\tilde{\mathbf{y}}}_{k_f} \end{bmatrix} + \begin{bmatrix} \boldsymbol{G}_j^T \\ \mathbf{0} \end{bmatrix} \boldsymbol{\lambda}_j = \begin{bmatrix} \boldsymbol{f}_j + \boldsymbol{B}_k^T (\boldsymbol{I} - \boldsymbol{M}_k \boldsymbol{H}_k (\boldsymbol{H}_k^T \boldsymbol{M}_k \boldsymbol{H}_k)^{-1} \boldsymbol{H}_k^T) (\boldsymbol{f}_k - \boldsymbol{M}_k \boldsymbol{d}_k) \\ \boldsymbol{D}_k^T (\boldsymbol{f}_k - \boldsymbol{M}_k (\dot{\widetilde{\boldsymbol{E}}}_k \dot{\tilde{\mathbf{y}}}_{k_c} + \dot{\widetilde{\boldsymbol{D}}}_k \dot{\tilde{\mathbf{y}}}_{k_f}) \end{bmatrix} \tag{46}$$

where $\boldsymbol{d}_k = \dot{\boldsymbol{B}}_k \dot{\mathbf{y}}_j + \dot{\boldsymbol{H}}_k \dot{\boldsymbol{q}}_k + \dot{\boldsymbol{c}}_k$, with $\boldsymbol{B}_k$, $\boldsymbol{H}_k$, and $\boldsymbol{c}_k$ as given in Eq. (A4). Details of simplification of Eq. (46) are presented in Appendix C.3.

Note that if j and k (k treated as a terminal node) are the only two bodies of the multibody system, then Eq. (8), with Eqs. (9) and (10) used for $\hat{\boldsymbol{M}}_j$ and $\hat{\boldsymbol{f}}_j$, is the same as the $\mathbf{y}_j$ part of Eq. (45). Similarly, Eq. (8), with Eqs. (11) and (12) used for $\hat{\boldsymbol{M}}_j$ and $\hat{\boldsymbol{f}}_j$, is the same as the $\mathbf{y}_j$ part of Eq. (46). We recall that Eqs. (9) and (10) are presented in Ref. [7], and Eqs. (11) and (12) are presented in Refs. [7,3,2]. Thus, we have reduced the equations of RFDA obtained by our method into standard form found in literature.

5.4 Visualization of Coordinates for Planar Revolute Joint Example

5.4.1 Coordinates of Step 1. For the planar-revolute joint system, using Eq. (36) and $\boldsymbol{M}_k$ given in Sec. 3.2.1, $\widetilde{\boldsymbol{A}}_k$ of Eq. (42) evaluates to

$$\begin{bmatrix} -\dfrac{m_k (\sin(\phi_k) s_{k_x}'^{P_k} + \cos(\phi_k) s_{k_y}'^{P_k})}{J_k + m_k ((s_{k_x}'^{P_k})^2 + (s_{k_y}'^{P_k})^2)} & \dfrac{m_k (\cos(\phi_k) s_{k_x}'^{P_k} - \sin(\phi_k) s_{k_y}'^{P_k})}{J_k + m_k ((s_{k_x}'^{P_k})^2 + (s_{k_y}'^{P_k})^2)} \end{bmatrix} \tag{47}$$

Let the two elements in the above matrix be represented by $\tilde{\alpha}$ and $\tilde{\beta}$.

The coordinate $\tilde{\mathbf{y}}_k$ of Step 1 is the same as the coordinate $\breve{\mathbf{y}}_k$, defined in Eq. (39), except that α and β are replaced with $\tilde{\alpha}$ and $\tilde{\beta}$. It turns out that the equation (after replacing with $\tilde{\alpha}$ and $\tilde{\beta}$) is nonintegrable. Hence, $\tilde{\mathbf{y}}_k$ is a pseudocoordinate for the system. We can visualize it by examining the changes that body k undergoes, due to small changes in the components of $\tilde{\mathbf{y}}_k$. Figures 4(d)–4(f)

[6] Appendix A shows how to find such an $\boldsymbol{E}_k$ and $\boldsymbol{D}_k$.

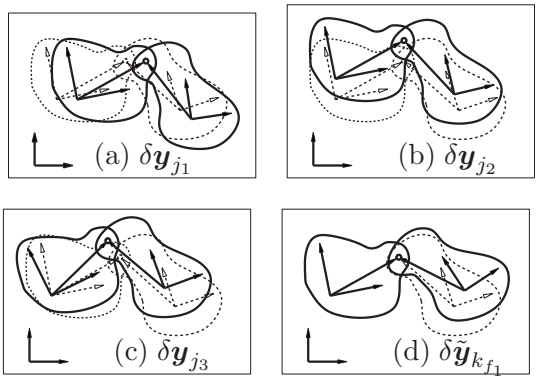

Fig. 5 Changes in system due to small changes in the coordinate $[\boldsymbol{y}_j^T \ \tilde{\boldsymbol{y}}_{k_f}^T]^T$ defined in Eq. (48)

hold good here also. The rotation in Fig. 4(*d*) is $\tilde{\alpha}$ times the translation along the *x*-axis. The rotation in Fig. 4(*e*) is $\tilde{\beta}$ times the translation along the *y*-axis.

5.4.2 Coordinates of Step 2. Coordinates of RFDA. Equation (31) gives the relation between $\boldsymbol{y}_k$ and $[\tilde{\boldsymbol{y}}_{k_c}^T \ \tilde{\boldsymbol{y}}_{k_f}^T]^T$. Equation (26) gives the relation between $[\boldsymbol{y}_j^T \ \tilde{\boldsymbol{y}}_{k_c}^T \ \tilde{\boldsymbol{y}}_{k_f}^T]^T$ and $[\boldsymbol{y}_j^T \ \tilde{\boldsymbol{y}}_{k_f}^T]^T$. These two relations could be composed to obtain the relation between $[\boldsymbol{y}_j^T \ \boldsymbol{y}_k^T]^T$ and $[\boldsymbol{y}_j^T \ \tilde{\boldsymbol{y}}_{k_f}^T]^T$. For the planar-revolute joint example, such a relation assumes the following form:

$$\begin{bmatrix} \dot{\boldsymbol{y}}_j \\ \dot{\boldsymbol{y}}_k \end{bmatrix} = \begin{bmatrix} \boldsymbol{I} & \boldsymbol{0} \\ -(\boldsymbol{E}_k + \boldsymbol{D}_k[\tilde{\alpha} \quad \tilde{\beta}])\boldsymbol{Q}_k & \boldsymbol{D}_k \end{bmatrix} \begin{bmatrix} \dot{\boldsymbol{y}}_j \\ \dot{\tilde{\boldsymbol{y}}}_{k_f} \end{bmatrix} \tag{48}$$

where $[\tilde{\alpha} \quad \tilde{\beta}] = \tilde{\boldsymbol{A}}$ is given in Eq. (47), $\boldsymbol{E}_k$ and $\boldsymbol{D}_k$ in Eq. (36), and $\boldsymbol{Q}_k$ in Sec. 3.2.1.

To get a feel for the coordinates of RFDA, Figs. 5(*a*)–5(*d*) show (highly exaggerated) displacement of the system due to infinitesimal changes in each of the components of $[\boldsymbol{y}_j^T \ \tilde{\boldsymbol{y}}_{k_f}^T]^T$. Also, to see how different these coordinates are from standard coordinates, in Figs. 6(*a*)–6(*d*), we have shown the exaggerated displacement of the system due to infinitesimal change in each of the components of $\bar{\boldsymbol{y}}$ defined in Eq. (20).

The comparison between the two coordinates is summarized as follows: If, $[\delta\bar{\boldsymbol{y}}_1 \ \delta\bar{\boldsymbol{y}}_2 \ \delta\bar{\boldsymbol{y}}_3 \ \delta\bar{\boldsymbol{y}}_4]^T = [\delta\boldsymbol{y}_{j_1} \ \delta\boldsymbol{y}_{j_2} \ \delta\boldsymbol{y}_{j_3} \ \delta\tilde{\boldsymbol{y}}_{k_{f_1}}]^T$, then we arrive at the following.

1. The displacement of body *j* is the same in the corresponding figures for the two coordinates.
2. The corresponding figures differ only in the rotation that the body *k* undergoes about the point P^k. The rotations of body *k* in Figs. 5(*a*)–5(*d*) are $\tilde{\alpha}\delta\boldsymbol{y}_{j_1}$, $\tilde{\boldsymbol{\beta}}\delta\boldsymbol{y}_{j_2}$, $((-\boldsymbol{S}'^{P_k}_{k_x} s\phi_k - \boldsymbol{S}'^{P_k}_{k_y} c\phi_k)\tilde{\alpha} + (\boldsymbol{S}'^{P_k}_{k_x} c\phi_k - \boldsymbol{S}'^{P_k}_{k_y} s\phi_k)\tilde{\beta})\delta\boldsymbol{y}_{j_3}$, and $\delta\tilde{\boldsymbol{y}}_{k_{f_1}}$, respectively ($s\phi_k$ represent $\sin\phi_k$ and $c\phi_k$ represent $\cos\phi_k$). The rotations in Figs. 6(*a*)–6(*d*) are 0, 0, $\delta\tilde{\boldsymbol{y}}_3$, and $\delta\tilde{\boldsymbol{y}}_4$, respectively.

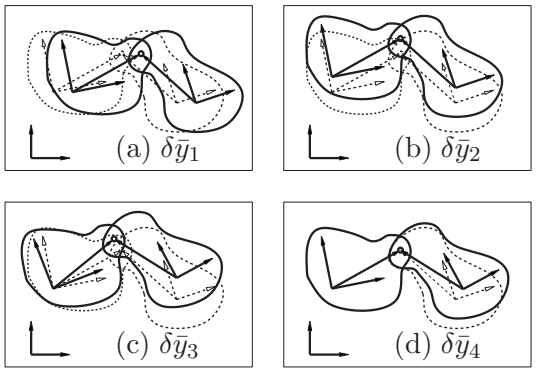

Fig. 6 Changes in system due to small changes in the coordinate $\bar{\boldsymbol{y}}$, defined in equation (20)

In this section, we defined the coordinates of Step 1 by the relation given in Eq. (31) and gave explicit expressions for $\tilde{\boldsymbol{E}}_k$ and $\tilde{\boldsymbol{D}}_k$ using two methods. The first method leads to Eqs. (37) and (38), while the second method resulted in Eqs. (43) and (44). Kinematic observation was used to motivate the second method. We further simplified equations of RFDA to the form generally found in literature. We illustrated the $\tilde{\boldsymbol{y}}_k$ coordinates of Step 1, and the coordinates of RFDA $[\boldsymbol{y}_j^T \ \tilde{\boldsymbol{y}}_{k_f}^T]^T$, using planar-revolute joint example.

6 Generalization to All Nodes

Consider any nonterminal node, *j*, of the branched multibody system. Suppose that for every child, *k*, of node *j*, there are coordinates $[\boldsymbol{y}_k^T \ \boldsymbol{\xi}_k^T]^T$, having the following properties.

1. $[\boldsymbol{y}_k^T \ \boldsymbol{\xi}_k^T]^T$ describes the system consisting of node *k* and all its descendants. In other words, the relation between $[\boldsymbol{y}_k^T \ \boldsymbol{\xi}_k^T]^T$ and absolute coordinates of *k* and its descendants is of the form
$$\begin{bmatrix} \dot{\boldsymbol{y}}_k \\ \begin{bmatrix} \dot{\boldsymbol{y}}_{h(k,1)} \\ \vdots \\ \dot{\boldsymbol{y}}_{h(k,d_k)} \end{bmatrix} \end{bmatrix} = \begin{bmatrix} \boldsymbol{I} & \boldsymbol{0} \\ \boldsymbol{P}_k & \boldsymbol{R}_k \end{bmatrix} \begin{bmatrix} \dot{\boldsymbol{y}}_k \\ \dot{\boldsymbol{\xi}}_k \end{bmatrix} + \begin{bmatrix} \boldsymbol{0} \\ \bar{\boldsymbol{\omega}}_k \end{bmatrix}, \quad \forall\, k{:}j = \mathcal{P}(k)$$
where $h(i,p)$ is the *p*th descendant of node *i*, with the descendants arranged in some order.[7] ($\mathcal{P}(i)$ denotes parent index of *i* and $k{:}j = \mathcal{P}(k)$ denotes *k* such that *j* is its parent.) An example for the above equation is Eq. (48), where there is a single descendant node.
2. Any value for $[\dot{\boldsymbol{y}}_k^T \ \dot{\boldsymbol{\xi}}_k^T]^T$ is consistent with all the joint constraints among body *k* and its descendants. The only constraint on the coordinates $[\dot{\boldsymbol{y}}_k^T \ \dot{\boldsymbol{\xi}}_k^T]^T$ is due to joint between body *k* and body *j*, given by
$$\boldsymbol{Q}_k\dot{\boldsymbol{y}}_j + \boldsymbol{G}_k\dot{\boldsymbol{y}}_k + [\boldsymbol{0}]\dot{\boldsymbol{\xi}}_k = \boldsymbol{\nu}_k, \quad \forall\, k{:}j = \mathcal{P}(k) \tag{49}$$
3. The equation of motion in terms of $[\boldsymbol{y}_k^T \ \boldsymbol{\xi}_k^T]^T$, for the system consisting of body *k* and all its descendants, is of the form
$$\begin{bmatrix} \hat{\boldsymbol{M}}_k & \boldsymbol{0} \\ \boldsymbol{0} & \boldsymbol{\Lambda}_k \end{bmatrix} \begin{bmatrix} \ddot{\boldsymbol{y}}_k \\ \ddot{\boldsymbol{\xi}}_k \end{bmatrix} + \begin{bmatrix} \boldsymbol{G}_k^T\boldsymbol{\lambda}_k \\ \boldsymbol{0} \end{bmatrix} = \begin{bmatrix} \hat{\boldsymbol{f}}_k \\ \boldsymbol{\eta}_k \end{bmatrix}, \quad \forall\, k{:}j = \mathcal{P}(k) \tag{50}$$
then we claim that we can find coordinate $[\boldsymbol{y}_j^T \ \boldsymbol{\xi}_j^T]^T$, which has the same properties listed above, i.e., (1) $[\boldsymbol{y}_j^T \ \boldsymbol{\xi}_j^T]^T$ describes body *j* and all its descendants, (2) the coordinates are consistent with all the joint constraints between node *j* and its descendants, and (3) mass matrix with respect to the coordinates is block diagonal.

Proof. Find $\tilde{\boldsymbol{E}}_k$ and $\tilde{\boldsymbol{D}}_k$ (with $[\tilde{\boldsymbol{E}}_k \ \tilde{\boldsymbol{D}}_k]$ being nonsingular) that satisfy Conditions 1 and 2 of Sec. 5.1, with $\boldsymbol{M}_k$ replaced with $\hat{\boldsymbol{M}}_k$. The only property of $\boldsymbol{M}_k$ used in deriving $\tilde{\boldsymbol{E}}_k$ and $\tilde{\boldsymbol{D}}_k$ in Sec. 5.2

[7] Descendants of node *i* can always be arranged in a sequence. For example, the descendants of Node 2 in Fig. 1 can be arranged as 4, 5, 7, 10, 11, and 12. For this order, $h(2,3) = 7$.

was positive definiteness of $\boldsymbol{M}_k$. $\hat{\boldsymbol{M}}_k$ is diagonal block of the positive definite matrix given in Eq. (50). Hence, $\hat{\boldsymbol{M}}_k$ is also positive definite. Thus, we can use the theory in Sec. 5.2 to find $\tilde{\boldsymbol{E}}_k$ and $\tilde{\boldsymbol{D}}_k$, even after the replacement.

Define new coordinates for the system consisting of node k and its descendants, as

$$\begin{bmatrix} \dot{\boldsymbol{y}}_k \\ \dot{\boldsymbol{\xi}}_k \end{bmatrix} = \begin{bmatrix} \tilde{\boldsymbol{E}}_k & \tilde{\boldsymbol{D}}_k & \boldsymbol{0} \\ \boldsymbol{0} & \boldsymbol{0} & \boldsymbol{I} \end{bmatrix} \begin{bmatrix} \dot{\tilde{\boldsymbol{y}}}_{k_c} \\ \dot{\tilde{\boldsymbol{y}}}_{k_f} \\ \dot{\boldsymbol{\xi}}_k \end{bmatrix}, \quad \forall\, k{:}j = \mathcal{P}(k) \tag{51}$$

Since $[\tilde{\boldsymbol{E}}_k\ \tilde{\boldsymbol{D}}_k]$ is nonsingular, the above transformation as a whole is nonsingular.

Under the transformation from $[\boldsymbol{y}_k^T\ \boldsymbol{\xi}_k^T]^T$ coordinates to $[\tilde{\boldsymbol{y}}_{k_c}^T\ \tilde{\boldsymbol{y}}_{k_f}^T\ \boldsymbol{\xi}_k^T]^T$, the only constraint equation involving $[\boldsymbol{y}_k^T\ \boldsymbol{\xi}_k^T]^T$, i.e., Eq. (49), becomes (see Eq. (B1))

$$\boldsymbol{Q}_k\dot{\boldsymbol{y}}_j + \boldsymbol{G}_k\tilde{\boldsymbol{E}}_k\dot{\tilde{\boldsymbol{y}}}_{k_c} + [\boldsymbol{0}]\dot{\tilde{\boldsymbol{y}}}_{k_f} + [\boldsymbol{0}]\dot{\boldsymbol{\xi}}_k = \boldsymbol{\nu}_k, \quad \forall\, k{:}j = \mathcal{P}(k) \tag{52}$$

(from Condition 1 of Sec. 5, $\boldsymbol{G}_k\tilde{\boldsymbol{D}}_k = 0$). This is the only constraint equation involving $[\tilde{\boldsymbol{y}}_{k_c}^T\ \tilde{\boldsymbol{y}}_{k_f}^T\ \boldsymbol{\xi}_k^T]^T$. Hence, both $\tilde{\boldsymbol{y}}_{k_f}$ and $\dot{\boldsymbol{\xi}}_k$ are kinematically unconstrained. $\dot{\tilde{\boldsymbol{y}}}_{k_c}$ is determined by $\dot{\boldsymbol{y}}_j$ by the following equation:

$$\dot{\tilde{\boldsymbol{y}}}_{k_c} = \boldsymbol{S}_k\dot{\boldsymbol{y}}_j + \boldsymbol{a}_k, \quad \forall\, k{:}j = \mathcal{P}(k) \tag{53}$$

where $\boldsymbol{S}_k = -(\boldsymbol{G}_k\tilde{\boldsymbol{E}}_k)^{-1}\boldsymbol{Q}_k$, and $\boldsymbol{a}_k = (\boldsymbol{G}_k\tilde{\boldsymbol{E}}_k)^{-1}\boldsymbol{\nu}_k$. The above equation follows from Eq. (52). The equation of motion of the system consisting of node k and its descendants, written in terms of coordinates $[\tilde{\boldsymbol{y}}_{k_c}^T\ \tilde{\boldsymbol{y}}_{k_f}^T\ \boldsymbol{\xi}_k^T]^T$, becomes (see Eq. (B3))

$$\begin{bmatrix} \tilde{\boldsymbol{M}}_{k_c} & \boldsymbol{0} \\ \boldsymbol{0} & \tilde{\boldsymbol{M}}_{k_f} \end{bmatrix} \begin{bmatrix} \ddot{\tilde{\boldsymbol{y}}}_{k_c} \\ \ddot{\boldsymbol{\xi}}_k \end{bmatrix} = \begin{bmatrix} \tilde{\boldsymbol{f}}_{k_c} \\ \tilde{\boldsymbol{\eta}}_k \end{bmatrix} + \begin{bmatrix} (\boldsymbol{G}_k\tilde{\boldsymbol{E}}_k)^T\boldsymbol{\lambda}_k \\ \boldsymbol{0} \end{bmatrix}, \quad \forall\, k{:}j = \mathcal{P}(k) \tag{54}$$

where $\boldsymbol{M}_{k_c} = \tilde{\boldsymbol{E}}_k^T\hat{\boldsymbol{M}}_k\tilde{\boldsymbol{E}}_k$, $\tilde{\boldsymbol{M}}_{k_f} = \begin{bmatrix} \tilde{\boldsymbol{D}}_k^T\hat{\boldsymbol{M}}_k\tilde{\boldsymbol{D}}_k & \boldsymbol{0} \\ \boldsymbol{0} & \boldsymbol{\Lambda}_k \end{bmatrix}$, $\tilde{\boldsymbol{\xi}}_k = \begin{bmatrix} \tilde{\boldsymbol{y}}_{k_f} \\ \boldsymbol{\xi}_k \end{bmatrix}$,

$$\tilde{\boldsymbol{f}}_{k_c} = \tilde{\boldsymbol{E}}_k^T(\hat{\boldsymbol{f}}_k - \hat{\boldsymbol{M}}_k(\dot{\tilde{\boldsymbol{E}}}_k\dot{\tilde{\boldsymbol{y}}}_{k_c} + \dot{\tilde{\boldsymbol{D}}}_k\dot{\tilde{\boldsymbol{y}}}_{k_f})),$$

and

$$\tilde{\boldsymbol{\eta}}_k = \begin{bmatrix} \tilde{\boldsymbol{D}}_k^T(\hat{\boldsymbol{f}}_k - \hat{\boldsymbol{M}}_k(\dot{\tilde{\boldsymbol{E}}}_k\dot{\tilde{\boldsymbol{y}}}_{k_c} + \dot{\tilde{\boldsymbol{D}}}_k\dot{\tilde{\boldsymbol{y}}}_{k_f})) \\ \boldsymbol{\eta}_k \end{bmatrix}$$

Let $g(i,p)$ denote the pth child of node i, with the children of node i arranged in some order. Also, let h_i represent the number of children of node i. Then, the coordinates

$$[\boldsymbol{y}_j^T\ \ \tilde{\boldsymbol{y}}_{g(j,1)_c}^T\ \ \tilde{\boldsymbol{\xi}}_{g(j,1)}^T\ \ \cdots\ \ \tilde{\boldsymbol{y}}_{g(j,h_j)_c}^T\ \ \tilde{\boldsymbol{\xi}}_{g(j,h_j)}^T]^T$$

describe node j and all its descendants. The constraints on these coordinates are Eq. (52), and the constraint due to joint between body j and its parent, i.e., $\boldsymbol{Q}_j\dot{\boldsymbol{y}}_{\mathcal{P}(j)} + \boldsymbol{G}_j\dot{\boldsymbol{y}}_j = \boldsymbol{\nu}_j$.

Using relation (53), we obtain a smaller coordinate $[\boldsymbol{y}_j^T\ \tilde{\boldsymbol{\xi}}_{g(j,1)}^T \cdots \tilde{\boldsymbol{\xi}}_{g(j,h_j)}^T]^T$ by the following transformation:

$$\begin{bmatrix} \dot{\boldsymbol{y}}_j \\ \dot{\tilde{\boldsymbol{y}}}_{g(j,1)_c} \\ \dot{\tilde{\boldsymbol{\xi}}}_{g(j,1)} \\ \vdots \\ \dot{\tilde{\boldsymbol{y}}}_{g(j,h_j)_c} \\ \dot{\tilde{\boldsymbol{\xi}}}_{g(j,h_j)} \end{bmatrix} = \begin{bmatrix} \boldsymbol{I} & \boldsymbol{0} & \cdots & \boldsymbol{0} \\ \boldsymbol{S}_{g(j,1)} & \boldsymbol{0} & \cdots & \boldsymbol{0} \\ \boldsymbol{0} & \boldsymbol{I} & \cdots & \boldsymbol{0} \\ \vdots & \vdots & \ddots & \vdots \\ \boldsymbol{S}_{g(j,h_j)} & \boldsymbol{0} & \cdots & \boldsymbol{0} \\ \boldsymbol{0} & \boldsymbol{0} & \cdots & \boldsymbol{I} \end{bmatrix} \begin{bmatrix} \dot{\boldsymbol{y}}_j \\ \dot{\tilde{\boldsymbol{\xi}}}_{g(j,1)} \\ \vdots \\ \dot{\tilde{\boldsymbol{\xi}}}_{g(j,h_j)} \end{bmatrix} + \begin{bmatrix} \boldsymbol{0} \\ \boldsymbol{a}_{g(j,1)} \\ \boldsymbol{0} \\ \vdots \\ \boldsymbol{a}_{g(j,h_j)} \\ \boldsymbol{0} \end{bmatrix} \tag{55}$$

From the expression of $\boldsymbol{S}_k$ and $\boldsymbol{a}_k$ given in Eq. (53), it is easy to see that constraint equation (52) becomes redundant under the new coordinates defined above. Let $\boldsymbol{\xi}_j = [\tilde{\boldsymbol{\xi}}_{g(j,1)}^T \cdots \tilde{\boldsymbol{\xi}}_{g(j,h_j)}^T]^T$. Then, the only constraint equation on $[\boldsymbol{y}_j^T\ \boldsymbol{\xi}_j^T]^T$ coordinates is due to joint between j and its parent can be written as

$$\boldsymbol{Q}_j\dot{\boldsymbol{y}}_{\mathcal{P}(j)} + \boldsymbol{G}_j\dot{\boldsymbol{y}}_j + \boldsymbol{0}\dot{\boldsymbol{\xi}}_j = \boldsymbol{\nu}_j \tag{56}$$

Analogous to Eq. (28), the equation of motion in terms of $[\boldsymbol{y}_j^T\ \boldsymbol{\xi}_j^T]^T$ is obtained as follows.

$$\begin{bmatrix} \boldsymbol{M}_j + \sum_{k:\mathcal{P}(k)=j} \boldsymbol{S}_k^T\tilde{\boldsymbol{M}}_{k_c}\boldsymbol{S}_k & \boldsymbol{0} \\ \boldsymbol{0} & \Lambda_j \end{bmatrix} \begin{bmatrix} \ddot{\boldsymbol{y}}_j \\ \ddot{\boldsymbol{\xi}}_j \end{bmatrix} + \begin{bmatrix} \boldsymbol{G}_j^T\boldsymbol{\lambda}_j \\ \boldsymbol{0} \end{bmatrix} = \begin{bmatrix} \boldsymbol{f}_{d_j} \\ \boldsymbol{\eta}_j \end{bmatrix}$$

$$\text{where } \boldsymbol{\Lambda}_j = \begin{bmatrix} \tilde{\boldsymbol{M}}_{g(j,1)_f} & \cdots & \boldsymbol{0} \\ \vdots & \ddots & \vdots \\ \boldsymbol{0} & \cdots & \tilde{\boldsymbol{M}}_{g(j,h_j)_f} \end{bmatrix}, \quad \boldsymbol{\eta}_j = \begin{bmatrix} \tilde{\boldsymbol{\eta}}_{g(j,1)} \\ \vdots \\ \tilde{\boldsymbol{\eta}}_{g(j,h_j)} \end{bmatrix} \tag{57}$$

and

$$\boldsymbol{f}_{d_j} = \boldsymbol{f}_j + \sum_{k:\mathcal{P}(k)=j} (\boldsymbol{S}_k^T\tilde{\boldsymbol{M}}_{k_c}\boldsymbol{b}_k)$$

Thus, associated with node j, we have found the coordinates $[\boldsymbol{y}_j^T\ \boldsymbol{\xi}_j^T]^T$ having the required properties and the proof is complete.

If k is a terminal node, then the coordinate y_k trivially satisfies all the properties mentioned in the claim at the beginning of this section. Now, from the result obtained above, we can recursively obtain $[\boldsymbol{y}_j^T\ \boldsymbol{\xi}_j^T]^T$ coordinates for all nodes of the tree structure.

Thus, associated with each node of the tree structure, we can obtain $[\boldsymbol{y}_j^T\ \boldsymbol{\xi}_j^T]^T$ coordinate, which has the constraint equation as in Eq. (56) and equation of motion as in Eq. (57). The row of matrix equation (57) associated with $\boldsymbol{y}_j$ is the first part of Eq. (8). The constraint equation (56) is the second part of the equation. So we have obtained equations of RFDA, based on finding coordinates of RFDA, $[\boldsymbol{y}_j^T\ \boldsymbol{\xi}_j^T]^T$, for every node of the tree.

Analogous to simplification from Eq. (28) to Eq. (45) or Eq. (46), we can show that the row of matrix equation (57) associated with $\boldsymbol{y}_j$ simplifies to $\hat{\boldsymbol{M}}_j + \boldsymbol{G}_j^T\boldsymbol{\lambda}_j = \hat{\boldsymbol{f}}_j$, with $\hat{\boldsymbol{M}}_j$ and $\hat{f}_j$ as given in Eqs. (9) and (10) or Eqs. (11) and (12).

7 Conclusions

In this paper, we derive equations of RFDA using a new method. The method has two parts: (1) finding coordinates of RFDA and (2) writing equations of motion in terms of it and extracting relevant portion of it as equations of RFDA. In Sec. 4, the method has been described for a simple two noded tree structure, in four steps, and the nontrivial coordinate of Step 1 has been worked out in Sec. 5. Steps 1 and 2 constitute the procedure to find the coordinates of RFDA. Steps 3 and 4 are about writing down equation of motion and extracting relevant portion of it.

The crux of this paper lies in Sec. 5.2, where coordinates required for Step 1 are defined. Two different methods of finding the

coordinates have been explained. We use linear algebraic arguments, motivated by kinematic intuition, to get the coordinates. The originality of this paper lies here.

We simplified the relevant portion of its equation of motion, in terms of coordinates of RFDA, to standard form in Eqs. (45) and (46). In Sec. 6, our approach based on coordinates of RFDA was extended to general tree structure. Different nodes have different coordinates of RFDA associated with them, which describe the rigid bodies of the node and all its descendants. The coordinates of RFDA get defined recursively, as in Eq. (55) and equations of motion with respect to them are as in Eq. (57).

This derivation conclusively shows that equations of RFDA are actually part of equations of motion. More importantly, this derivation gives coordinates associated with equation of motion, as well as left out part of equations of motion. These are significant insights into RFDA, an important algorithm in multibody dynamics.

Appendix A: Coordinate of Child Body in Terms of Coordinate of Parent and Joint Variables

Consider body j and k with a joint k between them. The constraint is represented as $\boldsymbol{Q}_k\dot{\boldsymbol{y}}_j+\boldsymbol{G}_k\dot{\boldsymbol{y}}_k=\boldsymbol{\gamma}_k$. If there are p_{k_c} rows in the constraint equation and p_k represent the degree of freedom of unconstrained body k, then one can associate joint variable $\boldsymbol{q}_k$ of dimension $(p_k-p_{k_c})$. For example, if the kth joint is a revolute joint, then $\boldsymbol{q}_k=[\theta_k]$, where θ_k is a joint rotation angle. If $\boldsymbol{q}_k$ is constrained as a function of time, say, $\dot{\boldsymbol{q}}=\boldsymbol{g}(t)$, then such a constraint is called driving constraint. Driving constraints have the form[8]

$$\bar{\boldsymbol{Q}}_{k_d}\dot{\boldsymbol{y}}_j+\bar{\boldsymbol{G}}_{k_d}\dot{\boldsymbol{y}}_k=\bar{\boldsymbol{\nu}}_{k_d}+\mathfrak{h}_{k_d}\dot{\boldsymbol{q}}_k \tag{A1}$$

Ref. [8] catalogs driving constraint and corresponding Jacobians for standard joints.) We consider only cases where $\mathfrak{H}_{k_d}$ is invertible.

For example, consider the planar-revolute joint example given in Fig. 3. The constraint equation is $\boldsymbol{Q}_k\dot{\boldsymbol{y}}_j+\boldsymbol{G}_k\dot{\boldsymbol{y}}_k=\boldsymbol{\nu}_k$, where $\dot{\boldsymbol{y}}_j$, $\dot{\boldsymbol{y}}_k$, $\boldsymbol{Q}_k$, and $\boldsymbol{G}_k$ are given in Sec. 3.2.1, and $\boldsymbol{\nu}_k=[0\ 0]^T$. The joint driving constraint can be written as $\phi_k-\phi_j=\theta_k(t)$, where θ_k is the joint angle. For this driving constraint, $\overline{\boldsymbol{Q}}_{k_d}=[0\ 0\ -1]$, $\overline{\boldsymbol{G}}_{k_d}=[0\ 0\ 1]$, $\overline{\boldsymbol{V}}_{k_d}=[0]$, and $\mathfrak{h}_{k_d}=[1]$.

Assume that driving constraints are present in the system so that we can write the constraint equation as

$$\begin{bmatrix}\boldsymbol{Q}_k\\ \boldsymbol{Q}_{k_d}\end{bmatrix}\dot{\boldsymbol{y}}_j+\begin{bmatrix}\boldsymbol{G}_k\\ \boldsymbol{G}_{k_d}\end{bmatrix}\dot{\boldsymbol{y}}_k=\begin{bmatrix}\boldsymbol{\nu}_k\\ \boldsymbol{\nu}_{k_d}\end{bmatrix}+\begin{bmatrix}\boldsymbol{0}\\ \dot{\boldsymbol{q}}_k\end{bmatrix} \tag{A2}$$

where $\boldsymbol{Q}_{k_d}=\mathfrak{h}_{k_d}^{-1}\overline{\boldsymbol{Q}}_{k_d}$, $\boldsymbol{G}_{k_d}=\mathfrak{H}_{k_d}^{-1}\overline{\boldsymbol{G}}_{k_d}$, and $\boldsymbol{\nu}_{k_d}=\mathfrak{H}_{k_d}^{-1}\overline{\boldsymbol{\nu}}_{k_d}$. We restrict ourselves to the cases where $\begin{bmatrix}\boldsymbol{G}_k\\ \boldsymbol{G}_{k_d}\end{bmatrix}$ is invertible. Let $\begin{bmatrix}\boldsymbol{G}_k\\ \boldsymbol{G}_{k_d}\end{bmatrix}^{-1}=[\boldsymbol{E}_k\ \boldsymbol{D}_k]$, so that

$$\begin{bmatrix}\boldsymbol{G}_k\\ \boldsymbol{G}_{k_d}\end{bmatrix}[\boldsymbol{E}_k\quad \boldsymbol{D}_k]=\begin{bmatrix}\boldsymbol{G}_k\boldsymbol{E}_k & \boldsymbol{G}_k\boldsymbol{D}_k\\ \boldsymbol{G}_{k_d}\boldsymbol{E}_k & \boldsymbol{G}_{k_d}\boldsymbol{D}_k\end{bmatrix}=\begin{bmatrix}\boldsymbol{I}_{p_{k_c}\times p_{k_c}} & \boldsymbol{0}_{p_{k_c}\times p_{k_f}}\\ 0_{p_{k_f}\times p_{k_c}} & \boldsymbol{I}_{p_{k_f}\times p_{k_f}}\end{bmatrix} \tag{A3}$$

Multiplying Eq. (A2) with $[\boldsymbol{G}_k\ \boldsymbol{G}_{k_d}]^{-1}$ and using Eq. (A3), we get

$$\dot{\boldsymbol{y}}_k=\boldsymbol{B}_k\dot{\boldsymbol{y}}_j+\boldsymbol{H}_k\dot{\boldsymbol{q}}_k+\boldsymbol{c}_k \tag{A4}$$

where $\boldsymbol{B}_k=-(\boldsymbol{E}_k\boldsymbol{Q}_k+\boldsymbol{D}_k\boldsymbol{Q}_{k_d})$, $\boldsymbol{H}_k=\boldsymbol{D}_k$, and $\boldsymbol{c}_k=(\boldsymbol{E}_k\boldsymbol{\nu}_k+\boldsymbol{D}_k\boldsymbol{\nu}_{k_d})$. Equation (A4) essentially gives coordinate of body k in terms of coordinate of parent body j and joint coordinate.

[8] If the driving constraint is holonomic, then the constraint can be written as $\bar{\boldsymbol{\Phi}}(\boldsymbol{y}_j,\boldsymbol{y}_k,\boldsymbol{q}_k(t),t)=\boldsymbol{0}$. Its differentiation gives $(\boldsymbol{\partial}\bar{\boldsymbol{\Phi}}/\boldsymbol{\partial y}_j)\dot{\boldsymbol{y}}_j+(\boldsymbol{\partial}\bar{\boldsymbol{\Phi}}/\boldsymbol{\partial y}_k)\dot{\boldsymbol{y}}_k=-\partial\bar{\boldsymbol{\Phi}}/\partial t-(\partial\bar{\boldsymbol{\Phi}}/\boldsymbol{\partial q}_k)\dot{\boldsymbol{k}}_k$. The above equation is the motivation for Eq. (A1).

Appendix B: Equations of Motion and Change of Coordinates

Let $\boldsymbol{u}$ be coordinates describing a rigid multibody system. There could be constraints on $\dot{\boldsymbol{u}}$. We consider only those constraints that could be expressed in the form $\boldsymbol{\Psi}\dot{\boldsymbol{u}}=\boldsymbol{\nu}$ with $\boldsymbol{\Psi}$ having full row rank. Application of generalized d'Alembert's principle (see, for example, Ref. [10]) to the multibody system leads to equation of motion of form $\boldsymbol{M}_u\ddot{\boldsymbol{u}}=\boldsymbol{f}_u-\boldsymbol{\Psi}^T\boldsymbol{\lambda}$. $\boldsymbol{M}_u$ is a function of $\boldsymbol{u}$ and t. $\boldsymbol{f}_u$, in general, could be a function of $\boldsymbol{u}$, $\dot{\boldsymbol{u}}$, t, and even $\boldsymbol{\lambda}$. However, in this paper, we restrict ourselves to cases where $\boldsymbol{f}_u$ is a function of $\boldsymbol{u}$, $\boldsymbol{u}$, and t only.

Consider new coordinates $\boldsymbol{v}$, having the relation with $\boldsymbol{u}$ as $\dot{\boldsymbol{u}}=\boldsymbol{T}\boldsymbol{v}+\boldsymbol{e}$, where $\boldsymbol{T}$ is full column rank. The constraint equation in terms of $\boldsymbol{v}$ would be

$$(\boldsymbol{\Psi}\boldsymbol{T})\dot{\boldsymbol{v}}=\boldsymbol{\nu}-\boldsymbol{\Psi}\boldsymbol{e} \tag{B1}$$

When $\boldsymbol{T}$ is nonsquare ($rows>columns$), $\boldsymbol{T}$ and $\boldsymbol{e}$ used to define $\boldsymbol{v}$ cannot be arbitrary. The sufficient conditions on $\boldsymbol{T}$ and e are as follows: (1) Eq. (B1) should be consistent, and (2) if $n_{\boldsymbol{u}}$ and $n_{\boldsymbol{v}}$ represent number of components of coordinates $\boldsymbol{u}$ and $\boldsymbol{v}$, respectively, then $n_{\boldsymbol{u}}-n_{\boldsymbol{v}}$ equations in (B1) should be redundant. The constraint equation in terms of $\boldsymbol{v}$ is obtained after removing redundant equations from Eq. (B1).

The equation of motion in terms of $\boldsymbol{v}$ would be of the form

$$\boldsymbol{M}_{\boldsymbol{v}}\ddot{\boldsymbol{v}}=\boldsymbol{f}_{\boldsymbol{v}}-(\boldsymbol{T}^T\boldsymbol{\Psi}^T)\boldsymbol{\lambda} \tag{B2}$$

where

$$\boldsymbol{M}_{\boldsymbol{v}}=\boldsymbol{T}^T\boldsymbol{M}_{\boldsymbol{u}}\boldsymbol{T}\quad\text{and}\quad\boldsymbol{f}_{\boldsymbol{v}}=\boldsymbol{T}^T(\boldsymbol{f}_{\boldsymbol{u}}-\boldsymbol{M}_u(\dot{\boldsymbol{e}}-\dot{\boldsymbol{T}}\dot{\boldsymbol{v}})) \tag{B3}$$

Appendix C: Simplifications

C.1 A Useful Relation

$$\begin{aligned}
&\boldsymbol{Q}_k^T(\boldsymbol{G}_k\tilde{\boldsymbol{E}}_k)^{-T}\tilde{\boldsymbol{E}}_k^T\boldsymbol{M}_k(\dot{\tilde{\boldsymbol{E}}}_k\dot{\tilde{\boldsymbol{y}}}_{k_c}+\dot{\tilde{\boldsymbol{D}}}_k\dot{\tilde{\boldsymbol{y}}}_{k_f}+\tilde{\boldsymbol{E}}_k(\dot{\boldsymbol{S}}_k\dot{\boldsymbol{y}}_j+\dot{\boldsymbol{a}}_k))\\
&=\boldsymbol{Q}_k^T(\boldsymbol{G}_k\tilde{\boldsymbol{E}}_k)^{-T}\tilde{\boldsymbol{E}}_k^T\boldsymbol{M}_k(\ddot{\boldsymbol{y}}_k-\tilde{\boldsymbol{E}}_k\ddot{\tilde{\boldsymbol{y}}}_{k_c}-\tilde{\boldsymbol{D}}_k\ddot{\tilde{\boldsymbol{y}}}_{k_f}+\tilde{\boldsymbol{E}}_k(\ddot{\tilde{\boldsymbol{y}}}_{k_c}-\boldsymbol{S}_k\ddot{\boldsymbol{y}}_j))\\
&\quad\text{(see Eqs. (31) and (22))}\\
&=\boldsymbol{Q}_k^T(\boldsymbol{G}_k\tilde{\boldsymbol{E}}_k)^{-T}\tilde{\boldsymbol{E}}_k^T\boldsymbol{M}_k(\ddot{\boldsymbol{y}}_k+\tilde{\boldsymbol{E}}_k(\boldsymbol{G}_k\tilde{\boldsymbol{E}}_k)^{-1}\boldsymbol{Q}_k\ddot{\boldsymbol{y}}_j)\\
&\quad-\boldsymbol{Q}_k^T(\boldsymbol{G}_k\tilde{\boldsymbol{E}}_k)^{-T}(\tilde{\boldsymbol{E}}_k^T\boldsymbol{M}_k\tilde{\boldsymbol{D}}_k)\ddot{\tilde{\boldsymbol{y}}}_{k_f}\quad\text{(see }\boldsymbol{S}_k\text{ given in Sec. 5.3)}\\
&=\boldsymbol{Q}_k^T(\boldsymbol{G}_k\tilde{\boldsymbol{E}}_k)^{-T}\tilde{\boldsymbol{E}}_k^T\boldsymbol{M}_k(\ddot{\boldsymbol{y}}_k+\tilde{\boldsymbol{E}}_k(\boldsymbol{G}_k\tilde{\boldsymbol{E}}_k)^{-1}\boldsymbol{Q}_k\ddot{\boldsymbol{y}}_j)\\
&\quad\text{(from Condition 1 in Sec. 5.1, }\tilde{\boldsymbol{E}}_k^T\boldsymbol{M}_k\tilde{\boldsymbol{D}}_k=\boldsymbol{0})
\end{aligned} \tag{C1}$$

C.2 Simplification Related to Equation (45)

$$\begin{aligned}
&\boldsymbol{Q}_k^T(\boldsymbol{G}_k\tilde{\boldsymbol{E}}_k)^{-T}\tilde{\boldsymbol{E}}_k^T\boldsymbol{M}_k(\dot{\tilde{\boldsymbol{E}}}_k\dot{\tilde{\boldsymbol{y}}}_{k_c}+\dot{\tilde{\boldsymbol{D}}}_k\dot{\tilde{\boldsymbol{y}}}_{k_f}+\tilde{\boldsymbol{E}}_k(\dot{\boldsymbol{S}}_k\dot{\boldsymbol{y}}_j+\dot{\boldsymbol{a}}_k))\\
&=\boldsymbol{Q}_k^T(\boldsymbol{G}_k\tilde{\boldsymbol{E}}_k)^{-T}\tilde{\boldsymbol{E}}_k^T\boldsymbol{M}_k(\ddot{\boldsymbol{y}}_k+\tilde{\boldsymbol{E}}_k(\boldsymbol{G}_k\tilde{\boldsymbol{E}}_k)^{-1}\boldsymbol{Q}_k\ddot{\boldsymbol{y}}_j)\quad\text{(see Eq. (C1))}\\
&=\boldsymbol{Q}_k^T(\boldsymbol{G}_k\boldsymbol{M}_k^{-1}\boldsymbol{G}_k^T)^{-T}\boldsymbol{C}_c^{-T}\boldsymbol{C}_c^T\boldsymbol{G}_k\boldsymbol{M}_k^{-T}\boldsymbol{M}_k(\ddot{\boldsymbol{y}}_k\\
&\quad+\boldsymbol{M}_k^{-1}\boldsymbol{G}_k^T\boldsymbol{C}_c\boldsymbol{C}_e^{-1}(\boldsymbol{G}_k\boldsymbol{M}_k^{-1}\boldsymbol{G}_k^T)^{-1}\boldsymbol{Q}_k\ddot{\boldsymbol{y}}_j)\quad\text{(see Eq. (38))}
\end{aligned}$$

$\boldsymbol{C}_c$ is invertible. $(\boldsymbol{G}_k\boldsymbol{M}_k^{-1}\mathbf{G}_k^T)$ and $\boldsymbol{M}_k$ are positive definite.

$$\begin{aligned}
&=\boldsymbol{Q}_k^T(\boldsymbol{G}_k\boldsymbol{M}_k^{-1}\boldsymbol{G}_k^T)^{-1}(\boldsymbol{G}_k\ddot{\boldsymbol{y}}_k+(\boldsymbol{G}_k\boldsymbol{M}_k^{-1}\boldsymbol{G}_k^T)(\boldsymbol{G}_k\boldsymbol{M}_k^{-1}\boldsymbol{G}_k^T)^{-1}\boldsymbol{Q}_k\ddot{\boldsymbol{y}}_j)\\
&=\boldsymbol{Q}_k^T(\boldsymbol{G}_k\boldsymbol{M}_k^{-1}\boldsymbol{G}_k^T)^{-1}(\boldsymbol{\gamma})\quad\text{(from Eq. (3))}
\end{aligned} \tag{C2}$$

C.3 Simplifications Related to Equation (46)

$$\text{Let } \widetilde{\boldsymbol{B}}_k = \widetilde{\boldsymbol{E}}_k \boldsymbol{Q}_k = \boldsymbol{E}_k \boldsymbol{Q}_k - \boldsymbol{D}_k (\boldsymbol{D}_k^T \boldsymbol{M}_k \boldsymbol{D}_k)^{-1} \boldsymbol{D}_k^T \boldsymbol{M}_k \boldsymbol{E}_k \boldsymbol{Q}_k \quad \text{(see Eq. (43))}$$

$$= -\boldsymbol{B}_k + \boldsymbol{D}_k \boldsymbol{Q}_{k_d} + \boldsymbol{D}_k (\boldsymbol{D}_k^T \boldsymbol{M}_k \boldsymbol{D}_k)^{-1} \boldsymbol{D}_k^T \boldsymbol{M}_k \boldsymbol{B}_k - \boldsymbol{D}_k (\boldsymbol{D}_k^T \boldsymbol{M}_k \boldsymbol{D}_k)^{-1} (\boldsymbol{D}_k^T \boldsymbol{M}_k \boldsymbol{D}_k) \boldsymbol{Q}_{k_d}$$

(because from Eq. (43), we have $\boldsymbol{B}_k = -(\boldsymbol{E}_k \boldsymbol{Q}_k + \boldsymbol{D}_k \boldsymbol{Q}_{k_d})$) (C3)

It may be noted that

$$\widetilde{\boldsymbol{B}}_k = -\boldsymbol{B}_k + \boldsymbol{D}_k (\boldsymbol{D}_k^T \boldsymbol{M}_k \boldsymbol{D}_k)^{-1} \boldsymbol{D}_k^T \boldsymbol{M}_k \boldsymbol{B}_k \tag{C4}$$

$$\widetilde{\boldsymbol{B}}_k = (-\boldsymbol{I} + \boldsymbol{D}_k (\boldsymbol{D}_k^T \boldsymbol{M}_k \boldsymbol{D}_k)^{-1} \boldsymbol{D}_k^T \boldsymbol{M}_k) \boldsymbol{B}_k \tag{C5}$$

It may be noted that

$$\boldsymbol{D}_k^T \boldsymbol{M}_k \widetilde{\boldsymbol{B}}_k = -\boldsymbol{D}_k^T \boldsymbol{M}_k \boldsymbol{B}_k + \boldsymbol{D}_k^T \boldsymbol{M}_k \boldsymbol{D}_k (\boldsymbol{D}_k^T \boldsymbol{M}_k \boldsymbol{D}_k)^{-1} \boldsymbol{D}_k \boldsymbol{M}_k \boldsymbol{B}_k = \boldsymbol{0} \tag{C6}$$

Also, using Eqs. (43) and (43), we get

$$\boldsymbol{G}_k \widetilde{\boldsymbol{E}}_k = \boldsymbol{G}_k (\boldsymbol{E}_k + \boldsymbol{D}_k \widetilde{\boldsymbol{A}}_k) = \boldsymbol{G}_k \boldsymbol{E}_k + (\boldsymbol{G}_k \boldsymbol{D}_k) \widetilde{\boldsymbol{A}}_k = \boldsymbol{I} + \boldsymbol{0} = \boldsymbol{I} \tag{C7}$$

C.3.1 Mass Matrix Related Term

$$\boldsymbol{Q}_k^T (\boldsymbol{G}_k \widetilde{\boldsymbol{E}}_k)^{-T} \widetilde{\boldsymbol{E}}_k^T \boldsymbol{M}_k \widetilde{\boldsymbol{E}}_k (\boldsymbol{G}_k \widetilde{\boldsymbol{E}}_k)^{-1} \boldsymbol{Q}_k$$

$$= \boldsymbol{Q}_k^T \widetilde{\boldsymbol{E}}_k^T \boldsymbol{M}_k \widetilde{\boldsymbol{E}}_k \boldsymbol{Q}_k = \widetilde{\boldsymbol{B}}_k^T \boldsymbol{M}_k \widetilde{\boldsymbol{B}}_k \quad \text{(see Eqs. (C7) and (C3))}$$

$$= \widetilde{\boldsymbol{B}}_k^T \boldsymbol{M}_k (-\boldsymbol{B}_k + \boldsymbol{D}_k (\boldsymbol{D}_k^T \boldsymbol{M}_k \boldsymbol{D}_k)^{-1} \boldsymbol{D}_k \boldsymbol{M}_k \boldsymbol{B}_k) \quad \text{(see Eq. (C4))}$$

$$= -\widetilde{\boldsymbol{B}}_k \boldsymbol{M}_k \boldsymbol{B}_k + \boldsymbol{0} \quad \text{(see Eq. (C6))}$$

$$= \boldsymbol{B}_k^T (\boldsymbol{I} - \boldsymbol{M}_k \boldsymbol{D}_k (\boldsymbol{D}_k^T \boldsymbol{M}_k \boldsymbol{D}_k)^{-1} \boldsymbol{D}_k^T) \boldsymbol{M}_k \boldsymbol{B}_k \quad \text{(see Eq. (C5))} \tag{C8}$$

$$= \boldsymbol{B}_k^T (\boldsymbol{I} - \boldsymbol{M}_k \boldsymbol{H}_k (\boldsymbol{H}_k^T \boldsymbol{M}_k \boldsymbol{H}_k)^{-1} \boldsymbol{H}_k^T) \boldsymbol{M}_k \boldsymbol{B}_k \quad \text{(from Eq. (A4), } \boldsymbol{D}_k = \boldsymbol{H}_k) \tag{C9}$$

C.3.2 Force Vector Related Term

$$-\boldsymbol{Q}_k^T (\boldsymbol{G}_k \widetilde{\boldsymbol{E}}_k)^{-T} \widetilde{\boldsymbol{E}}_k^T \boldsymbol{f}_k = -\boldsymbol{Q}_k^T \widetilde{\boldsymbol{E}}_k \boldsymbol{f}_k \quad \text{(see Eq. (C7))}$$

$$= -\widetilde{\boldsymbol{B}}_k^T \boldsymbol{f}_k = \boldsymbol{B}_k^T (\boldsymbol{I} - \boldsymbol{M}_k \boldsymbol{D}_k (\boldsymbol{D}_k^T \boldsymbol{M}_k \boldsymbol{D}_k)^{-1} \boldsymbol{D}_k^T) \boldsymbol{f}_k \quad \text{(see Eqs. (C3) and (C5))}$$

$$= \boldsymbol{B}_k^T (\boldsymbol{I} - \boldsymbol{M}_k \boldsymbol{H}_k (\boldsymbol{H}_k^T \boldsymbol{M}_k \boldsymbol{H}_k)^{-1} \boldsymbol{H}_k^T) \boldsymbol{f}_k \quad \text{(from Eq. (A4), } \boldsymbol{D}_k = \boldsymbol{H}_k) \tag{C10}$$

C.3.3 Velocity Related Term.

$$\boldsymbol{Q}_k^T (\boldsymbol{G}_k \widetilde{\boldsymbol{E}}_k)^{-T} \widetilde{\boldsymbol{E}}_k^T \boldsymbol{M}_k (\dot{\widetilde{\boldsymbol{E}}}_k \dot{\boldsymbol{y}}_{k_c} + \dot{\widetilde{\boldsymbol{D}}}_k \dot{\boldsymbol{y}}_{k_f} + \widetilde{\boldsymbol{E}}_k (\dot{\boldsymbol{S}}_k \dot{\boldsymbol{y}}_j + \dot{\boldsymbol{a}}_k))$$

$$= \boldsymbol{Q}_k^T (\boldsymbol{G}_k \widetilde{\boldsymbol{E}}_k)^{-T} \widetilde{\boldsymbol{E}}_k^T \boldsymbol{M}_k (\ddot{\boldsymbol{y}}_k + \widetilde{\boldsymbol{E}}_k (\boldsymbol{G}_k \widetilde{\boldsymbol{E}}_k)^{-1} \boldsymbol{Q}_k \ddot{\boldsymbol{y}}_j) \quad \text{(see Eq. (C1))}$$

$$= \boldsymbol{Q}_k^T \widetilde{\boldsymbol{E}}_k^T \boldsymbol{M}_k \ddot{\boldsymbol{y}}_k + (\boldsymbol{Q}_k^T \widetilde{\boldsymbol{E}}_k^T \boldsymbol{M}_k \widetilde{\boldsymbol{E}}_k \boldsymbol{Q}_k) \ddot{\boldsymbol{y}}_j \quad \text{(from Eq. (C7))} = \widetilde{\boldsymbol{B}}_k^T \boldsymbol{M}_k \ddot{\boldsymbol{y}}_k$$

$$- \widetilde{\boldsymbol{B}}_k^T \boldsymbol{M}_k \boldsymbol{B}_k \ddot{\boldsymbol{y}}_j \quad \text{(see Eqs. (C3) and (C8))} = \widetilde{\boldsymbol{B}}_k^T \boldsymbol{M}_k \ddot{\boldsymbol{y}}_k$$

$$- \widetilde{\boldsymbol{B}}_k^T \boldsymbol{M}_k \boldsymbol{B}_k \ddot{\boldsymbol{y}}_j - (\widetilde{\boldsymbol{B}}_k^T \boldsymbol{M}_k \boldsymbol{D}_k) \ddot{\boldsymbol{q}}_j \quad (\widetilde{\boldsymbol{B}}_k \boldsymbol{M}_k \boldsymbol{D}_k = \boldsymbol{0}, \text{ Eq. (C6))} =$$

$$- \widetilde{\boldsymbol{B}}_k^T \boldsymbol{M}_k (-\ddot{\boldsymbol{y}}_k + \boldsymbol{B}_k \ddot{\boldsymbol{y}}_j + \boldsymbol{D}_k \ddot{\boldsymbol{q}}_k) = -\widetilde{\boldsymbol{B}}_k^T \boldsymbol{M}_k (-(\dot{\boldsymbol{B}}_k \ddot{\boldsymbol{y}}_j + \dot{\boldsymbol{D}}_k \dot{\boldsymbol{q}}_k + \dot{\boldsymbol{c}}_k)) \quad \text{(from Eq. (A4), } \ddot{\boldsymbol{y}}_k = \boldsymbol{B}_k \ddot{\boldsymbol{y}}_j + \boldsymbol{D}_k \ddot{\boldsymbol{q}}_k + \dot{\boldsymbol{B}}_k \dot{\boldsymbol{y}}_j + \dot{\boldsymbol{D}}_k \dot{\boldsymbol{q}}_k + \dot{\boldsymbol{c}}_k)$$

$$= \boldsymbol{B}_k^T (\boldsymbol{I} - \boldsymbol{M}_k \boldsymbol{H}_k (\boldsymbol{H}_k^T \boldsymbol{M}_k \boldsymbol{H}_k)^{-1} \boldsymbol{H}_k^T) \boldsymbol{M}_k (-\boldsymbol{d}_k) \quad \text{(see Eq. (C5))}$$

where $\boldsymbol{d}_k = (\dot{\boldsymbol{B}}_k \dot{\boldsymbol{y}}_j + \dot{\boldsymbol{D}}_{\mathbf{k}} \dot{\boldsymbol{q}}_k + \dot{\boldsymbol{c}}_k)$

References

[1] Armstrong, W. W., 1979, "Recursive Solution to the Equations of Motion of an n-Link Manipulator," *Proceedings of the Fifth World Congress on Theory of Machines and Mechanisms*, Montreal.

[2] Featherstone, R., 1983, "The Calculation of Robot Dynamics Using Articulated-Body Inertias," Int. J. Robot. Res., **2**, pp. 13–30.

[3] Bae, D. S., and Haug, E. J., 1987, "A Recursive Formulation for Constrained Mechanical System Dynamics: Part I. Open Loop Systems," Mech. Struct. Mach., **15**(), pp. 359–382.

[4] Rodriguez, G., 1987, "Kalman Filtering, Smoothing, and Recursive Robot Arm Forward and Inverse Dynamics," IEEE J. Rob. Autom., **3**(), pp. 624–639.

[5] Rodriguez, G., and Kreutz-Delgado, K., 1992, "Spatial Operator Factorization and Inversion of the Manipulator Mass Matrix," IEEE Trans. Rob. Autom., **8**(), pp. 65–76.

[6] Saha, S. K., 1999, "Dynamics of Serial Multibody Systems Using the Decoupled Natural Orthogonal Complement Matrices," ASME J. Appl. Mech., **666**, pp. 986–996.

[7] Lubich, Ch., Nowak, U., Phle, U., and Engstler, Ch., 1992, "MEXX—Numerical Software for the Integration of Constrained Mechanical Multibody Systems," Technical Report SC 92–12, Konrad-Zuse-Zentrum Berlin.

[8] Haug, E. J., 1989, *Computer-Aided Kinematics and Dynamics of Mechanical Systems, Vol. 1: Basic Methods*, Allyn and Bacon, Needham Heights, MA.

[9] Strang, G., 1998, *Linear Algebra and Its Applications*, 3rd ed., Thomson International, Australia.

[10] Meirovitch, L., 1970, *Methods of Analytical Dynamics*, McGraw-Hill, New York.

A Noncanonically Shape Laminated Plate Subjected to Impact Loading: Theory and Experiment

Natalia V. Smetankina
Senior Research Associate
e-mail: nsmet@ipmach.kharkov.ua

Alexander N. Shupikov
Professor, Chief Research Associate

Sergei Yu. Sotrikhin
Senior Research Associate

Vladimir G. Yareshchenko
Research Associate

A.N. Podgorny Institute for Mechanical Engineering Problems,
National Academy of Sciences of Ukraine,
2/10 Dm. Pozharsky Street,
Kharkov 61046, Ukraine

This paper suggests an analytical approach to investigating vibrations of a laminated plate with a noncanonical shape in plan view under impact with an impactor having a semispherical end. The approach suggested is based on the immersion method. The dynamic behavior of the plate is described by the first-order theory accounting for transverse shear strain, thickness reduction, and normal element rotation inertia in each layer. Impact has been analyzed for different points of the plate whose contour consists of straight lines and circle arcs. The theoretical results are consistent with experimental data obtained with the dynamic wide-range strain measurement technique.
[DOI: 10.1115/1.2936925]

Keywords: mechanical engineering, laminated plate, impact, immersion method, strain measurement

1 Introduction

Laminated structures are advantageous as compared to the homogeneous ones. Hence, they are used widely in mechanical engineering. Calculating dynamic response parameters for shock loading is a key effort in analyzing vibrations of composite structures. References [1–7] discuss in detail the methods of theoretical and experimental investigation of homogeneous and composite structures subjected to shock in a wide range of velocities.

Qiu et al. [8] and McShane et al. [9] used the finite-element method to analyze round plates under shock loading. Reference [8] investigates the response of clamped circular sandwich plates to shock loading in air and water. The optimal configurations of plates with maximum shock resistance were defined. Reference [9] numerically and experimentally analyzes the dynamic response of clamped circular monolithic and sandwich plates to impacts with projectiles. It was found that sandwich plates are more shock resistant than monolithic plates of equal mass. The results of finite-element modeling are consistent with experimental measurements.

Malekzadeh et al. [10] suggested an analytical model of impact interaction between the impactor and composite sandwich panels. The panels are rectangular simply supported plates. A normal impact was applied to the face surface with impactors of different masses and various initial velocities. The finite-element method was used to calculate displacements, stresses, and strains in the face sheets and the core.

Naidu and Sinha [11] analyzed the transient responses of simply supported laminated composite cylindrical and spherical shell panels subjected to low-velocity impact in hygrothermal environments. Finite-element analysis was conducted within the geometrically nonlinear theory. The impact model is based on the modified Hertzian contact law. The impact force was computed by a nonlinear equation solved with the Newmark average acceleration method jointly with an incremental modified Newton–Raphson scheme.

Schubel et al. [12] experimentally studied the quasistatic behavior and that during low-velocity impact of composite sandwich panels comprising woven carbon/epoxy face sheets and a PVC foam core. The panels are simply supported square plates and the impactor has a spherical head. Experimental results were compared to those of analytical and finite-element analysis.

Lataillade et al. [13] suggested combining analytical methods and the finite-element one for designing approximate strain models for monolithic and sandwich composite plates subjected to a low-velocity shock. The mathematical relations between inputs and outputs were polynomials whose coefficients were defined experimentally. The authors numerically and experimentally investigated simply supported circular monolithic and sandwich plates as well as square plates under impact with a steel ball.

Banerjee et al. [14] suggested a semianalytical method of analyzing the wave field under action of localized dynamic sources. The method is based on the wave number integral representation of the elastodynamic field. The wave field was investigated for a thin unidirectional graphite/epoxy composite laminate under the action of a dynamic surface point load.

Olsson [15] obtained an analytical solution of the impact problem as a trigonometric series for a ball colliding with simply supported rectangular orthotropic plates.

Anderson et al. [16] also presented the analytical solution of the problem in nonstationary strain of a rectangular laminated especially orthotropic plates resting on roller supports effected by an irregularly distributed impulse load. The governing equations were obtained with Reissner's functional. The equations were solved with the Fourier or Laplace transform in time and by expanding the sought for functions in double Fourier series about plane coordinates. This method was extended by Anderson and Madenci [17] when studying quasistatic loading of sandwich rectangular panels with a rigid sphere. The response of sandwich panels to low-velocity impact was experimentally investigated in Ref. [18].

A review of the above studies shows that numerical methods are used widely to analyze nonstationary vibrations of laminated structures subjected to shock loads. The finite-element method is used most often. The analytical solution of these problems is given only for laminated plates and shells with a canonical plan-view shape.

In Ref. [19], the authors of this paper used the immersion

Contributed by the Applied Mechanics Division for publication in the JOURNAL OF APPLIED MECHANICS. Manuscript received March 12, 2007; final manuscript received February 4, 2008; published online July 2, 2008. Review conducted by Professor Sridhar Krishnaswamy.

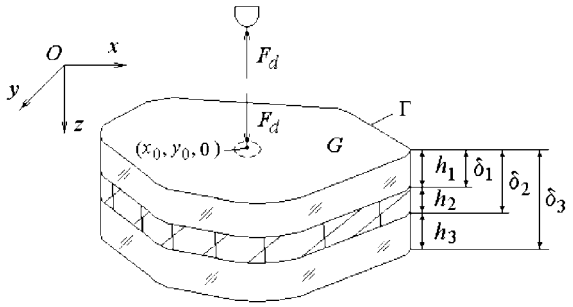

Fig. 1 Laminated plate

method to obtain an analytical solution of the problem in nonstationary vibrations of an elliptical plate with account of wave strain. In this paper, the method was extended to vibrations of an impact-loaded laminated plate with a noncanonical plan-view shape. The solution was derived as a trigonometric series. Since a low-velocity impact was considered, the contact interaction of the indenter and plate is described by Hertzian law. The applicability of Hertzian law to this case was substantiated by analyzing Goldsmith [1], Timoshenko [20], Tan and Sun [21], Lin and Lee [22], and Nosier et al. [23] studies. The numerical results were compared to experimental data. Experiments were based on the dynamic wide-range strain measurement technique [24].

2 Impact Problem Statement

A constant-thickness laminated plate is considered. It comprises isotropic layers with constant thickness h_i (Fig. 1). The layers have a different thickness and various physical and mechanical properties. The number of layers I and their layout is arbitrary. The plate is referred to the Cartesian system of coordinates fixed to the outer surface of the first layer. In the coordinate plane xOy, it occupies domain G limited by boundary Γ,

$$\Gamma: x_\Gamma = x_\Gamma(s), \quad y = y_\Gamma(s) \tag{1}$$

where s is current arc length.

The laminated plate is arranged horizontally. An indenter of mass M with a semispherical end of radius R impacts the outer surface of the plate's first layer. The indenter is dropped onto the plate from height H. The velocity of its impact with the plate is

$$V_z = \sqrt{2gH}$$

where g is the gravity acceleration.

The domain of interaction of the indenter and plate is a circle of radius $a(t)$ with a center in point (x_0, y_0) (t is time). The contact pressure of the indenter on the plate is distributed over the load area according to function [19]

$$p_z(x,y,t) = F_0(t)\left[1 - \frac{(x-x_0)^2 + (y-y_0)^2}{a^2(t)}\right]^{1/2} \tag{2}$$

The resultant load (2) is equal to the indenter's contact force of action on the plate

$$F_d(t) = \int\int_S p_z dS = \frac{2}{3}F_0(t)\pi a^2(t)$$

whence

$$F_0(t) = \frac{3}{2}\frac{F_d(t)}{\pi a^2(t)}$$

The contact area radius $a(t)$ is found from formula [24]

$$a(t) = \left[\frac{3}{16}F_d(t)(\theta_1 + \theta)\right]^{1/3}$$

where

$$\theta_1 = \frac{4(1-\nu_1^2)}{E_1}, \quad \theta = \frac{4(1-\nu^2)}{E}$$

E_1 and ν_1 are Young's module and Poisson's ratio of the material of the plate's first layer, and E and ν are the similar properties of the indenter material.

The indenter equation of motion is

$$Mz_{,tt} = Mg - F_d(t), \quad z(0) = 0, \quad z_{,t}(0) = V_z \tag{3}$$

where $z = z(t)$ is the indenter displacement. In these expressions and elsewhere, the index following the comma means differentiation for the respective variable.

The condition of joint displacement of the indenter and plate is [24]

$$w_0 + \alpha_c - z \geq 0 \tag{4}$$

Here, α_c is the contact approach of the indenter and plate in the contact point (x_0, y_0); $w(x_0, y_0, t)$ is the deflection of the plate's first layer outer surface in point (x_0, y_0).

The indenter and plate come into contact when inequality (4) becomes equality

$$w_0 + \alpha_c - z = 0 \tag{5}$$

Contact approach α_c is found by solving Hertzian problem [25] on ball indentation into an elastic semispace,

$$\alpha_c(t) = \kappa_1 F_d^{2/3}(t), \quad \kappa_1 = \left[\frac{9(\theta + \theta_1)}{256R}\right]^{1/3}$$

3 Key Relations for a Laminated Plate

The behavior of a laminated plate is described by the first-order theory accounting for transverse shear strain, thickness reduction, and normal element rotation inertia in each layer.

Hence, the displacements of layer points are defined as

$$u^i = u + \sum_{j=1}^{i-1} h_j \psi_x^j + (z - \delta_{i-1})\psi_x^j, \quad v^i = v + \sum_{j=1}^{i-1} h_j \psi_y^j + (z - \delta_{i-1})\psi_y^j$$

$$w^i = w + \sum_{j=1}^{i-1} h_j \psi_z^j + (z - \delta_{i-1})\psi_z^j \quad i = \overline{1,I} \tag{6}$$

where

$$\delta_i = \sum_{j=1}^{i} h_j, \quad \delta_{i-1} \leq z \leq \delta_i, \quad i = \overline{1,I}$$

$u = u(x,y,t)$, $v = v(x,y,t)$, and $w = w(x,y,t)$ are the displacements of coordinate plane points to coordinate axes; $\psi_x^j = \psi_x^j(x,y,t)$ and $\psi_y^j = \psi_y^j(x,y,t)$ are the angles of rotation of the normal element in the ith layer about the coordinate axes $0x$ and $0y$; $\psi_z^j = \psi_z^j(x,y,t)$ is the normal element reduction within the ith layer.

Strains are found by Cauchy's formulas:

$$\varepsilon_x^i = u_{,x} + \sum_{j=1}^{i-1} h_j \psi_{x,x}^j + (z - \delta_{i-1})\psi_{x,x}^j,$$

$$\varepsilon_y^i = v_{,y} + \sum_{j=1}^{i-1} h_j \psi_{y,y}^j + (z - \delta_{i-1})\psi_{y,y}^j, \quad \varepsilon_z^i = \psi_z^j$$

$$\gamma_{xy}^j = \gamma_{yx}^j = u_{,y} + v_{,x} + \sum_{j=1}^{i-1} h_j(\psi_{x,y}^j + \psi_{y,x}^j) + (z - \delta_{i-1})(\psi_{x,y}^j + \psi_{y,x}^j)$$

$$\gamma_{xz}^i = \gamma_{zx}^i = w_{,x} + \psi_x^i + \sum_{j=1}^{i-1} h_j \psi_{z,x}^j + (z - \delta_{i-1})\psi_{z,x}^i$$

$$\gamma_{yz}^i = \gamma_{zy}^i = w_{,y} + \psi_y^i + \sum_{j=1}^{i-1} h_j \psi_{z,y}^j + (z - \delta_{i-1})\psi_{z,y}^i \tag{7}$$

Stresses and strains are related by Hooke's law,

$$\sigma_x^i = \frac{E_i}{1+\nu_i}\left(\varepsilon_x^i + \frac{\nu_i}{1-2\nu_i}\theta^i\right), \quad \sigma_y^i = \frac{E_i}{1+\nu_i}\left(\varepsilon_y^i + \frac{\nu_i}{1-2\nu_i}\theta^i\right)$$

$$\sigma_z^i = \frac{E_i}{1+\nu_i}\left(\varepsilon_z^i + \frac{\nu_i}{1-2\nu_i}\theta^i\right)$$

$$\tau_{xy}^i = G_i\gamma_{xy}^i, \quad \tau_{xz}^i = G_i\gamma_{xz}^i, \quad \tau_{yz}^i = G_i\gamma_{yz}^i, \quad i = \overline{1,I} \tag{8}$$

where

$$G_i = \frac{E_i}{2(1+\nu_i)}, \quad \theta^i = \varepsilon_x^i + \varepsilon_y^i + \varepsilon_z^i$$

E_i is Young's modulus for the material of the ith layer, and ν_i is Poisson's ratio for the material of the ith layer.

The equations of motion of a laminated plate affected by impact load $\mathbf{P}$,

$$\mathbf{\Omega}_\rho \mathbf{U}_{,tt} - \mathbf{\Lambda U} = \mathbf{P}, \quad x,y \in G, \quad \mathbf{U} = \mathbf{U}_{,t} = 0, \quad t = 0 \tag{9}$$

as well as the respective boundary conditions on boundary Γ,

$$\mathbf{B}^\Gamma \mathbf{U} = 0, \quad x,y \in \Gamma \tag{10}$$

are derived by Hamilton's variational principle [24,26].

In Eqs. (9) and (10), $\mathbf{U}$ is the displacement vector,

$$u_1 = u, \quad u_2 = v, \quad u_3 = w, \quad u_{3+i} = \psi_x^i, \quad u_{3+I+i} = \psi_y^i,$$

$$u_{3+2I+i} = \psi_z^i, \quad i = \overline{1,I}$$

$\mathbf{\Omega}_\rho$, $\mathbf{\Lambda}$, and $\mathbf{B}^\Gamma$ are the symmetric matrices with dimensions $(3I+3)\times(3I+3)$ whose components are given in the Appendix; $\mathbf{P}$ is the external load vector,

$$p_1 = p_2 = p_{3+i} = p_{3+I+i} = p_{3+2I+i} = 0, \quad i = \overline{1,I}, \quad p_3 = p_z(x,y,t)$$

Hence, the problem of investigating nonstationary vibrations of a laminated plate subjected to a impact load is reduced to integrating a system of motion equations for a plate (9) with account of boundary conditions (10) jointly with the indenter equation of motion (3) and the condition of joint displacement of the indenter and plate (5).

4 Solution Method

The analytical solution of the problem described by Eqs. (3), (5), (9), and (10) was derived by the immersion method [26]. According to this method, a laminated plate is immersed into an auxiliary enveloping plate with the same composition of layers. It is loaded within domain G similar to that for the primary plate (Fig. 2). An auxiliary plate is the one whose contour shape and boundary conditions yield a simple analytical solution. In this case, the auxiliary plate is a simply supported rectangular laminated one, allowing to find the problem solution as trigonometric series. To satisfy actual boundary conditions (10), the auxiliary plate is subjected over the trace of boundary Γ to additional distributed compensating loads $\mathbf{Q}^{\text{comp}} = \{q_j^{\text{comp}}(x,y,t)\}$, $j = \overline{1,3I+3}$ (Fig. 2) whose intensities must be defined. In motion equation (9), the compensating loads are presented as curvilinear patterns $\mathbf{P}^{\text{comp}} = \{p_j^{\text{comp}}(x,y,t)\}$,

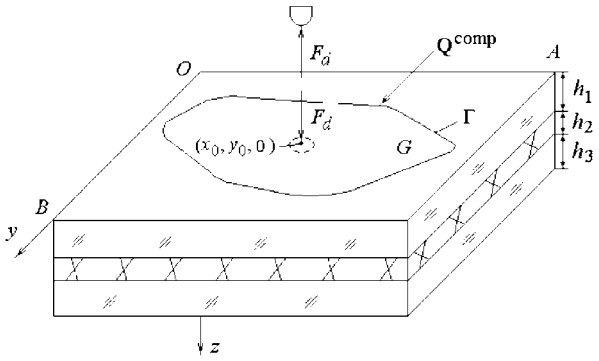

Fig. 2 Auxiliary rectangular plate

$$p_j^{\text{comp}}(x,y,t) = \oint_\Gamma q_j^{\text{comp}}(s,t)\,\delta(x - x_\Gamma, y - y_\Gamma)ds, \quad j = \overline{1,3I+3} \tag{11}$$

where $\delta(x-x_\Gamma, y-y_\Gamma)$ is the two-dimensional δ-function.

To satisfy boundary conditions (10), a system of integral equations for finding the intensities of compensating loads

$$\mathbf{B}^\Gamma \mathbf{U}[\mathbf{Q}^{\text{comp}}(x,y,t)] = 0, \quad x,y \in \Gamma \tag{12}$$

is formed on the trace of boundary Γ.

Displacements $\mathbf{U}$ and loads $\mathbf{P}$ and $\mathbf{P}^{\text{comp}}$ Eq. (11) are expanded in the rectangular plate domain in trigonometric series for functions satisfying simply supported conditions:

$$u_j(x,y,t) = \sum_{m=1}^{\infty}\sum_{n=1}^{\infty} \phi_{jmn}(t)B_{jmn}(x,y) \tag{13}$$

$$p_j(x,y,t) = \sum_{m=1}^{\infty}\sum_{n=1}^{\infty} p_{jmn}(t)B_{jmn}(x,y) \tag{14}$$

$$p_j^{\text{comp}}(x,y,t) = \sum_{m=1}^{\infty}\sum_{n=1}^{\infty} p_{jmn}^{\text{comp}}(t)B_{jmn}(x,y), \quad j = \overline{1,3I+3} \tag{15}$$

where

$$B_{1mn} = \cos\frac{m\pi x}{A}\sin\frac{n\pi y}{B}, \quad B_{2mn} = \sin\frac{m\pi x}{A}\cos\frac{n\pi y}{B},$$

$$B_{3mn} = \sin\frac{m\pi x}{A}\sin\frac{n\pi y}{B}$$

$$B_{3+imn} = B_{1mn}, \quad B_{3+I+imn} = B_{2mn}, \quad B_{3+2I+imn} = B_{3mn}, \quad i = \overline{1,I},$$

$$m = \overline{1,m^*}, \quad n = \overline{1,n^*}$$

$$p_{jmn}(t) = \frac{4}{AB}\int_0^A\int_0^B p_j(t)B_{jmn}(x,y)dxdy, \quad j = \overline{1,3I+3}$$

A and B are the dimensions of auxiliary rectangular plate.

The expansion coefficients of the given impulse load Eq. (14) are

$$p_{jmn} = 0, \quad j = \overline{1,3I+3}, \quad j \neq 3, \quad p_{3mn} = D_{mn}F_d(t) \tag{16}$$

where

$$D_{mn} = \frac{12}{AB\rho_{mn}^2}\sin\frac{m\pi x_0}{A}\sin\frac{n\pi y_0}{B}\left(\frac{\sin\rho_{mn}}{\rho_{mn}} - \cos\rho_{mn}\right),$$

$$\rho_{mn} = \pi a(t)\sqrt{\frac{m^2}{A^2} + \frac{n^2}{B^2}}$$

The relationships for expansion coefficients $\mathbf{P}^{\text{comp}}$ Eq. (15) are written as

$$p_{jmn}^{\text{comp}}(t) = \frac{4}{AB}\oint_{\Gamma} q_j^{\text{comp}}(s,t)B_{jmn}(x_\Gamma, y_\Gamma)ds, \quad j = \overline{1,3I+3} \tag{17}$$

In so doing, the following δ-function properties were accounted for

$$\delta(x - x_0, y - y_0) = \delta(x - x_0)\delta(y - y_0)$$

$$\int_{\alpha}^{\beta} f(x)\delta(x - x_0)dx = f(x_0)$$

The system of motion equations (9) for each pair of m and n with account of expansions (13)–(17) is reduced to a system of ordinary second-order differential equations

$$\mathbf{\Omega}_\rho \mathbf{\Phi}_{mn,tt} + \mathbf{\Lambda}^{mn}\mathbf{\Phi}_{mn} = \mathbf{P}_{mn} + \mathbf{P}_{mn}^{\text{comp}}, \quad \mathbf{\Phi}_{mn} = \mathbf{\Phi}_{mn,t} = 0, \quad t = 0 \tag{18}$$

where

$$\mathbf{P}_{mn} = \{p_{jmn}(t)\}, \quad \mathbf{P}_{mn}^{\text{comp}} = \{p_{jmn}^{\text{comp}}(t)\}, \quad \mathbf{\Phi}_{mn} = \{\phi_{jmn}(t)\}$$

$$\mathbf{\Phi}_{mn,t} = \{\phi_{jmn,t}(t)\}, \quad \mathbf{\Phi}_{mn,tt} = \{\phi_{jmn,tt}(t)\}, \quad j = \overline{1,3I+3}$$

Matrix $\mathbf{A}^{mn}$ is given in the Appendix.

The system of differential equations (18) is integrated by expansion into Taylor series [27]. For this, we transform the system of differential equations (18),

$$\mathbf{\Phi}_{mn,tt} - \mathbf{A}^{mn}\mathbf{\Phi}_{mn} = \mathbf{B}^{mn}(\mathbf{P}_{mn} + \mathbf{P}_{mn}^{\text{comp}})$$

where

$$\mathbf{A}^{mn} = -\mathbf{\Omega}_\rho^{-1}\mathbf{\Lambda}_{mn}, \quad \mathbf{B}^{mn} = \mathbf{\Omega}_\rho^{-1}$$

The system

$$\mathbf{\Phi}_{mn,t} = \mathbf{E}\mathbf{\Psi}_{mn}$$

by substitution of variables and simple manipulations is reduced to

$$\mathbf{G}_{mn,t} = \mathbf{R}^{mn}\mathbf{G}_{mn} + \mathbf{H}_{mn}$$

where $\mathbf{E}$ is the unit matrix.

The integration interval $[0,t]$ is divided into k^* segments, each with a length of Δt so that $t = k\Delta t$, $k = \overline{1,k^*}$. We denote $\mathbf{G}_{mn}(k\Delta t) = \mathbf{G}_{mn}^k$.

At each kth integration step, the system solution is expanded in Taylor series,

$$\mathbf{G}_{mn}^k = \mathbf{G}_{mn}^{k-1} + \frac{\mathbf{G}_{mn,t}^{k-1}}{1!}\Delta t + \frac{\mathbf{G}_{mn,tt}^{k-1}}{2!}\Delta t^2 + \cdots$$

For each integration step, function $\mathbf{H}_{mn}(t)$ is assumed constant,

$$\mathbf{H}_{mn}(t) = \mathbf{H}_{mn}^k, \quad (k-1)\Delta t \le t \le k\Delta t$$

After such manipulations, the solution of system (18) at the $(k+1)$th time step is

$$\mathbf{\Phi}_{mn}^{k+1} = \mathbf{\Delta}^{mn}\mathbf{\Phi}_{mn}^k + \mathbf{\Pi}^{mn}(\mathbf{P}_{mn}^{k+1} + \mathbf{P}_{mn}^{\text{comp}k+1})$$

or

$$\phi_{jmn}^{k+1} = \frac{4}{AB}\sum_{l=1}^{3I+3} \pi_{jl}^{mn} p_{lmn}^{\text{comp}k+1} + \varepsilon_{jmn}^{k+1}, \quad j = \overline{1,3I+3}$$

where

$$\varepsilon_{jmn}^{k+1} = \sum_{l=1}^{3I+3} (\Delta_{jl}^{mn}\phi_{lmn}^k + \pi_{jl}^{mn}p_{lmn}^{k+1})$$

k is the time interval number, and $\mathbf{\Delta}^{mn}$ and $\mathbf{\pi}^{mn}$ are matrix elements yielded by numerical transformations of matrices $\mathbf{A}^{mn}$ and $\mathbf{B}^{mn}$.

The solution of the equation of motion for indenter (3) is derived by the Laplace integral transform,

$$z(t) = z(t_0) + z_{,t}(t_0)(t - t_0) + \frac{g}{2}(t - t_0)^2 - \frac{1}{M}\int_{t_0}^{t} F_d(\tau)(t - \tau)d\tau$$

where t_0 is the time of first contact of the indenter and plate.

The unknown contact force at the $(k+1)$th time step F_d^{k+1} is found from the condition of joint displacement of the indenter and plate, Eq. (5), which is a nonlinear equation for F_d^{k+1}

$$\kappa_2 F_d^{k+1} + \kappa_1 (F_d^{k+1})^{2/3} + \kappa_3 = 0 \tag{19}$$

where

$$\kappa_2 = \sum_{m=1}^{\infty}\sum_{n=1}^{\infty} D_{mn}\pi_{33}^{mn}B_{3mn}(x_0, y_0) + \frac{\Delta t^2}{2M}$$

$$\kappa_3 = \sum_{m=1}^{\infty}\sum_{n=1}^{\infty}\sum_{l=1}^{3I+3} \Delta_{3l}^{mn}\phi_{lmn}^k B_{3mn}(x_0, y_0) - z^{k+1} - z_{,t}^{k+1}\Delta t - \frac{g\Delta t^2}{2},$$

$$m = \overline{1,m^*}, \quad n = \overline{1,n^*}$$

Nonlinear equation (19) is solved by the Newton method [28].

The compensating loads are found from the system of integral equations (12). Similar to Ref. [26], the compensating forces and moments $\mathbf{Q}^{\text{comp}}$ are expanded in a series over the trace of boundary Γ,

$$q_j^{\text{comp}k+1}(s) = \sum_{\alpha=1,2}\sum_{\mu=0}^{\infty} f_{j\alpha\mu}^{k+1} d_{\alpha\mu}(s), \quad j = \overline{1,3I+3} \tag{20}$$

where

$$d_{1\mu} = \sin[\mu\gamma(s)], \quad d_{2\mu} = \cos[\mu\gamma(s)], \quad \mu = \overline{0,\mu^*},$$

$$\gamma(s) = 2\pi\int_0^s ds \Big/ \oint_{\Gamma} ds, \quad 0 \le \gamma(s) \le 2\pi$$

With account of Eq. (20), coefficients Eq. (19) are transformed to

$$p_{jmn}^{\text{comp}k+1} = \sum_{\alpha=1,2}\sum_{\mu=0}^{\infty} f_{j\alpha\mu}^{k+1}\theta_{j\alpha\mu}^{mn}, \quad j = \overline{1,3I+3}$$

where

$$\theta_{j\alpha\mu}^{mn} = \oint_{\Gamma} B_{jmn}(x_\Gamma, y_\Gamma)d_{\alpha\mu}(s)ds$$

The boundary conditions on boundary Γ, system (12), are also expanded at each time step in a series over the trace of boundary Γ,

$$\sum_{\beta=1,2}\sum_{\nu=0}^{\infty} \mathrm{s}_{j\beta\nu}^{k+1} d_{\beta\nu}(s) = 0 \tag{21}$$

where

$$\mathrm{s}_{j\beta\nu}^{k+1} = \frac{1}{\lambda_\nu}\oint_{\Gamma}\sum_{j=1}^{3I+3}\oint_{\Gamma} b_{ij}^{\Gamma} u_j^{k+1}(x_\Gamma, y_\Gamma)d_{\beta\nu}ds, \quad j = \overline{1,3I+3},$$

$$\beta = 1,2, \quad \nu = \overline{0,\nu^*}$$

$$\lambda_0 = 2\pi, \quad \lambda_\nu = \pi, \quad \nu = \overline{1,\nu^*}$$

Evidently, conditions (21) shall be fulfilled when equalities

$$s_{j\beta\nu}^{k+1} = 0, \quad j = \overline{1,3I+3}, \quad \beta = 1,2, \quad \nu = \overline{0,\nu^*}$$

are satisfied. At each time step, these equalities form a system of algebraic equations for compensation coefficients of compensating loads,

$$\sum_{j=1}^{3I+3} \sum_{\alpha=1,2} \sum_{\mu=0}^{\mu^*} T_{ij\alpha\mu\beta\nu} f_{j\alpha\mu}^{k+1} = R_{i\beta\nu}^{k+1}, \quad i = \overline{1,3I+3}, \quad \beta = 1,2,$$

$$\nu = \overline{0,\nu^*}$$

where

$$T_{ij\alpha\mu\beta\nu} = \sum_{m=1}^{m^*} \sum_{n=1}^{n^*} \sum_{l=1}^{3I+3} \bar{\theta}_{il\beta\nu}^{mn} \sum_{r=1}^{3I+3} \pi_{lr}^{mn} \theta_{rj\alpha\mu}^{mn} + \frac{\xi_{1i} AB}{8} \delta_{ij},$$

$$j = \overline{1,3I+3}, \quad \alpha = 1,2, \quad \mu = \overline{0,\mu^*}$$

$$R_{i\beta\nu}^{k+1} = -\frac{AB}{4} \sum_{m=1}^{m^*} \sum_{n=1}^{n^*} \sum_{l=1}^{3I+3} \bar{\theta}_{il\beta\nu}^{mn} \varepsilon_{lmn}^{k+1}$$

$$\bar{\theta}_{il\beta\nu}^{mn} = \frac{1}{\lambda_\nu} \oint_\Gamma b_{il}^\Gamma B_{lmn}(x_\Gamma, y_\Gamma) d_{\beta\nu} ds, \quad l = \overline{1,3I+3}$$

δ_{ij} is the Kronecker symbol and ξ_{1i} is the coefficient defining the kind of boundary conditions. The coefficients $\xi_{ki} (k = 1,2, i = \overline{1,3I+3})$ for a simply supported plate are given in the Appendix.

Having calculated the intensities of compensating loads, Eq. (20), the solution of the problem (Eqs. (3), (5), (9), and (10)) takes the final form

$$u_j^{k+1}(x,y) = \sum_{m=1}^{m^*} \sum_{n=1}^{n^*} \left[\sum_{l=1}^{3I+3} \sum_{\alpha=1,2} \sum_{\mu=0}^{\mu^*} \pi_{jl}^{mn} \theta_{l\alpha\mu}^{mn} f_{l\alpha\mu}^{k+1} + \varepsilon_{jmn}^{k+1} \right] B_{jmn}(x,y), \quad j = \overline{1,3I+3} \tag{22}$$

where

$$u_1 = u, \quad u_2 = v, \quad u_3 = w, \quad u_{3+i} = \psi_x^i, \quad u_{3+I+i} = \psi_y^i, \quad u_{3+2I+i} = \psi_z^i, \quad i = \overline{1,I}$$

Then, formulas (22) and (6)–(8) are used to find the parameters of the dynamic response of the laminated plate.

5 Experimental Setup and Procedure

The procedure and equipment for running experiments were developed at A.N. Podgorny Institute for Mechanical Engineering Problems of National Academy of Sciences of Ukraine. They allow for strain measurements with adequate accuracy and recording measurement time intervals. Dynamic wide-range strain gauging was used to measure strain under impact loads [19,24].

Figure 3 shows the experimental setup. Plate 3 fastening along the edge simulates the required type of boundary conditions. Plate (3) is installed on bearing plate (4). Loading was done by dropping an indenter (1) on the outer surface of the first layer of plate (3) by using dropping device (2). Small-base (1 mm measurement base) strain gauges (5) were bonded to the back face of plate (3).

At plate impact loading, the signals from strain gauges bonded to the plate along metering lines are output to a wide-range strain-gauge amplifier (6) (WSA), and therefrom to a multichannel analog-to-digital converter (7) (MADC).

A bridge circuit was used to measure strain. The WSA functions with amplitude modulation at a carrier frequency of 1 MHz. Prior to the experiment, the amplifying channel is calibrated for each strain gauge and $\varepsilon = \varepsilon(U)$ is defined, where ε is the measured strain and U is the signal voltage recorded by the MADC. The signal recording frequency is input on the computer keyboard. For this, the WSA has a clock pulse generator to provide the required signal recording frequency. The maximum clocking frequency is 40 MHz, which is defined by the MADC circuit. The storage capacity in each MADC channel is 1 kbyte. The synchronization pulse generator simultaneously enables all instrumentation channels when it receives a trigger signal. This signal can be applied from one of the strain gauges or the acceleration gauge. An adapter located in the computer serves to maintain a dialog between the computer and the measuring system.

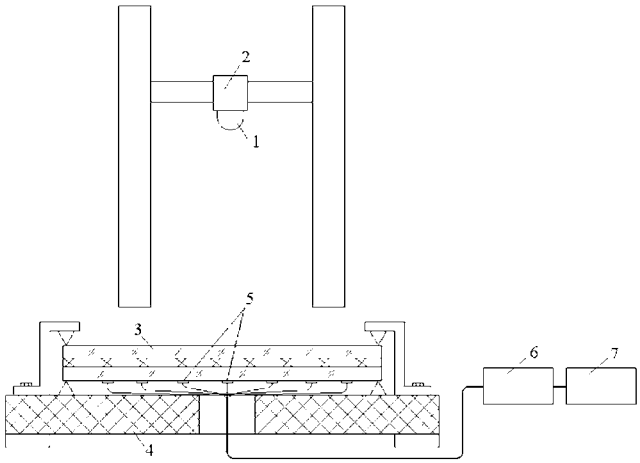

Fig. 3 Experimental setup: (1) indenter, (2) indenter dropping device, (3) laminated plate, (4) bearing plate, (5) strain gauges, (6) WSA, and (7) MADC

The WSA has the following specifications:

(a) number of instrumentation channels 8
(b) carrier frequency, kHz 1000
(c) operating frequency range, kHz 0.04–200
(d) amplitude-frequency response nonlinearity, dB, max ± 1.2
(e) minimal detected strain, relative strain units (RSU) 30×10^{-6}
(f) dynamic range, dB 80
(g) calibration range, RSU $30 \times 10^{-6} - 2.4 \times 10^{-3}$
(h) resistance of strain gauges, Ω 50–200

The application program package supports the following measuring system functions:

(1) creating a file of the test sequence
(2) testing the MADC and certifying its operability
(3) carrying out the experiment with recording of data in the working file
(4) graphic presentation with subsequent output to the monitor or printer
(5) searching for maximum and minimum values
(6) spectral analysis

6 Numerical Results

The numerical results that demonstrate the theoretical and experimental approach were obtained for a simply supported nine-layer plate ($I = 9$). The plate plan view is shown in Fig. 4. Impact loading in different plate points was investigated. A low-velocity impact was considered when strains of the plate were elastic. The contact interaction of the indenter and plate was described by Hertzian law.

The indenter was made of organic glass. The mechanical properties and dimensions of the indenter are as follows: $E = 5.7$

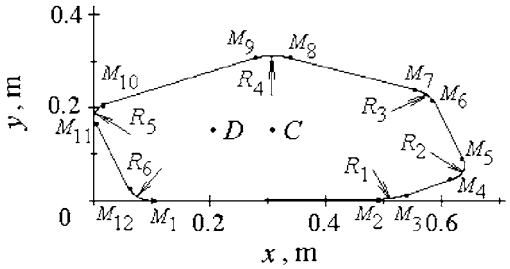

Fig. 4 Plate plan view shape

$\times 10^3$ MPa, $\nu=0.38$, $\rho=1.2\times10^3$ kg/m^3 (indenter material density), $M=0.123$ kg, and $R=0.03$ m. The indenter dropping height was $H=0.62$ m. The parameters of the indenter are such that the diameter of the loading area is much less than the characteristic dimension of the plate.

The carrying layers of the plate ($i=1,3,5,7,9$) were made of silica glass and interconnected by layers from polymer materials ($i=2,4,6,8$). Data for the plate layers are as follows: $E_i=6.12\times10^4$ MPa, $\nu_i=0.22$, and $\rho_i=2.5\times10^3$ kg/m^3 for $i=1,3,5,7,9$; $E_2=10^2$ MPa, $\nu_2=0.39$, and $\rho_2=1.2\times10^3$ kg/m^3; $E_i=2.8\times10^2$ MPa, $\nu_i=0.38$, and $\rho_i=1.2\times10^3$ kg/m^3 for $i=4,6,8$; $h_1=h_9=4\times10^{-3}$ m, $h_2=3\times10^{-3}$ m, $h_3=h_5=5\times10^{-3}$ m, $h_4=h_6=h_8=2\times10^{-3}$ m, and $h_7=7\times10^{-3}$ m. Here, ρ_i is the density of the ith layer material.

The plate contour consists of K straight segments and K adjoint circle arcs ($K=6$). Contour s_{2k-1} segments, being straight lines, are defined by the following equations:

$$x = x_{2k-1} + (S - S_{2(k-1)})\cos\alpha_{2k-1},$$

$$y = y_{2k-1} + (S - S_{2(k-1)})\sin\alpha_{2k-1}, \quad k = \overline{1,K}$$

where point $M_{2k-1}(x_{2k-1},y_{2k-1})$ is beginning of the $(2k-1)$th straight-line segment.

Contour segments s_{2k}, being arcs of circles, are defined as

$$x = x_{2k} + R_k\left[\sin\left(\frac{S - S_{2k-1}}{R_k} + \alpha_{2k-1}\right) - \sin\alpha_{2k-1}\right]$$

$$y = y_{2k} - R_k\left[\cos\left(\frac{S - S_{2k-1}}{R_k} + \alpha_{2k-1}\right) - \cos\alpha_{2k-1}\right], \quad k = \overline{1,K}$$

where point $M_{2k}(x_{2k},y_{2k})$ is the end of the $(2k-1)$th straight-line segment;

$$S_k = \sum_{i=1}^{k} s_i, \quad S_0 = 0$$

α_{2k-1} is the angle between the $(2k-1)$th straight-line segment on the contour and the positive direction of axis Ox; S is the length of contour segment from the reference point (point $M_1(x_1,y_1)$) to the current one $M(x,y)$ on the given contour segment; $s_1=|M_1M_2|=0.5$ m, $s_3=|M_3M_4|=0.23$ m, $s_5=|M_5M_6|=0.44$ m, $s_7=|M_7M_8|=0.34$ m, $s_9=|M_9M_{10}|=0.31$ m, and $s_{11}=|M_{11}M_{12}|=0.31$ m; $R_1=0.15$ m, $R_2=0.03$ m, $R_3=0.06$ m, $R_4=0.11$ m, $R_5=0.035$ m, and $R_6=0.045$ m; $\alpha_1=2$, $\alpha_3=23$ deg, $\alpha_5=113$ deg, $\alpha_7=164$ deg, $\alpha_9=204$ deg, and $\alpha_{11}=294$ deg.

The loading area center coordinates are $(x_0,y_0,0)$ (Figs. 1 and 2) and those of the point where the dynamic response is calculated are (x_p,y_p,z_p). The response investigated was the strain occurring on the outer surface of the ninth plate layer.

First, we conducted experimental runs for an impact in Point C, $x_0=0.31$ m and $y_0=0.155$ m. Strains were measured simultaneously in points $x_p=0.31$ m, $y_p=0.155$ m, and $z_p=0.034$ m, and $x_p=0.205$ m, $y_p=0.155$ m, and $z_p=0.034$ m. Then we conducted

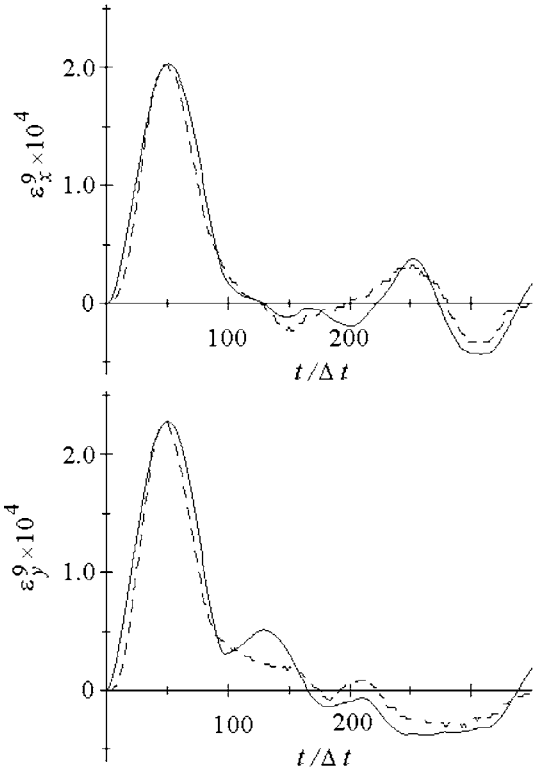

Fig. 5 Strain ε_x^9 and ε_y^9 in point $x_p=0.31$ m, $y_p=0.155$ m, $z_p=0.034$ m for impact in point $C(0.31;0.155;0)$

experimental runs for an impact in Point D, $x_0=0.205$ m, and $y_0=0.155$ m. Strains were measured in the same points. Each run included 20 experiments.

Figures 5–8 show the theoretical and experimental results for strain ε_x^9 and ε_y^9 versus time. The time step Δt was 4×10^{-6} s. The mismatch between the maximum numerical and experimental strains in points under the contact area (Figs. 5 and 7) was within 5%, and in other points (Figs. 6 and 8) it was within 10%, confirming the validity of results.

7 Conclusion

An effective analytical method for investigating the dynamic response of plates, developed earlier for one-layer plates, was extended to investigating the response of laminated plates having a noncanonical shape. This method yielded a solution of the plate-indenter impact problem in the form of a trigonometric series. The impact was effected by dropping an indenter with a semispherical end.

The method potentialities are demonstrated by calculating the strain in a nine-layer plate when the indenter is dropped in different points of the plate. A good match of theoretical and experimental results for different cases of applying the impact load confirms the feasibility and effectiveness of the method offered.

The developed approach can be easily extended to impulse loading and impact applied to plates of noncanonical shape in plan view with arbitrary boundary conditions.

Appendix

The nonzero elements of matrix $\mathbf{\Omega}_\rho$ are

$$\Omega_{\rho\,1\,1} = \Omega_{\rho\,2\,2} = \Omega_{\rho\,3\,3} = C_\rho^I$$

$$\Omega_{\rho\,1\,3+i} = \Omega_{\rho\,3+i\,1} = \Omega_{\rho\,2\,3+I+i} = \Omega_{\rho\,3+I+i\,2} = \Omega_{\rho\,3\,3+2I+i} = \Omega_{\rho\,3+2I+i\,3} = D_\rho^i$$

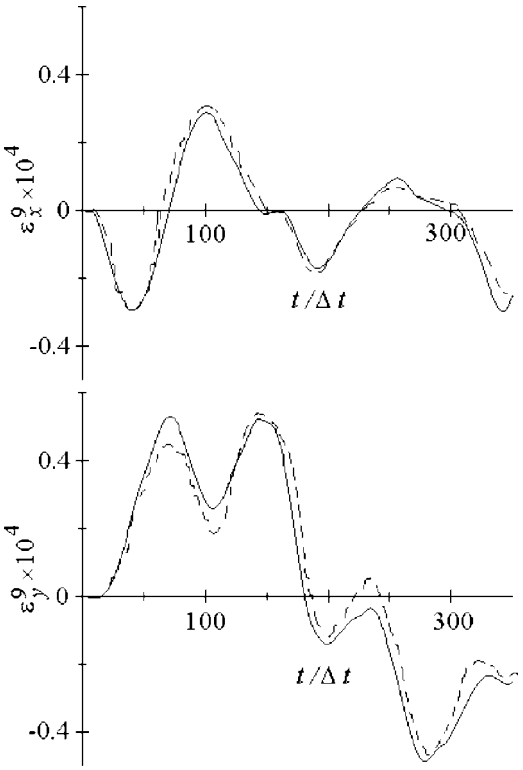

Fig. 6 Strain ε_x^9 and ε_y^9 in point x_p=0.205 m, y_p=0.155 m, z_p =0.034 m for impact in point C(0.31;0.155;0)

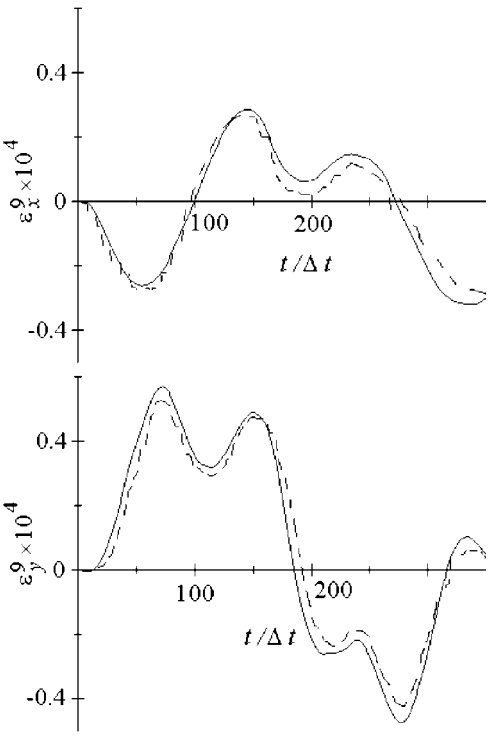

Fig. 8 Strain ε_x^9 and ε_y^9 in point x_p=0.31 m, y_p=0.155 m, z_p =0.034 m for impact in point D(0.205;0.155;0)

$$\Omega_{\rho\ 3+i\ 3+j} = \Omega_{\rho\ 3+I+i\ 3+I+j} = \Omega_{\rho\ 3+2I+i\ 3+2I+j} = \eta_\rho^{ij}, \quad i,j = \overline{1,I}$$

where

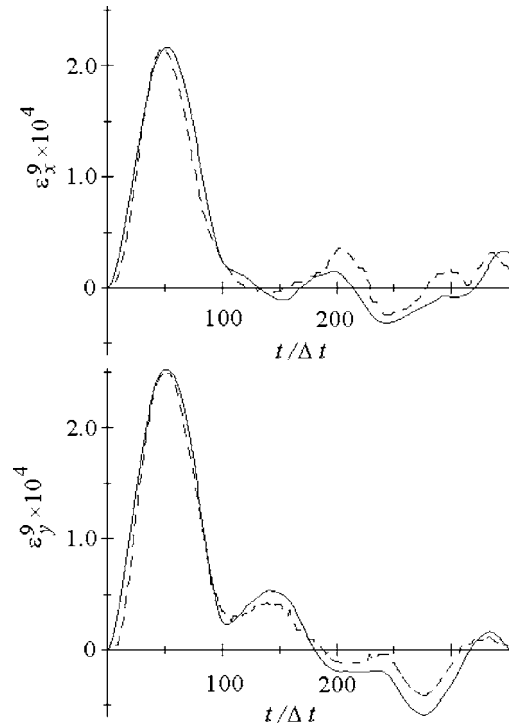

Fig. 7 Strain ε_x^9 and ε_y^9 in point x_p=0.205 m, y_p=0.155 m, z_p =0.034 m for impact in point D(0.205;0.155;0)

$$\alpha_\rho^i = \rho_i h_i, \quad C_\rho^i = \sum_{j=1}^{i} \alpha_\rho^j, \quad D_\rho^i = h_i(C_\rho^I - C_\rho^i) + \beta_\rho^i,$$

$$K_\rho^i = h_i^2(C_\rho^I - C_\rho^i) + \gamma_\rho^j$$

$$\eta_\rho^{ij} = \begin{cases} h_j D_\rho^i, & j < i, \\ K_\rho^i, & j = i, \\ h_i D_\rho^j, & j > i, \end{cases} \qquad i,j = \overline{1,I}$$

ρ_i is density of ith layer

The elements of stiffness matrix $\mathbf{\Lambda}$ are

$$\Lambda_{1\ 1} = C_1^I \frac{\partial^2}{\partial x^2} + C_3^I \frac{\partial^2}{\partial y^2}, \quad \Lambda_{1\ 2} = \Lambda_{2\ 1} = (C_2^I + C_3^I)\frac{\partial^2}{\partial x \partial y},$$

$$\Lambda_{1\ 3} = -\Lambda_{3\ 1} = 0$$

$$\Lambda_{1\ 3+i} = \Lambda_{3+i\ 1} = D_1^i \frac{\partial^2}{\partial x^2} + D_3^i \frac{\partial^2}{\partial y^2},$$

$$\Lambda_{1\ 3+I+i} = \Lambda_{3+I+i\ 1} = (D_2^i + D_3^i)\frac{\partial^2}{\partial x \partial y}$$

$$\Lambda_{1\ 3+2I+i} = -\Lambda_{3+2I+i\ 1} = \alpha_2^i \frac{\partial}{\partial x}, \quad \Lambda_{2\ 2} = C_3^I \frac{\partial^2}{\partial x^2} + C_1^I \frac{\partial^2}{\partial y^2},$$

$$\Lambda_{2\ 3} = \Lambda_{3\ 2} = 0$$

$$\Lambda_{2\ 3+i} = \Lambda_{3+i\ 2} = (D_2^i + D_3^i)\frac{\partial^2}{\partial x \partial y},$$

$$\Lambda_{2\ 3+I+i} = \Lambda_{3+I+i\ 2} = D_3^i \frac{\partial^2}{\partial x^2} + D_1^i \frac{\partial^2}{\partial y^2}$$

$$\Lambda_{2\ 3+2I+i} = -\Lambda_{3+2I+i\ 2} = \alpha_2^i \frac{\partial}{\partial y}, \quad \Lambda_{3\ 3} = C_3^I \left(\frac{\partial^2}{\partial x^2} + C_3^I \frac{\partial^2}{\partial y^2} \right)$$

$$\Lambda_{3\ 3+i} = -\Lambda_{3+i\ 3} = \alpha_3^i \frac{\partial}{\partial x}, \quad \Lambda_{3\ 3+I+i} = -\Lambda_{3+I+i\ 3} = \alpha_3^i \frac{\partial}{\partial y}$$

$$\Lambda_{3\ 3+2I+i} = \Lambda_{3+2I+i\ 3} = D_3^i \left(\frac{\partial^2}{\partial x^2} + \frac{\partial^2}{\partial y^2} \right),$$

$$\Lambda_{3+i\ 3+j} = \eta_1^{ij} \frac{\partial^2}{\partial x^2} + \eta_3^{ij} \frac{\partial^2}{\partial y^2} - \delta_{ij} \alpha_3^i$$

$$\Lambda_{3+i\ 3+I+j} = \Lambda_{3+I+j\ 3+i} = (\eta_2^{ij} + \eta_3^{ij}) \frac{\partial^2}{\partial x \partial y},$$

$$\Lambda_{3+i\ 3+2I+j} = -\Lambda_{3+2I+j\ 3+i} = \overline{\eta}_1^{ij} \frac{\partial}{\partial x}$$

$$\Lambda_{3+I+i\ 3+I+j} = \eta_3^{ij} \frac{\partial^2}{\partial x^2} + \eta_1^{ij} \frac{\partial^2}{\partial y^2} - \delta_{ij} \alpha_3^i,$$

$$\Lambda_{3+I+i\ 3+2I+j} = -\Lambda_{3+2I+j\ 3+I+i} = \overline{\eta}_1^{ij} \frac{\partial}{\partial y}$$

$$\Lambda_{3+2I+i\ 3+2I+j} = \eta_3^{ij} \left(\frac{\partial^2}{\partial x^2} + \frac{\partial^2}{\partial y^2} \right) - \delta_{ij} \alpha_1^i, \quad i,j = \overline{1,I}$$

where

$$C_k^i = \sum_{j=1}^{i} \alpha_k^j, \quad D_k^i = h_i (C_k^I - C_k^i) + \frac{\beta_k^i}{2}, \quad K_k^i = h_i^2 (C_k^I - C_k^i) + \frac{\gamma_k^j}{3}$$

$$\eta_k^{ij} = \begin{Bmatrix} D_k^i h_j, & j < i \\ K_k^i, & j = i \\ D_k^j h_i, & j > i \end{Bmatrix}, \quad \overline{\eta}_1^{ij} = \begin{Bmatrix} -h_j \alpha_3^i, & j < i \\ (\beta_2^i - \beta_3^i)/2, & j = i \\ h_i \alpha_2^j, & j > i \end{Bmatrix},$$

$$\delta_{ij} = \begin{Bmatrix} 1, & i = j \\ 0, & i \neq j \end{Bmatrix}$$

$$\alpha_1^i = \frac{E_i h_i}{1 - \nu_i^2}, \quad \alpha_2^i = \alpha_1^i \nu_i, \quad \alpha_3^i = \alpha_1^i \frac{1 - \nu_i}{2}$$

$$\beta_k^i = \alpha_k^i h_i, \quad \gamma_k^i = \beta_k^i h_i, \quad i,j = \overline{1,I}, \quad k = 1,2,3$$

The elements of matrix $\mathbf{B}^\Gamma$ that defines the boundary conditions are

$$b_{ij}^\Gamma = \xi_{1i} A_{ij}^1 + \xi_{2i} A_{ij}^2, \quad i,j = \overline{1,3I+3}$$

Here, $\mathbf{A}^1$ and $\mathbf{A}^2$ are matrices whose nonzero elements are

$$A_{11}^1 = (C_1^I n_x^2 + C_2^I n_y^2) \frac{\partial}{\partial x} + 2 C_3^I n_x n_y \frac{\partial}{\partial y},$$

$$A_{12}^1 = 2 C_3^I n_x n_y \frac{\partial}{\partial x} + (C_2^I n_x^2 + C_1^I n_y^2) \frac{\partial}{\partial y}$$

$$A_{1\ 3+i}^1 = A_{3+i\ 1}^1 = (D_1^i n_x^2 + D_2^i n_y^2) \frac{\partial}{\partial x} + 2 D_3^i n_x n_y \frac{\partial}{\partial y}$$

$$A_{1\ 3+I+i}^1 = A_{3+i\ 2}^1 = 2 D_3^i n_x n_y \frac{\partial}{\partial x} + (D_2^i n_x^2 + D_1^i n_y^2) \frac{\partial}{\partial y}, \quad A_{1\ 3+2I+i}^1 = \alpha_2^i$$

$$A_{21}^1 = (C_2^I - C_1^I) n_x n_y \frac{\partial}{\partial x} + C_3^I (n_x^2 - n_y^2) \frac{\partial}{\partial y}$$

$$A_{22}^1 = C_3^I (n_x^2 - n_y^2) \frac{\partial}{\partial x} - (C_2^I - C_1^I) n_x n_y \frac{\partial}{\partial y}$$

$$A_{2\ 3+i}^1 = A_{3+I+i\ 1}^1 = (D_2^i - D_1^i) n_x n_y \frac{\partial}{\partial x} + D_3^i (n_x^2 - n_y^2) \frac{\partial}{\partial y}$$

$$A_{2\ 3+I+i}^1 = A_{3+I+i\ 2}^1 = D_3^i (n_x^2 - n_y^2) \frac{\partial}{\partial x} - (D_2^i - D_1^i) n_x n_y \frac{\partial}{\partial y}$$

$$A_{33}^1 = C_3^I \left(n_x \frac{\partial}{\partial x} + n_y \frac{\partial}{\partial y} \right), \quad A_{3\ 3+i}^1 = \alpha_3^i n_x, \quad A_{3\ 3+I+i}^1 = \alpha_3^i n_y$$

$$A_{3\ 3+2I+i}^1 = A_{3+2I+i\ 3}^1 = D_3^i \left(n_x \frac{\partial}{\partial x} + n_y \frac{\partial}{\partial y} \right)$$

$$A_{3+i\ 3+j}^1 = (\eta_1^{ij} n_x^2 + \eta_2^{ij} n_y^2) \frac{\partial}{\partial x} + 2 \eta_3^{ij} n_x n_y \frac{\partial}{\partial y}$$

$$A_{3+i\ 3+I+j}^1 = 2 \eta_3^{ij} n_x n_y \frac{\partial}{\partial x} + (\eta_2^{ij} n_x^2 + \eta_1^{ij} n_y^2) \frac{\partial}{\partial y}, \quad A_{3+i\ 3+2I+j}^1 = \overline{\eta}_2^{ij}$$

$$A_{3+I+i\ 3+j}^1 = (\eta_2^{ij} - \eta_1^{ij}) n_x n_y \frac{\partial}{\partial x} + \eta_3^{ij} (n_x^2 - n_y^2) \frac{\partial}{\partial y}$$

$$A_{3+I+i\ 3+I+j}^1 = \eta_3^{ij} (n_x^2 - n_y^2) \frac{\partial}{\partial x} - (\eta_2^{ij} - \eta_1^{ij}) n_x n_y \frac{\partial}{\partial y}$$

$$A_{3+2I+j\ 3+i}^1 = \overline{\eta}_3^{ij} n_x, \quad A_{3+2I+j\ 3+I+i}^1 = \overline{\eta}_3^{ij} n_y$$

$$A_{3+2I+i\ 3+2I+j}^1 = \eta_3^i \left(n_x \frac{\partial}{\partial x} + n_y \frac{\partial}{\partial y} \right)$$

$$A_{11}^2 = A_{22}^2 = A_{3+i\ 3+j}^2 = A_{3+I+i\ 3+I+j}^2 = n_x, \quad A_{33}^2 = A_{3+2I+i\ 3+2I+i}^2 = 1$$

$$A_{12}^2 = -A_{21}^2 = A_{3+i\ 3+I+j}^2 = -A_{3+I+i\ 3+j}^2 = n_y$$

$$\overline{\eta}_k^{ij} = \begin{Bmatrix} 0, & j < i \\ \beta_k^i/2, & j = i \\ h_i \alpha_k^j, & j > i \end{Bmatrix}, \quad i,j = \overline{1,I}, \quad k = 2,3$$

where n_x and n_y are the directional cosines of the normal to boundary Γ.

Coefficients ξ_{1i} and ξ_{2i} allow selecting the boundary conditions on the support contour. For simply supported

$$\xi_{11} = \xi_{12} = \xi_{23} = \xi_{1\ 3+i} = \xi_{1\ 3+I+i} = \xi_{1\ 3+2I+i} = 1$$

$$\xi_{21} = \xi_{22} = \xi_{13} = \xi_{2\ 3+i} = \xi_{2\ 3+I+i} = \xi_{2\ 3+2I+i} = 0, \quad i = \overline{1,I}$$

The elements of matrix $\mathbf{\Lambda}^{mn}$ are

$$\Lambda_{11}^{mn} = C_1^I \frac{m^2 \pi^2}{A^2} + C_3^I \frac{n^2 \pi^2}{B^2}, \quad \Lambda_{1\ 2}^{mn} = \Lambda_{2\ 1}^{mn} = (C_2^I + C_3^I) \frac{mn\pi^2}{AB}$$

$$\Lambda_{1\ 3}^{mn} = \Lambda_{3\ 1}^{mn} = 0, \quad \Lambda_{1\ 3+i}^{mn} = \Lambda_{3+i\ 1}^{mn} = D_1^i \frac{m^2 \pi^2}{A^2} + D_3^i \frac{n^2 \pi^2}{B^2}$$

$$\Lambda_{1\ 3+I+i}^{mn} = \Lambda_{3+I+i\ 1}^{mn} = (D_2^i + D_3^i) \frac{mn\pi^2}{AB},$$

$$\Lambda_{1\ 3+2I+i}^{mn} = \Lambda_{3+2I+i\ 1}^{mn} = -\alpha_2^i \frac{m\pi}{A}$$

$$\Lambda_{2\ 2}^{mn} = C_3^I \frac{m^2 \pi^2}{A^2} + C_1^I \frac{n^2 \pi^2}{B^2}, \quad \Lambda_{2\ 3}^{mn} = \Lambda_{3\ 2}^{mn} = 0$$

$$\Lambda^{mn}_{2\ 3+i} = \Lambda^{mn}_{3+i\ 2} = (D^i_2 + D^i_3)\frac{mn\pi^2}{AB},$$

$$\Lambda^{mn}_{2\ 3+I+i} = \Lambda^{mn}_{3+I+i\ 2} = D^i_3\frac{m^2\pi^2}{A^2} + D^i_1\frac{n^2\pi^2}{B^2}$$

$$\Lambda^{mn}_{2\ 3+2I+i} = \Lambda^{mn}_{3+2I+i\ 2} = -\alpha^i_2\frac{n\pi}{B}, \quad \Lambda^{mn}_{33} = C^I_3\left(\frac{m^2\pi^2}{A^2} + \frac{n^2\pi^2}{B^2}\right)$$

$$\Lambda^{mn}_{3\ 3+i} = \Lambda^{mn}_{3+i\ 3} = \alpha^i_3\frac{m\pi}{A}, \quad \Lambda^{mn}_{3\ 3+I+i} = \Lambda^{mn}_{3+I+i\ 3} = \alpha^i_3\frac{n\pi}{B}$$

$$\Lambda^{mn}_{3\ 3+2I+i} = \Lambda^{mn}_{3+2I+i\ 3} = D^i_3\left(\frac{m^2\pi^2}{A^2} + \frac{n^2\pi^2}{B^2}\right),$$

$$\Lambda^{mn}_{3+i\ 3+j} = \eta^{ij}_1\frac{m^2\pi^2}{A^2} + \eta^{ji}_3\frac{n^2\pi^2}{B^2} + \delta_{ij}\alpha^i_3$$

$$\Lambda^{mn}_{3+i\ 3+I+j} = \Lambda^{mn}_{3+I+j\ 3+i} = (\eta^{ij}_2 + \eta^{ij}_3)\frac{mn\pi^2}{AB},$$

$$\Lambda^{mn}_{3+i\ 3+2I+j} = \Lambda^{mn}_{3+2I+j\ 3+i} = -\overline{\eta}^{ij}_1\frac{m\pi}{A}$$

$$\Lambda^{mn}_{3+I+i\ 3+I+j} = \eta^{ij}_3\frac{m^2\pi^2}{A^2} + \eta^{ij}_1\frac{n^2\pi^2}{B^2} - \delta_{ij}\alpha^i_3,$$

$$\Lambda^{mn}_{3+I+i\ 3+2I+j} = \Lambda^{mn}_{3+2I+j\ 3+I+i} = \overline{\eta}^{ij}_1\frac{n\pi}{B}$$

$$\Lambda^{mn}_{3+2I+i\ 3+2I+j} = \eta^{ij}_3\left(\frac{m^2\pi^2}{A^2} + \frac{n^2\pi^2}{B^2}\right) - \delta_{ij}\alpha^i_1, \quad i,j = \overline{1,I}$$

References

[1] Goldsmith, W., 1960, *Impact. The Theory and Physical Behaviour of Colliding Solids*, Edward Arnold, London.

[2] Jones, N., 1989, *Structural Impact*, Cambridge University Press, Cambridge.

[3] 1990, *High Velocity Impact Dynamics*, J. A. Zukas, ed., Wiley, New York.

[4] Corbett, G. G., Reid, S. R., and Johnson, W., 1996, "Impact Loading of Plates and Shells by Free-Flying Projectiles: A Review," Int. J. Impact Eng., **18**(2), pp. 141–230.

[5] Abrate, S., 1998, *Impact on Composite Structures*, Cambridge University Press, Cambridge.

[6] Fields, J. E., Walley, S. M., Proud, W. G., Goldrein, H. T., and Siviour, C. R., 2004, "Review of Experimental Techniques for High Rate Deformation and Shock Studies," Int. J. Impact Eng., **30**(7), pp. 725–775.

[7] Alhazza, Kh. A., and Alhazza, A. A., 2004, "A Review of the Vibrations of Plates and Shells," Shock Vib. Dig., **36**(5), pp. 377–395.

[8] Qiu, X., Deshpande, V. S., and Fleck, N. A., 2004, "Dynamic Response of a Clamped Circular Sandwich Plate Subject to Shock Loading," ASME J. Appl. Mech., **71**(5), pp. 637–645.

[9] McShane, G. J., Radford, D. D., Deshpande, V. S., and Fleck, N. A., 2006, "The Response of Clamped Sandwich Plates With Lattice Cores Subjected to Shock Loading," Eur. J. Mech. A/Solids, **25**(2), pp. 215–229.

[10] Malekzadeh, K., Khalili, M. R., and Mittal, R. K., 2006, "Analytical Prediction of Low-velocity Impact Response of Composite Sandwich Panels Using New TDOF Spring-Mass-Damper Model," J. Compos. Mater., **40**(18), pp. 1671–1689.

[11] Naidu, N. V. S., and Sinha, P. K., 2005, "Nonlinear Impact Behaviour of Laminated Composite Shells in Hygrothermal Environments," Int. J. Crashworthiness, **10**(4), pp. 389–402.

[12] Schubel, P. M., Luo, J.-J., and Daniel, I. M., 2005, "Low Velocity Impact Behavior of Composite Sandwich Panels," Composites, Part A, **36**(10), pp. 1389–1396.

[13] Lataillade, J. L., Guillaumat, L., and Vidal, B., 2001, "Materials and Structures: Some Experimental and Calculations Procedures for the Responses of Composites Plates and Sandwich Panels to Low Velocity Impacts," *New Experimental Methods in Material Dynamics and Impact*, W. K. Nowacki and J. R. Klepaczko, eds., Institute of Fundamental Technological Research, Warsaw, Poland, pp. 267–307.

[14] Banerjee, S., Prosser, W., and Mal, A., 2005, "Calculation of the Response of a Composite Plate to Localized Dynamic Surface Loads Using a New Wave Number Integral Method," ASME J. Appl. Mech., **72**(1), pp. 18–24.

[15] Olsson, R., 1992, "Impact Response of Orthotropic Composite Plates Predicted From a One-Parameter Differential Equation," AIAA J., **30**(6), pp. 1587–1596.

[16] Anderson, T., Madenci, E., Burton, W. S., and Fish, J. C., 1998, "Analytical Solution of Finite-Geometry Composite Panels Under Transient Surface Loading," Int. J. Solids Struct., **35**(12), pp. 1219–1239.

[17] Anderson, T., and Madenci, E., 2000, "Graphite/Epoxy Foam Sandwich Panels Under Quasi-Static Indentation," Eng. Fract. Mech., **67**(4), pp. 329–344.

[18] Anderson, T., and Madenci, E., 2000, "Experimental Investigation of Low-Velocity Impact Characteristics of Sandwich Composites," Compos. Struct., **50**(3), pp. 239–247.

[19] Smetankina, N. V., Shupikov, A. N., Sotrikhin, S. Yu., and Yareschenko, V. G., 2007, "Dynamic Response of an Elliptic Plate to Impact Loading. Theory and Experiment," Int. J. Impact Eng., **34**(2), pp. 264–276.

[20] Timoshenko, S. P., Young, D. H., and Weaver, W. Jr., 1974, *Vibration Problems in Engineering*, Wiley, New York.

[21] Tan, T. M., and Sun, C. T., 1988, "Use of Statical Indentation Laws in the Impact Analysis of Laminated Composite Plates," ASME J. Appl. Mech., **52**(1), pp. 6–12.

[22] Lin, H. J., and Lee, Y. J., 1990, "Use of Statical Indentation Laws in the Impact Analysis of Composite Laminated Plates and Shells," ASME J. Appl. Mech., **57**(3), pp. 787–789.

[23] Nosier, A., Kapania, R. K., and Reddy, J. N., 1994, "Low-Velocity Impact of Laminated Composites Using a Layerwise Theory," Comput. Mech., **13**(5), pp. 360–379.

[24] Smetankina, N. V., Sotrikhin, S. Yu., and Shupikov, A. N., 1995, "Theoretical and Experimental Investigation of Vibration of Multilayer Plates Under the Action of Impulse and Impact Loads," Int. J. Solids Struct., **32**(8/9), pp. 1247–1258.

[25] Dinnik, A. N., 1952, *Selected Works*, Academy of Sciences of the Ukrainian S.S.R. Publishers, Kiev.

[26] Shupikov, A. N., and Smetankina, N. V., 2001, "Non-Stationary Vibration of Multilayer Plates of an Uncanonical Form. The Elastic Immersion Method," Int. J. Solids Struct., **38**(14), pp. 2271–2290.

[27] Shupikov, A. N., and Ugrimov, S. V., 1999, "Vibrations of Multilayer Plates Under the Effect of Impulse Loads. Three-Dimensional Theory," Int. J. Solids Struct., **36**(22), pp. 3391–3402.

[28] Lanczos, C., 1956, *Applied Analysis*, Prentice Hall, Englewood Cliffs, NJ.

Active Absorption of Viscously Damped System With Time Delay

Yitshak M. Ram
Department of Mechanical Engineering,
Louisiana State University,
Baton Rouge, LA 70803

Kumar Vikram Singh
Department of Mechanical and Manufacturing Engineering,
Miami University,
Oxford, OH 45056

In general, it is not possible to obtain total motion absorption of a certain degree of freedom in a harmonically excited damped system by passive control. This paper presents a method of obtaining total absorption in viscously damped system by active control, including time delay, which is unavoidable in digital controlled system. The control is applied on one degree of freedom and the absorption is achieved at another point. This study is carried out by both complex and real analyses. The necessary and sufficient condition for obtaining total absorption is given. Examples demonstrate the various results. [DOI: 10.1115/1.2936926]

1 Introduction

By total absorption, we mean that the motion of a certain degree of freedom in harmonically excited system vanishes. Total absorption is important in applications where sensitive equipment and devices may be placed at a steady degree of freedom. Frahm has shown that total absorption is possible in a two degree-of-freedom conservative system such as that shown in Fig. 1(*a*) where the rigidity $k_2=\omega^2/m_2$ [1]. In this case, $x_1=0$ is a possible solution. There is a wealth of literature dealing with extensions of this result and with its applications [2–5]. Mottershead and Lallement [6] have shown how to create a nodal point in a vibrating system by applying a Rank 1 structural modification. Assignment of zeros in the frequency response function using added masses was first achieved experimentally by Mottershead [7]. The sensitivity of the zeros of the frequency response function in a conservative system has been studied by Mottershead [8]. The theory was generalized to multidegrees of freedom conservative system with a multiple frequency dynamic absorber in Ref. [9] and a continuous system in Ref. [10].

We have shown in Ref. [11] that, in general, it is not possible to achieve total absorption in a harmonically excited damped system by adjusting the rigidity of one of the springs and the damping coefficient of one of the dashpots. We have proved this result by contradiction. Consider the three degrees-of-freedom system shown in Fig. 1(*b*), and suppose that by changing k_2 and c_2 to $\hat{k}_2$ and $\hat{c}_2$ total absorption $x_1=0$ is achieved. Then, the motion of the other two degrees of freedom x_2 and x_3 is equivalent to that of the system shown in Fig. 1(*c*). Obviously, the steady state motion of the system of Fig. 1(*c*) vanishes. Hence, if $x_1=x_2=x_3=0$, no force is able to oppose the external force $\sin(\omega t)$. Total absorption in a nonconservative system is possible by active control that mimics the dynamics of a spring and a dashpot, since by active control we can produce the effect of spring or dashpot with negative coefficients. Time delay, however small, is inherent to digital active controlled systems. This paper deals with total absorption in nonconservative system when time delay in the control is accounted for.

In Sec. 2, we derive an explicit solution for the control parameters. In Sec. 3, we present analogues formulation using real number analysis. It gives an insight to the solution in terms of equivalent rigidity and damping coefficients and provides a framework for verification of the result. Section 4 extends the result to a continuous system, namely, the nonuniform damped vibrating rod. Conclusions are drawn in Sec. 5.

Contributed by the Applied Mechanics Division of ASME for publication in the JOURNAL OF APPLIED MECHANICS. Manuscript received March 28, 2007; final manuscript received March 31, 2008; published online July 2, 2008. Review conducted by Wei-Chau Xie.

2 Control Parameters

Since the degrees of freedom may be numbered arbitrarily, we may without loss of generality consider an n degree of freedom where the harmonic excitation of frequency ω applies on x_n and the control acts on x_1. The dynamics of such a system is described by

$$\mathbf{M}\ddot{\mathbf{x}}+\mathbf{C}\dot{\mathbf{x}}+\mathbf{K}\mathbf{x}=\mathbf{e}_n e^{j\omega t}+\mathbf{e}_1 u(t-\tau) \tag{1}$$

where the control is

$$u(t-\tau)=\alpha\dot{x}_1(t-\tau)+\beta x_1(t-\tau) \tag{2}$$

and where $\mathbf{e}_k$ is the kth unit vector of appropriate dimension. Unlike passive control, here the control parameters may be positive or negative. Time delay τ that must exist between the state measurement of x_1 and the actuation of the control force u is accounted for in this formulation.

We assume that $\mathbf{M}$, $\mathbf{C}$, $\mathbf{K}$, ω, and τ are known and we wish to find α and β such that $x_n=0$ for all time t. Symmetry or even definiteness of the mass matrix $\mathbf{M}$, the damping matrix $\mathbf{C}$, and the stiffness matrix $\mathbf{K}$ is not crucial in the ensuing analysis.

If the controlled system is stable, then its steady state response is

$$\mathbf{x}(t)=\mathbf{a}e^{j\omega t} \tag{3}$$

where $\mathbf{a}$ is a constant vector, independent of time t. Substituting Eq. (3) in Eq. (2) gives

$$u(t-\tau)=a_1 s e^{j\omega t} \tag{4}$$

where

$$s=e^{-j\omega\tau}(j\omega\alpha+\beta) \tag{5}$$

and from Eq. (1) we have

$$(-\omega^2\mathbf{M}+j\omega\mathbf{C}+\mathbf{K})\mathbf{a}=\mathbf{e}_n+a_1 s\mathbf{e}_1 \tag{6}$$

For any matrix $\mathbf{Z}\in\Re^{n\times n}$, let $\hat{\mathbf{Z}}$ be the $(n-1)\times(n-1)$ matrix obtained by deleting the last row and column of $\mathbf{Z}$, and for any vector $\mathbf{z}\in\Re^n$ let $\hat{z}$ be the $(n-1)$ vector obtained by deleting the last row of $\mathbf{z}$. Then the requirement $a_n=0$ substituted in Eq. (6) gives

$$(-\omega^2\hat{\mathbf{M}}+j\omega\hat{\mathbf{C}}+\hat{\mathbf{K}}-s\hat{\mathbf{e}}_1\hat{\mathbf{e}}_1^T)\hat{\mathbf{a}}=\mathbf{0} \tag{7}$$

So s is the finite eigenvalue of

$$(\hat{\mathbf{A}}-s\hat{\mathbf{B}})\hat{\mathbf{a}}=\mathbf{0} \tag{8}$$

where

$$\hat{\mathbf{A}}=-\omega^2\hat{\mathbf{M}}+j\omega\hat{\mathbf{C}}+\hat{\mathbf{K}} \quad \text{and} \quad \hat{\mathbf{B}}=\hat{\mathbf{e}}_1\hat{\mathbf{e}}_1^T \tag{9}$$

The only finite eigenvalue of Eq. (8) is, in fact,

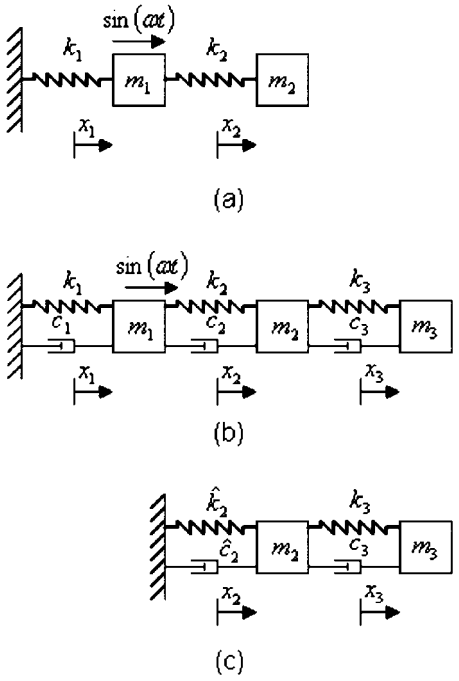

Fig. 1 Illustrative systems

$$s = \frac{\det(\hat{\mathbf{A}})}{\det(\tilde{\mathbf{A}})} \tag{10}$$

where for any matrix $\mathbf{Z} \in \Re^{n\times n}$, $\tilde{\mathbf{Z}}$ is the $(n-2)\times(n-2)$ matrix obtained by deleting the first and last rows and columns of $\mathbf{Z}$. Note that s is the inverse of a collocated reacceptance at x_1 of the system under the constraint $x_n=0$. The control gains α and β are thus obtained from Eq. (5) as follows:

$$\alpha = \frac{1}{\omega}\,\mathrm{Im}(se^{j\omega\tau}) \quad \text{and} \quad \beta = \mathrm{Re}(se^{j\omega\tau}) \tag{11}$$

It follows from Eq. (10) that $s=s(\omega)$ independent of the time delay τ. Hence, for a given ω, the control parameters vary in a sinusoidal manner with τ according to

$$\alpha = \frac{1}{\omega}(\mathrm{Re}(s)\sin(\omega\tau) + \mathrm{Im}(s)\cos(\omega\tau)) \tag{12}$$

and

$$\beta = \mathrm{Re}(s)\cos(\omega\tau) - \mathrm{Im}(s)\sin(\omega\tau) \tag{13}$$

For any change in the time delay, the variations in α and β are bounded by $-|s|/\omega \le \alpha \le |s|/\omega$ and $-|s| \le \beta \le |s|$. Another remarkable property is obtained by considering the last equation of Eq. (6), namely,

$$\mathbf{e}_n^T(-\omega^2\mathbf{M} + j\omega\mathbf{C} + \mathbf{K})\mathbf{a} = 1, \quad a_n = 0 \tag{14}$$

which imply that for a given frequency of excitation ω the norm of $\mathbf{a}$ is invariant of the time delay τ. The physical meaning is that total absorption is achieved by increasing the amplitude of vibrations in the other degrees of freedom.

It follows from Eq. (10) that if $\det(\tilde{\mathbf{A}})=0$, the problem is not solvable. This case corresponds to the situation where an eigenvalue of $\lambda^2\tilde{\mathbf{M}}+\lambda\tilde{\mathbf{C}}+\tilde{\mathbf{K}}$ is purely imaginary, i.e., $\lambda = \pm j\omega_k$, and the exciting frequency if $\omega=\omega_k$. While generally the eigenvalues of $\lambda^2\tilde{\mathbf{M}}+\lambda\tilde{\mathbf{C}}+\tilde{\mathbf{K}}$ have negative real part, in some instances where $\tilde{\mathbf{C}}$ for particular configurations of dashpots some eigenvalues may be purely imaginary. In such cases, total absorption cannot be attained for these particular frequencies.

3 Real Analysis

It is instructive to formulate the system response in terms of real analysis. Since the time origin may be chosen arbitrarily, it is enough to consider the case where

$$\mathbf{M}\ddot{\mathbf{x}} + \mathbf{C}\dot{\mathbf{x}} + \mathbf{K}\mathbf{x} = \mathbf{e}_n \sin\omega t + \mathbf{e}_1 u(t-\tau) \tag{15}$$

where $u(t-\tau)$ is given in Eq. (2). The steady state response of a stable system takes the form

$$\mathbf{x} = \mathbf{a}\sin\omega t + \mathbf{b}\cos\omega t \tag{16}$$

so that

$$u(t-\tau) = \alpha a_1\omega\cos\omega(t-\tau) - \alpha b_1\omega\sin\omega(t-\tau) + \beta a_1\sin\omega(t-\tau) + \beta b_1\cos\omega(t-\tau)$$

Recall that

$$\sin\omega(t-\tau) = \sin\omega t\cos\omega\tau - \cos\omega t\sin\omega\tau \tag{17}$$

and

$$\cos\omega(t-\tau) = \cos\omega t\cos\omega\tau + \sin\omega t\sin\omega\tau \tag{18}$$

We obtain the following from Eq. (15):

$$\begin{bmatrix} \mathbf{K} - \omega^2\mathbf{M} - (\alpha\omega\sin\omega\tau + \beta\cos\omega\tau)\mathbf{e}_1\mathbf{e}_1^T & -\omega\mathbf{C} + (\alpha\omega\cos\omega\tau - \beta\sin\omega\tau)\mathbf{e}_1\mathbf{e}_1^T \\ \omega\mathbf{C} - (\alpha\omega\cos\omega\tau - \beta\sin\omega\tau)\mathbf{e}_1\mathbf{e}_1^T & \mathbf{K} - \omega^2\mathbf{M} - (\alpha\omega\sin\omega\tau + \beta\cos\omega\tau)\mathbf{e}_1\mathbf{e}_1^T \end{bmatrix} \begin{pmatrix} \mathbf{a} \\ \mathbf{b} \end{pmatrix} = \begin{pmatrix} \mathbf{e}_n \\ \mathbf{0} \end{pmatrix} \tag{19}$$

If α and β are chosen according to Eq. (11), then $a_n=b_n=0$. It thus follows that the control action is equivalent to the addition of spring

$$\kappa = -\alpha\omega\sin\omega\tau - \beta\cos\omega\tau \tag{20}$$

and dashpot

$$\gamma = -\alpha\cos\omega\tau + \frac{\beta}{\omega}\sin\omega\tau \tag{21}$$

between x_1 and the ground. The determining factor weather the time delay is negligible or not is the magnitude of $\omega\tau$. It is expected that when the excitation is near resonance frequency even for small τ, the effect of time delay may be profound.

Example 1. Consider the system shown in Fig. 2. Its dynamics is governed by Eq. (1) where

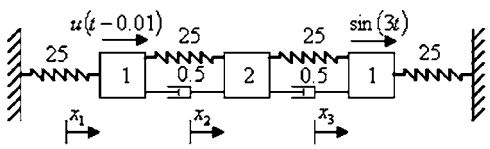

Fig. 2 The actively controlled system of Example 1

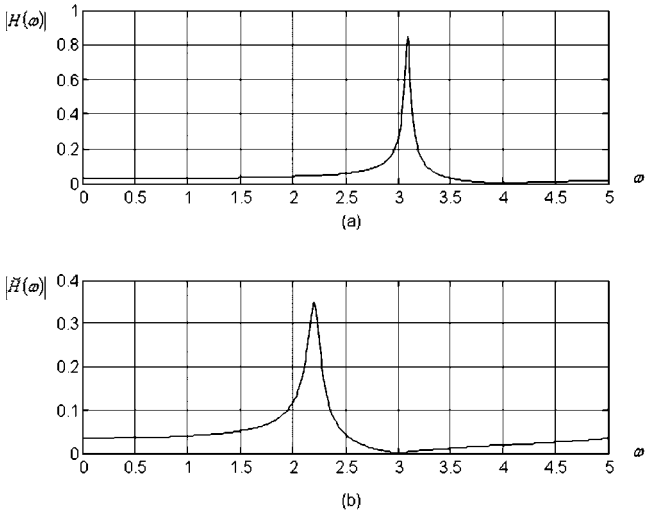

Fig. 3 Absolute values of the frequency response function at x_3 for (*a*) the uncontrolled system and (*b*) the controlled one

$$\mathbf{M}=\begin{bmatrix}1&0&0\\0&2&0\\0&0&1\end{bmatrix},\quad \mathbf{C}=\begin{bmatrix}0.5&-0.5&0\\-0.5&1.0&-0.5\\0&-0.5&0.5\end{bmatrix},$$

$$\mathbf{K}=\begin{bmatrix}50&-25&0\\-25&50&-25\\0&-25&50\end{bmatrix}$$

For $\omega=3$ and $\tau=0.01$, we have by Eq. (10)

$$s=\frac{\det\left(\begin{bmatrix}41+j1.5&-25-j1.5\\-25-j1.5&32+j3\end{bmatrix}\right)}{32+j3}=21.4908+j0.9852$$

By Eqs. (12) and (13), we have $\alpha=0.5431$ and $\beta=21.4516$. For such a control, the steady state motion of the third mass vanishes.

If time delay is ignored, then the control gains become $\alpha=0.3284$ and $\beta=21.4908$. In this case, the third mass vibrates at steady state with an amplitude of $x_3=0.0016$.

The magnitude of the frequency response function $|H(\omega)|$, representing the amplitude of the harmonic response of x_3 in the uncontrolled system, is shown in Fig. 3(*a*). Figure 3(*b*) shows the function $|\breve{H}(\omega)|$ corresponding to the associated controlled system with time delay. As expected, $|\breve{H}(3)|=0$.

4 Axially Vibrating Rod

The results obtained so far extend naturally for continuous systems. Consider the axially vibrating rod with axial rigidity $p(x)$ and mass per unit length $q(x)$, which is supported by spring k and dashpot c at $x=0$ and it is harmonically excited at $x=1$, as shown in Fig. 4. The control $u(t-\tau)$ acts at the end $x=0$. The motion of the rod is determined by

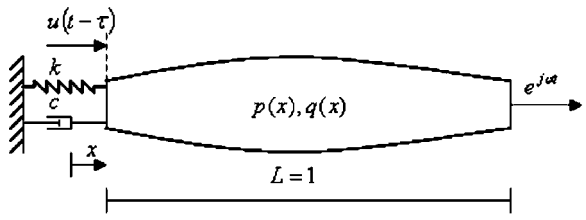

Fig. 4 The axially vibrating rod

$$\frac{\partial}{\partial x}\left(p\frac{\partial v}{\partial x}\right)=q\frac{\partial^2 v}{\partial t^2},\quad 0<x<1,\quad t>0 \tag{22}$$

and the boundary conditions

$$\left[p\frac{\partial v}{\partial x}\right]_{x=0,t}=\left[kv+c\frac{\partial v}{\partial t}+u(t-\tau)\right]_{x=0,t},\quad \left[p\frac{\partial v}{\partial x}\right]_{x=0,t}=e^{j\omega t} \tag{23}$$

where

$$u(t-\tau)=\left[\alpha\frac{\partial v}{\partial t}+\beta v\right]_{x=0,t} \tag{24}$$

If the controlled rod is stable, the steady state response of the system is

$$v(x,t)=a(x)e^{j\omega t} \tag{25}$$

Substituting Eq. (25) in Eq. (22) gives

$$(pa')'=-\omega^2 qa \tag{26}$$

and Eq. (23) yields

$$p(0)a'(0)=ka(0)+j\omega ca(0)+sa(0) \tag{27}$$

and

$$p(1)a'(1)=1 \tag{28}$$

where

$$s=(j\omega\alpha+\beta)e^{j\omega\tau} \tag{29}$$

by virtue of Eq. (24). For total absorption,

$$a(1)=0 \tag{30}$$

Equations (26), (27), and (30) define an eigenvalue problem of determining an eigenvalue s_i with corresponding eigenfunction $a\neq 0$. Equations (26) and (30) determine a up to a multiplication by an arbitrary constant. The eigenvalue s is then determined by Eq. (27) as follows:

$$s=p(0)\frac{a'(0)}{a(0)}-k-j\omega c \tag{31}$$

and Eq. (11) determines the control parameters by virtue of Eq. (28).

Example 2. Suppose that the rod is uniform. Then,

$$a''+\theta^2 a=0 \tag{32}$$

where

$$\theta^2=\omega^2\frac{q}{p} \tag{33}$$

The general solution to Eq. (32) is

$$a(x)=C_1\sin\theta x+C_2\cos\theta x \tag{34}$$

Equation (30) gives

$$C_2=C_1\tan\theta \tag{35}$$

so that

$$a(x)=C_1(\sin\theta x+\tan\theta\cos\theta x) \tag{36}$$

By Eq. (31),

$$s=\frac{p\theta}{\tan\theta}-k-j\omega c \tag{37}$$

and, in view of Eqs. (12) and (13), the control parameters are

$$\alpha=\frac{1}{\omega}\left(\left(\frac{p\theta}{\tan\theta}-k\right)\sin(\omega\tau)-\omega c\cos(\omega\tau)\right) \tag{38}$$

and

$$\beta = \left(\frac{p\theta}{\tan \theta} - k \right) \cos(\omega\tau) + \omega c \sin(\omega\tau) \tag{39}$$

5 Conclusions

It has been shown that total absorption in damped system may be achieved by active vibration control. The control is applied on one degree of freedom and the absorption is achieved at another point. An explicit formula for calculating the control gains was derived. The analysis was carried out for the case where there is time delay between the measured state and the applied control force. The control strategy used is equivalent to addition of spring and damper of constants β and γ given in Eqs. (20) and (21). It follows from Eq. (20) that neglecting small time delay may have considerable consequence for high frequency of excitation.

The results extend to vibration of continuous systems. We have demonstrated this for the case of a nonuniform, damped, axially vibrating rod, and achieved total absorption at a predefined point.

Acknowledgment

The research for Y.M.R. was supported in part by National Science Foundation Grant No. CMS-0324628

References

[1] den Hartog, J. P., 1947, *Mechanical Vibrations*, 3rd ed., McGraw-Hill, New York.

[2] Cha, P. D., 2005, "Enforcing Nodes at Required Locations in a Harmonically Excited Structure Using Simple Oscillators," J. Sound Vib., **279**, pp. 799–816.

[3] Lee, E. C., Nian, C. Y., and Tarng, Y. S., 2001, "Design of Dynamic Vibration Absorber Against Vibrations in Turning Operations," J. Mater. Process. Technol., **108**, pp. 278–285.

[4] Song, Y., Sato, H., Iwata, Y., and Komatsuzaki, T., 2003, "The Response of a Dynamic Vibration Absorber System With a Parametrically Excited Pendulum," J. Sound Vib., **259**, pp. 747–759.

[5] Yamashita, S., Seto, K., and Hara, F., 1989, "Vibration Control In Piping System by Dual Dynamic Absorber (3-Dimensional Vibration Analysis and Absorber Design Using Transfer-Matrix Method)," JSME Int. J., Ser. III, **32**, pp. 531–537.

[6] Mottershead, J. E., and Lallement, G., 1999, "Vibration Nodes, and the Cancellations of Poles and Zeros by Unit-Rank Modifications to Structures," J. Sound Vib., **222**, pp. 833–851.

[7] Mottershead, J. E., 2001, "Structural Modification for the Assignment of Zeros Using Measured Receptances," ASME J. Appl. Mech., **68**, pp. 791–798.

[8] Mottershead, J. E., 1998, "On the Zeros of Structural Frequency Response Functions and Their Sensitivities," Mech. Syst. Signal Process., **12**, pp. 591–597.

[9] Ram, Y. M., and Elhay, S., 1996, "The Theory of a Multi Degree of Freedom Dynamic Absorber," J. Sound Vib., **195**, pp. 607–615.

[10] Ram, Y. M., 2002, "Nodal Control of a Vibrating Rod," Mech. Syst. Signal Process., **16**, pp. 69–81.

[11] Singh, K. V., and Ram, Y. M., 2000, "Dynamic Absorption by Passive and Active Control," ASME J. Vibr. Acoust., **122**, pp. 429–433.

Stiffness Design of Continuum Structures by a Bionics Topology Optimization Method

Kun Cai

Biao-song Chen[1]
e-mail: chenbs@dlut.edu.cn

Hong-wu Zhang

State Key Laboratory of Structural Analysis for Industrial Equipment,
Department of Engineering Mechanics,
Dalian University of Technology,
Dalian 116024, P.R.C.

Jiao Shi
College of Water Resources and Architectural Engineering,
Northwest A&F University,
Yangling 712100, P.R.C.

A heuristic approach is presented to solve continuum topology optimization problems with specified constraints, e.g., structural volume constraint and/or displacement constraint(s). The essentials of the present approach are summarized as follows. First, the structure is regarded as a piece of bone and the topology optimization process is viewed as bone remodeling process. Second, a second-rank positive and definite fabric tensor is introduced to express the microstructure and anisotropy of a material point in the design domain. The eigenpairs of the fabric tensor are the design variables of the material point. Third, Wolff's law, which states that bone microstructure and local stiffness tend to align with the stress principal directions to adapt to its mechanical environment, is used to renew the eigenvectors of the fabric tensor. To update the eigenvalues, an interval of reference strain, which is similar to the concept of dead zone in bone remodeling theory, is suggested. The idea is that, when any one of the absolute values of the principal strains of a material point is out of the current reference interval, the fabric tensor will be changed. On the contrary, if all of the absolute values of the principal strains are in the current reference interval, the fabric tensor remains constant and the material point is in a state of remodeling equilibrium. Finally, the update rule of the reference strain interval is established. When the length of the interval equals zero, the strain energy density in the final structure distributes uniformly. Simultaneously, the volume and the displacement field of the final structure are determined uniquely. Therefore, the update of the reference interval depends on the ratio(s) between the current constraint value(s) and their critical value(s). Parameters, e.g., finite element mesh the initial material and the increments of the eigenvalues of fabric tensors, are studied to reveal their influences on the convergent behavior. Numerical results demonstrate the validity of the method developed.
[DOI: 10.1115/1.2936929]

1 Introduction

Topology optimization is often called as layout optimization or generalized shape optimization. The importance of topology optimization is that the choice of the appropriate topology of a structure in the conceptual design phase is generally the most decisive factor for the efficiency of a novel product. Therefore, topology optimization is very valuable as a preprocessing tool for shape and size optimization. Due to its complexity, topology optimization becomes an intellectually challenging field and attracts so much attention in the past two decades. Most efforts in this field are put on the development of continuum topology optimization methods. According to the classification in the work by Eschenauer and Olhoff [1], those methods can be briefly separated into two types, i.e., the microstructure methods and the geometry (or macrostructure) methods. For example, the homogenization design method (HDM) (Bendsøe and Kikuchi [2] and Bendsøe [3]) and the solid isotropic microstructures with penalization (SIMP) method (Rozvany et al. [4]) belong to the first type. The latter type contains such methods as SHAPE method (Atrek and Kodali [5]), evolutionary structural optimization (ESO) method (Xie and Steven [6]), bidirectional ESO (BESO) method (Querin et al. [7]), bubble method (Eschenauer et al. [8]), level set (LST) method (Wang et al. [9]), and so on.

The microstructural method is called as free material design approach, which is to find the topology of the structure as well as the material properties at each point in the structure. There exist many meaningful works on the topic (Bendsøe [3], Rozvany et al. [4], Sigmund and Torquato [10], Bendsøe and Sigmund [11,12], Rodrigues et al. [13], etc).

In the current work, a new microstructural method is presented. Different from the methods mentioned above, a fabric tensor approach is adopted to express both of the microstructure properties and elasticity of material in design domain. To restrict the elastic symmetry of the porous material, only a second-rank fabric tensor is used. Therefore, in an optimization process, the design variables of a material point in design domain are the eigenpairs of the second-rank fabric tensor. In the optimization process, the update rule of design variables is performed by an intuitive evolutionary method based on bone remodeling theories. Two concepts in bone remodeling theories (Pauwels [14], Carter et al. [15], Cowin [16], Frost [17], Huiskes et al. [18], Mullender et al. [19] and Huiskes et al. [20]) are involved in the current work. One is Wolff's law [21], which states that bone microstructure and local stiffness tend to align with the stress principal directions according to its mechanical environment. Wolff's law is the primary principle and is accepted widely in this field (e.g., Gibson [22] and Odgaard et al. [23]). The other is the dead zone theory (Pauwels [14] and Frost [18]), which indicates that the local material will change when the stimuli of growth are out of the zone in bone remodeling process.

Corresponding to the dead zone in bone mechanics, the interval of the reference strain is introduced in our work [24,25]. It means that all the absolute values of the principal strains in the final structure should locate in the interval. However, in that work, the reference interval is specified directly and fixed during iterations. The method can only solve the optimization problems with strain constraint. When a structural stiffness design problem has other types of constraints, e.g., volume constraint of structure and/or

[1]Corresponding author.

Contributed by the Applied Mechanics Division of ASME for publication in the JOURNAL OF APPLIED MECHANICS. Manuscript received May 24, 2007; final manuscript received March 27, 2008; published online July 15, 2008. Review conducted by Yonggang Huang.

displacement constraint(s), one can hardly give the appropriate interval of the reference strain. In order to overcome the difficulty, a floating interval approach is presented in the current work.

Briefly, the present approach can be summarized as follows. First, a structural topology optimization process is equivalent to the bone remodeling process. The optimal structural topology is obtained when the bone is in a state of remodeling equilibrium. Second, a second-rank positive and definite fabric tensor is introduced to be the design variable of a material point in design domain. Third, a floating interval method of the reference strain is presented. During the process of optimization, the fabric tensor of a material point will be changed when any one of the absolute values of its principal strains is out of the current reference interval. On the contrary, if all of the absolute values of its principal strains are in the current reference interval, the fabric tensor remains constant and the material point is in the state of remodeling equilibrium. Finally, the update rule of the floating interval can be established according to the constraint types, e.g., volume constraint, displacement constraint, etc.

This paper is organized as follows. In Sec. 2, material properties, e.g., geometry of microstructure, elastic constitutive tensor, and volume fraction of a material point, are introduced. Section 3 presents the optimal model of the proposed method, it includes the update of design variables and the update of the interval of the reference strain, etc. Numerical examples are given in Sec. 4. Section 5 summarizes the discussion of the proposed method for continuum topology optimization.

2 Material Properties

2.1 Notation. Tr and Det denote the trace and the determinant of a square matrix or an even-rank tensor, respectively. $\nabla(\cdot)$ denotes the gradient operator. Italic bold roman letters denote vectors and higher-rank tensors; capital letters are used for the latter. The scalar and tensorial product of two vectors or tensors is designed by symbols $\bullet$. The tensorial products are designed by symbols $\otimes$ and $\bar{\otimes}$. They are defined in such a way that, to any given triplet of arbitrary second-rank tensors $\boldsymbol{A}$, $\boldsymbol{C}$, and $\boldsymbol{G}$,

$$\boldsymbol{A}:\boldsymbol{G} = \mathrm{Tr}(\boldsymbol{A}\cdot\boldsymbol{G}) \tag{1}$$

$$(\boldsymbol{A}\otimes\boldsymbol{G}):\boldsymbol{C} = (\boldsymbol{G}:\boldsymbol{C})\boldsymbol{A} \tag{2}$$

$$(\boldsymbol{A}\bar{\otimes}\boldsymbol{G}):\boldsymbol{C} = \frac{1}{2}(\boldsymbol{A}\cdot\boldsymbol{C}\cdot\boldsymbol{G}^{\boldsymbol{T}} + \boldsymbol{A}\cdot\boldsymbol{C}^{\boldsymbol{T}}\cdot\boldsymbol{G}^{\boldsymbol{T}}) \tag{3}$$

The superimposed symbol $(\cdot)^T$ denotes the transpose of the quantity over which it applies.

2.2 Definitions of Fabric Tensor and Elastic Tensor. In porous materials, mechanical properties are related closely to microstructure of materials. Clearly, porous ratio alone is not sufficient to characterize the geometric configuration of the local solid structure for a porous material. Since 1970s, many researchers (e.g., Whitehouse and Dyson [26], Harrigan and Mann [27], Cowin [28], Kanatani [29], Boehler [30], Zysset and Curnier [31], He and Curnier [32], and Odgaard et al. [23]) tried to establish theoretical foundation to characterize the accurate relationships between the anisotropy and the microstructure. It was found that microstructural properties can be described as invariant form by a set of even-rank fabric tensors (He and Curnier [32]) and can be assessed accurately using stereological methods (Kanatani [29] and Odgaard et al. [23]). There is a similar conclusion which considers that the principal directions of the fabric tensor coincide with those of the orthotropic elastic tensor. Especially, these methods are employed to identify the symmetry group and the degree of anisotropy of the microstructure. The results coincide well with those obtained from experiments.

The linear elastic properties of anisotropic porous materials characterized by a fourth-rank tensor are dependent on both the solid volume fraction of the material and the geometric configuration of the microstructure. In most applications, anisotropy material properties seem to be sufficiently well described by a scalar and a symmetric, traceless second-rank fabric tensor, and this approach restricts the material symmetry to be orthotropy. In the work by Zysset and Curnier [31], a general approach was introduced to express the anisotropic elasticity with fabric tensors. Based on the work by Zysset and Curnier [31], here we suggest a second-rank positive and definite fabric tensor with two material parameters to express the elasticity tensor.

2.2.1 Fabric Tensor

$$\boldsymbol{B} = \sum_{i=1}^{3} b_i \boldsymbol{q}_i \otimes \boldsymbol{q}_i \tag{4}$$

where $b_i \in (0\ 1.0]$, $\boldsymbol{q}_i$ $(i=1,2,3)$ are eigenpairs of the fabric tensor $\boldsymbol{B}$. $\boldsymbol{q}_i$ $(i=1,2,3)$ represent three material principal axes.

2.2.2 Stiffness Tensor. From an experimental point of view, anisotropic elasticity $(\boldsymbol{D}_0)$ of a material can be identified using two independent material constants (λ_0, μ_0), a second-rank fabric tensor $(\boldsymbol{B})$, and an exponent (ω) (Zysset and Curnier [31])

$$\boldsymbol{D}_0 = \lambda_0 \boldsymbol{B}^{\omega} \otimes \boldsymbol{B}^{\omega} + 2\mu_0 \boldsymbol{B}^{\omega} \bar{\otimes} \boldsymbol{B}^{\omega} \tag{5}$$

In the present work, a particular elasticity model with $\lambda=\lambda_0$, $\mu=\mu_0$, and $\omega=1.0$ in Eq. (5) is adopted, i.e.,

$$\boldsymbol{D} = \lambda \boldsymbol{B} \otimes \boldsymbol{B} + 2\mu \boldsymbol{B} \bar{\otimes} \boldsymbol{B} \tag{6}$$

where λ and μ are Lame constants of the base material. Clearly, $\boldsymbol{D}$ in Eq. (6) expresses an isotropic material when $\boldsymbol{B}$ has only one distinct eigenvalue. When $\boldsymbol{B}$ has more than one distinct eigenvalue, then $\boldsymbol{D}$ expresses a set of orthotropic materials. There are no more than five independent variables (three eigenvalues and two Lame constants of solid phase) to express the elastic tensor of a porous material point. So, the number of independent variables of each material point is less than that of a full orthotropic material (nine independent components). Actually, from an experimental point of view, such elastic constitutive expression is precise enough for practical engineering (Zysset and Curnier [31]). The compliance tensor is given by

$$\boldsymbol{D}^{-1} = \frac{-\lambda}{2\mu(3\lambda+2\mu)} \boldsymbol{B}^{-1} \otimes \boldsymbol{B}^{-1} + \frac{1}{2\mu} \boldsymbol{B}^{-1} \bar{\otimes} \boldsymbol{B}^{-1} \tag{7}$$

2.3 Effective Volume Fraction of a Porous Material Point. From above, the fabric tensor is employ to express the geometric configuration of the microstructure of a porous material point. When the material point stiffness tensor is expressed as Eq. (6), the effective volume fraction (EVF) of the porous material point can be expressed as a function with respect to the invariants of the fabric tensor of the point by a mathematical condensation method (Cai et al. [24]).

The EVF of a 3D case has the following form:

$$\rho = \mathrm{Tr}(\boldsymbol{B}\cdot\boldsymbol{B}) - 2\,\mathrm{Det}(\boldsymbol{B}) \tag{8}$$

For a 2D case, the EVF can be expressed as

$$\rho = \mathrm{Tr}(\boldsymbol{B}\cdot\boldsymbol{B}) - \mathrm{Det}(\boldsymbol{B}\cdot\boldsymbol{B}) \tag{9}$$

3 Optimization Model

3.1 Basic Equations of Linear Elasticity Theory. In the present work, the classical linear theory of elasticity is considered. The load process is quasistatic and the deformation process takes an isothermal course simultaneously. Only single load case is considered for structural analysis. Then, the basic equations are summarized as follows:

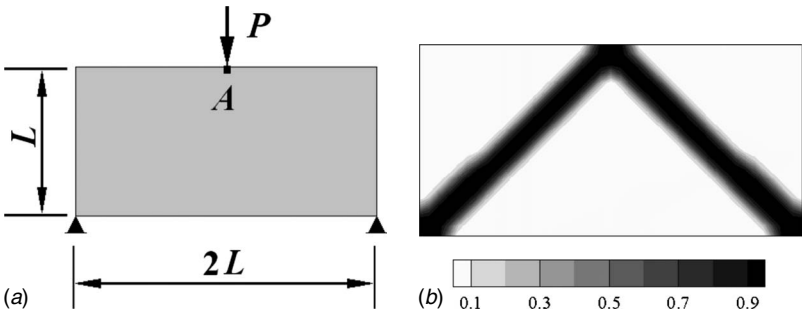

Fig. 1 (*a*) Design domain and (*b*) optimal topology obtained by SIMP method

$$\boldsymbol{\sigma} = \boldsymbol{D}:\boldsymbol{\varepsilon}$$

$$\boldsymbol{\varepsilon} = \tfrac{1}{2}[\nabla \boldsymbol{u} + (\nabla \boldsymbol{u})^T] \tag{10}$$

$$\nabla \cdot \boldsymbol{\sigma} + \boldsymbol{f} = \boldsymbol{0}$$

and boundary conditions are

$$\Gamma_\sigma: \quad \boldsymbol{\sigma} \cdot \boldsymbol{n} = \boldsymbol{F}^*$$

$$\Gamma_u: \quad \boldsymbol{u} = \boldsymbol{u}^* \tag{11}$$

where $\boldsymbol{\sigma}$ is the stress tensor, $\boldsymbol{\varepsilon}$ is the strain tensor, $\boldsymbol{u}$ is the displacement vector, $\boldsymbol{f}$ is the body force vector, $\boldsymbol{F}^*$ is the boundary force on the boundary Γ_σ with the normal direction $\boldsymbol{n}$, and $\boldsymbol{u}^*$ is the assigned displacement on the boundary Γ_u.

3.2 Formulations of Topology Optimization Problem

3.2.1 Fixed Reference Interval Method. For the fixed reference interval method proposed in Refs. [24,25], the formulations of topology optimization can be expressed as

$$\text{Find } \{\boldsymbol{B}_m(b_{i,m}, \boldsymbol{q}_{i,m})\}$$

$$\text{such that } |\varepsilon_{i,m}| \in [\varepsilon_{\text{inf}}^{\text{ref}} \ \varepsilon_{\text{sup}}^{\text{ref}}] \tag{12}$$

$$b_{i,m} \in [\beta \ 1.0] \quad (i = 1,2,3)$$

where $\boldsymbol{B}_m$ is the fabric tensor of the mth material point. $\varepsilon_{i,m}$ is the ith principal strain of the mth material point. $[\varepsilon_{\text{inf}}^{\text{ref}} \ \varepsilon_{\text{sup}}^{\text{ref}}]$ is the specified fixed interval of the reference strain. β is a very small scalar to keep the fabric tensor to be positive and definite.

The reference interval of cancellous bone is the dead zone and the physical meaning of the interval is clear. However, the reference interval of an engineering material is ambiguous. In fact, the interval indicates the scope of the deformation potential energy per volume of the optimal structure.

If a structural optimization problem has a strain constraint, it can be solved by the fixed reference interval method. If the constraints of an optimization problem have other types, i.e., volume constraint, displacement constraint, etc., obviously, one cannot give directly an appropriate reference interval to find the final results of such problem. Hence, a floating interval method of the reference strain is suggested in the current work.

3.2.2 Floating Interval of Reference Strain Method. The optimization problem in its general form is constructed as

$$\text{Find } \{\boldsymbol{B}_m(b_{i,m}, \boldsymbol{q}_{i,m})\} \quad \text{and } [\varepsilon_{\text{inf}}^{\text{ref}} \ \varepsilon_{\text{sup}}^{\text{ref}}]$$

$$\text{to minimize } \psi(\{\boldsymbol{B}_m\})$$

$$\text{subject to } \phi_n(\{\boldsymbol{B}_m\}) \le 0 \quad (n = 1,2, \ldots, N^*) \tag{13}$$

$$|\varepsilon_{i,m}| \in [\varepsilon_{\text{inf}}^{\text{ref}} \ \varepsilon_{\text{sup}}^{\text{ref}}] \quad (m = 1,2, \ldots, M^*)$$

$$b_{i,m} \in [\beta \ 1.0] \quad (i = 1,2,3)$$

where $\boldsymbol{B}_m$ is the fabric tensor of the mth material point. $[\varepsilon_{\text{inf}}^{\text{ref}} \ \varepsilon_{\text{sup}}^{\text{ref}}]$ is the floating interval of the reference strain, which will be changed during the iterations of optimization analysis. ψ is the objective function (commonly, the compliance of a structure or the amount of material in structure). ϕ_n is the constraint function and N^* is the total number of constraints. $\varepsilon_{i,m}$ is the ith principal strain of the mth material point. M^* is the total number of material points in design domain.

3.3 Update Rule of Design Variables. According to Wolff's law, we introduce the following update rule. In order to obtain the optimal topology of a structure, a state of remodeling equilibrium, which requires that all the absolute values of the principal strains at each material point within the admissible design domain are in an interval of the reference strain, should be reached. Based on the rule, the material distribution within the design domain will be changed as the iteration proceeds. As the design variables of a material point, the fabric tensor should be updated. If both of the

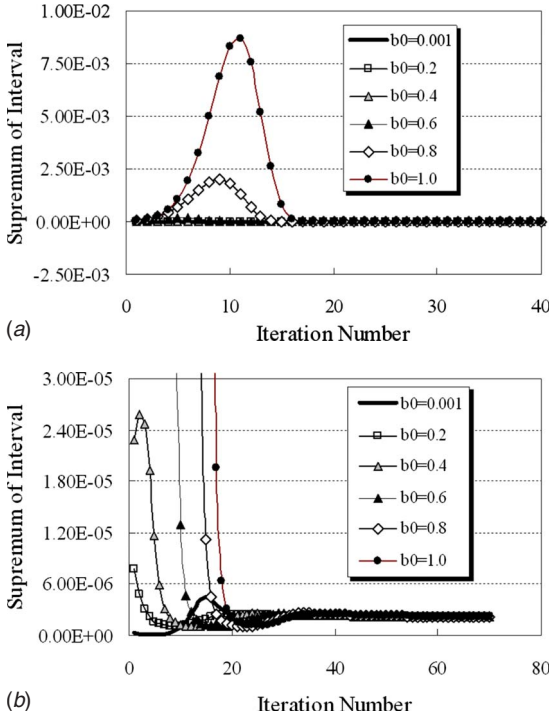

Fig. 2 Iteration histories of the supremums of the intervals of the reference strain of the structure with different initial designs: (*a*) 1–40 steps and (*b*) 1–80 steps

Table 1 Material distributions of structure with different initial designs

b_0	At iteration 10	At iteration 30	At iteration 50	At iteration 70
0.001	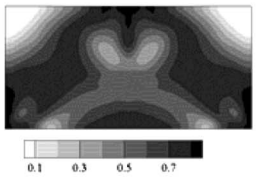	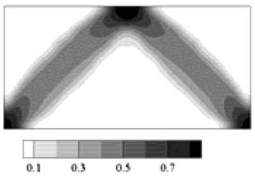	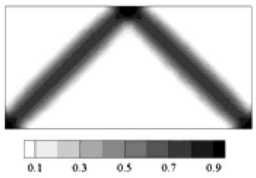	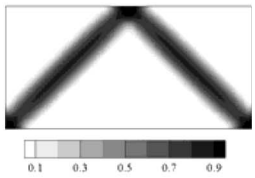
0.2	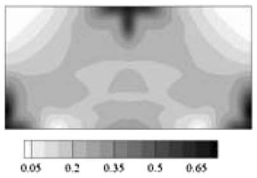	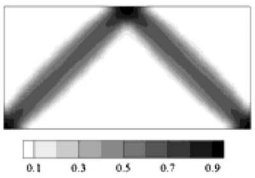	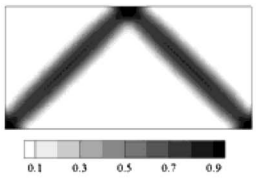	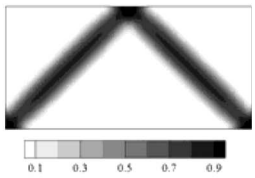
0.4	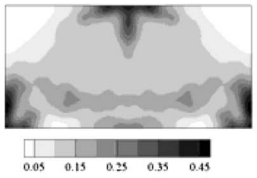	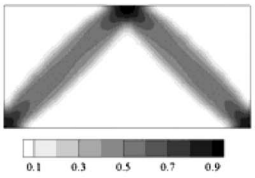	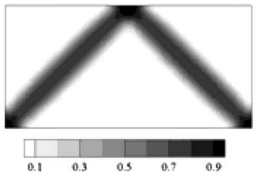	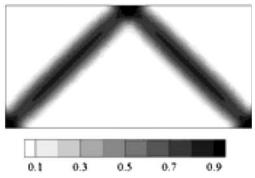
0.6	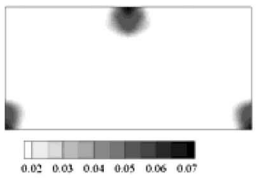	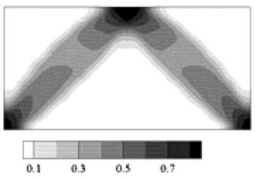	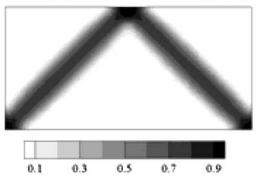	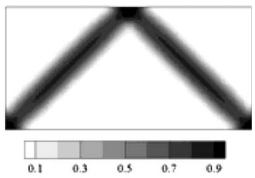
0.8	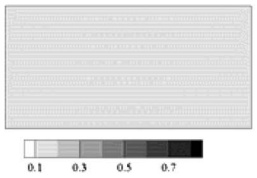	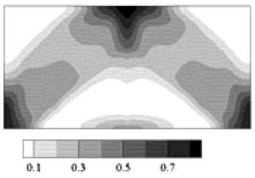	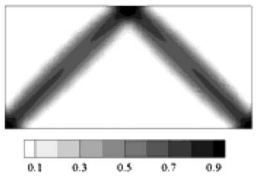	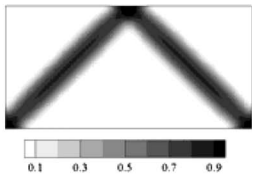
1.0	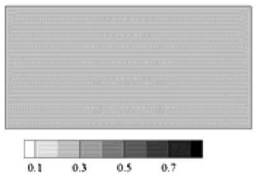	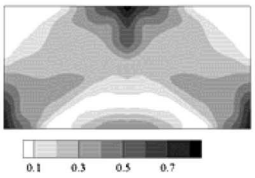	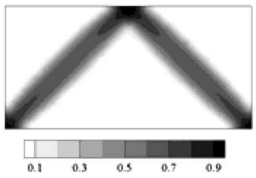	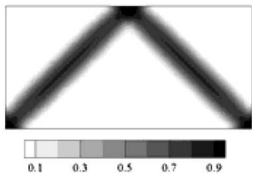

eigenvectors and the eigenvalues of the fabric tensors are defined as design variables and are changed in a simulation process, the process is called as anisotropic growth (AG).

Supposing a structure under a single load case, during a numerical simulation, (a) the update rule of eigenvectors of a fabric tensor can be given according to Wolff's law, i.e., the eigenvectors of a fabric tensor at the $(k+1)$th step should be identical to those of stress tensor at the kth step for the same material point. (b) The update rule of eigenvalues of a fabric tensor can be defined briefly as follows: The increments of the eigenvalues of the fabric tensor of a material point are called as growth speeds and are determined by the absolute values of the principal strains along the corresponding directions. When any one of the absolute values is out of the interval, then the growth speed is nonzero. The opposite case

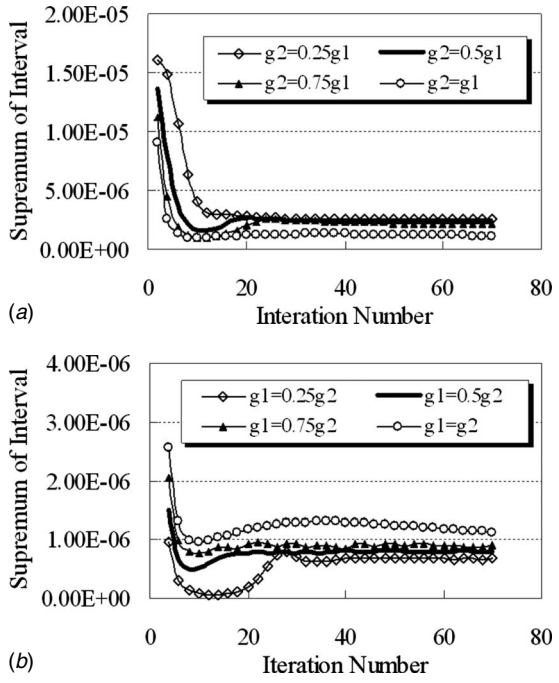

Fig. 3 Iteration histories of the supremums of reference intervals for different grow speed pairs: (*a*) $g_1=0.08$ and (*b*) $g_2=0.08$

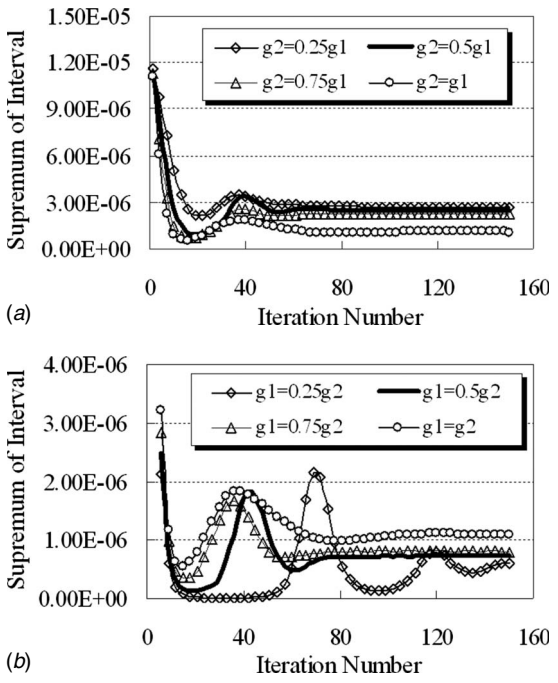

Fig. 4 Iteration histories of the supremums of reference strain intervals when the growth speed pairs are different

is that, if all of the absolute values of its principal strains locate in the interval, the growth speeds are equal to zero. Mathematically, the increments of the eigenvalues of a fabric tensor can be expressed as

$$\Delta b_{i,k,m}=\begin{cases} g_1>0 & \text{if } |\varepsilon_{i,k,m}|>\varepsilon_{\sup}^{k-1} & \text{deposition} \\ 0 & \text{if } \varepsilon_{\inf}^{k-1}\le|\varepsilon_{i,k,m}|\le\varepsilon_{\sup}^{k-1} & \text{equilibrium,} \\ -g_2<0 & \text{if } |\varepsilon_{i,k,m}|<\varepsilon_{\inf}^{k-1} & \text{dissipation} \end{cases} \quad i=1,2(,3) \tag{14}$$

where $\Delta b_{i,k,m}$ $i=1,2(,3)$ are increments of the eigenvalues of the fabric tensor of the mth material point at the kth iteration step. g_1 is the deposition speed. g_2 is the dissipation speed.

The update of the eigenvalues of the fabric tensor is given below:

$$b_{i,k+1,m}=\begin{cases} \beta & \text{if } b_{i,k,m}+\Delta b_{i,k+1,m}\le\beta \\ b_{i,k,m}+\Delta b_{i,k,m} & \text{others} \\ 1.0 & \text{if } b_{i,k,m}+\Delta b_{i,k+1,m}\ge 1.0 \end{cases} \quad i=1,2,3 \tag{15}$$

$$\boldsymbol{B}_{k+1,m}=\boldsymbol{Q}_{k,m}\begin{bmatrix} b_{1,k+1,m} & 0 & 0 \\ 0 & b_{2,k+1,m} & 0 \\ 0 & 0 & b_{3,k+1,m} \end{bmatrix}\boldsymbol{Q}_{k,m}^{\mathrm{T}} \tag{16}$$

where

$$\boldsymbol{Q}_{k,m}=[\boldsymbol{q}_{1,k,m}\quad \boldsymbol{q}_{2,k,m}\quad \boldsymbol{q}_{3,k,m}] \tag{17}$$

Equation (17) gives the transfer tensor from the global Cartesian coordinate system to the local one.

During the growth process, for the mth material point at the kth step, the operation of updating elastic tensor can be expressed as

$$\boldsymbol{D}_{k+1,m}=\lambda^*\boldsymbol{B}_{k+1,m}\otimes\boldsymbol{B}_{k+1,m}+2\mu\boldsymbol{B}_{k+1,m}\underline{\bar{\otimes}}\boldsymbol{B}_{k+1,m} \tag{18}$$

where

$$\lambda^*=\begin{cases} \lambda & \text{for plane strain or 3D} \\ \dfrac{2\lambda\mu}{\lambda+2\mu} & \text{for plane stress} \end{cases}$$

Particularly, if the fabric tensors are kept to be proportional to the second-rank identity tensor in a simulation process, then the process is called as isotropic growth (IG). For IG algorithm, the following formulation is used in the optimization process:

$$\boldsymbol{B}_{k+1,m}^{\mathrm{iso}}=\frac{1}{N}\mathrm{Tr}(\boldsymbol{B}_{k+1,m})\boldsymbol{I}_N \tag{19}$$

where N is the spatial dimension (2 or 3) of the structure to be analyzed, $\boldsymbol{I}_N$ is the N-dimensional second-rank identity tensor, and $\boldsymbol{B}_{k+1,m}$ has been given in Eq. (16).

3.4 Update of Interval of Reference Strain. Commonly, the length of the interval of the reference strain is kept to be approxi-

Table 2 Convergent values of the supremums of the reference strain intervals when the growth speed pairs are different

	$g_2=\frac{1}{4}g_1$	$g_2=\frac{1}{2}g_1$	$g_2=\frac{3}{4}g_1$	$g_2=g_1$	$g_2=\frac{4}{3}g_1$	$g_2=2g_1$	$g_2=4g_1$
$g_1=0.08$	2.52E−06	2.25E−06	2.15E−06	1.09E−06	8.61E−07	8.01E−07	6.67E−07
$g_1=0.06$	2.50E−06	2.32E−06	2.18E−06	1.07E−06	8.67E−07	7.83E−07	6.71E−07
$g_1=0.04$	2.54E−06	2.39E−06	2.24E−06	1.08E−06	8.49E−07	7.71E−07	6.41E−07
$g_1=0.02$	2.67E−06	2.43E−06	2.26E−06	1.08E−06	8.01E−07	7.34E−07	*6.02E−07

Table 3 Final topologies of structure with different growth speeds

	$g_1 = 0.08$; at iteration 60	$g_1 = 0.02$; at iteration 140
$g_2 = \frac{1}{4} g_1$	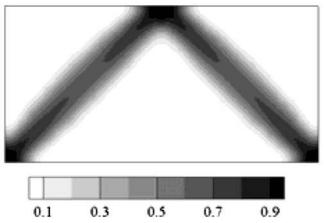	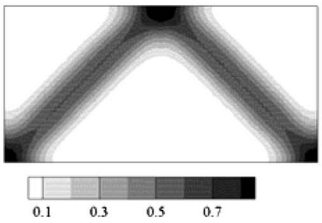
$g_2 = \frac{1}{2} g_1$	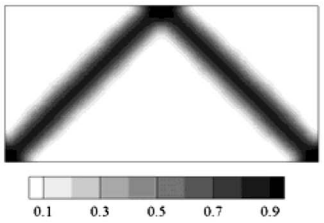	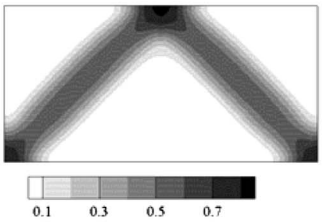
$g_2 = \frac{3}{4} g_1$	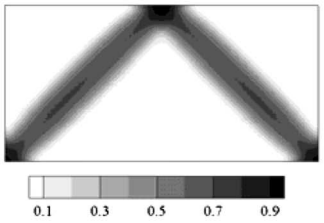	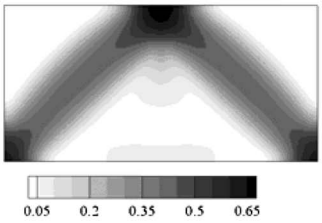
$g_2 = g_1$	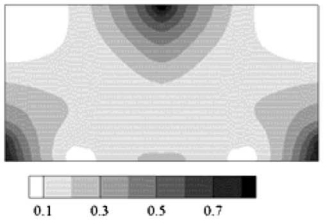	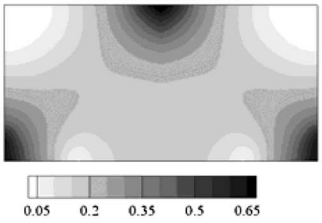
$g_2 = \frac{4}{3} g_1$	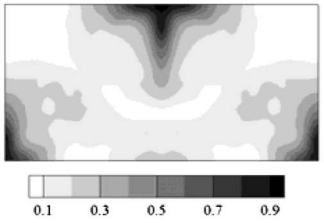	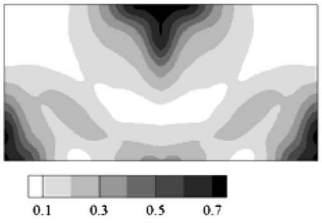
$g_2 = 2 g_1$	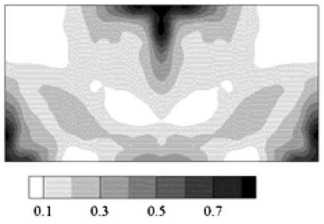	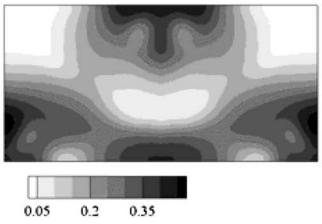
$g_2 = 4 g_1$	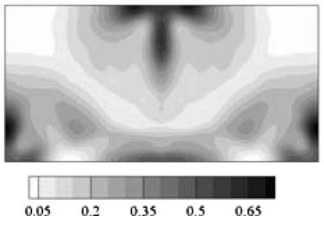	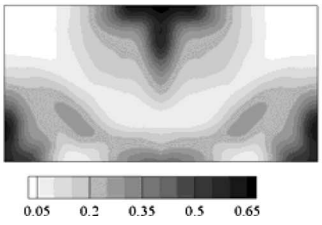

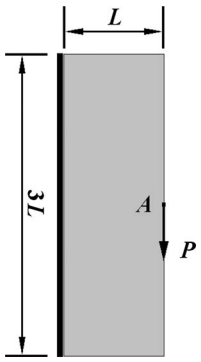

Fig. 5 Initial design domain

mately null in order to keep the strain energy density distributing uniformly in the structure. Therefore, only the supremum of the interval needs to be updated.

3.4.1 Single Constraint. For an optimization problem with single constraint, the supremum of the interval of the reference strain can be updated as follows:

$$\varepsilon_{\sup}^{k} = \left(\frac{H^{k-1}}{H_0}\right)^{\alpha} \varepsilon_{\sup}^{k-1} \tag{20}$$

where H_0 is the critical value of physical constraint (e.g., volume constraint or displacement constraint). H^{k-1} is the current value in the $(k-1)$th iteration step.

For example, if a stiffness optimization problem has a volume constraint, H_0 is the given supremum of the volume of the structure and H^{k-1} is the total volume of the solid phase (i.e., base material) after the $(k-1)$th finite element analysis (FEA) and optimization of the structure. Simultaneously, the exponent α is positive. It means that when the current volume is less than the given volume constraint value, the current supremum of the interval of the reference strain is too big and needs to be decreased.

When the objective is to minimize the structural volume and the constraint type is the specified displacement, H_0 is the critical value of displacement and H^{k-1} is the current displacement of the same location in the structure. At the same time, α is negative. It shows that if H^{k-1} is less than H_0, the current supremum of the interval of the reference strain is too small and should be increased.

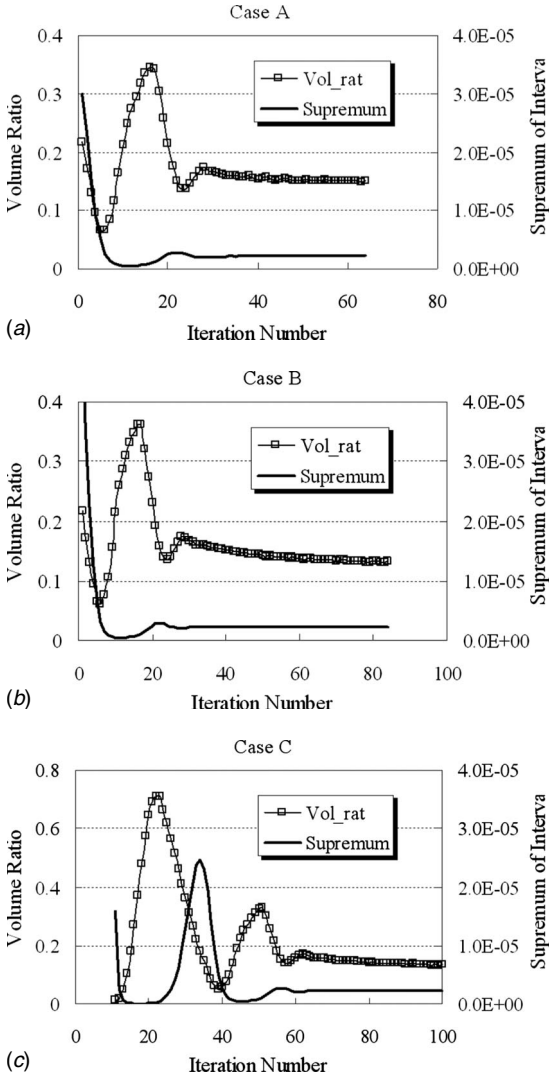

Fig. 6 Iteration histories of the supremums of the intervals of the reference strain and the volume ratios of structure with different mesh schemes: (*a*) results of Case A, (*b*) results of Case B, and (*c*) results of Case C

3.4.2 Multiple Constraints. In general, an optimization problem may have more than one constraint. Such problem can be solved easily by mathematical programming approaches. When a structural stiffness optimal design problem with multiple constraints is solved by the floating interval method of the reference strain, the update rule of the supremum of the reference interval may be different from that with a single constraint. Here, two types of multiconstraint problem are considered. One is the problems with multidisplacement constraints. The other is the problems with both of displacement constraints and structural volume constraint. The corresponding update rules of both types are given below.

Multidisplacement constraints. We suppose that an optimization problem is expressed as follows: The objective is to minimize the structural compliance, and the total number of locations with displacement constraints is I^*. The update rule of the supremum of interval is determined by the maximum of the ratios between the current displacements and the specified values on the correspond-

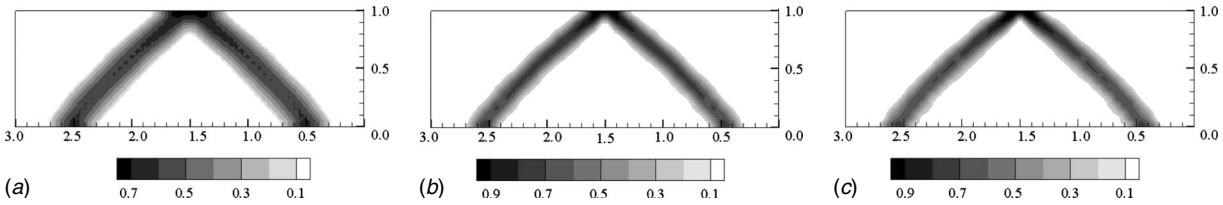

Fig. 7 Optimal material distributions of structure with different FE mesh cases: (*a*) results of structure with Mesh Case A after 64 iterations, (*b*) results of structure with Mesh Case B after 84 iterations, and (*c*) results of structure with Mesh Case C after 100 iterations

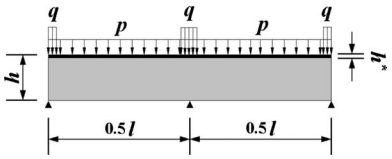

Fig. 8 Initial design domain

ing locations. It implies that at least one of the displacements approaches the critical value and the rest are less than the given values in an optimal structure.

$$\varepsilon_{\sup}^{k} = \min_{i=1,2,\ldots,I^*} \left\{ \left| \frac{H_i^{k-1}}{H_i^*} \right|^{\alpha} \right\} \varepsilon_{\sup}^{k-1} \tag{21}$$

where H_i^* is the given displacement value of the ith location. Correspondingly, H_i^{k-1} is the current displacement of the location after $(k-1)$th iteration. The exponent α is negative.

Combining the displacement constraints with the volume constraint. Supposing a stiffness optimal design problem has both of volume constraint and displacement constraints. Such problem may have no optimal result. If it has optimal result, the update of the supremum of interval is determined by the volume constraint. The reasons can be given as follows: First, if one of the displacements of the specified locations in the final structure reaches the critical value, the final structural volume should be no more than the given value. At the same time, let the structural compliance be S_1. Second, if the final structural volume approaches the given maximum, the other displacements should be no more than their critical values. Let the structural compliance be S_2. One can easily conclude that S_2 is no more than S_1 when the structure is under the same loading conditions. Thus, the update rule of the supremum of the interval can be expressed by Eq. (20). It means that the original optimization problem with multiconstraints is transformed into a problem with a single constraint, i.e., volume constraint.

3.5 Optimization Procedure for a Floating Interval of Reference Strain Method

S1: Construct the finite element model and initiate all parameters, such as the growth speeds g_1, g_2; the interval of the reference strain $[\varepsilon_{\inf}^0 \ \varepsilon_{\sup}^0]$ and set initial fabric tensors and define the initial design, let $k=1$.

S2: Analyze the structure to obtain the strain and stress fields by using Eqs. (10) and (11).

S3: Update the fabric tensor (Eq. (16)) of each element: (1) obtain the eigenvectors of the fabric tensor based on Wolff's law (Eq. (17)); (2) obtain the eigenvalues of the strain tensor and update the eigenvalues of the fabric tensor by using Eqs. (14) and (15), renew the interval of the reference strain (Eq. (20) or (21)).

S4: Determine iteration criterion: If the convergent conditions are satisfied or k is equal to a given maximum number of iteration, then go to S5; otherwise, let $k=k+1$ and go to S2.

S5: Stop.

For an initial design, it is normal to distribute evenly the porous materials, of which all the eigenvalues of the fabric tensors are initialized to be a positive scalar (b_0 a constant no more than unity), over the admissible design domain. Commonly, the initial supremum of the interval of the reference strain is approximately equal to the maximum of the absolute values of the principal strains of the solid structure (each material point has $b_0=1.0$) under the given loading conditions.

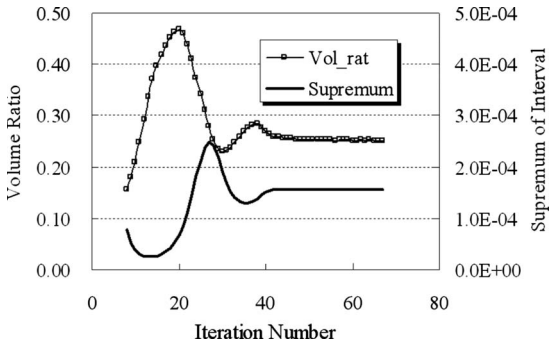

Fig. 9 Iteration histories of the supremum of the interval of the reference strain and the structural volume ratio

The convergent conditions are given by Eq. (22).

$$\left| \frac{H^k}{H^{k-1}} - 1.0 \right| \le \eta_1$$
$$\max_{0 \le i_1 < i_2 \le J} \left(\left| \frac{\varepsilon_{\sup}^{k-i_1} - \varepsilon_{\sup}^{k-i_2}}{\varepsilon_{\sup}^{k-i_1}} \right| \right) \le \eta_2 \tag{22}$$

where η_1 and η_2 are the tolerance parameters and J is a specified integer.

4 Numerical Examples

In the following examples, a uniformly fixed finite element mesh is used to describe the geometry and mechanical response within the entire design domain. Three-node plane stress element is employed. All numerical examples are analyzed by using IG algorithm.

4.1 Study of the Algorithm Parameters With Volume Constraint. In this subsection, a structure with specified volume constraint is investigated. The rectangular design domain shown in Fig. 1(*a*) is a fixed-supported deep beam ($L=1000$ mm) with a thickness of 10 mm and the beam is subjected to a concentrated force $P=1000$ N at the middle point of the upper side. The properties of the base material are Young's modulus $E=210.0$ GPa and Poisson's ratio $\nu=0.3$. The design domain is divided into 6400 elements with 3321 nodes. Figure 1(*b*) gives the optimal topology of the structure with a maximum volume ratio of 20% obtained by using SIMP method.

4.1.1 Optimal Results With Different Initial Designs. To investigate the influence of the initial material distribution on the optimum topology, it sets all of the initial eigenvalues of the fabric tensors to be $b_0=0.001$, 0.2, 0.4, 0.6, 0.8, and 1.0, respectively.

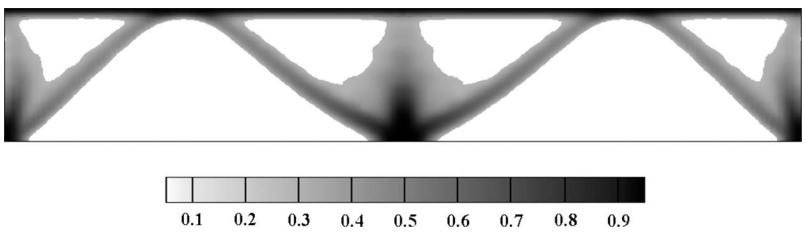

Fig. 10 The final material distribution of structure

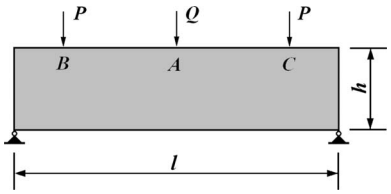

Fig. 11 Initial design domain

The volume ratio of the available material relative to the design domain is set to be 20%. The initial infimum and supremum of the interval of the reference strain are assigned as the maximum of the absolute values of the principal strains of the solid structure in Fig. 1(*a*). During the growth process, the growth speeds are $g_1=0.09$ and $g_2=0.06$, respectively. α in Eq. (20) is set to be 0.5.

Figure 2 shows the iteration histories of the supremums of the intervals of the reference strain of the structure with different initial eigenvalues of fabric tensors. All of the supremums converge at 2.18×10^{-6}. At Iteration 70 (in Table 1), the final material distribution of the structure is the same as that shown in Fig. 1(*b*). So, a conclusion can be given, i.e., the initial material distribution does not affect the final topology of a structure. It is necessary to demonstrate that the oscillation degree of the supremum depends on the initial material distribution (Fig. 2). When $b_0=1.0$ or $b_0=0.8$, the peak value of the supremum is far more than the convergent value. From Fig. 2(*b*), it can be found that the convergence behavior is much better when $b_0\leqslant0.4$. To avoid the extreme fluctuation of the supremum in iteration, we suggest that the value of b_0 should be determined by Eq. (8) or (9), i.e.,

$$b_0=f^{-1}[\rho=f(\boldsymbol{B}=b_0\boldsymbol{I})=R_v] \tag{23}$$

where function $\rho=f(\boldsymbol{B}=b_0\boldsymbol{I})$ is shown in Eq. (8) for 3D case or Eq. (9) for 2D case. R_v is the specified volume ratio of the structure.

4.1.2 Effects of the Growth Speeds on the Convergent Behavior. In this subsection, all of the initial eigenvalues of the fabric tensors are set to be $b_0=0.3$. The volume fraction of the available material relative to the design domain is set to be 20%. The initial infimum and supremum of the interval of the reference strain are assigned as the maximum of the absolute values of the principal strains of the solid structure in Fig. 1(*a*). Parameter α in Eq. (20) is set to be 0.5. Fourteen pairs of growth speeds are discussed in detail, i.e.,

(1) $g_1=0.08$ is fixed and $g_2=0.25g_1,0.5g_1,0.75g_1,1.0g_1$, respectively
(2) $g_2=0.08$ is fixed and $g_1=0.25g_2,0.5g_2,0.75g_2$, respectively
(3) $g_1=0.02$ is fixed and $g_2=0.25g_1,0.5g_1,0.75g_1,1.0g_1$, respectively
(4) $g_2=0.02$ is fixed and $g_1=0.25g_2,0.5g_2,0.75g_2$, respectively

When the structure grows with high speed pairs, the iteration histories of the supremums of reference intervals are shown in Fig. 3, which implies that the convergency appears after around 60 times of iteration. Figure 4 shows the iteration histories of the supremums of reference intervals of the structure growing with lower speed pairs. Obviously, the convergency appears after around 100 iterations. Especially, when the growth speed pair is $g_2=0.02$ and $g_1=0.25g_2$, the high oscillations of the supremum exist and the convergency does not appear after 140 times of iteration. Both Figs. 3 and 4 show that the convergent values of the supremums are different.

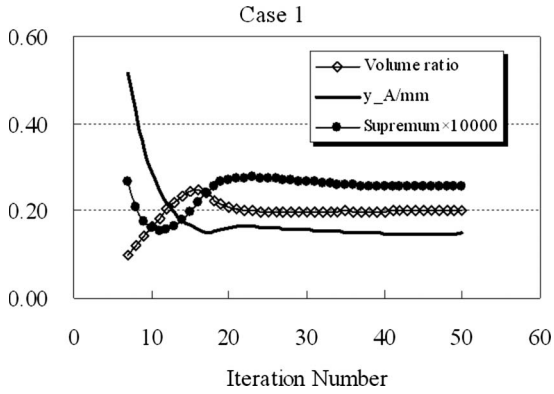

Fig. 13 Iteration histories of the volume ratio of the structure, *y*-deflection of Point *A*, and the supremum of the reference strain interval

Table 2 gives the values in detail. When the deposition speed g_1 is fixed and the dissipation speed increases, the supremum of the interval becomes smaller rapidly. When the dissipation speed g_2 is fixed and the deposition speed increases, the convergent value of the supremum of the interval changes slightly. Obviously, the convergent value of the supremum of the reference interval depends on the growth speeds. The reason is that the structural displacement field is sensitive to the growth speeds when the structure is in an equilibrium state of "remodeling."

Table 3 shows the final topology of the structure growing with different growth speed pairs. One can find that the structure cannot reach the optimal topology when the dissipation speed is not less than the deposition speed. At the same time, the material distribution in the final structural topology appears loose as for lower growth speed pairs, and it appears compactly when the speed pair is selected as $g_1=0.08$ and $g_2=0.5g_1$.

4.2 Study of Algorithmic Mesh-Dependency With Displacement Constraint. The design domain shown in Fig. 5 is a deep cantilever beam with a thickness of 10.0 mm, $L=1.0$ m. The concentrated force $P=1.0$ kN is imposed on the center (Point A) of the right edge vertically. The properties of the base material are Young's modulus $E=210.0$ MPa and Poisson's ratio $\nu=0.3$. The initial supremum of the interval of the reference strain is assigned as the maximum of the absolute values of the principal strains of the solid structure under loading conditions. The growth speeds are set to be $g_1=0.08$ and $g_2=0.5g_1$. All of the initial eigenvalues of the fabric tensors of each finite element are set to be $b_0=0.3$. The parameters of the algorithm are $\alpha=-0.5$, $\eta_1=0.2\%$, $\eta_2=1.0\%$, and $J=10$, respectively. The maximum iteration number is 100. The objective is to minimize the structural volume, and the

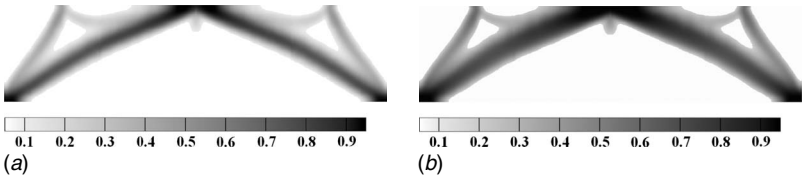

Fig. 12 Optimal topologies of structure in different cases: (*a*) Case 1 and (*b*) Case 2

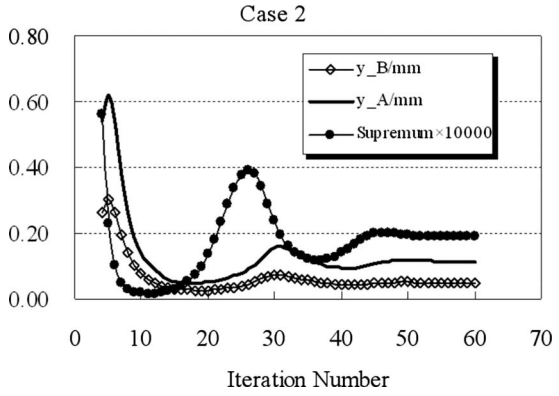

Fig. 14 Iteration histories of the *y*-deflections of Points *A* and *B* and the supremum of the reference strain interval

maximum displacement of Point A is no more than 0.5×10^{-5} m.

To investigate the mesh dependency of the optimal results of the structure, here we mesh the design domain with three cases: (A) 21×61 nodes, (B) 41×121 nodes and (C) 51×151 nodes.

Figure 6 shows the iteration histories of the supremums of the intervals of the reference strain with different mesh schemes. It is clear that the supremums converge at 2.19×10^{-6} after 64 times of iteration with Mesh Case A, at 2.28×10^{-6} after 84 iterations with Case B, and at 2.27×10^{-6} after 100 iterations with Case C. It is worth noting that the supremums oscillate slightly in Cases A and B. However, the oscillation of the supremum in Case C is very violent during the first 60 times of iteration.

The structural volume ratios approach 15.0%, 13.3%, and 13.4% in Cases A, B, and C, respectively. From the convergent values of the supremums of the interval and the structural volume ratios, one can find that the results have no mesh dependence if the mesh is refined enough.

Figure 7 shows the final topologies with different mesh cases. All topologies are almost the same, i.e., the distance between the two ends of the two bars on the fixed boundary is two times of the structural breadth. It implies that the optimal topology of the structure does not depend on the meshes.

4.3 Application of Current Approach. As an application, a 2D bridge problem is analyzed. The initial design domain is shown in Fig. 8, where the height $h=10.0$ m, length $l=60.0$ m, and unit thickness. The base material of the bridge has Young's modulus $E=21.0$ GPa and Poisson's ratio $\nu=0.2$. The structure is subjected to a uniform pressure $p=300.0$ kN/m on the upper edge. Three points on the bottom are fixed. Three additional loadings ($q=300.0$ kN/m) are exposed onto the upper edge right upon the three fixed points. The widths of the segments with additional loadings are 0.75 m, 1.5 m, and 0.75 m, respectively. The subdomain near the upper edge with height $h^*=0.5$ m is not a design domain. The initial supremum of the interval of the reference strain is assigned as the maximum of the absolute values of the principal strains of the solid structure under loading conditions. During the growth process, the parameters of the algorithm are $g_1=0.06$, $g_2=0.5g_1$, $b_0=0.3$, $\alpha=-0.5$, $\eta_1=0.5\%$, $\eta_2=0.5\%$, and $J=10$, respectively. The objective is to minimize the structural volume, and the maximum displacement on the upper edge must be no more than 0.005 m.

Figure 9 shows the iteration history of the interval supremum and the structural volume ratio. After 67 iterations, the supremum converges at 1.58×10^{-4} and the structural volume ratio approaches 25.3%. Figure 10 shows the final topology of the structure, which is like an arch bridge.

4.4 Optimization Problem With Multiple Constraints. Figure 11 shows the initial design of a structure with fixed conjuncted two ends at the bottom, where $l=4.0$ m, $h=1.0$ m, and thickness of 10.0 mm. A concentrated force $Q=5.0$ kN is supplied on the center (Point A) of the upper boundary. Two concentrated forces with $P=2.5$ kN are supplied symmetrically on the upper boundary, where $l_{AB}=l_{AC}=1.4$ m. Young's modulus and Poisson's ratio of the base material in the design domain are $E=210.0$ GPa and $\nu=0.3$, respectively. The initial supremum of the interval of the reference strain is assigned as the maximum of the absolute values of the principal strains of the solid structure under loading conditions. During the growth process, the parameters of the algorithm are $g_1=0.08$, $g_2=0.5g_1$, $b_0=0.3$, $\eta_1=0.5\%$, $\eta_2=0.5\%$, and $J=10$, respectively. The maximum iteration times is 100. Two types of design are considered as follows:

Case 1. The objective is to minimize the structural compliance, and the constraints are (a) the y-displacement of Point A $y_A^*\le0.2$ mm and (b) the final structural volume is no more than 20% of the total volume. In Eq. (20), $\alpha=0.5$.

Case 2. The objective is to minimize the structural volume, and the constraints are (a) the y-displacement of Point A $y_A^*\le0.2$ mm and (b) the y-displacement of Point B $y_B^*\le0.05$ mm. In Eq. (20), $\alpha=-0.5$.

From Fig. 12, one can find that the final topologies are the same. The difference between two final structures is the local material densities.

Figure 13 shows the iteration histories of the volume ratio of the structure, the y-deflection of Point A, and the supremum of the interval of the reference strain in Case 1. After 50 times of iteration, the volume ratio approaches 20%, the y-deflection of Point A reaches 0.149 mm, and the supremum of the interval converges at 0.257×10^{-4}.

For Case 2, from Fig. 14, one can find that the y-deflections of Points A and B reach 0.11 mm and 0.05 mm, respectively, after 61 times of iteration. Simultaneously, the supremum of the interval approaches 0.188×10^{-04}.

5 Conclusions

A heuristic approach is presented to solve continuum topology optimization problems with specified constraints, e.g., structural volume constraint and/or displacement constraint(s). Different from the other methods such as HDM and SIMP, a second-rank fabric tensor is adopted to express the geometry of the microstructure and the constitutive properties of a material point in design domain. In the optimization process, the design variables of a material point are the eigenpairs of its fabric tensor. The update of the design variables contains the update rule of the eigenvectors of fabric tensors based on Wolff's law and the update rule of the eigenvalues of fabric tensors by adopting a floating interval of the reference strain, which is similar to the dead zone of the bone. The update rule of the reference interval, which depends on the ratio(s) between the current constraint value(s) and the corresponding critical value(s), is given. Several optimization problems with different constraints are analyzed and the results imply the following.

(1) The optimal topology of the structure is independent of the initial design.
(2) The convergent value of the supremum of the interval of the reference strain of the structure depends on the growth speeds slightly.
(3) The optimal topology of the structure can be obtained rapidly when the deposition speed is not less than 0.04 and the material distributes compactly when the dissipation speed is approximately half of the deposition speed.

Acknowledgment

The financial support of the National Natural Science Foundation of China (10225212, 10721062, and 10402005), the National Key Basic Research Special Foundation of China (2005CB321704), and the Program for Changjiang Scholars and

Innovative Research Team in University of China (PCSIRT), SRF for ROCS, SEM is greatly acknowledged. Many thanks to anonymous reviewers for their suggestions.

References

[1] Eschenauer, H. A., and Olhoff, N., 2001, "Topology Optimization of Continuum Structures: A Review," Appl. Mech. Rev., **54**, pp. 331–390.

[2] Bendsøe, M. P., and Kikuchi, N., 1988, "Generating Optimal Topologies in Structural Design Using a Homogenization Method," Comput. Methods Appl. Mech. Eng., **71**, pp. 197–224.

[3] Bendsøe, M. P., 1989, "Optimal Shape Design as a Material Distribution Problem," Struct. Optim., **1**, pp. 193–202.

[4] Rozvany, G. I. N., Zhou, M., and Birker, T., 1992, "Generalized Shape Optimization Without Homogenizaiton," Struct. Optim., **4**, pp. 250–252.

[5] Atrek, E., and Kodali, R., 1989, "Optimum Design of Continuum Structures With SHAPE," *CAD/CAM Robotics and Factories of the Future*, Vol. 2, B. Prasad, ed., Springer, Berlin.

[6] Xie, Y. M., and Steven, G. P., 1993, "A Simple Evolutionary Procedure for Structural Optimization," Comput. Struct., **49**, pp. 885–896.

[7] Querin, O. M., Steven, G. P., and Xie, Y. M., 1998, "Evolutionary Structural Optimization (ESO) Using a Bidirectional Algorithm," Eng. Comput., **15**, pp. 1031–1048.

[8] Eschenauer, H. A., Kobelev, V. V., and Schumacher, A., 1994, "Bubble Method for Topology and Shape Optimization of Structures," Struct. Optim., **8**, pp. 42–51.

[9] Wang, M. Y., Wang, X., and Guo, D., 2003, "A Level Set Method for Structural Topology Optimization," Comput. Methods Appl. Mech. Eng., **192**, pp. 227–246.

[10] Sigmund, O., and Torquato, S., 1997, "Design of Materials With Extreme Thermal Expansion Using a Three-Phase Topology Optimization Method," J. Mech. Phys. Solids, **45**, pp. 1037–1067.

[11] Bendsøe, M. P., and Sigmund, O., 1999, "Material Interpolation Schemes in Topology Optimization," Appl. Mech. Rev., **69**, pp. 635–654.

[12] Bendsøe, M. P., and Sigmund, O., 2003, *Topology Optimization: Theory, Method and Applications*, Springer, Berlin.

[13] Rodrigues, H., Guedes, J. M., and Bendsøe, M. P., 2002, "Hierarchical Optimization of Material and Structure," Struct. Multidiscip. Optim., **24**, pp. 1–10.

[14] Pauwels, F., 1965, *Gesammelte Abhandlungen zur Funktionellen Anatomic des Bewegungsapparates*, Springer-Verlag, Berlin.

[15] Carter, D. T., Harris, W. H., Vasu, R., and Caler, W. E., 1981, "The Mechanical and Biological Response of Cortical Bone to In Vivo Strain Histories," *Mechanical Properties of Bone*, S. C. Cowin, ed., ASME, New York.

[16] Cowin, S. C., 1986, "Wolff'S Law of Trabecular Architecture at Remodeling Equilibrium," ASME J. Biomech. Eng., **108**, pp. 83–88.

[17] Frost, H. M., 1987, "Bone "Mass" and the "Mechanostat:" A Proposal," Anat. Rec., **219**, pp. 1–9.

[18] Huiskes, R., Weinans, H., Grootenboer, H. J., Dalstra, M., Fudala, B., and Slooff, T. J., 1987, "Adaptive Bone-Remodeling Theory Applied to Prosthetic-Design Analysis," J. Biomech., **20**, pp. 1135–1150.

[19] Mullender, M. G., Huiskes, R., and Weinans, H., 1994, "A Physiological Approach to the Simulation of Bone Remodeling as a Self-Organizational Control Process," J. Biomech., **27**, pp. 1389–1394.

[20] Huiskes, R., Ruimerman, R., van Lenthe, G. H., and Janssen, J. D., 2000, "Effects of Mechanical Forces on Maintenance and Adaptation on Form in Trabecular Bone," Nature (London), **405**, pp. 704–706.

[21] Wolff, J., 1986, *The Law of Bone Remodelling (Das Gesetz der Transformation der Knochen, Hirschwald, 1892)*, translated by P. Maquet and R. Furlong, Springer, Berlin.

[22] Gibson, L. J., 1985, "The Mechanical Behaviour of Cancellous Bone," J. Biomech., **18**, pp. 317–328.

[23] Odgaard, A., Kabel, J., van Rietbergen, B., Dalstra, M., and Huiskes, R., 1997, "Fabric and Elastic Principal Directions of Cancellous Bone Are Closely Related," J. Biomech., **30**, pp. 487–495.

[24] Cai, K., Zhang, H. W., and Chen, B. S., 2006, "Wolff'S Law Based Topology Optimization for Continuum Structure," Acta Mech. Sin., **38**, pp. 514–521, in Chinese.

[25] Cai, K., Chen, B. S., and Zhang, H. W., 2007, "Topology Optimization of Continuum Structures Based on a New Bionics Method," Int. J. Comput. Meth. Eng. Sci. Mech., **8**, pp. 233–242.

[26] Whitehouse, W. J., and Dyson, E. D., 1974, "Scanning Electron Microscope Studies of Trabecular Bone in the Proximal End of the Human Femur," J. Anat., **118**, pp. 417–444.

[27] Harrigan, T. P., and Mann, R. W., 1984, "Characterization of Microstructural Anisotropy in Othotropic Materials Using a Second Rank Tensor," J. Mater. Sci., **19**, pp. 761–767.

[28] Cowin, S. C., 1985, "The Relationship Between the Elasticity Tensor and the Fabric Tensor," Mech. Mater., **4**, pp. 137–147.

[29] Kanatani, K., 1984, "Distribution of Directional Data and Fabric Tensors," Int. J. Eng. Sci., **22**, pp. 149–164.

[30] Boehler, J. P., 1987, *Applications of Tensor Functions in Solid Mechanics*, Springer, Wien.

[31] Zysset, P. K., and Curnier, A., 1995, "An Alternative Model for Anisotropic Elasticity Based on Fabric Tensors," Mech. Mater., **21**, pp. 243–250.

[32] He, Q. C., and Curnier, A., 1995, "A More Fundamental Approach to Damaged Elastic Stress-Strain Relations," Int. J. Solids Struct., **32**, pp. 1433–1457.

Buckling of a Circular Plate Resting Over an Elastic Foundation in Simple Shear Flow

Haoxiang Luo[1]
Department of Mechanical Engineering,
Vanderbilt University,
VU Station B 351592,
2301 Vanderbilt Pl,
Nashville, TN 37235-1592
e-mail: haoxiang.luo@vanderbilt.edu

C. Pozrikidis
Department of Mechanical and Aerospace Engineering,
University of California, San Diego,
La Jolla, CA 92093-0411

The elastic instability of a circular plate adhering to an elastic foundation modeling the exposed surface of a biological cell resting on the cell interior is considered. Plate buckling occurs under the action of a uniform body force due to an overpassing simple shear flow distributed over the plate cross section. The problem is formulated in terms of the linear von Kármán plate bending equation incorporating the body force and the elastic foundation spring constant, subject to clamped boundary conditions around the rim. The coupling of the plate to the substrate delays the onset of the buckling instability and may have a strong effect on the shape of the bending eigenmodes. Contrary to the case of uniform compression, as the shear stress of the overpassing shear flow increases, the plate always first buckles in the left-to-right symmetric mode.
[DOI: 10.1115/1.2937137]

Keywords: membrane wrinkling, winkler foundation, elastic instability, plate buckling, shear flow

1 Introduction

The elastic instability of beams and plates is of prime interest in mainstream engineering design where critical conditions for structural stability under a compressive edge load must be established. Analytical and numerical results are available in the classical mechanics and applied engineering literature for plates with various shapes and a variety of boundary conditions (e.g., see Refs. [1,2]). The buckling of beams and plates with rectangular and circular shapes adhering to an elastic foundation has been studied by analytical and numerical methods on several occasions. Recently, Wang [3] studied the nonaxisymmetric buckling of a Kirchhoff plate resting on a Winkler foundation, provided analytical solutions for the eigenfunctions, and identified the most unstable buckling mode.

In this paper, we consider the buckling of a plate resting on an elastic foundation under a distributed tangential body force. Motivation is provided by the possible buckling of the membrane of an endothelium or cultured cell adhering to a substrate under the influence of an overpassing shear flow. In the physical model, the membrane is a composite medium consisting of the bilayer and the cytoskeleton, tethered to the cell interior by macromolecules that resist deflection and introduce an elastic response. Fung and Liu [4] discussed the mechanics of the endothelium and proposed that the main effect of an overpassing shear flow is to generate tensions over the exposed part of the cell membrane, while the cell interior is virtually unstressed. In an idealized depiction, the exposed membrane is a thin elastic patch anchored around its edges on the endothelium wall and connected to the basal lamina by sidewalls. In the present model, we also account for the elastic coupling between the cell membrane and the cell interior. Luo and Pozrikidis [5] considered the problem in the absence of the elastic substrate and uncovered the spectrum of eigenvalues corresponding to symmetric and antisymmetric deflection modes. Subsequently, Luo and Pozrikidis [6] investigated the effect of prestress with the goal of evaluating the buckling of the rotating capsule membrane. The present formulation extends these analyses and delineates critical conditions in the particular context of membrane mechanics and in the broader context of elastic stability pertinent to flow-structure interaction.

2 Theoretical Model

We consider a circular membrane patch modeled as an elastic plate flush mounted on a plane wall with the edge clamped around the rim (Fig. 1.) The upper surface of the membrane is exposed to an overpassing shear flow along the x axis with velocity $u_x = Gz$, where G is the shear rate and the z axis is normal to the wall. The lower surface of the membrane adheres to an elastic medium modeled as an elastic foundation.

The shear flow imparts to the upper surface of the membrane a uniform hydrodynamic shear stress, $\tau = \mu G$, where μ is the fluid viscosity. In the context of thin-shell theory for a zero thickness membrane, the shear stress can be smeared from the upper surface into the cross section of the membrane. When this is done, the shear stress effectively amounts to an in-plane body force uniformly distributed over the cross section with components

$$b_x = \frac{\tau}{h} = \frac{\mu G}{h}, \quad b_y = 0 \tag{1}$$

where h is the membrane thickness.

We assume that the in-plane stresses developing due to the in-plane deformation in the absence of buckling, σ_{ij}, are related to the in-plane strains ϵ_{ij} by the linear constitutive equation

$$\begin{bmatrix} \sigma_{xx} \\ \sigma_{yy} \\ \sigma_{xy} \end{bmatrix} = \frac{E}{1-\nu^2} \begin{bmatrix} 1 & \nu & 0 \\ \nu & 1 & 0 \\ 0 & 0 & 1-\nu \end{bmatrix} \cdot \begin{bmatrix} \epsilon_{xx} \\ \epsilon_{yy} \\ \epsilon_{xy} \end{bmatrix} \tag{2}$$

where

$$\epsilon_{kl} = \frac{1}{2}\left(\frac{\partial v_k}{\partial x_l} + \frac{\partial v_l}{\partial x_k} \right) \tag{3}$$

(v_x, v_y) is the tangential displacement of membrane point particles in the xy plane, E is the membrane modulus of elasticity, and ν is the Poisson ratio. Force equilibrium requires the differential balances

[1]Corresponding author.

Contributed by the Applied Mechanics Division of ASME for publication in the JOURNAL OF APPLIED MECHANICS. Manuscript received July 3, 2007; final manuscript received March 27, 2008; published online July 15, 2008. Review conducted by Krishna Garikipati.

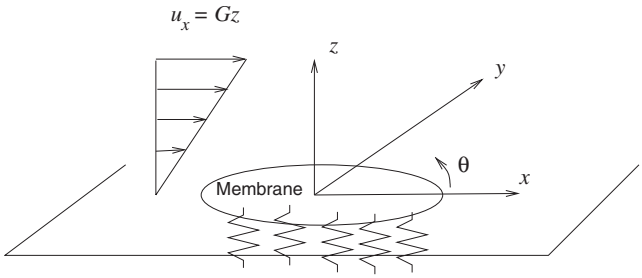

Fig. 1 Shear flow past a membrane patch modeled as an elastic plate flush mounted on a plane wall. The lateral deformation of the membrane is resisted by an elastic material supporting the membrane from underneath.

$$\frac{\partial \sigma_{xx}}{\partial x} + \frac{\partial \sigma_{yx}}{\partial y} + b_x = 0, \quad \frac{\partial \sigma_{xy}}{\partial x} + \frac{\partial \sigma_{yy}}{\partial y} + b_y = 0 \tag{4}$$

subject to the boundary conditions $v_x=0$ and $v_y=0$ around the clamped rim of the plate. For a circular plate of radius a, we obtain the simplified expressions

$$v_x = \frac{\tau}{Eh}\frac{1-\nu^2}{3-\nu}(a^2 - x^2 - y^2), \quad v_y = 0 \tag{5}$$

and associated stresses

$$\sigma_{xx} = -\frac{2}{3-\nu}\frac{\tau}{h}x, \quad \sigma_{xy} = -\frac{1-\nu}{3-\nu}\frac{\tau}{h}y, \quad \sigma_{yy} = \nu\sigma_{xx} \tag{6}$$

These expressions confirm that the streamwise component of the in-plane normal stress, σ_{xx}, is positive (tensile) on the upstream half and negative (compressive) on the downstream half of the plate. The transverse component of the normal stress, σ_{yy}, is also positive or negative depending on the sign of the Poisson ratio. Compression raises the possibility of buckling and wrinkling when the shear stress τ exceeds a critical threshold.

To compute the transverse deflection along the z axis upon inception of buckling, $z=f(x,y)$, we work under the auspices of linear elastic stability of thin plates and shells and derive the linear von Kármán equation,

$$\nabla^4 f \equiv \nabla^2\nabla^2 f = \frac{\partial^4 f}{\partial x^4} + 2\frac{\partial^4 f}{\partial x^2 \partial y^2} + \frac{\partial^4 f}{\partial y^4} = \frac{h}{E_B}\left(\sigma_{xx}\frac{\partial^2 f}{\partial x^2} + 2\sigma_{xy}\frac{\partial^2 f}{\partial x \partial y} + \sigma_{yy}\frac{\partial^2 f}{\partial y^2} - b_x\frac{\partial f}{\partial x} - b_y\frac{\partial f}{\partial y}\right) - \frac{k}{E_B}f \tag{7}$$

where E_B is the bending modulus and k is the spring constant of the foundation with dimensions of force over cubed length (F/L^3). In a physiological context, the bending modulus of a typical biological membrane is $E_B \simeq 1\times 10^{-12}$ dyn·cm. In the human circulation, μ is on the order of 1 cP, or 1 mPa·s, and the shear stress varies in the range of 1–2 Pa through all branches, corresponding to $G \sim 100\ \mathrm{s}^{-1}$.

The fourth-order differential equation (Eq. (7)) incorporates position-dependent coefficients multiplying the second derivatives on the right-hand side. Since the membrane is assumed to be clamped around the rim, the deflection satisfies homogeneous Dirichlet and Neumann boundary conditions around the rim in the xy plane, $f=0$ and $\partial f/\partial n=0$, where $\partial/\partial n$ denotes the normal derivative.

Substituting the expressions for the in-plane shear stresses in Eq. (7) and nondimensionalizing lengths by the plate radius a, we derive the dimensionless parameters

$$\hat{\tau} = \frac{\tau a^3}{E_B}, \quad \gamma = \frac{k a^4}{E_B} \tag{8}$$

expressing, respectively, the strength of the shear flow and the stiffness of the spring relative to the developing bending moments. Equation (7) admits the trivial solution, $f=0$, for any value of $\hat{\tau}$ and nontrivial eigensolutions at a sequence of discrete eigenvalues. Numerical solutions for $\gamma=0$ were derived by Luo and Pozrikidis [5] using analytical and finite-element methods. The computation of these eigenvalues and corresponding eigenfunctions in the more general case where γ is nonzero is the main objective of our analysis.

When the plate is uniformly compressed, $\sigma_{xx}=-N/h$, $\sigma_{yy}=-N/h$, $\sigma_{xy}=0$, and $\sigma_{yx}=0$, and in the absence of a body force, the governing equation (Eq. (7)) reduces to

$$\nabla^4 f = -\frac{N}{E_B}\nabla^2 f - \frac{k}{E_B}f \tag{9}$$

where N is the magnitude of the isotropic compressive tension. Nondimensionalizing lengths by the plate radius a, we find that the solution depends on the dimensionless group $\Lambda \equiv Na^2/E_B$, and stiffness parameter γ. The eigensolutions of this equation were computed by Wang [3] for several types of boundary conditions using Fourier–Bessel expansions.

3 Fourier Series Solution

Following Luo and Pozrikids [5], we introduce the plane polar coordinates defined in Fig. 1 and nondimensionalize the position, radial distance, and membrane deflection by the patch radius a. Dimensionless variables are indicated by a hat; thus, $\hat{r}=r/a$ and $\hat{f}=f/a$. The eigenfunctions of Eq. (7) are expanded in Fourier series,

$$\hat{f}(\hat{r},\theta) = \frac{1}{2}p_0(\hat{r}) + \sum_{n=1}^{\infty}\left(p_n(\hat{r})\cos n\theta + q_n(\hat{r})\sin n\theta\right) = \sum_{n=-\infty}^{\infty} F_n(\hat{r})\exp(-in\theta) \tag{10}$$

where i is the imaginary unit, $p_n(\hat{r})$ and $q_n(\hat{r})$ are real functions, and $F_n(\hat{r})$ is a complex dimensionless function defined by

$$F_n(\hat{r}) \equiv \frac{1}{2}(p_n(\hat{r}) + iq_n(\hat{r})) \tag{11}$$

for $n \geqslant 0$. For $n<0$, $F_n(\hat{r}) = F^*_{-n}(\hat{r})$, where an asterisk denotes the complex conjugate. To ensure that the membrane shape is smooth at the origin, we require $F_n(0)=0$ for $n \geqslant 1$. A straightforward computation yields the following expressions for the Laplacian and bi-Laplacian in-plane polar coordinates:

$$\hat{\nabla}^2\hat{f} = \sum_{n=-\infty}^{\infty} Q_n(\hat{r})\exp(-in\theta), \quad \hat{\nabla}^4\hat{f} = \sum_{n=-\infty}^{\infty}\Omega_n(\hat{r})\exp(-in\theta) \tag{12}$$

where $\hat{\nabla}$ is the gradient with respect to $\hat{x}\equiv x/a$ and $\hat{y}\equiv y/a$,

$$Q_n \equiv F_n'' + \frac{F_n'}{\hat{r}} - n^2\frac{F_n}{\hat{r}^2} \tag{13}$$

a prime denotes a derivative with respect to $\hat{r}$, and

$$\Omega_n(\hat{r}) \equiv Q_n'' + \frac{Q_n'}{\hat{r}} - n^2\frac{Q_n}{\hat{r}^2} = F_n'''' + \frac{2}{\hat{r}}F_n''' - \frac{1+2n^2}{\hat{r}^2}F_n'' + \frac{1+2n^2}{\hat{r}^3}F_n' + n^2\frac{n^2-4}{\hat{r}^4}F_n \tag{14}$$

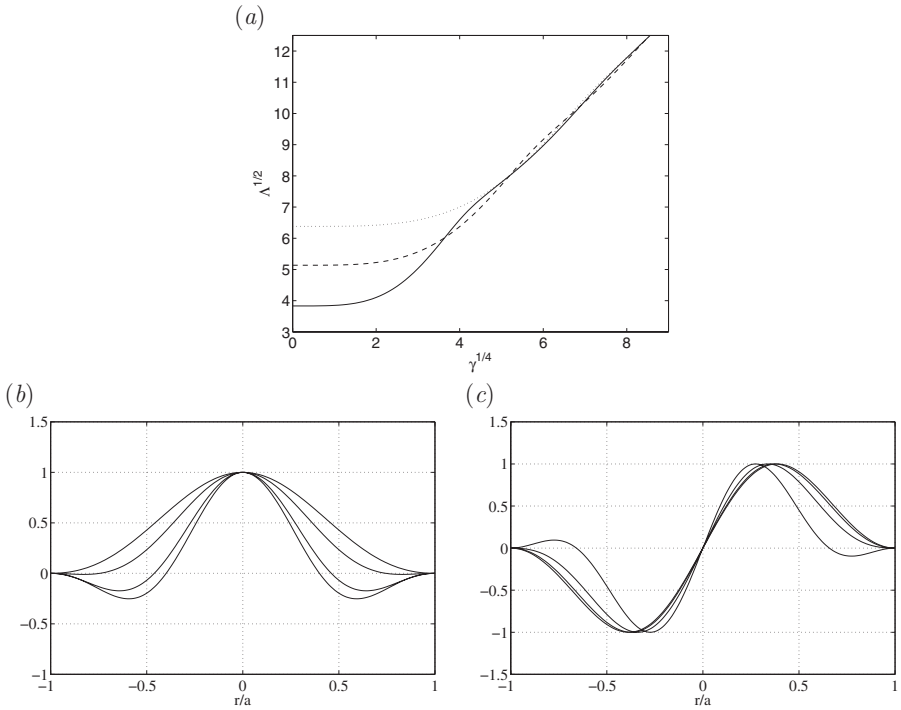

Fig. 2 (*a*) Effect of the elastic foundation constant γ on the lowest eigenvalues of a radially compressed circular plate for $n=0$ (solid line), $n=1$ (dashed line), and $n=2$ (dotted line). This figure reproduces Fig. 1 of Wang [3]. (*b*) and (*c*) Eigenfunctions, p_n, for $\gamma^{1/4}=3, 4, 5, 6$, and (*b*) $n=0$ and (*c*) $n=1$.

Expressing the right-hand side of Eq. (7) in plane polar coordinates and substituting the Fourier expansion, we find

$$\hat{\nabla}^4\hat{f} = -\sum_{n=-\infty}^{\infty}\left[\frac{\hat{\tau}}{3-\nu}\Psi_n e^{i\theta} + \gamma F_n + \frac{\hat{\tau}}{3-\nu}\Phi_n e^{-i\theta}\right]e^{-in\theta} \quad (15)$$

which can be restated as

$$\hat{\nabla}^4\hat{f} = -\sum_{n=-\infty}^{\infty}\left[\frac{\hat{\tau}}{3-\nu}\Psi_{n+1} + \gamma F_n + \frac{\hat{\tau}}{3-\nu}\Phi_{n-1}\right]e^{-in\theta} \quad (16)$$

where

$$\Psi_n = \hat{r}F_n'' + \left[\frac{3+\nu}{2} + (1-\nu)n\right]F_n' + n\left(\frac{1+\nu}{2} - \nu n\right)\frac{F_n}{\hat{r}}$$

$$\Phi_n = \hat{r}F_n'' + \left[\frac{3+\nu}{2} - (1-\nu)n\right]F_n' - n\left(\frac{1+\nu}{2} + \nu n\right)\frac{F_n}{\hat{r}} \quad (17)$$

Substituting Eq. (12) into Eq. (7) and equating corresponding Fourier coefficients, we derive an infinite tridiagonal system of ordinary differential equations,

$$\Omega_n + \gamma F_n = -\frac{\hat{\tau}}{3-\nu}(\Psi_{n+1} + \Phi_{n-1}) \quad (18)$$

for $n=0, \pm 1, \pm 2, \ldots$. Approximate eigenvalues are computed by truncating the system at a finite level, $n=\pm N$. In the case of eigensolutions with a left-to-right symmetry with respect to the zx plane, the Fourier series involves only cosine terms; the component functions F_n are real, $F_n=F_{-n}$, and $\Psi_{-n}=\Phi_n$. The general system (Eq. (18)) then reduces to

$$\Omega_0 + \gamma F_0 = -\frac{2\hat{\tau}}{3-\nu}\Psi_1$$

$$\Omega_n + \gamma F_n = -\frac{\hat{\tau}}{3-\nu}(\Psi_{n+1} + \Phi_{n-1}) \quad (19)$$

for $n=1,2,\ldots,N$. If the eigensolutions are antisymmetric with respect to the zx plane, the Fourier series involves only sine terms, the component functions F_n are imaginary, $F_n=-F_{-n}$, $\Psi_{-n}=-\Phi_n$, and the general system (Eq. (18)) reduces to $\Omega_0+\gamma F_0=0$ for the zeroth Fourier mode and the second equation in Eq. (19) for $n=1,2,\ldots,N$.

To solve the partial differential equations encapsulated in Eq. (18), we approximate the Fourier modulating modes $F_n(r)$ with polynomials, as discussed by Luo and Pozrikidis [5]. Collocating at Chebyshev nodes, we derive a generalized eigenvalue system of algebraic equations for the critical hydrodynamic stress. Physically, the smallest eigenvalue provides us with the minimum shear stress for the onset of buckling.

A similar method was implemented for solving Wang's compressed-plate equation (Eq. (9)). Substituting in Eq. (9) $\hat{f}(\hat{r},\theta)=p_n(\hat{r})\cos(n\theta)$, we derive the fourth-order ordinary differential equation

$$\mathcal{L}^2 p_n + \Lambda\mathcal{L}p_n + \gamma p_n = 0 \quad (20)$$

where

$$\mathcal{L} = \frac{d^2}{d\hat{r}^2} + \frac{1}{r}\frac{d}{d\hat{r}} - \frac{n^2}{r^2} \quad (21)$$

is a second-order differential operator. In this case, because of the uniform and isotropic tensions acting on the plate, the Fourier modes are decoupled.

4 Results and Discussion

To establish a point of reference, we first discuss the instability of the radially compressed plate governed by Eq. (20). Figure 2 demonstrates the effect of the elastic foundation parameter γ on

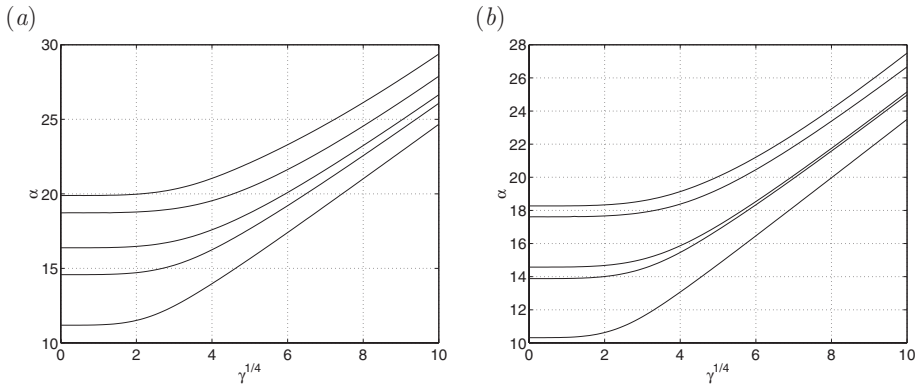

Fig. 3 Effect of the elastic foundation constant on the square root of the lowest eigenvalue, $\alpha=\sqrt{\hat{\tau}}$, for Poisson ratio (*a*) $\nu=0$ and (*b*) $\nu=0.25$. From bottom to top, the curves represent modes S1, S2, A1, A2, and S3, where "S" denotes a symmetric mode and "A" denotes an antisymmetric mode.

the lowest eigenvalues corresponding to $n=0$ (axisymmetric mode) and $n=1,2$ (nonaxisymmetric modes). The results precisely reproduce those shown in Fig. 1 of Wang [3] obtained by a different method. As γ is increased, the eigenvalue branches cross and then intertwine. Wang [3] noted that in the presence of a stiff elastic foundation, the axisymmetric mode is not necessarily the most dangerous buckling mode when the plate is strongly coupled to the foundation. As γ increases, the eigenfunctions of the axisymmetric mode and nonaxisymmetric modes take complicated shapes, as shown in Figs. 2(*b*) and 2(*c*).

Next, we discuss the instability of the circular plate under the action of a shear flow. Luo and Pozrikidis [5] found that, in the absence of the elastic substrate, $\gamma=0$, the buckling eigenfunctions consist of a sequence of symmetric modes, denoted as "S," interlaced with antisymmetric modes, denoted as "A." Figure 3 shows the effect of the substrate elastic parameter γ on the lowest few eigenvalues $\hat{\tau}$ for $\nu=0$ and 0.25. As γ increases, the eigenvalues increase monotonically while maintaining their relative position. In contrast to the radially compressed plate, the buckling modes caused by the hydrodynamic shear stress do not cross, and the symmetric mode S1 is always the most dangerous buckling mode. Selected eigenfunctions for $\nu=0.25$ and $\gamma=625$ are shown in Fig. 4.

Figure 5 illustrates the effect of γ on the profile of the eigenfunctions in the zx plane for the symmetric eigenmodes corresponding to $\nu=0.25$ and $\gamma=0$, 625, and 6561. For high values of γ, the buckled shape is convoluted even for the lowest mode. As γ increases, the deflection becomes more pronounced at the downstream portion of the plate.

Luo and Pozrikidis [5] found that the Poisson ratio may affect the order of appearance of the symmetric and antisymmetric eigenmodes, as illustrated in Fig. 6 for $\gamma=0$, 625, and 4096. In all cases, the eigenvalue $\hat{\tau}$ decreases as ν is increased, and the rate of decrease varies for each eigenmode. At certain critical Poisson ratios, the pair of the S2 and A1 modes and the pair of the S3 and

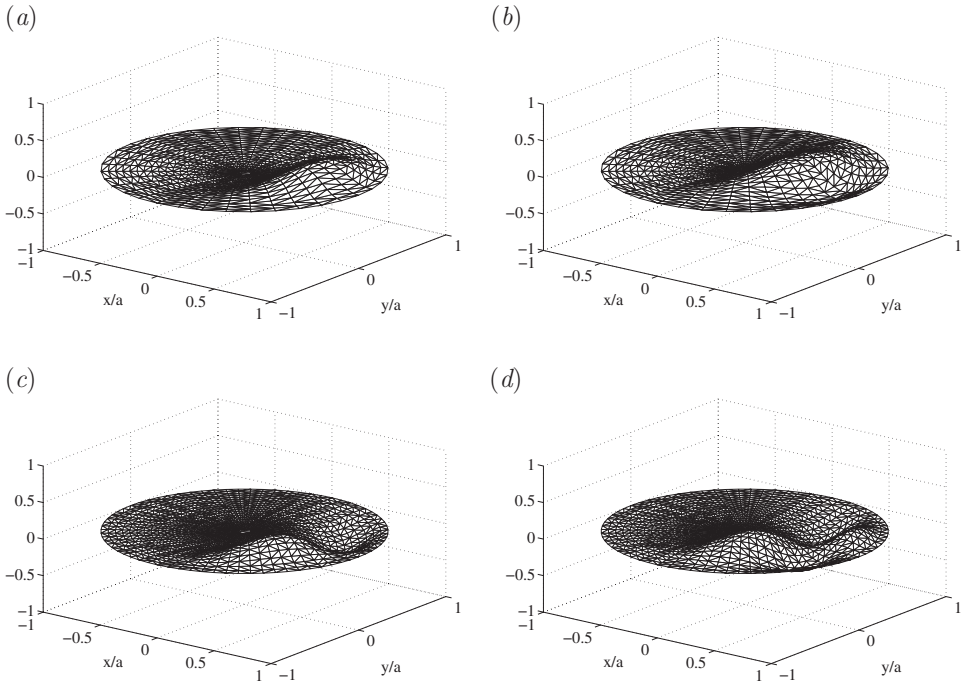

Fig. 4 Buckling eigenmodes for $\nu=0.25$, $\gamma=625$, and (*a*) $\hat{\tau}=217.24$ (S1), (*b*) $\hat{\tau}=282.93$ (S2), (*c*) $\hat{\tau}=291.82$ (A1), and (*d*) $\hat{\tau}=371.08$ (A2)

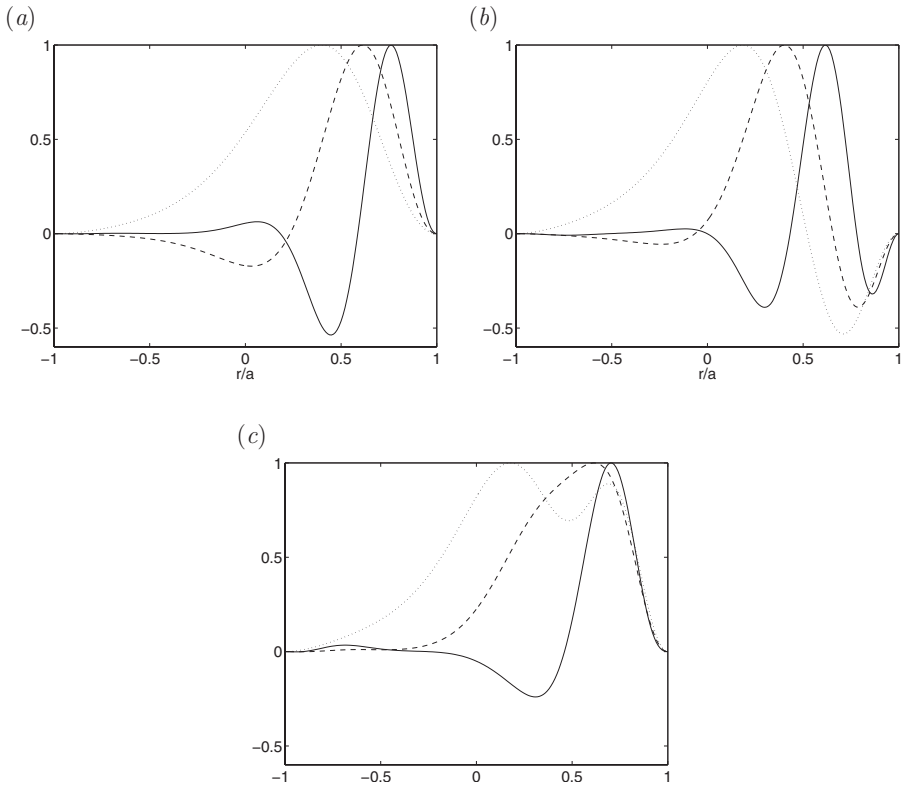

Fig. 5 Comparison of the buckling mode profiles for ν=0.25 and γ=0 (dash-dotted line), γ=625 (dashed line), and γ=6561 (solid line), and buckling modes (*a*) S1, (*b*) S2, and (*c*) S3

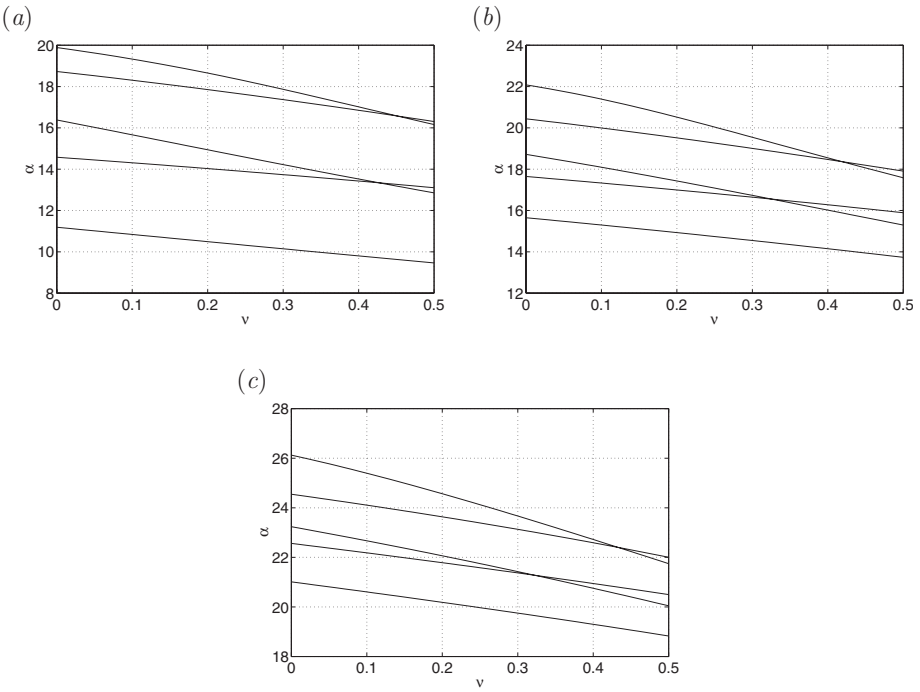

Fig. 6 First few eigenvalues, $\alpha=\sqrt{\hat{\tau}}$, plotted against ν for a circular membrane with the spring stiffness (*a*) γ=0, (*b*) γ=625, and (*c*) γ=4096. From bottom to top along ν=0, the curves represent modes S1, S2, A1, A2, and S3.

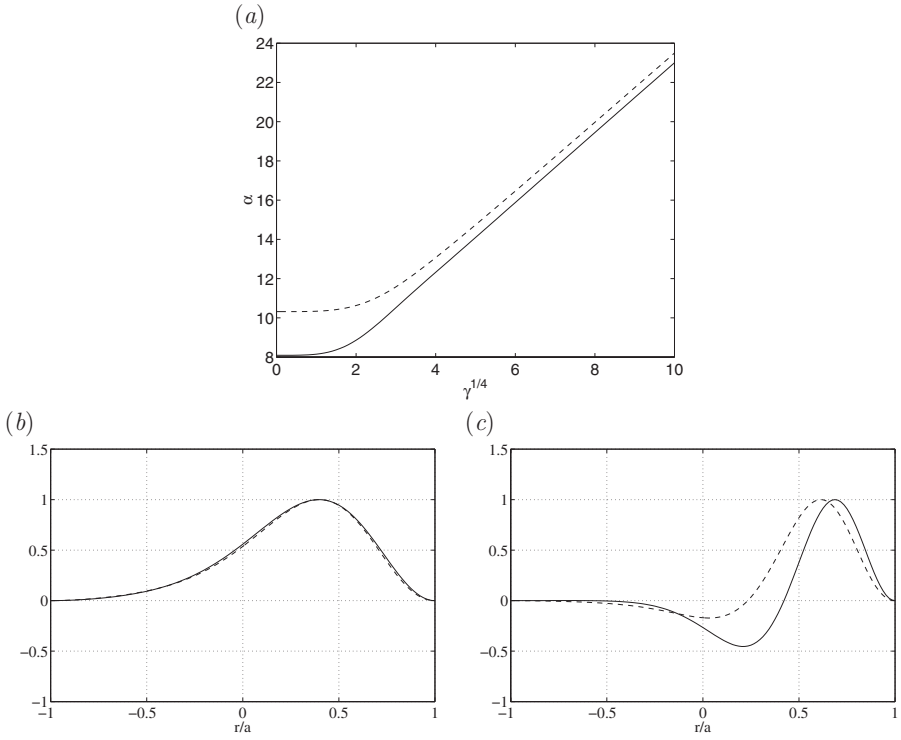

Fig. 7 (*a*) The lowest eigenvalues of the one-dimensional model, $\alpha=\sqrt{\hat{\tau}}$ (solid line), are compared with the S1 eigenvalues of the two-dimensional model (dashed line). (*b*) and (*c*) The solid lines illustrate the eigenfunctions of the one-dimensional model for (*b*) $\gamma=0$ and (*c*) $\gamma=625$. The profiles of the two-dimensional eigenfunction S1 at $y=0$ are shown as dashed lines.

A2 modes cross over. At these Poisson ratios, the eigenfunctions of the double eigenvalues are arbitrary superposition of the symmetric and antisymmetric modes and may thus have an arbitrary orientation in space. The critical Poisson ratios are affected only slightly by γ.

It is instructive to compare the numerical results of the full two-dimensional model with the predictions of a one-dimensional model that arises by applying the von Kármán equation at the midplane, $y=0$, and discarding the y dependence. The deflection is governed by a linear ordinary differential equation with position-dependent coefficients,

$$\frac{d^4f}{dx^4}+\frac{k}{E_B}f=-\frac{2\tau}{(3-\nu)E_B}\left(x\frac{d^2f}{dx^2}+\frac{3-\nu}{2}\frac{df}{dx}\right) \tag{22}$$

subject to the clamped-end boundary conditions $f=0$ and $f'=0$ at $x=\pm a$. The nondimensional form is

$$\frac{d^4\hat{f}}{d\hat{x}^4}+\gamma\hat{f}=-\frac{2\hat{\tau}}{3-\nu}\left(\hat{x}\frac{d^2\hat{f}}{d\hat{x}^2}+\frac{3-\nu}{2}\frac{d\hat{f}}{d\hat{x}}\right) \tag{23}$$

On physical grounds, we anticipate that the eigenvalues and corresponding eigenfunctions will be approximations of the symmetric circular membrane modes.

We were unable to solve the one-dimensional eigenvalue problem by analytical methods. Numerical solutions were produced instead using a finite-difference method resulting in a pentadiagonal system of algebraic equations for the nodal values of the eigenfunctions. Figure 7(*a*) compares the eigenvalues of the one-dimensional model with the S1 eigenvalues of the two-dimensional model. The critical buckling load predicted by the one-dimensional model is lower than that of the two-dimensional model and thus provides us a conservative prediction independent of the elastic foundation constant. Figures 7(*b*) and 7(*c*) compare the first buckling mode of the one-dimensional model for $\gamma=0$ and $\gamma=625$ with the corresponding eigenfunction profiles of the two-dimensional solution at $y=0$. The agreement is excellent for $\gamma=0$ and reasonable for $\gamma=625$. We conclude that the one-dimensional model is useful for making reliable engineering predictions.

5 Conclusion

We have investigated the effect of an elastic foundation on the buckling of a circular plate under the action of a uniform body force tangential to the plate, imparted by an overpassing simple shear flow. In the case of the radially compressed circular plate, a nonaxisymmetric deflection in an indeterminate meridional position may occur when the plate-substrate coupling is sufficiently strong. Buckling first occurs in the symmetric mode where the deflection is left-to-right symmetric with respect to the direction of the flow. Our results serve as a guide for future laboratory observations aimed at documenting the buckling of exposed cells and assessing their significance in mechanotransduction.

Acknowledgment

This research was supported by a grant provided by the National Science Foundation.

References

[1] Bloom, F., and Coffin, D., 2001, *Handbook of Thin Plate Buckling and Postbuckling*, Chapman and Hall/CRC, Boca Raton.
[2] Timoshenko, S. P., and Gere., J. M., 1961, *Theory of Elastic Stability*, 2nd ed., McGraw-Hill, New York.
[3] Wang, C. W., 2005, "On the Buckling of a Circular Plate on an Elastic Foundation," ASME J. Appl. Mech., **72**, pp. 795–796.
[4] Fung, Y. C., and Liu, S. Q., 1993, "Elementary Mechanics of the Endothelium of Blood Vessels," ASME J. Biomech. Eng., **115**, pp. 1–12.
[5] Luo, H., and Pozrikidis, C., 2006, "Buckling of a Flush Mounted Plate in Simple Shear Flow," Arch. Appl. Mech., **76**, pp. 549–566.
[6] Luo, H., and Pozrikidis, C., 2007, "Buckling of a Pre-Compressed or Pre-Stretched Membrane in Shear Flow," Int. J. Solids Struct., 44, pp. 8074–8085.

Scale-Dependent Homogenization of Inelastic Random Polycrystals

Shivakumar I. Ranganathan
Mem. ASME
e-mail: srangan3@uiuc.edu

Martin Ostoja-Starzewski
Fellow ASME
e-mail: martinos@uiuc.edu

Department of Mechanical Science and Engineering,
University of Illinois at Urbana-Champaign,
Urbana, IL 61801

Rigorous scale-dependent bounds on the constitutive response of random polycrystalline aggregates are obtained by setting up two stochastic boundary value problems (Dirichlet and Neumann type) consistent with the Hill condition. This methodology enables one to estimate the size of the representative volume element (RVE), the cornerstone of the separation of scales in continuum mechanics. The method is illustrated on the single-phase and multiphase aggregates, and, generally, it turns out that the RVE is attained with about eight crystals in a 3D system. From a thermodynamic perspective, one can also estimate the scale dependencies of the dissipation potential in the velocity space and its complementary potential in the force space. The viscoplastic material, being a purely dissipative material, is ideally suited for this purpose. [DOI: 10.1115/1.2912999]

Keywords: homogenization, random polycrystals, representative volume element (RVE), bounds, plasticity

1 Introduction

The motivation of this study is to determine the size of the representative volume element (RVE) and obtain rigorous bounds on the inelastic response of polycrystalline aggregates. In most of the existing literature, the response of polycrystalline aggregates is obtained using the Taylor hypothesis [1], the Sachs hypothesis [2], or the self-consistent methods (e.g., Refs. [3–6]). The Taylor and the Sachs hypotheses only give the upper and lower bounds on the aggregate response, which can be quite different depending on the orientation and material properties of single crystals comprising the aggregate. If a periodic cell of an elastoplastic composite is assumed, the classical homogenization method can be applied; see Ref. [7] for a thermodynamic perspective. However, none of the above approaches answer this question: "How many grains are needed to homogenize the response of polycrystalline aggregates?" This is equivalent to asking: "What is the size of the RVE in random polycrystals?"

One powerful way of approaching this problem is to set up and solve two stochastic boundary value problems consistent with the Hill condition, assuming the microstructure to be spatially homogeneous and ergodic, but not requiring any periodicity assumptions. In such an approach, one moves from the so called statistical volume element (SVE) to the RVE with an increasing number of grains. Basically, three types of boundary value problems can be set up—the Dirichlet, Neumann, and mixed-orthogonal ones—and the RVE is approached when the aggregate is sufficiently large so that its response becomes practically independent of the applied boundary conditions. In the process of increasing the scale of SVE, the Dirichlet and Neumann boundary value problems deliver scale-dependent bounds from above and from below, respectively. Jiang et al. [8] and more recently Li and Ostoja-Starzewski [9] have employed such an approach to study responses of two-phase elastoplastic random composites. A comparative review of scaling trends in linear and finite elasticity and/or thermoelasticity, elastoplasticity, and Stokesian flow in porous media has been given in Ref. [10], while a broad study of this and many related issues in stochastic mechanics of materials is given in Ref. [11].

Contributed by the Applied Mechanics Division of ASME for publication in the JOURNAL OF APPLIED MECHANICS. Manuscript received September 1, 2007; final manuscript received November 14, 2007; published online July 15, 2008. Review conducted by Robert M. McMeeking.

2 Mathematical Formulation

2.1 Note on the Hill Condition. The Hill condition establishes the equivalence between the energetic and the mechanical approaches for setting up constitutive equations. To demonstrate this, let the Cauchy stress $\boldsymbol{\sigma}$ and the rate of deformation tensor $\mathbf{D}$ be decomposed into their mean and fluctuating parts

$$\boldsymbol{\sigma}(x,\omega) = \bar{\boldsymbol{\sigma}}(\omega) + \boldsymbol{\sigma}'(x,\omega)$$
$$\mathbf{D}(x,\omega) = \bar{\mathbf{D}}(\omega) + \mathbf{D}'(x,\omega) \tag{2.1}$$

Here, $\omega(\in\Omega)$ indicates a specific realization of the microstructure, while x accounts for the point to point dependence. Both fields are split into the mean fields and zero-mean fluctuations

$$\bar{\boldsymbol{\sigma}}_\delta(\omega) = \frac{1}{V}\int \boldsymbol{\sigma}(x,\omega)dV, \quad \int \boldsymbol{\sigma}'(x,\omega)dV = 0$$
$$\bar{\mathbf{D}}_\delta(\omega) = \frac{1}{V}\int \mathbf{D}(x,\omega)dV, \quad \int \mathbf{D}'(x,\omega)dV = 0 \tag{2.2}$$

In Eq. (2.2), the subscript δ represents the window size and is defined as follows:

$$\delta = \frac{d}{l} = (N_G)^{1/3} \tag{2.3}$$

where d is some characteristic length scale, l is the scale of observation, and N_G is the total number of grains in the aggregate. Using Eqs. (2.1) and (2.2), the volume averaged contracted scalar product of $\boldsymbol{\sigma}$ and $\mathbf{D}$ is given by

$$\overline{\sigma_{ij}:D_{ij}} = \frac{1}{V}\int_{\partial V} \sigma_{ij}:D_{ij}dV = \bar{\sigma}_{ij}:\bar{D}_{ij} + \frac{1}{V}\int_{\partial V} \sigma'_{ij}:D'_{ij}dV \tag{2.4}$$

The Hill condition follows from Eq. (2.4), so that, in an incremental setting [12],

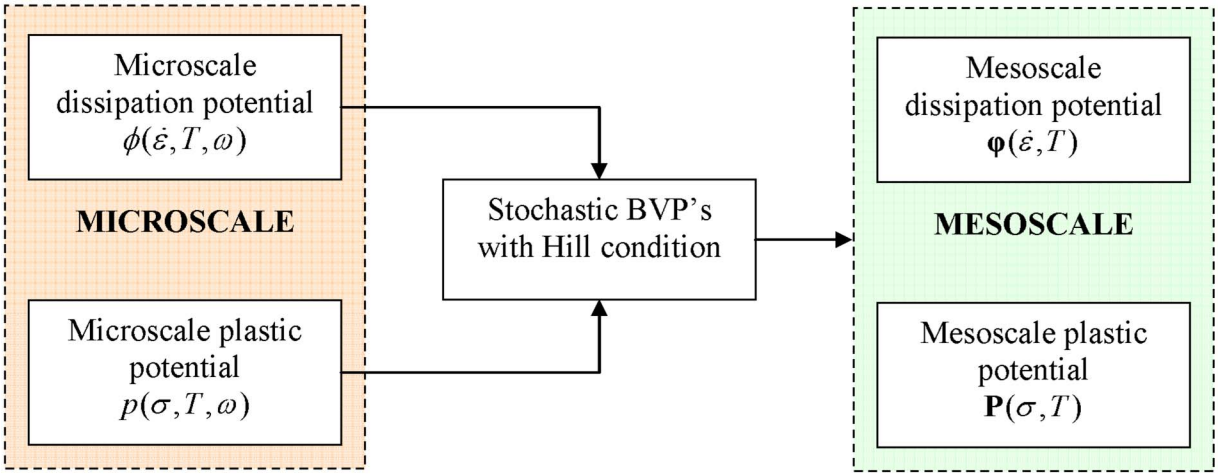

Fig. 1 The homogenization methodology

$$\overline{\sigma_{ij}:D_{ij}} = \overline{\sigma_{ij}}:\overline{D_{ij}} \Leftrightarrow \overline{\sigma_{ij}:d\varepsilon_{ij}} = \overline{\sigma_{ij}}:\overline{d\varepsilon_{ij}} \tag{2.5}$$

The relation (2.5) holds provided the following condition is satisfied:

$$\frac{1}{V}\int_{\partial V} \boldsymbol{\sigma}':\mathbf{D}'\,dV = 0 \tag{2.6}$$

On account of the Green–Gauss theorem, Eq. (2.6) becomes

$$\frac{1}{V}\int_{\partial V} \sigma'_{ij}d\varepsilon'_{ij}dV = 0 \Leftrightarrow \int_{\partial B_\delta} (t_i - \overline{\sigma_{ij}}n_j)(du_i - \overline{d\varepsilon_{ij}}x_j)dS = 0, \quad \forall\, x \in \partial B_\delta \tag{2.7}$$

Equation (2.7) suggests three types of boundary conditions that satisfy Eq. (2.5):

(i) uniform displacement (Dirichlet): $du_i = \overline{d\varepsilon_{ij}}x_j$ (2.8*a*)

(ii) uniform traction (Neumann): $t_i = \overline{\sigma_{ij}}n_j$ (2.8*b*)

(iii) mixed orthogonal: $(t_i - \overline{\sigma_{ij}}n_j)(du_i - \overline{d\varepsilon_{ij}}x_j) = 0$ (2.8*c*)

By increasing the window size (effectively, the number of grains in $\mathbf{B}_\delta$) and by setting up stochastic boundary value problems with the above boundary conditions, upon ensemble averaging, one obtains bounds on the constitutive response of the aggregate.

Statistical Homogeneity and Ergodicity. The methodology outlined works provided the hypotheses of spatial homogeneity and ergodicity hold for any spatial material random field $\boldsymbol{\Theta}(x,\omega)$. A random field is called *strict-sense stationary* (SSS) if all n-order distributions F_n are invariant with respect to arbitrary shifts x' for all $x'_i s$ [11,13]

$$F_n(\theta_1,\theta_2,\ldots,\theta_n;x_1,x_2,\ldots,x_n) = F_n(\theta_1,\theta_2,\ldots,\theta_n;x_1+x',x_2+x',\ldots,x_n+x') \tag{2.9a}$$

In a *wide-sense stationary* (WSS) random field, the mean is constant and its finite-valued autocorrelation only depends on the shift $h=x_2-x_1$ [11,13]

$$\langle\Theta(x_1)\rangle = \mu$$
$$\langle\Theta(x_1)\langle\Theta(x_1)\Theta(x_1+h)\rangle\rangle = R_\Theta(h) < \infty \tag{2.9b}$$

As is well known, Eq. (2.9*b*) is a weaker requirement than Eq. (2.9*a*), but it is sufficient for the proposed scale-dependent homogenization. The approach to obtain scale-dependent bounds for inelastic polycrystalline aggregates is illustrated in Fig. 1. Note that the response is realization dependent at microscales.

The random field $\boldsymbol{\Theta}(x,\omega)$ is *mean ergodic* if its spatial average equals the ensemble average [11,13]

$$\frac{1}{V}\int_v \boldsymbol{\Theta}(x,\omega)dV = \overline{\boldsymbol{\Theta}(\omega)} = \langle\boldsymbol{\Theta}(x)\rangle = \int_\Omega \boldsymbol{\Theta}(x,\omega)dP \tag{2.9c}$$

2.2 Basic Relations of Thermodynamics With Internal Variables. Ziegler [14] presented a broad methodology through which constitutive responses of a wide range of elastic-inelastic materials could be obtained by an appropriate choice of two potentials—the dissipation potential and the free energy (or their Legendre transforms)—consistent with the energy balance and the second law of thermodynamics. One such choice for the dissipation potential is shown in Fig. 2. A similar quartet can be set up for the quasiconservative potential.

Let $\boldsymbol{\varepsilon}$, $\boldsymbol{\alpha}$, and T represent the strain, the internal variable, and the temperature—these are the state variables. Note that in Fig. 2, the dependence on $\boldsymbol{\alpha}$ has been ignored for simplicity. Thus, we have four possible potentials to choose from. If the $\boldsymbol{\alpha}$-dependence is retained, we have eight possible potentials to work with. Let the Helmholtz energy $\psi(\boldsymbol{\varepsilon},\boldsymbol{\alpha},T)$ be a homogeneous function of degree a, such that

$$\psi(k_1\boldsymbol{\varepsilon},k_1\boldsymbol{\alpha},k_1T) = k_1^a\psi(\boldsymbol{\varepsilon},\boldsymbol{\alpha},T) \tag{2.10}$$

Let the dissipation potential $\phi(\dot{\boldsymbol{\varepsilon}},\dot{\boldsymbol{\alpha}},T)$ be a homogeneous function of degree s,

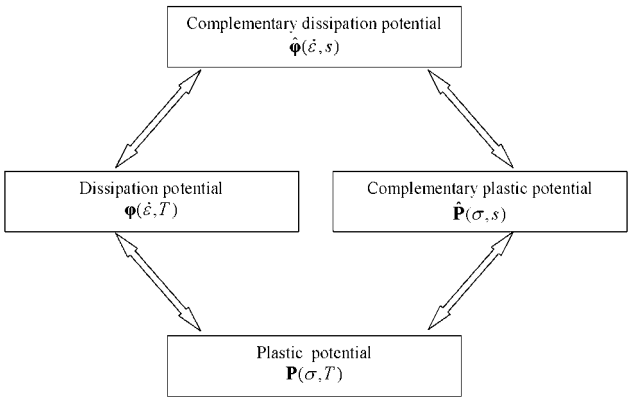

Fig. 2 Quartet for the selection of dissipation potential (at macroscale)

$$\phi(k_2\dot{\boldsymbol{\varepsilon}},k_2\dot{\boldsymbol{\alpha}},k_2T)=k_2^s\phi(\dot{\boldsymbol{\varepsilon}},\dot{\boldsymbol{\alpha}},T) \tag{2.11}$$

Thus, by applying Euler's theorem, we set up the microscale (single crystal) free energy and dissipation potentials

$$\psi(\boldsymbol{\varepsilon},\boldsymbol{\alpha},T)=\frac{1}{a}\left[\boldsymbol{\sigma}^{(q)}:\boldsymbol{\varepsilon}+\boldsymbol{\beta}^{(q)}:\boldsymbol{\alpha}+\frac{\partial\psi}{\partial T}:T\right] \tag{2.12a}$$

$$\phi(\dot{\boldsymbol{\varepsilon}},\dot{\boldsymbol{\alpha}},T)=\frac{1}{s}\left[\boldsymbol{\sigma}^{(d)}:\dot{\boldsymbol{\varepsilon}}+\boldsymbol{\beta}^{(d)}:\dot{\boldsymbol{\alpha}}+\frac{\partial\phi}{\partial T}:T\right]\geq 0 \tag{2.12b}$$

The inequality $\phi\geqslant 0$ ensures that the second law of thermodynamics is satisfied. The microstresses (at the single crystal level) are defined as follows:

$$\boldsymbol{\sigma}^{(q)}=\frac{\partial\psi}{\partial\boldsymbol{\varepsilon}},\quad \boldsymbol{\beta}^{(q)}=\frac{\partial\psi}{\partial\boldsymbol{\alpha}},\quad \boldsymbol{\sigma}^{(d)}=\frac{\partial\phi}{\partial\dot{\boldsymbol{\varepsilon}}},\quad \boldsymbol{\beta}^{(d)}=\frac{\partial\phi}{\partial\dot{\boldsymbol{\alpha}}},\quad \boldsymbol{\beta}^{(q)}+\boldsymbol{\beta}^{(d)}=0 \tag{2.13}$$

$\boldsymbol{\sigma}^{(q)}$ represents the quasiconservative stress, $\boldsymbol{\beta}^{(q)}$ is the internal quasiconservative stress, $\boldsymbol{\sigma}^{(d)}$ is the dissipative stress, and $\boldsymbol{\beta}^{(d)}$ represents the internal dissipative stress. The total stress is the sum of its dissipative and quasiconservative parts

$$\boldsymbol{\sigma}=\boldsymbol{\sigma}^{(q)}+\boldsymbol{\sigma}^{(d)} \tag{2.14}$$

The volume averaging of the microscale potentials (dropping the explicit temperature dependence) gives

$$\boldsymbol{\psi}(\boldsymbol{\varepsilon},\omega)=\frac{1}{V}\left[\int_v(\boldsymbol{\sigma}^{(q)}:\boldsymbol{\varepsilon})dv+\int_v(\boldsymbol{\beta}^{(q)}:\boldsymbol{\alpha})dv\right] \tag{2.15}$$

$$\boldsymbol{\phi}(\dot{\boldsymbol{\varepsilon}},\omega)=\frac{1}{V}\left[\int_v(\boldsymbol{\sigma}^{(d)}:\dot{\boldsymbol{\varepsilon}})dv+\int_v(\boldsymbol{\beta}^{(d)}:\dot{\boldsymbol{\alpha}})dv\right] \tag{2.16}$$

For a viscoplastic material, the desired forms of macroscopic potentials $\boldsymbol{\psi}(\boldsymbol{\varepsilon})$ and $\boldsymbol{\phi}(\dot{\boldsymbol{\varepsilon}})$ are given by

$$\boldsymbol{\psi}=0,\quad \boldsymbol{\sigma}^{(q)}=0,\quad \boldsymbol{\beta}^{(q)}=0\Rightarrow\boldsymbol{\beta}^{(d)}=0[\because\boldsymbol{\beta}^{(d)}+\boldsymbol{\beta}^{(q)}=0] \tag{2.17}$$

$$\boldsymbol{\phi}(\dot{\boldsymbol{\varepsilon}},\omega)=\frac{1}{V}\left[\int_v(\boldsymbol{\sigma}^{(d)}:\dot{\boldsymbol{\varepsilon}})dv\right] \tag{2.18}$$

It follows from Eq. (2.17) that the viscoplastic material is a purely dissipative material.

2.3 Bounds on the Dissipation Function and Plastic Potential. Under proportional monotonic loading, a hardening material may be considered to be equivalent to a physically nonlinear elastic material. In such a case, one can use variational principles and establish hierarchy of bounds for the polycrystalline aggregates. Further details on the methodology can be found in Ref. [8]. Thus, upon ensemble averaging of Eq. (2.18), one obtains the following bounds for a viscoplastic material:

$$\langle\boldsymbol{\phi}(\dot{\boldsymbol{\varepsilon}})\rangle_\Delta\leq\langle\boldsymbol{\phi}(\dot{\boldsymbol{\varepsilon}})\rangle_\delta\leq\langle\boldsymbol{\phi}(\dot{\boldsymbol{\varepsilon}})\rangle_{\delta'}\leq\langle\boldsymbol{\phi}(\dot{\boldsymbol{\varepsilon}})\rangle_1\quad\text{for } 1\leq\delta'\leq\delta\leq\Delta \tag{2.19}$$

Also, the following expression holds for the aggregate:

$$\mathbf{P}(\boldsymbol{\sigma})+\boldsymbol{\phi}(\dot{\boldsymbol{\varepsilon}})=\boldsymbol{\sigma}:\dot{\boldsymbol{\varepsilon}} \tag{2.20}$$

Thus, if one sets up $\mathbf{P}(\boldsymbol{\sigma})$, then on mesoscale, it can be bounded as follows:

$$\langle\mathbf{P}(\boldsymbol{\sigma})\rangle_\Delta\geq\langle\mathbf{P}(\boldsymbol{\sigma})\rangle_\delta\geq\langle\mathbf{P}(\boldsymbol{\sigma})\rangle_{\delta'}\geq\langle\mathbf{P}(\boldsymbol{\sigma})\rangle_1\quad\text{for } 1\leq\delta'\leq\delta\leq\Delta \tag{2.21}$$

2.4 Special Case: Anisotropic Yielding. *Single crystals*. The anisotropic yield criterion for a single crystal in stress space is

$$F^c(\boldsymbol{\sigma}^c)=\boldsymbol{\Pi}^c_{ijkl}\boldsymbol{\sigma}^c_{ij}\boldsymbol{\sigma}^c_{kl}-1=f(\boldsymbol{\sigma}^c)-1=0 \tag{2.22}$$

The plastic part of the deformation rate tensor in a single crystal is

$$\mathbf{D}^{pc}_{ij}=\dot{\lambda}\frac{\partial F(\boldsymbol{\sigma}^c)}{\partial\boldsymbol{\sigma}^c_{ij}}=2\dot{\lambda}\boldsymbol{\Pi}^c_{ijkl}\boldsymbol{\sigma}^c_{kl} \tag{2.23a}$$

$$\mathbf{D}^{pc}_{ij}\boldsymbol{\sigma}^c_{ij}=2\dot{\lambda}\boldsymbol{\Pi}^c_{ijkl}\boldsymbol{\sigma}^c_{ij}\boldsymbol{\sigma}^c_{kl}>0 \tag{2.23b}$$

Here, $\boldsymbol{\Pi}^c_{ijkl}$ represents the positive definite fourth-order plastic modulus tensor with the following symmetries:

$$\boldsymbol{\Pi}^c_{ijkl}=\boldsymbol{\Pi}^c_{jikl}=\boldsymbol{\Pi}^c_{ijlk}=\boldsymbol{\Pi}^c_{klij} \tag{2.24}$$

Note that $\boldsymbol{\Pi}^c_{ijkl}$ has 21 (respectively, 6) independent components in the most general 3D (2D) anisotropic case. The incompressibility assumption further reduces the number of independent constants ($\boldsymbol{\Pi}^c_{ijkk}=0$). Note that Hill's orthotropic yield criteria and the von Mises isotropic yield criteria are the special forms of Eq. (2.22).

The anisotropic yield criterion for a single crystal in the velocity (plastic deformation rate) space is given by

$$\Phi(\mathbf{D}^{pc})=\boldsymbol{\Lambda}_{ijkl}\mathbf{D}^{pc}_{ij}\mathbf{D}^{pc}_{kl}-1=\phi(\mathbf{D}^{pc})-1=0 \tag{2.25}$$

The stress is thus given as follows:

$$\boldsymbol{\sigma}^c_{ij}=\dot{\gamma}\frac{\partial F(\boldsymbol{\sigma}^c)}{\partial\mathbf{D}^{pc}_{ij}}=2\dot{\gamma}\boldsymbol{\Lambda}^c_{ijkl}\mathbf{D}^{pc}_{kl} \tag{2.26a}$$

$$\mathbf{D}^{pc}_{ij}\boldsymbol{\sigma}^c_{ij}=2\dot{\gamma}\boldsymbol{\Lambda}^c_{ijkl}\mathbf{D}^{pc}_{ij}\mathbf{D}^{pc}_{kl}>0 \tag{2.26b}$$

where $\boldsymbol{\Lambda}_{ijkl}$ represents positive definite fourth-order plastic modulus tensor with the following symmetries:

$$\boldsymbol{\Lambda}^c_{ijkl}=\boldsymbol{\Lambda}^c_{jikl}=\boldsymbol{\Lambda}^c_{ijlk}=\boldsymbol{\Lambda}^c_{klij} \tag{2.27}$$

$\boldsymbol{\Lambda}^c_{ijkl}$ has 21 (respectively, 6) independent components in the most general 3D (2D) anisotropic case. The incompressibility assumption further reduces the number of independent constants ($\boldsymbol{\Lambda}^c_{ijkk}=0$).

Polycrystalline aggregates. Depending on the orientation of any individual crystal, the plastic modulus and compliance tensors may be computed as follows:

$$\begin{aligned}\boldsymbol{\Pi}^{c(i)}_{ijkl}&=\mathbf{R}^{(i)}_{ip}\mathbf{R}^{(i)}_{jq}\mathbf{R}^{(i)}_{kr}\mathbf{R}^{(i)}_{ls}\boldsymbol{\Pi}^{\text{ref}}_{pqrs},\\ \boldsymbol{\Lambda}^{c(i)}_{ijkl}&=\mathbf{R}^{(i)}_{ip}\mathbf{R}^{(i)}_{jq}\mathbf{R}^{(i)}_{kr}\mathbf{R}^{(i)}_{ls}\boldsymbol{\Lambda}^{\text{ref}}_{pqrs},\quad \mathbf{R}^{(i)}_{ij}\mathbf{R}^{(i)}_{jq}=\boldsymbol{\delta}^{(i)}_{iq}\end{aligned} \tag{2.28}$$

In Eq. (2.28), $\mathbf{R}^{(i)}$ is the rotation tensor associated with the ith crystal. Following the methodology of Ref. [15] and observing the quadratic form in Eq. (2.25), one can set up the Dirichlet bound-

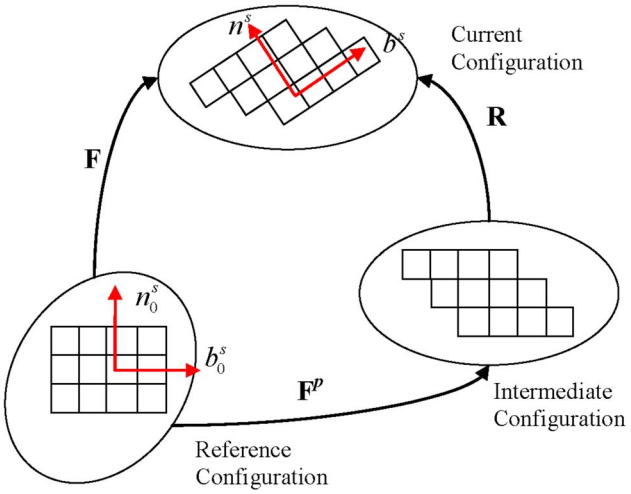

Fig. 3 The multiplicative decomposition

Table 1 Material parameters

$\dot{\varepsilon}$	1.0 s^{-1}	u	2
T	573 K	$g_{0\varepsilon}$	1.6
n	5	$\dot{\varepsilon}_0$	1.0*E*7 s^{-1}
μ_0	28,815 MPa	$\dot{\varepsilon}_{0es}$	1.0*E*7 s^{-1}
D_0	3440 MPa	$\hat{\tau}_{0es}$	665.3 MPa
T_0	215 K	g_{0es}	0.1058
k/b^3	0.5899 MPa/K	p_ε	2/3
θ_0	800 MPa	q_ε	1
τ_a	3.333 MPa	g_{0i}	1.196
$\hat{\tau}_i/\mu_0$	0.0034383	p_i	1/2
$\dot{\varepsilon}_{0i}$	1.0*E*7 s^{-1}	q_i	1.5

ary value problem and postulate the following hierarchy of bounds for the aggregate:

$$\langle \mathbf{\Lambda}^d_\infty \rangle \leqslant \cdots \leqslant \langle \mathbf{\Lambda}^d_\delta \rangle \leqslant \langle \mathbf{\Lambda}^d_{\delta\prime} \rangle \leqslant \cdots \leqslant \langle \mathbf{\Lambda}^d_1 \rangle, \quad \delta' < \delta \tag{2.29}$$

Similarly, by setting up the Neumann boundary value problem, one can postulate the following hierarchy of bounds for the aggregate:

$$\langle \mathbf{\Pi}^t_\infty \rangle \leqslant \cdots \leqslant \langle \mathbf{\Pi}^t_\delta \rangle \leqslant \langle \mathbf{\Pi}^t_{\delta\prime} \rangle \leqslant \cdots \leqslant \langle \mathbf{\Pi}^t_1 \rangle, \quad \delta' < \delta \tag{2.30}$$

Thus, we obtain the following hierarchy of bounds for the polycrystalline aggregate with anisotropic yield criteria:

$$\langle \mathbf{\Pi}^t_1 \rangle^{-1} \leqslant \cdots \leqslant \langle \mathbf{\Pi}^t_{\delta\prime} \rangle^{-1} \leqslant \langle \mathbf{\Pi}^t_\delta \rangle^{-1} \leqslant \cdots \leqslant \mathbf{\Lambda}^{\text{eff}} \leqslant \cdots \leqslant \langle \mathbf{\Lambda}^d_\delta \rangle \leqslant \langle \mathbf{\Lambda}^d_{\delta\prime} \rangle \leqslant \cdots \leqslant \langle \mathbf{\Lambda}^d_1 \rangle, \quad \delta' < \delta \tag{2.31}$$

2.5 Crystal Plasticity Model. The responses of a single crystal with a given orientation under Sachs and Taylor hypotheses are identical—this will be demonstrated in the subsequent section. This is due to the fact that a single crystal is homogeneous although anisotropic. In general, it is more efficient to obtain results using the Sachs hypothesis since it is numerically much faster than the Taylor based model. Furthermore, by introducing the orientation dependence, two stochastic boundary value problems (Dirichlet and Neumann) on polycrystalline aggregates can be set up in order to get tighter bounds (compared to the upper or lower bound estimates) on the aggregate response.

The kinematics of the deformation is illustrated in Fig. 3. By neglecting elastic effects, the deformation gradient can be expressed as

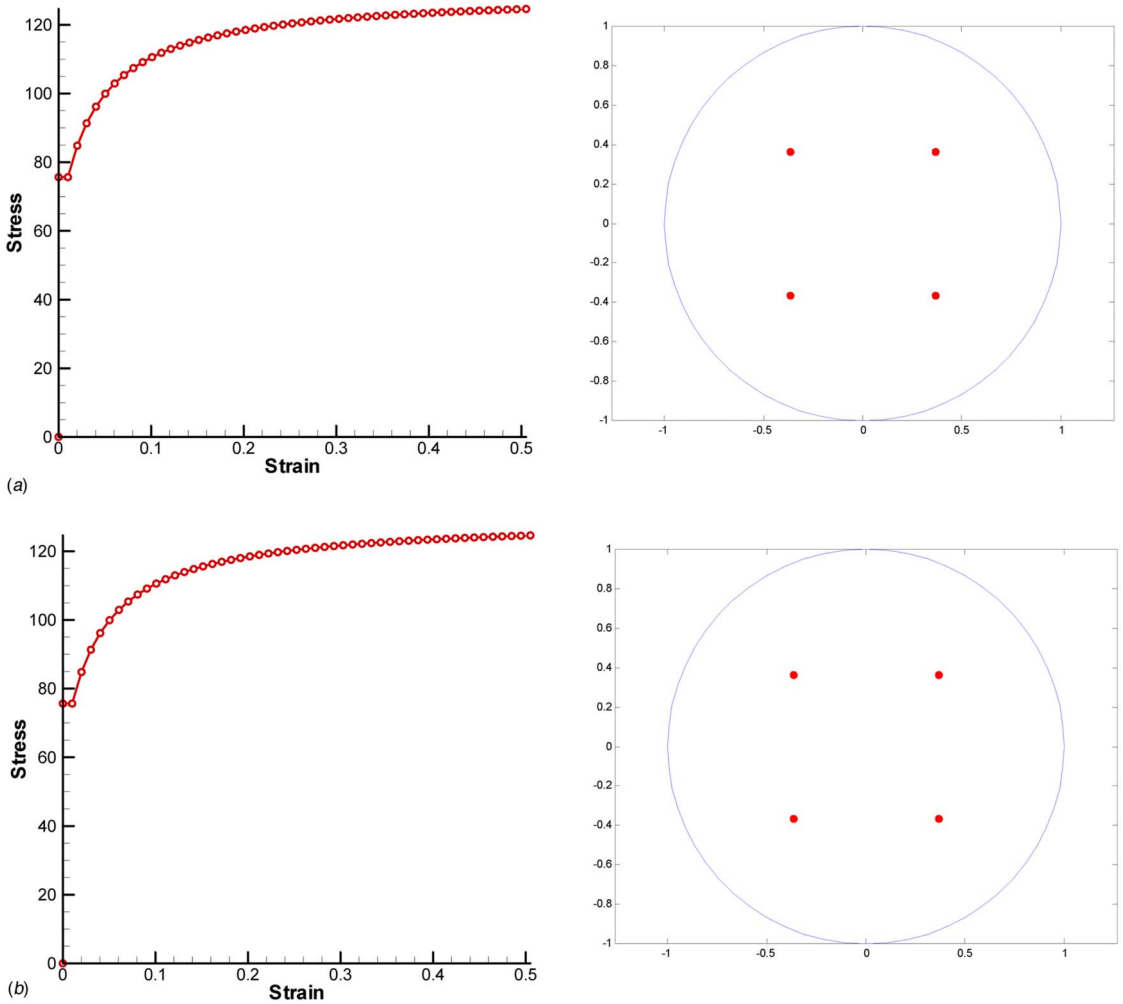

Fig. 4 Single crystal compression test: *L*11=*L*22=0.5, *L*33=−1, *L*12=*L*13=*L*21=*L*23=*L*31=*L*32=0: (*a*) Sachs type and (*b*) Taylor type

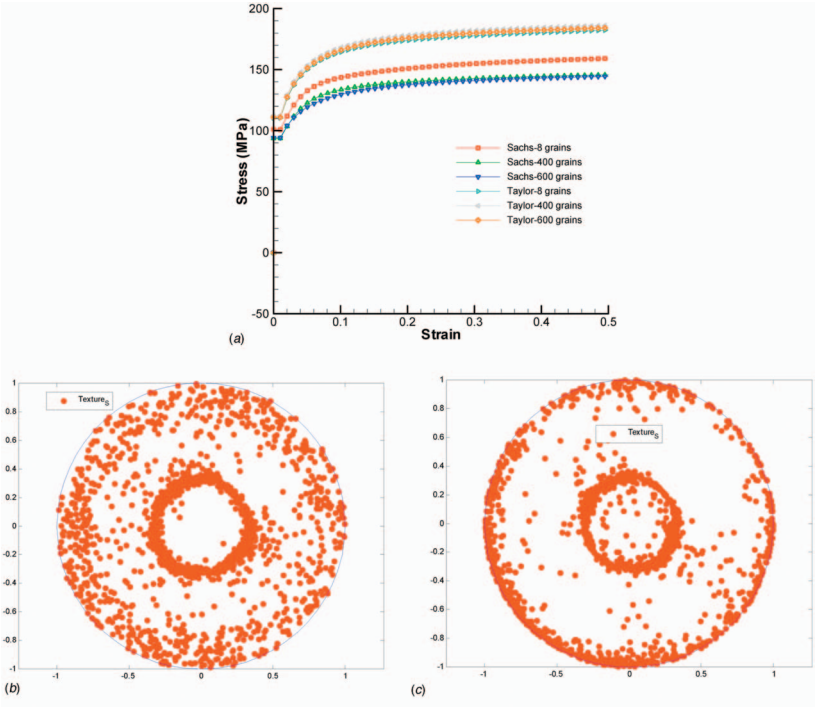

Fig. 5 (*a*) **The polycrystal compression test:** $L11=L22=0.5$, $L33=-1$, $L12=L13=L21=L23=L31=L32=0$, (*b*) **texture-Taylor type, and** (*c*) **texture-Sachs type**

$$\mathbf{F} = \mathbf{R}\mathbf{F}^p, \quad \det(\mathbf{R}) = 1 \tag{2.32}$$

where $\mathbf{R}$ represents an orthogonal tensor and $\mathbf{F}^p$ is the plastic part of the deformation gradient. We assume the elastic part of the deformation to be negligible in this viscoplastic formulation. The velocity gradient is given by

$$\mathbf{L} = \dot{\mathbf{F}}\mathbf{F}^{-1} = \dot{\mathbf{R}}\mathbf{R}^T + \mathbf{R}\dot{\mathbf{F}}^p\mathbf{F}^{p^{-1}}\mathbf{R}^T = \dot{\mathbf{R}}\mathbf{R}^T + \mathbf{R}\mathbf{L}^p\mathbf{R}^T \tag{2.33}$$

The Schmidt tensor in the reference configuration is given as

$$\mathbf{S}_0^s = \mathbf{b}_0^s \otimes \mathbf{n}_0^s \tag{2.34}$$

The velocity gradient is decomposed into its symmetric ($\mathbf{D}$) and skew parts ($\mathbf{W}$),

$$\mathbf{L} = \mathbf{D} + \mathbf{W}, \quad \mathbf{D} = \mathbf{R}\left(\sum_s \dot{\gamma}^{(s)}\mathbf{m}_0^s\right)\mathbf{R}^T,$$
$$\mathbf{W} = \dot{\mathbf{R}}\mathbf{R}^T + \mathbf{R}\left(\sum_s \dot{\gamma}^{(s)}\mathbf{q}_0^s\right)\mathbf{R}^T \tag{2.35}$$

$\dot{\gamma}^{(s)}$ is the shear rate of the slip system s. $\mathbf{m}_0^s$ and $\mathbf{q}_0^s$ are the symmetric and skew parts of the Schmidt tensor in the reference configuration. The lattice rotation evolution equation is given by

$$\dot{\mathbf{R}} = \mathbf{W}\mathbf{R} + \mathbf{R}\mathbf{A}, \quad \mathbf{A} = -\sum_s \dot{\gamma}^{(s)}\mathbf{q}_0^s \tag{2.36}$$

The mechanical threshold strength (MTS) model [16] will be used to obtain the single crystal response. The model is used to describe the constitutive relation between the slip system shear rate $\dot{\gamma}^s$ and the traction component acting on the slip plane in the slip direction τ^s,

$$\tau^s = \boldsymbol{\sigma}' : (\mathbf{R}\mathbf{m}_0^s\mathbf{R}^T) \tag{2.37a}$$

$$\dot{\gamma}^s = \dot{\varepsilon}\left|\frac{\tau^s}{\tau_0^s}\right|^n \mathrm{sgn}(\tau^s), \quad \dot{\varepsilon} = \sqrt{\frac{2}{3}\mathbf{D}:\mathbf{D}} \tag{2.37b}$$

By using Eqs. (2.35), (2.37*a*), and (2.37*b*), one obtains the following quasilinear relationship between the rate of deformation tensor and the Cauchy stress tensor $\boldsymbol{\sigma}$:

$$\mathbf{D} = \mathfrak{I}\boldsymbol{\sigma}' \tag{2.38}$$

Here, $\mathfrak{I}$ is the fourth-order fluidity tensor defined as follows:

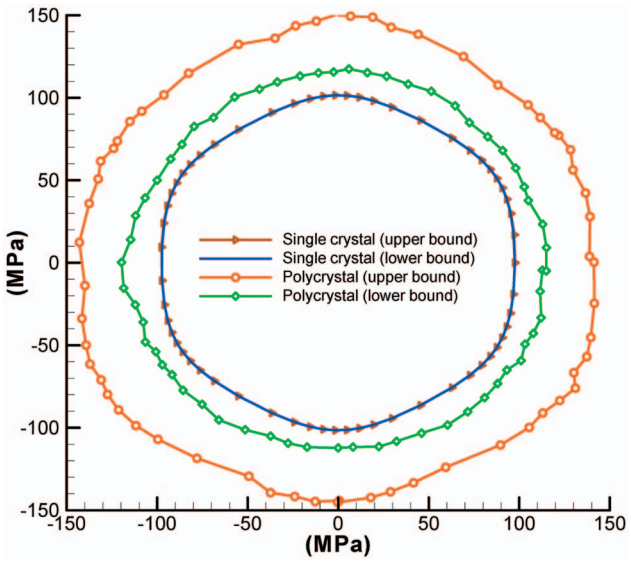

Fig. 6 Single crystal and the polycrystalline aggregate yield surfaces at a strain of 0.5 (in the "π-plane")

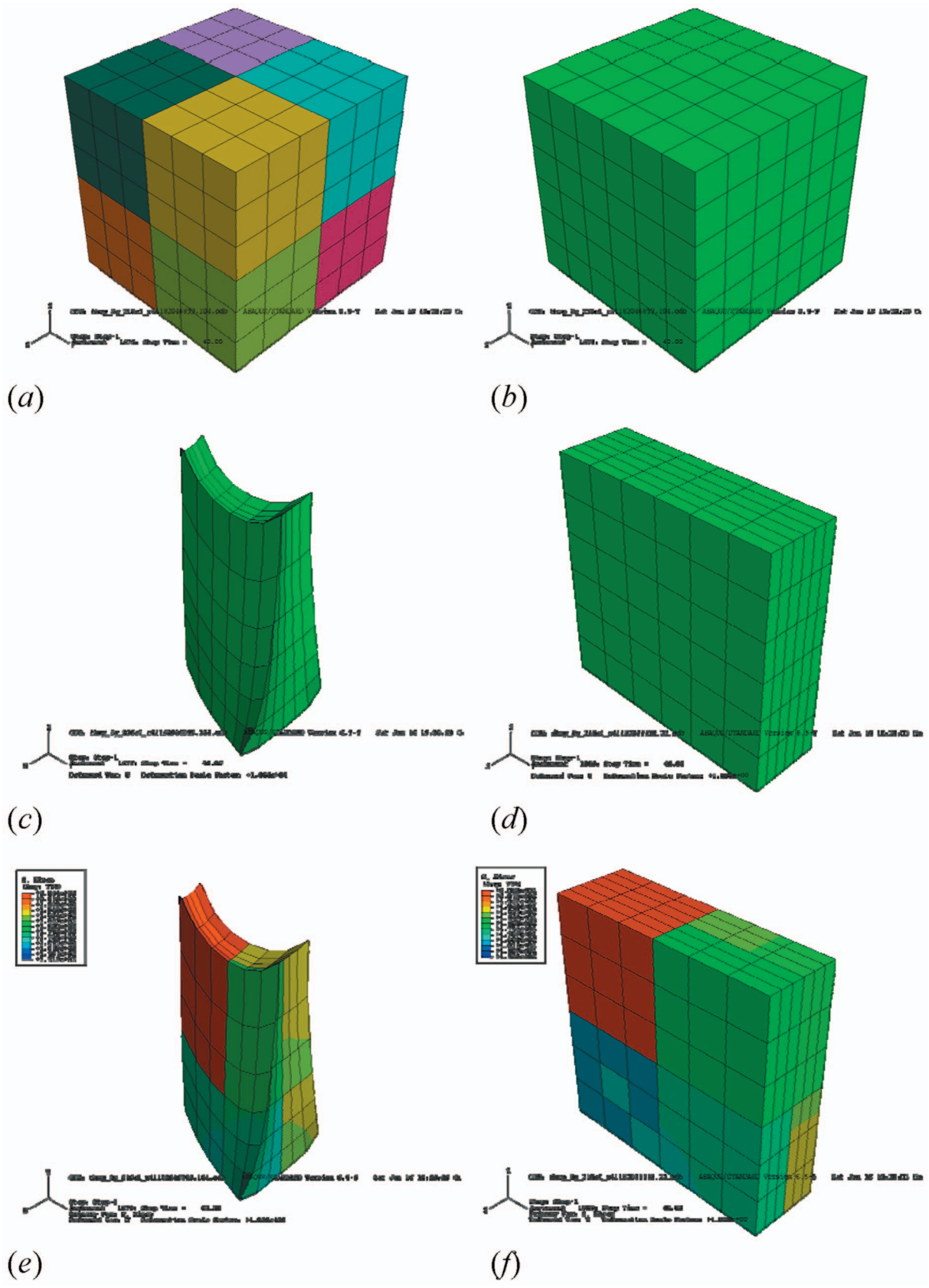

Fig. 7 (*a*) **Geometry of eight grains,** (*b*) **mesh,** (*c*) **deformed view-Neumann problem,** (*d*) **deformed view-Dirichlet problem,** (*e*) **von Mises stress-Neumann problem, and** (*f*) **von Mises stress-Dirichlet problem**

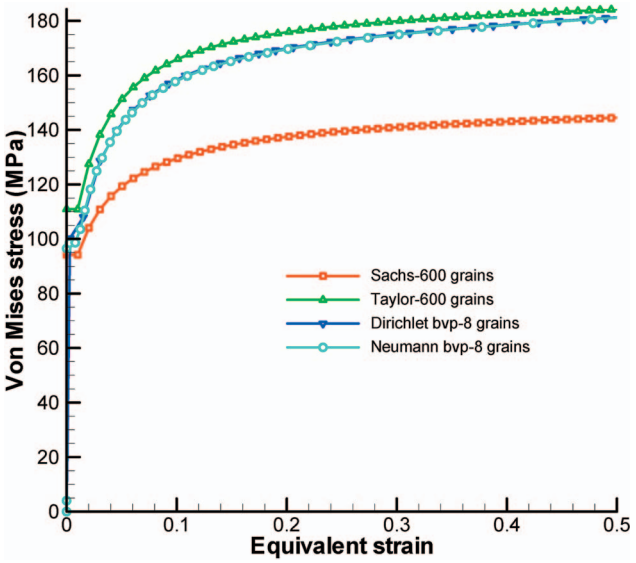

Fig. 8 Bounds on the aggregate response

$$\mathfrak{I} = \sum \frac{\dot{\varepsilon}}{\dot{\tau}_0^s} \left| \frac{\tilde{\tau}^s}{\tau_0^s} \right|^{n-1} (\mathbf{R}\mathbf{m}_0^s\mathbf{R}^T) \otimes (\mathbf{R}\mathbf{m}_0^s\mathbf{R}^T) \tag{2.39}$$

and τ_0^s is the slip system flow stress at the reference shear rate, which in a simplified form is given by [17]

$$\tau_0^s = \tau_a + \frac{\mu}{\mu_0} S_i(\dot{\varepsilon}, T)\hat{\tau}_i + \frac{\mu}{\mu_0} S_\varepsilon(\dot{\varepsilon}, T)\hat{\tau}_\varepsilon \tag{2.40a}$$

$$S_i(\dot{\varepsilon}, T) = \left[1 - \left[\frac{kT}{\mu b^3 g_{0i}} \ln\left(\frac{\dot{\varepsilon}_0}{\dot{\varepsilon}} \right) \right]^{1/q_i} \right]^{1/p_i}$$

$$S_\varepsilon(\dot{\varepsilon}, T) = \left[1 - \left[\frac{kT}{\mu b^3 g_{0\varepsilon}} \ln\left(\frac{\dot{\varepsilon}_0}{\dot{\varepsilon}} \right) \right]^{1/q_\varepsilon} \right]^{1/p_\varepsilon} \tag{2.40b}$$

In the above, k is the Boltzmann constant, b is the magnitude of Burgers vector, g_0 is the normalized activation energy, $\dot{\varepsilon}_0$ is a constant, and p_i, q_i, p_ε, and q_ε are statistical constants. Also, μ is the shear modulus, whose temperature dependence is given as [18]

$$\mu = \mu_0 - \frac{D_0}{\exp\left(\frac{T_0}{T} \right) - 1} \tag{2.41}$$

while $\hat{\tau}_\varepsilon$ accounts for the interaction of the mobile dislocations with the forest dislocation structure. Henceforth, the following equation is used to obtain the evolution of $\hat{\tau}_\varepsilon$:

$$\dot{\hat{\tau}}_\varepsilon = \theta_0 \left(1 - \frac{\hat{\tau}_\varepsilon}{\hat{\tau}_{\varepsilon s}} \right)^u \sum_s |\dot{\gamma}^{(s)}| \tag{2.42}$$

where $\hat{\tau}_{\varepsilon s}$ is the saturation threshold stress dependent on the temperature and the strain rate [19]

$$\ln \frac{\dot{\varepsilon}}{\dot{\varepsilon}_{0\varepsilon s}} = \frac{\mu b^3 g_{0\varepsilon s}}{kT} \ln \frac{\hat{\tau}_{\varepsilon s}}{\hat{\tau}_{\varepsilon s 0}} \tag{2.43}$$

with $\dot{\varepsilon}_{0\varepsilon s}$, $g_{0\varepsilon s}$, and $\hat{\tau}_{\varepsilon s 0}$ being empirically obtained constants.

2.6 Algorithm for Constitutive Response via Sachs Hypothesis. As previously mentioned, every single crystal is homogeneous and hence it really does not matter whether one drives the problem via uniform stress or uniform deformation rate. The algorithm is as follows:

- define the normal and the Burgers vectors
- obtain the Schmidt tensor $\mathbf{S}_0^s$ as the dyadic product of the normal and the Burgers vector, Find its symmetric ($\mathbf{m}_0^s$) and skew parts ($\mathbf{q}_0^s$), and represent these tensors in a vectorial form
- impose the velocity gradient $\mathbf{L}=\mathbf{D}+\mathbf{W}$
- compute the time step for explicit integration scheme based on the value of the total strain
- read the initial orientation of the crystals and guess the starting value of stress
- obtain the vector forms of $\boldsymbol{\sigma}$ and $\mathbf{D}$
- transform $\boldsymbol{\sigma}$ and $\mathbf{D}$ relationship to the laboratory configuration by rotating the Schmidt tensor from the crystal to the laboratory frame
- invoke the Newton algorithm in the laboratory frame to solve for the stress vector based on the quasilinear constitutive relationship between the stress and $\mathbf{D}$; such an estimate of stress satisfies equilibrium; the value of $\mathbf{D}$ is thus the average value of all individual crystals
- convert the stress vector to a tensorial form and rotate the stress in the laboratory frame back to the crystal frame
- update the resolved shear stress values by contracting the Schmidt tensor with the stress tensor
- update the shear rates based on the power law relationship connecting the rates and the resolved shear stresses
- use the exponential map to find the incremental change in the rotation tensor $d\mathbf{R}$ and update the orientation matrix for each crystal by using $d\mathbf{R}$ and $\mathbf{R}(t)$ to obtain $\mathbf{R}(t+dt)$
- invoke the pole figure subroutine and plot the pole figures
- repeat the above steps for other time steps until the total effective strain value is reached

3 Bounds on the Response of Polycrystalline Aggregates

3.1 Single-Phase Materials. In this section, we numerically demonstrate that the response of the single crystal is identical irrespective of the method in which the problem is driven. It is also shown that for polycrystalline aggregates, there can be large differences in the predicted response depending on the manner in which the problem is driven. This is our motivation to set up stochastic boundary value problems satisfying the Hill condition so as to obtain a response of the aggregate that is independent of the boundary conditions and the manner in which the problem is driven. Such a methodology also gives us an estimate of the number of grains necessary to homogenize the response of inelastic polycrystalline aggregates.

Sachs and Taylor bounds. The parameters for the numerical simulation of the compression test are given in Table 1. Figures 4(*a*) and 4(*b*) show that a single crystal's response, with any given orientation, does not depend on how the problem is driven.

Now, consider the response of the aggregate. The initial orientations (in terms of the rotation tensor) for individual crystals have been chosen to be uniformly distributed by using the algorithm after Shoemake [20]. In the case of polycrystalline aggregates, the response inherently depends on the manner in which one drives the problem and the number of grains in the aggregate, Fig. 5(*a*). Even the texture differently evolves, see Figs. 5(*b*) and 5(*c*).

Note that Fig. 5 represents the upper and lower bounds for one particular realization of the aggregate. In principle, one must find the ensemble average based on a number of realizations to reduce the scatter. In general, with a higher number of grains, one obtains less scatter in the predicted response and vice versa.

The yield surfaces for a single crystal driven by Taylor's or Sachs hypothesis are identical (Fig. 6). For polycrystalline aggregates, the yield surface obtained using Sachs hypothesis is enclosed within the one obtained using Taylor's hypothesis (Fig. 6). One is interested in finding the effective response of the aggre-

gate, which depends on the number of grains or the size of the RVE. In general, the effective response and the effective yield surface lies somewhere in between the Sachs and the Taylor estimates.

Scale-dependent bounds. In this section, we compute Dirichlet-type and Neumann-type bounds on the aggregate response, recall Sec. 2.1. In the process, we also determine the number of grains needed to homogenize the aggregate response. To demonstrate the concept, we assume the grains to be piecewise homogeneous and isotropic. The following loading conditions have been imposed to drive the stochastic boundary value problems:
In Neumann problem,

$$\overline{\sigma_{11}} = \overline{\sigma_{22}} = 300 \text{ MPa}, \quad \overline{\sigma_{33}} = -600 \text{ MPa}, \quad \overline{\sigma_{12}} = \overline{\sigma_{13}} = \overline{\sigma_{23}} = 0$$

In Dirichlet problem,

$$\overline{\varepsilon_{11}} = \overline{\varepsilon_{22}} = 0.3, \quad \overline{\varepsilon_{33}} = -0.6, \quad \overline{\varepsilon_{12}} = \overline{\varepsilon_{13}} = \overline{\varepsilon_{23}} = 0$$

Based on the results of a mesh sensitivity analysis on an eight grain aggregate, we decided to mesh each grain with 27 brick elements with reduced integration to accurately capture the grains' deformation. The response of one particular realization of an aggregate with eight grains is shown in Fig. 7. For simplicity and to demonstrate the concept, cubical grains are used, Fig. 7(*a*). The entire approach can be easily generalized to other grains of geometrically disordered tessellations. The undeformed mesh is shown in Fig. 7(*b*). Figures 7(*c*) and 7(*d*) show the deformed mesh for the traction controlled and the displacement controlled problems, respectively. Unlike the displacement controlled problems, traction controlled problems can cause numerical difficulties due to uncontrolled deformation of the mesh. Figures 7(*e*) and 7(*f*) show the von Mises stress contour on the deformed mesh.

The above boundary value problems are then solved for many realizations, and upon ensemble averaging, we obtain tighter bounds on the aggregate response, as shown in Fig. 8. As expected, the overall behavior of the aggregate lies in between the Taylor and the Sachs bounds. It appears that for the aggregate under consideration, eight grains are sufficient to produce a response, which is almost independent of the applied boundary conditions, and this gives the RVE size. Also, note that the effective response is closer to the upper bound (Taylor) response, although it is distinct.

3.2 Multiphase Materials. Consider an aggregate having two

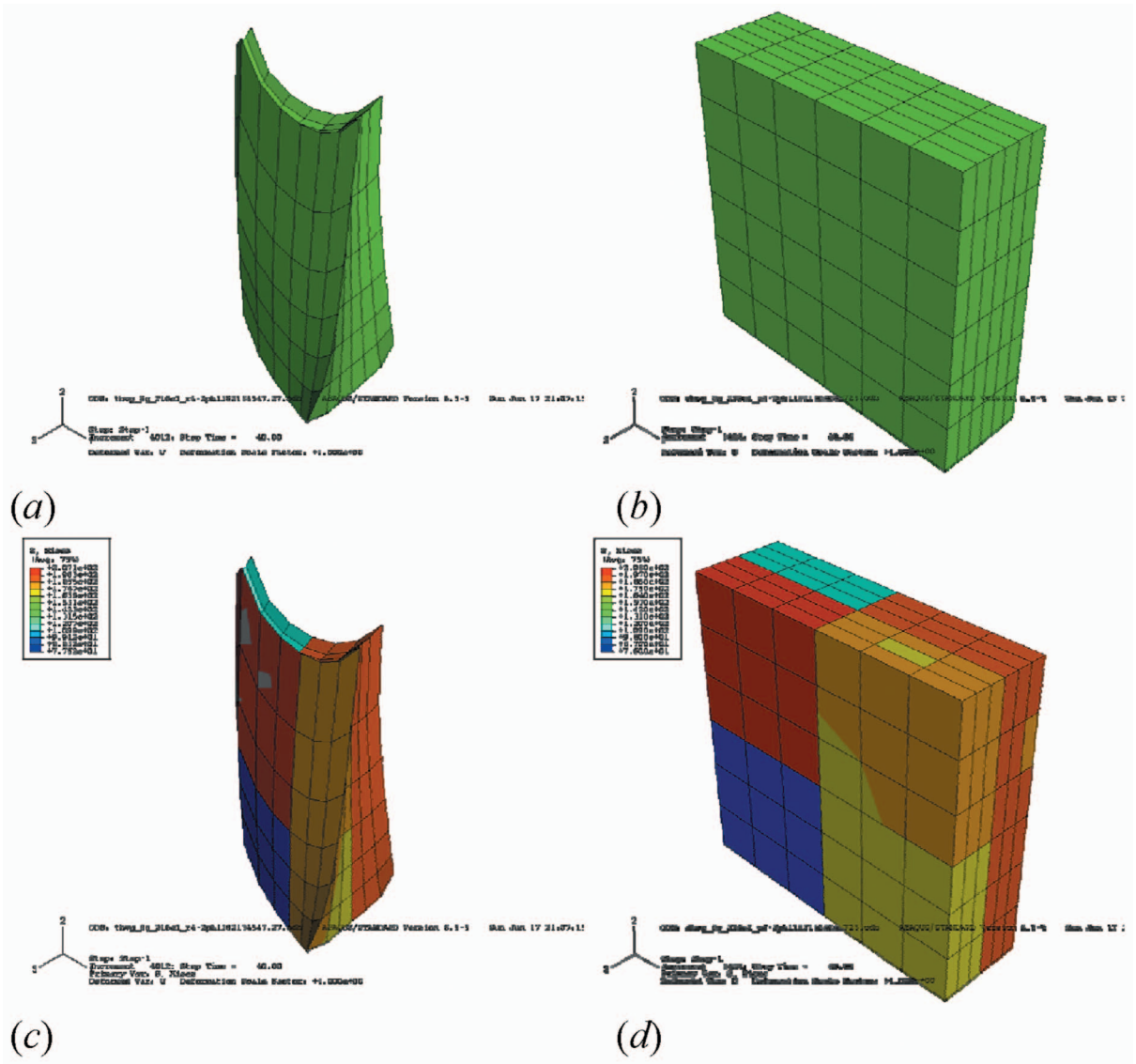

Fig. 9 (*a*) **Deformed view in the Neumann problem (two-phase material), (*b*) deformed view in the Dirichlet problem (two-phase material), (*c*) the von Mises stress in the Neumann problem, and (*d*) the von Mises stress in the Dirichlet problem**

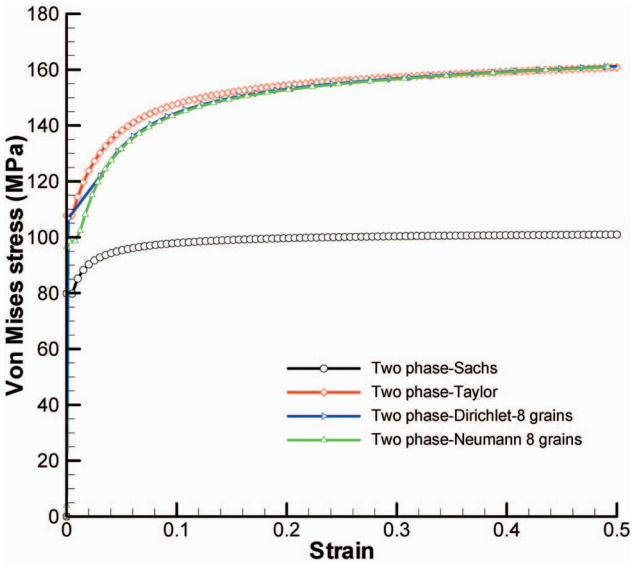

Fig. 10 Bounds on the multiphase aggregate response

distinct phases, a hard phase with a volume fraction of 0.75 and a soft phase with a volume fraction of 0.25. The hard phase material is chosen to be the same as the one discussed in the previous section. The soft material is chosen to be rigid/perfectly plastic. The response of the two-phase aggregate for one particular realization is illustrated in Fig. 9.

Figure 10 illustrates the bounds on the aggregate response after ensemble averaging. As expected, the overall response is much softer due to the presence of the soft phase. It is interesting to note that the Sachs estimate shows almost no hardening and behaves almost as a rigid perfectly-plastic material. This is because the Sachs bound computes the harmonic mean of the tangent modulus of individual phases, which is dominated by the behavior of the soft phase. On the other hand, the Taylor estimate and the predictions obtained by setting up the boundary conditions almost overlap. Even for this particular two-phase aggregate, one obtains a response virtually independent of the boundary conditions. Thus, the RVE is attained with just eight grains.

4 Conclusions

A scale-dependent homogenization has been developed to determine the size of the RVE for inelastic polycrystalline aggregates, given the statistics of geometric and physical properties. It has been demonstrated on this basis that neither the Taylor model nor the Sachs model gives the correct estimate of the aggregate response, but a method based on uniform Dirichlet and Neumann boundary value problems stemming from the Hill condition is recommended. The proposed methodology is very general and advantageous relative to other homogenization and bounding methods.

It turns out that the RVE comprises about eight crystals for both the single- and the multiphase systems, so that the RVE's length scale $\delta=2$. It is a straightforward matter to extend this methodology to other type of grains or geometrically disordered microstructures. A related investigation of scaling trends in elastic random polycrystals is carried out in Ref. [21]. Finally, based on the upper and lower bound models, it was observed that the evolution of texture depends on the manner in which the problem is driven. Given this observation, we end with a hypothesis that, by using our methodology, one can also obtain rigorous bounds on the evolution of texture in polycrystals.

Acknowledgment

The authors are thankful to Professor Armand Beaudoin and Daniel Tortorelli for useful discussions.

References

[1] Taylor, G. I., 1938, "Plastic Strain in Metals," J. Inst. Met., **62**, pp. 307–324.
[2] Sachs, G., 1928, "Zur Ableitung einer Fliessbedingung," Z. Ver. Deutsch. Ing., **72**, pp. 734–736.
[3] Canova, G. R., 1994, "Self-Consistent Methods: Application to the Prediction of the Deformation Texture of Polyphase Materials," Mater. Sci. Eng., A, **175**, pp. 37–42.
[4] Hill, R., 1965, "Continuum Micro-Mechanics of Elastoplastic Polycrystals," J. Mech. Phys. Solids, **13**, pp. 89–101.
[5] Hutchinson, J. W., 1970, "Elastic-Plastic Behaviour of Polycrystalline Metals and Composites," Proc. R. Soc. London, Ser. A, **319**, pp. 247–272.
[6] Tome, C. N., and Canova, G. R., 1998, "Self-Consistent Modeling of Heterogeneous Plasticity," *Texture and Anisotropy: Preferred Orientations in Polycrystals and Their Effect on Materials Properties*, U. F. Kocks, C. N. Tomé, and H.-R. Wenk, eds., Cambridge University Press, Cambridge, pp. 466–511.
[7] Maugin, G. A., 1992, *The Thermomechanics of Plasticity and Fracture*, Cambridge University Press, Cambridge, pp. 174–205.
[8] Jiang, M., Ostoja-Starzewski, M., and Jasiuk, I., 2001, "Scale-Dependent Bounds on Effective Elastoplastic Response of Random Composites," J. Mech. Phys. Solids, **49**, pp. 655–673.
[9] Li, W., and Ostoja-Starzewski, M., 2006, "Yield of Random Elasto-Plastic Materials," J. Mech. Mater. Struct., **1**, pp. 1055–1073.
[10] Ostoja-Starzewski, M., Du, X., Khisaeva, Z. F., and Li, W., 2007, "On the Size of Representative Volume Element in Elastic, Plastic, Thermoelastic, and Permeable Random Microstructures," Mater. Sci. Forum, **539–543**, pp. 201–206.
[11] Ostoja-Starzewski, M., 2007, *Microstructural Randomness and Scaling in Mechanics of Materials*, Chapman and Hall, London.
[12] Hazanov, S., 1998, "Hill Condition and Overall Properties of Composites," Arch. Appl. Mech., **68**, pp. 385–394.
[13] Ostoja-Starzewski, M., 2006, "Material Spatial Randomness—From Statistical to Representative Volume Element," Probab. Eng. Mech., **21**, pp. 112–132.
[14] Ziegler, H., 1983, *An Introduction to Thermomechanics*, North-Holland, Amsterdam.
[15] Ostoja-Starzewski, M., 2005, "Scale Effects in Plasticity of Random Media: Status and Challenges," Int. J. Plast., **21**, pp. 1119–1160.
[16] Kok, S., Beaudoin, A. J., and Tortorelli, D. A., 2002, "A Polycrystal Plasticity Model Based on the Mechanical Threshold," Int. J. Plast., **18**, pp. 715–741.
[17] Kocks, U. F., Argon, A. S., and Ashby, M. F., 1975, *Thermodynamics and Kinetics of Slip* (Progress in Materials Science Vol. 19) Pergamon, New York.
[18] Varshni, Y. P., 1970, "Temperature Dependence of the Elastic Constants," Phys. Rev. B, **2**, pp. 3952–3958.
[19] Chen, S. R., and Gray, G. T., 1996, "Constitutive Behaviour of Tantalum and Tantalum-Tungsten Alloys," Metall. Mater. Trans. A, **27A**, pp. 2994–3006.
[20] Shoemake, K., 1992, in *Uniform Random Rotations*, Graphics Gems Vol. III, D. Kirk, ed., Academic, London, pp. 124–132.
[21] Ranganathan, S. I., and Ostoja-Starzewski, M., 2008, "Scaling Function, Anisotropy and the Size of RVE in Elastic Random Polycrystals," J. Mech. Phys. Solids, to be published.

Effect of Fluctuations in the Brush Conformation on the Interaction Between Polymer Brushes in a Good Solvent

Yan Xing Shen

Jen Fin Lin[1]
e-mail: jflin@mail.ncku.edu.tw

Department of Mechanical Engineering,
National Cheng Kung University,
Tainan 701, Taiwan

*This study presents a novel approach for analyzing the interaction between two parallel surfaces grafted with polymer brushes in a good solvent. In the proposed approach, molecular dynamics simulations are performed to establish the mean brush height and the standard deviation of the brush height distribution for a given value of the surface separation. The corresponding probability density function (PDF) of the brush height is then determined and a statistical technique is applied to compute the corresponding interaction free energy per unit area of the grafted substrates. Finally, the Derjaguin approximation is employed to determine the corresponding value of the interaction force between the two surfaces. At relatively high surface grafting density as well as under low to moderate compressions of these two parallel plates, the interdigitation effect of the brushes is quite weak and is not considered in the present study. The results obtained for the interaction free energy and interaction force are compared with those derived using the Alexander and de Gennes (AdG) model [1977, "Adsorption of Chain Molecules With a Polar Head. A Scaling Approach," J. Phys. (Paris), **38**, pp. 983–989, 1985, "Films of Polymer-Solutions," C. R. Acad. Sci., **300**, pp. 839–843] and the Milner, Witten, and Cates (MWC) model [1988, "Theory of the Grafted Polymer Brush," Macromolecules, **21**, pp. 2610–2619], respectively. The value of the normalized interaction free energy computed using the present method is higher than that obtained from the AdG and MWC models at larger surface separations. However, the three sets of results are in good agreement particularly at smaller values of the surface separation. In addition, the results obtained by the current method for the interaction force are found to be in better agreement with the experimental data than those obtained using the AdG or MWC models. The enhanced performance of the proposed method is attributed primarily to the use of an adaptive non-Gaussian PDF of the brush height to model the effects of fluctuations in the brush conformation at different distances from the grafting plane.*
[DOI: 10.1115/1.2937155]

Keywords: polymer brush, probability density function, conformation fluctuations

1 Introduction

In a good solvent, polymers densely end grafted on a solid surface with no attractive interaction between polymers and the surface will stretch away from the surface, forming the so-called "polymer brush." Polymer brushes are a central model in many important problems of polymer science, and are relevant in colloid stabilization, adhesion, lubrication, tribology, and rheology. For all of these applications, the brush structure of the polymer chains is responsible for behavior. A key issue is the monomer density profile, i.e., the variation of the monomer density as a function of the distance from the grafting plane. The brush height and the segment density profile in a good solvent have been experimentally studied using neutron reflectometry [1–4]. Another significant property is the interaction between two plates grafted with polymer brushes, which has been directly measured by a surface force apparatus (SFA) [5–7] and an atomic force microscope (AFM) [8–10].

Alexander and de Gennes [11,12] adopted scaling arguments and assumed the monomer density to be constant throughout the brush, i.e., the step-function profile. This assumption is valid only for very dense brushes, where the chains are nearly completely extended. Milner et al. [13] used the self-consistent-field (SCF) model and demonstrated that the monomer density decreases parabolically from a finite value at the grafting plane to zero at the edge of the brush. Experimental results show that the step-function profile is not adequate to describe the inner structure of the brush and the tail of the experimental profile is smoother than the parabolic one [4]. Murat and Grest [14,15] performed molecular dynamics (MD) simulations based on a simple bead-spring model of the polymer chains to investigate the interaction characteristics of two parallel surfaces bearing end-grafted polymers. The results showed that the edge of the brush was characterized by an extended tail region in which the monomer density decayed smoothly toward zero [14]. Furthermore, a good agreement was observed between the simulation results obtained for the force-separation profile between the two opposing surfaces and that observed experimentally [15]. However, while MD simulation methods provide detailed insights into the properties of polymer brushes, appropriate scaling factors must be applied to the length and energy scales utilized in the simulations in order to enable a reliable comparison to be made between the simulation results and the corresponding experimental data. In practice, assigning appropriate scaling values is problematic since the lack of theoretical basis.

[1]Corresponding author.

Contributed by the Applied Mechanics Division for publication in the JOURNAL OF APPLIED MECHANICS. Manuscript received September 27, 2007; final manuscript received March 9, 2008; published online July 17, 2008. Review conducted by Krishna Garikipati.

The current study presents a hybrid approach comprising MD simulations and a statistical technique for analyzing the interaction between two parallel surfaces grafted with identical polymer brushes in a good solvent. The proposed method resolves the limitations of pure MD simulation schemes described above and provides a convenient and accurate means of establishing the interaction free energy and interaction force per unit area between the two parallel substrates. In the proposed approach, MD simulations are performed to establish the mean brush height and the standard deviation of the brush height distribution for discrete values of the surface separation. Having done so, the skewness and kurtosis parameters of the brush height distributions are derived such that the corresponding probability density functions (PDFs) of the brush height can be obtained. A statistical method is then applied to compute the corresponding interaction free energy per unit area of the grafted plates. Finally, the Derjaguin approximation [16] is employed to determine the corresponding values of the interaction force between the two plates. The results obtained by the current method for the interaction free energy are compared to those obtained from the Alexander and de Gennes (AdG) scaling model [11,12] and the Milner, Witten, and Cates (MWC) SCF model [13]. The discrepancies between the results obtained by the three models at various values of the surface separation are systematically evaluated and discussed. Finally, the validity of the proposed approach is confirmed by comparing the force-distance profiles obtained from the proposed scheme for PS-*X* polymer grafted on mica surfaces and immersed in toluene with the experimental results presented in the literature [6].

2 Theoretical Models

2.1 Free Energy of a Single Brush. Alexander [11] considered a chain with a polymerization degree, N, which has one end grafted at a surface with a mean spacing s between two adjacent grafting points. This chain extends out from the surface into the good solvent with a height L. For a high grafting density such that $s \ll R_F$ (R_F, the Flory radius), the grafted layer is in the semidilute region and is assumed to have an essentially uniform concentration density in the region far away from the surface. There are two components of the free energy at each chain. One is related to the osmotic repulsion among monomers [6]:

$$\frac{F_{\text{osm}}}{k_B T} = V_{\text{chain}} \Pi_{\text{osmotic}} \cong N^{9/4} a^{15/4} s^{-5/2} L^{-5/4} \tag{1}$$

where k_B represents the Boltzmann constant, which has the unit of energy; V_{chain} represents the volume of a chain; Π_{osmotic} is the osmotic pressure; and a is the monomer size. The osmotic repulsion between monomers tends to stretch the chains out of the surface. This tendency is opposite to the increase in the entropic elasticity of the chains when being overstretched. Each chain is then taken as a body consisting of some connected semidilute "blobs" [17] in a good solvent. The entropic elastic free energy F_{stretch} related to the chain stretch can be expressed as [6]

$$\frac{F_{\text{stretch}}}{k_B T} \cong \frac{L^2}{\left(\frac{N}{g}\right)\xi^2} \cong N^{-3/4} a^{-5/4} s^{-1/2} L^{7/4} \tag{2}$$

where g is the number of monomers in one blob and ξ represents the size of the blob. Combining Eqs. (1) and (2) gives the total free energy at one chain as

$$\frac{F}{k_B T} \cong N^{9/4} a^{15/4} s^{-5/2} L^{-5/4} + N^{-3/4} a^{-5/4} s^{-1/2} L^{7/4} \tag{3}$$

Minimizing the overall free energy with respect to L gives the equilibrium height of the brush, L_0, as

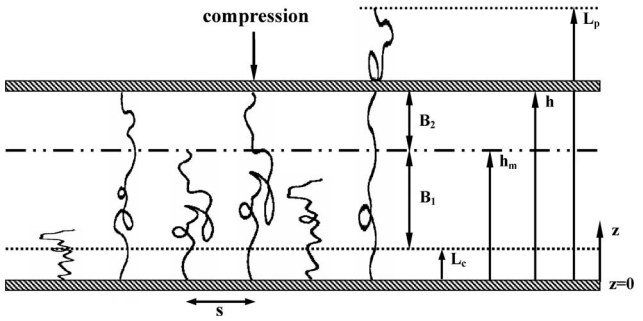

Fig. 1 Schematic of one solid surface grafted with polymer brushes compressed by another parallel solid surface

$$L_0 \cong Na\left(\frac{a}{s}\right)^{2/3} \cong Na^{5/3}\rho_a^{1/3} \tag{4}$$

where $\rho_a = M/S = 1/s^2$ is the grafting density, M represents the number of polymer chains grafted on the surface, and S is the grafting surface area. Substituting Eq. (4) back into Eq. (3) gives the one-chain free energy for the brush as

$$\frac{F(L)}{k_B T} \cong \frac{L_0}{s}\left[\left(\frac{L_0}{L}\right)^{5/4} + \left(\frac{L}{L_0}\right)^{7/4}\right] \tag{5}$$

Both terms on the right-hand side of the above equation are denoted using the scaling method such that a numerical prefactor with an order of unity is missing. This treatment assumes a uniform monomer density within the brush. If the more realistic parabolic density profile is assumed [18], scaling exponents calculated for the brush height are the same as those for the uniform density. Therefore, the same scaling exponents are used in the present study. For each polymer brush, the interaction force $f(z)$ can be derived by differentiating Eq. (5) with respect to z. It is expressed as

$$\frac{f(z)}{k_B T} = -\frac{1}{k_B T}\frac{\partial F(z)}{\partial z} = \frac{A}{s}\left[\left(\frac{L_0}{z}\right)^{9/4} - \left(\frac{z}{L_0}\right)^{3/4}\right] \tag{6}$$

where A represents the missing prefactor in Eq. (5), which is given directly dependent on the nature of the chain. In the next section, a statistical method is applied to expand the interaction force of a single brush to the interactions of polymer brushes under different compressions.

2.2 Compressibility of Polymer Brushes. In the present study, polymer brushes are end grafted at a solid surface and are compressed by another parallel solid surface without polymer brushes. As Fig. 1 shows, when a compression force is applied, the separation between the two parallel plates is reduced from its initial value of L_p, i.e., the initial equilibrium brush thickness, to some arbitrary separation,h. The interaction force formed in a unit area between the two parallel plates would be zero if the separation h is equal to L_p. The assumption of a uniform concentration density is inappropriate to describe the brush conformation because it restricts the chains in two aspects. First, all chains are constrained to exhibit the same behavior. Second, all chains are grouped together, and the fluctuations of a chain far away from its most likely path are suppressed. However, in practice, the polymer chains have different lengths and exhibit considerable conformational variations. As a result, in order to model the compression effect more precisely, it is necessary to treat each polymer brush on an individual basis. Accordingly, the current study analyzes the compression of the polymer brushes by constructing a PDF to describe the heights of the individual brushes within the brush layer. The PDF for brush heights denoted by $p(z)$ defines the probability of locating the maximum extent of the brushes at a height of z. This function can be obtained from a statistical analy-

sis method, which is discussed in the next section as a function of surface separation between the two parallel plates. In the present study, the heights of all polymer brushes satisfy the distribution function $p(z)$, which is varied with different compression forces, rather than assuming the Gaussian distribution function. The probability that a polymer brush has a height between z and $z+dz$ is $p(z)dz$. The interaction force formed in a unit area between the two parallel plates with a separation h is expressed as

$$\bar{f}(h) = \rho_a \int_{L_c}^{h} f(z)p(z)dz \tag{7}$$

where L_c, as shown in Fig. 1, represents the fully compressed brush thickness, at which thickness the polymer layers are effectively incompressible. Here, the distribution function $p(z)$ is assumed to be a symmetry distribution before compression ($h=L_p$). Moreover, the relationship between L_0 and L_p can be determined by setting $\bar{f}(L_p)=0$. This raises the question of how to express the compression between the two parallel plates all grafted with polymer brushes at a separation D. The interdigitation effect of the polymer brushes can be expressed as $d \cong (2L_P/D)^{1/3}s$, where d represents the interpenetration thickness, and s denotes the mean spacing between the two adjacent grafting points [19,20]. At relatively high surface grafting density (a small s value) as well as under low to moderate compressions of these two parallel plates, the brushes interdigitate weakly. The interdigitation effect is not considered in the present study. Therefore, the free energy of two brushes compressed against each other is approximately equal to twice the free energy of a single brush whose height is imposed to be $h=D/2$. The interaction free energy W formed in a unit area between two parallel plates with a separation D is given as

$$W(D) = 2\int_{L_p}^{h} \bar{f}(h)dh \tag{8}$$

The force formed between the two cylindrical surfaces via the Derjaguin approximation [16] is expressed as a function of $W(D)$:

$$\frac{F(D)}{R} = 2\pi W(D) \tag{9}$$

where R denotes the radius of curvature of the curved cylinder.

2.3 Determination of the Brush Height Probability Density Function. The PDF of the brush heights, $p(z)$, can be expressed as [21]

$$p(z) = y_e\left(1 + \frac{z-h_m}{B_1}\right)^{m_1}\left(1 - \frac{z-h_m}{B_2}\right)^{m_2} \quad -B_1 + h_m \le z \le B_2 + h_m \tag{10}$$

where z is the z-coordinate, and h_m, as shown in Fig. 1, represents the mean value of brush heights. It is a phenomenological model. In Eq. (10), m_1, m_2, B_1, and B_2 can be derived from the expressions [21]

$$\frac{(m_1+1)}{B_1} = \frac{(m_2+1)}{B_2} \tag{11}$$

$$B_1 + B_2 = \frac{\sigma}{2}\{\mathrm{Sk}^2(r+2)^2 + 16(r+1)\}^{1/2} \tag{12}$$

where σ represents the standard deviation of the brush height distribution, and Sk is the skewness parameter. The mean brush height, h_m, and the standard deviation of the brush height distribution, σ, depend on several factors, most notably the material properties of the brushes, and are virtually impossible to determine theoretically or via direct experimental methods. Accordingly, in the present study, the values of h_m and σ are obtained via the MD simulations. For the case where the brushes are assumed to compress only (i.e., no interdigitation effect takes place) in the present study, the simulation model contains100 polymer chains with a polymerization degree $N=50$ end grafted on the lower substrate and compressed by a parallel solid surface with no polymer brushes. In the simulations, the grafting density corresponding to the semidilute regime is specified as $\rho_a=0.03$ [15]. The conformations of the polymer brushes obtained from the simulations are then used to determine the brush height PDF at different values of the surface separation. Figure 2 illustrates the variation of the mean brush height (h_m) with the separation distance. For convenience, let $(h_m)_d$ denote the mean brush height for the case where h/L_p has a value close to 1 (i.e., small compressions), and let $(h_m)_u$ be the mean brush height for the case where h/L_p has a value closer to zero (i.e., large compressions). The simulation results obtained for the variation of the mean brush height (h_m) with the surface separation can be fitted as follows:

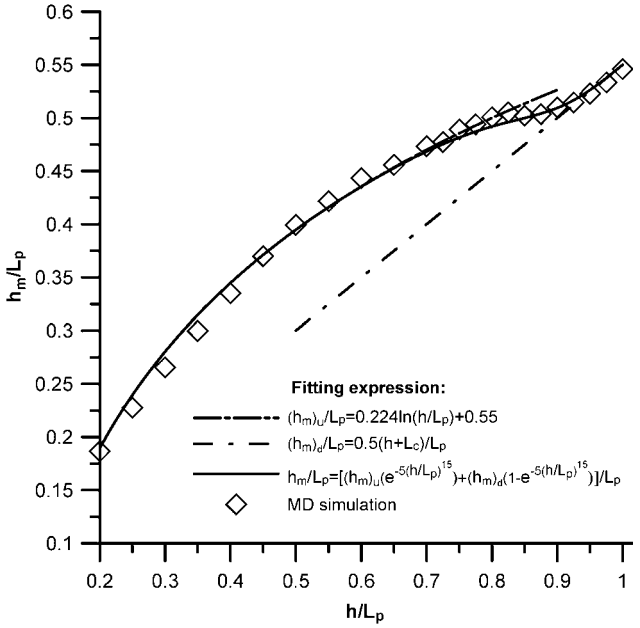

Fig. 2 The mean values of brush heights h_m obtained from the MD simulations at different compressions and the fitting curve

$$(h_m)_u/L_p = 0.224\ln(h/L_p) + [(h_m)_0/L_p]$$

$$(h_m)_d/L_p = 0.5(h + L_c)/L_p$$

$$h_m/L_p = [(h_m)_u e^{-5(h/L_p)^{15}} + (h_m)_d(1 - e^{-5(h/L_p)^{15}})]/L_p \tag{13}$$

where $(h_m)_0$ represents the initial value of the mean brush height ($=0.5(L_p+L_c)$). The simulation result shows that $(h_m)_0/L_p=0.55$, which indicates that $L_c/L_p=0.1$. Figure 3 illustrates the MD simulation results obtained for the variation of the standard deviation of the brush height distribution,σ, as a function of the surface separation. From inspection, it is found that the variation of σ can be described as

$$\sigma/L_p = \begin{cases} 0.231(h/L_p) - 0.031 & \text{for } 0.2 \le h/L_p \le 0.65 \\ 0.140(h/L_p) + 0.028 & \text{for } 0.65 \le h/L_p \le 1.0 \end{cases} \tag{14}$$

In the present study, the MD simulation model of Murat and Grest [14] was adopted in the present simulation because it provides detailed insights into the conformational properties of polymer brushes. MD simulations are performed to evaluate the mean brush height and the standard deviation of the brush height distribution for various surface separations. Accordingly, the variations of the mean brush height and the standard deviation of the brush height distribution with the surface separation can be established

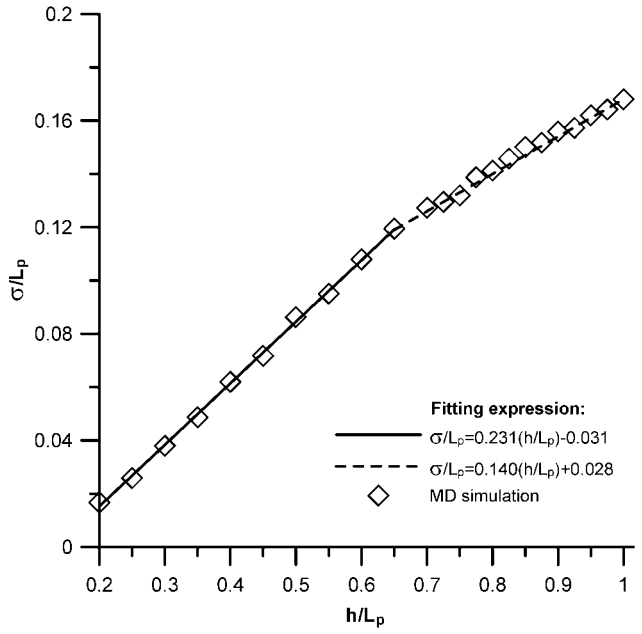

Fig. 3 The standard deviation σ of brush heights distributions obtained from the MD simulations at different compressions and the fitting expressions

from Eqs. (13) and (14). In computing the values of B_1 and B_2 in Eq. (12) in order to establish the brush height PDF (given in Eq. (10)), the parameter r is determined in accordance with [21]

$$r = \frac{6(\mathrm{Kt} - \mathrm{Sk}^2 - 1)}{(6 + 3\mathrm{Sk}^2 - 2\mathrm{Kt})} \tag{15}$$

where Kt is the kurtosis parameter and represents a measure of the flatness of the brush height profile. Having determined the value of r, the values of m_1 and m_2 in Eq. (10) can be obtained from [21]

$$m_1 = \frac{1}{2}\left\{ r - 2 + r(r+2)\left(\frac{\mathrm{Sk}^2}{\mathrm{Sk}^2(r+2)^2 + 16(r+1)} \right)^{1/2} \right\} \tag{16a}$$

$$m_2 = \frac{1}{2}\left\{ r - 2 - r(r+2)\left(\frac{\mathrm{Sk}^2}{\mathrm{Sk}^2(r+2)^2 + 16(r+1)} \right)^{1/2} \right\} \tag{16b}$$

Finally, the term y_e in Eq. (10) is determined in accordance with [21]

$$y_e = \frac{1}{(B_1 + B_2)} \frac{(m_1+1)^{m_1}(m_2+1)^{m_2}}{(m_1+m_2+2)^{m_1+m_2}} \frac{\Gamma(m_1+m_2+2)}{\Gamma(m_1+1)\Gamma(m_2+1)} \tag{17}$$

where Γ is the Gamma function. The PDF $p(z)$ adopted in the present study, as Eq. (10) shows, is expressed as a function of the y_e, m_1, m_2, B_1, and B_2 coefficients. These five coefficients are further expressed as a function of the skewness Sk and the kurtosis Kt. Therefore, in the evaluations, only the skewness and the kurtosis are the independent parameters.

From the discussions above, it is clear that computing the PDF of the brush height at any given value of the surface separation,h, requires a prior knowledge of the values of the skewness (Sk) and kurtosis (Kt) parameters of the brush height distribution. In the present study, these parameter values are derived using an iterative numerical method. In the PDF formulation given in Eq. (10), the lower bound of z, i.e., $(-B_1+h_m)$, represents the minimum value of the brush height and corresponds to the fully compressed brush thickness,L_c (see Fig. 1). Furthermore, the value of B_1 at an arbitrary surface separation is equal to (h_m-L_c), while the upper bound of the PDF, i.e., B_2+h_m, represents the maximum value of the brush height and is equal to h, i.e., the surface separation between the two parallel surfaces. In other words, the value of the PDF drops to zero for values of z greater than h. In Eq. (10), the values of B_1 and B_2 vary with the surface separation, h, in such a way that integrating the non-Gaussian PDF over the entire range of z between the lower $(-B_1+h_m)$ and upper bounds (B_2+h_m) yields a value of 1 for any surface separation h. Prior to compression, the mean brush height,h_m, lies at the center of the brush height distribution range, and thus the initial skewness, Sk_0, is equal to zero, indicating a perfectly symmetrical distribution. From Fig. 1, it can be seen that the initial value of (B_1+B_2) on the left-hand side of Eq. (12) is equal to (L_p-L_c). The initial value of parameter r_0 can be determined by substituting the values of Sk_0, (B_1+B_2), and σ into Eq. (12). Having done so, the initial value of the kurtosis parameter, Kt_0, can be obtained directly from Eq. (15). When a surface compression effect is applied, the left-hand side of Eq. (12) is given by $B_1+B_2=h-L_c$. The corresponding value of r_i is determined by substituting the values of Sk_i, (B_1+B_2), and σ into Eq. (12). The kurtosis, Kt_i, is then obtained from Eq. (15). Having obtained values for both Sk_i and r_i, the corresponding values of m_1 and m_2 are derived from Eqs. (16*a*) and (16*b*), respectively. Finally, the value of $(B_2)_i$ is determined from Eq. (11) using the formulation $B_1=h_m-L_c$. In the event that the value of $(B_2)_i$ is exactly equal to $h-h_m$, integrating the non-Gaussian PDF over the range $-B_1+h_m \leqslant z \leqslant B_2+h_m$ yields a value of 1 and therefore the current values of Sk and Kt are the true values of the skewness and kurtosis parameters of the brush height PDF. However, if the integration of the non-Gaussian PDF over the range $-B_1+h_m \leqslant z \leqslant B_2+h_m$ yields a value other than 1, the solution procedure computes new values of Sk_i, Kt_i, and the PDF. This process is repeated iteratively at each value of the surface separation distance until the integration of the non-Gaussian PDF over the range $-B_1+h_m \leqslant z \leqslant B_2+h_m$ yields the required value of 1. Using the procedure described above, the true values of Sk and Kt are obtained for a given surface separation h such that the corresponding value of the brush height PDF can be determined.

3 Results and Discussion

Figure 2 shows the mean values of brush heights h_m obtained from the MD simulations at different compressions, and they can be fitted well by Eq. (13). The normalized fully compressed brush thickness, $L_c/L_p=0.1$, is assumed. Before a compression $(h=L_p)$, h_m lies at the center in the distribution range $(=1/2(L_p+L_c))$. At small compressions $(h/L_p=0.9-1.0)$, the polymer brushes between the two parallel plates with a separation h undergo a uniform compression such that h_m is decreased linearly with the decrease in the separation h $(=(h_m)_d)$. As compressions become strong $(h/L_p<0.9)$, more brushes are pressed against the upper plate such that h_m is finally asymptotic to the value of $(h_m)_u$. The h_m value exhibits a logarithmic increase with surface separation h in a form of $(h_m)_u=0.224L_p \ln(h/L_p)+(h_m)_0$. When the upper surface moves to the full compression $(h/L_p=0.2)$, $(h_m)_u$ is obtained to have a value of $0.224L_p \ln(0.2)+(h_m)_0$.

Figure 3 shows the standard deviation of brush height distributions σ obtained from the MD simulations (symbolized by "◇") and the fitting curve predicted by Eq. (14). At small compressions $(h/L_p=0.65-1.0)$, the standard deviations σ is linearly decreased with a slope of 0.14 as the separation h decreases. As compressions become strong $(h/L_p<0.65)$, the standard deviations σ is still linearly decreased by decreasing the h value, but with a slope of 0.231.

Alexander [11] assumed the monomer density to be constant throughout the brushes and neglected the details of the brush

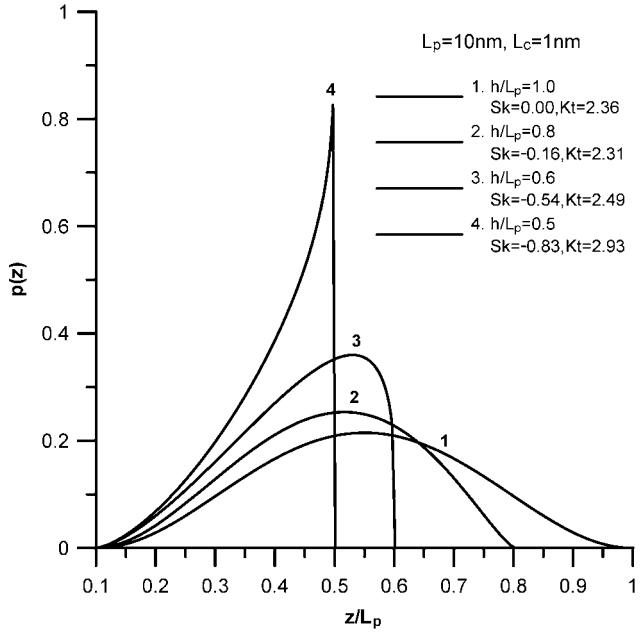

Fig. 4 PDF of brush heights under different compressions (h/L_p). The distance z is normalized by the equilibrium thickness of the brushes L_p.

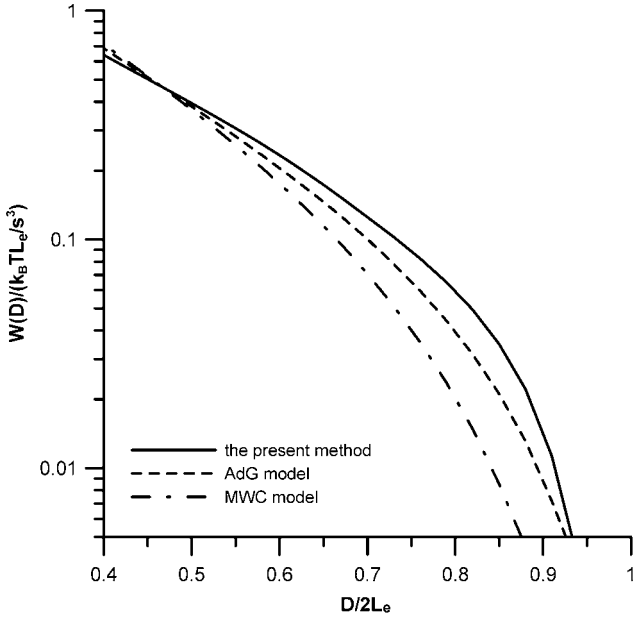

Fig. 5 Normalized interaction free energy per unit area between the two parallel plates grafted with polymer brushes versus dimensionless surface separation. The results predicted by the AdG model and the MWC model are rescaled to compare to that of the present method.

structure. Milner et al. [13] took the brush structure into account, with the density being expressed in a parabolic form. However, the MWC model [13] is limited by a strong stretching and the discrepancy between brush analyses that assume an infinite chain length for brushes and a finite one. This discrepancy in the brush analysis can be made up by the fluctuations in the brush conformation. This fluctuation effect apparently arises at small compressions. The fluctuation effect is evaluated in terms of the brush height PDF varying in the non-Gaussian form. In the present study, a statistical analysis method is applied to evaluate the brush height PDF under different compressions. Figure 4 shows the PDFs of brush heights obtained by the present method under different compressions. Here, the equilibrium brush thickness L_p is set to be 10 nm and the fully compressed brush thickness L_c is set to be 1 nm. The distance z is normalized by the equilibrium thickness of the brushes, L_p. At equilibration ($h/L_p=1.0$), the PDF approximates the Gaussian distribution, which is symmetrical with respect to the surface placed in the midway between the surface of $z=L_c$ and the upper surface shown in Fig. 1. This situation implies that there is no compression and that chains show large fluctuations in the conformation. When a small compression is applied ($h/L_p=0.8$), the distribution is skewed toward the compressing surface slightly, which corresponds to the mean value of brush heights shifting toward the upper surface, as shown in Fig. 2. It means that the compression has manifested but is still insignificant. Both the skewness and kurtosis of the $p(z)$ profile are enhanced by decreasing the h/L_p value or increasing the compression force. At a further compression of $h/L_p=0.5$, the $p(z)$ profile becomes sharp and with a high peak near the upper surface. This behavior indicates that most of the brushes stretching out from the grafting surface are pressed against the upper surface such that a layer full of maximum extent of the brushes is formed.

In the present study, two models, which can predict the interaction force between the two parallel plates grafted with polymer brushes, are presented to compare their results with that of the present method. The AdG model, developed for the interaction force formed in a unit area with a separation D between two parallel surfaces, is given as [22]

$$f(D) \cong \frac{k_B T}{s^3}\left[\left(\frac{2L_0}{D}\right)^{9/4} - \left(\frac{D}{2L_0}\right)^{3/4}\right], \quad D < 2L_0 \tag{18}$$

Applying the Derjaguin approximation [16], the measured force between two cylindrical surfaces, $F(D)$, can be expressed in relation to the interaction free energy in a unit area, $W(D)$, as [23]

$$\frac{F(D)}{R} = 2\pi W(D) \cong \frac{16 k_B T \pi L_0}{35 s^3}\left[7\left(\frac{2L_0}{D}\right)^{5/4} + 5\left(\frac{D}{2L_0}\right)^{7/4} - 12\right], \quad D < 2L_0 \tag{19}$$

where R denotes the radius of curvature of the two cylinders, L_0 represents the equilibrium brush thickness in the model, and s is the average distance between the two adjacent grafting points on the surface. Kenworthy et al. [24] used the MWC model to express the interaction force between the grafted polyethylene oxide (PEO) chains as a function of surface separation, D. The force formed in a unit area of two parallel surfaces can be expressed as

$$f(D) = P_0[L_m/(D/2)^2 - D/L_m^2 + (D/2)^4/(L_m)^5] \tag{20}$$

where

$$P_0 = \frac{k_B T N}{2}\left(\frac{\pi^2}{12}\right)^{1/3}\frac{a^{4/3}}{s^{10/3}}$$

In Eq. (20), L_m represents the equilibrium brush thickness in the model. Then, the force formed between the two cylindrical surfaces can be expressed as [25]

$$\frac{F(D)}{R} = 2\pi W(D) = 4\pi P_0\left[\frac{2L_m}{D} + \left(\frac{D}{2L_m}\right)^2 - \frac{1}{5}\left(\frac{D}{2L_m}\right)^5 - \frac{9}{5}\right] \tag{21}$$

The results in Fig. 5 show the normalized interaction free energy per unit area, $W(D)/(k_B T L_e/s^3)$, obtained from the present method and the comparison with the AdG and MWC models. The normalized fully compressed brush thickness L_c/L_p is assumed to be 0.1. It should be mentioned that the values of the equilibrium brush thickness in the present method L_p, in the AdG model L_0, and in

the MWC model L_m are not the same among them. If the normalized fully compressed brush thickness L_c/L_p is assumed to be 0.1, a relationship of $L_0=0.46L_p$ was obtained by setting $\bar{f}(L_p)=0$. In addition, a simple relationship of $L_m=1.3L_0$ had been derived in the study of Milner et al. [13]. To make an appropriate comparison, a single value of equilibrium brush thickness L_e is set for the present method and the other two models. Moreover, the surface separation D is normalized by $2L_e$. A numerical prefactor is given in order to rescale the results of the AdG and the MWC models so that they can be compared to the present method. At relatively high surface grafting density as well as under low to moderate compressions of these two parallel plates, the brushes interdigitate quite weakly. With the assumption that no interdigitation due to a compression exists in the present method, the interaction free energy of two brushes compressed against each other is approximately equal to twice the interaction free energy of a single brush whose height is imposed to be $h=D/2$. In the present study, the compressions can operate only in a region larger than the mean value of brush heights such that a maximum compression value, $D/2L_e=0.4$, is set. For small $D/2L_e$ values, the interaction forces predicted by these three models are quite close to each other. Significant differences in the interaction free energy among the present method and the other two models are present at the $D/2L_e$ values larger than 0.5. The results show the interaction free energy in the sequence $W(D)_{\mathrm{MWC}}<W(D)_{\mathrm{AdG}}<W(D)_{\mathrm{present}}$. In this strong compression region ($D/2L_e<0.5$), the fluctuation effect due to the brush conformation is reduced and the interaction free energy is actually dominated by osmotic repulsions. On the contrary, substantial differences in the interaction free energy among the present method and the other two models are present at small compressions (or large $D/2L_e$ values). Large fluctuation effects of the brushes tend to enhance the monomer density at the outer extremity of the brushes, and thus increase the interaction free energy at small compressions. In the present method, this fluctuation effect is evaluated using the change in the PDF of brush heights formed at different separations, as shown in Fig. 4. This PDF is different from the step-function profile given in the AdG model, which leads the brush ends to be confined to the outer extremity of the brushes, and the assumption of a parabolic profile given in the MWC model. The present method makes the interaction free energy higher than those of the other two models when operating at small compressions.

In order to examine the validity of the present method, the experimental force profile of PS-X(X: $-\mathrm{N(CH_3)_2}$) grafted on mica surfaces in toluene obtained using the surface force balance (SFB) technique [6] is shown to compare it to the results predicted by the present method. This experimental material was obtained following the method of Taunton et al. [26] to produce well-defined polymer brushes using monodisperse chains, with small end groups physisorbing to the mica surface. The force results of the AdG and MWC models and the present method are compared to the experimental data and shown in Fig. 6. The mean spacing between two adjacent grafting points with $s=6.7$ nm and the equilibrium brush thickness with $L_e=50$ nm were used. In the small compression region that $D>50$ nm, the results predicted by the present method fit the experimental results much better than those of the other two models. The AdG and MWC models underestimated the forces. The large fluctuation effect in the brush conformation is the main cause of different interaction forces forming in the present method and the other two models. This effect has been considered in the present method. Small compressions are generally important in applications, such as colloidal stabilization. In this region, the force is quite small and is hard to detect due to the limitation in the instrument resolution. The results indicate that the present method can provide more accurate predictions of the interaction force than the other two models because of a significant improvement in the fluctuation effect formed in the brush conformation.

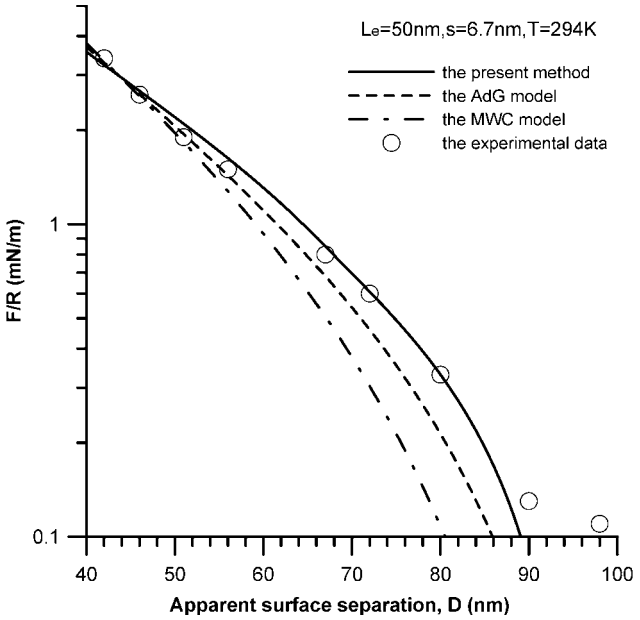

Fig. 6 The measured force parameters obtained at different apparent surface separations between mica surfaces in a $(5.6\pm1)\times10^{-5}$ weight fraction solution of PS-X ($\bar{M}_w$=65 kDa) in toluene [6]. The experimental force profiles are presented to compare them to that of the present method, the AdG model, and the MWC model.

4 Conclusions

The fluctuation effect in the brush conformation is successfully evaluated in terms of the brush height PDF varying in the non-Gaussian form. The present method is developed to find the non-Gaussian PDF, and the skewness and the kurtosis evaluated at various surface separations, no matter what the initial values of the above three parameters are given before compression. The interaction free energy and the force due to a compression can be attained directly if the material factor A is available.

Both the skewness and kurtosis of the PDF profile are enhanced by decreasing the surface separation or increasing the compression force. The variation of the non-Gaussian PDF is the main cause of having significant differences in the interaction free energy at small compressions among the present method and the other two models.

The interaction force results predicted by the present method show a better fit with the experimental results than those of the AdG and MWC models. The results of the interaction free energy predicted by the present method at small compressions are always higher than those predicted by the AdG and MWC models. The differences among the present method and the other two models are enhanced by increasing the apparent surface separation.

References

[1] Anastassopoulos, D. L., Vradis, A. A., Toprakcioglu, C., Smith, G. S., and Dai, L., 1998, "Neutron Reflectivity Study of End-Attached Telechelic Polymers in a Good Solvent," Macromolecules, **31**, pp. 9369–9371.

[2] Levicky, R., Koneripalli, N., Tirrell, M., and Satija, S. K., 1998, "Concentration Profiles in Densely Tethered Polymer Brushes," Macromolecules, **31**, pp. 3731–3734.

[3] Currie, E., P. K., Wagemaker, M., Cohen Stuart, M. A., and van Well, A. A., 2000, "Structure of Grafted Polymers, Investigated With Neutron Reflectometry," Physica B, **283**, pp. 17–21.

[4] Marzolin, C., Auroy, P., Deruelle, M., Folkers, J. P., Léger, L., and Menelle, A., 2001, "Neutron Reflectometry Study of the Segment-Density Profiles in End-Grafted and Irreversibly Adsorbed Layers of Polymer in Good Solvents," Macromolecules, **34**, pp. 8694–8700.

[5] Taunton, H. J., Toprakcioglu, C., Fetters, L. J., and Klein, J., 1988, "Forces Between Surfaces Bearing Terminally Anchored Polymer Chains in Good Solvents," Nature (London), **332**, pp. 712–714.

[6] Dunlop, I. E., Briscoe, W. H., Titmuss, S., Sakellariou, G., Hadjichristidis, N., and Klein, J., 2004, "Interactions Between Polymer Brushes: Varying the Number of End-Attaching Groups," Macromol. Chem. Phys., **205**, pp. 2443–2450.
[7] Drobek, T., Spencer, N. D., and Heuberger, M., 2005, "Compressing PEG Brushes," Macromolecules, **38**, pp. 5254–5259.
[8] Yamamoto, S., Ejaz, M., Tsujii, Y., Matsumoto, M., and Fukuda, T., 2000, "Surface Interaction Forces of Well-Defined, High-Density Polymer Brushes Studied by Atomic Force Microscopy. 1. Effect of Chain Length," Macromolecules, **33**, pp. 5602–5607.
[9] Yamamoto, S., Ejaz, M., Tsujii, Y., and Fukuda, T., 2000, "Surface Interaction Forces of Well-Defined, High-Density Polymer Brushes Studied by Atomic Force Microscopy. 2. Effect of Graft Density," Macromolecules, **33**, pp. 5608–5612.
[10] McLean, S. C., Lioe, H., Meagher, L., Craig, V. S. J., and Gee, M. L., 2005, "Atomic Force Microscopy Study of the Interaction between Adsorbed Poly-(ethylene oxide) Layers: Effects of Surface Modification and Approach Velocity," Langmuir, **21**, pp. 2199–2208.
[11] Alexander, S., 1977, "Adsorption of Chain Molecules With a Polar Head. A scaling Approach," J. Phys. (Paris), **38**, pp. 983–989.
[12] de Gennes, P. G., 1985, "Films of Polymer-Solutions," C. R. Acad. Sci., **300**, pp. 839–843.
[13] Milner, S., Witten, T., and Cates, M., 1988, "Theory of the Grafted Polymer Brush," Macromolecules, **21**, pp. 2610–2619.
[14] Murat, M., and Grest, G. S., 1989, "Structure of a Grafted Polymer Brush: A Molecular Dynamics Simulation," Macromolecules, **22**, pp. 4054–4059.
[15] Murat, M. and Grest, G. S., 1989, "Interaction Between Grafted Polymeric Brushes—A Molecular-Dynamics Study," Phys. Rev. Lett., **63**, pp. 1074–1077.
[16] Israelachvili, J. N., 1992, *Intermolecular and Surface Forces*, 2nd ed., Academic, London.
[17] de Gennes, P. G., 1979, *Scaling Concepts in Polymer Physics*, Cornell University Press, Ithaca, NY.
[18] Milner, S. T., Witten, T. A., and Cates, M. E., 1988, "A Parabolic Density Profile for Grafted Polymers," Europhys. Lett., **5**, pp. 413–418.
[19] Klein, J., 1996, "Shear, Friction, and Lubrication Forces Between Polymer-Bearing Surfaces," Annu. Rev. Mater. Sci., **26**, pp. 581–612.
[20] Witten, T. A., Leibler, L., and Pincus, P., 1990, "Stress Relaxation in the Lamellar Copolymer Mesophase," Macromolecules, **23**, pp. 824–830.
[21] Gibra, I. N., 1973, *Probability and Statistical Inference for Scientists and Engineers*, Prentice-Hall, Englewood Cliffs, NJ.
[22] de Gennes, P. G., 1987, "Polymers at Interfaces: A Simplified View," Adv. Colloid Interface Sci., **27**, pp. 189–209.
[23] Kuhl, T. L., Leckband, D. E., Lasic, D. D., and Israelachvili, J. N., 1995, Stealth Liposomes, CRC, Boca Raton, FL.
[24] Kenworthy, A. K., Hristova, K., Needham, D., and McIntosh, T. J., 1995, "Range and Magnitude of the Steric Pressure Between Bilayers Containing Phospholipids with Covalently Attached Poly(Ethylene Glycol)," Biophys. J., **68**, pp. 1921–1936.
[25] Efremova, N. V., Bondurant, B., O'Brien, D. F., and Leckband, D. E., 2000, "Measurements of Interbilayer Forces and Protein Adsorption on Uncharged Lipid Bilayers Displaying Poly(Ethylene Glycol) Chains," Biochemistry, **39**, pp. 3441–3451.
[26] Taunton, H. J., Toprakcioglu, C., Fetters, L. J., and Klein, J., 1990, "Interactions Between Surfaces Bearing End-Adsorbed Chains in a Good Solvent," Macromolecules, **23**, pp. 571–580.

A Locally Exact Homogenization Theory for Periodic Microstructures With Isotropic Phases

Anthony S. Drago

Marek-Jerzy Pindera

Civil Engineering Department,
University of Virginia,
Charlottesville, VA 22904-4742

Elements of the homogenization theory are utilized to develop a new micromechanics approach for unit cells of periodic heterogeneous materials based on locally exact elasticity solutions. The interior inclusion problem is exactly solved by using Fourier series representation of the local displacement field. The exterior unit cell periodic boundary-value problem is tackled by using a new variational principle for this class of nonseparable elasticity problems, which leads to exceptionally fast and well-behaved convergence of the Fourier series coefficients. Closed-form expressions for the homogenized moduli of unidirectionally reinforced heterogeneous materials are obtained in terms of Hill's strain concentration matrices valid under arbitrary combined loading, which yield homogenized Hooke's law. Homogenized engineering moduli and local displacement and stress fields of unit cells with offset fibers, which require the use of periodic boundary conditions, are compared to corresponding finite-element results demonstrating excellent correlation. [DOI: 10.1115/1.2913043]

Keywords: homogenization, periodicity, variational principle, heterogeneous materials

1 Introduction

Micromechanical analyses of heterogeneous media are based on two related but fundamentally distinct concepts rooted in different geometric representations of material microstructures, namely, the concepts of a repeating unit cell (RUC) and a representative volume element (RVE). The RVE is used in the analysis of statistically homogeneous microstructures, while RUC is employed for periodic composites [1]. In particular, the RVE is the smallest element of a heterogeneous material with a statistically homogeneous distribution of phases that responds in a manner identical to that of the entire assemblage under homogeneous tractions or displacement boundary conditions, ensuring that the effective moduli are independent of the manner in which the boundary conditions are applied as in the case of purely homogeneous materials. Unfortunately, there are no geometric models that satisfy the homogeneous displacement and traction boundary condition equivalence under **all** loading conditions. Therefore, for a general statistically homogeneous microstructure, Hill [2] proposed an energetic definition for the RVE based on the equivalence of strain energies induced by homogeneous displacement and traction boundary conditions. Nonetheless, this equivalence needs to be established for each microstructure to within an acceptable error. In contrast to the RVE, the RUC is the smallest element of a heterogeneous periodic microstructure that provides the basic building block for the entire microstructure's construction through replication. Since each RUC is indistinguishable from the next, the response of the entire array under macroscopically uniform loading is identical to the response of an arbitrary RUC under the same loading. This loading is specified by periodic boundary conditions that involve both surface displacements and tractions.

Intrinsic difficulties of simultaneously satisfying homogeneous displacement and traction boundary conditions necessary in fulfilling the RVE requirement for subvolumes with arbitrary statistically homogeneous microstructures have contributed to greater emphasis on the development of methods for the analysis of periodic materials in the past 20 years. Specifically, the homogenization technique has emerged as a powerful tool in the analysis of this class of materials, cf. Sanchez-Palencia [3] and Suquet [4]. This technique employs a multiscale displacement representation in the solution of the RUC problem, which leads to the determination of effective or homogenized moduli and internal strain and stress fields. The solution of the RUC boundary-value problem, however, is typically generated using the finite-element method with the attendant limitations, noting some exceptions such as the semianalytical finite-volume approach [5,6].

Conversely, elasticity-based solutions of periodic unit cell problems have been attempted outside of the homogenization theory's framework in the 1960s and 1970s with varying degrees of success. Typically, Fourier series representations of stress or displacement fields were employed in conjunction with boundary conditions applied in an approximate manner that reflected the symmetry of the problem for specified loading. For instance, Chen and Chang [7], Pickett [8], and Leissa and Clausen [9] used series representation of the Airy stress function, which satisfied the biharmonic equation for doubly symmetric unit cells. The boundary conditions were approximately satisfied by using collocation or least-squares techniques at both the fiber-matrix interface and the exterior boundary. Similarly, Heaton [10] used series representation of the Airy stress function such that the fiber-matrix interface conditions were exactly satisfied for circular inclusions while pointwise collocation was applied on the unit cell boundary. Complex potential methods were also employed in the solution of specific plane problems involving periodic inclusions [11–14]. Interest in elasticity-based methods has recently revived in light of advances in the computational technology, as well as due to the potential advantages offered by these techniques, cf. Wang et al. [15] and Crouch and Mogilevskaya [16]. One obvious area is microstructural optimization, which can profit from the use of analytical solution techniques for unit cell problems due to the significantly smaller design variable space, more efficient specifi-

Contributed by the Applied Mechanics Division of ASME for publication in the JOURNAL OF APPLIED MECHANICS. Manuscript received September 27, 2007; final manuscript received February 5, 2008; published online July 17, 2008. Review conducted by Anthony Waas.

cation of objective functions, and the implementation of more efficient search procedures. Another application is related to the recent work aimed at reconstructing local fields from homogenized-based results within a multiscale analysis framework [17], presently carried out by using the numerical approach.

Herein, we employ elements of the homogenization framework to develop a new micromechanics theory for periodic materials based on locally exact unit cell elasticity solutions rather than the unit cell discretization used in the finite-element and finite-volume techniques. This approach differs from previous stress or displacement-based formulations of unit cell solutions that employed Fourier series, which were limited to centered inclusions and symmetric boundary conditions. Herein, a consistent framework is developed, which is applicable to unit cells with or without planes of material symmetry wherein the interior problem is exactly solved and the exterior unit cell periodic boundary-value problem is tackled by using a new variational principle. This contrasts with the common but problematic use of collocation or least-squares techniques employed in the solution of nonseparable problems. Closed-form expressions for the homogenized moduli of unidirectionally reinforced materials are obtained in terms of Hill's strain concentration matrices valid under arbitrary combined loading, which, in fact, yield homogenized Hooke's law. Homogenized effective moduli generated by the locally exact solution are compared to the finite-element predictions, as are local displacement and stress fields generated under unidirectional loadings, demonstrating the new approach's accuracy and promise.

The paper is organized as follows. In Sec. 2, we present the analytical framework for the single-inclusion unit cell problem subjected to periodic loading by macroscopic (or average) strains, including implementation of periodic boundary conditions by using the new variational approach, and the calculation of Hill's strain concentration factors. Comparison of the homogenized moduli for two unidirectional composites with large fiber/matrix property contrast predicted by the locally exact analytical solution with the corresponding finite-element results is given in Sec. 3. Local displacement and stress fields predicted by the analytical and finite-element approaches are also illustrated in this section. Discussion of the implemented variational principle, method's limitations and future extensions, and summary and conclusions are given in Secs. 4, 5, and 6, respectively.

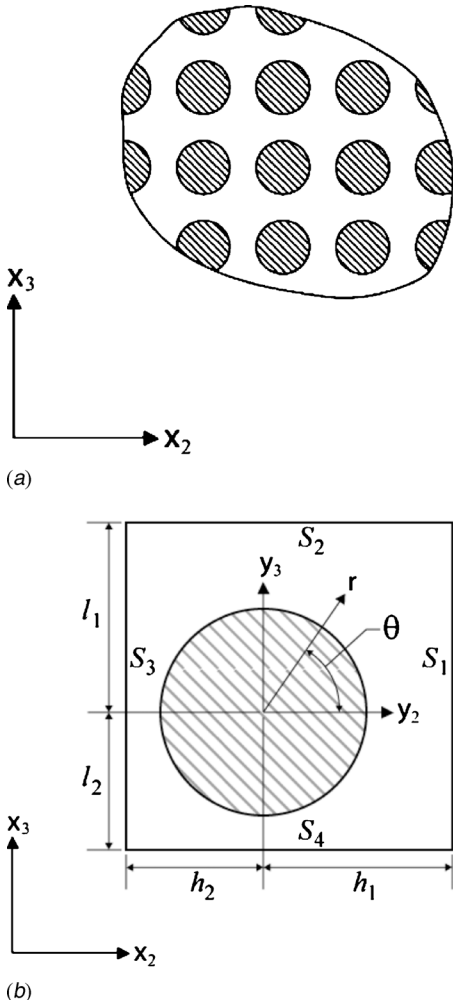

Fig. 1 (*a*) Periodically arranged inclusions in a square array and (*b*) RUC with an offset fiber that is the fundamental building block for the entire array

2 Analytical Framework

We consider a periodic material with continuous reinforcement along the x_1 axis, characterized by a RUC that defines the material's microstructure, Fig. 1. To demonstrate the fundamental approach, we limit our analysis to unit cells with single inclusions that are offset from the center. This requires the use of periodic boundary conditions that involve both surface displacements and tractions. Periodic displacement boundary conditions are defined by

$$u_i(\mathbf{x}_o + \mathbf{d}) = u_i(\mathbf{x}_o) + \bar{\varepsilon}_{ij} d_j, \quad (\mathbf{x}_o, \mathbf{x}_o + \mathbf{d}) \in S \tag{1}$$

where $\bar{\varepsilon}_{ij}$ are the average strain components of the entire array, $\mathbf{x}_o$ is a coordinate point on the unit cell boundary S, and $\mathbf{d}$ is a characteristic distance that defines the RUC array microstructure. This characteristic distance separates image points between adjacent RUCs and defines the microstructural scale of the periodic array. The above boundary conditions ensure that displacements are continuous at the interfaces between adjacent RUCs. Furthermore, tractions must also be continuous at these interfaces, which is ensured by the periodic traction boundary conditions

$$T_i(\mathbf{x}_o + \mathbf{d}) + T_i(\mathbf{x}_o) = 0, \quad (\mathbf{x}_o, \mathbf{x}_o + \mathbf{d}) \in S \tag{2}$$

The analysis of local displacement and stress fields is motivated by the homogenization theory's framework wherein the global coordinates $\mathbf{x}=(x_1,x_2,x_3)$ describe the average response of the entire periodic array and the local coordinates $\mathbf{y}=(y_1,y_2,y_3)$ describe the interior unit cell response. Accordingly, a two-scale displacement field expansion is employed for the fiber and matrix phases within the unit cell as follows:

$$u_i^{(k)}(\mathbf{x},\mathbf{y}) = \bar{\varepsilon}_{ij} x_j + u_i'^{(k)}(\mathbf{y}) \tag{3}$$

where $\bar{\varepsilon}_{ij}$ are the specified average strain components, the fluctuating displacement components u_i' caused by the heterogeneity of the medium are functions of the local coordinates (y_2,y_3) given the unidirectional constraint along the x_1 direction by the continuous reinforcement, and the superscripts $k=f,m$ denote the fiber and matrix phases, respectively. Within the constraint of infinitesimal deformations, the strain field in the fiber and matrix phases generated by the above displacement representation is obtained from the strain-displacement relations

$$\varepsilon_{ij}^{(k)} = \bar{\varepsilon}_{ij} + \frac{1}{2}\left(\frac{\partial u_i'^{(k)}}{\partial y_j} + \frac{\partial u_j'^{(k)}}{\partial y_i} \right) \tag{4}$$

so that the local fiber and matrix strains are obtained in terms of the average strains $\bar{\varepsilon}_{ij}$ and contributions from the fluctuating displacement components

$$\varepsilon_{11}^{(k)} = \bar{\varepsilon}_{11}$$

$$\varepsilon_{22}^{(k)} = \bar{\varepsilon}_{22} + \frac{\partial u_2'^{(k)}}{\partial y_2}$$

$$\varepsilon_{33}^{(k)} = \bar{\varepsilon}_{33} + \frac{\partial u_3'^{(k)}}{\partial y_3}$$

$$\varepsilon_{23}^{(k)} = \bar{\varepsilon}_{23} + \frac{1}{2}\left(\frac{\partial u_2'^{(k)}}{\partial y_3} + \frac{\partial u_3'^{(k)}}{\partial y_2}\right) \tag{5}$$

$$\varepsilon_{12}^{(k)} = \bar{\varepsilon}_{12} + \frac{1}{2}\frac{\partial u_1'^{(k)}}{\partial y_2}$$

$$\varepsilon_{13}^{(k)} = \bar{\varepsilon}_{13} + \frac{1}{2}\frac{\partial u_1'^{(k)}}{\partial y_3}$$

The unidirectional reinforcement imposes the constraint that the normal strain $\varepsilon_{11}^{(k)}$ is the same in all phases and, in fact, is equal to the macroscopic axial strain $\bar{\varepsilon}_{11}$. Furthermore, the normal and shear in-plane strains $\varepsilon_{22}^{(k)}, \varepsilon_{33}^{(k)}, \varepsilon_{23}^{(k)}$ are uncoupled from the out-of-plane shear strains $\varepsilon_{12}^{(k)}, \varepsilon_{13}^{(k)}$.

Given that the macrostrains are constant, the local stress equilibrium equations that need to be satisfied in the fiber and matrix phases $(k=f,m)$ reduce to

$$\frac{\partial \sigma_{ij}^{(k)}}{\partial y_j} = 0 \tag{6}$$

Since none of the stress components depends on the out-of-plane coordinate y_1, the three equilibrium equations become

$$\frac{\partial \sigma_{12}^{(k)}}{\partial y_2} + \frac{\partial \sigma_{13}^{(k)}}{\partial y_3} = 0$$

$$\frac{\partial \sigma_{22}^{(k)}}{\partial y_2} + \frac{\partial \sigma_{23}^{(k)}}{\partial y_3} = 0 \tag{7}$$

$$\frac{\partial \sigma_{23}^{(k)}}{\partial y_2} + \frac{\partial \sigma_{33}^{(k)}}{\partial y_3} = 0$$

where the out-of-plane shear stress components are uncoupled from the in-plane normal and shear components. By assuming isotropic phases, the stress equilibrium equations are subsequently expressed in terms of the displacement components through the use of the stress-strain equations

$$\sigma_{ij}^{(k)} = \lambda_{(k)}\varepsilon_{nn}^{(k)}\delta_{ij} + 2\mu_{(k)}\varepsilon_{ij}^{(k)} \tag{8}$$

and the strain-displacement equations, Eq. (5). The resulting Navier equations are then compactly written in terms of the Cartesian displacements as

$$(\lambda_{(k)} + \mu_{(k)})\frac{\partial^2 u_j'^{(k)}}{\partial y_i \partial y_j} + \mu_{(k)}\frac{\partial^2 u_i'^{(k)}}{\partial y_j \partial y_j} = 0 \tag{9}$$

where the subscripts i,j assume integer values 1,2,3 subject to $\partial/\partial y_1 = 0$. Extension of the above formulation to transversely isotropic phases in order to model unidirectionally reinforced materials with graphite or carbon fibers, for instance, can be easily accomplished by following the approach of Davison et al. [18].

In the present approach, we first solve the local problem exactly by satisfying the Navier equations in each phase and the fiber-matrix interfacial continuity conditions in a pointwise fashion in the cylindrical coordinate system (z,r,θ), given that the local problem is separable in this coordinate system. Then, we impose periodicity conditions on the external unit cell boundaries in an approximate manner by using a new variational principle, given that the exterior problem is nonseparable in Cartesian coordinates.

2.1 Local Problem in Cylindrical Coordinates. By using the standard transformation equations for the displacement components

$$u_1' = u_z'$$

$$u_2' = u_r'\cos\theta - u_\theta'\sin\theta \tag{10}$$

$$u_3' = u_r'\sin\theta + u_\theta'\cos\theta$$

together with the relations between the in-plane cylindrical and Cartesian coordinates $y_2 = r\cos\theta$, $y_3 = r\sin\theta$ and their differential operators, the Navier equations (Eq. (9)) become

$$\frac{\partial^2 u_z'}{\partial r^2} + \frac{1}{r}\frac{\partial u_z'}{\partial r} + \frac{1}{r^2}\frac{\partial^2 u_z'}{\partial \theta^2} = 0 \tag{11}$$

$$2(1-\nu)\left(\frac{\partial^2 u_r'}{\partial r^2} + \frac{1}{r}\frac{\partial u_r'}{\partial r} - \frac{u_r'}{r^2}\right) + \frac{(1-2\nu)}{r^2}\frac{\partial^2 u_r'}{\partial \theta^2} + \frac{1}{r}\frac{\partial^2 u_\theta'}{\partial r \partial \theta} - \frac{(3-4\nu)}{r^2}\frac{\partial u_\theta'}{\partial \theta} = 0 \tag{12}$$

$$(1-2\nu)\left(\frac{\partial^2 u_\theta'}{\partial r^2} + \frac{1}{r}\frac{\partial u_\theta'}{\partial r} - \frac{u_\theta'}{r^2}\right) + \frac{2(1-\nu)}{r^2}\frac{\partial^2 u_\theta'}{\partial \theta^2} + \frac{1}{r}\frac{\partial^2 u_r'}{\partial r \partial \theta} + \frac{(3-4\nu)}{r^2}\frac{\partial u_r'}{\partial \theta} = 0 \tag{13}$$

Since the out-of-plane and in-plane displacement components u_z' and u_r', u_θ', respectively, are uncoupled in the governing differential equations, the two problems are independently solved below for the displacement field that generates the effective shear moduli G_{12}^*, G_{13}^* and the displacement field that generates the effective normal and shear moduli E_{11}^*, E_{22}^*, E_{33}^*, G_{23}^*, ν_{12}^*, ν_{13}^*, and ν_{23}^*.

2.1.1 Axial Shear Loading. We assume the displacement field $u_z'(r,\theta)$ of the form given below for the fiber and matrix phases

$$u_z' = \sum_{n=0}^{\infty}[h_n(r)\cos n\theta + h_n^*(r)\sin n\theta] \tag{14}$$

By substituting the above equation into Eq. (11) and solving for the unknown functions $h_n(r)$ and $h_n^*(r)$ to obtain single-valued displacement field, the solution for $u_z'(r,\theta)$ in the fiber and matrix regions becomes

$$u_z' = H_{01} + \sum_{n=1}^{\infty} a[(\zeta^n H_{n1} + \zeta^{-n}H_{n3})\cos n\theta + (\zeta^n H_{n2} + \zeta^{-n}H_{n4})\sin n\theta] \tag{15}$$

where $\zeta = r/a$ is the nondimensionalized radial coordinate with respect to the fiber radius a, and $H_{nj}^{f,m}$ $(j=1,2,3,4)$, with the superscripts designating fiber and matrix phases omitted in the above equation for ease of notation, are unknown coefficients. The rigid body coefficient H_{01} is determined by constraining the total displacement u_z at a point within the RUC. In order to ensure that the displacement field at the fiber center remains bounded, we take

$$H_{n3}^f = H_{n4}^f = 0 \tag{16}$$

The remaining coefficients $H_{n1}^{f,m}, \ldots, H_{n4}^{f,m}$ are obtained from the fiber/matrix continuity conditions and the periodic boundary conditions.

The interfacial traction and displacement continuity conditions are applied first to express the unknown coefficients $H_{n1}^m, \ldots, H_{n4}^m$ in the matrix displacement field in terms of the coefficients H_{n1}^f, H_{n2}^f associated with the fiber displacement field. These conditions ensure that the fluctuating axial displacement component $u_z'(\zeta,\theta)$ is continuous at the fiber/matrix interface, as is the radial traction component $\sigma_{zr}(\zeta,\theta)$,

$$u_z'^f(1,\theta) = u_z'^m(1,\theta)$$
$$\sigma_{zr}^f(1,\theta) = \sigma_{zr}^m(1,\theta) \tag{17}$$

The shear stress components σ_{zr} in the fiber and matrix regions are obtained from Hooke's law, Eq. (8), expressed in cylindrical coordinates

$$\sigma_{zr} = 2\mu\varepsilon_{zr} = 2\mu(\bar{\varepsilon}_{zr} + \varepsilon_{zr}') \tag{18}$$

using the strain-displacement relation $2\varepsilon_{zr}' = \partial u_z'/\partial r$ to generate the expression for the shear strain ε_{zr}' from the displacement field of Eq. (15). This yields

$$\sigma_{zr} = 2\mu\bar{\varepsilon}_{zr} + \mu\sum_{n=1}^{\infty} n[(\zeta^{n-1}H_{n1} - \zeta^{-n-1}H_{n3})\cos n\theta + (\zeta^{n-1}H_{n2} - \zeta^{-n-1}H_{n4})\sin n\theta] \tag{19}$$

where $\bar{\varepsilon}_{zr} = \bar{\varepsilon}_{12}\cos\theta + \bar{\varepsilon}_{13}\sin\theta$, since the periodic boundary conditions imposed on a rectangular unit cell in the Cartesian coordinate system are given in terms of the macroscopic axial shear strains $\bar{\varepsilon}_{12}$ and $\bar{\varepsilon}_{13}$.

By applying the two interfacial continuity conditions and using the orthogonality of the $\cos n\theta$ and $\sin n\theta$ terms, we obtain the following solution for the coefficients $H_{n1}^m, \ldots, H_{n4}^m$:

$$\begin{bmatrix} H_{n1}^m \\ H_{n2}^m \\ H_{n3}^m \\ H_{n4}^m \end{bmatrix} = \begin{bmatrix} c_1 & 0 \\ 0 & c_1 \\ c_2 & 0 \\ 0 & c_2 \end{bmatrix} \begin{bmatrix} H_{n1}^f \\ H_{n2}^f \end{bmatrix} + \delta_{n1}c_2 \begin{bmatrix} -1 & 0 \\ 0 & -1 \\ 1 & 0 \\ 0 & 1 \end{bmatrix} \begin{bmatrix} 2\bar{\varepsilon}_{12} \\ 2\bar{\varepsilon}_{13} \end{bmatrix} \tag{20}$$

where $c_1 = (\mu^m + \mu^f)/2\mu^m$ and $c_2 = 1 - c_1$.

The unknown coefficients $\mathbf{H}_n^f = [H_{n1}^f, H_{n2}^f]^T$ are then determined from the application of periodic boundary conditions in a variational sense described in Sec. 2.2. This requires expressions for the axial shear stresses obtained from Hooke's law in Cartesian coordinates

$$\sigma_{12} = 2\mu(\bar{\varepsilon}_{12} + \varepsilon_{12}')$$
$$\sigma_{13} = 2\mu(\bar{\varepsilon}_{13} + \varepsilon_{13}') \tag{21}$$

where the fluctuating Cartesian strains are obtained from the transformation relations

$$\varepsilon_{12}' = \varepsilon_{zr}'\cos\theta - \varepsilon_{z\theta}'\sin\theta$$
$$\varepsilon_{13}' = \varepsilon_{zr}'\sin\theta + \varepsilon_{z\theta}'\cos\theta \tag{22}$$

and $2\varepsilon_{zr}' = \partial u_z'/\partial r$ and $2\varepsilon_{z\theta}' = (1/r)\partial u_z'/\partial\theta$.

2.1.2 Axial Normal and Transverse Loading. Since unit cells without planes of material symmetry in the $r-\theta$ plane are considered, a fully coupled displacement field $u_r'(r,\theta)$, $u_\theta'(r,\theta)$ is assumed of the form

$$u_r' = \sum_{n=0}^{\infty}[f_n(r)\cos n\theta + g_n(r)\sin n\theta]$$
$$u_\theta' = \sum_{n=0}^{\infty}[f_n^*(r)\sin n\theta + g_n^*(r)\cos n\theta] \tag{23}$$

By substituting the above series representations into Eqs. (12) and (13) and solving for the unknown functions $f_n(r)$, $f_n^*(r)$ and $g_n(r)$, $g_n^*(r)$ to obtain single-valued displacement field, the solutions for $u_r'(r,\theta)$, $u_\theta'(r,\theta)$ in the fiber and matrix regions become

$$u_r' = F_{01}a\zeta + F_{02}a\zeta^{-1} + F_{12}\cos\theta + G_{12}\sin\theta + \sum_{n=2}^{\infty}\sum_{j=1}^{4} a\zeta^{p_{nj}}[F_{nj}\cos n\theta + G_{nj}\sin n\theta]$$
$$u_\theta' = -F_{12}\sin\theta + G_{12}\cos\theta + \sum_{n=2}^{\infty}\sum_{j=1}^{4} a\beta_{nj}\zeta^{p_{nj}}[F_{nj}\sin n\theta - G_{nj}\cos n\theta] \tag{24}$$

where $\zeta = r/a$ is the nondimensionalized radial coordinate as before, and the eigenvalues p_{nj} are

$$p_{n1} = n+1, \quad p_{n2} = n-1, \quad p_{n3} = -(n+1), \quad p_{n4} = -(n-1) \tag{25}$$

The eigenvectors β_{nj} are

$$\beta_{nj} = \frac{2(1-\nu)(1-p_{nj}^2) + (1-2\nu)n^2}{n(p_{nj} - 3 + 4\nu)} \tag{26}$$

and $F_{nj}^{f,m}$, $G_{nj}^{f,m}$ $(j=1,2,3,4)$, with the superscripts designating fiber and matrix phases omitted for ease of notation, are unknown coefficients. In order to ensure that the displacement field at the fiber center remains bounded, we must have

$$F_{02}^f = 0 \quad \text{and } F_{n3}^f = F_{n4}^f = 0, \quad G_{n3}^f = G_{n4}^f = 0 \quad \text{for } n \geq 2 \tag{27}$$

The remaining coefficients $F_{nj}^{f,m}$ and $G_{nj}^{f,m}$ are obtained from the fiber/matrix continuity conditions and the periodic boundary conditions.

As in the case of axial shear, the interfacial traction and displacement continuity conditions are applied first to express the unknown coefficients F_{nj}^m, G_{nj}^m in the matrix displacement field in terms of the coefficients F_{nj}^f, G_{nj}^f associated with the fiber displacement field. These conditions ensure that the radial and circumferential fluctuating displacement components $u_r'(\zeta,\theta)$, $u_\theta'(\zeta,\theta)$ and the corresponding stress components $\sigma_{rr}(\zeta,\theta)$, $\sigma_{r\theta}(\zeta,\theta)$ are continuous at the fiber/matrix interface,

$$u_r'^m(1,\theta) = u_r'^f(1,\theta), \quad u_\theta'^m(1,\theta) = u_\theta'^f(1,\theta)$$
$$\sigma_{rr}^m(1,\theta) = \sigma_{rr}^f(1,\theta), \quad \sigma_{r\theta}^m(1,\theta) = \sigma_{r\theta}^f(1,\theta) \tag{28}$$

The radial and shear stress components σ_{rr} and $\sigma_{r\theta}$ in the fiber and matrix regions are obtained from Hooke's law, Eq. (8), expressed in cylindrical coordinates

$$\sigma_{rr} = (\lambda + 2\mu)(\bar{\varepsilon}_{rr} + \varepsilon_{rr}') + \lambda(\bar{\varepsilon}_{zz} + \bar{\varepsilon}_{\theta\theta} + \varepsilon_{\theta\theta}')$$
$$\sigma_{r\theta} = 2\mu(\bar{\varepsilon}_{r\theta} + \varepsilon_{r\theta}') \tag{29}$$

since $\varepsilon_{zz} = \bar{\varepsilon}_{zz}$ in light of the unidirectional constraint, Eq. (5). By using the strain-displacement relations $\varepsilon_{rr}' = \partial u_r'/\partial r$, $\varepsilon_{\theta\theta}' = u_r'/r + (1/r)\partial u_\theta'/\partial\theta$, and $2\varepsilon_{r\theta}' = (1/r)\partial u_r'/\partial\theta + \partial u_\theta'/\partial r - u_\theta'/r$ to generate the expression for the normal and shear strains ε_{rr}', $\varepsilon_{\theta\theta}'$, and $\varepsilon_{r\theta}'$ from the displacement field of Eq. (24), the radial and shear stress components become

$$\sigma_{rr} = (\lambda + 2\mu)\bar{\varepsilon}_{rr} + \lambda(\bar{\varepsilon}_{zz} + \bar{\varepsilon}_{\theta\theta}) + 2kF_{01} - 2\mu F_{02}\zeta^{-2} + \sum_{n=2}^{\infty}\sum_{j=1}^{4} P_{nj}\zeta^{p_{nj}-1}(F_{nj}\cos n\theta + G_{nj}\sin n\theta)$$
$$\sigma_{r\theta} = 2\mu\bar{\varepsilon}_{r\theta} + \sum_{n=2}^{\infty}\sum_{j=1}^{4} R_{nj}\zeta^{p_{nj}-1}(F_{nj}\sin n\theta - G_{nj}\cos n\theta) \tag{30}$$

where $k = \lambda + \mu$, $P_{nj} = (\lambda + 2\mu)p_{nj} + \lambda(1 + n\beta_{nj})$, $R_{nj} = \mu[(p_{nj} - 1)\beta_{nj} - n]$, and

$$\bar{\varepsilon}_{zz} = \bar{\varepsilon}_{11}$$

$$\bar{\varepsilon}_{rr} = \frac{1}{2}(\bar{\varepsilon}_{22} + \bar{\varepsilon}_{33}) + \frac{1}{2}(\bar{\varepsilon}_{22} - \bar{\varepsilon}_{33})\cos 2\theta + \bar{\varepsilon}_{23}\sin 2\theta$$

$$\bar{\varepsilon}_{\theta\theta} = \frac{1}{2}(\bar{\varepsilon}_{22} + \bar{\varepsilon}_{33}) - \frac{1}{2}(\bar{\varepsilon}_{22} - \bar{\varepsilon}_{33})\cos 2\theta - \bar{\varepsilon}_{23}\sin 2\theta \tag{31}$$

$$\bar{\varepsilon}_{r\theta} = -\frac{1}{2}(\bar{\varepsilon}_{22} - \bar{\varepsilon}_{33})\sin 2\theta + \bar{\varepsilon}_{23}\cos 2\theta$$

By applying the four interfacial continuity conditions and using orthogonality of the $\cos n\theta$ and $\sin n\theta$ terms, we obtain systems of equations for the different order terms in the Fourier series representation of the displacement field. From the $n=0$ contributions, we have

$$\begin{bmatrix} F_{01}^m \\ F_{02}^m \end{bmatrix} = \begin{bmatrix} b_{01} \\ b_{02} \end{bmatrix} F_{01}^f + \begin{bmatrix} c_{01} \\ c_{02} \end{bmatrix} \bar{\varepsilon}_{11} + \begin{bmatrix} d_{01} \\ d_{02} \end{bmatrix} (\bar{\varepsilon}_{22} + \bar{\varepsilon}_{33}) \tag{32}$$

where

$$b_{01} = \frac{k^f + \mu^m}{k^m + \mu^m}, \quad c_{01} = \frac{\lambda^f - \lambda^m}{2(k^m + \mu^m)}, \quad d_{01} = -\frac{1}{2} b_{02}$$

$$b_{02} = \frac{k^m - k^f}{k^m + \mu^m}, \quad c_{02} = -c_{01}, \quad d_{02} = -d_{01}$$

From the $n=1$ contributions, we have

$$F_{12}^m = F_{12}^f, \quad G_{12}^m = G_{12}^f \tag{33}$$

and from the $n \geqslant 2$ contributions, we have

$$\mathbf{A}_n^m \mathbf{F}_n^m = \mathbf{A}_n^f \mathbf{F}_n^f + \delta_{n2} \mathbf{A}_0 (\bar{\varepsilon}_{22} - \bar{\varepsilon}_{33})$$

$$\mathbf{A}_n^m \mathbf{G}_n^m = \mathbf{A}_n^f \mathbf{G}_n^f + \delta_{n2} \mathbf{A}_0 2\bar{\varepsilon}_{23} \tag{34}$$

where $\mathbf{F}_n^m = [F_{n1}^m, F_{n2}^m, F_{n3}^m, F_{n4}^m]^T$, $\mathbf{F}_n^f = [F_{n1}^f, F_{n2}^f]^T$, $\mathbf{G}_n^m = [G_{n1}^m, G_{n2}^m, G_{n3}^m, G_{n4}^m]^T$, $\mathbf{G}_n^f = [G_{n1}^f, G_{n2}^f]^T$, and the matrices $\mathbf{A}_n^m$, $\mathbf{A}_n^f$, and $\mathbf{A}_0$ are given by

$$\mathbf{A}_n^m = \begin{bmatrix} 1 & 1 & 1 & 1 \\ \beta_{n1}^m & \beta_{n2}^m & \beta_{n3}^m & \beta_{n4}^m \\ P_{n1}^m & P_{n2}^m & P_{n3}^m & P_{n4}^m \\ R_{n1}^m & R_{n2}^m & R_{n3}^m & R_{n4}^m \end{bmatrix}, \quad \mathbf{A}_n^f = \begin{bmatrix} 1 & 1 \\ \beta_{n1}^f & \beta_{n2}^f \\ P_{n1}^f & P_{n2}^f \\ R_{n1}^f & R_{n2}^f \end{bmatrix},$$

$$\mathbf{A}_0 = \begin{bmatrix} 0 \\ 0 \\ (\mu^f - \mu^m) \\ -(\mu^f - \mu^m) \end{bmatrix} \tag{35}$$

The Kronecker delta term δ_{n2} is present because the average strains are introduced only through the $n=2$ terms $\cos 2\theta$ and $\sin 2\theta$.

The unknown coefficients F_{n1}^f, F_{n2}^f and G_{n1}^f, G_{n2}^f are determined from the application of the periodic boundary conditions in a variational sense described in Sec. 2.2. This requires expressions for the transverse normal and shear stresses in the Cartesian coordinate system along the unit cell's boundary obtained from Hooke's law

$$\sigma_{22} = (\lambda + 2\mu)(\bar{\varepsilon}_{22} + \varepsilon'_{22}) + \lambda(\bar{\varepsilon}_{11} + \bar{\varepsilon}_{33} + \varepsilon'_{33})$$

$$\sigma_{33} = (\lambda + 2\mu)(\bar{\varepsilon}_{33} + \varepsilon'_{33}) + \lambda(\bar{\varepsilon}_{11} + \bar{\varepsilon}_{22} + \varepsilon'_{22}) \tag{36}$$

$$\sigma_{23} = 2\mu(\bar{\varepsilon}_{23} + \varepsilon'_{23})$$

where the fluctuating Cartesian strains are obtained from the transformation relations

$$\varepsilon'_{22} = \frac{1}{2}(\varepsilon'_{rr} + \varepsilon'_{\theta\theta}) + \frac{1}{2}(\varepsilon'_{rr} - \varepsilon'_{\theta\theta})\cos 2\theta - \varepsilon'_{r\theta}\sin 2\theta$$

$$\varepsilon'_{33} = \frac{1}{2}(\varepsilon'_{rr} + \varepsilon'_{\theta\theta}) - \frac{1}{2}(\varepsilon'_{rr} - \varepsilon'_{\theta\theta})\cos 2\theta + \varepsilon'_{r\theta}\sin 2\theta \tag{37}$$

$$\varepsilon'_{23} = \frac{1}{2}(\varepsilon'_{rr} - \varepsilon'_{\theta\theta})\sin 2\theta + \varepsilon'_{r\theta}\cos 2\theta$$

2.2 Implementation of Periodic Boundary Conditions. To complete the solution to the unit cell problem, the unknown coefficients $\mathbf{F}_n^f$, $\mathbf{G}_n^f$, and $\mathbf{H}_n^f$ are determined from the periodic boundary conditions given by Eqs. (1) and (2) with the average strains $\bar{\varepsilon}_{ij}$ acting as loading parameters. This is accomplished using a new variational principle whose origin is rooted in the principle originally proposed by Jirousek [19] in the context of a large-deformation, finite-element methodology based on elements that locally satisfy the governing field equations of elasticity. Specifically, we propose to minimize the functional

$$H_{D-P} = \frac{1}{2}\int_V \sigma_{ij}\varepsilon_{ij} dV - \int_{S_u} T_i u_i^o dS - \int_{S_t} T_i^o u_i dS \tag{38}$$

where $\mathbf{T} = \mathbf{T}^o$ and $\mathbf{u} = \mathbf{u}^o$ are *periodic* traction and displacement constraints imposed on S_t and S_u, respectively. The difference between this and Jirousek's variational principle with its attendant problems in the context of periodic boundary conditions is discussed in Sec. 4.

By taking the first variation of H_{D-P} and using the fact that our local elasticity solutions satisfy the stress equilibrium equations a priori so that

$$\frac{1}{2}\int_V \sigma_{ij}\varepsilon_{ij} dV = \frac{1}{2}\int_S T_i u_i dS \tag{39}$$

we obtain after some manipulation the variational principle in the final form

$$\int_{S_T} \delta u_i (T_i - T_i^o) dS + \int_{S_u} \delta T_i (u_i - u_i^o) dS = 0 \tag{40}$$

where the displacement and traction components on the four surfaces $S_1, \ldots, S_4$ shown in Fig. 1(*b*) are obtained from the periodicity conditions, Eqs. (1) and (2), in the form

$$u_i(S_1) = u_i(S_3) + \bar{\varepsilon}_{i2} d_2, \quad u_i(S_2) = u_i(S_4) + \bar{\varepsilon}_{i3} d_3$$

$$T_i(S_1) = -T_i(S_3), \quad T_i(S_2) = -T_i(S_4) \tag{41}$$

for $i=1,2,3$ with $d_2 = h_1 + h_2$ and $d_3 = l_1 + l_2$. Use of the two-scale displacement representation given by Eq. (3) in the above periodic displacement boundary conditions reduces these periodicity conditions to constraints on the fluctuating displacement components

$$u'_i(S_1) = u'_i(S_3), \quad u'_i(S_2) = u'_i(S_4) \tag{42}$$

Since the out-of-plane and in-plane problems are uncoupled, the coefficients $\mathbf{F}_n^f$ and $\mathbf{G}_n^f$ are found independent of the coefficients $\mathbf{H}_n^f$ upon utilizing the reduced periodicity conditions in the variational principle. By implementing the reduced periodicity conditions for the in-plane problem in the first variation of the functional, Eq. (40), we obtain

$$\sum_{i=1}^{2} \int_{S_i} \{\delta T_2(S_i)[u'_2(S_i) - u'_2(S_{i+2})] + \delta T_3(S_i)[u'_3(S_i) - u'_3(S_{i+2})]\} dS$$
$$+ \sum_{i=3}^{4} \int_{S_i} \{\delta u'_2(S_i)[T_2(S_i) + T_2(S_{i-2})] + \delta u'_3(S_i)[T_3(S_i)$$
$$+ T_3(S_{i-2})]\} dS = 0 \tag{43}$$

from which the system of equations for the unknown coefficients $\mathbf{F}_n^f$ and $\mathbf{G}_n^f$ is obtained in the form

$$\hat{\mathbf{A}}[\mathbf{F}^f\mathbf{G}^f]^{\mathrm{T}} = \hat{\mathbf{B}}\bar{\varepsilon}_{\mathrm{in}} \tag{44}$$

where $\bar{\varepsilon}_{\mathrm{in}}=[\bar{\varepsilon}_{11},\bar{\varepsilon}_{22},\bar{\varepsilon}_{33},2\bar{\varepsilon}_{23}]^T$ and $\mathbf{F}^f=[\mathbf{F}_1^f,\ldots,\mathbf{F}_{N_{\max}}^f]$, $\mathbf{G}^f=[\mathbf{G}_1^f,\ldots,\mathbf{G}_{N_{\max}}^f]$. Similarly, for the out-of-plane loading, the first variation of the functional becomes

$$\sum_{i=1}^{2}\int_{S_i}\delta T_1(S_i)[u_1'(S_i)-u_1'(S_{i+2})]dS+\sum_{i=3}^{4}\int_{S_i}\delta u_1'(S_i)[T_1(S_i)+T_1(S_{i-2})]dS=0 \tag{45}$$

from which the system of equations for the unknown coefficients $\mathbf{H}_n^f$ is obtained in the form

$$\tilde{\mathbf{A}}\mathbf{H}^f = \tilde{\mathbf{B}}\bar{\varepsilon}_{\mathrm{out}} \tag{46}$$

where $\bar{\varepsilon}_{\mathrm{out}}=[2\bar{\varepsilon}_{12},2\bar{\varepsilon}_{13}]^T$ and $\mathbf{H}^f=[\mathbf{H}_1^f,\ldots,\mathbf{H}_{N_{\max}}^f]$. The elements of the matrices $\hat{\mathbf{A}},\tilde{\mathbf{A}}$ and $\hat{\mathbf{B}},\tilde{\mathbf{B}}$ in the above equations are obtained in terms of surface integrals along the four sides $S_1,\ldots,S_4$ of the unit cell.

2.3 Homogenized Constitutive Equations. Once the solution for the coefficients $\mathbf{F}_n^f$, $\mathbf{G}_n^f$, and $\mathbf{H}_n^f$ is obtained, the average fiber strains $\bar{\boldsymbol{\varepsilon}}^f$ are then related to average macroscopic strains through the localization relation

$$\bar{\boldsymbol{\varepsilon}}^f = \mathbf{A}^f\bar{\boldsymbol{\varepsilon}} \tag{47}$$

where $\mathbf{A}^f$ is Hill's elastic strain concentration matrix for the fiber phase [2]. The average fiber strains are obtained in closed form upon integrating the local expressions over the fiber cross section. The resulting expressions for the average fiber strains contain only the applied average strains and the displacement coefficients associated with the $n=0,2$ harmonics in the case of transverse normal and shear strains, and the $n=1$ harmonic in the case of axial shear strains

$$\begin{aligned}
\bar{\varepsilon}_{22}^f &= \bar{\varepsilon}_{22}+F_{01}^f+\frac{3}{4\nu_f}F_{21}^f+F_{22}^f\\
\bar{\varepsilon}_{33}^f &= \bar{\varepsilon}_{33}+F_{01}^f-\frac{3}{4\nu_f}F_{21}^f-F_{22}^f\\
\bar{\varepsilon}_{23}^f &= \bar{\varepsilon}_{23}+\frac{3}{4\nu_f}G_{21}^f+G_{22}^f\\
\bar{\varepsilon}_{12}^f &= \bar{\varepsilon}_{12}+\frac{1}{2}H_{11}^f\\
\bar{\varepsilon}_{13}^f &= \bar{\varepsilon}_{13}+\frac{1}{2}H_{12}^f
\end{aligned} \tag{48}$$

Use of the above relations in the expression for the average unit cell stress, in conjunction with the volume-averaged stress-strain relations within each phase, leads to the macroscopic constitutive equation for the two-phase composite considered herein in the form

$$\bar{\boldsymbol{\sigma}} = \mathbf{C}^*\bar{\boldsymbol{\varepsilon}} \tag{49}$$

where the homogenized stiffness matrix $\mathbf{C}^*$ is given in terms of the fiber volume fraction v_f, phase elastic moduli $\mathbf{C}^f$, $\mathbf{C}^m$, and the elastic Hill strain concentration matrix for the fiber phase,

$$\mathbf{C}^* = \mathbf{C}^m + v_f(\mathbf{C}^f-\mathbf{C}^m)\mathbf{A}^f \tag{50}$$

when the RUC contains just the two phases. Because the out-of-plane and the inplane loading are uncoupled, the localization relations can be separately written for each loading type in matrix form as follows:

$$\begin{bmatrix}\bar{\varepsilon}_{11}\\ \bar{\varepsilon}_{22}\\ \bar{\varepsilon}_{33}\\ 2\bar{\varepsilon}_{23}\end{bmatrix}^f=\begin{bmatrix}1&0&0&0\\ A_{21}&A_{22}&A_{23}&A_{24}\\ A_{31}&A_{32}&A_{33}&A_{34}\\ A_{41}&A_{42}&A_{43}&A_{44}\end{bmatrix}^f\begin{bmatrix}\bar{\varepsilon}_{11}\\ \bar{\varepsilon}_{22}\\ \bar{\varepsilon}_{33}\\ 2\bar{\varepsilon}_{23}\end{bmatrix} \tag{51}$$

for in-plane loading and

$$\begin{bmatrix}2\bar{\varepsilon}_{13}\\ 2\bar{\varepsilon}_{12}\end{bmatrix}^f=\begin{bmatrix}A_{55}&A_{56}\\ A_{65}&A_{66}\end{bmatrix}^f\begin{bmatrix}2\bar{\varepsilon}_{13}\\ 2\bar{\varepsilon}_{12}\end{bmatrix} \tag{52}$$

for out-of-plane loading.

To determine the elements of the $\mathbf{A}^f$ matrix for the fiber phase, we impose one nonzero average strain of a known magnitude at a time, with the remaining average strains kept zero. By solving the appropriate global system of equations for this particular average strain state, we obtain the unknown coefficients $\mathbf{F}_n^f$, $\mathbf{G}_n^f$, or $\mathbf{H}_n^f$, depending on the applied loading, and thus the average fiber strains. The elements of the strain concentration matrix occupying the column that corresponds to the applied nonzero average strain in Eqs. (51) and (52) are then obtained by taking the ratio of the averaged strain for the fiber phase and the average applied strain. For instance, for the loading involving the nonzero average axial strain: $\bar{\varepsilon}_{11}=0.01$ with $\bar{\varepsilon}_{22}=0$, $\bar{\varepsilon}_{33}=0$, and $\bar{\varepsilon}_{23}=0$, we pick up the elements of the first column of $\mathbf{A}^f$,

$$A_{11}^f=\frac{\bar{\varepsilon}_{11}^f}{\bar{\varepsilon}_{11}}=1,\quad A_{21}^f=\frac{\bar{\varepsilon}_{22}^f}{\bar{\varepsilon}_{11}},\quad A_{31}^f=\frac{\bar{\varepsilon}_{33}^f}{\bar{\varepsilon}_{11}},\quad A_{41}^k=\frac{2\bar{\varepsilon}_{23}^f}{\bar{\varepsilon}_{11}}$$

The elements of the second, third, and fourth columns of the in-plane strain concentration matrix are generated in a similar way, as are the elements of the out-of-plane concentration matrix.

Incorporation of spatially uniform temperature change to determine the homogenized thermal expansion coefficient presents no problem. Extension of the above approach to multi-inclusion unit cells will be presented elsewhere.

3 Numerical Results

We demonstrate the developed approach's accuracy and efficacy by calculating the homogenized moduli and local displacement and stress fields of a unit cell containing a single offset fiber, Fig. 1(*b*), and compare the results with those generated by the commercial finite-element code FEMLAB. The homogenized moduli were calculated as a function of the fiber volume fraction up to $v_f=0.70$ in increments of 0.05, which is just below the maximum allowed for the considered square array. Alternatively, the local displacement and stress fields were generated for the specific fiber volume fraction of 0.35. For the homogenized moduli calculations, the finite-element results were generated by using a unit cell containing a centered fiber which, when subjected to periodic boundary conditions, must produce the same results as those of the same unit cell with the offset fiber for the considered square array, providing an additional check. On the other hand, the microlevel stress fields were generated by using the same unit cell geometry with offset fiber as that employed in the analytical model calculations. Two cases with the relatively large moduli contrast $E_f/E_m=10$ and 10^{-6} were considered, with the second case practically representing a porous composite. For the first case, the material properties of the elastic inclusions are representative of glass, with $E=70$ GPa and $\upsilon=0.22$, and those of the matrix are representative of epoxy, $E=7$ GPa and $\upsilon=0.3$. For the second case, Young's modulus of the fiber was accordingly adjusted.

When comparing the homogenized moduli and local fields predicted by the locally exact theory with the finite-element results, we also demonstrate the convergence of these quantities with increasing number of harmonics employed in the analytical solution of the unit cell problem.

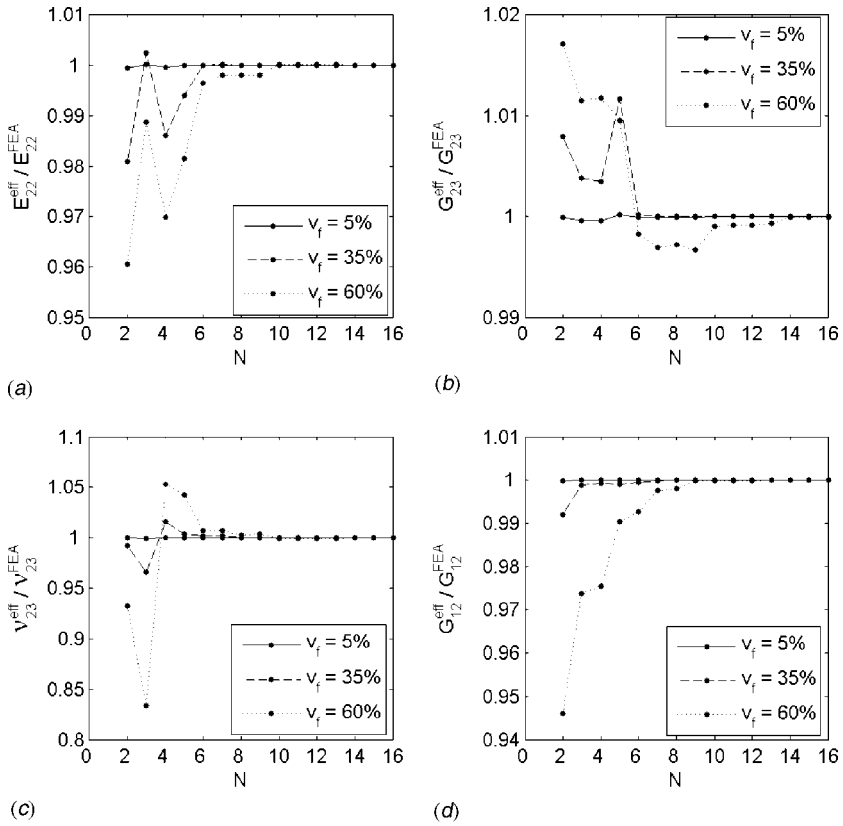

Fig. 2 Convergence of the predicted homogenized moduli with the number of harmonics used in the displacement field representation relative to the finite-element results for a unit cell with an off-center fiber for fiber volume fractions of 0.05, 0.35, and 0.60 with $E_f/E_m=10$ moduli ratio: (*a*) E_{22}^*, (*b*) G_{23}^*, (*c*) ν_{23}^*, and (*d*) G_{12}^*

3.1 Homogenized Engineering Moduli. The effective engineering moduli were determined from the knowledge of the effective compliance matrix $\mathbf{S}^*$. This matrix is the inverse of the effective stiffness matrix $\mathbf{C}^*$ appearing in homogenized Hooke's law in Eqs. (49) and (50). Given that the elements of $\mathbf{S}^*$ are directly expressed in terms of the engineering moduli, and $\mathbf{S}^*=[\mathbf{C}^*]^{-1}$, the effective engineering moduli $E_{11}^*, E_{22}^*, E_{33}^*, \nu_{12}^*, \nu_{23}^*, \nu_{13}^*, G_{23}^*, G_{12}^*, G_{13}^*$ for an orthotropic material then become

$$E_{11}^*=\frac{1}{S_{11}^*},\quad E_{22}^*=\frac{1}{S_{22}^*},\quad E_{33}^*=\frac{1}{S_{33}^*}$$

$$\frac{\nu_{12}^*}{E_{11}^*}=-S_{21}^*,\quad \frac{\nu_{13}^*}{E_{11}^*}=-S_{31}^*,\quad \frac{\nu_{23}^*}{E_{22}^*}=-S_{32}^* \tag{53}$$

$$G_{23}^*=\frac{1}{S_{44}^*},\quad G_{13}^*=\frac{1}{S_{55}^*},\quad G_{12}^*=\frac{1}{S_{66}^*}$$

In our case, the considered square array produces six independent elastic moduli with $E_{22}^*=E_{33}^*$, $G_{12}^*=G_{13}^*$, and $\nu_{12}^*=\nu_{13}^*$.

An alternative manner of calculating the homogenized moduli involves direct imposition of unidirectional loading in the form of one nonzero macroscopic stress component applied at a time, in conjunction with the use of engineering definitions. To accomplish this requires the determination of correct proportions of macroscopic strains using homogenized Hooke's law since the macroscopic strains serve as the loading parameters in our theory. This alternative approach was indeed verified to produce identical results.

Figure 2 illustrates the convergence of the homogenized moduli E_{22}^*, G_{23}^*, ν_{23}^*, and G_{12}^*, normalized by the corresponding finite-element results, with the number of harmonics employed in the displacement fields given by Eqs. (15) and (24) for the fiber volume fractions of 0.05, 0.35, and 0.60, and the moduli contrast $E_f/E_m=10$. Remarkably, even with $n=2$ harmonics, the analytical solution produces homogenized moduli, which differ little from the finite-element results. Generally, the initial differences for a particular modulus depend on the fiber volume fraction and typically become larger with increasing volume fraction. As the number of harmonics increases, the predicted moduli converge to the finite-element results in a manner that depends on the fiber volume fraction and the particular modulus. In the case of $E_{22}^*, G_{23}^*, \nu_{23}^*$, initially oscillatory behavior is observed, while in the case of G_{12}^*, monotonic convergence occurs. The relatively small initial oscillations are generally largest for high fiber volume fractions, becoming smaller with decreasing volume fraction, and are typically limited to the low harmonic number range (up to $n=4-5$) beyond which the convergence is monotonic. While for the lower fiber volume fractions convergence rapidly occurs, (by $n=6$), greater number of harmonics is required for $v_f=0.6$, typically $n=10$ for the employed moduli contrast $E_f/E_m=10$. Decreasing the moduli contrast to $E_f/E_m=10^{-6}$ (not shown) only affects the extent of deviation from the finite-element predictions in the low harmonic number range without affecting the asymptotic convergence, which is similar to that for the large moduli contrast. Homogenized moduli of unit cells with large porosity content ($v_f=0.60$) exhibit initial deviations from the finite-element predictions that are substantially larger than those of the large moduli contrast, while the intermediate and low porosity content unit cells produce comparable homogenized moduli deviations.

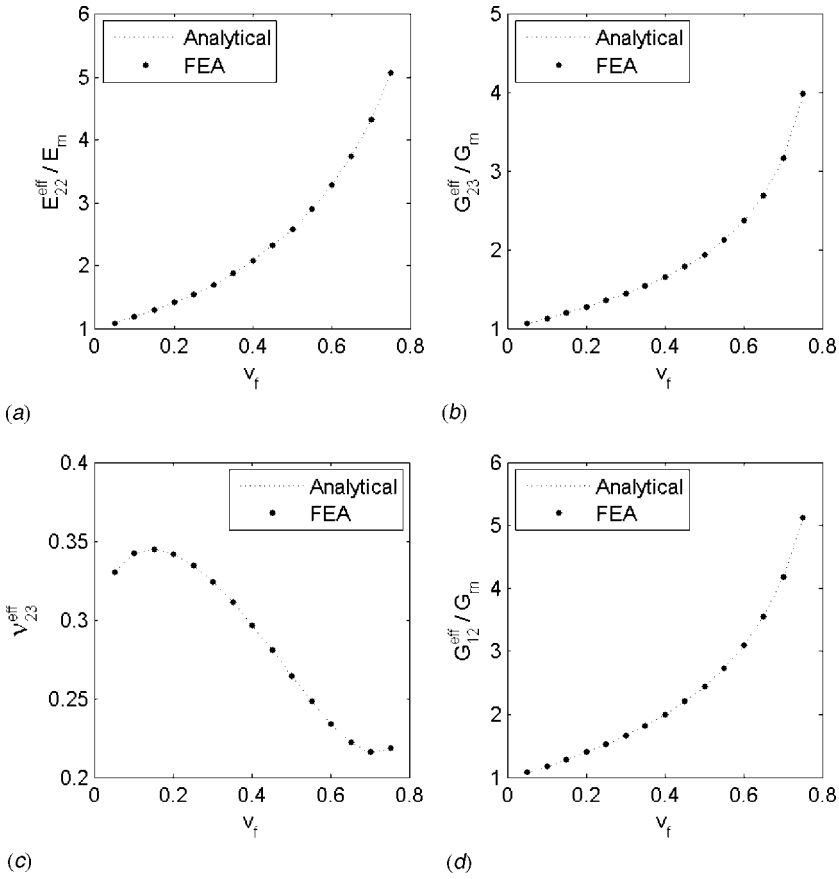

Fig. 3 Comparison of the locally exact predictions for the effective moduli as a function of the fiber volume fraction with the finite-element calculations for unidirectional composites with $E_f/E_m=10$ moduli ratio: (*a*) E_{22}^*, (*b*) G_{23}^*, (*c*) ν_{23}^*, and (*d*) G_{12}^*

We note that the convergence of homogenized moduli to the finite-element results in the low harmonic number range depends on the position of the fiber within the unit cell. The results shown in Fig. 2 were generated by keeping the fiber center fixed while increasing the fiber radius to generate the desired volume fractions. Somewhat different results were obtained by placing the fiber center as close to the lower left hand corner of the unit cell shown in Fig. 1(*b*) as possible for the three fiber volume fractions. In this case, the deviations of the homogenized moduli in the low harmonic number range were not as consistent vis-a-vis the fiber volume fraction as those observed in Fig. 2, but the asymptotic behavior was the same.

Figure 3 presents comparison of the converged homogenized moduli E_{22}^*, G_{23}^*, ν_{23}^*, and G_{12}^* as a function of the fiber volume fraction predicted by the present solution with the corresponding moduli obtained from the finite-element analysis of a unit cell with a centered fiber. The moduli contrast $E_f/E_m=10$ was employed in the calculations. The homogenized moduli were normalized by the corresponding matrix modulus (with the exception of major transverse Poisson's ratio ν_{23}^*). The analytical results were generated using typically 16 harmonics for each fiber volume fraction. This number ensured converged results based on the study shown in Fig. 2. As observed, no visible difference is evident between the two sets of results for all homogenized moduli in the entire range of the employed fiber volume fractions. The corresponding results for the moduli contrast $E_f/E_m=10^{-6}$, which simulates a porous composite, are presented in Fig. 4, where again no differences between the analytical and finite-element predictions are observed.

3.2 Local Displacement and Stress Fields. Convergence of the local displacement fields given in Eqs. (15) and (24) and the derived stresses depends on the applied loading. We first demonstrate this convergence for unidirectional loading by the applied macroscopic strain $\bar{\varepsilon}_{22}^o$ with the remaining strain components equal to zero for $v_f=0.35$ and $E_f/E_m=10$. Figure 5 presents the F_{nj}^f coefficients appearing in the displacement field given by Eq. (24) for this uniaxial strain loading in two ways, which demonstrate the convergence behavior of the analytical solution. In Fig. 5(*a*), the first four coefficients F_{01}^f, F_{12}^f, F_{21}^f, and F_{22}^f normalized with respect to the asymptotic values are given as a function of the harmonic number n, where rapid convergence with harmonic number is observed for F_{01}^f, F_{21}^f, and F_{22}^f, with somewhat greater number required for F_{12}^f. In Fig. 5(*b*), we present the magnitudes of all F_{nj}^f coefficients when 20 harmonics are used to approximate the displacement field for this uniaxial loading in order to demonstrate that they decrease with increasing number (although initially in a nonmonotonic manner), so that convergent behavior is obtained in the limit. In fact, these coefficients become very small beyond the $n=4$ harmonic, and remain small and well behaved for larger harmonic numbers. Included in this figure is the convergence behavior of the average strain $\bar{\varepsilon}_{22}$ calculated from the determined displacement field for each harmonic relative to the imposed macroscopic strain $\bar{\varepsilon}_{22}^o$. Similar results are obtained for unidirectional loading by the applied macroscopic strain $\bar{\varepsilon}_{23}^o$ with the remaining strain components equal to zero (not shown). The above results demonstrate that the employed manner of calculating the unknown coefficients for the most demanding loading

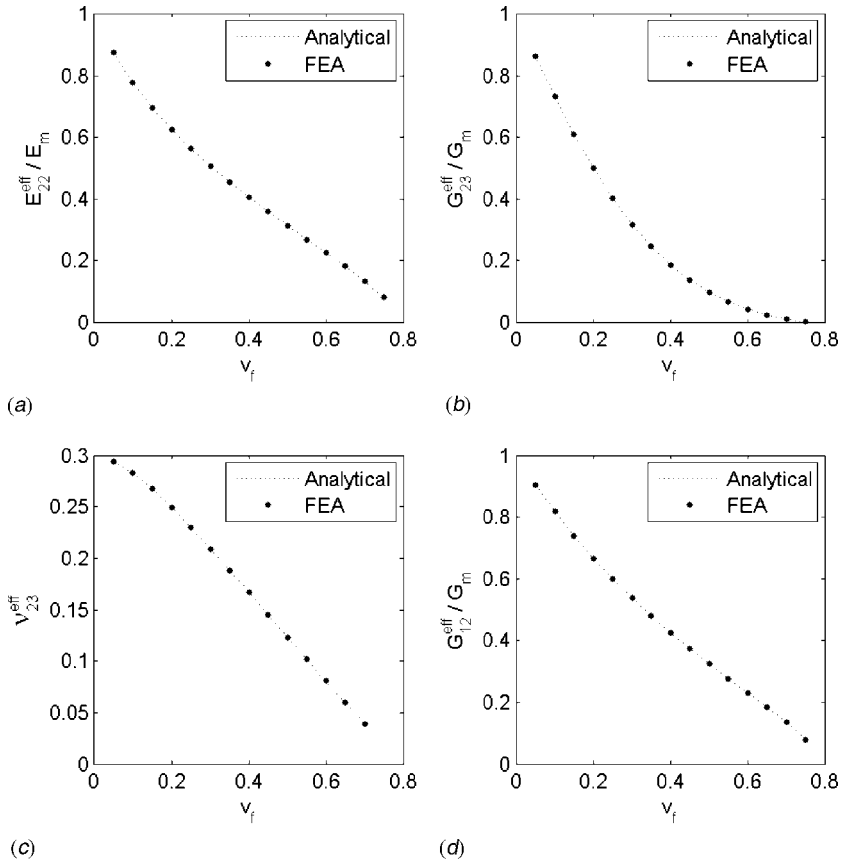

Fig. 4 Comparison of the locally exact predictions for the effective moduli as a function of the fiber volume fraction with the finite-element calculations for unidirectional composites with $E_f/E_m=10^{-6}$ moduli ratio: (*a*) E_{22}^*, (*b*) G_{23}^*, (*c*) ν_{23}^*, and (*d*) G_{12}^*

types (axial normal and shear loading are less demanding) is a stable one that produces convergent results, in contrast with the commonly used and more problematic collocation technique discussed later.

Figure 6 illustrates the local $u_2(y_2,y_3)$ and $u_3(y_2,y_3)$ displacement fields generated by using $n=2$, 8, and 16 harmonics in Eq. (24), and the corresponding converged finite-element results obtained by using 938 quadratic triangular elements. Even with $n=8$ harmonics, the analytical results are of graphical quality that is comparable to the finite-element results. The corresponding local $\sigma_{22}(y_2,y_3)$, $\sigma_{23}(y_2,y_3)$, and $\sigma_{33}(y_2,y_3)$ stress fields generated by this loading are shown in Fig. 7. Again, only $n=8$ harmonics are needed to yield high-fidelity stress fields relative to the finite-element results. We note that for the lowest number of harmonics that can be employed, $n=2$, the predicted local stress fields exhibit correct qualitative characteristics that become refined with increasing number of harmonics. For instance, in the case of the $\sigma_{22}(y_2,y_3)$ stress field, the stress in the fiber is uniform as would be expected of the Eshelby problem solution [20], and its magnitude is relatively close to that of the converged solution. Furthermore, the matrix stress has the same qualitative distribution. Increasing the number of harmonics introduces more nonuniformity in the fiber stress distribution and more refinement in the matrix stress distribution, as would be expected due to the interaction with adjacent fibers for this unit cell with the fiber volume fraction of 0.35. Similar observations hold for the $\sigma_{23}(y_2,y_3)$ and $\sigma_{33}(y_2,y_3)$ stress fields where increasing the number of harmonics has a greater effect on the matrix than the fiber stresses. Generally, increasing the number of harmonics improves the stress distributions around periphery of the unit cell and to a lesser extent within the fiber. The details of stress fields at the fiber/matrix interface are well captured with small numbers of harmonics.

For computational efficiency comparison, we present the execution times (up to and including the solution of Eqs. (44) and (46)) as a function of the number of harmonics for the above unidirectional loading of the considered unit cell in Fig. 8. The data points were determined by taking the average of 20 run times for each harmonic number. We note that the determination of the elements of the global matrices $\hat{\mathbf{A}},\tilde{\mathbf{A}}$ in the above equations involved the evaluation of eight and four integrals, respectively, which were calculated by using 32 Gauss points. As an example, the analytical results generated using 16 harmonics in the displacement field representation, which resulted in 63 unknown coefficients, were obtained in 17.57 s in an uncompiled MATLAB environment. In contrast, the finite-element results generated by using 938 quadratic triangular elements, which resulted in 3875 degrees of freedom, required 0.5 s in the FEMLAB environment on the same 2 GHz machine with 2 Gbytes of RAM. Decreasing the number of harmonics to 8, which produces acceptably accurate homogenized moduli and local displacement and stress fields, reduced the execution time to 4.39 s. On the other hand, use of 16 harmonics in our analytical solution based on periodic boundary conditions implemented in a pointwise collocation sense produced a solution in 0.047 s [21]. The large difference between the collocation and variational principle-based implementation of the periodic boundary conditions is due to the time-consuming calculation of the integrals required in the accurate determination of the ele-

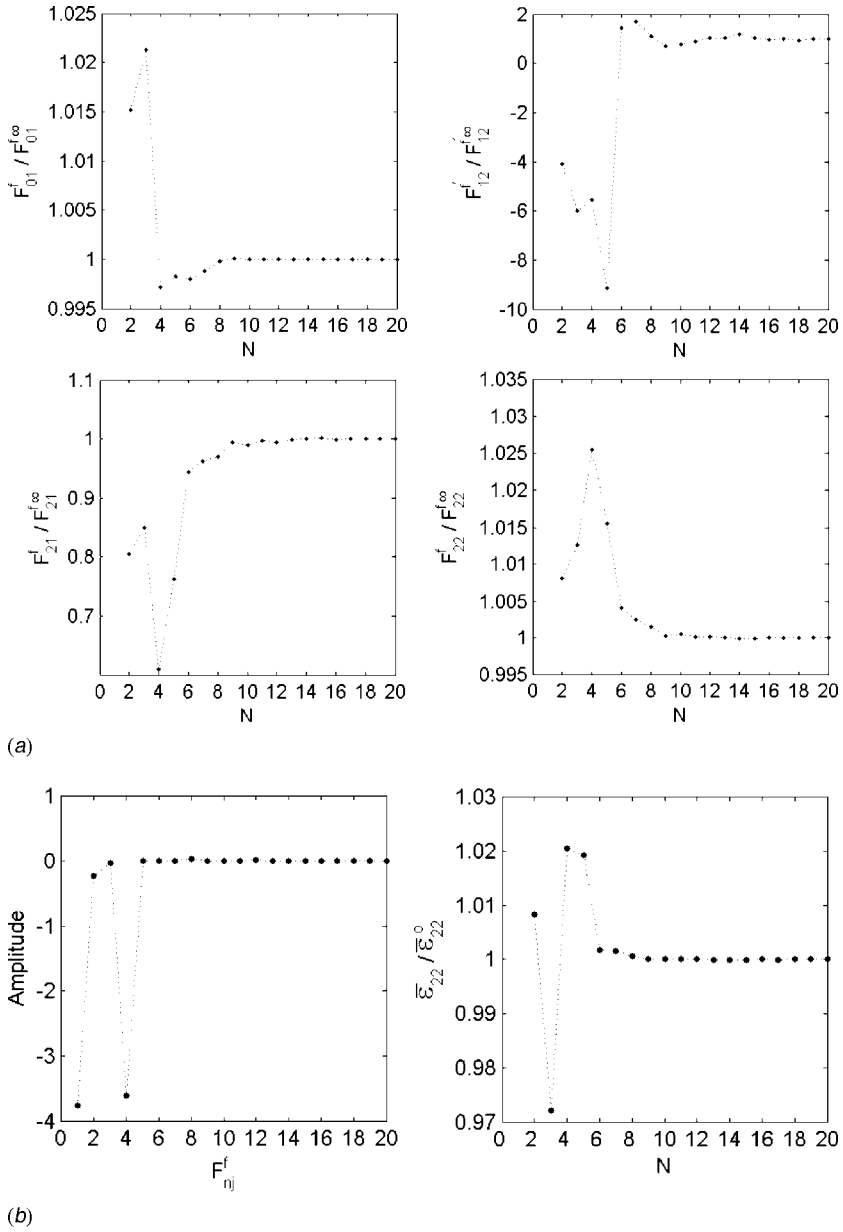

Fig. 5 (*a*) **Convergence of the coefficients F^f_{nj} with the number of harmonics for a unit cell with an off-center fiber, v_f=0.35, and E_f/E_m=10 moduli ratio subjected to loading by $\bar{\varepsilon}_{22}$ only and** (*b*) **amplitude** ($\times 10^{-3}$) **of 20 coefficients** (**left**) **and the convergence of $\bar{\varepsilon}_{22}$ with the number of harmonics** (**right**)

ments of $\hat{\mathbf{A}}, \tilde{\mathbf{A}}$, which is the price for superior stability and rapid convergence. Means of reducing the boundary integral calculation time without sacrificing accuracy will be investigated in our future studies. However, it should be noted that a realistic comparison of the analytical and finite-element solutions would also include the time consumed in defining the problem (mesh generation, etc.), which is virtually insignificant for our approach compared to the finite-element method.

Figure 9 presents comparison of the converged $\sigma_{23}(y_2, y_3)$, $\sigma_{22}(y_2, y_3)$, and $\sigma_{33}(y_2, y_3)$ stress fields generated by using 16 harmonics in the displacement field representation with the finite-element results for unidirectional loading by $\bar{\varepsilon}_{23}$ only. Comparison of local $\sigma_{12}(y_2, y_3)$ and $\sigma_{13}(y_2, y_3)$ stress fields produced by unidirectional loading by $\bar{\varepsilon}_{13}$ only is shown in Fig. 10. In both cases, the moduli contrast E_f/E_m=10 was employed to generate the results. As in the preceding case, no differences are observed between the analytical and finite-element predictions of the local stress fields.

4 Discussion

Our variational principle has been motivated by the work of Jirousek [19] who had proposed the following augmented functional in developing a finite-element procedure locally satisfying all field equations:

$$H_J = \frac{1}{2}\int_V \sigma_{ij}\varepsilon_{ij}dV - \int_{S_t} T_i^o u_i dS - \int_{S_u} T_i(u_i - u_i^o)dS \qquad (54)$$

This functional represents the potential energy subject to the displacement constraint over S_u, which can be interpreted in the con-

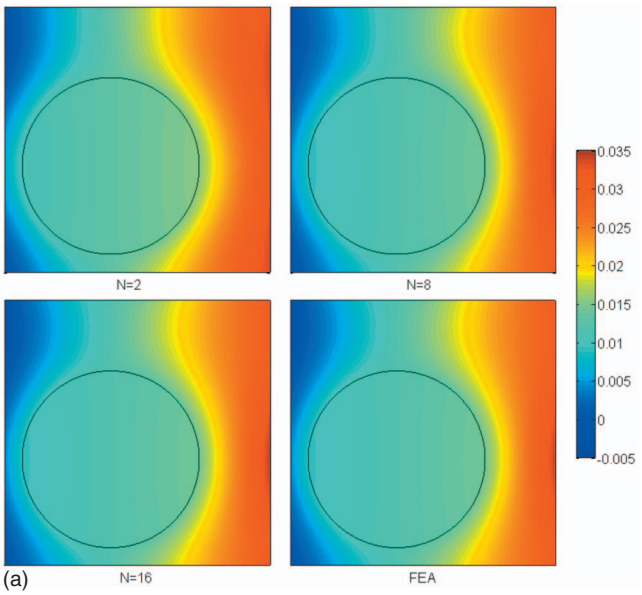

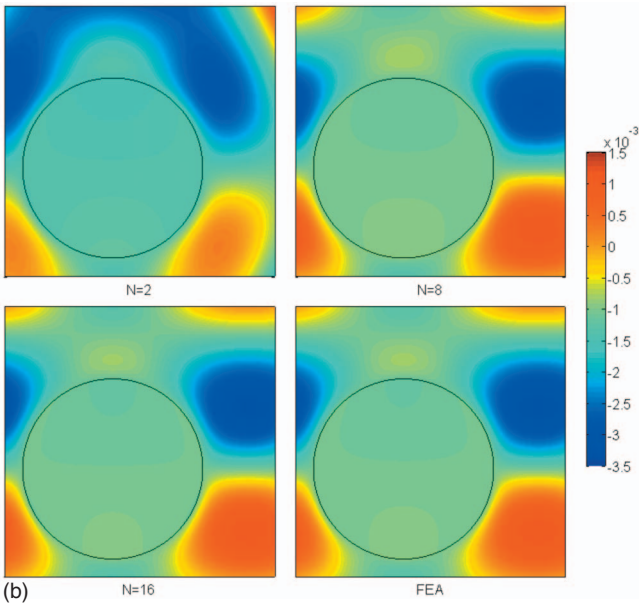

Fig. 6 Convergence of the predicted local displacement fields with the number of harmonic terms used in the displacement field representation relative to the finite-element results under loading by $\bar{\varepsilon}_{22}$ only for a unit cell with an off-center fiber and $E_f/E_m=10$ moduli ratio: (*a*) u_2 and (*b*) u_3

text of our problem as a constraint on the periodic displacement boundary conditions over a portion of the RUC boundary. This principle leads to the variational statement

$$\int_{S_T} \delta u_i (T_i - T_i^o) dS - \int_{S_u} \delta T_i (u_i - u_i^o) dS = 0 \qquad (55)$$

which is almost identical to the statement that follows from our principle, Eq. (40), except for the sign difference. The implementation of the above variational statement into the periodic unit cell problem based on our locally exact interior elasticity solution produced results that exhibited erratic convergence characteristics, but often yielded acceptably good results relative to the finite-element predictions with sufficiently large number of harmonics.

The search for a new variational principle was motivated by the need to satisfy periodic boundary conditions on the unit cell

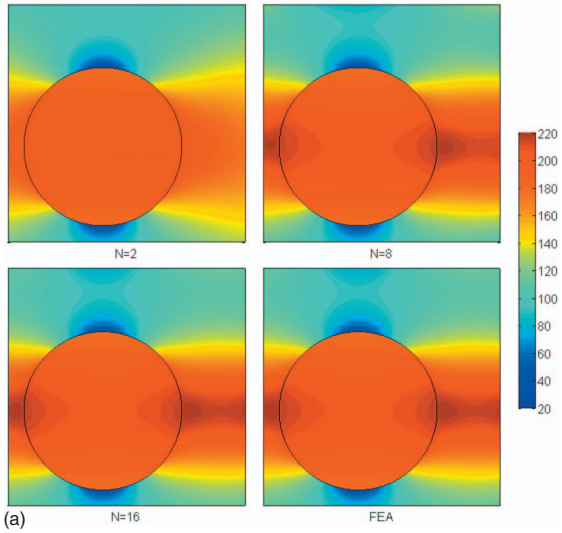

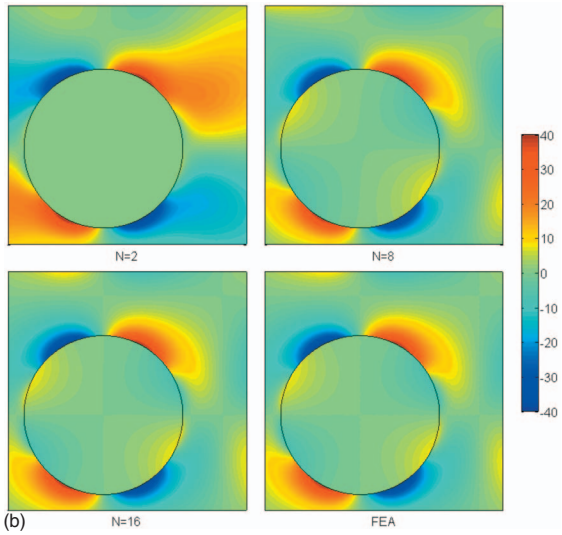

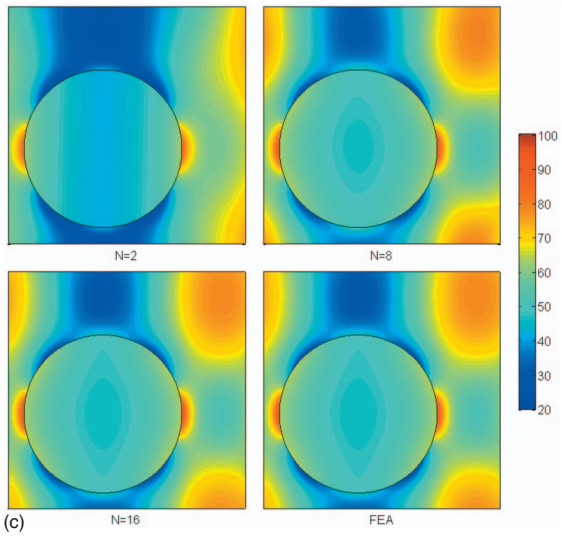

Fig. 7 Convergence of the predicted local stress fields with number of harmonics used in the displacement field representation relative to the finite-element results under loading by $\bar{\varepsilon}_{22}$ only for a unit cell with an off-center fiber and $E_f/E_m=10$ moduli ratio: (*a*) σ_{22}, (*b*) σ_{23}, and (*c*) σ_{33}

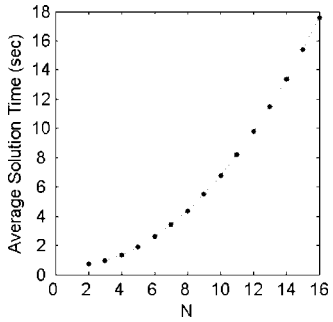

Fig. 8 Average solution time as a function of the number of harmonic terms in the displacement field representation in a unit cell with an off-center fiber and $E_f/E_m=10$ moduli ratio loaded by $\bar{\varepsilon}_{22}$ only

boundary displacements as well as on the tractions, Eqs. (1) and (2), which are not specified in explicit form, in contrast with the standard minimization problems involving potential or complementary energy. The proposed functional puts the periodic boundary displacements and tractions on the same footing.

The use of the proposed variational principle in satisfying the periodic boundary conditions substantially improves the convergence of the homogenized moduli and local fields with increasing number of harmonics used in the displacement field approximation relative to the results based on the constrained potential energy principle as well as the collocation technique. As an illustration, Fig. 11 shows the convergence of the homogenized moduli E_{22}^* and G_{23}^* as a function of the harmonic number n generated for the moduli contrast $E_f/E_m=10$ and $v_f=0.35$ by using the collocation technique in satisfying periodic boundary conditions. While the transverse Young's modulus E_{22}^* fluctuates with increasing harmonic number before converging at $n=24$, the transverse shear modulus G_{23}^* converges much more quickly and generally in an asymptotic manner without substantial fluctuations. This is in contrast with the homogenized moduli based on our variational principle, which exhibited similar convergence characteristics independent of the given modulus. Furthermore, the magnitudes of these moduli in the low harmonic number range are much greater than the corresponding values based on our variational principle shown in Fig. 2. On the other hand, the local stress fields based on the collocation technique generated with $n=16$ compared well to the finite-element results and were of comparable quality as those generated with $n=8$ based on the proposed variational principle. Nonetheless, increasing the number of harmonics produced often unstable behavior and yielded ill-conditioned system of equations for the unknown coefficients.

The implemented variational principle produces much better convergence and exhibits better stability than the collocation technique employed by others in constructing elasticity-based solutions to unit cell problems, cf. Zielinski and Herrera [22]. This feature, in addition to the two-scale expansion representation of the displacement field within the unit cell based on the homogenization framework, and the use of periodicity conditions that makes the analysis of unit cells lacking apparent planes of symmetry possible, sets our locally exact homogenization theory apart from others.

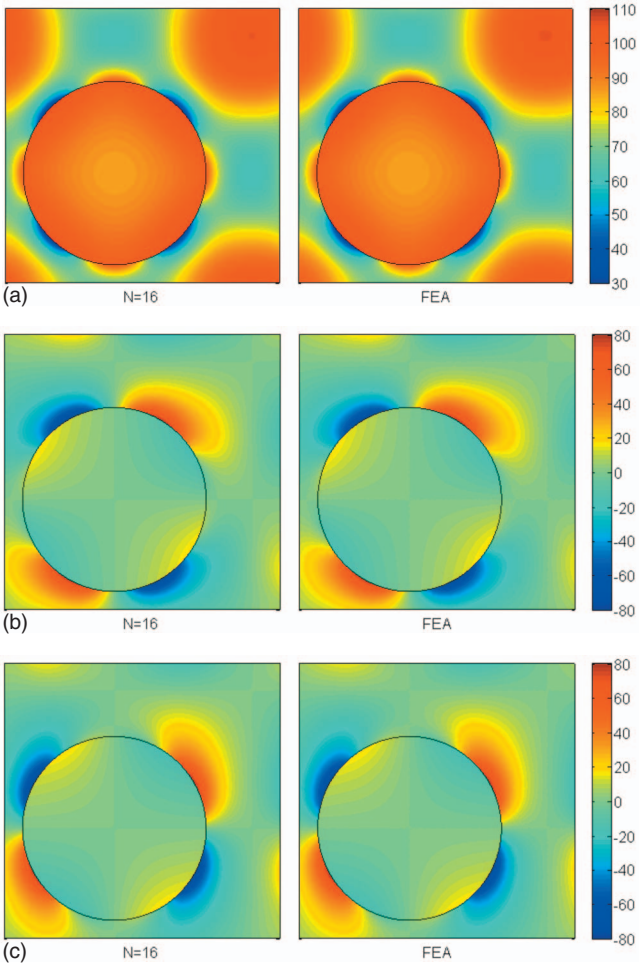

Fig. 9 Comparison of the converged local stress fields predicted by the locally exact homogenization theory with the finite-element results for loading by $\bar{\varepsilon}_{23}$ only for a unit cell with an off-center fiber and $E_f/E_m=10$ moduli ratio: (*a*) σ_{23}, (*b*) σ_{22}, and (*c*) σ_{33}

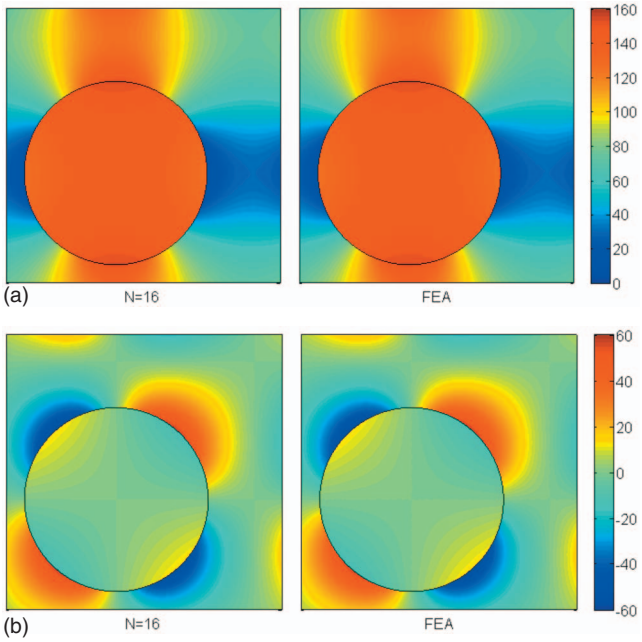

Fig. 10 Comparison of the converged local stress fields predicted by the locally exact homogenization theory with the finite-element results for loading by $\bar{\varepsilon}_{13}$ only for a unit cell with an off-center fiber and $E_f/E_m=10$ moduli ratio: (*a*) σ_{13} and (*b*) σ_{12}

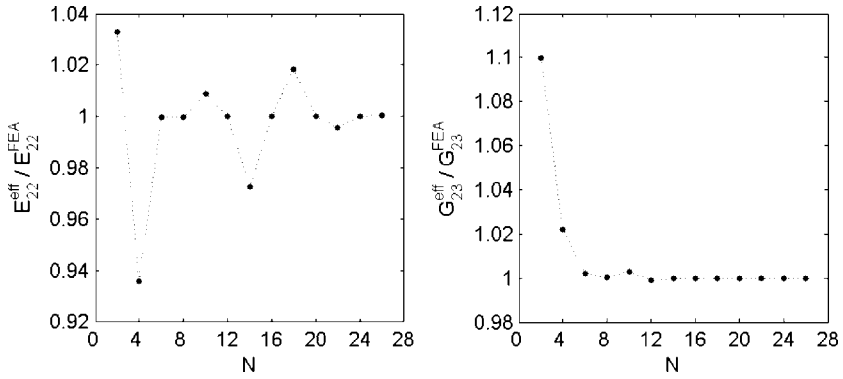

Fig. 11 Convergence of the predicted homogenized moduli with the number of harmonics used in the displacement field representation relative to the finite-element results for a unit cell with an off-center fiber, fiber volume fraction $\nu_f = 0.35$, and $E_f/E_m = 10$ moduli ratio using collocation-based periodic boundary conditions

5 Limitations and Future Extensions

The present development is limited to periodic materials with unidirectionally oriented isotropic phases, which are characterized by unit cells containing single inclusions with circular cross sections arranged in a rectangular or a square array. Thus, homogenized moduli of periodic materials with cubic or orthotropic material symmetries can be generated by the present analysis. Calculation of homogenized transversely isotropic moduli of periodic materials with planes of isotropy perpendicular to the reinforcement direction requires analysis of hexagonal arrays. The present framework is sufficiently general to accommodate such arrays and this will be accomplished in our future work, as will the generalization to accommodate transversely isotropic or orthotropic constituents based on the solutions developed by Davison et al. [18] for the problem of a multiple concentric cylinder under arbitrary transverse loading. The full utility of the present approach for the elastic response of periodic unidirectionally reinforced materials will be realized upon extending the framework to multi-inclusion unit cells, which we are presently considering. Locally exact solutions are also possible for continuous inclusion cross sections other than circular, as well as for three-dimensional inclusions such as spheres and ellipsoids, and this is also a direction worth pursuing based on the quality of presented results.

Thus, the locally exact homogenization approach has its place in the area of micromechanics of heterogeneous materials, and it holds promise with further development. Nonetheless, its applicability does have limitations given the difficulty of constructing locally exact solutions in the presence of inelastic and finite-deformation effects. In fact, only few exact elasticity solutions are available in the presence of these effects, which are typically limited to axisymmetric loading situations.

6 Summary and Conclusions

A new analytical micromechanics technique for the elastic response of periodic, unidirectionally reinforced heterogeneous materials has been developed by using elements of the homogenization theory and Fourier series representation of the local displacement fields. At present, unit cells with circular isotropic inclusions that may lack planes of material symmetry (i.e., containing offset fibers) can be accommodated. The governing elasticity equations for the displacement and stress fields within the fiber and matrix phases, and the concomitant fiber/matrix continuity conditions, are exactly satisfied, but the boundary conditions are enforced by using a new variational principle given that the outer problem is not separable.

The conducted convergence study indicates that the number of harmonics necessary to obtain accurate results does not depend on the desired homogenized modulus, with relatively few harmonics required for converged results depending on the fiber volume fraction. This is in contrast with the homogenized moduli obtained by using the same solution based on collocation periodic boundary conditions, where different convergence behavior was observed for different moduli. Comparison of the homogenized moduli over a wide range of volume fractions calculated by using the present and finite-element approaches demonstrates the new model's accuracy for a unidirectional composite with relatively large fiber/matrix modulus mismatch. The local stress fields are also well captured with relatively few harmonics. The advantage of the present model over the finite-element approach lies in its implementability and relatively quick data generation, comprised of input data construction and execution times.

The results presented herein demonstrate the viability of using the locally exact solution approach in constructing homogenization theories for periodic materials. The difficulty occurs on the unit cell boundaries, which require a new method of implementing periodic boundary conditions that ensures smooth and predictable convergence behavior, such as the one proposed herein based on a variational principle.

Acknowledgment

The first author (A.S.D.) thanks the Civil Engineering Department at the University of Virginia for providing support that enabled him to conduct this investigation. The second author (M.J.P.) acknowledges the Engineered Materials Concepts, LLC for providing partial support.

References

[1] Drago, A. S., and Pindera, M.-J., 2007, "Micro-Macromechanical Analysis of Heterogeneous Materials: Macroscopically Homogeneous vs Periodic Microstructures," Compos. Sci. Technol. **67**(6), pp. 1243–1263.
[2] Hill, R., 1963, "Elastic Properties of Reinforced Solids: Some Theoretical Principles," J. Mech. Phys. Solids, **11**, pp. 357–372.
[3] Sanchez-Palencia, E., 1980, *Non-Inhomogeneous Media and Vibration Theory* Lecture Notes in Physics Vol. 127, Springer-Verlag Berlin.
[4] Suquet, P. M., 1987, *Elements of Homogenization for Inelastic Solid Mechanics* Lecture Notes in Physics Vol. 272, Springer-Verlag, Berlin, pp. 193–278.
[5] Bansal, Y., and Pindera, M.-J., 2005, "A Second Look at the Higher-Order Theory for Periodic Multiphase Materials," ASME J. Appl. Mech., **72**, pp. 177–195. see also NASA CR2004-213043.
[6] Bansal, Y., and Pindera, M.-J., 2006, "Finite-Volume Direct Averaging Micromechanics of Heterogeneous Materials With Elastic-Plastic Phases," Int. J. Plast., **22**(5), pp. 775–825.
[7] Chen, C. H., and Cheng, S., 1967, "Mechanical Properties of Fiber Reinforced Composites," J. Compos. Mater., **1**, pp. 30–41.
[8] Pickett, G., 1968, "Elastic Moduli of Fiber Reinforced Plastic Composites," *Fundamental Aspect of Fiber Reinforced Plastic Composites*, R. T. Schwartz and H. S. Schwartz, eds., Wiley, New York, pp. 13–27.
[9] Leissa, A. W., and Clausen, W. E., 1968, "Application of Point Matching to

Problems in Micromechanics," *Fundamental Aspects of Fiber Reinforced Plastic Composites*, R. T. Schwartz and H. S. Schwartz, eds., Wiley New York, pp. 29–44.
[10] Heaton, M. D., 1968, "A Calculation of the Elastic Constants of a Unidirectional Fibre-Reinforced Composite," Br. J. Appl. Phys., J. Phys. D, **2**(1), pp. 1039–1048.
[11] Koiter, W. T., 1960, "Stress Distribution in an Infinite Elastic Sheet With a Doubly-Periodic Set of Equal Holes," *Boundary Value Problems in Differential Equations*, R. E. Langer, ed., The University of Wisconsin Press, Madison, pp. 191–213.
[12] Fil'shtinskii, L. A., 1964, "Stresses and Displacements in an Elastic Plane Weakened by a Doubly Periodic System of Identical Circular Holes," Prikl. Mat. Mekh., **28**(3), pp. 430–441.
[13] Wilson, H. B., and Hill, J. L., 1965, "Plane Elastostatic Analysis of an Infinite Plate with a Doubly Periodic Array of Holes or Rigid Inclusions," Mathematical Studies of Composite Materials II, Report No. S-50, Rohm and Hass Company Redstone Arsenal Research Division, Huntsville, AL, pp. 39–66.
[14] Grigolyuk, E. I., and Fil'shtinskii, L. A., 1966, "Elastic Equilibrium of an Isotropic Plane With Doubly Periodic System of Inclusions," Sov. Appl. Mech., **2**(9), pp. 1–7.
[15] Wang, J., Mogilevskaya, S. G., and Crouch, S. L., 2005, "An Embedding Method for Modeling Micromechanical Behavior and Macroscopic Properties of Composite Materials," Int. J. Solids Struct., **42**, pp. 4588–4612.
[16] Crouch, S. L., and Mogilevskaya, S. G., 2006, "Loosening of Elastic Inclusions," Int. J. Solids Struct., **43**, pp. 1638–1668.
[17] Lipton, R. P., 2003, "Assessment of the Local Stress State Through Macroscopic Variables," Philos. Trans. R. Soc. London, Ser. A, **361**, pp. 921–946.
[18] Davison, T., Pindera, M.-J., and Wadley, H. N. G., 1994, "Elastic Behavior of a Layered Cylinder Subjected to Diametral Loading," Composites Eng., **4**(10), pp. 995–1009.
[19] Jirousek, J., 1978, "Basis for Development of Large Finite Elements Locally Satisfying all Fields Equations," Comput. Methods Appl. Mech. Eng., **14**, pp. 65–92.
[20] Eshelby, J. D., 1957, "The Determination of the Elastic Field of an Ellipsoidal Inclusion, and Related Problems," Proc. R. Soc. London, Ser. A, **241**, pp. 376–396.
[21] Drago, A. S., and Pindera, M.-J., 2008, "A Locally-Exact Homogenization Approach for Periodic Heterogeneous Materials," *Multiscale and Functionally Graded Materials, 2006*, G. H. Paulino, M.-J. Pindera, R. H. Dodds, Jr., F. A. Rochinha, E. V. Dave, and L. Chen, eds., AIP Conf. Proc. No. 973, American Institute of Physics, Melville, NY, pp. 203–208.
[22] Zielinski, A. P., and Herrera, I., 1987, "Trefftz Method: Fitting Boundary Conditions," Int. J. Numer. Methods Eng., **24**, pp. 871–891.

The Imperfection Sensitivity of Isotropic Two-Dimensional Elastic Lattices

Digby D. Symons

Norman A. Fleck

Engineering Department,
Cambridge University,
Trumpington Street,
Cambridge CB2 1PZ, UK

The imperfection sensitivity of the effective elastic properties is numerically explored for three planar isotropic lattices: fully triangulated, the Kagome grid, and the hexagonal honeycomb. Each lattice comprises rigid-jointed, elastic Euler–Bernoulli beams, which can both stretch and bend. The imperfections are in the form of missing bars, misplaced nodes, and wavy cell walls. Their effect on the macroscopic bulk and shear moduli is numerically investigated by considering a unit cell containing randomly distributed imperfections, and with periodic boundary conditions imposed. The triangulated and Kagome lattices have sufficiently high nodal connectivities that they are stiff, stretching dominated structures in their perfect state. In contrast, the perfect hexagonal honeycomb, with a low nodal connectivity of 3, is stretching dominated under pure hydrostatic loading but is bending dominated when the loading involves a deviatoric component. The high connectivity of the triangulated lattice confers imperfection insensitivity: Its stiffness is relatively insensitive to missing bars or to dispersed nodal positions. In contrast, the moduli of the Kagome lattice are degraded by these imperfections. The bulk modulus of the hexagonal lattice is extremely sensitive to imperfections, whereas the shear modulus is almost unaffected. At any given value of relative density and level of imperfection (in the form of missing bars or dispersed nodal positions), the Kagome lattice has a stiffness intermediate between that of the triangulated lattice and the hexagonal honeycomb. It is argued that the imperfections within the Kagome lattice switch the deformation mode from stretching to a combination of stretching and bending. Cell-wall waviness degrades the moduli of all three lattices where the behavior of the perfect structure is stretching dominated. Since the shear response of the perfect hexagonal honeycomb is by bar bending, the introduction of bar waviness has a negligible effect on the effective shear modulus. [DOI: 10.1115/1.2913044]

1 Introduction

There is a current interest in the mechanical properties of two-dimensional and three-dimensional lattice materials. For example, 2D lattices exist as an array of ceramic prismatic tubes in catalytic converters for automotive use. 2D lattices are also used in woven composites, such as triaxially woven carbon fiber epoxy laminates. Natural 2D lattices include the wax honeycomb of the honey bee, wood, and coral. In contrast, bone and sponges form 3D lattices, and 3D woven composites are under development for sandwich cores. In practical applications, these structures are loaded in the elastic regime and it is important to understand the relationship between their microstructure and mechanical properties. We consider in this paper the fundamental problem of the elastic properties of 2D imperfect but isotropic lattices.

It is now well established that the effective properties of lattices are dependent on the degree of nodal connectivity, but no systematic studies have been performed on the imperfection sensitivity of competing lattices of widely varying connectivity. Practical 2D and 3D lattice materials contain imperfections in the form of irregular cells, wavy bars, and possibly missing bars. It is of broad engineering significance to determine imperfection sensitivity of properties: If an imperfection causes a significant drop in a useful property then it may be worthwhile to put in serious effort to manufacture the lattice in as perfect a state as possible. This paper describes an investigation into the imperfection sensitivity of the elastic moduli of three planar *isotropic* lattices: the fully triangulated lattice with a nodal connectivity of $Z=6$, the Kagome lattice with a nodal connectivity of $Z=4$, and the hexagonal honeycomb with a nodal connectivity of $Z=3$, see Fig. 1. All three perfect lattices comprise uniform cell walls (bars) of length l and thickness t.

1.1 Recent Work on the Mechanical Properties of Planar Isotropic Lattices.

Deshpande et al. [1] have shown that whether a lattice is bending or stretching dominated may be informed by a consideration of its nodal connectivity Z, that is, the number of bars attached to each node. The approach is based on Maxwell's [2] equation for the rigidity of pin-jointed structures. If a pin-jointed structure contains a collapse mechanism under a particular loading, then the equivalent rigid-jointed structure will be flexible (bending dominated) under the same loading. Otherwise, both the pin-jointed and equivalent rigid-jointed structures will be stiff (stretching dominated). The necessary (but not sufficient) condition for rigidity of a planar lattice is $Z=4$. The Kagome lattice only just achieves this condition, and we shall show in this study that this has a major impact on its imperfection sensitivity.

The hexagonal honeycomb architecture (Fig. 1(*c*)) is ubiquitous in both natural and man-made materials. Although stiff under equibiaxial (i.e., hydrostatic) loading, it is flexible under deviatoric loading due to its low nodal connectivity. Hydrostatic loading is resisted by stretching of the cell walls, whereas deviatoric loading is resisted by bending of the cell walls. In contrast, the fully triangulated lattice (Fig. 1(*a*)) is stretching dominated under all loading states and is thereby stiff under both hydrostatic and shear loading.

Hyun and Torquato [3] have shown that the Kagome lattice attains the upper Hashin–Shtrikman bound for the stiffness of a two-phase isotropic composite, where one phase is empty space.

Contributed by the Applied Mechanics Division of ASME for publication in the JOURNAL OF APPLIED MECHANICS. Manuscript received September 28, 2007; final manuscript received October 11, 2007; published online July 17, 2008. Review conducted by Robert M. McMeeking.

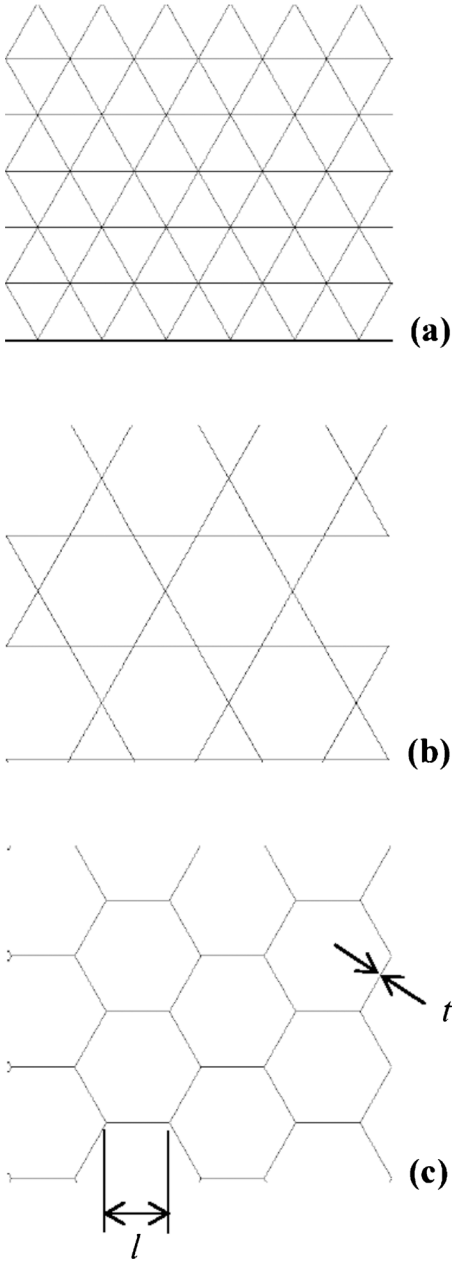

Fig. 1 Perfect geometries of three planar grids: (*a*) triangular, (*b*) Kagome, and (*c*) Hexagonal

In fact, the moduli of the Kagome lattice are identical to those of a triangulated grid of the same relative density $\bar{\rho}$. The high stiffness of the rigid-jointed Kagome lattice is consistent with the collapse response of the infinite pin-jointed version. Hutchinson and Fleck [4] have shown that the infinite pin-jointed Kagome lattice has an infinite number of internal periodic collapse mechanisms, yet none of these mechanisms produces macroscopic strain. Consequently, the Kagome lattice is stretching dominated under both hydrostatic and deviatoric loading.

Symons et al. [5] have explored the morphing potential of the Kagome lattice. They explored the static and kinematic determinacy of the finite, 2D pin-jointed Kagome truss and the finite, double layer grid with Kagome faces. They showed that the addition of patch bars to the periphery of the finite trusses converts them to forms which are statically and kinematically determinate. Thus, on external loading, the structure is stiff. However, if one of the bars is replaced by an axial actuator and extended, the remaining structure behaves as a mechanism with a single degree of freedom. Thus, the structure has a high morphing capability. In order to find application, however, additional studies are needed on the stiffness of the Kagome lattice and its imperfection sensitivity.

The low nodal connectivity of the rigid-jointed Kagome lattice also conveys to it a high fracture toughness. Fleck and Qiu [6] have shown that the lattice deforms by bar stretching remote from the crack tip and by a combination of bar bending and bar stretching within a characteristic elastic deformation zone near the crack tip. This elastic zone reduces the stress concentration at the crack tip in the Kagome lattice and the macroscopic toughness thereby exceeds that of the triangulated and hexagonal lattices.

1.2 Imperfection Sensitivity. Structures contain imperfections, either due to manufacturing or damage. The main aim of this study is to compare the imperfection sensitivity of elastic properties for the triangular lattice, the Kagome lattice, and the hexagonal honeycomb. It is anticipated that the large variation in nodal connectivity from one microstructure to the next will lead to marked differences in imperfection sensitivity. Partial information on the imperfection sensitivity of particular lattices can be gleaned from the existing literature, but no systematic comparisons have been reported to the authors' knowledge.

The sensitivity to node misplacement has been investigated by a number of authors for both 2D hexagonal honeycombs and 3D foams. Silva et al. [7] compared the elastic properties of 2D random Voronoi honeycombs to those of perfect hexagonal honeycombs. The Voronoi honeycomb is an arrangement of irregular hexagons and thereby has a connectivity $Z=3$. They found that the Voronoi honeycomb has a macroscopic shear modulus and Young's modulus slightly higher than that of a perfect hexagonal honeycomb (by 11% and 6%, respectively, for a relative density of $\bar{\rho}=0.15$). They concluded that the random (Voronoi) honeycomb has similar elastic properties to that of the perfect honeycomb. This conclusion is accurate for deviatoric loading but does not hold for hydrostatic loading; Zhu et al. [8] also observed an increase in shear and Young's modulus for increasingly imperfect 2D Voronoi honeycombs but showed that the bulk modulus decreased significantly. This increase in Young's modulus with increasing node misplacement in 2D hexagonal honeycombs is also observed for 3D open cell foams, see, for example, Van der Burg et al. [9]. Both structures are bending dominated in their perfect forms. In contrast, Grenestedt and Tanaka [10] show that perturbing the nodal positions of a 3D closed cell foam (a stretching-dominated structure in its perfect form) leads to a decrease in both bulk and shear moduli.

Chen et al. [11] examined the stiffness (and strength) of hexagonal honeycombs with imperfections in the form of rigid inclusions, holes, and missing cell walls. They found that the honeycomb was insensitive to the presence of rigid inclusions but that the presence of holes or missing cell walls causes a substantial knockdown in bulk modulus due to the induced cell-wall bending. Gan et al. [12] observed similar imperfection sensitivity in 3D open cell foams. Both Young's modulus and bulk modulus were reduced by the presence of broken cell edges, with the bulk modulus showing the greatest knockdown. However, stretching-dominated structures do not show the same sensitivity. Wallach and Gibson [13] found that Young's modulus of a fully triangulated 3D truss material is relatively insensitive to the removal of bars. For example, the removal of 10% of struts from the 3D truss decreases Young's modulus by only 17%.

The effect of cell-wall waviness in open and closed cell 3D foams has been investigated by Grenestedt [14]. A significant knockdown in bulk modulus of the open cell foam was observed for increasing bar waviness, with Young's modulus and shear modulus showing lesser sensitivities. The knockdown observed for closed cell foam was less significant and this was attributed to the dominance of stretching behavior in all deformation modes of this 3D structure, even in the presence of cell-wall waviness. Si-

Table 1 Relevant mechanical properties of the three perfect isotropic lattices

Topology	Relative density $\bar{\rho}$	Bulk modulus K	Shear modulus G	Poisson ratio ν
Triangular honeycomb	$2\sqrt{3}\frac{t}{l}$	$\frac{1}{4}\bar{\rho}E_s$	$\frac{1}{8}\bar{\rho}E_s$	1/3
Hexagonal honeycomb	$\frac{2}{\sqrt{3}}\frac{t}{l}$	$\frac{1}{4}\bar{\rho}E_s$	$\frac{3}{8}\bar{\rho}^3E_s$	1
Kagome lattice	$\sqrt{3}\frac{t}{l}$	$\frac{1}{4}\bar{\rho}E_s$	$\frac{1}{8}\bar{\rho}E_s$	1/3

mone and Gibson [15] also showed a knockdown in Young's modulus due to the cell-wall waviness of both 2D hexagonal honeycombs and closed cell 3D foams; they showed that the reduction is small unless the imperfection is very large.

The interaction of different types of imperfection in cellular materials may be of concern. However, Grenestedt [16] and Li et al. [17] examined combined imperfections in closed cell foams and Voroni honeycombs, respectively, and showed very little interaction between types of imperfection. For small levels of imperfection, the effects are additive. The imperfection sensitivity of Kagome type structures has received limited attention. Symons et al. [18] performed a number of morphing experiments on 3D Kagome lattices and showed that the presence of geometric imperfections significantly reduced the stiffness of the lattice against actuation. However, the imperfection sensitivity of in-plane stiffness under external loads was not explored.

1.3 Outline of the Study. The structure of this paper is as follows. First, the in-plane properties of the perfect triangulated, Kagome, and hexagonal lattices are reviewed. The numerical procedure for predicting the moduli of imperfect lattices is then described. The imperfection sensitivity of each of the three lattices is detailed for three types of imperfection: missing bars, a dispersion of nodes, and bar waviness. This paper concludes with a discussion of the relationship between imperfection sensitivity and nodal connectivity.

2 Review of the In-Plane Properties of Isotropic Lattice Materials

The relative density $\bar{\rho}$ of the three planar isotropic lattices are listed in Table 1 in terms of the cell-wall thickness t and length l. The table also gives the in-plane effective elastic properties in terms of $\bar{\rho}$ and Young's modulus E_s of the parent material, see Gibson and Ashby [19], Christensen [20], Fleck and Qiu [6], and Srikantha Phani et al. [21]. Define the bulk modulus K as the ratio of the mean applied biaxial stress to the in-plane hydrostatic strain. The in-plane shear modulus G has its usual definition.

Note that the elastic moduli of the triangular and Kagome lattices scale linearly with $\bar{\rho}$ in identical fashions. For both microstructures, the behavior is stretching dominated; we neglect here the very small additional contribution to stiffness associated with bending and shear deformation of the struts. The bulk modulus K of the perfect hexagonal honeycomb is identical to that of the other two lattices but the shear modulus G is dominated by bending and scales with $\bar{\rho}^3$.

3 Prediction of the Elastic Moduli of Imperfect Lattices

The finite element method was used to calculate the macroscopic modulus of imperfect lattices containing either missing bars or a dispersion of nodes. The effective elastic moduli were the mean values from multiple realizations of the imperfect lattices. The response of each realization has been determined by the finite element computer package ABAQUS/STANDARD [22]. In the simulations, a two-noded cubic beam element was used to represent each wall (element "B23" within ABAQUS). The B23 element is an Euler–Bernoulli beam that can both stretch and bend, but is rigid against shear.

A preliminary set of finite element calculations was performed to explore the degree to which a neglect of shear deformation leads to inaccurate predictions of the macroscopic stiffness. A perfect, hexagonal honeycomb was analyzed, and the macroscopic shear modulus was calculated using the B23 elements within ABAQUS. The results were then compared to the analytic expression given by Silva et al. [7], which includes the contribution from shear of the beam cross section. A comparison reveals that the neglect of shear deformation leads to too stiff a macroscopic shear modulus by a negligible factor: The finite element prediction is too stiff by 2.6% at a relative density of $\bar{\rho}=0.115$, with a smaller error at lower values of relative density. The Kagome and triangulated lattices are stretching-controlled structures and so the error introduced by a neglect of shear deformation is more minor for these lattices than the hexagonal honeycomb. We conclude that the B23 elements within ABAQUS are adequate for our purposes.

The macroscopic stiffness of the imperfect lattices was obtained by considering a representative unit cell containing a random distribution of imperfections. Periodic boundary conditions were applied such that the translation displacements u_α^i and rotation θ^i of every node on the boundary of the mesh satisfy

$$u_\alpha^J - u_\alpha^I = \varepsilon_{\alpha\beta}(x_\beta^J - x_\beta^I), \quad \theta^J - \theta^I = 0, \quad \alpha,\beta = 1,2 \tag{1}$$

where $\varepsilon_{\alpha\beta}$ is the average macroscopic strain and x_β^J and x_β^I are the coordinates of a pair of corresponding nodes I and J on opposite sides of the mesh. Periodic boundary conditions were also adopted in numerical studies of imperfection sensitivity of cellular materials by Chen [11,23], Grenestedt [10], Zhu et al. [8], and Gan et al. [12]. Li et al. [17] confirmed that for a regular honeycomb the computed moduli are independent of the number of cells with periodic boundary conditions; this is not the case for an analysis based on displacement boundary conditions.

In each simulation, a single-step linear calculation was performed to determine the response to uniform biaxial (hydrostatic) strain and then to deviatoric strain. The bulk modulus and shear modulus were calculated from the work-conjugate applied loads. Meshes of the imperfect lattice were generated from perfect parent meshes using a MATLAB [24] routine. For the imperfection of missing bars, the routine randomly removed a proportion f of the elements (see Fig. 2). For misplaced nodes, the routine displaced every node in the mesh from its perfect position along a randomly generated direction by a randomly generated distance up to a maximum distance of al, where a is the amplitude of nodal dispersion. The probability distribution of the random radial movement of nodes was chosen to give a uniform probability distribution with respect to area within a disk of radius al. Corresponding pairs of boundary nodes were assigned the same random displacement to ensure periodicity. Note that a can take values of the range of 0 to 0.5; for the choice $a=0.5$, occasional nodes touch in the undeformed configuration.

The unit cell of the imperfect lattice in the finite element simulations should be sufficiently large in order to give an accurate estimate of the modulus for the infinite imperfect lattice. A series of preliminary calculations was performed with the side length L of the unit cell varied from $12l$ to $96l$. For a given size of unit cell, 20 different randomly generated structural realizations were analyzed with the same level of imperfection in the form of missing bars. With increasing size of unit cell, it is anticipated that the standard deviation of modulus decreases (and asymptotes to zero in the limit of an infinite mesh), while the mean value of modulus asymptotes to the infinite lattice result. It is of interest to explore whether the rate of convergence of the standard deviation is the

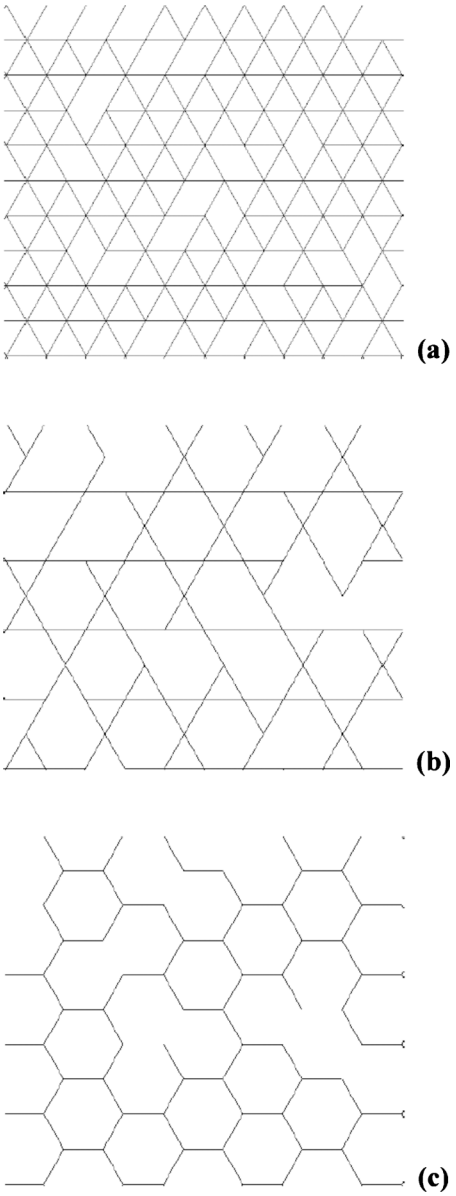

Fig. 2 **Planar grids with $f=0.1$ (10%) missing bars: (*a*) triangular, (*b*) Kagome, and (*c*) hexagonal**

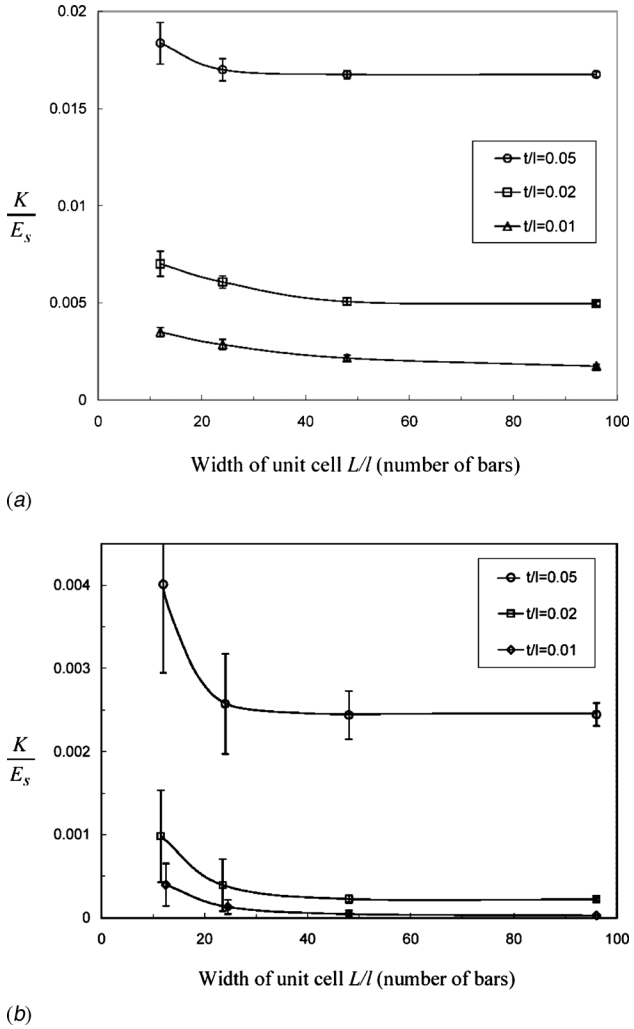

Fig. 3 **Convergence of bulk modulus of planar Kagome with increasing size of unit cell; (*a*) $f=0.01$ (1%) missing bars and (*b*) $f=0.1$ (10%) missing bars (means of 20 simulations plotted, error bars represent ±1 standard deviation)**

same as that for the mean value. A similar approach was adopted by Gan et al. [12]. They examined the mean and standard deviation of the moduli of randomly perturbed (Voronoi) 3D open cell foams and showed convergence of the results for increasing model size.

A representative set of calculations is reported in Fig. 3, for a Kagome unit cell with selected values of side lengths $12l$, $24l$, $48l$ and $96l$. In each case, the unit cell was rectangular with a height to width ratio of $\sqrt{3}/2$. The mean and standard deviation of the bulk modulus K were obtained from each set of 20 simulations. This exercise was performed for three different values of t/l (i.e., varying $\bar{\rho}$) and for two fractions of missing bars $f=0.01$ and $f=0.1$. It is clear from the results shown in Fig. 3 that the standard deviation of the bulk modulus K asymptotes to zero with increasing size of unit cell. The mean value decreases to a stabilized value, and this stable value is taken to represent the infinite lattice modulus. We note that the required size of unit cell to give a negligible standard deviation is essentially the same as that required to give a stable mean value. For any given size of unit cell and relative density, the standard deviation of the bulk modulus is lower for a smaller level of imperfection f of missing bars.

The Kagome lattice has the characteristic feature that the size of unit cell in order to give an acceptable estimate for the infinite lattice solution is dependent on t/l. For example, for the choice $f=0.01$, it is evident from Fig. 3(*a*) that a unit cell of width $L=24l$ is adequate for $t/l=0.05$, whereas a unit cell of width $L=96l$ is needed for $t/l=0.01$. The reason for this size dependence on t/l is evident from an examination of the deformed mesh, as follows. Consider the choice of a unit cell of size $L=96l$ and $f=0.01$. Then, the perturbation in deformation field around a missing bar is much larger for $t/l=0.02$ than for $t/l=0.05$, as shown in Fig. 4. This has already been noted in the study of Wicks and Guest [25] in the context of single member actuation of a Kagome lattice.

Similar preliminary investigations have been performed for the shear modulus of the Kagome lattice, and for both in-plane moduli of the triangular lattice and hexagonal honeycomb. The required sizes of unit cell to achieve accurate values of the effective shear modulus of the Kagome lattice are the same as that noted above for the bulk modulus. Smaller unit cells suffice for the triangular lattice and hexagonal honeycomb as these lattices do not have long decay lengths adjacent to missing bars, as dis-

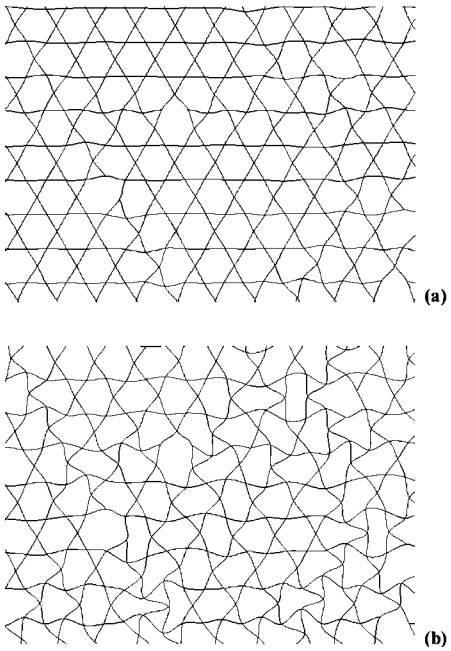

Fig. 4 Planar Kagome grids with $f=0.01$ (1%) missing bars: (*a*) equibiaxial strain $t/l=0.05$; (*b*) equibiaxial strain $t/l=0.02$

cussed by Wicks and Guest [25]. Detailed results for the effective moduli are now given for the three lattices employing a unit cell of width $96l$.

4 Imperfection Sensitivity

4.1 Imperfection Type 1: Missing Bars. The first imperfection investigated is that of missing (or broken) bars. All nodes are in their ideal (perfect) positions and all bars are perfectly straight, but a random distribution of the bars are missing. Figure 2 shows representative regions of the three planar lattices where the fraction of missing bars $f=0.1$.

4.1.1 Bulk Modulus. The dependence of bulk modulus of the three lattices on relative density $\bar{\rho}$ is plotted in Fig. 5(*a*) for $f=0$ and $f=0.1$. (Note that the relative density as plotted includes the correction associated with missing bars.) All lattices in their perfect state ($f=0$) have a slope of unity on this log-log plot. This is due to the stretching-dominated behavior: the bulk modulus scales linearly with $\bar{\rho}$.

The triangulated lattice is relatively unaffected by the introduction of missing bars; the modulus drops by 30% upon increasing f from zero to 0.1. However, the bulk modulus still scales linearly with $\bar{\rho}$ (a slope of unity), indicating that stretching behavior is preserved.

In contrast, for the Kagome and hexagonal lattices, an increase of f from 0 to 0.1 greatly reduces the bulk modulus. The bulk modulus now scales as $\bar{\rho}^3$ indicating that bending behavior now dominates. However, for the practical range of relative density, the Kagome is one order of magnitude stiffer than the honeycomb and is therefore much more tolerant to imperfections in the form of missing bars.

The knockdown in bulk modulus K/K_0 is plotted as a function of fraction f of missing bars in Fig. 5(*b*) for the three lattices. In this plot, an intermediate cell-wall (bar) thickness has been chosen of $t/l=0.02$ and K_0 is the bulk modulus of each lattice for $f=0$. (Note that a fixed value of t/l gives a different $\bar{\rho}$ for each lattice.) The extreme imperfection sensitivity of the hexagonal lattice is evident. In contrast the Kagome is much more imperfection tolerant and the triangular lattice is almost insensitive to missing bars.

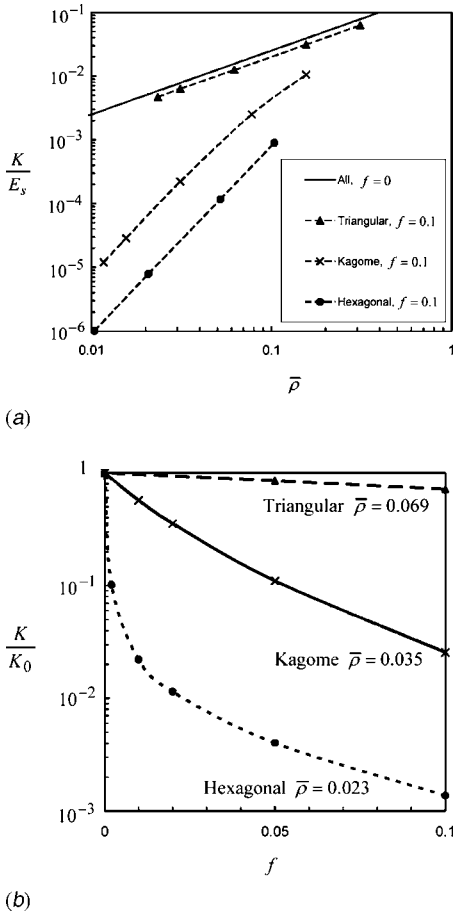

Fig. 5 Sensitivity of bulk modulus of planar grids to missing bars: (*a*) for varying relative density $\bar{\rho}$ with $f=0$ and $f=0.1$ (10%) missing bars; (*b*) for varying proportion of missing bars f with fixed cell-wall thickness $t/l=0.02$

4.1.2 Shear Modulus. The effective shear modulus G of the three lattices is plotted as a function of $\bar{\rho}$ in Fig. 6(*a*) for the two choices $f=0$ and $f=0.1$. For the perfect lattice, $f=0$, the triangulated and Kagome lattices have the same stiffness, as expected from Table 1. However, for $f=0.1$, the Kagome suffers a significant knockdown in shear stiffness whereas the triangulated grid is relatively unaffected by the imperfection. The perfect hexagonal honeycomb has a very low shear modulus due to its bending-dominated response, and the introduction of missing bars leads to only a small additional reduction in modulus.

The knockdown in shear modulus G/G_0 with increasing f is plotted in Fig. 6(*b*) for the choice $t/l=0.02$, where G_0 is the bulk modulus of each lattice for $f=0$. The Kagome is clearly the most sensitive to the introduction of missing bars but it must be recalled from Fig. 6(*a*) that the absolute shear modulus of the Kagome lattice is an order of magnitude greater than that of the hexagonal honeycomb at any given value of $\bar{\rho}$.

4.2 Imperfection Type 2: Stochastic Dispersion of Nodes. The second type of imperfection investigated is that of misplaced nodes. All bars are present and perfectly straight but are connected to nodes which are randomly displaced from their ideal (perfect) positions. As already noted, the random displacement has a uniform probability density function over a circular disk of radius al. Figure 7 shows the representative portions of each lattice with stochastically displaced nodes of amplitude $a=0.3$.

4.2.1 Bulk Modulus. The dependence of in-plane bulk modulus on relative density for the three lattices is shown in Fig. 8(*a*),

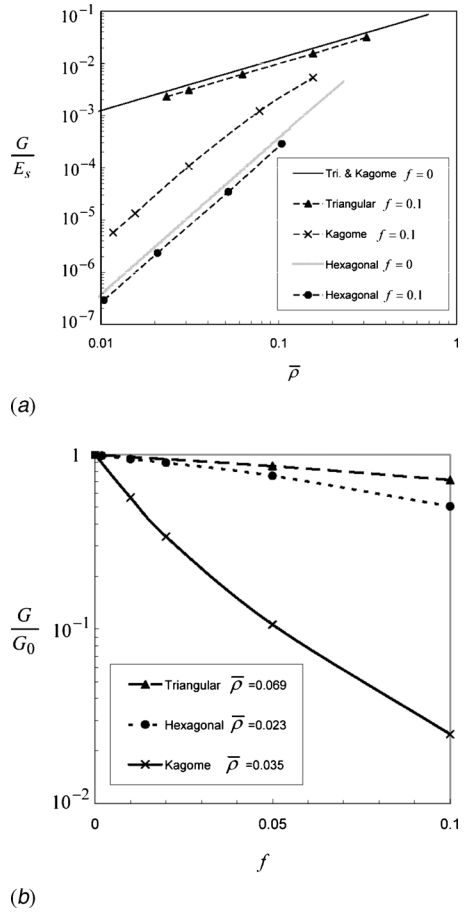

Fig. 6 Sensitivity of shear modulus of planar grids to missing bars: (*a*) for varying relative density with $f=0$ and $f=0.1$ missing bars; (*b*) for cell-wall thickness $t/l=0.02$

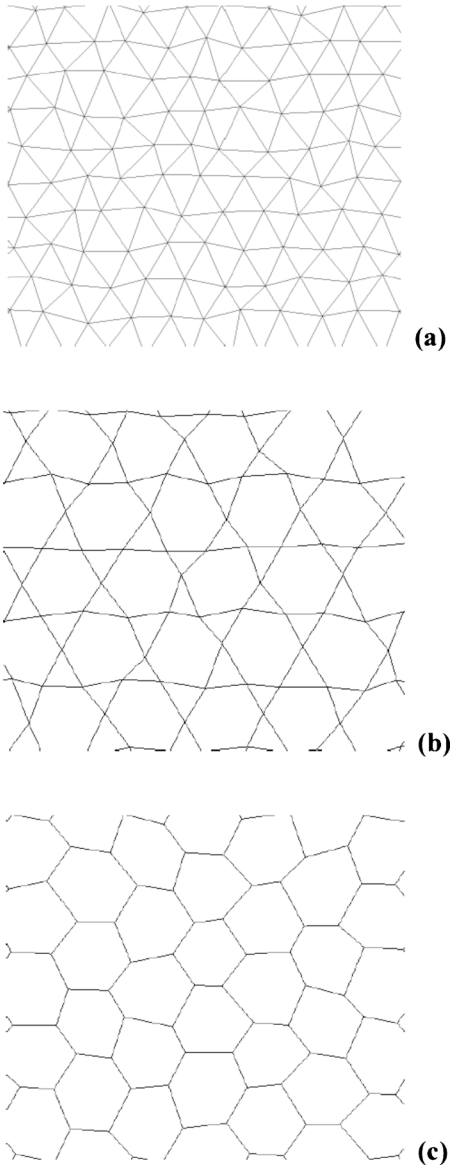

Fig. 7 Planar grids with stochastic nodal dispersion amplitude $a=0.3$: (*a*) triangular, (*b*) Kagome, and (*c*) hexagonal

for the choices $a=0$ and $a=0.5$. The triangulated lattice is relatively insensitive to nodal position. The bulk modulus of the imperfect triangulated lattice linearly scales with $\bar{\rho}$, indicating that stretching behavior remains dominant. In contrast, the stiffness of the hexagonal lattice is severely degraded by random movement of the nodes. The bulk modulus K of the imperfect honeycomb scales as $\bar{\rho}^3$. The Kagome is the intermediate case: The bulk modulus of the imperfect lattice scales as $\bar{\rho}^n$, with the index n increasing from unity to 2 with increasing a. In the extreme case shown for $a=0.5$, K scales as $\bar{\rho}^2$. It is argued that this intermediate behavior of the Kagome lattice is due to the fact that it deforms by a combination of bending and stretching, as discussed by Wicks and Guest [25]. The knockdown in bulk modulus K/K_0 is plotted as a function of dispersion amplitude a in Fig. 8(*b*) for the case $t/l=0.02$. This plot clearly shows the extreme sensitivity of the hexagonal honeycomb to the imperfection, while the Kagome lattice is moderately sensitive and the triangular lattice is almost insensitive.

4.2.2 Shear Modulus. Figures 9(*a*) and 9(*b*) show the effect of stochastic nodal dispersion on the shear modulus of the three lattices, again for $a=0$ and $a=0.5$. The shear modulus of the triangulated lattice decreases slightly while that of the hexagonal honeycomb increases slightly when a is increased from zero (perfect lattice) to 0.5 (imperfect lattice). In contrast, the shear modulus of the Kagome lattice is sensitive to nodal dispersion, as shown in Fig. 9(*b*). For the choice $a=0.5$, as shown in Fig. 9(*a*), the shear modulus approximately scales as $\bar{\rho}^2$. A similar behavior has already been noted for the bulk modulus.

The slight effect of nodal dispersion on the shear modulus of the hexagonal honeycomb is consistent with the observations by Silva et al. [7] that the shear modulus of a Voronoi honeycomb (with a nodal connectivity of $Z=3$) is slightly above that of the perfect hexagonal honeycomb.

4.3 Imperfection Type 3: Bar Waviness. The final type of imperfection considered here is bar waviness, that is, lack of straightness of cell walls. The waviness of a bar leads to a reduction in axial stiffness and to a negligible change of bending stiffness. The relationship between amplitude of waviness and axial stiffness of a bar can be straightforwardly determined, as follows.

Consider a bar of length l, with an integral number of sine waves of wavelength l'. Then, the misalignment w as a function of position along the bar x is

$$w(x) = w_0 \sin\left(\frac{2\pi x}{l'}\right) \tag{2}$$

where w_0 is the amplitude of waviness, as defined in Fig. 10(*a*). Now apply an axial tension T to the ends of the bar. This tension

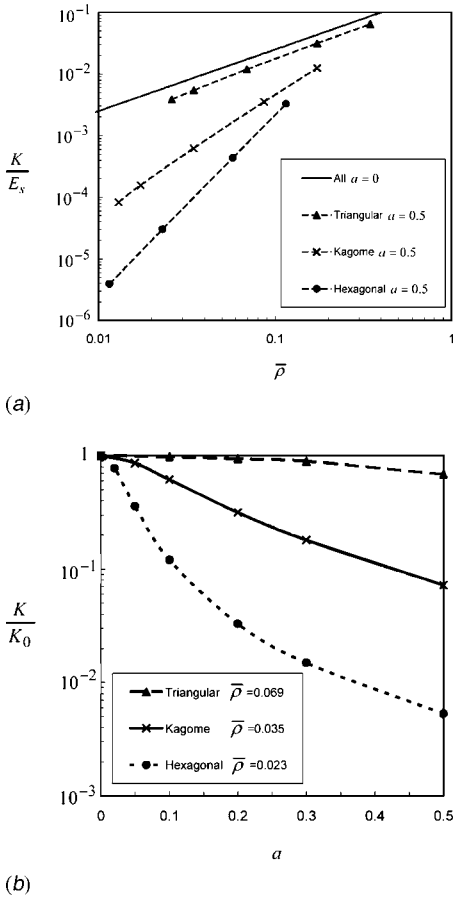

Fig. 8 Sensitivity of bulk modulus of planar grids to stochastic nodal dispersion: (*a*) for varying relative density with dispersion amplitude $a=0$ and $a=0.5$; (*b*) for varying dispersion amplitude with fixed cell-wall thickness $t/l=0.02$

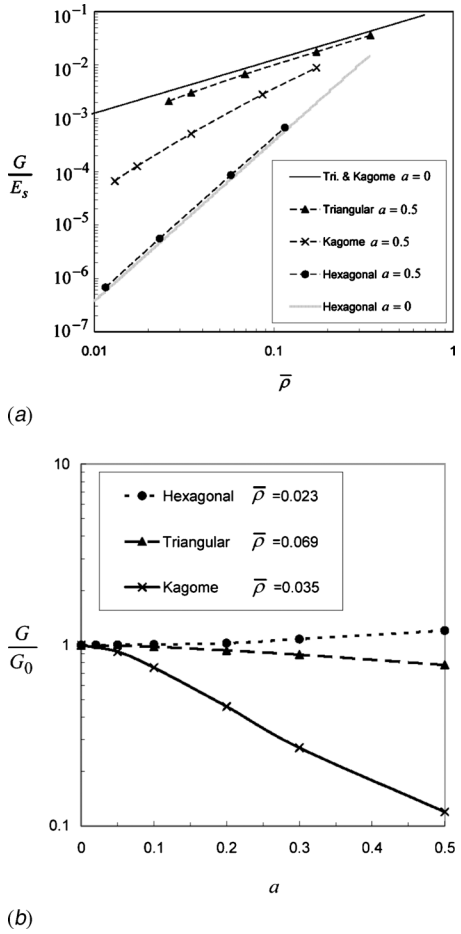

Fig. 9 Sensitivity of shear modulus of planar grids to stochastic nodal dispersion: (*a*) for varying relative density with dispersion amplitude $a=0$ and $a=0.5$; (*b*) for varying dispersion amplitude with fixed cell-wall thickness $t/l=0.02$

gives rise to a bending moment M and an additional transverse displacement u such that

$$M = -EI\frac{d^2u}{dx^2} = Tw(x) \tag{3}$$

where E is the axial modulus and I the second moment of area of the bar cross section.

$$I = t^3/12 \tag{4}$$

Substitute Eq. (2) into Eq. (3) and solve the resulting differential equation to obtain

$$u(x) = -\frac{T}{EI}\left(\frac{l'}{2\pi}\right)^2 w_0 \sin\left(\frac{2\pi x}{l'}\right) \tag{5}$$

The extension Δl of a bar of thickness t and total length l has two contributions: the stretching of the bar and the straightening due to its initial waviness. Hence,

$$\Delta l = \frac{Tl}{Et} - \int_0^l \left[\sqrt{1+\left(\frac{du}{dx}+\frac{dw}{dx}\right)^2} - \sqrt{1+\left(\frac{dw}{dx}\right)^2}\right]dx \tag{6}$$

Upon assuming that the elastic deflection $du/dx \ll dw/dx \ll 1$, we obtain

$$\Delta l = \frac{Tl}{Et}\left(1+\frac{w_0^2 t}{2I}\right) \tag{7}$$

The axial stiffness k of the bar is therefore

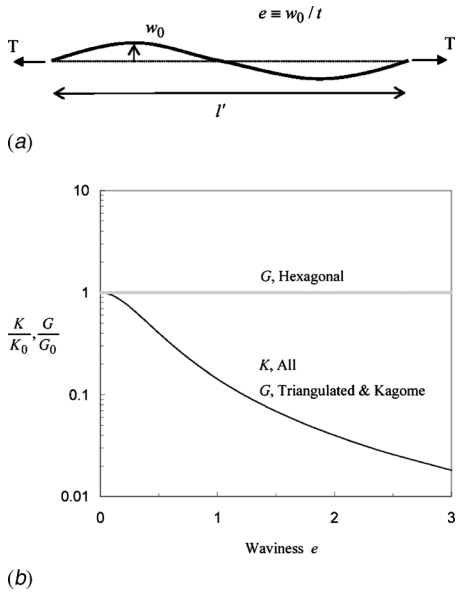

Fig. 10 (*a*) Definition of bar waviness; (*b*) sensitivity of bulk and shear moduli of triangular, Kagome, and hexagonal planar grids to bar waviness

$$k = \frac{T}{\Delta l} = \frac{Et}{l}\frac{1}{(1+6e^2)} \tag{8}$$

where $e \equiv w_0/t$ is a nondimensional measure of waviness given by the ratio of the amplitude of waviness w_0 to the bar thickness t. This result agrees with the knockdown factor calculated by Grenestedt [14].

Thus, the presence of waviness reduces the axial stiffness of the bar by the factor $1+6e^2$. Consequently, stretching-dominated deformation modes of lattices will have the relevant modulus reduced by this factor upon introducing bar waviness. This knockdown factor is potent: The effective modulus drops by a factor of 25 for a waviness amplitude $w_0=2t$. For the three isotropic lattices considered in this study, all moduli are degraded except for the shear modulus of the hexagonal honeycomb. This result is shown in Fig. 10(*b*).

5 Concluding Remarks

Perfect triangulated and Kagome lattices are stiff, stretching-dominated structures under all loadings and their bulk and shear moduli scale with $\bar{\rho}$. The hexagonal honeycomb is only stretching dominated under hydrostatic loading. Under deviatoric loading, it is a flexible, bending-dominated structure. Consequently, the bulk modulus of the perfect hexagonal honeycomb scales with $\bar{\rho}$, whereas its shear modulus scales with $\bar{\rho}^3$.

The high nodal connectivity $Z=6$ of the triangulated lattice confers insensitivity to imperfections in the form of missing bars and nodal dispersion: It remains a stiff stretching structure under all loadings. In contrast, the bulk and shear moduli of the Kagome lattice ($Z=4$) are significantly degraded by these imperfections. The bulk modulus of the hexagonal lattice ($Z=3$) is extremely sensitive to the presence of missing bars and nodal dispersion as the deformation mode switches from stretching dominated to bending dominated. Its shear modulus is almost unaffected since it is bending governed for both the perfect and imperfect geometries.

This study has highlighted the relative ranking of the in-plane moduli of three isotropic lattices in the presence of missing bars and nodal dispersion. For the same relative density and level of imperfection, both the bulk and shear moduli of the Kagome are intermediate between those of the imperfection-insensitive triangulated lattice and the hexagonal honeycomb. This suggests that the Kagome lattice is a promising topology for morphing applications: The imperfect structure is stiff under external loads, yet compliant when one or more bars are axially actuated.

Cell wall lack of straightness (bar waviness) degrades the moduli of all three lattices where the behavior is stretching dominated. Consequently, it is only the shear modulus of the hexagonal honeycomb that is insensitive to this imperfection, since in this case the behavior is already bending controlled.

References

[1] Deshpande, V. S., Ashby, M. F., and Fleck, N. A., 2001, "FoamTopology Bending Versus Stretching Dominated Architectures," Acta Mater., **49**, pp. 1035–1040.

[2] Maxwell, J. C., 1864, "On the Calculation of the Equilibrium and Stiffness of Frames," Philos. Mag., **27**, pp. 294–299, 1890, *Collected Papers, XXVI*, Cambridge University Press, Cambridge.

[3] Hyun, S., and Torquato, S., 2002, "Optimal and Manufacturable Two-Dimensional, Kagomé-Like Cellular Solids," J. Mater. Res., **17**(1), pp. 137–144.

[4] Hutchinson, R. G., and Fleck, N. A., 2006, "The Structural Performance of the Periodic Truss," J. Mech. Phys. Solids, **54**(4), 756–782.

[5] Symons, D. D., Hutchinson, R. G., and Fleck, N. A., 2005, "Actuation of the Kagome Double Layer Grid. Part 1: Prediction of Performance of the Perfect Structure," J. Mech. Phys. Solids, **53**, pp. 1855–1874.

[6] Fleck, N. A., and Qiu, X., 2006, "The Damage Tolerance of Elastic-Brittle, Two-Dimensional Isotropic Lattices," J. Mech. Phys. Solids, **55**, 562–588.

[7] Silva, M. J., Hayes, W. C., and Gibson, L. J., 1995, "The Effects of Non-Periodic Microstructure on the Elastic Properties of Two-Dimensional Cellular Solids," Int. J. Mech. Sci., **37**(11), 1161–1177.

[8] Zhu, H. X., Hobdell, J. R., and Windle, A. H., 2001, "Effects of Cell Irregularity on the Elastic Properties of 2D Voronoi Honeycombs," J. Mech. Phys. Solids, **49**, 857–870.

[9] Van Der Burg, M. W. D., and Shulmeister, V., Van Der Geissen, E., Marissen, R., 1997, "On the Linear Elastic Properties of Regular and Random Open-Cell Foam Models," J. Cell. Plast., **33**(1), 31–54.

[10] Grenestedt, J. L., and Tanaka, K., 1999, "Influence of Cell Shape Variations on Elastic Stiffness of Closed Cell Cellular Solids," Scr. Mater., **40**(1), 71–77.

[11] Chen, C., Lu, T. J., and Fleck, N. A., 2001, "Effect of Inclusions and Holes on the Stiffness and Strength of Honeycombs," Int. J. Mech. Sci., **43**, pp. 487–504.

[12] Gan, Y. X., Chen, C., and Shen, Y. P., 2005, "Three-Dimensional Modeling of the Mechanical Property of Linearly Elastic Open Cell Foams," Int. J. Solids Struct., **42**, pp. 6628–6642.

[13] Wallach, J. C., and Gibson, L. J., 2001, "Defect Sensitivity of a 3D Truss Material," Scr. Mater., **45**(6), pp. 639–644.

[14] Grenestedt, J. L., 1998, "Influence of Wavy Imperfections in Cell Walls on Elastic Stiffness of Cellular Solids," J. Mech. Phys. Solids, **46**(1), pp. 29–50.

[15] Simone, A. E., and Gibson, L. J., 1998, "The Effects of Cell Face Curvature and Corrugations on the Stiffness and Strength of Metallic Foams," Acta Mater., **46**(11), pp. 3929–3935.

[16] Grenestedt, J. L., 2005, "On Interactions Between Imperfections in Cellular Solids," J. Mater. Sci., **40**, pp. 5853–5857.

[17] Li, K., Gao, X.-L., and Subhash, G., 2005, "Effects of Cell Shape and Cell Wall Thickness Variations on the Elastic Properties of Two-Dimensional Cellular Solids," Int. J. Solids Struct., **42**, pp. 1777–1795.

[18] Symons, D. D., Shieh, J., and Fleck, N. A., 2005, "Actuation of the Kagome Double Layer Grid. Part 2: Effect of Imperfections on the Measured and Predicted Actuation Stiffness," J. Mech. Phys. Solids, **53**, pp. 1875–1891.

[19] Gibson, L. J., and Ashby, M. F., 1997, *Cellular Solids: Structure and Properties*, 2nd ed., Cambridge University Press, Cambridge.

[20] Christensen, R. M., 2000, "Mechanics of Cellular and Other Low-Density Materials," Int. J. Solids Struct., **37**, pp. 93–104.

[21] Srikantha Phani, A., Woodhouse, J., and Fleck, N. A., 2006, "Wave Propagation in Two-Dimensional Periodic Lattices," J. Acoust. Soc. Am., **119**(4), pp. 1995–2005.

[22] HKS, 2003, ABAQUS/STANDARD, Version 6.4.1, Hibbit, Karlsson and Sorenson Inc., Providence, RI.

[23] Chen, C., Lu, T. J., and Fleck, N. A., 1999, "Effect of Imperfections on the Yielding of Two-Dimensional Foams," J. Mech. Phys. Solids, **47**, pp. 2235–2272.

[24] MathWorks, 2002, MATLAB, Version 6.5, The MathWorks Inc., Natick, MA.

[25] Wicks, N., and Guest, S. D., 2004, "Single Member Actuation in Large Repetitive Truss Structures," Int. J. Solids Struct., **41**, pp. 965–978.

Kwang Ho Lee
Professor
Department of Automotive Engineering,
Kyungpook National University,
Sangju City, Kyeongbuk 742-711,
Republic of Korea

Vijaya Bhaskar Chalivendra
Assistant Professor
Department of Mechanical Engineering,
University of Massachusetts Dartmouth,
North Dartmouth, MA 02747

Arun Shukla[1]
Simon Ostrach Professor
ASME Fellow
e-mail: shuklaa@egr.uri.edu
Dynamic Photomechanics Laboratory,
Department of Mechanical Engineering and
Applied Mechanics,
University of Rhode Island,
Kingston, RI 02881

Dynamic Crack-Tip Stress and Displacement Fields Under Thermomechanical Loading in Functionally Graded Materials

Thermomechanical stress and displacement fields for a propagating crack in functionally graded materials (FGMs) are developed using displacement potentials and asymptotic analysis. The shear modulus, mass density, and coefficient of thermal expansion of the FGMs are assumed to vary exponentially along the gradation direction. Temperature and heat flux distribution fields are also derived for an exponential variation of thermal conductivity. The mode mixity due to mixed-mode loading conditions around the crack tip is accommodated in the analysis through the superposition of opening and shear modes. Using the asymptotic stress fields, the contours of isochromatics (contours of constant maximum shear stress) are developed and the results are discussed for various crack-tip thermomechanical loading conditions. [DOI: 10.1115/1.2932093]

Keywords: functionally graded materials, thermomechanical loading, stress intensity factors, mixed mode, isochromatics

1 Introduction

For the past two decades, research and applications of functionally graded materials (FGMs) have received considerable attention. Although their performances in real-life engineering applications are still under investigation, FGMs have shown promising results when they are subjected to thermomechanical loading [1]. Hasselman and Youngblood [2] were among the first to study thermal stresses in nonhomogeneous structures associated with thermomechanical loading. By introducing thermal conductivity gradient, they realized significant reductions in the magnitude of the tensile thermal stress in ceramic cylinders. In other studies, thermal residual stresses are relaxed in metal-ceramic layered materials by inserting a functionally graded interface layer between the metal and the ceramic [3–5]. In their studies, Kudora et al. [6] and Takashashi et al. [7] reported that when subjected to thermal shocks, FGM coatings suffer significantly less damage than conventional ceramic coatings.

In a continuation of the above studies, several studies on the quasistatic fracture of FGMs under thermomechanical loading have been reported. Assuming exponential variation of material properties, Jin and Noda [8] investigated the steady thermal stress intensity factor in the functionally gradient semi-infinite space with an edge crack subjected to thermal load. Later, Erdogan and Wu [9] also studied the steady thermal stress intensity factor of a FGM layer with a surface crack perpendicular to the boundaries. By further assuming the exponential variation of thermal and mechanical properties of the materials, Jin and Batra [10] investigated the stress intensity relaxation problem at the tip of an edge crack in a FGM subjected to a thermal shock. Using both experimental and numerical techniques, Kokini and Choules [11] and Kokini and Case [12] studied surface and interface cracking in FGM coatings subjected to thermal shocks. By employing a finite element method (FEM), Noda [13] analyzed an edge crack problem in a zirconia/titanium FGM plate subjected to cyclic thermal loads. Using integral equation method, Jin and Paulino [14] studied transient thermal stresses in a FGM with an edge crack and having constant Young's modulus and Poisson's ratio but varying thermal properties along the thickness direction. Walters et al. [15] developed general domain integral methods to obtain stress intensity factors for surface cracks in FGMs under Mode I thermomechanical loading conditions. El-Borgi et al. [16] investigated crack-tip stress intensity factors for a partially insulated embedded crack in an infinite functionally graded medium under thermomechanical loading. They studied the effect of nonhomogeneity parameters, crack closure, and partial crack surface on the stress intensity factors using the integral transform method. Zhang and Paulino [17] investigated the effect of gradation on wave propagation and dynamic analysis in smoothly graded heterogeneous continua using graded finite elements. The above studies provide closed form solutions for stress intensity factors under thermomechanical loading conditions. However, for extracting fracture parameters from experimental studies, asymptotic expansion of crack-tip stress fields around the crack tip is essential. In this direction, very recently, Jain et al. [18] developed quasistatic stress and displacement fields for a crack in an infinite FGM medium under thermomechanical loading conditions.

In this paper, the stress and displacement fields for a propagating crack at uniform speed along the direction of mechanical and thermal property variation in a FGM under thermomechanical loading conditions are developed. The elastodynamic problem for FGM is formulated in terms of displacement potentials, and the solutions are obtained through an asymptotic analysis. In analyzing this problem, we transform the general partial differential equation in the dynamic equilibrium into Laplace's equation whose solution involves harmonic functions. Using these developed stress fields, the effects of mechanical nonhomogeneity on isochromatics for a propagating crack under different dynamic crack-tip thermomechanical loading conditions in FGMs are discussed.

2 Theoretical Formulation

At a continuum level, the properties at any given point in a FGM can be assumed to be the same in all directions. Hence, FGMs can be treated as isotropic nonhomogeneous solids. Spatial

[1]Corresponding author.

Contributed by the Applied Mechanics Division of ASME for publication in the JOURNAL OF APPLIED MECHANICS. Manuscript received May 11, 2007; final manuscript received February 8, 2008; published online July 10, 2008. Review conducted by Marek-Jerzy Pindera.

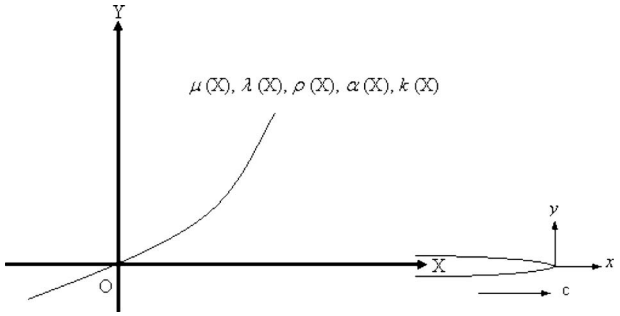

Fig. 1 Propagating crack-tip orientation with respect to reference coordinate configuration

variation of elastic properties, mass density, and thermal properties make analytical solutions to the elastodynamic equations extremely difficult. Hence, an asymptotic analysis similar to that employed by Freund [19] is used to expand the stress field around a propagating crack under thermomechanical loading conditions.

The shear modulus (μ), Lame's constant (λ), density (ρ), thermal expansion (α), and heat conductivity (k) of the FGM are assumed to vary in an exponential manner as given by Eqs. (1*a*)–(1*e*), whereas Poisson's ratio (ν) is assumed to be a constant,

$$\mu = \mu_0 \exp(\zeta X) \tag{1a}$$

$$\lambda = \lambda_0 \exp(\zeta X) \tag{1b}$$

$$\rho = \rho_0 \exp(\zeta X) \tag{1c}$$

$$\alpha = \alpha_0 \exp(\beta X) \tag{1d}$$

$$k = k_0 \exp(\delta X) \tag{1e}$$

The relationship between stresses and strains can be written as

$$\sigma_{XX} = \exp(\zeta X)[(\lambda_0 + 2\mu_0)\varepsilon_{XX} + \lambda_0 \varepsilon_{YY} - (3\lambda_0 + 2\mu_0)\alpha_0 \exp(\beta X)T] \tag{2a}$$

$$\sigma_{YY} = \exp(\zeta X)[\lambda_0 \varepsilon_{XX} + (\lambda_0 + 2\mu_0)\varepsilon_{YY} - (3\lambda_0 + 2\mu_0)\alpha_0 \exp(\beta X)T] \tag{2b}$$

$$\tau_{XY} = \exp(\zeta X)\mu_0 \gamma_{XY} \tag{2c}$$

where X is the reference coordinate, σ_{ij} and ε_{ij} (where $i=X,Y$ and $j=X,Y$) are in-plane stress and strain components, λ and μ denote Lame's constant and shear modulus, respectively, and the subscript 0 means at $X=0$, as shown in Fig. 1. T represents the change in temperature in the infinite medium. ζ, β, and δ are nonhomogeneity constants that have the dimension $(\text{length})^{-1}$. For plane strain deformation, the displacements u and v are derived from dilatational and shear wave potentials Φ and Ψ. These potentials can be expressed as

$$u = \frac{\partial \Phi}{\partial X} + \frac{\partial \Psi}{\partial Y}, \quad v = \frac{\partial \Phi}{\partial Y} - \frac{\partial \Psi}{\partial X} \tag{3}$$

The equations of motion for a plane problem are given by

$$\frac{\partial \sigma_{XX}}{\partial X} + \frac{\partial \tau_{XY}}{\partial Y} = \rho \frac{\partial^2 u}{\partial t^2}, \quad \frac{\partial \tau_{XY}}{\partial X} + \frac{\partial \sigma_{YY}}{\partial Y} = \rho \frac{\partial^2 v}{\partial t^2} \tag{4}$$

For a propagating crack shown in Fig. 1, the transformed crack-tip coordinates can be written as $x=X-ct$, $y=Y$, where c is the constant crack-tip speed. The constant velocity assumption is justified because of the fact that both Mode I and mixed-mode cracks propagate at constant velocity in moderately graded materials, as shown by Shukla and Jain in their experimental studies [20,21].

Substituting displacement potentials (Eq. (3)) into Hooke's law (Eqs. (2*a*)–(2*c*)) and then substituting Hooke's law into the equations of motion (Eq. (4)), the equations for the dynamic equilibrium can be expressed in terms of crack-tip coordinates (x,y) as

$$\alpha_l^2 \frac{\partial^2 \Phi}{\partial x^2} + \frac{\partial^2 \Phi}{\partial y^2} + \zeta \frac{\partial \Phi}{\partial x} + \frac{\zeta}{K+2} \frac{\partial \Psi}{\partial y} - \frac{3K+2}{K+2} \alpha_c \left[T + \Delta^{-1} \left[(\zeta + 2\beta) \frac{\partial T}{\partial x} + \beta(\zeta + \beta) T \right] \right] = 0 \tag{5a}$$

$$\alpha_s^2 \frac{\partial^2 \Psi}{\partial x^2} + \frac{\partial^2 \Psi}{\partial y^2} + \zeta \frac{\partial \Psi}{\partial x} + \zeta K \frac{\partial \Phi}{\partial y} - (3K+2)\alpha_c \zeta \Delta^{-1} \left(\frac{\partial T}{\partial y} \right) = 0 \tag{5b}$$

where $\alpha_l = \sqrt{1-(c/c_l)^2}$, $\alpha_s = \sqrt{1-(c/c_s)^2}$, $c_s = \sqrt{\mu_c/\rho_c}$, $\nabla^2 = \Delta = \partial^2/\partial x^2 + \partial^2/\partial y^2$, and $K = \lambda_0/\mu_0$; $c_l = c_s\sqrt{2(1-\nu)/(1-2\nu)}$ for plane strain and $c_l = c_s\sqrt{2/(1-\nu)}$ for plane stress.

c_l and c_s are the elastic dilatational wave speed and elastic shear wave speed of the materials at the crack tip, respectively, and α_c is the coefficient of thermal expansion in the vicinity of the instantaneous crack tip and is assumed to be constant. To obtain an asymptotic expansion of the mechanical fields around the crack tip, we define the general solutions of Eqs. (5*a*) and (5*b*) in terms of complex functions Φ, Ψ, and T as given in

$$\Phi_n(z_l) = -\,\text{Re} \int \phi_n(z_l) dz_l, \quad \Psi_n(z_s) = -\,\text{Im} \int \psi_n(z_s) dz_s$$
$$T_n(z) = -\,\text{Re}\, \Im_n(z) dz \tag{6}$$

and $\phi_n(z_l)$, $\psi_n(z_l)$, and $\Im_n(z)$ can be expanded by a power series as

$$\phi_n(z_l) = \sum_{n=1}^{\infty} A_n z_l^{n/2}, \quad \psi_n(z_s) = \sum_{n=1}^{\infty} B_n z_s^{n/2}, \quad \Im_n(z) = \sum_{n=1}^{\infty} C_n z^{n/2} \tag{7}$$

where $A_n = A_n^o + iA_n^*$, $B_n = B_n^o + iB_n^*$, $C_n = C_n^o + iC_n^*$, $z_{l(s)} = x + m_{l(s)} y$, and $z = x + iy$.

When Φ, Ψ, and T in Eq. (6) are expanded as an infinite series as given in Eq. (7), the structure of Eqs. (5*a*) and (5*b*) can be expressed as Eqs. (8*a*), (8*b*), (9*a*), and (9*b*) for $n=1,2$ and $n=3,4$, respectively.

$$\alpha_l^2 \frac{\partial^2 \Phi_n}{\partial x^2} + \frac{\partial^2 \Phi_n}{\partial y^2} = 0, \quad n = 1,2 \tag{8a}$$

$$\alpha_s^2 \frac{\partial^2 \Psi_n}{\partial x^2} + \frac{\partial^2 \Psi_n}{\partial y^2} = 0, \quad n = 1,2 \tag{8b}$$

$$\alpha_l^2 \frac{\partial^2 \Phi_n}{\partial x^2} + \frac{\partial^2 \Phi_n}{\partial y^2} = -\zeta \left[\frac{\partial \Phi_{n-2}}{\partial x} + \frac{1}{K+2} \frac{\partial \Psi_{n-2}}{\partial y} \right] + \frac{3K+2}{K+2} \alpha_c T_{n-2}, \quad n = 3,4 \tag{9a}$$

$$\alpha_s^2 \frac{\partial^2 \Psi_n}{\partial x^2} + \frac{\partial^2 \Psi_n}{\partial y^2} = -\zeta \left[\frac{\partial \Psi_{n-2}}{\partial x} + K \frac{\partial \Phi_{n-2}}{\partial y} \right], \quad n = 3,4 \tag{9b}$$

2.1 Stress and Displacement Fields for $n=1$ and $n=2$. Equations (8*a*) and (8*b*) is Laplace's equation in complex domain $z_{l(s)} = x + m_{l(s)} y$, and this representation is similar to that for a homogeneous material. Equations (8*a*) and (8*b*) can be rewritten as $(\alpha_l^2 + m_l^2)\Phi_n''(z_l) = 0$ and $(\alpha_s^2 + m_s^2)\Psi_n''(z_s) = 0$, where $m_l = i\alpha_l$ and $m_s = i\alpha_s$. Substituting Eq. (6) into Eq. (3) and the derivatives of the

resulting equations into Eqs. (2*a*)–(2*c*), and applying traction free boundary conditions [20] on the crack surface, A_n and B_n in Eq. (7) can be obtained as

$$A_n^o = -\frac{2B_{\mathrm{I}}(c)K_n^o}{\mu_c\sqrt{2\pi}}, \quad A_n^* = \frac{2B_{\mathrm{II}}(c)K_n^*}{\mu_c\sqrt{2\pi}},$$
$$B_n^o = \frac{2h_n^oB_{\mathrm{I}}(c)K_n^o}{\mu_c\sqrt{2\pi}}, \quad B_n^* = -\frac{2h_n^*B_{\mathrm{II}}(c)K_n^*}{\mu_c\sqrt{2\pi}} \tag{10}$$

where $B_{\mathrm{I}}(c)=(1+\alpha_s^2)/[4\alpha_l\alpha_s-(1+\alpha_s^2)^2]$, $B_{\mathrm{II}}(c)=2\alpha_s/[4\alpha_l\alpha_s-(1+\alpha_s^2)^2]$, $h_1^o=h_2^*=2\alpha_l/(1+\alpha_s^2)$, $h_1^*=h_2^o=(1+\alpha_s^2)/2\alpha_s$, and μ_c is the shear modulus at the crack tip. Substituting Eq. (10) into Eq. (6) and substituting Eq. (6) into Eqs. (2*a*)–(2*c*) and (3), the stresses and displacements for a propagating crack are obtained as

$$\sigma_{ijn} = \exp(\zeta x)\sum_{n=1}^{2} n\sigma_{ijn}^o$$
$$u_n = \exp(-\zeta a)\sum_{n=1}^{2} u_n^o \tag{11}$$
$$v_n = \exp(-\zeta a)\sum_{n=1}^{2} v_n^o$$

where

$$\sigma_{xxn}^o = \frac{K_n^oB_{\mathrm{I}}(c)}{\sqrt{2\pi}}\{f_1r_l^{(n-2)/2}C(n,\theta_l) - f_1^o(n)r_s^{(n-2)/2}C(n,\theta_s)\} + \frac{K_n^*B_{\mathrm{II}}(c)}{\sqrt{2\pi}}\{f_1r_l^{(n-2)/2}S(n,\theta_l) - f_1^*(n)r_s^{(n-2)/2}S(n,\theta_s)\}$$

$$\sigma_{yyn}^o = \frac{K_n^oB_{\mathrm{I}}(c)}{\sqrt{2\pi}}\{-f_2r_l^{(n-2)/2}C(n,\theta_l) + f_1^o(n)r_s^{(n-2)/2}C(n,\theta_s)\} + \frac{K_n^*B_{\mathrm{II}}(c)}{\sqrt{2\pi}}\{-f_2r_l^{(n-2)/2}S(n,\theta_l) + f_1^*(n)r_s^{(n-2)/2}S(n,\theta_s)\}$$

$$\tau_{xyn}^o = \frac{K_n^oB_{\mathrm{I}}(c)}{\sqrt{2\pi}}\{-2\alpha_lr_l^{(n-2)/2}S(n,\theta_l) + f_2^o(n)r_s^{(n-2)/2}S(n,\theta_s)\} + \frac{K_n^*B_{\mathrm{II}}(c)}{\sqrt{2\pi}}\{2\alpha_lr_l^{(n-2)/2}C(n,\theta_l) - f_2^*(n)r_s^{(n-2)/2}C(n,\theta_s)\}$$

$$u_n^o = \frac{K_n^oB_{\mathrm{I}}(c)}{\mu_0}\sqrt{\frac{2}{\pi}}\left\{r_l^{n/2}\cos\left(\frac{n}{2}\right)\theta_l - g_1^o(n)r_s^{n/2}\cos\left(\frac{n}{2}\right)\theta_s\right\} + \frac{K_n^*B_{\mathrm{II}}(c)}{\mu_0}\sqrt{\frac{2}{\pi}}\left\{r_l^{n/2}\sin\left(\frac{n}{2}\right)\theta_l - g_1^*(n)r_s^{n/2}\sin\left(\frac{n}{2}\right)\theta_s\right\}$$

$$v_n^o = \frac{K_n^oB_{\mathrm{I}}(c)}{\mu_0}\sqrt{\frac{2}{\pi}}\left\{-\alpha_lr_l^{n/2}\sin\left(\frac{n}{2}\right)\theta_l + g_2^o(n)r_s^{n/2}\sin\left(\frac{n}{2}\right)\theta_s\right\} + \frac{K_n^*B_{\mathrm{II}}(c)}{\mu_0}\sqrt{\frac{2}{\pi}}\left\{\alpha_lr_l^{n/2}\cos\left(\frac{n}{2}\right)\theta_l - g_2^*(n)r_s^{n/2}\cos\left(\frac{n}{2}\right)\theta_s\right\}$$

$$f_1 = 1 + 2\alpha_l^2 - \alpha_s^2, \quad f_2 = 1 + \alpha_s^2$$

$$C(n,\theta_j) = \cos\left(\frac{n-2}{2}\right)\theta_j, \quad S(n,\theta_j) = \sin\left(\frac{n-2}{2}\right)\theta_j$$

$$f_1^o(n) = 2\alpha_sh_n^o, \quad f_1^*(n) = 2\alpha_sh_n^*, \quad f_2^o(n) = f_2h_n^o$$
$$f_2^*(n) = f_2h_n^*, \quad g_1^o(n) = \alpha_sh_n^o$$
$$g_1^*(n) = \alpha_sh_n^*, \quad g_2^o(n) = h_n^o$$
$$g_2^*(n) = h_n^*, \quad r_j = \sqrt{x^2 + (\alpha_jy)^2}$$
$$\theta_j = \tan^{-1}(\alpha_jy/x) \quad j = l,s$$

where K_1^o and K_1^* for $n=1$ denote the stress intensity factors K_{I} and K_{II}, respectively.

2.2 Stress and Displacement Fields for $n=3$ and $n=4$. For $n\geqslant 3$, the solutions of Φ_n and Ψ_n have nonhomogeneous coefficients in addition to temperature field terms, as shown in Eqs. (9*a*) and (9*b*). For $n=3$ and $n=4$, the relation between $\Phi_{n-2}(z_l)$ and $\Psi_{n-2}(z)$ in equilibrium equation (Eqs. (9*a*) and (9*b*)) can be written as shown in Eq. (12). The details for the derivation of Eq. (12) can be seen in Ref. [22],

$$\frac{\partial}{\partial y}\Psi_{n-2}(z_s) = -(K+2)\frac{\partial}{\partial x}\Phi_{n-2}(z_l)$$
$$\frac{1}{K+2}\frac{\partial}{\partial x}\Psi_{n-2}(z_s) = \frac{\partial}{\partial y}\Phi_{n-2}(z_l) \tag{12}$$

Thus, Eqs. (9*a*) and (9*b*) can be expressed as

$$\alpha_l^2\frac{\partial^2\Phi_n}{\partial x^2} + \frac{\partial^2\Phi_n}{\partial y^2} = \frac{3K+2}{K+2}\alpha_cT_{n-2}(z)$$
$$\alpha_s^2\frac{\partial^2\Psi_n}{\partial x^2} + \frac{\partial^2\Psi_n}{\partial y^2} = -\zeta\left[D_s\frac{\partial\Psi_{n-2}(z_s)}{\partial x}\right] \tag{13}$$

where $D_s=1+K/(K+2)=2(\alpha_l^2-\alpha_s^2)/(1-\alpha_s^2)$.

Applying $z=x+my$ in Eq. (13), we get

$$(\alpha_l^2 + m_l^2)\Phi_n''(z_l) = \frac{3K+2}{K+2}\alpha_cT_{n-2}(z)$$
$$(\alpha_s^2 + m_s^2)\Psi_n''(z_s) = -\varsigma[D_s\Psi_{n-2}'(z_s)] \tag{14}$$

where

$$m_l = i\hat{\alpha}_l, \quad m_s = i\hat{\alpha}_s \tag{15}$$

and $\hat{\alpha}_l=\sqrt{\alpha_l^2-(2/n)R_n^o[(3K+2)/(K+2)]\alpha_c}$, $\hat{\alpha}_s=\sqrt{\alpha_s^2+(2/n)\zeta k_n^oD_s}$ for the Mode I case, where $k_n^o=B_{n-2}^o/B_n^o=A_{n-2}^o/A_n^o$, and $(3K+2)/(K+2)=3(a_l^2-a_s^2)/(1-a_l^2)-1$ and $\hat{\alpha}_l=\sqrt{\alpha_l^2-(2/n)R_n^o[(3K+2)/(K+2)]\alpha_c}$, $\hat{\alpha}_s=\sqrt{\alpha_s^2+(2/n)\zeta k_n^oD_s}$ for the Mode II case, where $k_n^*=B_{n-2}^*/B_n^*=A_{n-2}^*/A_n^*$ and $R_n^*=C_{n-2}^*/A_n^*$.

Thus, Eq. (13) can be expressed as

$$\hat{\alpha}_l^2\frac{\partial^2\Phi_n(\hat{z}_l)}{\partial x^2} + \frac{\partial^2\Phi_n(\hat{z}_l)}{\partial y^2} = 0, \quad \hat{\alpha}_s^2\frac{\partial^2\Psi_n(\hat{z}_s)}{\partial x^2} + \frac{\partial^2\Psi_n(\hat{z}_s)}{\partial y^2} = 0 \tag{16}$$

where $\hat{z}_l=x+i\hat{\alpha}_ly$ and $\hat{z}_s=x+i\hat{\alpha}_sy$. $\hat{\alpha}_l$ is dependent on the crack propagation speed, physical properties, and thermal expansion and $\hat{\alpha}_s$ is dependent on a nonhomogeneity constant, physical properties, crack propagation speed, and stress intensity factors (Modes I and II). Equation (16) is also Laplace's equation in complex domains $\hat{z}_l$ and $\hat{z}_s$. This form of the equation is similar to that for a homogeneous material and can be rewritten as $(\hat{\alpha}_l^2+m_l^2)\Phi_n''(z_l)=0$ and $(\hat{\alpha}_s^2+m_s^2)\Psi_n''(z_s)=0$, where $m_l=i\hat{\alpha}_l$ and $m_s=i\hat{\alpha}_s$.

Similar to $n=1$ and $n=2$, the solutions for Laplace's equations

of $n=3$ and $n=4$ can be obtained in terms of harmonic functions. Thus, $\Phi_n(\hat{z}_l)$ and $\Psi_n(\hat{z}_s)$ in Eq. (16) can be written as

$$\Phi_n(\hat{z}_l) = -\,\mathrm{Re}\int \phi_n(\hat{z}_l)d\hat{z}_l, \quad \Psi_n(\hat{z}_s) = -\,\mathrm{Im}\int \psi_n(\hat{z}_s)d\hat{z}_s \tag{17}$$

where $\phi_n(\hat{z}_l)$ and $\psi_n(\hat{z}_s)$ can be written as power series as given in Eq. (7), and $\hat{z}_j = x + \hat{m}_j y = x + i\hat{\alpha}_j y$, $\hat{r}_j = \sqrt{x^2 + (\hat{\alpha}_j y)^2}$, $\hat{\theta}_j = \tan^{-1}[\hat{\alpha}_j y/x]$, $j = l, s$

Substituting the solutions $\Phi_n(\hat{z}_l)$ and $\Psi_n(\hat{z}_s)$ from Eq. (17) into Eq. (3), the displacements u and v for $n=3,4$ can be expressed as

$$u = -\,\mathrm{Re}\{\phi_n(\hat{z}_l) + \hat{\alpha}_s\psi_n(\hat{z}_s)\}, \quad v = \mathrm{Im}\{\hat{\alpha}_l\phi_n(\hat{z}_l) + \psi_n(\hat{z}_s)\} \tag{18}$$

After differentiating the displacement expressions of Eq. (18) and substituting these strains into Eqs. (2*a*)–(2*c*), the stresses σ_{ij} for $n=3,4$ can be expressed as

$$\sigma_{xx} = -\,\mu\,\mathrm{Re}\left\{\frac{1-\alpha_s^2}{1-\alpha_l^2}(1-\hat{\alpha}_l^2)\phi_n'(\hat{z}_l) + 2\hat{\alpha}_l^2\phi_n'(\hat{z}_l) + 2\hat{\alpha}_s\psi_n'(\hat{z}_s) + (3K+2)\alpha_c e^{\beta x}T_{n-2}(z)\right\}$$

$$\sigma_{yy} = -\,\mu\,\mathrm{Re}\left\{\frac{1-\alpha_s^2}{1-\alpha_l^2}(1-\hat{\alpha}_l^2)\phi_n'(\hat{z}_l) - 2\phi_n'(\hat{z}_l) - 2\hat{\alpha}_s\psi_n'(\hat{z}_s) + (3K+2)\alpha_c e^{\beta x}T_{n-2}(z)\right\} \tag{19}$$

$$\tau_{xy} = \mu\,\mathrm{Im}\{2\hat{\alpha}_l\phi_n'(\hat{z}_l) + (1+\hat{\alpha}_s^2)\psi_n'(\hat{z}_s)\}$$

$\phi_n(\hat{z}_l)$ and $\psi_n(\hat{z}_l)$ can be written as

$$\phi_n(\hat{z}_l) = \sum_{n=3}^{4}(\hat{A}_n^o + i\hat{A}_n^*)\hat{z}_l^{n/2}$$

$$\psi_n(\hat{z}_l) = \sum_{n=3}^{4}(\hat{B}_n^o + i\hat{B}_n^*)\hat{z}_s^{n/2} \tag{20}$$

$$T_{n-2} = \sum_{n=3}^{4}(C_{n-2}^o + iC_{n-2}^*)z^{(n-2)/2}$$

Now, applying the traction free boundary conditions on the crack surface, $\hat{A}_n^o$, $\hat{B}_n^o$, $\hat{A}_n^*$, and $\hat{B}_n^*$ can be obtained as

$$\hat{A}_n^o = -\frac{2}{\mu_c\sqrt{2\pi}}\hat{B}_{\mathrm{I}}(c)\hat{K}_n^o$$

$$\hat{A}_n^* = \frac{2}{\mu_c\sqrt{2\pi}}\hat{B}_{\mathrm{II}}(c)\hat{K}_n^* \tag{21}$$

$$\hat{B}_n^o = -\,h_n^o\hat{A}_n^o, \quad \hat{B}_n^* = -\,h_n^*\hat{A}_n^*$$

where

$$\hat{B}_{\mathrm{I}}(c) = \frac{(1+\hat{\alpha}_s^2)(1-\alpha_l^2)}{4\alpha_l\hat{\alpha}_s(1-\alpha_l^2) + (1+\alpha_s^2)[(1-\alpha_s^2)(1-\hat{\alpha}_l^2) - 2(1-\alpha_l^2)]}$$

$$\hat{B}_{\mathrm{II}}(c) = \frac{2\hat{\alpha}_s(1-\alpha_l^2)}{4\alpha_l\hat{\alpha}_s(1-\alpha_l^2) + (1+\alpha_s^2)[(1-\alpha_s^2)(1-\hat{\alpha}_l^2) - 2(1-\alpha_l^2)]}$$

Using the relations $\hat{A}_n^{o(*)} = \eta_{n-2}^{o(*)}A_{n-2}^{o(*)}/k_n^{o(*)}$ and $R_n^{o(*)} = C_{n-2}^{o(*)}/\hat{A}_n^{o(*)}$ and substituting Eqs. (20) and (21) into Eq. (19), the thermomechanical stress fields σ_{ijn} for $n=3,4$ can be obtained as

$$\sigma_{xxn} = \sum_{n=3}^{4}\frac{nK_n^oB_{\mathrm{I}}(c)}{\sqrt{2\pi}}\exp(\zeta x)\left\{\left[\frac{1-\alpha_s^2}{1-\alpha_l^2}(1-\hat{\alpha}_l^2) + 2\hat{\alpha}_l^2\right]\hat{r}_l^{(n-2)/2}\cos\left(\frac{n-2}{2}\right)\hat{\theta}_l - 2h_n^o\hat{\alpha}_s\hat{r}_s^{(n-2)/2}\cos\left(\frac{n-2}{2}\right)\hat{\theta}_s + \frac{R_n^o}{n}\left[\frac{3(\alpha_l^2-\alpha_s^2)}{1-\alpha_l^2} - 1\right]\alpha_c e^{\beta x}r^{(n-2)/2}\cos\left(\frac{n-2}{2}\right)\theta\right\}$$
$$+ \sum_{n=3}^{4}\frac{nK_n^*B_{\mathrm{II}}(c)}{\sqrt{2\pi}}\exp(\zeta x)\left\{\left[\frac{1-\alpha_s^2}{1-\alpha_l^2}(1-\hat{\alpha}_l^2) + 2\hat{\alpha}_l^2\right]\hat{r}_l^{(n-2)/2}\sin\left(\frac{n-2}{2}\right)\hat{\theta}_l - 2h_n^*\hat{\alpha}_s\hat{r}_s^{(n-2)/2}\sin\left(\frac{n-2}{2}\right)\hat{\theta}_s - \frac{R_n^*}{n}\left[\frac{3(\alpha_l^2-\alpha_s^2)}{1-\alpha_l^2} - 1\right]\alpha_c e^{\beta x}r^{(n-2)/2}\sin\left(\frac{n-2}{2}\right)\theta\right\}$$

$$\sigma_{yyn} = \sum_{n=3}^{4}\frac{nK_n^oB_{\mathrm{I}}(c)}{\sqrt{2\pi}}\exp(\zeta x)\left\{\left[\frac{1-\alpha_s^2}{1-\alpha_l^2}(1-\hat{\alpha}_l^2) - 2\right]\hat{r}_l^{(n-2)/2}\cos\left(\frac{n-2}{2}\right)\hat{\theta}_l + 2h_n^o\hat{\alpha}_s\hat{r}_s^{(n-2)/2}\cos\left(\frac{n-2}{2}\right)\hat{\theta}_s + \frac{R_n^o}{n}\left[\frac{3(\alpha_l^2-\alpha_s^2)}{1-\alpha_l^2} - 1\right]\alpha_c e^{\beta x}r^{(n-2)/2}\cos\left(\frac{n-2}{2}\right)\theta\right\}$$
$$+ \sum_{n=3}^{4}\frac{nK_n^*B_{\mathrm{II}}(c)}{\sqrt{2\pi}}\exp(\zeta x)\left\{\left[\frac{1-\alpha_s^2}{1-\alpha_l^2}(1-\hat{\alpha}_l^2) - 2\right]\hat{r}_l^{(n-2)/2}\sin\left(\frac{n-2}{2}\right)\hat{\theta}_l + 2h_n^*\hat{\alpha}_s\hat{r}_s^{(n-2)/2}\sin\left(\frac{n-2}{2}\right)\hat{\theta}_s + \frac{R_n^*}{n}\left[\frac{3(\alpha_l^2-\alpha_s^2)}{1-\alpha_l^2} - 1\right]\alpha_c e^{\beta x}r^{(n-2)/2}\sin\left(\frac{n-2}{2}\right)\theta\right\} \tag{22}$$

$$\tau_{xyn} = \sum_{n=3}^{4}\frac{nK_n^oB_{\mathrm{I}}(c)}{\sqrt{2\pi}}\exp(\zeta x)\left\{-2\hat{\alpha}_l\hat{r}_l^{(n-2)/2}\sin\left(\frac{n-2}{2}\right)\hat{\theta}_l + (1+\hat{\alpha}_s^2)h_n^o\hat{r}_s^{(n-2)/2}\sin\left(\frac{n-2}{2}\right)\hat{\theta}_s\right\} + \sum_{n=3}^{4}\frac{nK_n^*B_{\mathrm{II}}(c)}{\sqrt{2\pi}}\exp(\zeta x)\times\left\{2\hat{\alpha}_l\hat{r}_l^{(n-2)/2}\cos\left(\frac{n-2}{2}\right)\hat{\theta}_l - (1+\hat{\alpha}_s^2)h_n^*\hat{r}_s^{(n-2)/2}\cos\left(\frac{n-2}{2}\right)\hat{\theta}_s\right\}$$

where

$$h_3^o = h_4^* = \frac{2\hat{\alpha}_l}{(1+\hat{\alpha}_s^2)}, \quad h_3^* = h_4^o = \frac{2(1-\alpha_l^2) - (1-\alpha_s^2)(1-\hat{\alpha}_l^2)}{2\hat{\alpha}_s(1-\alpha_l^2)}$$

$$K_3^o = \eta_1^oK_1^o(K_{\mathrm{I}})/k_3^o, \quad K_4^o = \eta_2^oK_2^o/k_4^o$$

$$K_3^* = \eta_1^*K_1^*(K_{\mathrm{II}})/k_3^*, \quad K_4^* = \eta_2^*K_2^*/k_4^*$$

$$R_3^o = C_1^o/\hat{A}_3^o = 0, \quad R_4^* = C_2^*/\hat{A}_4^* = 0 \text{ (see Sec. 3)}$$

$$\hat{r}_l = \sqrt{x^2 + (\hat{\alpha}_l y)^2}, \quad \hat{r}_s = \sqrt{x^2 + (\hat{\alpha}_s y)^2}$$

$$\hat{\theta}_l = \tan^{-1}[\hat{\alpha}_l y/x], \quad \hat{\theta}_s = \tan^{-1}[\hat{\alpha}_s y/x]$$

Substituting Eqs. (20) and (13) into Eq. (18), the displacement fields for $n=3,4$ can be obtained as

$$u_n = \sum_{n=3}^{4} \frac{K_n^o B_{\mathrm{I}}(c)}{\mu_0 \exp(\zeta a)} \sqrt{\frac{2}{\pi}} \left\{ \hat{r}_l^{n/2} \cos\left(\frac{n}{2}\right)\hat{\theta}_l - \hat{\alpha}_s h_n^o r_s^{n/2} \cos\left(\frac{n}{2}\right)\hat{\theta}_s \right\} + \sum_{n=3}^{4} \frac{K_n^* B_{\mathrm{II}}(c)}{\mu_0 \exp(\zeta a)} \sqrt{\frac{2}{\pi}} \left\{ \hat{r}_l^{n/2} \sin\left(\frac{n}{2}\right)\hat{\theta}_l - \hat{\alpha}_s h_n^* \hat{r}_s^{n/2} \sin\left(\frac{n}{2}\right)\hat{\theta}_s \right\}$$

$$v_n = \sum_{n=3}^{4} \frac{K_n^o B_{\mathrm{I}}(c)}{\mu_0 \exp(\zeta a)} \sqrt{\frac{2}{\pi}} \left\{ -\hat{\alpha}_l \hat{r}_l^{n/2} \sin\left(\frac{n}{2}\right)\hat{\theta}_l + h_n^o \hat{r}_s^{n/2} \sin\left(\frac{n}{2}\right)\hat{\theta}_s \right\} + \sum_{n=3}^{4} \frac{K_n^* B_{\mathrm{II}}(c)}{\mu_0 \exp(\zeta a)} \sqrt{\frac{2}{\pi}} \left\{ \hat{\alpha}_l \hat{r}_l^{n/2} \cos\left(\frac{n}{2}\right)\hat{\theta}_l - h_n^* \hat{r}_s^{n/2} \cos\left(\frac{n}{2}\right)\hat{\theta}_s \right\} \tag{23}$$

Finally, the stress and displacement fields σ_{ij}, u, and v for the FGM are given by

$$\sigma_{ij} = \sum_{n=1}^{4} \sigma_{ijn}, \quad u = \sum_{n=1}^{4} u_n^o, \quad v = \sum_{n=1}^{4} v_n^o \tag{24}$$

In Eq. (23), a is the half crack length for a center crack or the crack length for an edge crack. μ_0 is the shear modulus at $x=-a$. Thus, crack-tip shear modulus μ_c is equal to $\mu_0 \exp(-\zeta a)$. When the nonhomogeneity parameter $\zeta=0$, Eq. (22) reduces to the stress field equations for an isotropic homogeneous material.

2.3 Temperature and Heat Flux Distribution Fields for an Exponential Variation of Heat Conductivity. For steady state heat conduction (without heat generation), heat conduction equation can be expressed as

$$\frac{\partial}{\partial X}\left(k\frac{\partial T}{\partial X}\right) + \frac{\partial}{\partial Y}\left(k\frac{\partial T}{\partial Y}\right) = 0 \tag{25}$$

Substituting the heat conductivity k from Eq. (1*e*) into Eq. (25), Eq. (25) can be expressed as

$$\nabla^2 T + \delta\frac{\partial T}{\partial X} = 0 \tag{26}$$

where $\nabla^2 = \partial^2/\partial X^2 + \partial^2/\partial Y^2$. By using crack-tip coordinates, the above equation can be transformed into crack tip coordinates as given in

$$\nabla^2 T + \delta\frac{\partial T}{\partial x} = 0 \tag{27}$$

where $\nabla^2 = \partial^2/\partial x^2 + \partial^2/\partial y^2$.

Now, applying $z=x+my$ and substituting $T_n(z)$ in Eqs. (6) into Eq. (27) gives

$$(1+m^2)T_n''(z) = -\delta T_{n-2}'(z) \tag{28}$$

For $n=1,2$, Eq. (28) can be expressed as

$$(1+m^2)T_n''(z) = 0 \tag{29}$$

Equation (29) is Laplace's equation in the complex domain $z=x+my$ and $m=i$. Substituting Eq. (6) into Eq. (29), and assuming the crack surface to be insulated, that is, $\partial T/\partial\theta=0$, C_n in Eq. (7) can be obtained as

$$C_1^o = 0, \quad C_1^* = \frac{2K_1^t}{\sqrt{2\pi}} \quad \text{for } n=1$$
$$C_2^* = 0, \quad C_2^o = -\frac{2K_2^t}{\sqrt{2\pi}} \quad \text{for } n=2 \tag{30}$$

Substituting Eq. (30) into Eq. (7) and then into Eq. (6), the temperature distribution for $n=1,2$ can be expressed as

$$T_n = \sqrt{\frac{2}{\pi}}\left(K_1^t r^{1/2} \sin\frac{\theta}{2} + K_2^t r \cos\theta\right) \tag{31}$$

where K_1^t is the heat flux intensity factor K_T. For $n=3,4$, m in Eq. (28) can be expressed as

$$m = i\eta \tag{32}$$

where

$$\eta = \sqrt{1+\delta_3^2 k_3^*}, \quad k_3^* = C_1^*/C_3^* \quad \text{for } n=3$$
$$\eta = \sqrt{1+\delta_2^1 k_4^o}, \quad k_4^o = C_2^o/C_4^o \quad \text{for } n=4$$

Thus, Eq. (28) can be expressed as $(1-\eta^2)T_n''(z)=0$. Applying $\partial T/\partial\theta=0$ on the crack surface, C_3 and C_4 in Eq. (7) can be obtained as

$$C_3^o = 0, \quad C_3^* = \frac{2K_3^t}{\sqrt{2\pi}} \quad \text{for } n=3$$
$$C_4^* = 0, \quad C_4^o = -\frac{2K_4^t}{\sqrt{2\pi}} \quad \text{for } n=4 \tag{33}$$

Substituting Eq. (33) into Eq. (7) and then Eq. (6), the temperature distribution for $\mathbf{n}=3,4$ can be expressed as

$$T_n = \sqrt{\frac{2}{\pi}}\left(K_3^t r_t^{3/2} \sin\frac{\theta_t}{2} + K_4^t r_t^2 \cos 2\theta_t\right) \tag{34}$$

Thus, the total temperature distribution at the crack tip can be expressed as

$$T = \sqrt{\frac{2}{\pi}}\left(K_1^t r^{1/2} \sin\frac{\theta}{2} + K_2^t r\cos\theta + K_3^t r_t^{3/2} \sin\frac{3\theta_t}{2} + K_4^t r_t^2 \cos 2\theta_t\right) \tag{35}$$

Now, heat flux $q_i=-kT_i$, thus, q_i can be written as

$$q_x = -k_c \exp(\delta x)\sqrt{\frac{2}{\pi}}\left(-\frac{1}{2}K_1^t r^{-1/2}\sin\frac{\theta}{2} + K_2^t + \frac{3}{2}K_3^t r_t^{1/2}\sin\frac{\theta_t}{2} + 2K_4^t r_t^2\cos\theta_t + \cdots\right)$$
$$q_y = -k_c \exp(\delta x)\sqrt{\frac{2}{\pi}}\left(\frac{1}{2}K_1^t r^{-1/2}\cos\frac{\theta}{2} + \frac{3}{2}\eta K_3^t r_t^{1/2}\cos\frac{\theta_t}{2} - 2\eta K_4^t r_t^2 \sin\theta_t + \cdots\right) \tag{36}$$

where k_c is heat conductivity at the crack tip, $r_t=\sqrt{x^2+(\eta y)^2}$, and $\theta_t=\tan^{-1}[\eta y/x]$.

3 Discussion of Solutions

The effect of nonhommogeniety on the stress field around the crack tip was evaluated by plotting contours of constant maximum shear stress also called the isochromatic fringes. The isochromatic fringes were generated to elucidate the effect of crack velocity, heating and material gradation on the whole field stress distribution under Mode I and mixed-mode loading. In order to generate these isochromatic fringes, we made use of the stress optic law [23] given in

$$\sqrt{(\sigma_{xx}-\sigma_{yy})^2 + 4\tau_{xy}^2} = \frac{Nf_\sigma}{h} \tag{37}$$

where N is the fringe order, h is the plate thickness, and f_σ is the material fringe constant. The normal and shear stresses in Eq. (37) were substituted from Eq. (22) for $n=1$, 2, 3, and 4. The following material parameters were used to plot the stress contours: f_σ

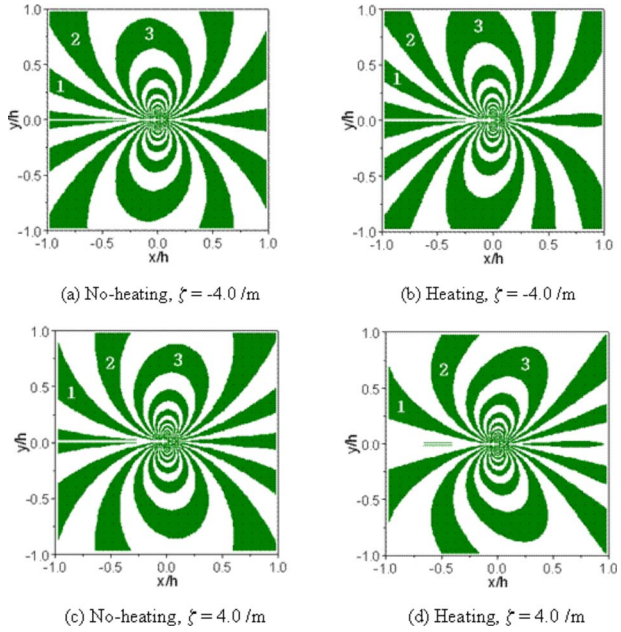

Fig. 2 The isochromatics associated with a stationary crack tip in FGM under heating for $k^o_{3(4)}=0.1$ m, $K^o_1(K_I)=1.0$ MPa $\sqrt{\text{m}}$, $K^o_2=0$, $K^o_3=5\times10^{-4}K_I/k^o_3$, $K^o_4=0.2K^o_3$, $M(c/c_s)=0.02$, $R^o_4=-1\times10^4(^\circ\text{C})$, $\alpha_0=0.00008/^\circ\text{C}$, and $\beta=0$

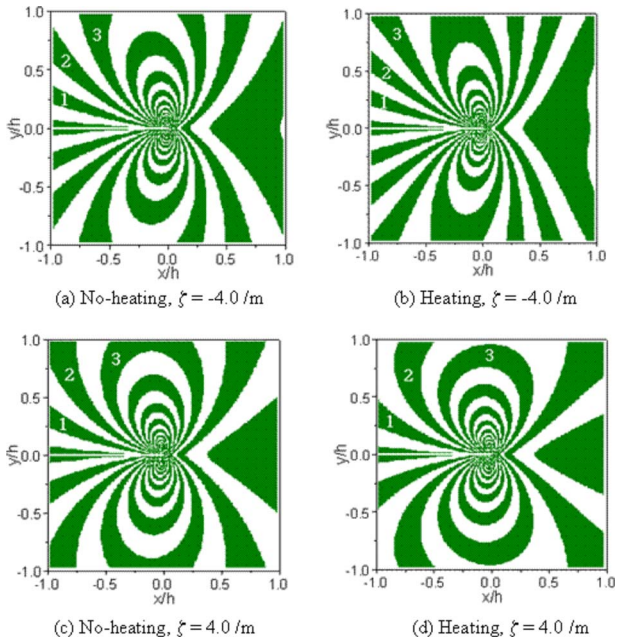

Fig. 3 The isochromatics associated with a propagating crack tip in FGM under heating for $k^o_{3(4)}=10^5$ m, $K^o_1(K_I)=1.0$ MPa $\sqrt{\text{m}}$, $K^o_2=0$, $K^o_3=K_I/k^o_3$, $M(c/c_s)=0.5$, $K^o_4=0.5K^o_3$, $R^o_4=-1\times10^4(^\circ\text{C})$, and $\alpha_0=0.00008/^\circ\text{C}$, and $\beta=0$

$=15$ kN/m, $h=9.5$ mm, $\mu(X)=1.316\exp(\zeta X)$ GPa, $\varsigma=4.0/\text{m}$ or $-4.0/\text{m}$, $\nu=0.33$, and $\rho_o=1200$ kg/m^3.

Figure 2 shows the isochromatic fringes for a stationary crack under Mode I loading conditions in a FGM in the direction of increasing or decreasing properties and under heating or no-heating conditions. All the frames show typical ovaloid shaped fringes associated with the crack tip. For nonheating conditions, the fringes match well with the corresponding fringes obtained by Parameswaran and Shukla [24] for FGMs under quasistatic mechanical loading conditions. Heating increases the stress intensity around the crack tip and tilts the fringes toward the stiffer region of the nonhomogeneous material in both cases of either increasing or decreasing nonhomogeneous properties. This stress intensity increase and the tilt are in agreement with the observations for a stationary crack under heating reported by Jain et al. [18].

Figure 3 shows the isochromatic fringes for a crack propagating under Mode I loading in a FGM in the direction of increasing or decreasing properties and under heating or no-heating conditions. From Figs. 3(*a*) and 3(*b*) one can see that the intensity of stresses increases around the crack tip as the plate is heated if the properties decrease ahead of the crack tip. Also, the tilt of the fringes indicates a stronger stress component acting parallel to the crack when heating is applied. These effects are reversed when the material properties increase ahead of the crack tip, as shown in Figs. 3(*c*) and 3(*d*). Both the intensity of stress field as well as the stress component parallel to the crack are reduced with heating for a FGM with increasing material properties. A comparison of Figs 3(*a*)–3(*d*) clearly shows that for the same loading conditions with or without heating, the stress field is more intense when the properties ahead of the crack tip decrease. This is evident by the size of the fringes around the crack tip. The tilt of the fringes also indicates that the stress acting parallel to the crack is much higher when the properties decrease ahead of the crack tip. The tilt of the fringes toward the stiffer region in both cases is due to higher $\tau_{\max}$ in the stiffer region for a given thermomechanical loading.

Figure 4 shows the isochromatic fringes for a crack propagating under mixed-mode loading in a FGM in the direction of increasing or decreasing properties and under heating or no-heating conditions. All the frames show typical inclined fringes associated with the mixed-mode crack-tip loading conditions. From Figs. 4(*a*) and 4(*b*), it can be seen that the intensity of stresses increases around the crack tip in the third quadrant and the same decreases in the first quadrant as the plate is heated if the properties decrease ahead of the crack tip. Also, similar to the Mode I conditions, the tilt of the fringes indicates a stronger stress component acting parallel to the crack when heating is applied. These effects are

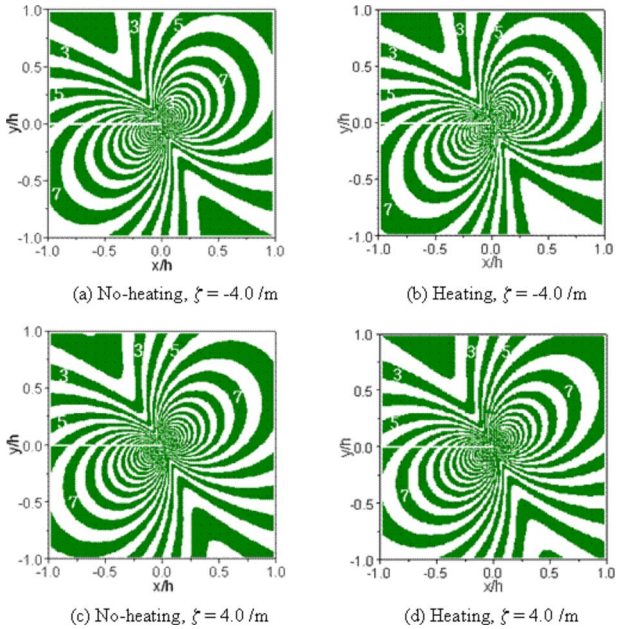

Fig. 4 The isochromatics associated with a mixed-mode propagating crack tip in FGM under heating for $K^o_1(K_I)=1.0$ MPa $\sqrt{\text{m}}$, $K^*_1(K_{II})=K^o_1$, $K^o_2=K^*_2=0$, $K^o_3=K_I/k^o_3$, $K^*_3=0.1K^o_3$, $k^{o(*)}_{3(4)}=10^5$ m, $M(c/c_s)=0.5$, $K^o_4=0.5K^o_3$, $R^*_3=R^o_4=-1\times10^4(^\circ\text{C})$, $\alpha_0=0.00008/^\circ\text{C}$, and $\beta=0$

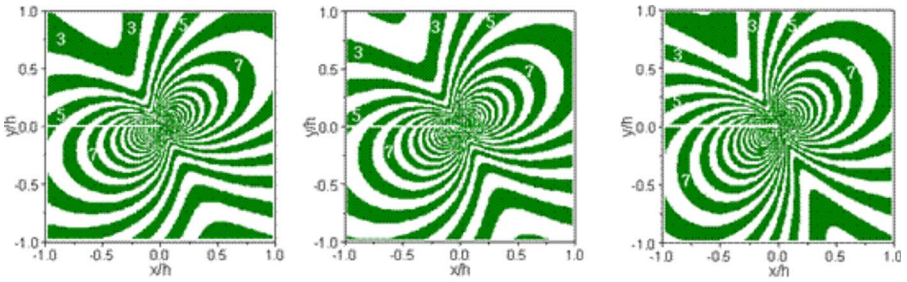

Fig. 5 The isochromatics associated with a mixed-mode propagating crack tip in FGM under heating for $K_1^o(K_I)=K_1^*(K_{II})=1.0$ MPa $\sqrt{m}$, $K_2^o=K_2^*=0$, $K_3^o=K_I/k_3^o$, $K_3^*=0.1K_3^o$, $k_{3(4)}^{o(*)}=10^5$ m, $M(c/c_s)=0.5$, $K_4^*=0.1K_3^o$, $R_3^*=R_4^o=-1\times10^4$(°C), and $\alpha_0=0.00008/°C$

reversed when the material properties increasine ahead of the crack tip, as shown in Figs. 4(*c*) and 4(*d*). The tilt of the fringes under mixed-mode conditions is complex and difficult to explain unless well-controlled experiments are conducted to visualize the tilt features.

Figure 5 shows the isochromatic fringes for a crack propagating under mixed-mode loading in a FGM in the direction of increasing properties and under heating conditions as a function of crack-tip speed. From Figs. 5(*a*)–5(*c*), it can be seen that, as the c/c_s increases, the intensity of stresses increase around the crack-tip in the third quadrant and the same decreases in the first quadrant. As the crack tip speed increases, the fringes tilt away from the crack face in the third quadrant and tilt toward the crack face in the first quadrant around the crack tip.

4 Summary of Results

Thermomechanical stress and displacement fields for a propagating crack in FGMs are developed using displacement potentials and an asymptotic analysis approach. In addition to mechanical fields, temperature and heat flux fields are also developed for exponential variation of thermal conductivity along the gradation direction. Using the asymptotic stress fields, the isochromatic fringes are developed as a function of heating or nonheating for both Mode I and mixed-mode mechanical loading conditions. In the case of Mode I loading conditions under heating, in the direction of decreasing properties ahead of the crack tip, the size of the isochromatic fringes increases and tilts toward the crack face. However, these effects are reversed when the material properties increase ahead of the crack tip. In the case of mixed-mode loading, the stress intensity significantly increases in the third quadrant ahead of the crack tip for decreasing material properties around the crack tip and the same decreases in the first quadrant. Similar to Mode I loading conditions, these effects are reversed when the material properties increase ahead of the crack tip.

Acknowledgment

The financial support of the Air Force Office of Scientific Research under Grant No. FA 95500610162 and the National Science Foundation under Grant No. CMS 0244330 is greatly acknowledged.

References

[1] Suresh, S., and Mortensen, A., 1998, *Fundamentals of Functionally Graded Materials, Processing and Thermomechanical Behavior of Graded Metals and Metal-Ceramic Composites*, IOM Communications Ltd., London.
[2] Hasselman, D. P. H., and Youngblood, G. E., 1978, "Enhanced Thermal Stress Resistance of Structural Ceramics with Thermal Conductivity Gradient," J. Am. Ceram. Soc., **61**, pp. 49–52.
[3] Kawasaki, A., and Wananabe, R., 1987, "Finite Element Analysis of Thermal Stress of the Metal/Ceramics Multi-layer Composites With Controlled Compositional Gradients," J. Jpn. Inst. Met., **51**, pp. 525–529.
[4] Drake, J. T., Williamson, R. L., and Rabin, B. H., 1993, "Finite Element Analysis of Thermal Residual Stresses at Graded Ceramic-Metal Interfaces—Part II: Interface Optimization for Residual Stress Reduction," J. Appl. Phys., **74**, pp. 1321–1326.
[5] Giannakopoulos, A. E., Suresh, S., Finot, M., and Olsson, M., 1995, "Elastoplastic Analysis of Thermal Cycling: Layered Materials With Compositional Gradient," Acta Metall. Mater., **43**, pp. 1335–1354.
[6] Kuroda, Y., Kusaka, K., Moro, A., and Togawa, M., 1993, "Evaluation Tests of ZrO_2/Ni Functionally Gradient Materials for Regeneratively Cooled Thrust Engine Applications," *Functionally Gradient Materials (Ceramic Transactions)*, J. B. Holt, M. Koisumi, T. Hirai, and Z. A. Munir, eds., American Ceramic Society, Westerville, OH, Vol. 34, pp. 289–296.
[7] Takahashi, H., Ishikawa, T., Okugawa, D., and Hashida, T., 1993, "Laser and Plasma-ARC Thermal Shock/Fatigue Fracture Evaluation Procedure for Functionally Gradient Materials," *Thermal Shock and Thermal Fatigue Behavior of Advanced Ceramics*, G. A. Scheneider and G. Petzow, eds., Kluwer Academic, Dordrecht, pp. 543–554.
[8] Jin, Z. H., and Noda, N., 1994, "Crack-Tip Singular Fields in Nonhomogeneous Materials," ASME J. Appl. Mech., **61**, pp. 738–740.
[9] Erdogan, F., and Wu, B., 1996, "Crack Problems in FGM Layers Under Thermal Stresses," J. Therm. Stresses, **19**, pp. 237–265.
[10] Jin, Z. H., and Batra, R. C., 1996, "Stress Intensity Relaxation at the Tip of an Edge Crack in a Functionally Graded Materials Subjected to a Thermal Shock," J. Therm. Stresses, **19**, pp. 317–339.
[11] Kokini, K., and Choules, B. D., 1995, "Surface Thermal Fracture of Functionally Graded Ceramic Coatings: Effect of Architecture and Materials," Composites Eng., **5**, pp. 865–877.
[12] Kokini, K., and Case, M., 1997, "Initiation of Surface and Interface Edge Cracks in Functionally Graded Ceramic Thermal Barrier Coatings," ASME J. Eng. Mater. Technol., **119**, pp. 148–152.
[13] Noda, N., 1997, "Thermal Stress Intensity for Functionally Graded Plate With an Edge Crack," J. Therm. Stresses, **20**, pp. 373–387.
[14] Jin, Z.-H., and Paulino, G. H., 2001, "Transient Thermal Stress Analysis of an Edge Crack in a Functionally Graded Material," Int. J. Fract., **107**, pp. 73–98.
[15] Walters, M. C., Paulino, G. C., and Dodds, R. H., Jr., 2004, "Stress-Intensity Factors for Surface Cracks in Functionally Graded Materials Under Mode-I Thermomechanical Loading," Int. J. Solids Struct., **41**, pp. 1081–1118.
[16] El-Borgi, S., Erdogan, F., and Hidri, L., 2004, "A Partially Insulated Embedded Crack in an Infinite Functionally Graded Medium Under Thermo-Mechanical Loading," Int. J. Eng. Sci., **42**(3–4), pp. 371–393.
[17] Zhang, Z. Y., Paulino, G. H., 2007, "Wave Propagation and Dynamic Analysis of Smoothly Graded Heterogeneous Continua Using Graded Finite Elements," Int. J. Solids Struct., **44**(11–12), pp. 3601–3626.
[18] Jain, N., Shukla, A., and Chona, R., 2006, "Asymptotic Stress Fields for Thermomechanically Loaded Cracks in FGMs," J. ASTM Int., **3**(7), pp. 88–90.
[19] Freund, L. B., 1990, *Dynamic Fracture Mechanics*, Cambridge University Press, Cambridge.
[20] Shukla, A., and Jain, N., 2004, "Dynamic Damage Growth in Particle Reinforced Graded Materials," Int. J. Impact Eng., **30**, pp. 777–803.
[21] Jain, N., and Shukla, A., 2006, "Mixed Mode Dynamic Fracture in Particulate Functionally Graded Materials," Exp. Mech., **46**(2), pp. 137–154.
[22] Lee, K. H., 2004, "Characteristics of a Crack Propagating Along the Gradient in Functionally Gradient Materials," Int. J. Solids Struct., **41**, pp. 2879–2898.
[23] Dally, J. W., and Riley, F. W., 2001, *Experimental Stress Analysis*, 3rd ed., College House Enterprises, TN.
[24] Parameswaran, V., and Shukla, A., 2002, "Asymptotic Stress Fields for Stationary Cracks in Functionally Graded Materials," ASME J. Appl. Mech., **69**, pp. 240–243.

Mixed-Mode Dynamic Crack Growth in a Functionally Graded Particulate Composite: Experimental Measurements and Finite Element Simulations

Madhu Kirugulige
The Goodyear Tire and Rubber Company,
Department of Mechanical Engineering,
Auburn University,
Auburn, AL 36849

Hareesh V. Tippur
Alumni Professor
Fellow ASME
Department of Mechanical Engineering,
Auburn University,
Auburn, AL 36849

Mixed-mode dynamic crack growth behavior in a compositionally graded particle filled polymer is studied experimentally and computationally. Beams with single edge cracks initially aligned in the direction of the compositional gradient and subjected to one-point eccentric impact loading are examined. Optical interferometry along with high-speed photography is used to measure surface deformations around the crack tip. Two configurations, one with a crack on the stiffer side of a graded sheet and the second with a crack on the compliant side, are tested. The observed crack paths are distinctly different for these two configurations. Furthermore, the crack speed and stress intensity factor variations between the two configurations show significant differences. The optical measurements are examined with the aid of crack-tip fields, which incorporate local elastic modulus variations. To understand the role of material gradation on the observed crack paths, finite element models with cohesive elements are developed. A user-defined element subroutine for cohesive elements based on a bilinear traction-separation law is developed and implemented in a structural analysis environment. The necessary spatial variation of material properties is introduced into the continuum elements by first performing a thermal analysis and then by prescribing material properties as temperature dependent quantities. The simulated crack paths and crack speeds are found to be in qualitative agreement with the observed ones. The simulations also reveal differences in the energy dissipation in the two functionally graded material (FGM) cases. T-stresses and hence the crack-tip constraint are significantly different. Prior to crack initiation, larger negative T-stresses near the crack tip are seen when the crack is situated on the compliant side of the FGM. [DOI: 10.1115/1.2932095]

1 Introduction

Functionally graded materials (FGMs) are a new class of materials having continuous spatial variation of properties (mechanical, thermal, piezoelectric, etc.). Generally, they are multiphase materials having continuously varying volume fractions of constituent phases along a desired spatial direction. Typical applications of FGM include thermal barrier coatings in high temperature components, impact resistant structures for armors and ballistics, interlayers in microelectronic packages, etc. The study of dynamic failure of FGM is essential in order to design structures involving these novel materials for elevated rates of loading. For example, Kirugulige et al. [1] have experimentally demonstrated (under Mode-I impact loading) that functionally graded sandwich structures perform better compared to their conventional counterparts at least in two respects. The face-sheet/core delamination can be mitigated by using a graded interfacial architecture in place of a conventional one. Also, the crack initiation can be delayed in the former when compared to the latter. Since a crack and/or loading directions can be inclined to the direction of material gradation in a FGM, fracture generally will be mixed mode in nature (say, Modes I and II). Therefore, it is important to understand the role spatial variation of properties has on the crack path under stress wave loading conditions.

The work of Delale and Erdogan [2] is among of the early studies on fracture behavior of FGM, where they have shown that stress intensity factors in nonhomogeneous materials are affected by compositional gradients even though the inverse $\sqrt{r}$ singularity is preserved near the crack tip. In a later work, Konda and Erdogan [3] have provided the expressions for stress intensity factors (SIFs) of a mixed-mode quasistatic fracture problem in nonhomogeneous materials. In the past few years, Shukla and coworkers [4,5] have reported crack-tip stress fields for dynamically growing cracks in FGM for Mode-I and mixed-mode loading conditions. There are relatively few experimental methods available to study mixed-mode dynamic fracture and measure fracture parameters. Butcher et al. [6] have demonstrated the feasibility of using optical interferometry to study fracture behavior of glass-filled epoxy FGM beams. Rousseau and Tippur [7] have reported on the role of material gradation on crack kinking under quasistatic conditions. They have also examined the effect of material gradation on Mode-I dynamic fracture in a separate study [8]. Kirugulige and Tippur [9] have conducted mixed-mode dynamic fracture experiments on FGM samples made of compositionally graded glass-filled epoxy sheets with edge cracks initially along the gradients. In that work [9], the authors have observed that when a crack is situated on the compliant side of the sample, it kinks significantly less compared to when it is on the stiffer side when impact loaded in eccentric one-point loading configuration. In order to further understand the role of material grading on ensuing crack paths, these experiments are reexamined here with

Contributed by the Applied Mechanics Division of ASME for publication in the JOURNAL OF APPLIED MECHANICS. Manuscript received May 24, 2007; final manuscript received February 7, 2008; published online July 10, 2008. Review conducted by Marek-Jerzy Pindera.

the aid of crack-tip fields for nonhomogeneous materials along with a complementary numerical investigation of the problem.

The numerical simulation of crack growth during mixed-mode dynamic fracture events is computationally challenging when compared to Mode-I counterparts. It is also more complex in case of FGM because mode mixity arises not only from geometrical and loading configurations but also from the material nonhomogeneity parameter. In order to predict the crack kinking direction in a FGM, the numerical scheme should be able to represent spatial variation of material properties and the evolution of crack path must be a natural outcome of the analysis. There are mainly three different approaches within the framework of finite element method to simulate this problem. The first is an automated moving finite element approach with local remeshing along the crack path. This approach requires a user-defined crack increment and relies on one of the mixed-mode fracture criteria for determining crack growth direction. Bittencourt et al. [10] and Nishioka [11] have successfully used this approach to simulate mixed-mode crack propagation in homogeneous materials. Nishioka et al. [12] were able to predict the crack path of a mixed-mode dynamic fracture experiment using moving singular finite element method based on Delaunay automatic mesh generation. In a comprehensive numerical work on mixed-mode crack growth simulations including FGM, Kim and Paulino [13] have used local remeshing technique to predict the crack path of mixed-mode quasistatic fracture tests of Rousseau and Tippur [7]. Recently, Tilbrook et al. [14] have simulated quasistatic crack propagation in FGMs under flexural loading conditions. The aforementioned approaches require a robust automatic remeshing algorithm, an elaborate bookkeeping system of node numbering to readjust the mesh pattern periodically, and a mesh rezoning procedure for mapping the solution fields of the previous mesh onto those in the current mesh.

The second approach is to use cohesive elements with the conceptual underpinnings found in the works of Dugdale [15] and Barenblatt [16]. There are two basic types of cohesive zone modeling approaches – intrinsic and extrinsic – methods. The former is characterized by its hardening and softening portions of the traction-separation law (TSL), whereas the latter has only the softening portion. The intrinsic cohesive element formulation in the context of finite element method was proposed early on by Needleman [17]. Numerous other investigators have used the intrinsic type of formulation with different shapes of TSL: exponential [18–21], bilinear [21–24], and trapezoidal [25,26] types. Xu and Needleman [18] have performed mixed-mode dynamic crack growth simulations in brittle solids. Wang and Nakamura [19] have used an exponential TSL to simulate dynamic crack propagation in elastic-plastic FGMs. The applicability of exponential and bilinear types of cohesive zone models to modified boundary layer analysis was conducted by Shim et al. [21]. Mode-I and mixed-mode dynamic fracture simulations in FGM have been reported by Zhang and Paulino [24]. Madhusudhana and Narasimhan [26] have used a trapezoidal TSL to simulate mixed-mode crack growth in ductile adhesive joints. The extrinsic type of formulation has also been used by many researchers [27,28].

Recently, Belytschko and co-workers [29,30] have proposed a third method called the extended finite element method (XFEM) to model arbitrary discontinuities in finite element meshes. In this method, discontinuous enrichment functions are added to the finite element approximation to account for the presence of a crack while preserving the classical displacement variational setting. This flexibility enables the method to simulate crack growth without remeshing.

Physical mechanisms governing dynamic crack propagation in FGM under mixed-mode loading are not clearly understood. Observations based on the study of quasistatic fracture indicate that under mixed-mode loading, the crack tends to grow according to a locally Mode-I dominated condition as predicted in the $K_{II}=0$ criterion or the maximum tensile stress criterion criterion [31]. Extending these methods to dynamic mixed-mode fracture of FGM requires evaluation of one of the fracture criterion and local remeshing. However, cohesive elements allow crack initiation and kinking to occur without the need for defining the crack path a priori. Therefore, in the current work, intrinsic cohesive element method with bilinear TSL is used to model dynamic mixed-mode crack growth in FGM. In order to implement this in the context of finite element analysis, a user subroutine is developed and augmented with ABAQUS™ (Version 6.5). The spatial variation of material properties in continuum elements is incorporated by conducting a thermal analysis and then applying temperature dependent material properties. The spatial variation of dynamic initiation toughness obtained by Mode-I dynamic fracture tests on homogeneous samples of different volume fractions of the filler material is also incorporated. The mixed-mode stress intensity factor histories up to crack initiation are computed by regression analyses of crack opening and sliding displacements. The simulated crack paths are found to be in qualitative agreement with the experimentally observed ones.

2 Experimental Details

In this section, we summarize the main experimental features and relevant results to the current work. Additional details can be found elsewhere [9].

2.1 Material Preparation and Test Configuration. FGM samples were prepared by continuously varying the volume fraction of solid glass filler particles (35 μm mean diameter) in an epoxy matrix. The gravity assisted casting method [6] was used to produce a monotonic variation of volume fraction of glass particles in the vertical direction of a cast sheet. A schematic of the specimen is shown in Fig. 1(*a*), where the gray scale is used to represent the compositional gradation. The elastic modulus and Poisson's ratio were estimated by measuring the elastic wave speeds in the cast sheet at several discrete locations using the ultrasonic pulse-echo method. The variations of elastic modulus and mass density along the width of a sample are shown in Fig. 1(*b*). The elastic modulus varies from $\sim$10 GPa to $\sim$4 GPa over a width of $\sim$43 mm. The mass density varies from $\sim$1750 kg/m^3 to $\sim$1175 kg/m^3 over the same width. The corresponding variation in Poisson's ratio was 0.33–0.37.

In cohesive element models, the fracture energy is an important input parameter, which has to be determined experimentally. To this end, Mode-I crack initiation toughness tests were conducted on *homogeneous* edge cracked beam samples of various volume fractions of the filler. Dally–Sanford single strain gage method [32] was used to record strain history in each case and was, in turn, used to obtain Mode-I crack initiation toughness (see Ref. [33] for details). Figure 1(*c*) shows the variation of the local Mode-I crack initiation toughness (K_{ICR}) as a function of position inferred from these tests. A monotonic increase in crack initiation toughness values can be seen at lower values of E and hence lower volume fraction of the filler. An increase in fracture toughness by a factor of $\sim$1.5 occurs when the filler volume fraction increases from 0% to 40% with a corresponding change in the elastic modulus by a factor of $\sim$2.4.

Mixed-mode fracture experiments were conducted on FGM samples in two separate configurations: (a) an edge crack on the compliant side of the sample with an impact on the stiffer side, and (b) an edge crack on the stiffer side of the sample with an impact on the compliant side. These configurations are shown schematically in Fig. 2. The specimens were impacted using a pneumatic hammer with a velocity of $\sim$5 m/s at an offset distance of 25.4 mm with respect to the initial crack orientation in both configurations. Here, the elastic modulus at the edge of the cracked sheet, behind the crack tip, is denoted by E_1 and the one ahead of the crack tip as E_2. With this notation, henceforth, Type-(a) experiments are denoted as $E_1 < E_2$ and Type-(b) experiments as $E_1 > E_2$. Except for this reversal of compositional gradient, all other conditions were the same for both cases. The coherent gra-

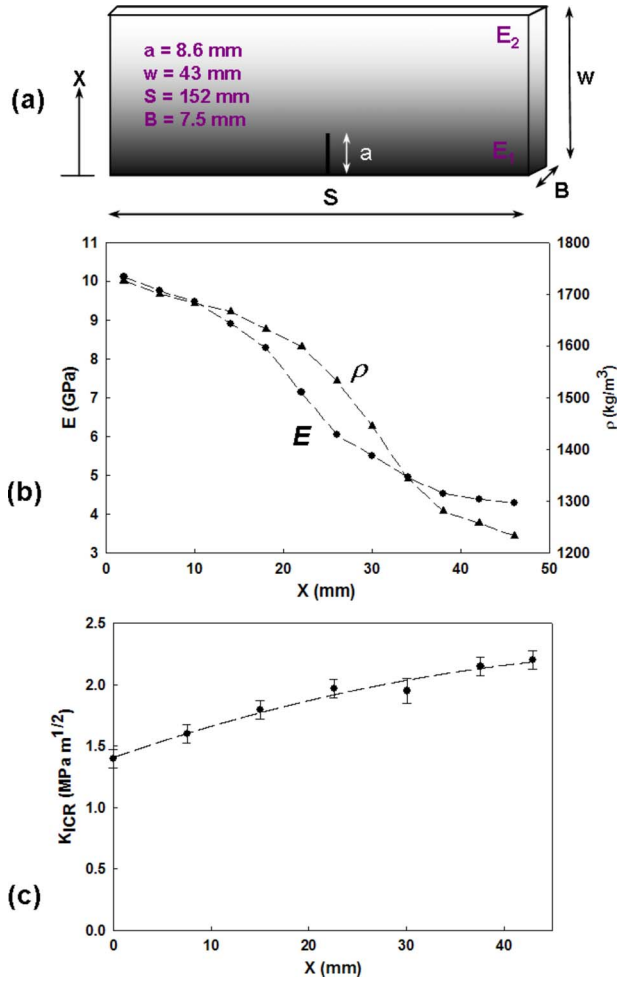

Fig. 1 (*a*) **Schematic of the FGM specimen (darker shades represent stiffer materials), (*b*) material property variation along the width of the sample, and (*c*) variation of dynamic crack initiation toughness along the width of the sample**

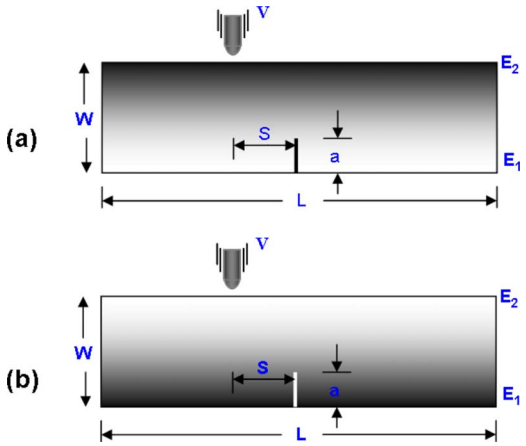

Fig. 2 Two mixed-mode FGM test configurations: (*a*) crack on the compliant side of the sample with impact occurring on the stiff side ($E_1<E_2$) and (*b*) crack on the stiff side of the sample with impact occurring on the compliant side ($E_1>E_2$). Impact velocity (V)=5 m/s. (Shading is used to denote compositional gradation; darker shades represent stiffer material.)

dient sensing (CGS) [34] method was used in conjunction with high-speed photography to measure instantaneous surface deformations around the crack tip. Specifically, angular deflections of the light rays proportional to $\partial w/\partial X_1$ (w being the out-of-plane displacement and X_1 is the initial crack orientation direction) were measured in the crack-tip vicinity as interference fringes. A framing rate of 200,000 was used and images were recorded at 5 μs intervals. A complete fracture of the specimen typically occurred after about 220 μs. Representative interferograms for both FGM configurations (one from the preinitiation and one from the postinitiation period) are shown in Fig. 3. Under the assumption of plane stress condition, out-of-plane displacement w can be related to the sum of the in-plane stresses $(\sigma_x+\sigma_y)$ using elastic constants.

2.2 Experimental Results: Crack Path History. Multiple experiments were conducted for both the FGM specimen configurations $E_1<E_2$ and $E_1>E_2$ to ensure repeatability. Four fractured samples from each configuration are shown in Figs. 4(*a*) and 4(*b*). A high degree of reproducibility in crack paths is clearly evident. More importantly, a distinctly different crack path can be seen in these two configurations. Figure 4(*c*) shows photographs of the fractured specimens for one representative experiment in each configuration. The impact point is located on the top edge of each image and the initial crack tip is at the bottom edge as indicated. The reflective area on each specimen surface is the region of interest where surface deformations were monitored optically. The crack was situated on the compliant side in Fig. 4(*c*) and on the stiffer side in Fig. 4(*d*). The difference in crack paths in the lower half of the specimen after initiation is quite striking in these images. For the case of $E_1<E_2$, crack growth occurs in a near Mode-I fashion with an initial kink angle of $\phi\sim 4$ deg with respect to the X_1-axis whereas for the case $E_1>E_2$, the crack growth occurs at an initial kink angle of $\phi\sim 16$ deg. Subsequent crack growth in the case of $E_1<E_2$ shows a tendency for the crack to grow nearly along the X_1-direction. On the other hand, in the case of $E_1>E_2$, the crack growth is essentially self-similar following initiation with a continued growth at an angle of $\sim$16 deg with respect to the X_1-direction. In the upper half of the sample, the crack growth is affected by a combination of free-edge and impact point interactions. Therefore, in the current work, the simulation results are compared with the experimental ones on initial crack growth in both configurations.

3 Evaluation of Stress Intensity Factors

The elastic crack-tip fields are available for nonhomogeneous materials having exponential variation of material properties. The use of exponential variation simplifies the process of deriving the crack-tip fields. However, processing a FGM having an exponential variation of elastic modulus is difficult. Recently, attempts have been made to derive crack-tip stress fields for a FGM with a linear variation of elastic modulus [35]. For an edge cracked beam having a linear material property, variation along the X_1-direction is described by the equation

$$E(X_1) = E_0(1 + \delta_f X_1) = E_0(1 + \alpha X_1' + \beta X_2') \tag{1}$$

where E_0 is the elastic modulus at the crack tip as shown in Fig. 5(*a*), and the parameters α and β are related to the nonhomogeneity parameter δ_f as

$$\alpha = \delta_f \cos\phi, \quad \beta = \delta_f \sin\phi \tag{2}$$

where ϕ is the crack kink angle. For a Mode-I crack propagation, ϕ=0, $\alpha=\delta_f$, and the axes X_1-X_2 and $X_1'-X_2'$ coincide. (In the current work, X_1 varies in the range $-0.0085\ \text{m}\leq X_1\leq 0.0345$ m.) The spatial variation of elastic modulus is approximated as a linear function (Fig. 5(*b*)) for both the FGM configurations. A four-term expansion for the sum of in-plane stresses $(\sigma_x+\sigma_y)$ is deduced from Eqs. (31) and (32) of Ref. [35] as

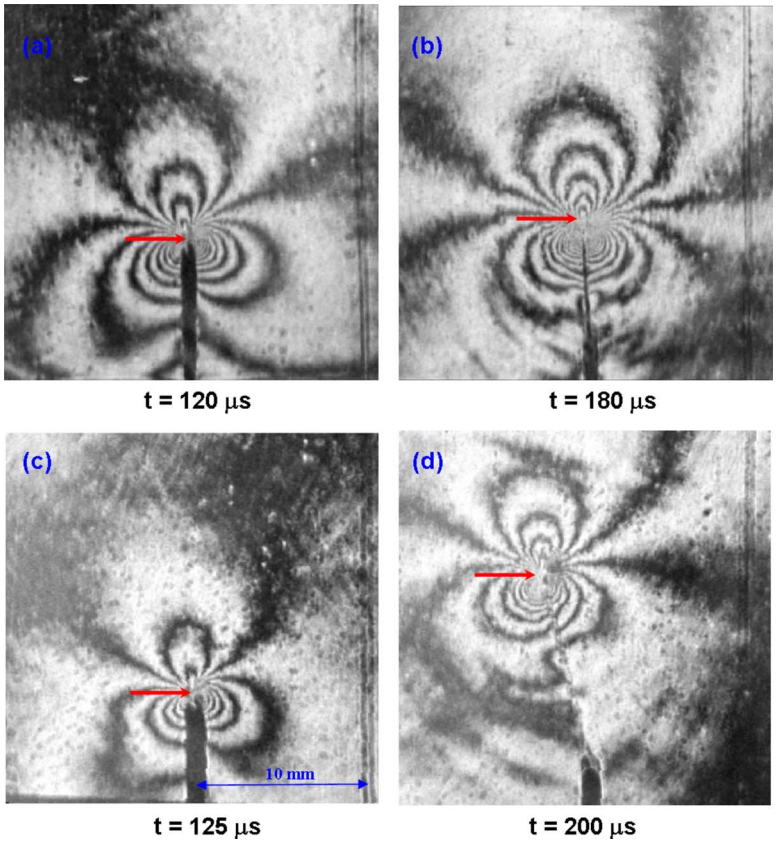

Fig. 3 Selected CGS interferograms representing contours of $\delta w/\delta X_1$ in FGM samples; (*a*) and (*b*) are for the case of $E_1 < E_2$ and (*c*) and (*d*) are for the case of $E_1 > E_2$. The time at which the images are taken after impact is indicated below each image. The current crack tip is indicated by an arrow.

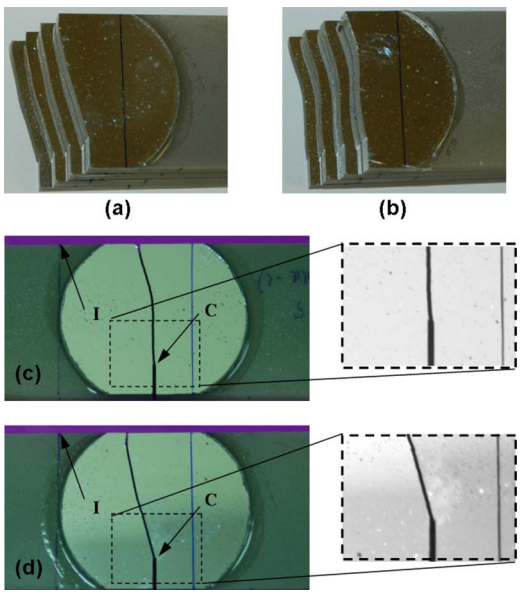

Fig. 4 Multiple fractured FGM specimens (right half) demonstrating experimental repeatability for (*a*) FGM with a crack on the stiffer side ($E_1 < E_2$) and (*b*) FGM with a crack on the compliant side ($E_1 > E_2$). Photograph showing fractured specimens for (*c*) FGM with a crack on the compliant side ($E_1 < E_2$) and (*d*) FGM with a crack on the stiffer side ($E_1 > E_2$). Impact point is indicated by letter "I" and initial crack tip by letter "C."

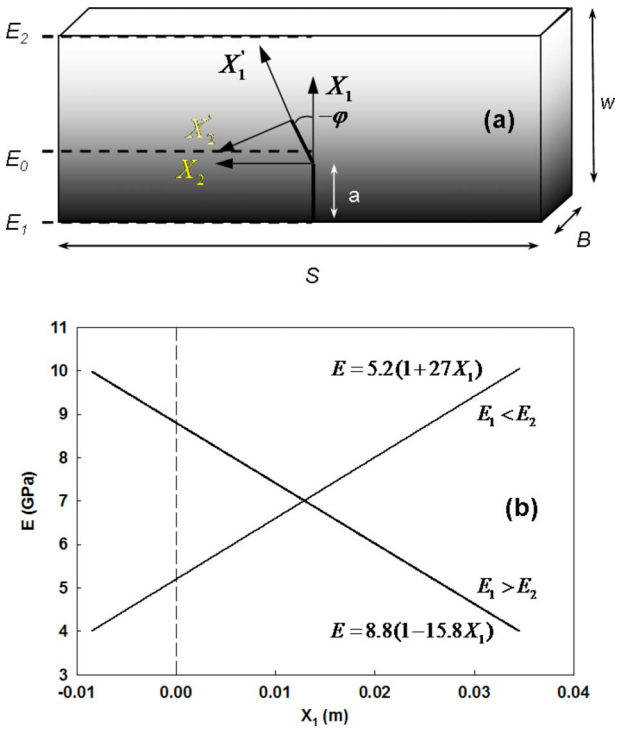

Fig. 5 (*a*) Schematic of FGM sample with linear material property variation, and (*b*) elastic modulus variation in graded samples (broken line denotes the crack tip location)

$$\sigma_x+\sigma_y=2\left[A_0(t)r^{-1/2}\cos\frac{\theta}{2}-C_0(t)r^{-1/2}\sin\frac{\theta}{2}+B_0(t)+A_1(t)r^{1/2}\cos\frac{\theta}{2}+C_1(t)r^{1/2}\sin\frac{\theta}{2}+B_1(t)r\cos\theta+D_1(t)r\sin\theta\right]$$
$$+\alpha\left[A_0(t)r^{1/2}\left\{-2\sin\theta\sin\frac{\theta}{2}-2\cos\frac{\theta}{2}\right\}+C_0(t)r^{1/2}\left\{-2\sin\theta\cos\frac{\theta}{2}-2\sin\frac{\theta}{2}\right\}-B_0(t)r\cos\theta-2D_0(t)r\sin\theta\right]$$
$$+\beta\left[A_0(t)r^{1/2}\left\{2\sin\theta\cos\frac{\theta}{2}+2\sin\frac{\theta}{2}\right\}+C_0(t)r^{1/2}\left\{-2\sin\theta\sin\frac{\theta}{2}-2\cos\frac{\theta}{2}\right\}+3B_0(t)r\sin\theta-D_0(t)r\cos\theta\right] \quad (3)$$

In the above equation, r and θ are the crack-tip coordinates instantaneously aligned with the current crack tip. The mixed-mode stress intensity factors, K_{I} and K_{II} are related to the constants of the singular terms in the above equation as $K_{\mathrm{I}}(t)=A_0(t)\sqrt{2\pi}$ and $K_{\mathrm{II}}(t)=C_0(t)\sqrt{2\pi}$. As already mentioned, the CGS fringes represent surface slopes in the principal direction of the grating (in the current work, the direction of initial crack orientation). These surface slopes can be related to the corresponding fringe orders N by using a difference approximation,

$$\frac{\partial w}{\partial X_1}\approx\frac{\delta w}{\delta X_1}=\frac{w_{i+1}-w_i}{\delta X_1}=\frac{Np}{2\Delta} \quad (4)$$

where δ represents the difference operator, p is the pitch of the grating, and Δ is the grating separation distance. By substituting the expression for the out-of-plane displacement w under plane stress assumption,

$$\frac{-\nu B}{2\delta X_1}\left[\left(\frac{\sigma_x+\sigma_y}{E_0(1+\alpha X_1'+\beta X_2')}\right)_{i+1}-\left(\frac{\sigma_x+\sigma_y}{E_0(1+\alpha X_1'+\beta X_2')}\right)_i\right]=\frac{Np}{2\Delta} \quad (5)$$

where B is the specimen thickness and ν is Poisson's ratio of the material. Furthermore, δX_1 denotes shearing distance ($\sim$1.05 mm in the current experimental setup). In the above equation, $\sigma_x+\sigma_y$ is substituted from Eq. (3) with r and θ being evaluated at locations denoted by i and $i+1$ as

$$r_i=\sqrt{X_1^2+X_2^2},\quad \theta_i=\tan^{-1}\frac{X_2}{X_1}$$
$$r_{i+1}=\sqrt{(X_1-\delta X_1)^2+X_2^2},\quad \theta_{i+1}=\tan^{-1}\frac{X_2}{X_1-\delta X_1} \quad (6)$$

The overdeterministic least-squares analysis [34] was carried out and mixed-mode stress intensity factors were extracted.

Equation (3) is used for a dynamically loaded stationary crack as well for a propagating crack under the following assumptions: The inertial effects enter the coefficients (A_n, B_n, C_n, and D_n)while retaining the functional form of the quasistatic counterpart. The velocity dependent terms were assumed to be small. It has been verified [8] that the contribution from the functions associated with the instantaneous crack-tip velocity is about 3% for a steadily propagating crack with a crack speed of $\sim$300 m/s. The crack-tip transient effects, namely, the rate of change of SIFs and crack accelerations/decelerations, were also small in the current experiments as identified in Ref. [9]. It should be noted that Eq. (3) used in the current work does not account for the spatial variation of mass density in FGM. There are difficulties associated with utilizing the earlier FGM crack-tip fields (which take into account spatial variation of modulus as well as mass density) to analyze the optical interferograms of the current work. The derivations [4,5] describe the spatial variation of elastic modulus and mass density with a single nonhomogeneity parameter in an exponential type of variation or assume mass density to be a constant. However, the glass-filled epoxy FGM used in the current experiments had significantly different elastic moduli and mass density variations. The elastic modulus varied 2.5-fold (4.0–10 GPa) over a width of 43 mm, whereas the mass density variation was 1.5-fold (1175–1700 kg/m^3) over the same length.

4 Computational Procedure

In this study, a cohesive element is developed (in FORTRAN) and implemented in ABAQUS/STANDARD environment as a user-defined element (UEL). The implicit time integration scheme is used to integrate the equations of motion. Generally, for large problems with material nonlinearities, explicit methods are preferred over implicit methods in view of minimizing the solution cost. However, in the current problem, only mild nonlinearity arises from the TSL. Therefore, using an implicit scheme can be justified considering superior convergence rate of Newton's method in ABAQUS/STANDARD. Also, developing a UEL instead of using the cohesive elements (provided in ABAQUS 6.5) gives an added flexibility of applying spatially varying cohesive properties for FGM.

4.1 Cohesive Element Formulation. Let A and B be two coincident material points on a prospective crack path at the time of impact ($t=0$) (see Fig. 6(a)). With the passage of time, their corresponding positions change to A' and B'. Let Δ_n and Δ_t be the normal and tangential components of separation between A' and B'. Let a cohesive element shown in Fig. 6(b) be present on this potential crack path. Then, the separation in the X- and Y-directions at a Gauss point of the element can be computed from nodal displacements $[U]$ as

$$\begin{bmatrix}U_X\\U_Y\end{bmatrix}=[N][U] \quad (7)$$

where

$$[N]=\begin{bmatrix}N_1&0&N_2&0&-N_2&0&-N_1&0\\0&N_1&0&N_2&0&-N_2&0&-N_1\end{bmatrix}$$

and

$$U=[U_1\ V_1\ U_2\ V_2\ U_3\ V_3\ U_4\ V_4]^T$$

Here, $N_1=(1-\xi)/2$ and $N_2=(1+\xi)/2$ are linear shape functions and $\xi=\pm 1/\sqrt{3}$ is the sampling location. The tangential and normal separations are computed by transforming U_X and U_Y into the local coordinate system of the element as

$$\begin{bmatrix}\Delta_t\\\Delta_n\end{bmatrix}=[Q]\begin{bmatrix}U_X\\U_Y\end{bmatrix}\quad\text{where}\quad[Q]=\begin{bmatrix}\cos\theta&\sin\theta\\-\sin\theta&\cos\theta\end{bmatrix} \quad (8)$$

Then, a nondimensional effective separation parameter λ can be defined as

$$\lambda=\sqrt{\left(\frac{\Delta_n}{\delta_n}\right)^2+\left(\frac{\Delta_t}{\delta_t}\right)^2} \quad (9)$$

Here, δ_t and δ_n are the critical values of tangential and normal separations, respectively. At time $t=0$, λ takes the value of zero. As the cohesive element separates, λ increases in magnitude and attains a value of unity when the separation is complete. The variation of pure normal traction (in the absence of tangential separation, $\Delta_t=0$) with normal separation is shown in Fig. 6(c).

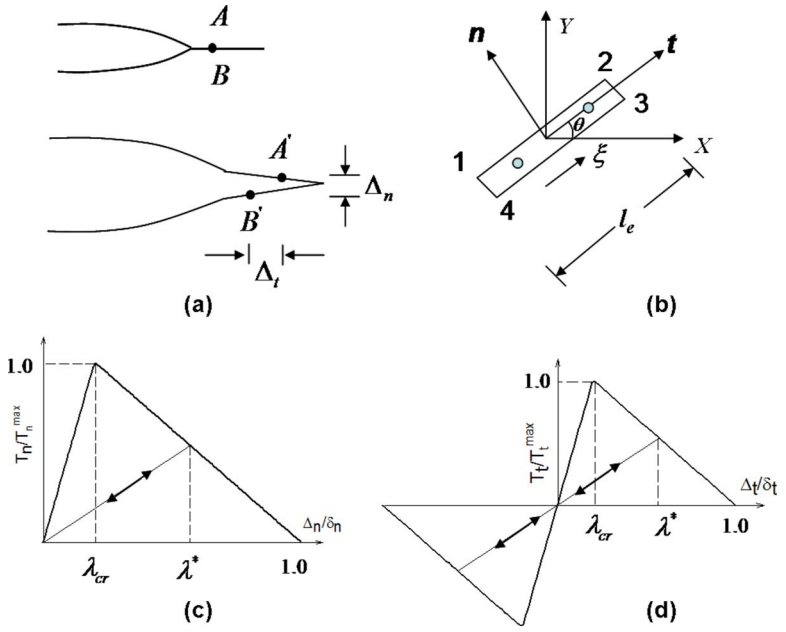

Fig. 6 Details on cohesive element formulations: (*a*) undeformed and deformed configurations of the crack tip region. (*b*) Local and global coordinate systems used for a cohesive element. Prescribed TSL for (*c*) pure normal separation and for (*d*) pure tangential separation.

Similarly, the variation of tangential traction with tangential separation (in the absence of normal separation, $\Delta_n=0$) is shown in Fig. 6(*d*). The critical values of normal and tangential separations are computed by equating the area under T-Δ curves to Mode-I and Mode-II fracture energies,

$$G_{IC} = \tfrac{1}{2}\delta_n T_n^{\max}, \quad G_{IIC} = \tfrac{1}{2}\delta_t T_t^{\max} \tag{10}$$

The traction-separation relations for various portions of the triangular variation are given as follows [24]:

For loading/unloading in the range $0 \leqslant \lambda \leqslant \lambda_{cr}$,

$$T_t = \frac{T_t^{\max}\Delta_t}{\lambda_{cr}\delta_t}, \quad T_n = \frac{T_n^{\max}\Delta_n}{\lambda_{cr}\delta_n} \tag{11}$$

For loading in the range $\lambda_{cr} < \lambda \leqslant 1$,

$$T_t = \frac{T_t^{\max}(1-\lambda)\Delta_t}{\lambda(1-\lambda_{cr})\delta_t}, \quad T_n = \frac{T_n^{\max}(1-\lambda)\Delta_n}{\lambda(1-\lambda_{cr})\delta_n} \tag{12}$$

For unloading/reloading in the range $0 < \lambda \leqslant \lambda^*$ where λ^* is the maximum value of λ after which unloading starts,

$$T_t = \frac{T_t^{\max}\Delta_t}{\lambda^*\delta_t}, \quad T_n = \frac{T_n^{\max}\Delta_n}{\lambda^*\delta_n} \tag{13}$$

For loading in the range $\lambda^* \leqslant \lambda \leqslant 1$,

$$T_t = \frac{T_t^{\max}(1-\lambda)\Delta_t}{\lambda(1-\lambda^*)\delta_t}, \quad T_n = \frac{T_n^{\max}(1-\lambda)\Delta_n}{\lambda(1-\lambda^*)\delta_n} \tag{14}$$

The stiffness coefficients are determined by differentiating tractions with respect to separations as follows:

$$[SS] = \begin{bmatrix} \partial T_t/\partial\Delta_t & \partial T_t/\partial\Delta_n \\ \partial T_n/\partial\Delta_t & \partial T_n/\partial\Delta_n \end{bmatrix} \tag{15}$$

Subsequently, both element stiffness matrix $[S]^e$ and internal force vector $[P]^e$ are computed by performing usual Gauss-quadrature numerical integration as

$$[S]^e_{8\times 8} = \int_{-1}^{1} [N^T]_{8\times 2}[Q^T]_{2\times 2}[SS]_{2\times 2}[Q]_{2\times 2}[N]_{2\times 8}\frac{l_e}{2}d\xi \tag{16}$$

and

$$[P]^e_{8\times 1} = \int_{\xi=-1}^{1} [N^T]_{8\times 2}[Q]_{2\times 2}[T]_{2\times 1}\frac{l_e}{2}d\xi \tag{17}$$

where l_e denotes the length of a cohesive element. The effect of introducing a UEL to the model during an analysis step is that the element should provide its contribution to the *residual force vector* and the *Jacobian matrix* of the overall system of equations [36]. In the current model, since there are no external forces applied to the cohesive elements, the internal force vector (tractions developed due to separation) as given by Eq. (17) becomes the residual force vector. Also, since there is no mass associated with the cohesive elements, the stiffness matrix given by Eq. (16) becomes the Jacobian matrix. Once these two quantities are computed and passed as arguments to ABAQUS, it internally assembles these to formulate a global system of equations and solution proceeds with an automatic time stepping.

4.2 Implicit Dynamic Scheme and Time Step Control. To integrate the equations of motion, implicit time integration is adopted, which uses the implicit operator of Hilber et al. [37] (see Appendix for details). In Eq. (A1), α_d is the parameter that controls algorithmic damping. In the current work, a value of −0.05 was chosen for α_d. This ensures that numerical dissipation is less than 1% of the total energy, which helps to remove the contribution of high frequency modal components and yet maintain good accuracy in the important lower modes. The implicit time step size has to be small enough to capture the transient effects of the problem. The corresponding stable time step size in an explicit dynamic analysis is the time taken by the dilatational wave to travel through the smallest element in the mesh, which is

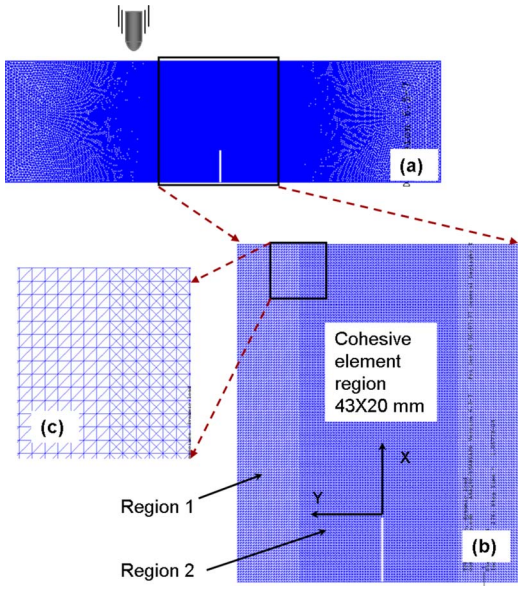

Fig. 7 Finite element discretization. (*a*) Overall view of the finite element discretization, (*b*) magnified view of the mesh showing Region 1 (continuum elements) and Region 2 (continuum and cohesive elements) and (*c*) enlarged view of the mesh near the interface of Regions 1 and 2.

$$\Delta t \leq \frac{L_c}{C_L} \tag{18}$$

where L_c is the smallest continuum element length ($\sim$0.23 mm in the current work) and C_L is the local dilatational wave speed,

$$C_L(X) = \sqrt{\frac{E(X)}{(1+\nu(X))(1-\nu(X))\rho(X)}} \tag{19}$$

for plane stress. Here, $E(X)$, $\nu(X)$, and $\rho(X)$ denote elastic modulus, Poisson's ratio, and mass density of the material at a location X. The maximum value of C_L for the FGM under consideration was 2580 m/s at the stiffer side of the sample. Therefore, the minimum value for Δt is $\sim$90 ns. However, it should be noted that time step size in implicit scheme can be several orders of magnitude greater than the corresponding stable time step size of the explicit scheme. In view of this, the upper limit for time step was set to 200 ns but once the crack initiation occurred, the program internally chose time increments as low as 40 ns.[1]

4.3 Modeling Aspects. The finite element mesh used is shown in Fig. 7(*a*). In mixed-mode dynamic crack growth simulations, the crack path is not known a priori. Therefore, cohesive elements need to be dispersed in a region where crack propagation is anticipated. Hence, the domain was divided into two parts: Region 1 in which crack propagation is not anticipated to occur and Region 2 where crack propagation was observed in experiments (see Fig. 7(*b*)). Accordingly, Region 1 was discretized with three-noded 2D plane stress continuum elements and Region 2 was discretized using three-noded plane stress elements with four-noded cohesive elements dispersed along their boundaries. These two mesh patterns are joined by merging the nodes selectively along their boundaries. The model contained about 117,000 nodes and 125,000 elements.

It is important to make sure that the smallest element size used in the mesh is less than the characteristic cohesive length scale δ so that mesh sensitivity is avoided. This was decided using the size of the cohesive zone based on Dugdale and Barrenblatt's model [15,16] for a Mode-I crack. The cohesive stress assumes a constant value of T_{av} up to a critical opening displacement δ_n and vanishes thereafter. Therefore, the size of the cohesive zone is given by [24,28,38]

$$\delta = \frac{\pi}{8}\frac{E}{1-\nu^2}\frac{G_{IC}}{T_{\text{av}}^2} \tag{20}$$

Here, E is the elastic modulus, G_{IC} is the Mode-I fracture energy, and $T_{\text{av}}=T_n^{\max}/2$, with $T_n^{\max}$ being the peak stress in a bilinear TSL. Minimum value for δ occurs at the stiffer side of the sample and is computed by substituting 10 GPa, 0.49 N/mm, and 100 MPa for E, G_{IC} (both measured under dynamic loading conditions), and $T_n^{\max}$, respectively. The value for δ so obtained is $\sim$845 μm. The smallest cohesive element size chosen in this work is $\sim$230 μm, which is less than one-third of the characteristic cohesive length scale.

While conducting experiments, the FGM samples were initially rested on soft putty blocks before imposing the impact load. This was to preclude support reactions affecting the fracture behavior of the sample. Accordingly, the sample was modeled as a "free-free" beam. The mass of the impactor was large compared to that of the sample. Therefore, a constant velocity of 5 m/s was imposed on the node located at the impact point.

4.4 Application of Graded Material Properties to Continuum Elements. One of the important aspects in finite element modeling of FGM is the implementation of spatially varying material properties. Anlas et al. [39] and Kim and Paulino [40] have developed graded finite elements in order to apply smoothly varying material properties. Rousseau and Tippur [41] used an alternative method to introduce the required spatial variation of material properties using standard elements in any commercial finite element software. Since simulations in the current work are conducted using ABAQUS, it is natural to think of using a user defined material constitutive law (UMAT) to apply spatial variations of material properties as previously done by Giannakopoulos and Suresh [42] under static conditions. However, it should be noted that for dynamic simulations, imposing spatial variation of mass density is also necessary. To our knowledge, currently this is not possible in ABAQUS by using the UMAT option. Therefore, in this work, the method suggested by Rousseau and Tippur [40] was extended to mixed-mode crack growth simulations.

Consider the finite element model shown in Fig. 7(*a*). In the current work, the material properties (elastic modulus, Poisson's ratio, and mass density) were approximated in a linear fashion along the width of the sample before applying to the model. In the first step, an uncoupled thermal analysis was conducted with temperature boundary conditions, $T=T_a$ at the bottom edge and $T=T_b$ at the top edge. No convective boundary conditions were imposed so that temperature variation from T_a to T_b across the width W occurs only through conduction. It should be noted here that as far as the thermal analysis is concerned, the elements in Region 2 (where the cohesive elements are present) are disconnected and no heat flow would occur in this region. In order to overcome this difficulty, first, all the cohesive elements were converted into thermally conductive elements (DGAP in ABAQUS). That is, each four-noded cohesive element was converted into two two-noded DGAP elements. (That is, in Fig. 8(*b*), Nodes 1 and 2 were tied to make first DGAP element and Nodes 3 and 4 were tied to make the next element and so on.) Next, for the DGAP elements, a high value of thermal conductance was assigned. This was to make sure that these elements act as good conductors of heat and both nodes attain the same temperature value. The resulting linear nodal temperature variation following the thermal analysis is shown in Fig. 8(*a*). In the second step, for performing structural analysis using implicit dynamic procedure in ABAQUS/Standard, nodal temperatures from the thermal analysis were im-

[1]The following parameters were used for convergence control [37]: the half-step residual tolerance=20, ratio of the largest residual to the corresponding average force norm (R_n^{α})=0.005, and the ratio of the largest solution correction to the largest corresponding incremental solution value (C_n^{α})=0.01.

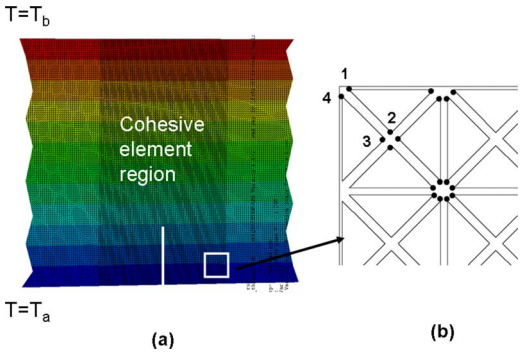

Fig. 8 Thermal analysis to apply graded material properties. (*a*) Nodal temperature results from thermal analysis, and (*b*) magnified view of the cohesive element region.

ported as initial conditions to the model. When nodal temperatures are imposed as boundary conditions, ABAQUS applies them in a ramped fashion over the entire time step and is undesirable. (For a static analysis, however, it does not matter whether temperature field is applied as boundary condition or as an initial condition but for a dynamic analysis, one has to ensure that the nodal temperature values remain the same throughout the time step.) Now, by applying the temperature dependent material properties to the model, a linear variation of elastic modulus and mass density across the sample width W was achieved. Any spurious thermal stresses resulting from the temperature field were avoided by setting thermal expansion coefficient to zero throughout the analysis.

4.5 Application of Material Properties to Cohesive Elements. There are five properties to be specified for cohesive elements. They are Mode-I and Mode-II fracture energies (G_{IC} and G_{IIC}), peak cohesive stresses ($T_n^{\max}$ and $T_t^{\max}$), and the damage parameter corresponding to the peak stress (λ_{cr}). In order to model cohesive elements in FGM realistically, spatial variations of fracture energy and cohesive stress have to be incorporated into the model. The spatial variation of K_{ICR} is available from Fig. 1(*c*) from which G_{IC} ($K_{ICR}^2(x)/E(x)$ for plane stress conditions) can be computed. There is no established physically based rationale for selecting the peak stress $T_n^{\max}$. For example, Xu and Needleman [18] have used $E/10$ in case of polymethyl methacrylate (PMMA), whereas Camacho and Ortiz [27] have used $E/200$ for ceramics. In view of this, several simulations were carried out in the current work by varying the peak stress in the range $E(x)/50$–$E(x)/100$ and the results did not show any significant difference in the crack path. However, the choice of cohesive stress seems to have a modest effect on crack initiation time. For example, when the value of $T_n^{\max}$ was changed from $E/100$ to $E/75$, the crack initiation time changed from 134.2 μs to 130.1 μs. It was desired to keep the value of $T_n^{\max}$ close to the tensile strength of the material which scales roughly by E/100 for the particulate composite used in the current work [43]. Therefore, $T_n^{\max}=T_t^{\max}=E(x)/100$ was chosen for all the simulations. Further more, the ratio of fracture energies and the ratio of peak normal traction to shear traction are also to be selected. It is relatively challenging to perform pure Mode-II experiments under dynamic loading conditions and hence the exact value G_{IIC} is not readily available in literature. Accordingly, a value of $G_{IIC}/G_{IC}=1.0$ was selected in this work. (Additional ratios in the range of $1.0 \leqslant G_{IIC}/G_{IC} \leqslant 3.0$ were attempted but crack path did not show any significant change.)

The variation of K_{ICR} and E over the sample width was approximated by linear functions. Thus, cohesive element properties for the specimen in Fig. 1(*a*) ($E_1 > E_2$) are applied in a linearly decreasing fashion as

$$K_{ICR}(x) = 2.2 - \frac{(2.2-1.4)}{43}x \ (\text{MPa}\sqrt{\text{m}}), \quad 0 \leq x \leq 43 \ \text{nm} \tag{21}$$

and

$$E(x) = 10.0 - \frac{(10.0-4.0)}{43}x \ (\text{GPa}), \quad 0 \leq x \leq 43 \ \text{mm} \tag{22}$$

$$G_{IC}(x) = \frac{K_{ICR}^2(x)}{E(x)}, \quad T_n^{\max}(x) = \frac{E(x)}{100} \quad \text{with}$$
$$G_{IIC}(x) = G_{IC}(x), \quad T_n^{\max}(x) = T_t^{\max}(x) \tag{23}$$

The centroidal location of each cohesive element was calculated and the graded cohesive properties were applied according to Eq. (23). Similarly, for the other configuration ($E_1 < E_2$) where crack is situated on the compliant side of the sample, the properties were applied using linearly increasing functions.

5 Results

The simulations were carried out with material properties applied to continuum and cohesive elements as explained in the previous section. A velocity of 5 m/s was specified to the node located at the impact point.

5.1 Mixed-Mode Stress Intensity Factor Histories. The SIF histories presented in Ref. [9] were based on the assumption that a locally homogeneous material behavior prevails in the crack-tip vicinity in a FGM. However, in the current work, the earlier results were reexamined with the aid of a crack-tip asymptotic expansion that takes into account the local nonhomogeneity. The SIFs were computed by considering a four-term expansion comprising of ($r^{-1/2}$, r^0, $r^{1/2}$, and r^1 terms for stresses, which incorporate the local elastic modulus variation in the sample. The stress intensity factors thus extracted (as explained in Sec. 3) for both configurations are shown in Fig. 9. In this plot, the crack initiation time is denoted by $t_i=0$ so that the positive values correspond to the postinitiation period and the negative ones to the preinitiation period. It should be noted here that SIFs have differences when compared to the ones reported in Ref. [9] since they are evaluated based on the nonhomogeneity parameters α and β (see Eq. (2)). In Fig. 9(*a*), K_I increases monotonically up to crack initiation for both configurations with initiation occurring at $\sim$1.5 MPa m$^{1/2}$. After crack initiation, K_I values show an increasing trend in the case of $E_1 < E_2$ as the crack propagates into a region of increasing reinforcement. However, for the case of $E_1 > E_2$, K_I values somewhat decrease in the observation window after initiation. This difference of K_I histories in the postinitiation region is similar to the one reported by Rousseau and Tippur [8] for the Mode-I case and Kirugulige et al. [1] for syntactic foam based FGMs. It is also confirmed in the finite element simulations to be discussed in the next section. The K_{II} (Fig. 9(*b*)) for both FGM configurations is initially negative and once initiation occurs, K_{II} continues to be a small but negative value for $E_1 < E_2$ whereas it attains a small but positive value for $E_1 > E_2$.

The quality of the least-squares fit (faithfulness of Eq. (5) to represent the surface slopes observed in experiments) is also tested. The synthetic contours generated from Eq. (5) are superimposed on the data points digitized from CGS interferograms and are shown in Figs. 9(*c*) and 9(*d*). One image from the preinitiation and one from the postinitiation period are reported for both FGM configurations. It should be noted here that only the lobes behind the crack tip were digitized while performing overdeterministic least-squares analysis. (The details of the same are available in Ref. [4].) Accordingly, the synthetic contours (order $N=-1$, -1.5, and -2) are superimposed on the data points behind the

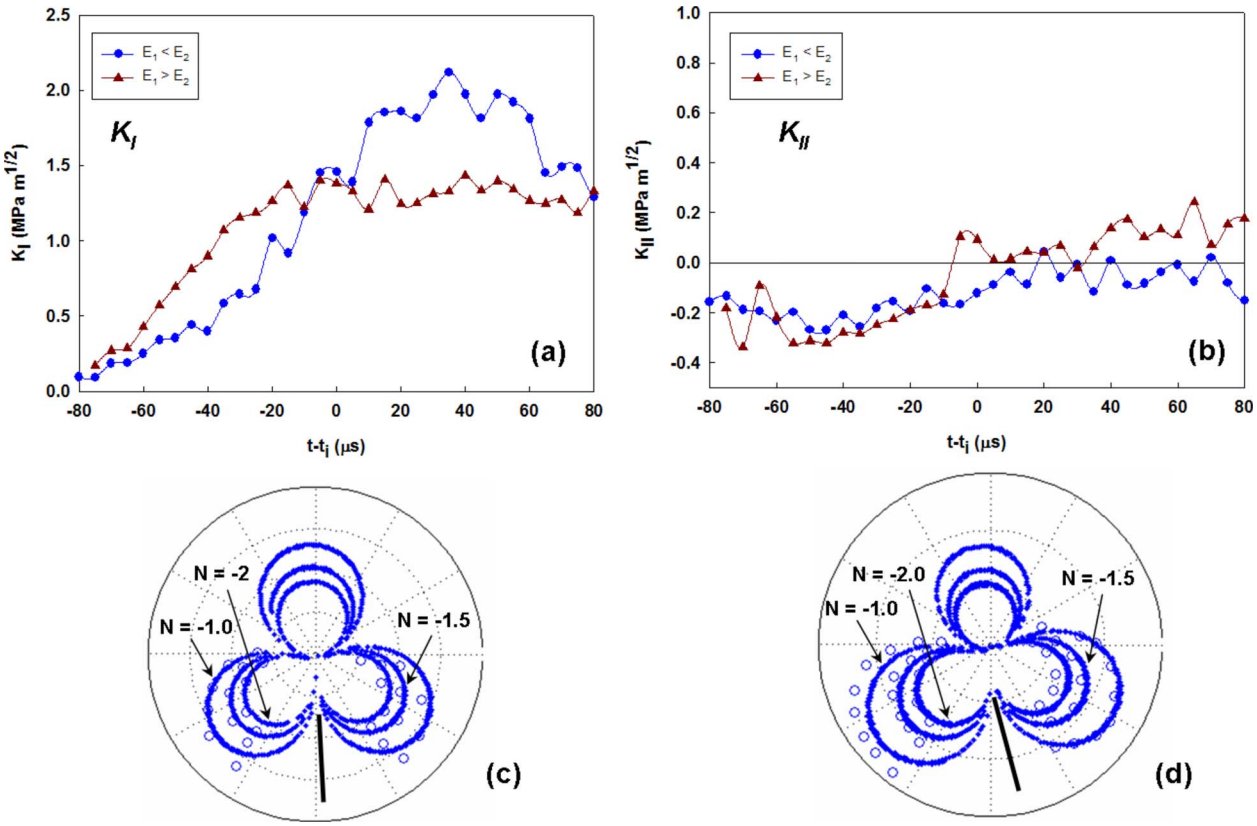

Fig. 9 Stress intensity factors extracted from CGS interferograms by performing overdeterministic least-squares analysis on difference formulation of CGS governing equation (Eq. (5)): (*a*) K_I history and (*b*) K_{II} history. The quality of least-squares fit for (*c*) $E_1 < E_2$ ($t-t_i=20$ μs) and (*d*) $E_1 > E_2$ ($t-t_i=-20$ μs).

crack tip. The least-squares fit considering a four-term FGM solution for the crack-tip stress field shows a good fit with the optical data.

5.2 Energy Computations. Additional insight into the differences in fracture behavior of the two FGM configurations can be obtained by studying the evolution of energy components in finite element simulations. For energy balance, the sum of all the internal energies should to be equal to the external work done on the system. Three types of energies can be identified here; kinetic energy (U_{KE}), strain energy (U_{SE}), and the energy absorbed by the cohesive elements (U_{CE}). The last one consists of two parts; the energy stored in the cohesive elements and the fracture energy. The external work is computed by multiplying impact load with the load point displacement throughout the history (in the current work, since displacement at the impact point is specified, the resulting nodal force is multiplied by the displacement). The energy balance was verified in the simulations for both configurations. Thus, the sum of all the energies (kinetic energy, strain energy, and the energy absorbed by cohesive elements) was found to be equal to the external work up to three significant digits. (For example, in the case of $E_1 < E_2$, at a time of $t=175$ μs, the sum of U_{KE}, U_{SE} and U_{CE} was 248.6286 *N* mm and the external work was 248.6280 *N* mm.) Evolution of U_{KE} and U_{SE} is shown in Fig. 10(*a*). A rapid increase in the kinetic energy for the case of $E_1 < E_2$ is attributed to the motion of denser material in the upper part of the sample. The strain energy is also stored rapidly for this case compared to the $E_1 > E_2$ case since stiffer material is located near the impact point. After about 90 μs for $E_1 < E_2$ and 120 μs for $E_1 > E_2$, the stored strain energy is gradually converted into the fracture energy. The energy absorbed by the cohesive elements is shown in Fig. 10(*b*). Initially, a small portion of the total energy is stored in the cohesive elements, which cause a slow increase of U_{CE} up to 120 μs. An abrupt change in the slope of U_{CE} curves at about 125 μs signifies crack initiation event after which the fracture energy becomes a major portion of U_{CE}. An important observation that can be made from this plot is that more energy is absorbed throughout the loading history by the cohesive elements for the case of $E_1 < E_2$. This can be directly linked to the higher crack speeds observed in experiments as well as in simulations for this configuration.

5.3 Initial Slope of Traction-Separation Law. Cohesive elements are known to introduce undesirable artificial compliance [19,24] into the finite element model. This is especially true when a large number of cohesive elements are dispersed in the model as in the current work. In order to realistically simulate the problem on hand, these artifacts have to be minimized. Therefore, a cohesive law with an initially stiff response was required. The initial slope of the TSL can be changed in the bilinear model rather easily and hence it is used in the current work. Simulations were carried out to study the effects of introducing cohesive elements into the model. The geometry considered for this study was same as the one shown in Fig. 7(*a*) except that *it did not have a crack*. Two beam models were created without a crack, the first one with cohesive elements (in Region 2) and continuum elements (in Region 1), as shown in Fig. 7(*b*). The second model had only continuum elements in Regions 1 and 2 and cohesive elements were absent. The assigned material properties in each case were $E=4.2$ GPa, $\nu=0.34$, and $\rho=1175$ kg/m^3 and the models were loaded with an impact velocity of 5 m/s. Several simulations were conducted (up to 100 μs after impact) by changing the initial slope of the TSL (that is, λ_{cr} was varied in the range 0.05–0.005). The opening displacement, u_y, and stress, σ_y, histories (with respect to the coordinate system shown in Fig. 7(*b*)) were collected at a node located at the midpoint of the lower edge in

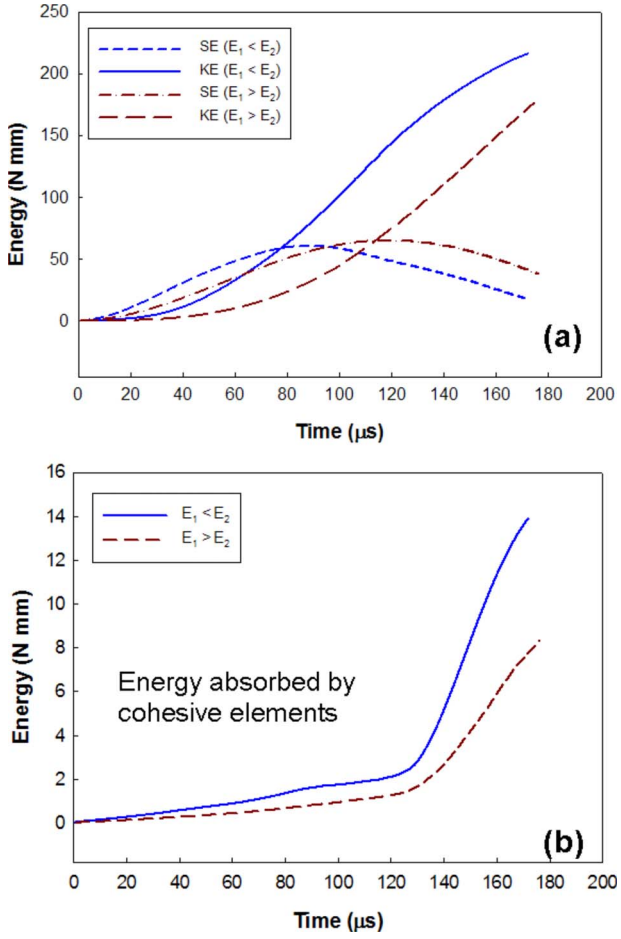

Fig. 10 Evolution of various energies in dynamic simulation for both FGM configurations: (*a*) kinetic energy and strain energy and (*b*) energy absorbed by cohesive elements

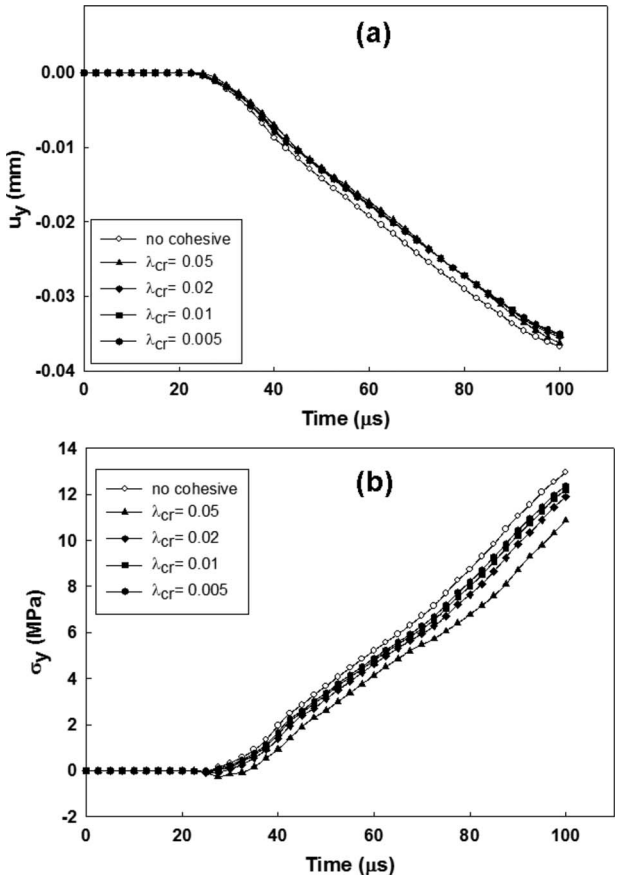

Fig. 11 Effect of the initial slope of the TSL on (*a*) displacement and (*b*) on stress results in elastodynamic simulations on uncracked beams at a node along the lower edge at mid-span

both the models.

The u_y displacement history is shown in Fig. 11(*a*). For an initial duration of 25 μs, there are no noticeable displacements as stress waves have not reached the lower edge of the beam yet. Upon the arrival of stress waves at the bottom edge, u_y monotonically increases up to 100 μs. From Fig. 11(*a*), it can be seen that the effect of introducing cohesive elements on displacements is relatively small. By comparing u_y displacements at 100 μs, a maximum of 4% difference between models without and with the cohesive elements having λ_{cr}=0.005 can be noted. The σ_y history is compared between the two models in Fig. 11(*b*). The effect of artificial compliance, however, can be seen here for larger values of λ_{cr}. For example, when λ_{cr}=0.05, the difference in σ_y between the two models is about 16%. This difference decreases as λ_{cr}. is decreased and stress histories for λ_{cr}=0.005 are rather close to that of the model without any cohesive elements. Also, it should be noted that there seems to be no significant gain in reducing λ_{cr} beyond 0.01 (the difference in σ_y between the two models is 5.8% when λ_{cr}=0.01 and 4.5% when λ_{cr}=0.005). Therefore, a value of λ_{cr}=0.01 was selected throughout this work.

5.4 Crack Path History. Figures 12(*a*) and 12(*b*) show instantaneous cracktip normal stresses before and after crack initiation, respectively, for the case of a crack on the compliant side ($E_1 < E_2$) of the beam. Similar results for the other configuration ($E_1 > E_2$) are shown in Figs. 12(*c*) and 12(*d*). The crack initiation is said to occur in the simulations when the first Gauss point of the first cohesive element is failed. The crack initiation times in simulations are nearly the same for both the configurations (131 μs for $E_1 < E_2$ and 133 μs for $E_1 > E_2$). The similarity in crack paths between experiments and simulations can be seen by comparing Fig. 12(*b*) with Fig. 3(*b*) and Fig. 12(*d*) with Fig. 3(*d*). When the crack is on the compliant side ($E_1 < E_2$), the crack growth trend is close to that of a Mode-I crack (crack kink angle α is ~2.4 deg in simulations whereas ~4 deg in experiments). For the other configuration ($E_1 < E_2$), the kink angle α is ~15 deg in simulations and ~16 deg in experiments. It should be noted here that only a qualitative comparison of crack paths can be made between experiments and simulations because a crack can grow only along element interfaces (in a zigzag fashion) in the model. The stress levels are higher at the beginning of the observation window for $E_1 > E_2$ and the stress contours shrink as the crack grows into a progressively compliant region. The opposite trend is observed for the other configuration where stress levels are lower before initiation and they increase following initiation. Figure 13 shows contour maps of u_y displacements at two instants of time: one before and one after crack initiation. Typical u_y displacement fields for a mixed-mode problem are shown in Figs. 13(*a*) and 13(*c*). As expected, prior to crack initiation, larger displacements occur in case of $E_1 < E_2$ compared to the one with $E_1 > E_2$. From Figs. 13(*b*) and 13(*d*), rapid increase in displacements for $E_1 > E_2$ configuration compared to $E_1 < E_2$ is evident as the crack grows into a progressively compliant material in the former.

The crack length histories from experiments and simulations are plotted in Fig. 14(*a*) and 14(*b*). Here, t_i denotes time at crack initiation. In simulations, cracks initiate at approximately 132 μs in both configurations. This is in contrast to the experimental results shown in Fig. 14(*a*) where the initiation time is in the range 145–155 μs. This difference is attributed to the fact that in ex-

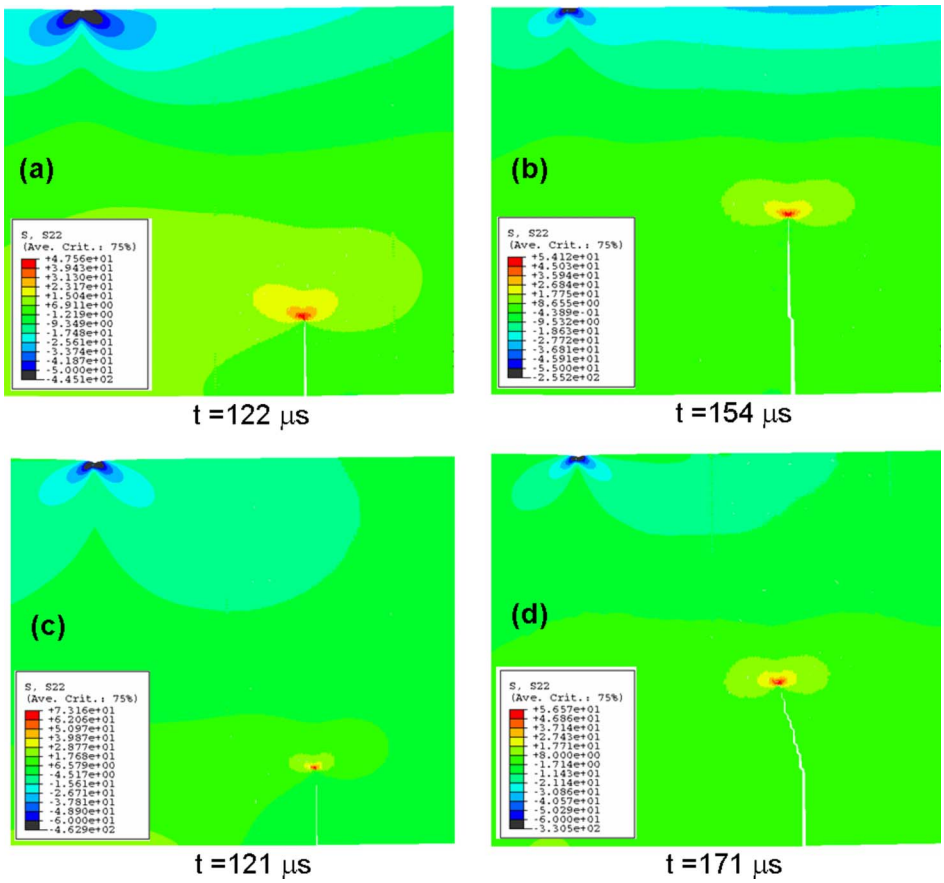

Fig. 12 Snapshots of σ_{yy} stress field at two different time instants: (*a*) 122 μs and (*b*) 154 μs for $E_1 < E_2$ (crack initiation time=131 μs), and (*c*) 121 μs and (*d*) 171 μs for $E_1 > E_2$ (crack initiation time=133 μs)

periments, the initial crack had a finite root radius of ~150 μm whereas in the finite element simulations, it was modeled as a sharp crack. Therefore, more energy had to accumulate at the notch tip before the crack initiated in experiments resulting a delayed response. Furthermore, the crack propagated at higher speeds when it initiated from the compliant side of the model. This agrees well with the experiments (higher slope for $E_1 < E_2$ in Figs. 14(*a*) and 14(*b*)). The higher crack speeds are associated with higher roughness of the fracture surfaces due to the formation of microcracks at the main crack tip resulting in greater energy dissipation.

5.5 *T*-Stress History. In order to understand the marked difference in crack paths for the two configurations, *T*-stress, a measure of in-plane crack tip constraint, was also computed up to crack initiation. Computation of *T*-stress in a mixed-mode dynamic simulation for FGM can be quite challenging. Paulino and Kim [44] have developed a robust and accurate interaction-integral based method to compute *T*-stress in FGM for mixed-mode cracks in the context of finite element simulations. However, in the current work, a modified stress difference method [33] was employed due to the ease of implementation. In this approach, the regression of normal stress difference $(\sigma_x - \sigma_y)$ ahead of the crack tip was used to find the instantaneous *T*-stress as

$$(\sigma_x - \sigma_y)_{\theta=0} = T + Dr \tag{24}$$

where D is the higher order coefficient associated with r^1 term in the asymptotic expansion of $(\sigma_x - \sigma_y)$. It can be seen from Fig. 15(*a*) that $(\sigma_x - \sigma_y)$ has an excellent linearity in the range where a straight line is fitted to the computed data. This process was repeated for all the time steps to get a *T*-stress history in each FGM configuration. The computed *T*-stress histories are plotted in Fig. 15(*b*) up to crack initiation for both configurations. A larger negative *T*-stress is observed for the case of $E_1 < E_2$. This indicates that the crack is likely to grow in its original direction and has lower tendency to kink compared to the other configuration. Similar behavior has been observed by Abanto-Bueno and Lambros [45] for a mixed-mode crack in homogeneous as well as FGM materials.

6 Conclusions

In this investigation, mixed-mode dynamic crack growth behavior in functionally graded glass-filled epoxy sheets is studied, using optical and finite element methods. The experimental study includes mapping deformations in the crack-tip vicinity as a crack initiates and propagates in a mixed-mode fashion in edge cracked FGM beams subjected to one-point impact at an offset distance relative to the initial crack and compositional gradient direction. Angular deflections of light rays proportional to surface slopes in the direction of initial crack orientation are recorded using reflection-mode CGS and high-speed photography. Marked differences in crack paths and crack speeds are observed experimentally. When the crack is initially situated on the compliant side of the beam, the crack growth occurred with a significantly small kink angle when compared to the case when the crack is on the stiffer side with all other experimental parameters being the same. The crack attained higher speeds (by about 100 m/s) in the former case when compared to the latter. The mixed-mode stress intensity factor histories, extracted based on a difference formulation of the crack-tip stress fields with linear variation of materials properties, also show differences. In both cases, the stress inten-

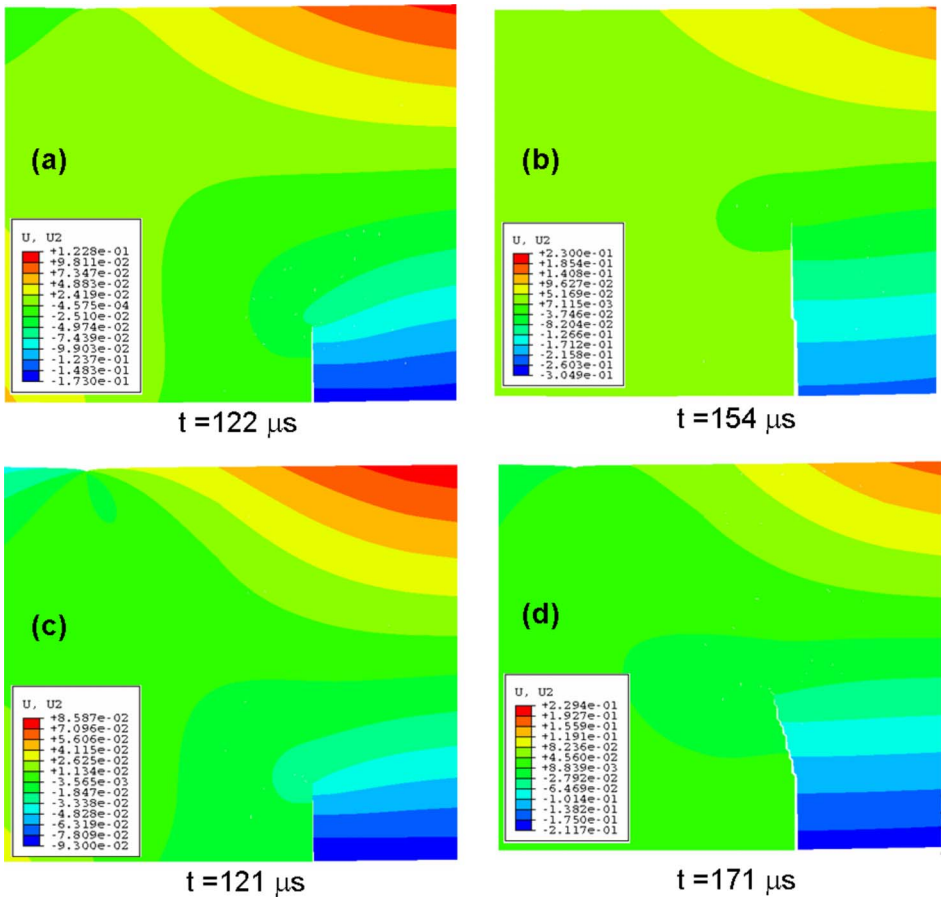

Fig. 13 Snapshots of u_y displacement field at two different time instants: (*a*) 122 μs and (*b*) 154 μs for $E_1 < E_2$ (crack initiation time=131 μs), and (*c*) 121 μs and (*d*) 171 μs for $E_1 > E_2$ (crack initiation time=133 μs)

sity factors increase with a negative (due to a negative K_{II} component) mode mixity up to crack initiation. After crack initiation, increasing Mode-I stress intensity factors accompanied by a small but positive Mode-II component is present in the case with a crack on the stiffer side of the FGM. On the other hand, Mode-I stress intensity factors show little variation after initiation from the compliant side of the FGM but propagate with a small but negative Mode-II component.

In order to understand the differences in crack path and other fracture parameters in the two FGM configurations, finite element simulations are undertaken. An intrinsic cohesive element method with a bilinear TSL was used to model mixed-mode dynamic crack growth. A user subroutine was developed and augmented with ABAQUS™ (Version 6.5) under the option UEL to implement the cohesive elements. The spatial variation of material properties in continuum elements was incorporated by performing a thermal analysis and then applying material properties (elastic properties, Poisson's ratio, and mass density) as temperature dependent quantities. The preinitiation *T*-stress was also computed by a modified stress difference method.

The finite element simulations have successfully captured the dominant characteristics of crack kinking under mixed-mode dynamic loading conditions. The simulated crack paths show a greater kink angle when the crack is on the stiffer side of the FGM. The computed *T*-stress values prior to crack initiation are more negative when the crack is situated on the compliant side of the sample indicating a greater likelihood of a crack to grow in its original direction and has a lower tendency to kink. Also, as in the experiments, higher crack speeds occur when the crack initiates from the compliant side of the FGM. The computed energy histories reveal greater energy dissipation throughout the observation window by the cohesive elements for the case of a crack on the compliant side of the FGM. Since higher crack speeds are accompanied by a greater fracture surface roughness due to microcracking during a dynamic fracture event, this observation is consistent with the higher crack speed seen in experiments when the crack initiates from the compliant side.

Acknowledgment

The authors would like to gratefully acknowledge the support of this research through a grant from the U.S. Army Research Office (Grant No. W911NF-04-10257). Alabama Supercomputer Center (ASC) provided some of the computational facilities for this research. The authors would like to thank the anonymous reviewers for their insightful comments.

Appendix: Direct Integration of Implicit Dynamic Equations

The dynamic equilibrium equations at the end of the current time step $t+\Delta t$ [36,37] is given by

$$M(\ddot{u})_{t+\Delta t} + (1+\alpha_d)\{(R^{\text{int}})_{t+\Delta t} - (R^{\text{ext}})_{t+\Delta t}\} - \alpha_d\{(R^{\text{int}})_t - (R^{\text{ext}})_t\} = 0 \tag{A1}$$

In the above, $\ddot{u}$ is the acceleration field and α_d is a parameter that controls algorithmic damping. Also, M, R^{int}, and R^{ext} are consistent mass matrix, internal force vector, and external force vector, respectively, and are given by

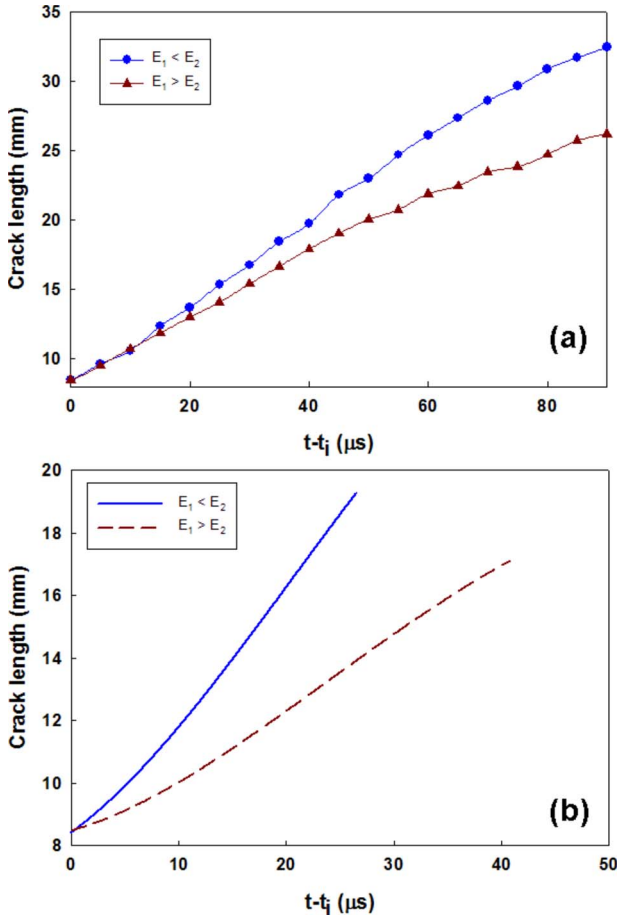

Fig. 14 Crack growth behavior in FGM sample under mixed-mode loading. Absolute crack length history from (*a*) experiments and (*b*) finite element simulations, t_i is crack initiation time (t_i=155 μs for $E_1<E_2$ and 145 μs for $E_1>E_2$ in experiments, and $t_i\sim$130 μs for both $E_1<E_2$ and $E_1>E_2$ in simulations).

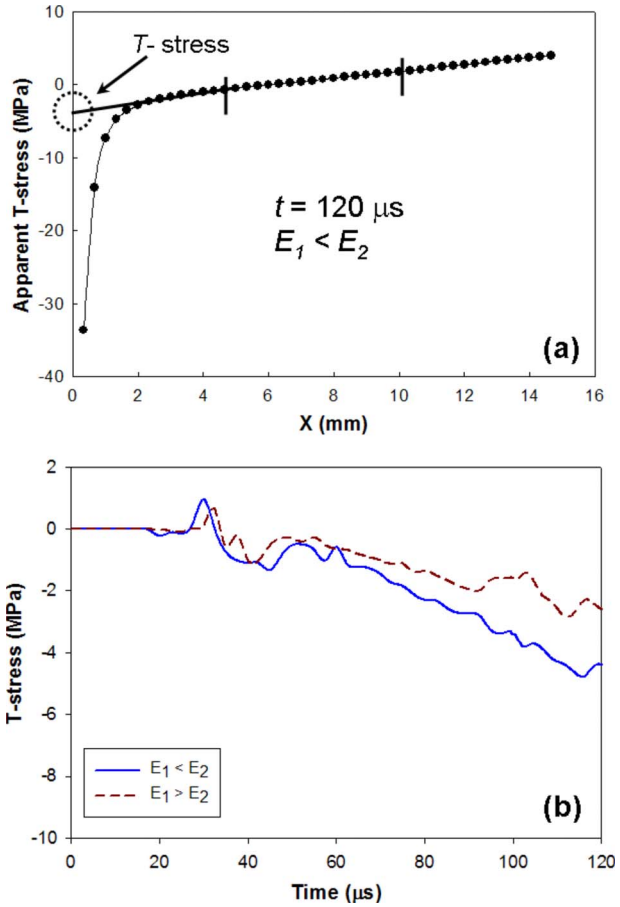

Fig. 15 Nonsingular crack-tip stress histories: (*a*) variation of apparent *T*-stress with radial distance at a certain time instant before crack initiation and (*b*) *T*-stress history up to crack initiation for $E_1<E_2$ and $E_1>E_2$

$$M = \int_{V_0} \rho_0 [N^T][N] dV_0 \tag{A2}$$

$$R^{\text{int}} = \int_{V_0} [B^T][\sigma] dV_0 \tag{A3}$$

and

$$R^{\text{ext}} = \int_S [N^T][T] dS + \int_V [N^T][F] dV \tag{A4}$$

Here, dV and dV_0 are elemental volumes in the current and the reference configurations, respectively, and dS is the current elemental surface area. Furthermore, $[\sigma]$ is the Cauchy stress tensor, $[B]$ is the strain-displacement matrix, and $[N]$ is the matrix of interpolation functions. The quantities $[F]$ and $[T]$ are body force and surface traction force vectors in the current configuration and ρ_0 is the reference mass density. The Newmark formulas for displacement and velocity integrations are as follows:

$$u_{t+\Delta t} = u_t + \Delta t \dot{u}_t + \Delta t^2((\tfrac{1}{2} - \beta_d)\ddot{u}_t + \beta_d \ddot{u}_{t+\Delta t}) \tag{A5}$$

and

$$\dot{u}_{t+\Delta t} = \dot{u}_t + \Delta t((1-\gamma)\ddot{u}_t + \gamma \ddot{u}_{t+\Delta t})$$

$$\beta_d = \tfrac{1}{4}(1-\alpha_d)^2, \quad \gamma_d = \tfrac{1}{2} - \alpha_d, \quad \text{and} \quad -\tfrac{1}{3} \leqslant \alpha_d \leqslant 0 \tag{A6}$$

when α_d=0, β_d and γ_d take the values of $\frac{1}{4}$ and $\frac{1}{2}$, respectively, which is the condition for unconditional stability in an implicit time integration scheme.

References

[1] Kirugulige, M. S., Kitey, R., and Tippur, H. V., 2005, "Dynamic Fracture Behavior of Model Sandwich Structures With Functionally Graded Core: A Feasibility Study," Compos. Sci. Technol., **65**, pp. 1052–1068.

[2] Delale, F., and Erdogan, F., 1983, "The Crack Problem for a Non-Homogeneous Plane," ASME J. Appl. Mech., **50**, pp. 609–614.

[3] Konda, N., and Erdogan, F., 1994, "The Mixed-Mode Crack Problem in a Nonhomogeneous Elastic Medium," Eng. Fract. Mech., **47**(4), pp. 533–545.

[4] Parameswaran, V., and Shukla, A., 1999, "Crack Tip Stress Fields for Dynamic Fracture in Functionally Graded Materials," Mech. Mater., **31**, pp. 579–596.

[5] Chalivendra, V., and Shukla, A., 2005, "Transient Elastodynamic Crack Growth in Functionally Graded Materials," ASME J. Appl. Mech., **72**, pp. 237–248.

[6] Butcher, R. J., Rousseau, C. E., and Tippur, H. V., 1998, "A Functionally Graded Particulate Composite: Preparation, Measurements and Failure Analysis," Acta Mater., **47**(1), pp. 259–268.

[7] Rousseau, C.-E., and Tippur, H. V., 2000, "Compositionally Graded Materials With Cracks Normal to the Elastic Gradient," Acta Mater., **48**, pp. 4021–4033.

[8] Rousseau, C.-E., and Tippur, H. V., 2001, "Dynamic Fracture of Compositionally Graded Materials With Cracks Along the Elastic Gradient: Experiments and Analysis," Mech. Mater., **37**, pp. 403–421.

[9] Kirugulige, M. S., and Tippur, H. V., 2006, "Mixed Mode Dynamic Crack Growth in Functionally Graded Glass-Filled Epoxy," Exp. Mech., **46**(2), pp. 269–281.

[10] Bittencourt, T. N., Wawrzynek, P. A., Ingraffea, A. R., and Sousa, J. L., 1996, "Quasi-Automatic Simulation of Crack Propagation for 2D LEFM Problems," Eng. Fract. Mech., **55**(2), pp. 321–334.

[11] Nishioka, T., 1997, "Computational Dynamic Fracture Mechanics," Int. J.

Fract., **86**, pp. 127–159.
[12] Nishioka, T., Tokudome, H., and Kinoshita, M., 2001, "Dynamic Fracture Path Prediction in Impact Fracture Phenomena Using Moving Finite Element Method Based on Delaunay Automatic Mesh Generation," Int. J. Solids Struct., **38**, pp. 5273–5301.
[13] Kim, J. H., and Paulino, G. H., 2004, "Simulation of Crack Propagation in Functionally Graded Materials Under Mixed-Mode and Non-Proportional Loading," Int. J. Mecha. Mater. Des., **1**, pp. 63–94.
[14] Tilbrook, M. T., Moon, R. J., and Hoffman, M., 2005, "Finite Element Simulations of Crack Propagation in Functionally Graded Materials Under Flexural Loading," Eng. Fract. Mech., **72**, pp. 2444–2467.
[15] Dugdale, D. C., 1960, "Yielding of Steel Sheets Containing Slits," J. Mech. Phys. Solids, **8**, pp. 100–104.
[16] Barenblatt, G. I., 1962, "The Mathematical Theory of Equilibrium Cracks in Brittle Fracture," Adv. Appl. Mech., **7**, pp. 55–129.
[17] Needleman, A., 1987, "A Continuum Model for Void Nucleation by Inclusion Debonding," ASME J. Appl. Mech., **54**, pp. 525–531.
[18] Xu, X. P., and Needleman, A., 1994, "Numerical Simulations of Fast Crack Growth in Brittle Solids," J. Mech. Phys. Solids, **42**(9), pp. 1397–1434.
[19] Wang, Z., and Nakamura, T., 2004, "Simulations of Crack Propagation is Elastic-Plastic Graded Materials," Mech. Mater., **36**, pp. 601–622.
[20] Jin, Z. H., Paulino, G. H., and Dodds, R. H., 2003, "Cohesive Fracture Modeling of Elastic-Plastic Crack Growth in Functionally Graded Materials," Eng. Fract. Mech., **70**(14), pp. 1885–1912.
[21] Shim, D. J., Paulino, G. H., and Dodds, R. H., 2006, "J Resistance Behavior in Functionally Graded Materials Using Cohesive Zone and Modified Boundary Layer Models," Int. J. Fract., **139**(1), pp. 91–117.
[22] Geubelle, P. H., and Baylor, J. S., 1998, "Impact Induced Delamination of Composites: A 2D Simulation," Composites, Part B, **29**, pp. 589–602.
[23] Zavattieri, P. D., Raghuram, P. V., and Espinosa, H. D., 2001, "A Computational Model of Ceramic Microstructures Subjected to Multi-Axial Dynamic Loading," J. Mech. Phys. Solids, **49**, pp. 27–68.
[24] Zhang, Z., and Paulino, G. H., 2005, "Cohesive Zone Modeling of Dynamic Failure in Homogeneous and Functionally Graded Materials," Int. J. Plast., **21**, pp. 1195–1254.
[25] Tvergaard, V., and Hutchinson, J. W., 1994, "The Relation Between Crack Growth Resistance and Fracture Process Parameters in Elastic-Plastic Solids," J. Mech. Phys. Solids, **40**, pp. 1377–1397.
[26] Madhusudhana, K. S., and Narasimhan, R., 2002, "Experimental and Numerical Investigations of Mixed Mode Crack Growth Resistance of a Ductile Adhesive Joint," Eng. Fract. Mech., **69**, pp. 865–883.
[27] Camacho, G. T., and Ortiz, M., 1996, "Computational Modeling of Impact Damage in Brittle Materials," Int. J. Solids Struct., **33**(20–22), pp. 2899–2938.
[28] Ortiz, M., and Pandolfi, A., 1999, "Finite-Deformation Irreversible Cohesive Elements for Three Dimensional Crack Propagation Analysis," Int. J. Numer. Methods Eng., **44**, pp. 1267–1282.
[29] Belytschko, T., and Black, A. T., 1999, "Elastic Crack Growth in Finite Elements With Minimal Re-Meshing," Int. J. Numer. Methods Eng., **45**, pp. 601–620.
[30] Moes, N., and Belytschko, T., 2002, "Extended Finite Elements for Cohesive Crack Growth," Eng. Fract. Mech., **69**, pp. 813–833.
[31] Erdogan, F., and Sih, G. C., 1963, "On the Crack Extension in Plates Under Plane Loading and Transverse Shear," ASME J. Basic Eng., **85D**(4), pp. 519–525.
[32] Dally, J. W., and Sanford, R. J., 1987, "Strain Gage Methods for Measuring the Opening Mode Stress Intensity Factor, K_I," Exp. Mech., **49**, pp. 381–388.
[33] Maleski, M. J., Kirugulige, M. S., and Tippur, H. V., 2004, "A Method for Measuring Mode-I Crack Tip Constraint Under Static and Dynamic Loading Conditions," Exp. Mech., **44**(5), pp. 522–532.
[34] Tippur, H. V., Krishnaswamy, S., and Rosakis, A. J., 1991, "Optical Mapping of Crack Tip Deformations Using the Methods of Transmission and Reflection Coherent Gradient Sensing: A. Study of Crack Tip K-Dominance," Int. J. Fract., **52**, pp. 91–117.
[35] Jain, N., Rousseau, C. E., and Shukla, A., 2004, "Crack Tip Stress Fields in Functionally Graded Materials With Linearly Varying Properties," Theor. Appl. Fract. Mech., **42**, pp. 155–170.
[36] 2004, "Theory and Users Manuals, I, II and III," ABAQUS, Version 6.5, Hibbit, Karlsson and Sorenson, RI.
[37] Hilber, H. M., Hughes, T. J. R., and Taylor, R. L., 1978, "Collocation, Dissipation and Overshoot for Time Integration Schemes in Structural Dynamics," Earthquake Eng. Struct. Dyn., **6**, pp. 99–117.
[38] Rice, J. R., 1968, "Mathematical Analysis in the Mechanics of Fracture," *Fracture, An Advanced Treatise*, Vol. 2, H. Liebowitz, ed., Academic, New York, pp. 191–311.
[39] Anlas, G., Santare, M. H., and Lambros, J., 2000, "Numerical Calculation of Stress Intensity Factors in Functionally Graded Materials," Int. J. Fract., **104**, pp. 131–143.
[40] Kim, J. H., and Paulino, G. H., 2002, "Isoparametric Graded Finite Elements for Nonhomogeneous Isotropic and Orthotropic Materials," ASME J. Appl. Mech., **69**, pp. 502–514.
[41] Rousseau, C.-E., and Tippur, H. V., 2002, "Evaluation of Crack Tip Fields and Stress Intensity Factors in Functionally Graded Elastic Materials: Cracks Parallel to Elastic Gradient," Int. J. Fract., **114**, pp. 87–111.
[42] Giannakopoulos, A. E., and Suresh, S., 1997, "Indentation of Solids With Gradients in Elastic Properties: Part—I. Point Force," Int. J. Solids Struct., **34**, pp. 2357–2392.
[43] Owens, A. T., 2007, "Development of a Split Hopkinson Bar for Testing Stress-Strain Response of Particulate Composites Under High Rates of Loading," MS thesis, Auburn University, Auburn TX.
[44] Paulino, G. H., and Kim, J. H., 2004, "A New Approach to Compute T-Stress in Functionally Graded Materials by Means of Interaction Integral Method," Eng. Fract. Mech., **71**, pp. 1907–1950.
[45] Abanto-Bueno, J., and Lambros, J., 2006, "An Experimental Study of Mixed Mode Crack Initiation and Growth in Functionally Graded Materials," Exp. Mech., **46**, pp. 179–196.

Green's Functions for a Half-Space and Two Half-Spaces Bonded to a Thin Anisotropic Elastic Layer

T. C. T. Ting
Professor Emeritus of University of Illinois at Chicago and Consulting Professor of Stanford University
Division of Mechanics and Computation,
Stanford University,
Durand 262,
Stanford, CA 94305-4040
e-mail: tting@uic.edu

The Green's function for an anisotropic elastic half-space that is bonded to a thin elastic material of different anisotropy subject to a line force and a line dislocation is presented. Also presented is the Green's function for two different anisotropic elastic half-spaces that are bonded to a thin elastic material of different anisotropy subject to a line force and a line dislocation in one of the half-spaces. The thickness h of the thin layer is assumed to be small compared with a reference length. Thus, instead of finding the solution in the thin layer and imposing the continuity conditions at the interface(s), we derive and apply effective boundary conditions for the interface between the layer and the body that take into account the existence of the layer. [DOI: 10.1115/1.2932097]

1 Introduction

When an elastic layer is bonded to another elastic body, one has to find the solutions in the layer as well as in the body and impose the continuity conditions across the interface. If the layer is very thin compared with some reference length, it is desirable to replace the existence of the layer by *effective boundary conditions* to avoid finding the solution in the layer. This was first considered by Bovik [1] who assumed that the layer is an isotropic elastic material. Niklasson et al. [2] studied the case when the layer is a monoclinic material with the symmetry plane parallel to the plane of the layer. The case in which the layer is a general anisotropic elastic material has been studied recently by Benveniste [3] and Ting [4]. We will employ the effective boundary conditions to construct the Green's functions for a half-space and two half-spaces bonded to a thin anisotropic elastic layer.

The basic governing equations for dynamics of a thin elastic layer derived in Ref. [4] are specialized for statics and are outlined in Sec. 2. In Sec. 3, we present the Stroh formalism [5–8] for two-dimensional deformation of an anisotropic elastic body. The Green's functions for a half-space and bimaterial subject to a line force and a line dislocation have been studied by many investigators [9–17]. The corresponding problem for a half-space bonded to a thin anisotropic elastic layer was investigated by Ma and Lin [18]. The solution involves an infinite series. If the thickness of the layer is much smaller than a reference length, we can replace the layer by the effective boundary conditions at the interface. We study this problem in Sec. 4 where the solution is in a closed form and explicit. It is valid only when the layer is very thin. In Sec. 5, we study the Green's function for two half-spaces bonded to a thin anisotropic layer subject to a line force and a line dislocation in one of the half-spaces.

2 Basic Equations

In a fixed rectangular coordinate system x_i $(i=1,2,3)$, the equation of equilibrium is

$$\sigma_{ij,j}=0 \tag{2.1}$$

where σ_{ij} is the stress, u_i is the displacement, and a comma denotes differentiation with x_i. The stress-strain relation is

$$\sigma_{ij}=C_{ijks}u_{k,s} \tag{2.2}$$

$$C_{ijks}=C_{jiks}=C_{ksij}=C_{ijsk} \tag{2.3}$$

where C_{ijks} is the elastic stiffness. The C_{ijks} is positive definite and possesses the full symmetry shown in Eq. (2.3). The third equality in Eq. (2.3) is redundant because the first two imply the third (p. 32, Ref. [8]).

Consider a layer of thickness h that is parallel to the plane $x_2=0$. If the layer is bonded to an elastic body, the stress components σ_{i2} $(i=1,2,3)$, are continuous across the interface between the layer and the body but not σ_{11}, σ_{13}, σ_{33}. Hence, let

$$\mathbf{t}=\begin{bmatrix}\sigma_{12}\\ \sigma_{22}\\ \sigma_{32}\end{bmatrix},\quad \hat{\mathbf{t}}=\begin{bmatrix}\sigma_{11}\\ \sigma_{13}\\ \sigma_{33}\end{bmatrix} \tag{2.4}$$

With Eq. (2.4), the equation of equilibrium (2.1) can be rewritten as

$$\mathbf{t}_{,2}+\mathbf{K}_1\mathbf{t}_{,1}+\mathbf{K}_3\mathbf{t}_{,3}+\hat{\mathbf{K}}_1\hat{\mathbf{t}}_{,1}+\hat{\mathbf{K}}_3\hat{\mathbf{t}}_{,3}=\mathbf{0} \tag{2.5}$$

where

$$\mathbf{K}_1=\begin{bmatrix}0&0&0\\1&0&0\\0&0&0\end{bmatrix},\quad \hat{\mathbf{K}}_1=\begin{bmatrix}1&0&0\\0&0&0\\0&1&0\end{bmatrix}$$
$$\mathbf{K}_3=\begin{bmatrix}0&0&0\\0&0&1\\0&0&0\end{bmatrix},\quad \hat{\mathbf{K}}_3=\begin{bmatrix}0&1&0\\0&0&0\\0&0&1\end{bmatrix} \tag{2.6}$$

Likewise, the stress-strain law (2.2) can be rewritten as

$$\mathbf{t}=\mathbf{C}_1\mathbf{u}_{,1}+\mathbf{C}_2\mathbf{u}_{,2}+\mathbf{C}_3\mathbf{u}_{,3} \tag{2.7a}$$

$$\hat{\mathbf{t}}=\hat{\mathbf{C}}_1\mathbf{u}_{,1}+\hat{\mathbf{C}}_2\mathbf{u}_{,2}+\hat{\mathbf{C}}_3\mathbf{u}_{,3} \tag{2.7b}$$

where, using the contracted notation $C_{\alpha\beta}$ for C_{ijks} [19],

Contributed by the Applied Mechanics Division of ASME for publication in the JOURNAL OF APPLIED MECHANICS. Manuscript received May 27, 2007; final manuscript received September 24, 2007; published online July 10, 2008. Review conducted by Marek-Jerzy Pindera.

$$\mathbf{C}_1=\begin{bmatrix} C_{61} & C_{66} & C_{65} \\ C_{21} & C_{26} & C_{25} \\ C_{41} & C_{46} & C_{45} \end{bmatrix},\quad \mathbf{C}_2=\begin{bmatrix} C_{66} & C_{62} & C_{64} \\ C_{26} & C_{22} & C_{24} \\ C_{46} & C_{42} & C_{44} \end{bmatrix}$$

$$\mathbf{C}_3=\begin{bmatrix} C_{65} & C_{64} & C_{63} \\ C_{25} & C_{24} & C_{23} \\ C_{45} & C_{44} & C_{43} \end{bmatrix}$$

$$\hat{\mathbf{C}}_1=\begin{bmatrix} C_{11} & C_{16} & C_{15} \\ C_{51} & C_{56} & C_{55} \\ C_{31} & C_{36} & C_{35} \end{bmatrix},\quad \hat{\mathbf{C}}_2=\begin{bmatrix} C_{16} & C_{12} & C_{14} \\ C_{56} & C_{52} & C_{54} \\ C_{36} & C_{32} & C_{34} \end{bmatrix} \tag{2.8}$$

$$\hat{\mathbf{C}}_3=\begin{bmatrix} C_{15} & C_{14} & C_{13} \\ C_{55} & C_{54} & C_{53} \\ C_{35} & C_{34} & C_{33} \end{bmatrix}$$

The three equations in Eqs. (2.5), (2.7*a*), and (2.7*b*) are the governing equations for $\mathbf{u}$, $\mathbf{t}$, and $\hat{\mathbf{t}}$. When the layer is bonded to an elastic body, $\mathbf{u}$, $\mathbf{t}$, $\mathbf{u}_{,1}$, $\mathbf{u}_{,3}$, $\mathbf{t}_{,1}$, $\mathbf{t}_{,3}$ are continuous across the interface but not $\hat{\mathbf{t}}$, $\mathbf{u}_{,2}$, and $\mathbf{t}_{,2}$. The idea is to eliminate $\hat{\mathbf{t}}$, $\mathbf{u}_{,2}$, and $\mathbf{t}_{,2}$. However, we have only three vector equations, Eqs. (2.5), (2.7*a*), and (2.7*b*). Thus, we can only eliminate two of the three.

The matrix $\mathbf{C}_2$ is positive definite so that Eq. (2.7*a*) can be solved for $\mathbf{u}_{,2}$ as

$$\mathbf{u}_{,2}=\mathbf{D}_0\mathbf{t}-\mathbf{D}_1^T\mathbf{u}_{,1}-\mathbf{D}_3^T\mathbf{u}_{,3} \tag{2.9}$$

where the superscript T denotes the transpose and

$$\mathbf{D}_0=\mathbf{C}_2^{-1},\quad \mathbf{D}_1=\mathbf{C}_1^T\mathbf{C}_2^{-1},\quad \mathbf{D}_3=\mathbf{C}_3^T\mathbf{C}_2^{-1} \tag{2.10}$$

Substitution of Eq. (2.9) into Eq. (2.7*b*) yields

$$\hat{\mathbf{t}}=\mathbf{E}_0\mathbf{t}+\mathbf{E}_1\mathbf{u}_{,1}+\mathbf{E}_3\mathbf{u}_{,3} \tag{2.11}$$

in which

$$\mathbf{E}_0=\hat{\mathbf{C}}_2\mathbf{C}_2^{-1},\quad \mathbf{E}_1=\hat{\mathbf{C}}_1-\mathbf{E}_0\mathbf{C}_1,\quad \mathbf{E}_3=\hat{\mathbf{C}}_3-\mathbf{E}_0\mathbf{C}_3 \tag{2.12}$$

Substitution of $\hat{\mathbf{t}}$ from Eq. (2.11) into Eq. (2.5) gives

$$\mathbf{t}_{,2}+\mathbf{D}_1\mathbf{t}_{,1}+\mathbf{D}_3\mathbf{t}_{,3}+\mathbf{G}_1\mathbf{u}_{,11}+\mathbf{G}_2\mathbf{u}_{,13}+\mathbf{G}_3\mathbf{u}_{,33}=\mathbf{0} \tag{2.13}$$

In the above,

$$\mathbf{D}_1=\mathbf{K}_1+\hat{\mathbf{K}}_1\mathbf{E}_0,\quad \mathbf{D}_3=\mathbf{K}_3+\hat{\mathbf{K}}_3\mathbf{E}_0$$

$$\mathbf{G}_1=\hat{\mathbf{K}}_1\mathbf{E}_1,\quad \mathbf{G}_3=\hat{\mathbf{K}}_3\mathbf{E}_3,\quad \mathbf{G}_2=\hat{\mathbf{K}}_1\mathbf{E}_3+\hat{\mathbf{K}}_3\mathbf{E}_1 \tag{2.14}$$

The $\mathbf{D}_1$ and $\mathbf{D}_3$ defined in Eqs. (2.10) and (2.14) can be shown to be equivalent using the identities

$$\mathbf{C}_1^T=\mathbf{K}_1\mathbf{C}_2+\hat{\mathbf{K}}_1\hat{\mathbf{C}}_2,\quad \mathbf{C}_3^T=\mathbf{K}_3\mathbf{C}_2+\hat{\mathbf{K}}_3\hat{\mathbf{C}}_2 \tag{2.15}$$

Equations (2.9) and (2.13) are two vector equations for the two unknowns $\mathbf{u}_{,2}$ and $\mathbf{t}_{,2}$. They and the auxiliary equation for $\hat{\mathbf{t}}$ in Eq. (2.11) are the key equations for a thin anisotropic elastic layer. It should be pointed out that the above derivation did not assume that the layer is thin. Hence, the results are valid regardless of whether the layer is thin or not.

The six matrices $\mathbf{C}_k$ and $\hat{\mathbf{C}}_k$ $(k=1,2,3)$, given in Eq. (2.8) are not independent of each other. Let

$$\mathbf{C}_0=\begin{bmatrix} C_{11} & C_{15} & C_{13} \\ C_{51} & C_{55} & C_{53} \\ C_{31} & C_{35} & C_{33} \end{bmatrix} \tag{2.16}$$

which is symmetric and positive definite. It can be shown that

$$\hat{\mathbf{C}}_1^T=\hat{\mathbf{K}}_1\mathbf{C}_0+\mathbf{K}_1\hat{\mathbf{C}}_2^T,\quad \hat{\mathbf{C}}_3^T=\hat{\mathbf{K}}_3\mathbf{C}_0+\mathbf{K}_3\hat{\mathbf{C}}_2^T \tag{2.17}$$

Hence, only $\mathbf{C}_0$, $\mathbf{C}_2$, and $\hat{\mathbf{C}}_2$ are independent. $\mathbf{C}_1$, $\mathbf{C}_3$, $\hat{\mathbf{C}}_1$, and $\hat{\mathbf{C}}_3$ can be computed from Eqs. (2.15) and (2.17).

We will show that the second columns of $\mathbf{E}_1$ and $\mathbf{E}_3$ vanish. Also, the matrices $\mathbf{G}_k$ $(k=1,2,3)$, are symmetric, and the second row and the second column of $\mathbf{G}_k$ $(k=1,2,3)$, vanish. To this end, let

$$\mathbf{w}=\mathbf{C}_0-\hat{\mathbf{C}}_2\mathbf{C}_2^{-1}\hat{\mathbf{C}}_2^T=\begin{bmatrix} w_{11} & w_{12} & w_{13} \\ w_{21} & w_{22} & w_{23} \\ w_{31} & w_{32} & w_{33} \end{bmatrix}=\mathbf{w}^T \tag{2.18}$$

The matrix $\mathbf{w}$ is symmetric, and can be shown to be positive definite. With the use of Eqs. (2.15) and (2.17), the $\mathbf{E}_1$ and $\mathbf{E}_3$ in Eq. (2.12) can be written in terms of $\mathbf{w}$ as

$$\mathbf{E}_1=\mathbf{w}\hat{\mathbf{K}}_1^T=\begin{bmatrix} w_{11} & 0 & w_{12} \\ w_{21} & 0 & w_{22} \\ w_{31} & 0 & w_{32} \end{bmatrix},\quad \mathbf{E}_3=\mathbf{w}\hat{\mathbf{K}}_3^T=\begin{bmatrix} w_{12} & 0 & w_{13} \\ w_{22} & 0 & w_{23} \\ w_{32} & 0 & w_{33} \end{bmatrix} \tag{2.19}$$

The $\mathbf{G}_k$ $(k=1,2,3)$, in Eq. (2.14) can also be written in terms of $\mathbf{w}$ as

$$\mathbf{G}_1=\hat{\mathbf{K}}_1\mathbf{w}\hat{\mathbf{K}}_1^T=\begin{bmatrix} w_{11} & 0 & w_{12} \\ 0 & 0 & 0 \\ w_{21} & 0 & w_{22} \end{bmatrix}=\mathbf{G}_1^T$$

$$\mathbf{G}_2=\hat{\mathbf{K}}_1\mathbf{w}\hat{\mathbf{K}}_3^T+\hat{\mathbf{K}}_3\mathbf{w}\hat{\mathbf{K}}_1^T=\begin{bmatrix} 2w_{12} & 0 & w_{13}+w_{22} \\ 0 & 0 & 0 \\ w_{31}+w_{22} & 0 & 2w_{23} \end{bmatrix}=\mathbf{G}_2^T \tag{2.20}$$

$$\mathbf{G}_3=\hat{\mathbf{K}}_3\mathbf{w}\hat{\mathbf{K}}_3^T=\begin{bmatrix} w_{22} & 0 & w_{23} \\ 0 & 0 & 0 \\ w_{32} & 0 & w_{33} \end{bmatrix}=\mathbf{G}_3^T$$

In conclusion, $\mathbf{D}_1$ and $\mathbf{D}_3$ shown in Eq. (2.14) depend on $\mathbf{E}_0$ only, whereas $\mathbf{E}_k$ $(k=1,3)$, and $\mathbf{G}_k$ $(k=1,2,3)$, given in Eqs. (2.19) and (2.20) depend on $\mathbf{w}$ only. Hence, it suffices to compute $\mathbf{D}_0$, $\mathbf{E}_0$, and $\mathbf{w}$. Since $\mathbf{D}_0$ and $\mathbf{w}$ are symmetric and $\mathbf{E}_0$ is not, there are a total of 21 independent parameters in $\mathbf{D}_0$. $\mathbf{E}_0$, and $\mathbf{w}$, same as $C_{\alpha\beta}$. Explicit expressions of $\mathbf{D}_0$, $\mathbf{E}_0$, and $\mathbf{w}$ in terms of the elastic stiffness $C_{\alpha\beta}$ and the elastic compliance $s_{\alpha\beta}$ have been given in Ref. [4].

3 Stroh Formalism

The Stroh formalism for two-dimensional problems for which the displacement $\mathbf{u}$ depends on x_1 and x_2 only has been extensively studied [5–8]. The solution to Eqs. (2.1) and (2.2) can be written as (see Chap. 5, Ref. [8])

$$\mathbf{u}=\mathrm{Im}\{\mathbf{A}\langle f(z_*)\rangle\mathbf{q}\},\quad \boldsymbol{\phi}=\mathrm{Im}\{\mathbf{B}\langle f(z_*)\rangle\mathbf{q}\} \tag{3.1a}$$

$\boldsymbol{\phi}$ is the stress function vector from which the stress is computed from

$$\sigma_{i1}=-\phi_{i,2},\quad \sigma_{i2}=\phi_{i,1} \tag{3.1b}$$

In the above, Im stands for the imaginary part, $\mathbf{q}$ is an arbitrary constant vector, $\mathbf{A}$ and $\mathbf{B}$ are 3×3 matrices, and $\langle f(z_*)\rangle$ is a diagonal matrix defined by

$$\mathbf{A}=[\mathbf{a}_1,\ \mathbf{a}_2,\ \mathbf{a}_3],\quad \mathbf{B}=[\mathbf{b}_1,\ \mathbf{b}_2,\ \mathbf{b}_3],$$

$$\langle f(z_*)\rangle=\mathrm{diag}[f(z_1),\ f(z_2),\ f(z_3)] \tag{3.2}$$

$f(z_\alpha)$ is an arbitrary function of

$$z_\alpha = x_1 + p_\alpha x_2 \tag{3.3}$$

The p_α and $\mathbf{a}_\alpha$ ($\alpha=1,2,3$), satisfy the eigenrelation

$$[\mathbf{Q} + p(\mathbf{R} + \mathbf{R}^T) + p^2\mathbf{T}]\mathbf{a} = \mathbf{0} \tag{3.4}$$

$$Q_{ik} = C_{i1k1}, \quad R_{ik} = C_{i1k2}, \quad T_{ik} = C_{i2k2} \tag{3.5}$$

It is known that p cannot be real. Hence, there are three pairs of complex conjugates for p. p_α ($\alpha=1,2,3$), are the p with a positive imaginary part. The associated eigenvectors are $\mathbf{a}_\alpha$ ($\alpha=1,2,3$),. The vectors $\mathbf{b}_\alpha$ ($\alpha=1,2,3$), are related to $\mathbf{a}_\alpha$ by

$$\mathbf{b} = (\mathbf{R}^T + p\mathbf{T})\mathbf{a} = -(\mathbf{R} + p^{-1}\mathbf{Q})\mathbf{a} \tag{3.6}$$

The second equality follows from Eq. (3.4).

It is useful to define the impedance tensor

$$\mathbf{M} = -i\mathbf{B}\mathbf{A}^{-1} \tag{3.7a}$$

and its inverse

$$\mathbf{M}^{-1} = i\mathbf{A}\mathbf{B}^{-1} \tag{3.7b}$$

They are positive definite Hermitian.

Before we study the Green's functions for a half-space and two half-spaces bonded to a thin elastic layer, we present Green's function for the infinite space subject to a line of concentrated force $\mathbf{f}$ and a line dislocation with Burgers vector $\hat{\mathbf{b}}$ applied along the x_3-axis. The solution is [8]

$$\mathbf{u} = \frac{1}{\pi}\,\mathrm{Im}\{\mathbf{A}\langle\ln(z_*)\rangle\mathbf{q}^\infty\}, \quad \boldsymbol{\phi} = \frac{1}{\pi}\,\mathrm{Im}\{\mathbf{A}\langle\ln(z_*)\rangle\mathbf{q}^\infty\} \tag{3.8}$$

$$\mathbf{q}^\infty = \mathbf{A}\mathbf{f} + \mathbf{B}\hat{\mathbf{b}} \tag{3.9}$$

In the case of a half-space $x_2 \geqslant 0$ subject to a line force $\mathbf{f}$ and a line dislocation with Burgers vector $\hat{\mathbf{b}}$ applied at

$$x_1 = 0, \quad x_2 = d > 0 \tag{3.10}$$

the Green's function is [8]

$$\mathbf{u} = \frac{1}{\pi}\,\mathrm{Im}\{\mathbf{A}\langle\ln(z_* - p_* d)\rangle\mathbf{q}^\infty + \mathbf{A}\langle\ln(z_* - \bar{p}_\beta d)\rangle\mathbf{q}_\beta\}$$

$$\boldsymbol{\phi} = \frac{1}{\pi}\,\mathrm{Im}\{\mathbf{B}\langle\ln(z_* - p_* d)\rangle\mathbf{q}^\infty + \mathbf{B}\langle\ln(z_* - \bar{p}_\beta d)\rangle\mathbf{q}_\beta\} \tag{3.11}$$

In the above, the repeated indices on β imply summation with $\beta=1,2,3$ and the overbar denotes the complex conjugate. If the boundary $x_2=0$ is a free surface,

$$\mathbf{q}_\beta = \mathbf{B}^{-1}\bar{\mathbf{B}}\mathbf{I}_\beta\mathbf{q}^\infty \tag{3.12}$$

where

$$\mathbf{I}_1 = \mathrm{diag}[1,\ 0,\ 0], \quad \mathbf{I}_2 = \mathrm{diag}[0,\ 1,\ 0] \quad \mathbf{I}_3 = \mathrm{diag}[0,\ 0,\ 1] \tag{3.13}$$

If the boundary $x_2=0$ is a rigid surface,

$$\mathbf{q}_\beta = \mathbf{A}^{-1}\bar{\mathbf{A}}\mathbf{I}_\beta\mathbf{q}^\infty \tag{3.14}$$

The first terms on the right of Eq. (3.11) are the Green's function for the infinite space subject to a line force and line dislocation applied at Eq. (3.10). The second terms are the *image singularities* that take care of the boundary condition at $x_2=0$.

4 Green's Function for a Half-Space Bonded to a Thin Layer

Let the half-space $x_2 \geqslant 0$ be subject to a line force $\mathbf{f}$ and a line dislocation with Burgers vector $\hat{\mathbf{b}}$ applied at

$$x_1 = 0, \quad x_2 = d > 0 \tag{4.1}$$

A thin elastic layer of thickness h and of different anisotropy is bonded to the half-space and occupies the region

$$-h \leq x_2 \leq 0 \tag{4.2}$$

Consider the solution

$$\mathbf{u} = \frac{1}{\pi}\,\mathrm{Im}\{\mathbf{A}\langle\ln(z_* - p_* d)\rangle\mathbf{q}^\infty + \mathbf{A}\langle\ln(z_* - \bar{p}_\beta d)\rangle\mathbf{q}_\beta + h\mathbf{A}\mathbf{g}(z_*)\} \tag{4.3}$$

$$\boldsymbol{\phi} = \frac{1}{\pi}\,\mathrm{Im}\{\mathbf{B}\langle\ln(z_* - p_* d)\rangle\mathbf{q}^\infty + \mathbf{B}\langle\ln(z_* - \bar{p}_\beta d)\rangle\mathbf{q}_\beta + h\mathbf{B}\mathbf{g}(z_*)\}$$

where

$$\mathbf{g}(z_*) = \begin{bmatrix} g_1(z_1) \\ g_2(z_2) \\ g_3(z_3) \end{bmatrix} \tag{4.4}$$

g_1, g_2, g_3 are, respectively, functions of z_1, z_2, z_3 to be determined. When $h=0$, Eq. (4.3) reduces to the solution (3.11) for the half-space without a layer. The last terms in Eq. (4.3) are the correction terms for the bonded thin layer.

At the interface boundary $x_2=0$, the displacement $\mathbf{u}$ in Eq. (4.3) simplifies to

$$\mathbf{u} = \frac{1}{\pi}\,\mathrm{Im}\{\mathbf{A}\langle\ln(x_1 - p_* d)\rangle\mathbf{q}^\infty + \mathbf{A}\mathbf{q}_\beta\ln(x_1 - \bar{p}_\beta d) + h\mathbf{A}\mathbf{g}(x_1)\}$$

Since

$$\mathrm{Im}\{\mathbf{A}\langle\ln(x_1 - p_* d)\rangle\mathbf{q}^\infty\} = \mathrm{Im}\{\mathbf{A}\mathbf{I}_\beta\mathbf{q}^\infty\ln(x_1 - p_\beta d)\}$$

$$= -\,\mathrm{Im}\{\bar{\mathbf{A}}\mathbf{I}_\beta\bar{\mathbf{q}}^\infty\ln(x_1 - \bar{p}_\beta d)\} \tag{4.5}$$

we have

$$\mathbf{u} = \frac{1}{\pi}\,\mathrm{Im}\{(\mathbf{A}\mathbf{q}_\beta - \bar{\mathbf{A}}\mathbf{I}_\beta\bar{\mathbf{q}}^\infty)\ln(x_1 - \bar{p}_\beta d) + h\mathbf{A}\mathbf{g}(x_1)\} \tag{4.6a}$$

Likewise, the stress function $\boldsymbol{\phi}$ in Eq. (4.3) at $x_2=0$ is

$$\boldsymbol{\phi} = \frac{1}{\pi}\,\mathrm{Im}\{(\mathbf{B}\mathbf{q}_\beta - \bar{\mathbf{B}}\mathbf{I}_\beta\bar{\mathbf{q}}^\infty)\ln(x_1 - \bar{p}_\beta d) + h\mathbf{B}\mathbf{g}(x_1)\} \tag{4.6b}$$

We now discuss separately the case when the surface $x_2=-h$ of the layer is traction free or rigid.

4.1 When the Surface $x_2=-h$ of the Layer is Traction Free. If the surface $x_2=-h$ of the layer is traction free, $\boldsymbol{\Phi}=0$ at $x_2=-h$. For the two-dimensional deformation considered here, Eq. (2.13) simplifies to

$$\mathbf{t}_{,2} + \mathbf{D}_1\mathbf{t}_{,1} + \mathbf{G}_1\mathbf{u}_{,11} = \mathbf{0} \tag{4.7}$$

Using Eqs. (2.4) and (3.1*b*), Eq. (4.7) is

$$\boldsymbol{\phi}_{,21} + \mathbf{D}_1\boldsymbol{\phi}_{,11} + \mathbf{G}_1\mathbf{u}_{,11} = \mathbf{0} \tag{4.8}$$

Without loss in generality, we may write Eq. (4.8) as

$$\boldsymbol{\phi}_{,2} + \mathbf{D}_1\boldsymbol{\phi}_{,1} + \mathbf{G}_1\mathbf{u}_{,1} = \mathbf{0} \tag{4.9}$$

Applying Eq. (4.9) at the interface $x_2=0$ and noticing that $\boldsymbol{\phi}=0$ at $x_2=-h$, $\boldsymbol{\phi}_{,2}$ can be approximated by $\boldsymbol{\phi}/h$ if terms of order higher than h are ignored. Hence,

$$\boldsymbol{\phi} + h(\mathbf{D}_1\boldsymbol{\phi}_{,1} + \mathbf{G}_1\mathbf{u}_{,1}) = \mathbf{0} \tag{4.10}$$

at $x_2=0$. Substitution of Eqs. (4.6*a*) and (4.6*b*) into Eq. (4.10) with the use of Eq. (3.12) leads to

$$h(\mathbf{D}_1\mathbf{B} + \mathbf{G}_1\mathbf{A})\mathbf{g}_{,1} + \mathbf{B}\mathbf{g} + \mathbf{G}_1(\mathbf{A}\mathbf{q}_\beta - \bar{\mathbf{A}}\mathbf{I}_\beta\bar{\mathbf{q}}^\infty)(x_1 - \bar{p}_\beta d)^{-1} = \mathbf{0} \tag{4.11}$$

Using Eqs. (3.7*a*) and (3.7*b*), we define

$$\mathbf{F}=\mathbf{B}^{-1}(\mathbf{D}_1-i\mathbf{G}_1\mathbf{M}^{-1})\mathbf{B},\quad \mathbf{m}_\beta=i\mathbf{B}^{-1}\mathbf{G}_1(\mathbf{M}^{-1}+\bar{\mathbf{M}}^{-1})\bar{\mathbf{B}}\mathbf{I}_\beta\bar{\mathbf{q}}^\infty \tag{4.12}$$

Equation (4.11) can be written as

$$h\mathbf{F}\mathbf{g}_{,1}+\mathbf{g}=\mathbf{m}_\beta(x_1-\bar{p}_\beta d)^{-1} \tag{4.13}$$

which is a first order differential equation for $\mathbf{g}(x_1)$.

Let λ_i and $\mathbf{y}_i$ $(i=1,2,3)$ be the eigenvalues and eigenvectors of $\mathbf{F}$. We then have

$$\mathbf{F}=\mathbf{Y}\langle\lambda_*\rangle\mathbf{Y}^{-1},\quad \mathbf{Y}=[\mathbf{y}_1,\ \mathbf{y}_2,\ \mathbf{y}_3] \tag{4.14}$$

The solution for $\mathbf{g}(x_1)$ in Eq. (4.13) can be shown to be

$$\mathbf{g}(x_1)=\mathbf{Y}\langle\eta_*(x_1-\bar{p}_\beta d)\rangle\mathbf{Y}^{-1}\mathbf{m}_\beta \tag{4.15}$$

where

$$\eta_k(\xi)=\frac{1}{h\lambda_k}\int^{\xi}e^{-(\xi-\gamma)/(h\lambda_k)}\gamma^{-1}d\gamma \tag{4.16}$$

To obtain $\mathbf{g}(z_*)$ in Eq. (4.4), we have to find $g_1(x_1)$, $g_2(x_1)$, $g_3(x_1)$, which are the components of $\mathbf{g}(x_1)$ in Eq. (4.15), and convert them to $g_1(z_1)$, $g_2(z_2)$, $g_3(z_3)$. Since

$$\mathbf{Y}\langle\eta_*(x_1-\bar{p}_\beta d)\rangle=\begin{bmatrix}Y_{11}\eta_1(x_1-\bar{p}_\beta d) & Y_{12}\eta_2(x_1-\bar{p}_\beta d) & Y_{13}\eta_3(x_1-\bar{p}_\beta d)\\ Y_{21}\eta_1(x_1-\bar{p}_\beta d) & Y_{22}\eta_2(x_1-\bar{p}_\beta d) & Y_{23}\eta_3(x_1-\bar{p}_\beta d)\\ Y_{31}\eta_1(x_1-\bar{p}_\beta d) & Y_{32}\eta_2(x_1-\bar{p}_\beta d) & Y_{33}\eta_3(x_1-\bar{p}_\beta d)\end{bmatrix} \tag{4.17}$$

we define

$$\mathbf{Z}(z_*-\bar{p}_\beta d)=\begin{bmatrix}Y_{11}\eta_1(z_1-\bar{p}_\beta d) & Y_{12}\eta_2(z_1-\bar{p}_\beta d) & Y_{13}\eta_3(z_1-\bar{p}_\beta d)\\ Y_{21}\eta_1(z_2-\bar{p}_\beta d) & Y_{22}\eta_2(z_2-\bar{p}_\beta d) & Y_{23}\eta_3(z_2-\bar{p}_\beta d)\\ Y_{31}\eta_1(z_3-\bar{p}_\beta d) & Y_{32}\eta_2(z_3-\bar{p}_\beta d) & Y_{33}\eta_3(z_3-\bar{p}_\beta d)\end{bmatrix} \tag{4.18a}$$

or

$$Z_{ij}(z_*-\bar{p}_\beta d)=Y_{ij}\eta_j(z_i-\bar{p}_\beta d),\quad (i,j\ \text{not summed}) \tag{4.18b}$$

We then have the explicit solution

$$\mathbf{g}(z_*)=\mathbf{Z}(z_*-\bar{p}_\beta d)\mathbf{Y}^{-1}\mathbf{m}_\beta \tag{4.19}$$

This completes the solution.

It should be pointed out that, in view of Eq. (3.12), the stress function at the interface $x_2=0$ obtained from Eq. (4.6*b*) is

$$\phi=\frac{h}{\pi}\,\mathrm{Im}\{\mathbf{B}\mathbf{g}(x_1)\} \tag{4.20}$$

4.2 When the Surface $x_2=-h$ of the Layer is Rigid. If the surface $x_2=-h$ of the thin layer is rigid, we have $\mathbf{u}=\mathbf{0}$ at $x_2=-h$. Equation (2.9) for the two-dimensional deformations considered here is

$$\mathbf{u}_{,2}+\mathbf{D}_1^T\mathbf{u}_{,1}-\mathbf{D}_0\boldsymbol{\phi}_{,1}=0 \tag{4.21}$$

Applying Eq. (4.21) at the interface $x_2=0$ and noticing that $\mathbf{u}=0$ at $x_2=-h$, $\mathbf{u}_{,2}$ can be approximated by $\mathbf{u}/h$ if terms of order higher than h are ignored. Hence,

$$\mathbf{u}=h(\mathbf{D}_0\boldsymbol{\phi}_{,1}-\mathbf{D}_1^T\mathbf{u}_{,1}) \tag{4.22}$$

at $x_2=0$. Substitution of Eqs. (4.6*a*) and (4.6*b*) into Eq. (4.22) with the use of Eq. (3.14) leads to

$$h(\mathbf{D}_1^T\mathbf{A}-\mathbf{D}_0\mathbf{B})\mathbf{g}_{,1}+\mathbf{A}\mathbf{g}=\mathbf{D}_0(\mathbf{B}\mathbf{q}_\beta-\bar{\mathbf{B}}\mathbf{I}_\beta\bar{\mathbf{q}}^\infty)(x_1-\bar{p}_\beta d)^{-1} \tag{4.23}$$

Equation (4.23) reduces to Eq. (4.13) if we define

$$\mathbf{F}=\mathbf{A}^{-1}(\mathbf{D}_1^T-i\mathbf{D}_0\mathbf{M})\mathbf{A},\quad \mathbf{m}_\beta=i\mathbf{A}^{-1}\mathbf{D}_0(\mathbf{M}+\bar{\mathbf{M}})\bar{\mathbf{A}}\mathbf{I}_\beta\bar{\mathbf{q}}^\infty \tag{4.24}$$

Thus, Eq. (4.15) provides the solution for $\mathbf{g}(x_1)$ and Eq. (4.19) is the explicit solution for $\mathbf{g}(z_*)$. The displacement at the interface $x_2=0$ obtained from Eq. (4.6*a*) is

$$\mathbf{u}=\frac{h}{\pi}\,\mathrm{Im}\{\mathbf{A}\mathbf{g}(x_1)\} \tag{4.25}$$

5 Green's Function for Two Half-Spaces Bonded to a Thin Layer

Let two half-spaces that are bonded to an anisotropic elastic layer of thickness h occupy the regions $x_2\geqslant h/2$ and $x_2\leqslant -h/2$, respectively. The thin layer lies in the region $h/2\geqslant x_2\geqslant -h/2$. The anisotropic elastic materials in $x_2\geqslant h/2$ and $x_2\leqslant -h/2$ will be denoted by Materials 1 and 2, respectively. A line force $\mathbf{f}$ and a line dislocation with Burgers vector $\hat{\mathbf{b}}$ are applied in Material 1 at

$$x_1=0,\quad x_2=(h/2)+d \tag{5.1}$$

When $h=0$, this is a problem of Green's function in a bimaterial for which the solution has been found [17]. We will find the Green's function for the case when the thickness h of the layer is very small.

As in the case of half-space, we employ the Green's function for a bimaterial obtained in Ref. [17] and add a correction term. Hence, let

$$\begin{aligned}\mathbf{u}^{(1)}=\frac{1}{\pi}\,\mathrm{Im}\{&\mathbf{A}_1\langle\ln(z_*^{(1)}-p_*^{(1)}d)\rangle\mathbf{q}^\infty+\mathbf{A}_1\langle\ln(z_*^{(1)}-\bar{p}_\beta^{(1)}d)\rangle\mathbf{q}_\beta^{(1)}\\&+h\mathbf{A}_1\mathbf{g}^{(1)}(z_*^{(1)})\}\end{aligned} \tag{5.2}$$

$$\begin{aligned}\boldsymbol{\phi}^{(1)}=\frac{1}{\pi}\,\mathrm{Im}\{&\mathbf{B}_1\langle\ln(z_*^{(1)}-p_*^{(1)}d)\rangle\mathbf{q}^\infty+\mathbf{B}_1\langle\ln(z_*^{(1)}-\bar{p}_\beta^{(1)}d)\rangle\mathbf{q}_\beta^{(1)}\\&+h\mathbf{B}_1\mathbf{g}^{(1)}(z_*^{(1)})\}\end{aligned}$$

for Material 1 and

$$\begin{aligned}\mathbf{u}^{(2)}&=\frac{1}{\pi}\,\mathrm{Im}\{\mathbf{A}_2\langle\ln(z_*^{(2)}-p_\beta^{(1)}d)\rangle\mathbf{q}_\beta^{(2)}+h\mathbf{A}_2\mathbf{g}^{(2)}(z_*^{(2)})\}\\ \phi^{(2)}&=\frac{1}{\pi}\,\mathrm{Im}\{\mathbf{B}_2\langle\ln(z_*^{(2)}-p_\beta^{(1)}d)\rangle\mathbf{q}_\beta^{(2)}+h\mathbf{B}_2\mathbf{g}^{(2)}(z_*^{(2)})\}\end{aligned} \tag{5.3}$$

for Material 2. In the above, the Superscripts (1) and (2) or the Subscripts 1 and 2 refer to Materials 1 and 2, respectively, and

$$z_\alpha^{(1)}=x_1+p_\alpha^{(1)}(x_2-h/2),\quad z_\alpha^{(2)}=x_1+p_\alpha^{(2)}(x_2+h/2) \tag{5.4}$$

$$\mathbf{g}^{(1)}(z_*^{(1)})=\begin{bmatrix}g_1^{(1)}(z_1^{(1)})\\ g_2^{(1)}(z_2^{(1)})\\ g_3^{(1)}(z_3^{(1)})\end{bmatrix},\quad \mathbf{g}^{(2)}(z_*^{(2)})=\begin{bmatrix}g_1^{(2)}(z_1^{(2)})\\ g_2^{(2)}(z_2^{(2)})\\ g_3^{(2)}(z_3^{(2)})\end{bmatrix} \tag{5.5}$$

The $\mathbf{g}^{(1)}(z_*^{(1)})$ and $\mathbf{g}^{(2)}(z_*^{(2)})$ are the correction terms that need to be determined. It is shown in Ref. [17] that

$$\mathbf{A}_1\mathbf{q}_\beta^{(1)}+\bar{\mathbf{A}}_2\bar{\mathbf{q}}_\beta^{(2)}=\bar{\mathbf{A}}_1\mathbf{I}_\beta\bar{\mathbf{q}}^\infty,\quad \mathbf{B}_1\mathbf{q}_\beta^{(1)}+\bar{\mathbf{B}}_2\bar{\mathbf{q}}_\beta^{(2)}=\bar{\mathbf{B}}_1\mathbf{I}_\beta\bar{\mathbf{q}}^\infty \tag{5.6}$$

The two equations in Eq. (5.6) can be solved for $\mathbf{q}_\beta^{(1)}$ and $\mathbf{q}_\beta^{(2)}$ as (p. 285, Ref. [7])

$$\mathbf{A}_1\mathbf{q}_\beta^{(1)}=(\mathbf{M}_1+\bar{\mathbf{M}}_2)^{-1}(\bar{\mathbf{M}}_2-\bar{\mathbf{M}}_1)\bar{\mathbf{A}}_1\mathbf{I}_\beta\bar{\mathbf{q}}^\infty$$

$$\bar{\mathbf{A}}_2\bar{\mathbf{q}}_\beta^{(2)} = (\mathbf{M}_1 + \bar{\mathbf{M}}_2)^{-1}(\mathbf{M}_1 + \bar{\mathbf{M}}_1)\bar{\mathbf{A}}_1\mathbf{I}_\beta\bar{\mathbf{q}}^\infty$$

$$\mathbf{B}_1\mathbf{q}_\beta^{(1)} = (\mathbf{M}_1^{-1} + \bar{\mathbf{M}}_2^{-1})^{-1}(\bar{\mathbf{M}}_2^{-1} - \bar{\mathbf{M}}_1^{-1})\bar{\mathbf{B}}_1\mathbf{I}_\beta\bar{\mathbf{q}}^\infty \tag{5.7}$$

$$\bar{\mathbf{B}}_2\mathbf{q}_\beta^{(2)} = (\mathbf{M}_1^{-1} + \bar{\mathbf{M}}_2^{-1})^{-1}(\mathbf{M}_1^{-1} + \bar{\mathbf{M}}_1^{-1})\bar{\mathbf{B}}_1\mathbf{I}_\beta\bar{\mathbf{q}}^\infty$$

At the interface $x_2 = h/2$, Eq. (5.2) simplifies to

$$\mathbf{u}^{(1)} = \frac{1}{\pi}\,\mathrm{Im}\{-\bar{\mathbf{A}}_2\bar{\mathbf{q}}_\beta^{(2)}\ln(x_1 - \bar{p}_\beta^{(1)}d) + h\mathbf{A}_1\mathbf{g}^{(1)}(x_1)\}$$

$$\boldsymbol{\phi}^{(1)} = \frac{1}{\pi}\,\mathrm{Im}\{-\bar{\mathbf{B}}_2\bar{\mathbf{q}}_\beta^{(1)}\ln(x_1 - \bar{p}_\beta^{(1)}d) + h\mathbf{B}_1\mathbf{g}^{(1)}(x_1)\} \tag{5.8}$$

where we have made use of Eqs. (4.5) and (5.6). At the interface $x_2 = -h/2$, Eq. (5.3) simplifies to

$$\mathbf{u}^{(2)} = \frac{1}{\pi}\,\mathrm{Im}\{-\bar{\mathbf{A}}_2\bar{\mathbf{q}}_\beta^{(2)}\ln(x_1 - \bar{p}_\beta^{(1)}d) - h\bar{\mathbf{A}}_2\bar{\mathbf{g}}^{(2)}(x_1)\}$$

$$\boldsymbol{\phi}^{(2)} = \frac{1}{\pi}\,\mathrm{Im}\{-\bar{\mathbf{B}}_2\bar{\mathbf{q}}_\beta^{(2)}\ln(x_1 - \bar{p}_\beta^{(1)}d) - h\bar{\mathbf{B}}_2\bar{\mathbf{g}}^{(2)}(x_1)\} \tag{5.9}$$

We now employ the effective boundary condition (4.21). Replacing $\mathbf{u}_{,2}$ by $(\mathbf{u}^{(1)} - \mathbf{u}^{(2)})/h$, Eq. (4.21) can be approximated by one of the following:

$$\mathbf{u}^{(1)} - \mathbf{u}^{(2)} + h\{\mathbf{D}_1^T\mathbf{u}_{,1}^{(1)} - \mathbf{D}_0\boldsymbol{\phi}_{,1}^{(1)}\} = \mathbf{0} \tag{5.10a}$$

$$\mathbf{u}^{(1)} - \mathbf{u}^{(2)} + h\{\mathbf{D}_1^T\mathbf{u}_{,1}^{(2)} - \mathbf{D}_0\boldsymbol{\phi}_{,1}^{(2)}\} = \mathbf{0} \tag{5.10b}$$

$$2(\mathbf{u}^{(1)} - \mathbf{u}^{(2)}) + h\{\mathbf{D}_1^T(\mathbf{u}_{,1}^{(1)} + \mathbf{u}_{,1}^{(2)}) - \mathbf{D}_0(\boldsymbol{\phi}_{,1}^{(1)} + \boldsymbol{\phi}_{,1}^{(2)})\} = \mathbf{0} \tag{5.10c}$$

Likewise, the effective boundary condition (4.9) can be approximated by one of the following:

$$\boldsymbol{\phi}^{(1)} - \boldsymbol{\phi}^{(2)} + h\{\mathbf{D}_1\boldsymbol{\phi}_{,1}^{(1)} + \mathbf{G}_1\mathbf{u}_{,1}^{(1)}\} = \mathbf{0} \tag{5.11a}$$

$$\boldsymbol{\phi}^{(1)} - \boldsymbol{\phi}^{(2)} + h\{\mathbf{D}_1\boldsymbol{\phi}_{,1}^{(2)} + \mathbf{G}_1\mathbf{u}_{,1}^{(2)}\} = \mathbf{0} \tag{5.11b}$$

$$2(\boldsymbol{\phi}^{(1)} - \boldsymbol{\phi}^{(2)}) + h\{\mathbf{D}_1(\boldsymbol{\phi}_{,1}^{(1)} + \boldsymbol{\phi}_{,1}^{(2)}) + \mathbf{G}_1(\mathbf{u}_{,1}^{(1)} + \mathbf{u}_{,1}^{(2)})\} = \mathbf{0} \tag{5.11c}$$

The differences between the three expressions in Eqs. (5.10*a*), (5.10*b*), (5.10*c*), (5.11*a*), (5.11*b*), and (5.11*c*) are of the order higher than h. Substitution of Eqs. (5.8) and (5.9) into Eqs. (5.10*a*) and (5.11*a*) leads to, after using Eq. (5.6),

$$h(\mathbf{D}_1^T\mathbf{A}_1 - \mathbf{D}_0\mathbf{B}_1)\mathbf{g}_{,1}^{(1)} + \mathbf{A}_1\mathbf{g}^{(1)} + \bar{\mathbf{A}}_2\bar{\mathbf{g}}^{(2)} = (\mathbf{D}_1^T\bar{\mathbf{A}}_2\bar{\mathbf{q}}_\beta^{(2)} - \mathbf{D}_0\bar{\mathbf{B}}_2\bar{\mathbf{q}}_\beta^{(2)})(x_1 - \bar{p}_\beta^{(1)}d)^{-1} \tag{5.12a}$$

$$h(\mathbf{D}_1\mathbf{B}_1 + \mathbf{G}_1\mathbf{A}_1)\mathbf{g}_{,1}^{(1)} + \mathbf{B}_1\mathbf{g}^{(1)} + \bar{\mathbf{B}}_2\bar{\mathbf{g}}^{(2)} = (\mathbf{D}_1\bar{\mathbf{B}}_2\bar{\mathbf{q}}_\beta^{(2)} + \mathbf{G}_1\bar{\mathbf{A}}_2\bar{\mathbf{q}}_\beta^{(2)})(x_1 - \bar{p}_\beta^{(1)}d)^{-1} \tag{5.12b}$$

The matrices $\mathbf{D}_0$, $\mathbf{D}_1$, and $\mathbf{G}_1$ in Eqs. (5.12*a*) and (5.12*b*) depend on the elastic constants of the thin layer.

Due to the choice of Eqs. (5.10*a*) and (5.11*a*). Eqs. (5.12*a*) and (5.12*b*) is a differential equation in $\mathbf{g}^{(1)}$, not in $\bar{\mathbf{g}}^{(2)}$. Any other choices would lead to coupled differential equations for $\mathbf{g}^{(1)}$ and $\bar{\mathbf{g}}^{(2)}$. We can now eliminate $\bar{\mathbf{g}}^{(2)}$ if we multiply Eq. (5.12*a*) by $\bar{\mathbf{B}}_2\bar{\mathbf{A}}_2^{-1}$ and subtract Eq. (5.12*b*). The result is

$$h\mathbf{F}\mathbf{g}_{,1}^{(1)} + \mathbf{g}^{(1)} = \mathbf{m}_\beta(x_1 - \bar{p}_\beta^{(1)}d)^{-1} \tag{5.13}$$

where

$$\mathbf{F} = \mathbf{A}_1^{-1}(\mathbf{M}^{(1)} + \bar{\mathbf{M}}^{(2)})^{-1}(\bar{\mathbf{M}}^{(2)}\mathbf{D}_1^T + \mathbf{D}_1\mathbf{M}^{(1)} - i\bar{\mathbf{M}}^{(2)}\mathbf{D}_0\mathbf{M}^{(1)} - i\mathbf{G}_1)\mathbf{A}_1 \tag{5.14}$$

$$\mathbf{m}_\beta = \mathbf{A}_1^{-1}(\mathbf{M}^{(1)} + \bar{\mathbf{M}}^{(2)})^{-1}(\bar{\mathbf{M}}^{(2)}\mathbf{D}_1^T - \mathbf{D}_1\bar{\mathbf{M}}^{(2)} + i\bar{\mathbf{M}}^{(2)}\mathbf{D}_0\bar{\mathbf{M}}^{(2)} - i\mathbf{G}_1)\bar{\mathbf{A}}_2\bar{\mathbf{q}}_\beta^{(2)}$$

Equation (5.13) is similar to Eq. (4.13) for which the solution is given in Eq. (4.15). Hence,

$$\mathbf{g}^{(1)}(x_1) = \mathbf{Y}\langle\eta_*(x_1 - \bar{p}_\beta^{(1)}d)\rangle\mathbf{Y}^{-1}\mathbf{m}_\beta \tag{5.15}$$

Following the derivation of Eqs. (4.17), (4.18*a*), (4.18*b*), and (4.19), we have

$$\mathbf{g}^{(1)}(z_*) = \mathbf{Z}(z_* - \bar{p}_\beta^{(1)}d)\mathbf{Y}^{-1}\mathbf{m}_\beta \tag{5.16}$$

in which $\mathbf{Z}(z_* - \bar{p}_\beta^{(1)}d)$ is defined in Eqs. (4.18*a*) and (4.18*b*) if we replace $\bar{p}_\beta$ by $\bar{p}_\beta^{(1)}$.

With $\mathbf{g}^{(1)}(x_1)$ obtained in Eq. (5.15), $\bar{\mathbf{g}}^{(2)}(x_1)$ can be computed from either Eq. (5.12*a*) or (5.12*b*). The result is too complicated to record here. It should be noted that, after $\bar{\mathbf{g}}^{(2)}(x_1)$ is computed, we have to convert $\bar{\mathbf{g}}^{(2)}(x_1)$ to $\bar{\mathbf{g}}^{(2)}(z_*)$ following the conversion of $\mathbf{g}(x_1)$ to $\mathbf{g}(z_*)$ shown in Eqs. (4.15)–(4.17), (4.18*a*), (4.18*b*), and (4.19).

6 Concluding Remarks

It should be noted that the two equations in Eq. (3.6) can be rewritten as [20] (see also Ref. [8])

$$\begin{bmatrix}\mathbf{N}_1 & \mathbf{N}_2\\ \mathbf{N}_3 & \mathbf{N}_1^T\end{bmatrix}\begin{bmatrix}\mathbf{a}\\ \mathbf{b}\end{bmatrix} = p\begin{bmatrix}\mathbf{a}\\ \mathbf{b}\end{bmatrix} \tag{6.1}$$

where

$$\mathbf{N}_1 = -\mathbf{T}^{-1}\mathbf{R}^T, \quad \mathbf{N}_2 = \mathbf{T}^{-1}, \quad \mathbf{N}_3 = \mathbf{R}\mathbf{T}^{-1}\mathbf{R}^T - \mathbf{Q} \tag{6.2}$$

The matrices $\mathbf{C}_1$ and $\mathbf{C}_2$ given in Eq. (2.8) are identical to the matrices $\mathbf{R}^T$ and $\mathbf{T}$ defined in Eq. (3.5), i.e.,

$$\mathbf{C}_1 = \mathbf{R}^T, \quad \mathbf{C}_2 = T \tag{6.3}$$

Hence, from Eqs. (2.10) and (6.2),

$$\mathbf{D}_1 = -\mathbf{N}_1^T, \quad \mathbf{D}_0 = \mathbf{N}_2, \quad \mathbf{G}_1 = -\mathbf{N}_3 \tag{6.4}$$

The last equality can be proved from the $\mathbf{G}_1$ in Eq. (2.20) and the explicit expression of w_{ij} given in Ref. [4]. Thus, the matrices $\mathbf{D}_1$, $\mathbf{D}_0$, and $\mathbf{G}_1$ that appeared in the Green's functions in Secs. 4 and 5 can be replaced by $-\mathbf{N}_1^T$, $\mathbf{N}_2$, and $-\mathbf{N}_3$, respectively. They are related to the material property of the thin layer.

References

[1] Bovik, P., 1994, "On the Modelling of Thin Interface Layers in Elastic and Acoustic Scattering Problems," Q. J. Mech. Appl. Math., **47**, pp. 17–40.

[2] Niklasson, A. J., Datta, S. K., and Dunn, M. L., 2000, "On Approximate Guided Waves in Plates With Thin Anisotropic Coatings by Means of Effective Boundary Conditions," J. Acoust. Soc. Am., **108**(3), pp. 924–933.

[3] Benveniste, Y., 2006, "A General Interface Model for a Three-Dimensional Curved Thin Anisotropic Interphase Between Two Anisotropic Media," J. Mech. Phys. Solids, **54**, pp. 708–734.

[4] Ting, T. C. T., 2007, "Mechanics of a Thin Anisotropic Elastic Layer and a Layer That is Bonded to an Anisotropic Elastic Body or Bodies," Proc. R. Soc. London, **463**(2085), pp. 2223–2239.

[5] Stroh, A. N., 1958, "Dislocations and Cracks in Anisotropic Elasticity," Philos. Mag., **3**, pp. 625–646.

[6] Barnett, D. M., and Lothe, J., 1973, "Synthesis of the Sextic and the Integral Formalism for Dislocations, Green's Function and Surface Waves in Anisotropic Elastic Solids," Phys. Norv., **7**, pp. 13–19.

[7] Chadwick, P., and Smith, G. D., 1977, "Foundations of the Theory of Surface Waves in Anisotropic Elastic Materials," Adv. Appl. Mech., **17**, pp. 303–376.

[8] Ting, T. C. T., 1996, *Anisotropic Elasticity: Theory and Applications*, Oxford University Press, New York.

[9] Willis, J. R., 1971, "Fracture Mechanics of Interfacial Cracks," J. Mech. Phys. Solids, **19**, pp. 353–368.

[10] Braekhus, J., and Loth, J., 1971, "Dislocations at and Near Planar Interface," Phys. Status Solidi B, **43**, pp. 651–657.

[11] Barnett, D. M., and Lothe, J., 1974, "An Image Force Theorem for Dislocations in Bicrystals," J. Phys. F: Met. Phys., **4**, pp. 1618–1635.

[12] Kirchner, H. O. K., and Lothe, J., 1987, "Displacements and Tractions Along Interfaces," Philos. Mag. A, **56**, pp. 583–594.

[13] Tewary, V. K., Wagoner, R. H., and Hirth, J. P., 1989, "Elastic Green's Function for a Composite Solid With a Planar Crack in the Interface," J. Mater. Res., **4**, pp. 124–136.
[14] Suo, Z., 1990, "Singularities, Interfaces and Cracks in Dissimilar Anisotropic Media," Proc. R. Soc. London, Ser. A, **427**, pp. 331–358.
[15] Qu, J., and Li, Q., 1991, "Interfacial Dislocations and Its Application to Interface Crack in Anisotropic Bimaterials," J. Elast., **26**, pp. 167–195.
[16] Qu, J., 1991, "Greens' Functions in Anisotropic Bimaterials," *Modern Theory of Anisotropic Elasticity and Applications*, (SIAM Proceedings Series), J. J. Wu, T. C. T. Ting, and D. M. Barnett, eds., SIAM, Philadelphia, pp. 62–73.
[17] Ting, T. C. T., 1992, "Image Singularities of Green's Functions for Anisotropic Elastic Half-Spaces and Bimaterials," Q. J. Mech. Appl. Math., **45**, pp. 119–139.
[18] Ma, C.-C., and Lin, R.-L., 2002, "Full-Field Analysis of a Planar Anisotropic Layered Half-Plane for Concentrated Forces and Edge Dislocations," Proc. R. Soc. London, Ser. A, **458**, pp. 2369–2392.
[19] Voigt, W., 1910, *Lehrbuch der Kristallphysik*, Teubner, Leipzig.
[20] Ingebrigtsen, K. A., and Tonning, A., 1969, "Elastic Surface Waves in Crystal," Phys. Rev., **184**, pp. 942–951.

Mixed-Mode Fracture Analysis of Orthotropic Functionally Graded Material Coatings Using Analytical and Computational Methods

Serkan Dag[1]
Mem. ASME
e-mail: sdag@metu.edu.tr

K. Ayse Ilhan

Department of Mechanical Engineering,
Middle East Technical University,
Ankara 06531, Turkey

This article presents analytical and computational methods for mixed-mode fracture analysis of an orthotropic functionally graded material (FGM) coating-bond coat-substrate structure. The analytical solution is developed by considering an embedded crack in the orthotropic FGM coating. The embedded crack is assumed to be loaded through arbitrary self-equilibrating mixed-mode tractions that are applied to its surfaces. Governing partial differential equations for each of the layers in the trilayer structure are derived in terms of the effective parameters of plane orthotropic elasticity. The problem is then reduced to a system of two singular integral equations, which is solved numerically to evaluate the mixed-mode crack tip parameters. The computational approach is based on the finite element method and is developed by applying the displacement correlation technique. The use of two separate methods in the analyses allowed direct comparisons of the results obtained for an embedded crack in the orthotropic FGM coating, leading to a highly accurate numerical predictive capability. The finite element based approach is used to generate further numerical results by considering periodic cracking in the orthotropic FGM coating. Parametric analyses presented in this article illustrate the influences of the material nonhomogeneity and orthotropy constants, the bond coat thickness, and the crack periodicity on the mixed-mode stress intensity factors and the energy release rate. [DOI: 10.1115/1.2932098]

1 Introduction

The past two decades have seen considerable progress in the development and applications of functionally graded materials (FGMs). These advanced composites are processed in such a way that they will induce continuous spatial variations in the volume fractions of the constituents. As a result, from the continuum perspective, modeling of FGMs requires that the physical properties be represented as functions of the spatial coordinates. Some of the processing methods used to deposit functionally graded coatings are known to lead to the formation of an orthotropic structure. For example, plasma sprayed coatings have a lamellar structure with weak cleavage planes parallel to the boundary [1]. Coatings processed by the electron beam physical vapor deposition technique, on the other hand, have a columnar structure with weak cleavage planes perpendicular to the free surface [2]. Both analytical and computational methods are developed in the literature to conduct fracture mechanics analysis of orthotropic FGMs. In the analytical studies, in order to incorporate the influence of directional dependence into the fracture mechanics analysis of FGMs, these materials are generally modeled as orthotropic, with principal directions parallel and perpendicular to the boundaries [3,4]. Among computational methods proposed, we can mention the displacement correlation technique (DCT) [5], the mixed-mode *J*-integral [6], and the interaction integral [7,8].

In the technical literature, the analytical solution techniques used to evaluate crack tip parameters for orthotropic FGMs are developed by considering either a single FGM layer [4,9] or an FGM coating-substrate structure [10,11]. However, in certain technological applications, such as thermal barrier coatings, a trilayer structure composed of an FGM coating, a bond coat, and a substrate is utilized. The bond coat is introduced between the FGM coating and the substrate in order to improve the bonding strength of the coating and to provide oxidation resistance. Therefore, the existence of the bond coat as an intermediate layer could significantly alter the fracture behavior of the overall structure. The objective of the present study is to develop analytical and computational methods to carry out mixed-mode fracture analysis of a trilayer structure by taking into account the orthotropic character of the functionally graded coating. The use of both analytical and computational techniques in the analyses allowed the verifications of both methods, leading to a highly accurate numerical predictive capability.

The analytical solution technique used in the present study is based on the method of singular integral equations and is outlined in Sec. 2. In the analytical solution, we consider an orthotropic FGM coating-bond coat-substrate structure. The orthotropic FGM coating is assumed to contain an embedded crack aligned parallel to the boundary and perpendicular to the direction of the material property gradation. The crack is loaded through arbitrary mixed-mode tractions that are applied to its surfaces. In Sec. 3, we describe the principal features of the computational approach, which is developed by using the finite element method in conjunction with the DCT. The numerical results generated by using the analytical and computational methods for a single embedded crack in an orthotropic FGM coating are presented in Sec. 4. These results illustrate the influences of the nonhomogeneity and orthotropy parameters and the bond coat thickness on the mixed-mode stress intensity factors (SIFs) and the energy release rate. Additional parametric analyses are also provided in Sec. 4 by considering

[1]Corresponding author.

Contributed by the Applied Mechanics Division of ASME for publication in the JOURNAL OF APPLIED MECHANICS. Manuscript received May 28, 2007; final manuscript received December 27, 2007; published online July 10, 2008. Review conducted by Marek-Jerzy Pindera.

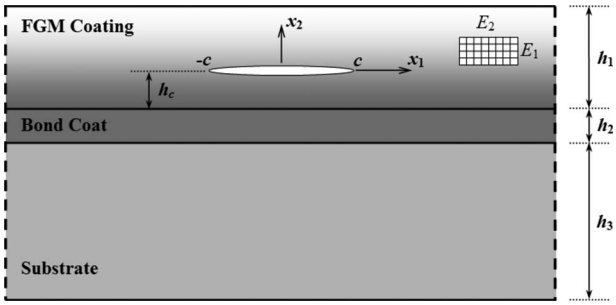

Fig. 1 The trilayer structure and an embedded crack in the orthotropic FGM coating

periodic cracks in an orthotropic FGM coating. The fracture parameters for the periodic cracks are evaluated by means of the developed computational method. A brief discussion and final remarks are provided in Sec. 5 to conclude the article.

2 Analytical Solution

The geometry of the trilayer structure considered in this section is shown in Fig. 1. The structure is composed of a graded orthotropic coating, a homogeneous orthotropic bond coat, and a homogeneous orthotropic substrate. In all three layers, x_1 and x_2 directions constitute the principal directions of orthotropy. The coating is graded in the x_2 direction and is assumed to possess a lamellar structure. Therefore, the planes that are parallel to the boundary in the coating are the weak cleavage planes. The FGM coating contains an embedded crack of length $2c$. The crack is assumed to be aligned parallel to the weak cleavage planes and therefore extends along the x_1 axis. The number of engineering parameters required to define constitutive relationships for orthotropic materials subjected to mechanical loads is equal to 4 for the case of plane stress and 7 for plane strain [12]. Krenk [13] previously showed that for both cases of plane stress and plane strain, the engineering parameters can be replaced by four parameters, which are named as the effective stiffness (S), the effective Poisson's ratio (ν), the stiffness ratio (δ), and the shear parameter (κ). The problem depicted in Fig. 1 is formulated by using the effective parameters that are introduced by Krenk [13]. For both cases of plane stress and (generalized) plane strain, linear elastic constitutive relations in terms of the effective parameters are given in the following form:

$$\begin{bmatrix} \varepsilon_{11} \\ \varepsilon_{22} \\ \varepsilon_{12} \end{bmatrix} = \frac{1}{S} \begin{bmatrix} \delta^{-2} & -\nu & 0 \\ -\nu & \delta^{2} & 0 \\ 0 & 0 & (\kappa+\nu) \end{bmatrix} \begin{bmatrix} \sigma_{11} \\ \sigma_{22} \\ \sigma_{12} \end{bmatrix} \tag{1}$$

For the case of plane stress, effective parameters are expressed in terms of the engineering parameters as follows:

$$S = \sqrt{E_{11}E_{22}}, \quad \nu = \sqrt{\nu_{12}\nu_{21}}, \quad \delta^4 = (E_{11}/E_{22}) = (\nu_{12}/\nu_{21}),$$
$$\kappa = S/(2G_{12}) - \nu \tag{2}$$

In the case of plane strain, the relations are given as

$$S = \sqrt{\frac{E_{11}E_{22}}{(1-\nu_{13}\nu_{31})(1-\nu_{23}\nu_{32})}} \tag{3}$$

$$\nu = \sqrt{\frac{(\nu_{12}+\nu_{13}\nu_{32})(\nu_{21}+\nu_{23}\nu_{31})}{(1-\nu_{13}\nu_{31})(1-\nu_{23}\nu_{32})}} \tag{4}$$

$$\delta^4 = \frac{1-\nu_{23}\nu_{32}}{1-\nu_{13}\nu_{31}}\frac{E_{11}}{E_{22}}, \quad \kappa = \frac{S}{2G_{12}} - \nu \tag{5}$$

Note that the terminology "effective parameters" used here is different from that often used to describe effective properties calculated using homogenization schemes [14]. There are certain limitations on the material parameters of orthotropic materials. These limitations require that $0<\nu<1$, $\kappa>-1$, and $(\kappa+\nu)>0$.

In order to make the defined problem analytically tractable, we make some simplifying assumptions regarding the material property distribution in the FGM coating. We assume that, in the FGM coating, the engineering parameters E_{11}, E_{22}, and G_{12} vary proportionally in the x_2 direction. Furthermore, the Poisson's ratios are assumed to be constants. These assumptions imply that in the graded layer ν, δ and κ are constants and S is variable. The variation in the effective stiffness is represented by using an exponential function. As a result, material properties in the orthotropic FGM coating are expressed as

$$S(x_1,x_2) = S_1 \exp(\beta x_2), \quad \kappa(x_1,x_2) = \kappa_1, \quad \delta(x_1,x_2) = \delta_1,$$
$$\nu(x_1,x_2) = \nu_1, \quad |x_1| < \infty, \quad -h_c < x_2 < (h_1 - h_c) \tag{6}$$

where S_1 is the value of the effective stiffness at $x_2=0$ and β is a nonhomogeneity constant. Note that if the variations in the engineering parameters are not taken as proportional, then the stiffness ratio δ, the shear parameter κ, and the effective Poisson's ratio ν will also be functions of the x_2 coordinate (see, for example, Eq. (2)). In that case, the governing partial differential equations will have variable coefficients and will not lend themselves to analytical treatment. The modeling approach of using proportional variations in engineering parameters is first proposed for the solutions of crack problems in orthotropic FGMs by Ozturk and Erdogan [15,16]. The material parameters of the homogeneous bond coat and the substrate are constant and are represented in the following way:

$$S = S_2, \quad \kappa = \kappa_2, \quad \delta = \delta_2, \quad \nu = \nu_2, \quad |x_1| < \infty,$$
$$-(h_c + h_2) < x_2 < -h_c \tag{7}$$

$$S = S_3, \quad \kappa = \kappa_3, \quad \delta = \delta_3, \quad \nu = \nu_3, \quad |x_1| < \infty$$
$$-(h_c + h_2 + h_3) < x_2 < -(h_c + h_2) \tag{8}$$

In order to derive the governing equations in a simpler form, we consider transformations for the coordinates and displacement and stress components in the trilayer structure. These transformations are given as follows:

$$x = x_1/\sqrt{\delta_1}, \quad y = x_2\sqrt{\delta_1} \tag{9}$$

$$u(x,y) = u_1(x_1,x_2)\sqrt{\delta_1}, \quad v(x,y) = u_2(x_1,x_2)/\sqrt{\delta_1} \tag{10}$$

$$\sigma_{xx}(x,y) = \sigma_{11}(x_1,x_2)/\delta_1, \quad \sigma_{yy}(x,y) = \sigma_{22}(x_1,x_2)\delta_1$$
$$\sigma_{xy}(x,y) = \sigma_{12}(x_1,x_2) \tag{11}$$

where (x,y), (u,v), and $(\sigma_{xx},\sigma_{yy},\sigma_{xy})$ are the coordinates, displacements, and stresses in the transformed domain, respectively. By using Eqs. (1) and (9)–(11) and the equations of equilibrium, the governing partial differential equations for the FGM coating, the bond coat and the substrate in the transformed coordinate system can be expressed as

$$\frac{\partial^2 u}{\partial y^2} + A_i\left(\frac{\delta_i}{\delta_1}\right)^2\frac{\partial^2 u}{\partial x^2} + B_i\frac{\partial^2 v}{\partial x \partial y} + \frac{\beta}{\sqrt{\delta_1}}\left(\frac{\partial u}{\partial y} + \frac{\partial v}{\partial x}\right) = 0 \tag{12}$$

$$\frac{\partial^2 v}{\partial x^2} + A_i\left(\frac{\delta_1}{\delta_i}\right)^2\frac{\partial^2 v}{\partial y^2} + B_i\frac{\partial^2 u}{\partial x \partial y} + \frac{A_i\beta}{\sqrt{\delta_1}}\left(\frac{\partial v}{\partial y} + \nu_1\frac{\partial u}{\partial x}\right) = 0 \tag{13}$$

$$A_i = \frac{2(\kappa_i+\nu_i)}{1-\nu_i^2}, \quad B_i = 1 + \nu_i A_i \tag{14}$$

where $i=1,2$, and 3 for the FGM coating, the bond coat, and the substrate, respectively. Note that in Eqs. (12) and (13), β should

be taken as zero for the homogeneous bond coat and the substrate.

In addition to the aforementioned governing partial differential equations, the solution of the crack problem has to satisfy the related boundary and continuity conditions. The free surface conditions at $x_2=h_1-h_c$ and $x_2=-(h_c+h_2+h_3)$ require that

$$\sigma_{22}(x_1,h_1-h_c)=\sigma_{12}(x_1,h_1-h_c)=0, \quad |x_1|<\infty \tag{15}$$

$$\sigma_{22}(x_1,-(h_c+h_2+h_3))=\sigma_{12}(x_1,-(h_c+h_2+h_3))=0, \quad |x_1|<\infty \tag{16}$$

By considering the continuity of the stresses and displacements at the orthotropic FGM coating–bond coat and bond coat–substrate interfaces, one can write

$$\sigma_{22}(x_1,-h_c^+)=\sigma_{22}(x_1,-h_c^-), \quad \sigma_{12}(x_1,-h_c^+)=\sigma_{12}(x_1,-h_c^-) \quad |x_1|<\infty \tag{17}$$

$$u_1(x_1,-h_c^+)=u_1(x_1,-h_c^-), \quad u_2(x_1,-h_c^+)=u_2(x_1,-h_c^-), \quad |x_1|<\infty \tag{18}$$

$$\sigma_{22}(x_1,-(h_c+h_2)^+)=\sigma_{22}(x_1,-(h_c+h_2)^-)$$
$$\sigma_{12}(x_1,-(h_c+h_2)^+)=\sigma_{12}(x_1,-(h_c+h_2)^-), \quad |x_1|<\infty \tag{19}$$

$$u_1(x_1,-(h_c+h_2)^+)=u_1(x_1,-(h_c+h_2)^-)$$
$$u_2(x_1,-(h_c+h_2)^+)=u_2(x_1,-(h_c+h_2)^-), \quad |x_1|<\infty \tag{20}$$

The displacement components are not continuous on the crack plane for $|x_1|<c$. However, stress continuity is valid on the crack plane if the crack surfaces are subjected to self-equilibrating tractions. Therefore, on the crack plane, we have the conditions of stress continuity, which can be expressed as

$$\sigma_{22}(x_1,0^+)=\sigma_{22}(x_1,0^-), \quad \sigma_{12}(x_1,0^+)=\sigma_{12}(x_1,0^-), \quad |x_1|<\infty \tag{21}$$

By considering the arbitrary mixed-mode tractions that are applied to crack surfaces, one can derive two more boundary conditions in the following form:

$$\sigma_{22}(x_1,0)=-p(x_1), \quad \sigma_{12}(x_1,0)=-q(x_1), \quad |x_1|<c \tag{22}$$

where $p(x_1)$ and $q(x_1)$ are arbitrary normal and shear tractions, respectively, applied to the crack faces. In the formulation of the problem, the derivatives of the relative displacements of the crack surfaces are used as the primary unknown functions. These functions are defined as follows:

$$f_1(x_1)=\frac{\partial}{\partial x_1}(u_2(x_1,0^+)-u_2(x_1,0^-))$$
$$f_2(x_1)=\frac{\partial}{\partial x_1}(u_1(x_1,0^+)-u_1(x_1,0^-)), \quad |x_1|<c \tag{23}$$

Note that the relative displacements are equal to zero for $|x_1|\geqslant c$.

In order to solve the embedded crack problem, first, the general solutions for the displacement components u and v and the stress components σ_{xx}, σ_{yy}, and σ_{xy} are derived for each of the layers in the trilayer structure. Displacement components are determined by taking Fourier transformations of Eqs. (12) and (13) in the x direction, and the stress components are determined through the constitutive relation given by Eq. (1). The boundary and continuity conditions given by Eqs. (15)–(21) are then satisfied by the use of these general solutions. Finally, Eq. (22) is used to reduce the problem to a system of two coupled singular integral equations. The details of this rather lengthy procedure are not provided here for brevity and can be found in the thesis of Ilhan [17]. The singular integral equations in the transformed coordinate system are expressed in the following form:

$$\int_{-c/\sqrt{\delta_1}}^{c/\sqrt{\delta_1}}\left\{\left(\frac{\lambda_1}{\pi(x-t)}+H_{11}(x,t)\right)\phi_1(t)+H_{12}(x,t)\phi_2(t)\right\}dt=-\frac{(1-\nu_1^2)\delta_1}{S_1}p(\sqrt{\delta_1}x), \quad |x|<\frac{c}{\sqrt{\delta_1}} \tag{24}$$

$$\int_{-c/\sqrt{\delta_1}}^{c/\sqrt{\delta_1}}\left\{H_{21}(x,t)\phi_1(t)+\left(\frac{\lambda_2}{\pi(x-t)}+H_{22}(x,t)\right)\phi_2(t)\right\}dt=-\frac{2(\kappa_1+\nu_1)}{S_1}q(\sqrt{\delta_1}x), \quad |x|<\frac{c}{\sqrt{\delta_1}} \tag{25}$$

where $\phi_1(x)=f_1(\sqrt{\delta_1}x)$, $\phi_2(x)=\sqrt{\delta_1}f_2(\sqrt{\delta_1}x)$, and $H_{ij}(x,t)$ $(i,j=1,2)$ are the known Fredholm kernels. λ_1 and λ_2 are known constants that depend on β, κ_1, δ_1, and ν_1. We observe that in both of the singular integral equations, the dominant singularity is the Cauchy type singularity. Hence, the unknown functions $\phi_1(t)$ and $\phi_2(t)$ possess square-root singularities near the end points $t=\pm c/\sqrt{\delta_1}$. The singular integral equations are solved numerically by applying an expansion-collocation technique. In the numerical solution, the integrals and intervals of definition are normalized by making use of the following transformations:

$$x=\frac{c}{\sqrt{\delta_1}}s, \quad |x|<\frac{c}{\sqrt{\delta_1}}, \quad |s|<1 \tag{26}$$

$$t=\frac{c}{\sqrt{\delta_1}}r, \quad |t|<\frac{c}{\sqrt{\delta_1}}, \quad |r|<1 \tag{27}$$

The solution can then be expressed in the following form:

$$\phi_1\left(\frac{c}{\sqrt{\delta_1}}r\right)=\frac{1}{\sqrt{1-r^2}}\sum_{n=1}^{N}A_nT_n(r),$$
$$\phi_2\left(\frac{c}{\sqrt{\delta_1}}r\right)=\frac{1}{\sqrt{1-r^2}}\sum_{n=1}^{N}B_nT_n(r) \tag{28}$$

where $T_n(r)$ is the Chebyshev polynomial of the first kind of order n and A_n and B_n $(n=1,\ldots,N)$ are unknown constants of the series expansions. The series forms given by Eq. (28) are substituted into Eqs. (24) and (25), and the resulting integral equation system is regularized by means of the method outlined by Erdogan [18]. The integral equations are then converted to a linear algebraic equation system of size $2N\times 2N$ by using collocation points. The linear equation system is solved numerically to compute the expansion constants A_n and B_n $(n=1,\ldots,N)$.

Fracture mechanics parameters, such as the mixed-mode SIFs and the energy release rate, are determined by using the computed expansion constants. Mixed-mode SIFs are defined by

$$k_1(\pm c)=\lim_{x_1\to\pm c^{\pm}}\sqrt{\pm 2(x_1\mp c)}(\sigma_{22}(x_1,0)) \tag{29}$$

$$k_2(\pm c)=\lim_{x_1\to\pm c^{\pm}}\sqrt{\pm 2(x_1\mp c)}(\sigma_{12}(x_1,0)) \tag{30}$$

By using the dominant parts of the stress components $\sigma_{22}(x_1,0)$ and $\sigma_{12}(x_1,0)$ near the crack tips and Eq. (28), mixed-mode SIFs are found as

$$k_1(\pm c)=\pm\frac{S_1\lambda_1\sqrt{c}}{\delta_1(1-\nu_1^2)}\sum_{n=1}^{N}A_nT_n(\pm 1) \tag{31}$$

$$k_2(\pm c) = \pm \frac{S_1\lambda_2\sqrt{c}}{2(\kappa_1+\nu_1)}\sum_{n=1}^{N} B_n T_n(\pm 1) \tag{32}$$

The crack closure energy method is employed to derive the expressions of the energy release rates at the crack tips. In an FGM coating that has a lamellar structure, the planes that are parallel to the boundary constitute the weak cleavage planes. Crack growth in this type of coatings is expected to be in the direction of the principal axis that is parallel to the weak cleavage planes. As a result, confining our analysis to the lamellar type of FGM coatings, we can assume that the embedded crack shown in Fig. 1 will propagate along the x_1 axis. Therefore, the expression for the energy release rate can be derived by considering the work done by the normal and shear stresses as the crack is closed along an infinitesimal distance in the x_1 direction [15]. Adopting this method, the expression for the energy release rate is found to be as follows:

$$G(\pm c) = -\frac{\pi}{S_1}\left(\frac{\delta_1(1-\nu_1^2)}{4\lambda_1}k_1^2(\pm c) + \frac{(\kappa_1+\nu_1)}{2\lambda_2\delta_1}k_2^2(\pm c)\right) \tag{33}$$

3 Computational Approach

In addition to the analytical solution described in Sec. 2, a finite element based approach developed by applying the DCT is used to evaluate the fracture parameters for orthotropic FGM coatings. The main advantage of this dual approach methodology is that it permits direct comparisons between analytical and computational results, leading to the development of a reliable numerical predictive capability. The developed finite element based procedure is integrated into the general purpose finite element analysis code ANSYS [19]. In the finite element models, quarter-point singular elements are utilized in order to take into account the square-root singular behavior of the strain components in the vicinity of a crack tip. The regions away from the crack tip are discretized by making use of regular six-noded triangular and eight-noded quadrilateral elements. In the finite element analyses of crack problems in FGMs, two different approaches are commonly used to take the continuous spatial variations of the material properties into account. In one of these approaches, the material parameters are specified at the centroid of each finite element. As a result, over a given finite element, the material property distribution is uniform in this method. The elements for which the material properties are constant are referred to as homogeneous elements. It is previously shown that with an appropriate degree of mesh refinement, the method of specifying the material properties at the centroid of a finite element leads to highly accurate numerical results [20]. In the second approach, the spatial distributions are incorporated into the finite element models by computing the properties at each integration point of a finite element during the formation of the element matrices. In the technical literature, these elements are generally referred to as graded finite elements [21–23]. In the present study, we employed the first method in which the properties are assigned at the centroids of the finite elements. As demonstrated in Sec. 4, a very good correlation is obtained between analytical and computational results, which is indicative of the effectiveness of the homogeneous finite element approach.

In the implementation of the DCT, the crack tip region is modeled by a ring of quarter-point elements. A quarter-point element is generated by using an eight-noded isoparametric element. Three nodes of the isoparametric element on one of its sides are merged at the crack tip. The midpoint nodes on the sides emanating from the crack tip are relocated to quarter points. The wedge-shaped elements generated by this method are known to possess a square-root singular strain field and a bounded stiffness matrix [24]. A quarter-point element in global and local coordinate systems and the distribution of the quarter-point elements around a crack tip are depicted in Fig. 2. Referring to Fig. 2(*a*), the displacement field of a quarter-point element can be expressed as follows:

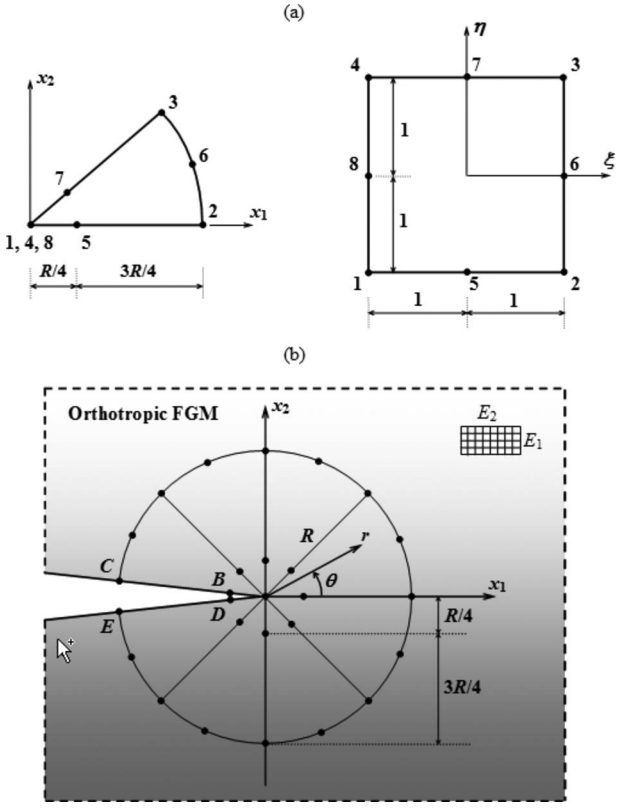

Fig. 2 (*a*) A quarter-point element in global and local coordinate systems; (*b*) quarter-point elements around a crack tip located in a graded orthotropic medium

$$u_1(\xi,\eta) = \sum_{i=1}^{8} N_i(\xi,\eta)u_{1i}, \quad u_2(\xi,\eta) = \sum_{i=1}^{8} N_i(\xi,\eta)u_{2i} \tag{34}$$

where $N_i(\xi,\eta)$ $(i=1,\ldots,8)$ are the shape functions and u_{1i}, u_{2i} $(i=1,\ldots,8)$ are the nodal displacements. The shape functions are given in the following form [24]:

$$N_i(\xi,\eta) = [(1+\xi\xi_i)(1+\eta\eta_i) - (1-\xi^2)(1+\eta\eta_i) - (1-\eta^2)(1+\xi\xi_i)]\frac{\xi_i^2\eta_i^2}{4} + (1-\xi^2)(1+\eta\eta_i)(1-\xi_i^2)\frac{\eta_i^2}{2} + (1-\eta^2)(1+\xi\xi_i)(1-\eta_i^2)\frac{\xi_i^2}{2}, \quad (i=1,\ldots,8) \tag{35}$$

The expressions for the mixed-mode SIFs can be derived directly by correlating the displacements of the crack surface nodes with the asymptotic analytical solutions. The crack surface nodes that are used in the evaluation of the mixed-mode SIFs (nodes *B*, *C*, *D*, and *E*) are shown in Fig. 2(*b*). Nodes *B* and *C* are located on the upper crack surface and nodes *D* and *E* are located on the lower one. Note that the asymptotic expressions for the displacement components derived for a homogeneous orthotropic medium can also be used for a graded orthotropic medium, provided that the required material parameters are calculated at the crack tip [10]. Considering the local polar coordinate system at the crack tip shown in Fig. 2(*b*), the asymptotic displacement expressions for a graded orthotropic medium can be written as [5]

$$u_1(r,\theta)=\sqrt{2r}\,\mathrm{Re}\left\{\frac{\mu_1^{\mathrm{tip}}p_2^{\mathrm{tip}}\sqrt{\cos\theta+\mu_2^{\mathrm{tip}}\sin\theta}-\mu_2^{\mathrm{tip}}p_1^{\mathrm{tip}}\sqrt{\cos\theta+\mu_1^{\mathrm{tip}}\sin\theta}}{\mu_1^{\mathrm{tip}}-\mu_2^{\mathrm{tip}}}\right\}k_1+\sqrt{2r}\,\mathrm{Re}\left\{\frac{p_2^{\mathrm{tip}}\sqrt{\cos\theta+\mu_2^{\mathrm{tip}}\sin\theta}-p_1^{\mathrm{tip}}\sqrt{\cos\theta+\mu_1^{\mathrm{tip}}\sin\theta}}{\mu_1^{\mathrm{tip}}-\mu_2^{\mathrm{tip}}}\right\}k_2 \tag{36}$$

$$u_2(r,\theta)=\sqrt{2r}\,\mathrm{Re}\left\{\frac{\mu_1^{\mathrm{tip}}q_2^{\mathrm{tip}}\sqrt{\cos\theta+\mu_2^{\mathrm{tip}}\sin\theta}-\mu_2^{\mathrm{tip}}q_1^{\mathrm{tip}}\sqrt{\cos\theta+\mu_1^{\mathrm{tip}}\sin\theta}}{\mu_1^{\mathrm{tip}}-\mu_2^{\mathrm{tip}}}\right\}k_1+\sqrt{2r}\,\mathrm{Re}\left\{\frac{q_2^{\mathrm{tip}}\sqrt{\cos\theta+\mu_2^{\mathrm{tip}}\sin\theta}-q_1^{\mathrm{tip}}\sqrt{\cos\theta+\mu_1^{\mathrm{tip}}\sin\theta}}{\mu_1^{\mathrm{tip}}-\mu_2^{\mathrm{tip}}}\right\}k_2 \tag{37}$$

where μ_j, p_j, and q_j $(j=1,2)$ are complex constants that depend on the coefficients of the compliance matrix of an orthotropic medium, and the superscript (tip) implies that the corresponding material parameter has to be calculated at the crack tip. By using Eqs. (36) and (37) and the properties of the quarter-point elements, mixed-mode SIFs can be obtained in the following form [5]:

$$k_1=\frac{1}{4}\sqrt{\frac{2}{R}}\frac{\{4(u_1^B-u_1^D)-(u_1^C-u_1^E)\}F_4-\{4(u_2^B-u_2^D)-(u_2^C-u_2^E)\}F_2}{F_1F_4-F_2F_3} \tag{38}$$

$$k_2=\frac{1}{4}\sqrt{\frac{2}{R}}\frac{\{4(u_2^B-u_2^D)-(u_2^C-u_2^E)\}F_1-\{4(u_1^B-u_1^D)-(u_1^C-u_1^E)\}F_3}{F_1F_4-F_2F_3} \tag{39}$$

where the superscripts B, C, D, and E refer to the crack surface nodes shown in Fig. 2(*b*), R is the radius of the quarter-point elements, and the constants F_j $(j=1,\ldots,4)$ are given by

$$F_1=\mathrm{Re}\left\{\frac{i(\mu_1^{\mathrm{tip}}p_2^{\mathrm{tip}}-\mu_2^{\mathrm{tip}}p_1^{\mathrm{tip}})}{\mu_1^{\mathrm{tip}}-\mu_2^{\mathrm{tip}}}\right\},\quad F_2=\mathrm{Re}\left\{\frac{i(p_2^{\mathrm{tip}}-p_1^{\mathrm{tip}})}{\mu_1^{\mathrm{tip}}-\mu_2^{\mathrm{tip}}}\right\} \tag{40}$$

$$F_3=\mathrm{Re}\left\{\frac{i(\mu_1^{\mathrm{tip}}q_2^{\mathrm{tip}}-\mu_2^{\mathrm{tip}}q_1^{\mathrm{tip}})}{\mu_1^{\mathrm{tip}}-\mu_2^{\mathrm{tip}}}\right\},\quad F_4=\mathrm{Re}\left\{\frac{i(q_2^{\mathrm{tip}}-q_1^{\mathrm{tip}})}{\mu_1^{\mathrm{tip}}-\mu_2^{\mathrm{tip}}}\right\} \tag{41}$$

Once the finite element solution for the displacement field is obtained for a given loading condition, Eqs. (38) and (39) can be used to evaluate the mixed-mode SIFs. The SIFs can then be substituted into Eq. (33) in order to compute the energy release rate.

4 Numerical Results

This section presents the numerical results evaluated by considering two separate problems. In Sec. 4.1, the numerical results generated for a single embedded crack in an orthotropic FGM coating are provided. Both analytical and computational approaches are used to evaluate the fracture parameters of the single embedded crack. Then, in Sec. 4.2, we examine the behavior of periodic cracks in an orthotropic FGM coating by using the developed computational method.

4.1 Embedded Crack in an Orthotropic FGM Coating. The results presented in this subsection are generated by considering the embedded crack problem described in Sec. 2. As depicted in Fig. 1, the embedded crack is located in an orthotropic FGM coating, which is perfectly bonded to an intermediate bond coat layer. The bond coat is assumed to be perfectly bonded to a substrate. The effective material parameters of the layers are given by Eqs. (6)–(8). The fracture parameters are evaluated by assuming that the crack surfaces are subjected to a uniform normal stress σ_0. By referring to Eq. (22), the normal and shear stresses applied to the crack surfaces can then be expressed as

$$p(x_1)=\sigma_0,\quad q(x_1)=0,\quad |x_1|<c \tag{42}$$

Note that due to the symmetry of the geometry and applied loading with respect to the x_2 axis, it suffices to provide the fracture

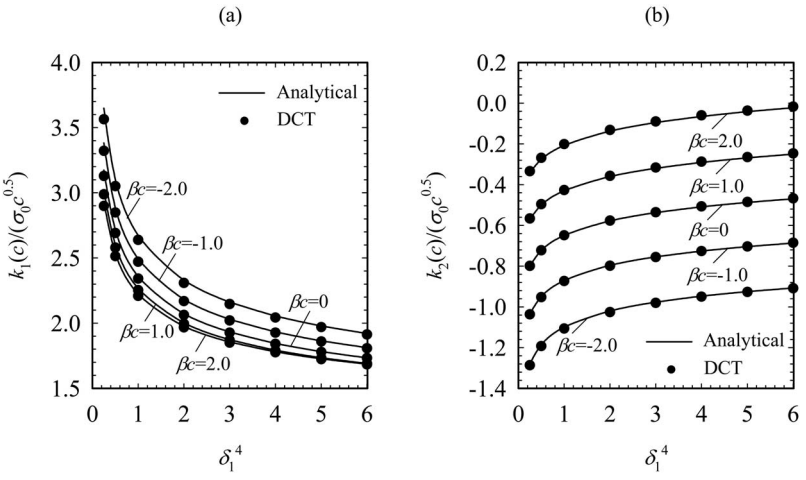

Fig. 3 Normalized mixed-mode SIFs versus δ_1^4 and βc for the crack problem depicted in Fig. 1: (*a*) Mode I SIFs; (*b*) Mode II SIFs. $S_2/S_1=\exp(-\beta h_c)$, $S_3/S_2=1.5$, $\kappa_1=\kappa_2=2$, $\kappa_3=1$, $\delta_1=\delta_2$, $\delta_3=1$, $\nu_1=\nu_2=0.25$, $\nu_3=0.3$, $h_1/c=1$, $h_c/c=0.5$, $h_2/c=0.5$, and $h_3/c=2$.

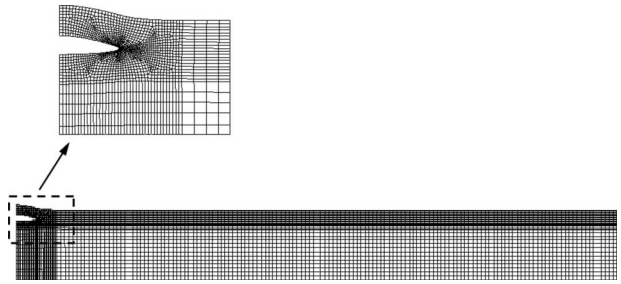

Fig. 4 Deformed shape of the finite element mesh and close-up view of the crack surfaces. $S_2/S_1=\exp(-\beta h_c)$, $\beta c=1$, $S_3/S_2=1.5$, $\kappa_1=\kappa_2=2$, $\kappa_3=1$, $\delta_1^4=\delta_2^4=2$, $\delta_3=1$, $\nu_1=\nu_2=0.25$, $\nu_3=0.3$, $h_1/c=1$, $h_c/c=0.5$, $h_2/c=0.5$, and $h_3/c=2$.

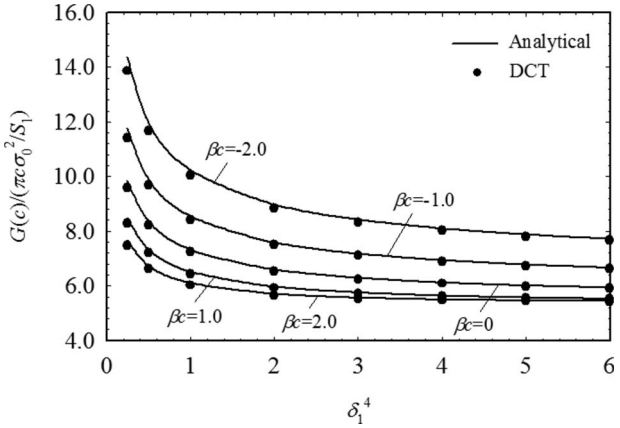

Fig. 5 Normalized energy release rate versus δ_1^4 and βc for the crack problem depicted in Fig. 1. $S_2/S_1=\exp(-\beta h_c)$, $S_3/S_2=1.5$, $\kappa_1=\kappa_2=2$, $\kappa_3=1$, $\delta_1=\delta_2$, $\delta_3=1$, $\nu_1=\nu_2=0.25$, $\nu_3=0.3$, $h_1/c=1$, $h_c/c=0.5$, $h_2/c=0.5$, and $h_3/c=2$.

parameters computed at the crack tip $x_1=c$. Under the action of the uniform normal stress σ_0, the mixed-mode SIFs and the energy release rate evaluated at the crack tips $x_1=\pm c$ are related as follows:

$$k_1(c)=k_1(-c), \quad k_2(c)=-k_2(-c), \quad G(c)=G(-c) \qquad (43)$$

As a result of the symmetry, only the region $x_1\geq 0$ is considered in the finite element analysis by setting the displacement component u_1 as zero at $x_1=0$.

Figure 3 illustrates the influences of the nondimensional nonhomogeneity parameter βc and the stiffness ratio of the coating δ_1 on the normalized mixed-mode SIFs, which are evaluated by considering an embedded crack. Note that the nonhomogeneity parameter β is defined in Sec. 2 by Eq. (6). In the present section, the numerical results are provided by using the nondimensional nonhomogeneity parameter βc, which is the product of β with the half crack length c. We use βc instead of β in this section in order to be able to present the numerical results in terms of nondimensional parameters. This approach is the accepted practice in the technical literature on crack problems in FGMs that possess exponential variations in their material properties (see, for example, Refs. [11,25]). In Fig. 3, the results generated by the analytical method are seen to agree quite well to those computed by the DCT. The normalized Mode I SIF decreases and the normalized Mode II SIF increases as the nonhomogeneity parameter βc is increased from −2 to 2. Similarly, the Mode I SIF is found to be a decreasing function of the stiffness ratio δ_1, whereas the Mode II SIF is an increasing function of δ_1. The deformed shape of the finite element mesh used in the computations and a close-up view of the crack surfaces are shown in Fig. 4. The normalized energy release rate values calculated by using the mixed-mode SIFs shown in Fig. 3 are given in Fig. 5. The trends observed for the energy release rate are similar to those observed for the Mode I SIF. An increase in βc or δ_1 leads to a corresponding decrease in the normalized energy release rate. In general, it is seen that the material properties, such as the nonhomogeneity parameter and the stiffness ratio, could have significant influences on the mixed-mode crack tip parameters.

The analytical solution developed in the present study is based on the effective parameters defined by Krenk [13]. The constitutive relation proposed by Krenk is given by Eq. (1). This equation is valid for both plane stress and plane strain. For both of these cases, the parameters defined by Krenk can be expressed in terms of the engineering parameters. Given the engineering constants, it is possible to evaluate Krenk's parameters using either Eq. (2) (plane stress) or Eqs. (3)–(5) (plane strain). Hence, the engineering parameters corresponding to a given set of effective parameters are different for plane stress and plane strain. Since our numerical results are presented in terms of the effective parameters, they can be considered to be valid for both of the cases of plane stress and plane strain. However, a given numerical result corresponds to a different set of engineering constants for plane

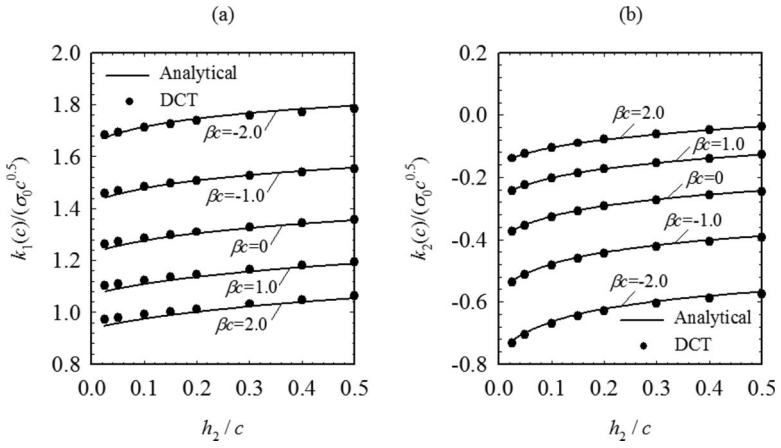

Fig. 6 Normalized mixed-mode SIFs versus h_2/c and βc for the crack problem depicted in Fig. 1: (*a*) Mode I SIFs; (*b*) Mode II SIFs. $S_2/S_1=\exp(-\beta h_c)$, $S_3/S_2=3$, $\kappa_1=\kappa_2=2$, $\kappa_3=1$, $\delta_1^4=\delta_2^4=2$, $\delta_3=1$, $\nu_1=\nu_2=0.25$, $\nu_3=0.3$, $h_1/c=1$, $h_c/c=0.05$, and $h_3/c=2$.

stress and plane strain. Also, note that the Poisson ratios related to loading and deformation in the out of plane direction, i.e. ν_{13}, ν_{23}, ν_{31}, and ν_{32}, are required to evaluate Krenk's parameters only for the case of plane strain. These parameters have no effect on the solution of the problem in the case of plane stress.

In a previous experimental study [26], it is shown that in an FGM coating–bond coat–substrate structure, embedded cracks often initiate in the close vicinity of the FGM coating–bond coat interface. Some numerical results are generated, in the present study, in order to examine the influence of the bond coat thickness on the fracture parameters of an embedded crack that is aligned close to the orthotropic FGM coating–bond coat interface. These results are provided in Figs. 6 and 7. The relative position of the embedded crack with respect to the interface is set by taking h_1/c and h_c/c as 1 and 0.05, respectively. Figure 6 shows the influence of the relative bond coat thickness h_2/c on the normalized Modes I and II SIFs. It can be seen that for all the βc values considered, both normalized Modes I and II SIFs increase slightly as h_2/c is increased from 0 to 0.5. The dependence of the normalized energy release rate on the relative bond coat thickness is illustrated in Fig. 7. The normalized energy release rate is also found to be an increasing function of h_2/c. The analytical and computational results presented in this subsection are seen to be in very good agreement. Hence, it can be inferred that the developed analytical and computational methods are reliable tools for mixed-mode fracture analysis of orthotropic FGM coatings.

The analytical solution developed in Sec. 2 is general in the sense that it allows the evaluation of fracture parameters for cracks that are subjected to both normal and shear stresses (see, for example, Eqs. (24) and (25)). However, in this section, the representative numerical results are provided by considering only a normal stress σ_0 that is applied to crack surfaces. The main reason for not considering shear loading is that under pure shear, there is always crack closure at one of the crack tips. This can be deduced by considering the fact that in the case of pure shear the problem will be antisymmetric with respect to the x_2 axis and $k_1(c)$ has to be equal to $-k_1(-c)$. In the present study, the solution of the singular integral equations is based on the assumption that the crack surfaces have no contact. If there is contact, a different approach is required in order to evaluate the size of the closed portion of the crack and the SIFs.

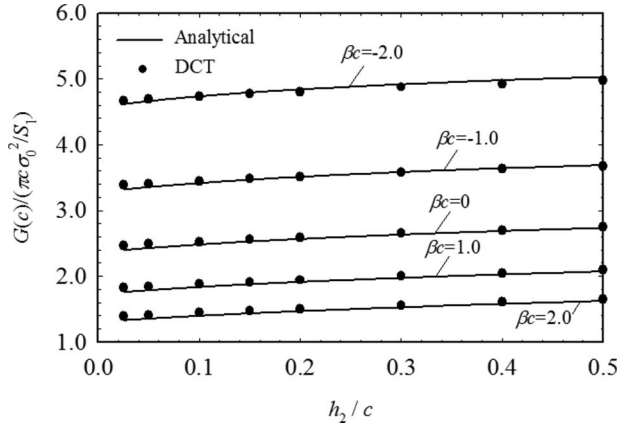

Fig. 7 Normalized energy release rate versus h_2/c and βc for the crack problem depicted in Fig. 1. $S_2/S_1=\exp(-\beta h_c)$, $S_3/S_2=3$, $\kappa_1=\kappa_2=2$, $\kappa_3=1$, $\delta_1^4=\delta_2^4=2$, $\delta_3=1$, $\nu_1=\nu_2=0.25$, $\nu_3=0.3$, $h_1/c=1$, $h_c/c=0.05$, and $h_3/c=2$.

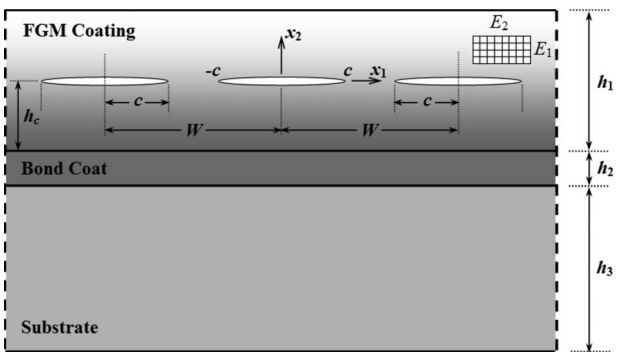

Fig. 8 Periodic cracks in an orthotropic FGM coating

4.2 Periodic Cracks in an Orthotropic FGM Coating. In this subsection, we examine the behavior of periodic cracks located in an orthotropic FGM coating by means of the developed computational technique. The geometry of the considered problem is depicted in Fig. 8. The orthotropic FGM coating contains periodic cracks of spacing W and is perfectly bonded to a homogeneous orthotropic bond coat. The bond coat is laid over and perfectly bonded to a homogeneous orthotropic substrate. The material property distributions in the trilayer structure are given by Eqs. (6)–(8). The surfaces of all the cracks are assumed to be subjected to a uniform normal stress σ_0. Due to the periodicity of the cracks, it is sufficient to consider a unit cell in the structure in finite element modeling. Figure 9 shows the unit cell and the boundary conditions used at planes $x_1=0$ and $x_1=W/2$. The trilayer structure is assumed to be infinitely long in the x_1 direction. As a result, each of the planes $x_1=\pm(n/2)W$ $(n=1,2,3,\ldots)$ could be considered to be a plane of reflective symmetry. Therefore, the shear stress is zero on all of these planes, which implies that these planes should remain as planes after deformation. This requirement can only be achieved in a finite element model by tying the horizontal displacements of the plane at $x_1=W/2$ with the horizontal displacements of a rigid block, as depicted in Fig. 9. In the developed finite element model, the unit cell is in contact with the rigid block at $x_1=W/2$. The horizontal displacements of the nodes of the unit cell are coupled with those of the rigid block at the contact interface. There are no constraints on the vertical displacements of the unit cell. Therefore, as the trilayer structure is subjected to mechanical loading, the unit cell

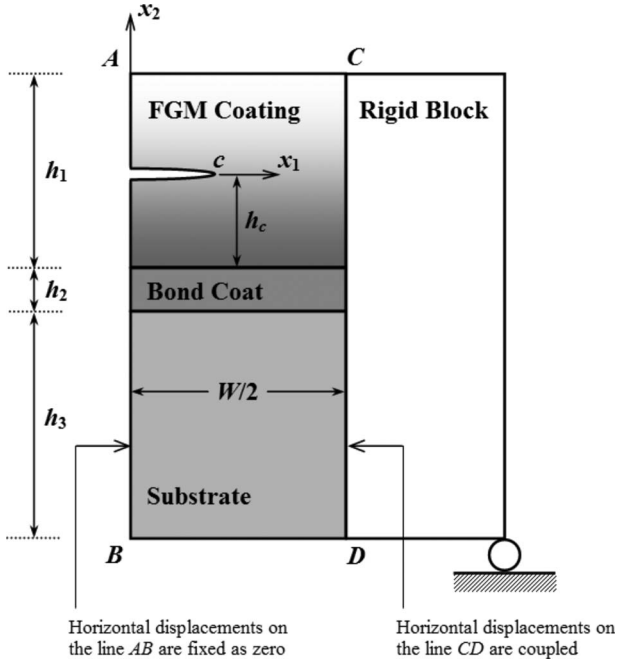

Fig. 9 Unit cell in the trilayer structure and the symmetry and periodicity conditions

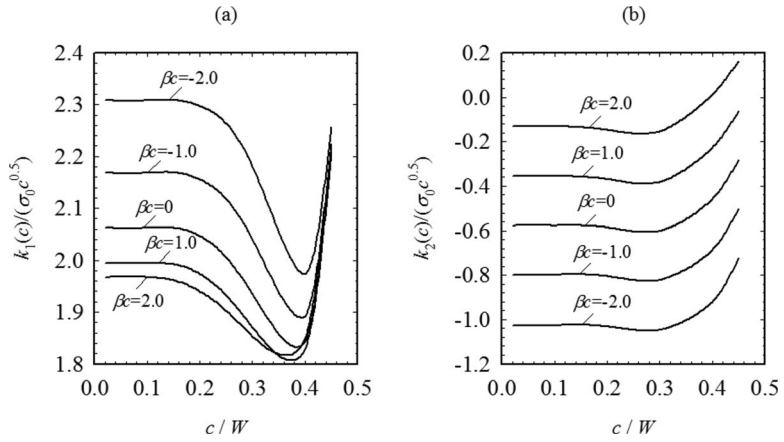

Fig. 10 Normalized mixed-mode SIFs versus c/W and βc for the crack problem depicted in Fig. 8: (*a*) Mode I SIFs; (*b*) Mode II SIFs. $S_2/S_1=\exp(-\beta h_c)$, $S_3/S_2=1.5$, $\kappa_1=\kappa_2=2$, $\kappa_3=1$, $\delta_1^4=\delta_2^4=2$, $\delta_3=1$, $\nu_1=\nu_2=0.25$, $\nu_3=0.3$, $h_1/c=1$, $h_c/c=0.5$, $h_2/c=0.5$, and $h_3/c=2$.

is free to undergo both rigid body translation and rotation at $x_1=W/2$. As a result of the symmetry about the x_2 axis, the displacement component u_1 is fixed as zero at $x_1=0$.

The computational results illustrating the influences of the nonhomogeneity parameter βc and the crack spacing parameter c/W on the normalized Modes I and II SIFs are shown in Fig. 10. The deformed shape of the finite element mesh used in the generation of the results given in Fig. 10 is depicted in Fig. 11. Note that for the periodic cracks, c/W is limited between 0 and 1/2. Examining the results shown in Fig. 10, we observe that for small values of c/W, the influence of the periodicity on the stress intensity values is not so significant. However, as c/W is increased, both Modes I and II SIFs first decrease and then go through minimum values. After going through the minima, SIFs increase significantly and become unbounded as the crack tips get closer to each other ($c/W \rightarrow 1/2$). Previously, Erdogan [27] showed analytically that the Mode I SIFs for two collinear cracks in a homogeneous isotropic medium approach infinity as the distance between the crack tips approaches zero. Hence, the trends depicted in Fig. 10 are in agreement with the findings of Erdogan [27]. It is also observed that the degree of nonhomogeneity in the orthotropic FGM coating, which is governed by the parameter βc, has a significant influence on the mixed-mode SIFs of the periodic cracks. Figure 12 shows the normalized energy release rates computed by using the Modes I and II SIFs given in Fig. 10. Similar to the trends observed for the mixed-mode SIFs, the energy release rate goes through a minimum before becoming unbounded as c/W approaches 1/2.

From Fig. 10, it is also observed that the normalized Mode II SIF is a monotonically decreasing function of βc regardless of the value of the crack spacing parameter c/W. However, for the normalized Mode I SIF (Fig. 10) and the normalized energy release rate (Fig. 12), different trends are observed depending on the value of c/W. For c/W approximately less than 0.34, the normalized Mode I SIF is seen to be a monotonically decreasing function of βc. The normalized energy release rate is a monotonically

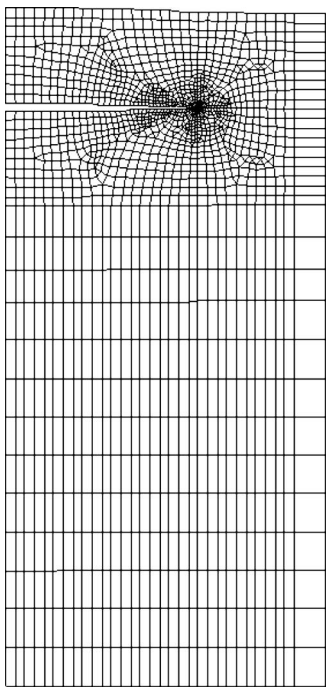

Fig. 11 Deformed shape of the unit cell. $S_2/S_1=\exp(-\beta h_c)$, $\beta c=1$, $S_3/S_2=1.5$, $\kappa_1=\kappa_2=2$, $\kappa_3=1$, $\delta_1^4=\delta_2^4=2$, $\delta_3=1$, $\nu_1=\nu_2=0.25$, $\nu_3=0.3$, $h_1/c=1$, $h_c/c=0.5$, $h_2/c=0.5$, $h_3/c=2$, and $c/W=0.3$.

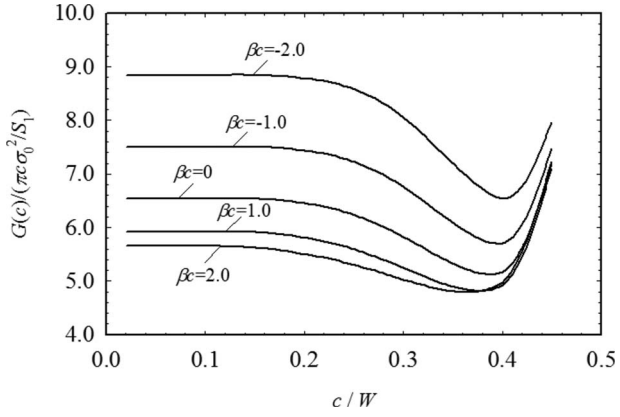

Fig. 12 Normalized energy release rate versus c/W and βc for the crack problem depicted in Fig. 8: (*a*) Mode I SIFs; (*b*) Mode II SIFs. $S_2/S_1=\exp(-\beta h_c)$, $S_3/S_2=1.5$, $\kappa_1=\kappa_2=2$, $\kappa_3=1$, $\delta_1^4=\delta_2^4=2$, $\delta_3=1$, $\nu_1=\nu_2=0.25$, $\nu_3=0.3$, $h_1/c=1$, $h_c/c=0.5$, $h_2/c=0.5$, and $h_3/c=2$.

decreasing function of βc for c/W approximately less than 0.38. For larger values of c/W, the normalized Mode I SIF and energy release rate calculated for $\beta c=2.0$ are seen to be greater than their corresponding values calculated for $\beta c=1.0$. This implies that as the crack tips get closer to each other, the interaction of the stress fields around the cracks leads to increases in the values of the normalized Mode I SIF and energy release rate. Therefore, for closely located cracks, an increase in either βc (for βc approximately greater than 1.0) or c/W will result in corresponding increases in both normalized Mode I SIF and energy release rate.

Our computational results, which are not presented in this article for brevity, do actually indicate that identical numerical results can also be obtained by using a simpler finite element model in which the horizontal displacements of the nodes at $x_1=W/2$ are tied among themselves. This simpler modeling method implies only translation in the x_1 direction. Hence, the bending of the plane $x_1=W/2$ is not significant under mechanical crack surface loads. The implementation of the boundary condition at $x_1=W/2$ in this article is more general and can also be used to examine periodic crack problems under thermal loads, which are known to lead to the bending of the layers.

5 Concluding Remarks

The work reported in this article is directed toward developing analytical and computational methods for a mixed-mode fracture analysis of orthotropic FGM coatings. In both analytical and computational studies, material behavior is modeled by using the effective parameters of plane orthotropic elasticity. In the analytical approach, a single embedded crack in the orthotropic FGM coating is considered. The general solutions of the governing partial differential equations are obtained by the application of the Fourier transformation method. The problem is then reduced to a system of two coupled singular integral equations, which is solved by following the numerical method outlined by Erdogan [18]. The computational approach is based on the DCT and is integrated into the general purpose finite element analysis software ANSYS. Both single and periodic crack problems are considered by using the developed computational technique. The primary numerical results generated by means of the analytical and computational approaches are the Modes I and II SIFs and the energy release rate.

The results presented in Sec. 4.1 indicate that the orthotropy and nonhomogeneity parameters significantly influence the fracture behavior of an orthotropic FGM coating. It is shown that the normalized energy release rate for a single embedded crack is a decreasing function of both the stiffness ratio of the coating and the nonhomogeneity parameter. An increase in the bond coat thickness, on the other hand, is shown to result in a corresponding increase in the energy release rate of a crack located close to the orthotropic FGM coating–bond coat interface. Further application of the developed computational method is demonstrated in Sec. 4.2 by considering periodic cracks in the orthotropic FGM coating. The finite element analysis is conducted by modeling a unit cell in the trilayer structure with the appropriate symmetry and periodicity conditions. Presented results point out that the mixed-mode SIFs and the energy release rate go through minimum values before becoming unbounded as the crack tips get close to each other. The comparisons provided in this article show that the results obtained by the analytical and computational methods are in very good agreement. Therefore, both of the methods are concluded to be effective ways of assessing the fracture behavior of orthotropic FGM coatings.

Acknowledgment

This work was partially supported by the Scientific and Technical Research Council of Turkey (TUBITAK) through Grant No. MISAG-TUN1-2004.

References

[1] Sampath, S., Herman, H., Shimoda, N., and Saito, T., 1995, "Thermal Spray Processing of FGMs," MRS Bull., **20**, pp. 27–31.

[2] Kaysser, W. A., and Ilschner, B., 1995, "FGM Research Activities in Europe," MRS Bull., **20**, pp. 22–26.

[3] Chen, J., Liu, Z., and Zou, Z., 2002, "Transient Internal Crack Problem for a Nonhomogeneous Orthotropic Strip (Mode I)," Int. J. Eng. Sci., **40**, pp. 1761–1774.

[4] Guo, L.-C., Wu, L.-Z., Zeng, T., and Ma, L., 2004, "Mode I Crack Problem for a Functionally Graded Orthotropic Strip," Eur. J. Mech. A/Solids, **23**, pp. 219–234.

[5] Kim, J.-H., and Paulino, G. H., 2002, "Mixed-Mode Fracture of Orthotropic Functionally Graded Materials Using Finite Elements and the Modified Crack Closure Method," Eng. Fract. Mech., **69**, pp. 1557–1586.

[6] Kim, J.-H., and Paulino, G. H., 2003, "Mixed-Mode *J*-Integral Formulation and Implementation Using Graded Elements for Fracture Analysis of Nonhomogeneous Orthotropic Materials," Mech. Mater., **35**, pp. 107–128.

[7] Kim, J.-H., and Paulino, G. H., 2003, "The Interaction Integral for Fracture of Orthotropic Functionally Graded Materials: Evaluation of Stress Intensity Factors," Int. J. Solids Struct., **40**, pp. 3967–4001.

[8] Kim, J. H., and Paulino, G. H., 2005, "Consistent Formulations of the Interaction Integral Method for Fracture of Functionally Graded Materials," Trans. ASME, J. Appl. Mech., **72**, pp. 351–364.

[9] Guo, L.-C., Wu, L.-Z., and Zeng, T., 2005, "The Dynamic Response of an Edge Crack in a Functionally Graded Orthotropic Strip," Mech. Res. Commun., **32**, pp. 385–400.

[10] Dag, S., Yildirim, B., and Erdogan, F., 2004, "Interface Crack Problems in Graded Orthotropic Media: Analytical and Computational Approaches," Int. J. Fract., **130**, pp. 471–496.

[11] Chen, J., 2005, "Determination of Thermal Stress Intensity Factors for an Interface Crack in a Graded Orthotropic Coating-Substrate Structure," Int. J. Fract., **133**, pp. 303–328.

[12] Dag, S., 2006, "Thermal Fracture Analysis of Orthotropic Functionally Graded Materials Using an Equivalent Domain Integral Approach," Eng. Fract. Mech., **73**, pp. 2802–2828.

[13] Krenk, S., 1979, "On the Elastic Constants of Plane Orthotropic Elasticity," J. Compos. Mater., **13**, pp. 108–116.

[14] Pindera, M.-J., and Chen, L., 2007, "Microstructural Effects in Finite Multilayers With Aligned Cracks," Eng. Fract. Mech., **74**, pp. 1697–1718.

[15] Ozturk, M., and Erdogan, F., 1999, "The Mixed Mode Crack Problem in an Inhomogeneous Orthotropic Medium," Int. J. Fract., **98**, pp. 243–261.

[16] Ozturk, M., and Erdogan, F., 1997, "Mode I Crack Problem in an Inhomogeneous Orthotropic Medium," Int. J. Eng. Sci., **35**, pp. 869–883.

[17] Ilhan, K. A., 2007, "Mixed-Mode Fracture Analysis of Orthotropic FGM Coatings Under Mechanical and Thermal Loads," Ph.D. thesis, Department of Mechanical Engineering, Middle East Technical University, Ankara, Turkey.

[18] Erdogan, F., 1978, "Mixed Boundary-Value Problems in Mechanics," *Mechanics Today*, S. Nemat-Nasser, ed., Pergamon, Elmsford, New York, pp. 1–84.

[19] 1997, ANSYS, Release 5.4, ANSYS Basic Analysis Procedures Guide, Canonsburg, PA.

[20] Yildirim, B., Dag, S., and Erdogan, F., 2005, "Three Dimensional Fracture Analysis of FGM Coatings Under Thermomechanical Loading," Int. J. Fract., **132**, pp. 371–397.

[21] Santare, M. H., and Lambros, J., 2000, "Use of Graded Finite Elements to Model the Behavior of Nonhomogeneous Materials," Trans. ASME, J. Appl. Mech., **67**, pp. 819–822.

[22] Li, C., Zou, Z., and Duan, Z., 2000, "Multiple Isoparametric Finite Element Method for Nonhomogeneous Media," Mech. Res. Commun., **27**, pp. 137–142.

[23] Kim, J.-H., and Paulino, G. H., 2002, "Isoparametric Graded Finite Elements for Nonhomogeneous Isotropic and Orthotropic Materials," Trans. ASME, J. Appl. Mech., **69**, pp. 502–514.

[24] Banks-Sills, L., and Sherman, D., 1986, "Comparison of Methods for Calculating Stress Intensity Factors With Quarter Point Elements," Int. J. Fract., **32**, pp. 127–140.

[25] Wang, B. L., and Mai, Y.-W., 2005, "A Periodic Array of Cracks in Functional Graded Materials Subjected to Thermo-Mechanical Loading," Int. J. Eng. Sci., **43**, pp. 432–446.

[26] Kokini, K., DeJonge, J., Rangaraj, S., and Beardsley, B., 2002, "Thermal Shock of Functionally Graded Thermal Barrier Coatings With Similar Thermal Resistance," Surf. Coat. Technol., **154**, pp. 223–231.

[27] Erdogan, F., 1962, "On the Stress Distribution in Plates With Collinear Cuts Under Arbitrary Loads," *Proceedings of the Fourth U.S. National Congress of Applied Mechanics*, Vol. 1, pp. 547–553.

Mechanical Modeling of Thin Films and Cover Plates Bonded to Graded Substrates

Mehmet A. Guler[1]
Department of Mechanical Engineering,
TOBB University of Economics and Technology,
Ankara 06560, Turkey
e-mail: mguler@etu.edu.tr

In this study, the contact problems of thin films and cover plates are considered. In these problems, the loading consists of any one or combination of stresses caused by uniform temperature changes and temperature excursions, far field mechanical loading, and residual stresses resulting from film processing or welding. The primary interest in this study is in examining stress concentrations or singularities near the film ends for the purpose of addressing the question of crack initiation and propagation in the substrate or along the interface. The underlying contact mechanics problem is formulated by assuming that the film is a "membrane" and the substrate a graded elastic continuum, and is solved analytically by reducing it to an integral equation. The calculated results are the interfacial shear stress between the film and the graded substrate, the Mode II stress intensity factor at the end of the film, and the axial normal stress in the film. The results indicate that grading the material properties of the substrate helps to decrease the film stresses and the stress intensity factors at the free edges and to lower the axial normal stresses at the midsection where the film is most likely to crack.
[DOI: 10.1115/1.2936237]

Keywords: thin film, contact stress, functionally graded material, cover plate, stress intensity factor

1 Introduction

In general, the mechanics of contact problems involving functionally graded materials (FGMs) may be studied in two broad categories. The first category is comprised of standard load transfer problems with or without friction, wherein the loading component may be rigid or deformable and the loaded component is usually deformable. These problems are known as "stamp" or "punch" problems and include bearings, gears, cams, cylinder linings/piston rings, and abradable seals in stationary gas turbines. For an in-depth review about the potential applications of FGMs, the reader is referred to Refs. [1,2]. In these applications, the concept of material property grading is used by coating the mechanical components with appropriate FGM layers, usually to improve wear resistance. Literature in this category is quite extensive and includes the works of Booker et al. [3], Giannakopoulos and Suresh [4] Suresh et al. [5,6], El-Borgi et al. [7], Ke and Wang [8–10], Zhang et al. [11], Watremetz et al. [12], Choi and Paulino [13], Dag and Erdogan [14] and Guler and Erdogan [15–17]. In this category, the contact problem is generally reduced to a singular integral equation involving the unknown contact pressure or the in-plane component of stress on the surface of the graded coating, which is solved from the perspective of crack initiation. Input for this kind of problems is the shape of the punch profile, and hence the singular integral equations formed are based on the displacement gradient in the thickness direction. The problem has to be solved with the consideration of equilibrium of the contact pressure generated and the load applied through the punch or stamp.

The second category of contact problems comprises thin films and cover plates bonded to FGM substrates. The main applications of cover plates involve aerospace and civil engineering structures in which they are used as reinforcements or stiffeners, whereas thin films are used mostly in microelectronics devices. This category of contact mechanics problems is quite different from the first kind and is characterized by deformable contacting medium whose thickness is very small in comparison with its in-plane dimensions. In contrast to contact problems of graded materials that belong in the first category, to the author's knowledge, there are not any studies conducted on thin films or cover plates bonded to functionally graded substrates, which focus on investigating the critical problem of crack initiation at the edge of the film and substrate that may cause delamination and consequently device malfunction in service. Therefore, it is an important task to study stress concentrations at the free edges of thin films to improve the reliability of devices for possible use on graded substrates. In this category, the elasticity problem of a thin membrane bonded to a graded substrate is reduced to a singular integral equation for the unknown shear stress based on the lateral gradient of the displacement field, as opposed to the component of displacement field in the thickness direction in the first category. The problem is solved using the compatibility of the strain field between the membrane and the graded surface. The inputs to this kind of problems are strains caused by external loads.

In this study, only the contact problems for thin films and cover plates will be considered. In these problems, the loading consists of any one or combination of stresses caused by uniform temperature changes and temperature excursions, far field mechanical loading, and residual stresses resulting from film processing or welding. A characteristic feature of this second category of contact problems is that generally the film or cover plate thickness is very small compared to other dimensions in the system. Consequently, in formulating the mechanics problem, it will be assumed that the substrate may be approximated by a semi-infinite graded elastic continuum and the film by an elastic "membrane." Freund and Suresh [18] explained the qualifier "small" used in their definition of thin films as the largest dimension, which is at least 20 times greater than the small dimension. With this definition, a minimum aspect ratio of 20 is assumed to be thin. They also added the following: "If a uniform all-around normal traction of magnitude

[1]Corresponding author.

Contributed by the Applied Mechanics Division of ASME for publication in the JOURNAL OF APPLIED MECHANICS. Manuscript received May 30, 2007; final manuscript received November 2, 2007; published online July 10, 2008. Review conducted by Marek-Jerzy Pindera.

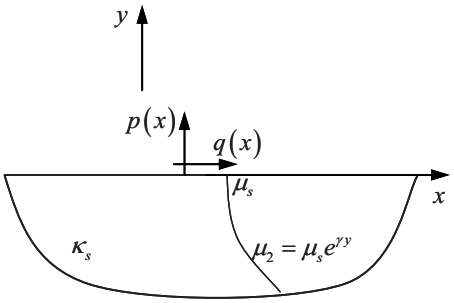

Fig. 1 Geometry of the problem

σ_m, either tension or compression, is applied to the edges of a film of thickness h, edge effect associated with the load transfer region is negligible when considering curvature of a film-substrate system with lateral dimensions more than $50h$ (aspect ratio 50)" [18].

The primary interest in this study is in examining stress concentrations or singularities near the film ends for the purpose of addressing the question of crack initiation and propagation in the substrate or along the interface. There are two approaches for studying these kinds of problems. One deals with the crack initiation process by assuming a preexisting crack [19,20]; the other deals with the singular stress field at the free edge that causes crack formation [21–29]. Erdogan and Gupta [21] provide one of the earliest and most relevant contributions to thin films, wherein they solved the problem of an elastic stiffener bonded to a half-plane using the membrane assumption. Later, Shield and Kim [30] used the plate assumption to model a thin film in order to accommodate bending stiffness. Alaca et al. [31] calculated the interfacial shear stress between a rectangular strip of thin aluminum film and a polyimide substrate in closed form by noting the similarity between the governing integrodifferential equation for the interfacial shear stress and Prandtl's integrodifferential equation that governs the circulation of air flow around a wing of finite span in aerodynamics. Takahashi and Shibuya [32] investigated the interfacial stress between a thin film and its substrate and the behavior of singular stress at the edge on the basis of thermoelasticity using the boundary element method.

The underlying contact mechanics problem is formulated [33] and solved analytically by reducing it to an integral equation. For the ideal interface model, it is shown that the integral equation has a simple Cauchy kernel. Hence, the contact stress has a standard square-root singularity. In the case of film/substrate bonding through an adhesive layer, the integral equation has only a logarithmic singularity and consequently, all stress components are bounded.

2 Green's Functions for the Graded Substrate

Before proceeding to the formulation of the problem, it is necessary to find the Green's functions for deriving the integral equations of the contact problem for a graded substrate. Consider the plane elasticity problem shown in Fig. 1. Medium 2 is the graded substrate with the shear modulus of the substrate given by $\mu_2(y)$ and approximated by

$$\mu_2(y) = \mu_s e^{\gamma y}, \quad y < 0 \tag{1}$$

where γ is a constant characterizing the material inhomogeneity and μ_s is the value of $\mu_2(y)$ at the surface $y=0$.

In the graded medium $-\infty < y < 0$, the spatial variation of Poisson's ratio is assumed to be negligible. Thus, we have $\nu_2(y) = \nu_s = \text{const}$.

For the plane contact problem under consideration, Hooke's law for the graded substrate can be written as

$$\sigma^s_{xx}(x,y) = \frac{\mu_2(y)}{\kappa_2 - 1}\left[(\kappa_2 + 1)\frac{\partial u_2}{\partial x} + (3 - \kappa_2)\frac{\partial \nu_2}{\partial y}\right] \tag{2a}$$

$$\sigma^s_{yy}(x,y) = \frac{\mu_2(y)}{\kappa_2 - 1}\left[(3 - \kappa_2)\frac{\partial u_2}{\partial x} + (\kappa_2 + 1)\frac{\partial \nu_2}{\partial y}\right] \tag{2b}$$

$$\tau^s_{xy}(x,y) = \mu_2(y)\left[\frac{\partial u_2}{\partial y} + \frac{\partial \nu_2}{\partial x}\right] \tag{2c}$$

where $\kappa_s = 3 - 4\nu_s$ for plane strain and $\kappa_s = (3 - \nu_s)/(1 + \nu_s)$ for the generalized plane stress conditions.

Substituting Eqs. (2*a*)–(2*c*) into the equilibrium equations, we obtain

$$(\kappa_2 + 1)\frac{\partial^2 \nu_2}{\partial y^2} + (\kappa_2 - 1)\frac{\partial^2 \nu_2}{\partial x^2} + 2\frac{\partial^2 u_2}{\partial x \partial y} + \gamma(3 - \kappa_2)\frac{\partial u_2}{\partial x} + \gamma(\kappa_2 + 1)\frac{\partial \nu_2}{\partial y} = 0, \quad y < 0 \tag{3a}$$

$$(\kappa_2 + 1)\frac{\partial^2 u_2}{\partial x^2} + (\kappa_2 - 1)\frac{\partial^2 u_2}{\partial y^2} + 2\frac{\partial^2 \nu_2}{\partial x \partial y} + \gamma(\kappa_2 - 1)\frac{\partial u_2}{\partial y} + \gamma(\kappa_2 - 1)\frac{\partial \nu_2}{\partial x} = 0, \quad y < 0 \tag{3b}$$

By using the Fourier transforms and a rather lengthy procedure outlined in Ref. [15], the derivatives of the displacement field $u_2(x,y)$ and $v_2(x,y)$ may be expressed as

$$-\omega q(x) + \frac{1}{\pi}\int_{-\infty}^{\infty}\left[\frac{1}{t - x} - k_{11}(t,x)\right]p(t)dt - \frac{1}{\pi}\int_{-\infty}^{\infty} q(t)k_{12}(t,x)dt = f_1(x), \quad -a < x < b \tag{4a}$$

$$\omega p(x) + \frac{1}{\pi}\int_{-\infty}^{\infty}\left[\frac{1}{t - x} - k_{21}(t,x)\right]q(t)dt - \frac{1}{\pi}\int_{-\infty}^{\infty} p(t)k_{22}(t,x)dt = f_2(x), \quad -a < x < b \tag{4b}$$

where $p(x)$ is the peel stress and $q(x)$ is the shear stress between the thin film and the graded medium, and the kernels $k_{ij}(t,x)$ are known bounded functions given in the Appendix and

$$f_1(x) = \frac{4\mu_s}{\kappa_s + 1}\frac{\partial}{\partial x}\nu_2(x,0) \tag{5a}$$

$$f_2(x) = \frac{4\mu_s}{\kappa_s + 1}\frac{\partial}{\partial x}u_2(x,0) \tag{5b}$$

$$\omega = \frac{\kappa_s - 1}{\kappa_s + 1} \tag{5c}$$

3 Formulation of the Plane Elasticity Problem

There are two approaches in modeling the film on a substrate from the continuum perspective. One is based on the membrane assumption in which the thin film acts as a membrane that cannot support peel stresses, and bending in the film is assumed to be negligible. This assumption was shown to hold over distances that are large compared to the film thickness. Shield and Kim [30] reported that the results obtained from the membrane assumption must be viewed as a first term in an expansion of the exact solution in the thickness of the film where the length scale in the expansion must also be compared to the geometry of the problem and thus the order of the expansion determines how close to the film edge such a model will yield accurate predictions. In order to get closer results, one should take into account the bending effects and the effect of peel stresses especially near the ends of the film. Clearly, the beam theory is only one more term in the expansion, and the results we obtain must still be viewed as being applicable only over distances on the order of film thickness from the film's end [30].

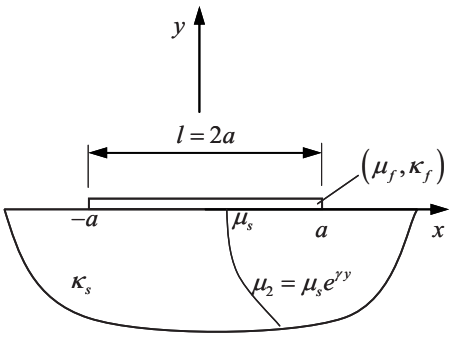

Fig. 2 Geometry of the thin film on a graded substrate problem

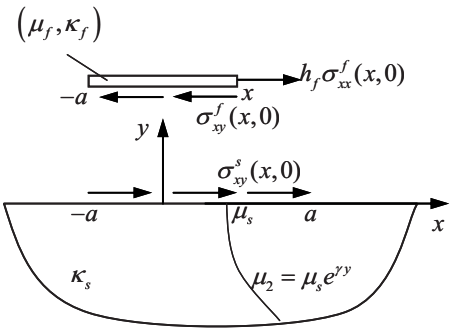

Fig. 3 Equilibrium diagram of the thin film and the graded substrate

The other approach is based on the plate assumption in which the thin film is modeled as a plate. Freund and Suresh [18] noted that near the edges (that is, the distance from the free edge is on the order of the film thickness), bending stresses in the thin film should be considered. This could be done by assuming the film acts as an elastic plate (this model is commonly known as a Kirchhoff plate). With this model, the effect of the peel stresses and bending in the film are no longer neglected. Now, the peel and shear stresses along the interface between the film and the substrate are coupled. Shield and Kim [30] studied these effects for homogeneous materials and the following conclusions were drawn from that study.

- For more compliant films, a large difference in the shear stress occurs near the ends of the film. Away from the ends, both theories predict similar values of shear stress.
- For films with large modulus ratios, the membrane model agrees well with the beam model.
- The lack of normal stress information in the membrane results may affect the ability to predict failures across interfaces that are sensitive to normal stresses. For films whose moduli differ little from the substrate modulus, it is necessary to use at least a beam theory to determine the interface stresses accurately.

In studying the factors influencing the nature of stress concentrations near the film edges, it is realistic to assume the film to behave like a membrane and the substrate a semi-infinite medium since the thickness of films used in the microelectronic industry is of the order of submicrons and the substrate is of the order of millimeters. This assumption can be validated by modeling the film by a plate. However, using the plate assumption couples the shear and peel stresses at the interface between the thin film and the graded substrate (see Eqs. (4*a*) and (4*b*)), complicating the problem at hand. The finite element method is a more suitable technique to study the differences between membrane and plate assumptions in this class of problems, and will be used in a future study to address this question.

The problem under consideration is shown in Fig. 2. Medium 1 is a homogeneous thin film with thickness h_f and length $l=2a$. The problem involves the determination of the contact stresses between a graded substrate and a "thin" film or cover plate of finite length, which is perfectly bonded to a graded substrate.

Let the thickness h_f be sufficiently small for generalized plane stress assumption for the thin film to be valid and let the contact stresses between the graded substrate and the film be

$$q(x) = \sigma^s_{xy}(x) = \begin{cases} 0, & |x| > a \\ f(x), & |x| < a \end{cases} \tag{6a}$$

$$p(x) = \sigma^s_{yy}(x) = 0 \tag{6b}$$

The equilibrium diagram of the thin film and graded substrate is shown in Fig. 3. It is assumed that the normal force per unit width of the film in the y direction is uniform across the thickness. Therefore, the change in normal force in the film is balanced by the interfacial shear σ^f_{xy} (see Fig. 3).

$$\int_{-a}^{x} \sigma^f_{xy}(t,0)dt = \int_{-a}^{x} f(t)dt = \sigma^f_{xx}(x,0)h(x) \tag{7}$$

Hence, the normal stress in the film may be expressed as

$$\sigma^f_{xx}(x,0) = \frac{1}{h(x)} \int_{-a}^{x} f(t)dt \tag{8}$$

For the plane strain conditions $\varepsilon^f_{zz}(x,y)=0$, and considering $\sigma^f_{yy}(x,y)=0$, the axial strain in the film can be written as

$$\varepsilon^f_{xx}(x,0) = \frac{\partial}{\partial x} u_1(x,0) = \frac{1+\kappa_f}{8\mu_f} \sigma^f_{xx} \tag{9}$$

Substituting the axial normal stress σ^f_{xx} found from Eq. (8) into the equilibrium equation (7), the strain in the thin film can be written as

$$\frac{\partial}{\partial x} u_1(x,0) = \frac{1+\kappa_f}{8\mu_f} \frac{1}{h(x)} \int_{-a}^{x} f(t)dt \tag{10}$$

Using the contact stresses from Eqs. (6*a*) and (6*b*), the strain on the surface of the FGM half-plane can be written from Eq. (4*b*) as

$$\frac{\partial}{\partial x} u_2(x,0) = \frac{\kappa_s+1}{4\mu_s} \frac{1}{\pi} \int_{-\infty}^{\infty} \left[\frac{1}{t-x} - k_{21}(t,x) \right] f(t)dt \tag{11}$$

Superposing the strains caused by the external loads other than $f(x)$, Eq. (11) becomes

$$\frac{\partial}{\partial x} u_2(x,0) = \frac{\kappa_s+1}{4\mu_s} \frac{1}{\pi} \int_{-\infty}^{\infty} \left[\frac{1}{t-x} - k_{21}(t,x) \right] f(t)dt + g(x) \tag{12}$$

where $g(x)=\varepsilon_0+\alpha T$: the resulting strain from the external loads other than $f(x)$.

If we consider a perfect bonding between the thin film and the FGM, compatibility condition at $y=0$ becomes

$$\varepsilon_{1xx}(x,0) = \varepsilon_{2xx}(x,0) \tag{13}$$

Using Eqs. (10) and (12), Eq. (13) becomes

$$\frac{1}{\pi} \int_{-a}^{a} \left[\frac{1}{t-x} - k_{21}(t,x) \right] f(t)dt - \frac{\lambda}{2h(x)} \int_{-a}^{x} f(t)dt = -\frac{4\mu_s}{\kappa_s+1} g(x) \tag{14}$$

where

$$\lambda = \frac{1+\kappa_f \mu_s}{1+\kappa_s \mu_f} \tag{15}$$

so that λ is a measure of relative stiffness of the substrate with respect to the film. In this study, Poisson's ratios of the film and the substrate were taken to be the same. Therefore, we have a soft film on a hard substrate if $\lambda > 1$, a hard film on a soft substrate if $\lambda < 1$, and equal stiffness of the film and substrate if $\lambda = 1$.

From the equilibrium of the film, it is clear that the integral equation should be solved subject to the following condition:

$$\int_{-a}^{a} f(t)dt = 0 \tag{16}$$

4 Solution of the Integral Equation

The loading parameter of the problem studied in this paper is the strain in the substrate, $\varepsilon_{xx}^{s}(x,0) = \varepsilon_0(x)$ due to external mechanical loads calculated by ignoring the film. By defining the following normalized quantities,

$$x = ar, \quad -a < x < a, \quad -1 < r < 1 \tag{17a}$$

$$t = as, \quad -a < s < a, \quad -1 < s < 1 \tag{17b}$$

$$h(x) = H(r) \tag{17c}$$

$$f(x) = -p_1 p(r) \tag{17d}$$

$$p_1 = \frac{4\mu_s \varepsilon_0}{\kappa_s + 1} \tag{17e}$$

the integral equation (14) and Eq. (16) may be expressed in the following form:

$$\frac{1}{\pi}\int_{-1}^{1}\left[\frac{1}{s-r} - k_{21}(s,r)\right]p(s)ds - \frac{\lambda}{2}\frac{a}{H(r)}\int_{-1}^{r} p(s)ds = 1, \quad -1 < r < 1 \tag{18}$$

$$\int_{-1}^{1} p(s)ds = 0 \tag{19}$$

where the kernel $k_{21}(s,r)$ is given by

$$k_{21}(s,r) = a k_{21}(t,x) \tag{20}$$

Assuming a solution of the form

$$p(s) = \phi(s)\frac{1}{\sqrt{1-s^2}} \tag{21}$$

where

$$\phi(s) = \sum_{0}^{\infty} a_n T_n(s) \tag{22}$$

Eqs. (18) and (19) become

$$\frac{1}{\pi}\int_{-1}^{1}\sum_{0}^{\infty} a_n \frac{T_n(s)}{\sqrt{1-s^2}}\left[\frac{1}{s-r} - k_{21}(s,r)\right]ds - \frac{\lambda}{2}\frac{a}{H(r)}\int_{-1}^{r}\sum_{0}^{\infty} a_n \frac{T_n(s)}{\sqrt{1-s^2}}ds = 1, \quad -1 < r < 1 \tag{23}$$

$$\int_{-1}^{1}\sum_{0}^{\infty} a_n T_n(s)\frac{1}{\sqrt{1-s^2}}ds = 0 \tag{24}$$

Using the orthogonality conditions

$$\frac{1}{\pi}\int_{-1}^{1}\frac{T_n(s)T_m(s)}{\sqrt{1-s^2}}ds = \begin{cases} 1, & m = n = 0 \\ 1/2, & m = n \geq 1 \\ 0, & m \neq n \end{cases} \tag{25}$$

and the following properties of the Chebyshev polynomials:

$$\frac{1}{\pi}\int_{-1}^{1}\frac{T_n(s)}{(s-r)\sqrt{1-s^2}}ds = \begin{cases} 0, & n = 0, \\ U_{n-1}(r), & n > 0, \end{cases} \quad |r| < 1 \tag{26}$$

$$\int_{-1}^{r}\frac{T_n(s)}{\sqrt{1-s^2}}ds = -\frac{1}{n}U_{n-1}(r)\sqrt{1-r^2}, \quad |r| < 1 \tag{27}$$

it may be seen that $a_0 = 0$, and the integral equation may be reduced to

$$\sum_{1}^{\infty} a_n[U_{n-1}(r) + R_n(r)] = 1, \quad -1 < r < 1 \tag{28}$$

where

$$R_n(r) = -\frac{1}{\pi}\int_{-1}^{1}\frac{T_n(s)}{\sqrt{1-s^2}}[k_{21}(s,r)]ds + \frac{\lambda}{2n}\frac{a}{H(r)}U_{n-1}(r)\sqrt{1-r^2} \tag{29}$$

The easiest way of solving Eq. (28) is to truncate the infinite series by retaining the first N terms and by collocating the equation at $r_1, \ldots, r_N$ [34]. Good convergence is obtained if the collocation points are concentrated near the ends. This may be accomplished by selecting the points as

$$T_N(r_i) = 0, \quad r_i = \cos\theta_i, \quad \theta_i = (2i-1)\frac{\pi}{2N}, \quad i = 1, \ldots, N \tag{30}$$

The shear stress at the interface $y = 0$ then becomes

$$\sigma_{xy}^{f}(x,0) = f(x) = -\frac{4\mu_s \varepsilon_0}{\kappa_s + 1}\sum_{1}^{N} a_n T_n\left(\frac{x}{a}\right)\frac{1}{\sqrt{1-\left(\frac{x}{a}\right)^2}} \tag{31}$$

After determining $\sigma_{xy}^{f}(x,0)$, the normal stress in the film may be obtained from

$$\sigma_{xx}^{f}(x,0) = \frac{1}{h(x)}\int_{-a}^{x} f(t)dt = p_1\frac{a}{h(x)}\sum_{1}^{N}\frac{1}{n}a_n U_{n-1}(x/a)\sqrt{1-(x/a)^2} \tag{32}$$

It may be seen that in the neighborhood of $x = \pm a$, the mixed boundary value problem for the film/substrate is identical to a crack problem under pure Mode II loading conditions.

Therefore, the Mode II stress intensity factor at $x = -a$ may be defined as

$$k_2 = \lim_{x \to -a}\sqrt{2(x+a)}\,\sigma_{xy}^{s}(x,0) \tag{33}$$

Substituting the shear stress found from Eq. (31) into Eg. (33), we have

$$\frac{k_2}{p_1\sqrt{a}} = -\sum_{1}^{N} a_n T_n(-1) \tag{34}$$

5 Results

Herein, the contact problem between a thin film and a graded substrate is investigated. The calculated results are the interfacial shear stress between the film and the graded substrate, Mode II stress intensity factor at the film's edge, and the axial normal stress in the film. Throughout this study, the thickness profile was

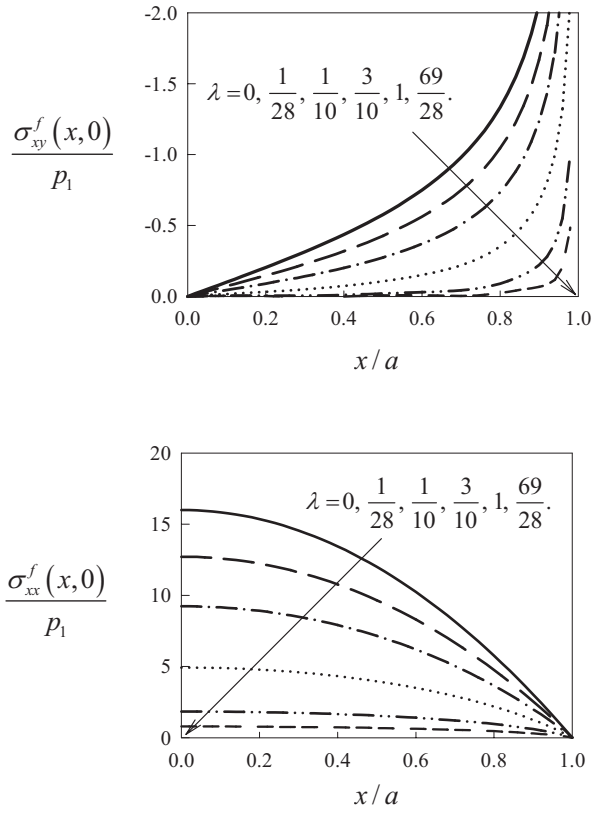

Fig. 4 Interfacial stress $\sigma_{xy}^f(x,0)$ and the axial normal stress in the film $\sigma_{xx}^f(x,0)$ for various values of the parameter λ for homogeneous substrate, $l/h_f=32$

taken to be constant, $h(x)=h_f$, and Poisson's ratios of the film and the substrate are the same, $\nu_s=\nu_f=0.3$. Here, it is worthwhile to mention that the selection of the parameter λ was not arbitrary. In fact, $\lambda=1/28$ corresponds to the results of Alaca et al. [31] where the motivation of his work was a micropump wherein a polymeric substrate was coated with a thin metal film, whereas $\lambda=69/28$ corresponds to the results of Erdogan and Joseph's study [25] where the film was taken to be silicon nitride (Si_3N_4) and the substrate was silicon (Si) used in the microelectronics industry.

We first consider the simple limiting case of the contact problem for a homogeneous substrate to set some ideas about the behavior of the solution to the general problem described in Fig. 1. The closed form solution of the problem is known and is described in the Appendix. Figure 4 shows some sample results obtained from the Appendix for specific values of the input parameters λ and aspect ratio $l/h_f=32$. From Fig. 4, it may be seen that for $\lambda=0$, we have an inextensible film and from the closed form solution (A18), the nondimensional normal stress at the midsection of the film is

$$\frac{\sigma_{xx}^f(0,0)}{p_1}=\frac{a}{h_f}=16 \tag{35}$$

As λ increases, that is, if the film gets softer than the substrate, both the interfacial stress and the normal stress in the film decrease. The figure also shows that the normal stress distribution in the film, $\sigma_{xx}^f(x,0)$, is symmetric with respect to $x=0$ plane due to symmetric boundary conditions and self-equilibrating nature of the interfacial shear stresses. Figure 5 shows the Mode II stress intensity factor versus the parameter λ for various values of the aspect ratio, l/h_f for homogeneous substrate. It can be seen that as λ increases, the stress intensity factor k_2 decreases. For the same value of the parameter λ, the stress intensity factor decreases as

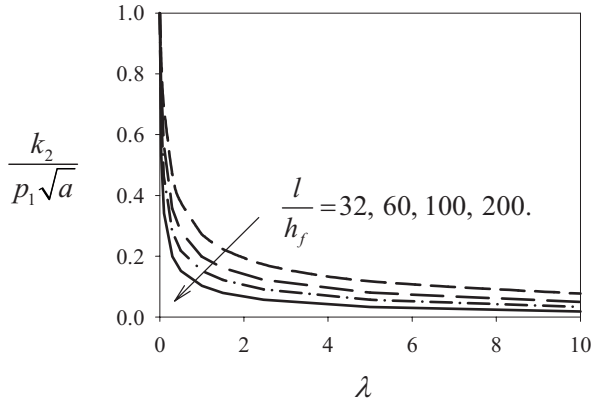

Fig. 5 Mode II stress intensity factor versus the parameter λ for various values of the aspect ratio l/h_f for homogeneous substrate, $l=2a$

the aspect ratio l/h_f increases. Therefore, for a fixed film length, a thicker film will be more likely to fail than a thinner one.

To compare the results with literature [31], the thickness profile is taken to be

$$h(x)=h_f\sqrt{1-\frac{x^2}{a^2}}\left(1+0.9\frac{x^2}{a^2}\right) \tag{36}$$

By defining the stress intensity factor at $x=-a$ as in Ref. [31],

$$K_2=\lim_{x\to -a}\sqrt{2\pi(x+a)}\sigma_{xy}^s(x,0) \tag{37}$$

Alaca et al. [31] found the stress intensity factor to be 0.47 for $\lambda=1/28$ (aluminum film on polyimide substrate) and $l/h_f=32$.

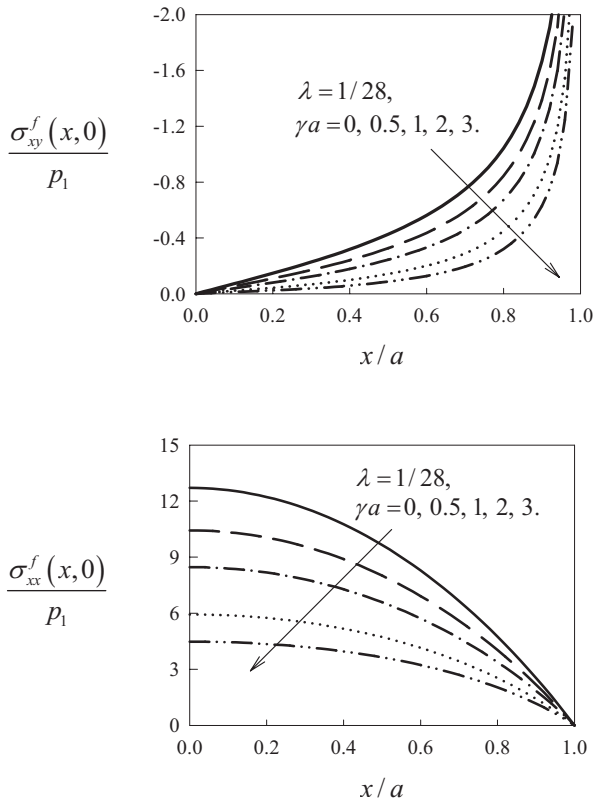

Fig. 6 Interfacial stress $\sigma_{xy}^f(x,0)$ and the axial normal stress in the film $\sigma_{xx}^f(x,0)$ for various values of the nonhomogeneity parameter γa for graded substrate, $\lambda=1/28$, $l/h_f=32$

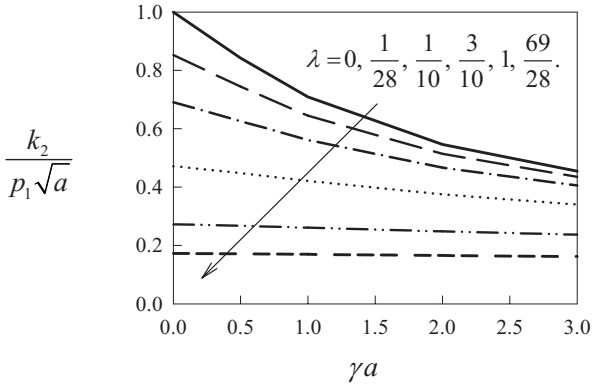

Fig. 7 Mode II stress intensity factor versus the nonhomogeneity parameter γa for various values of the parameter λ for graded substrate, $l/h_f=32$

According to this study, when the thickness profile is taken to be as in Eq. (36), with all the material and geometric parameters being equal, it is found that $K_2=0.4692$, in agreement with the previous work of Alaca et al. [31].

Returning to the graded substrates, some sample results for the general problem shown in Fig. 1 are given in Figs. 6–10. In the problem considered, the main variables are the nonhomogeneity parameter γa, the stiffness ratios $\lambda=(\kappa_f+1)/(\kappa_s+1)\mu_s/\mu_f$, the aspect ratio l/h_f, and the elastic constants κ_s, κ_f, which are taken to be equal, $\kappa_s=\kappa_f$, so that λ becomes $\lambda=\mu_s/\mu_f$. The full parametric study of the problem seems to be practically impossible. One may, however, select one of the variables a main parameter (in this case, γa or λ) and compute and plot the field quantities that deem to be important. In the results presented, these quantities were selected as the interfacial shear stress $\sigma^f_{xy}(x,0)$ and the normal stress in the film, $\sigma^f_{xx}(x,0)$, and the Mode II stress intensity factor, k_2. Material nonhomogeneity parameter γa is varied between 0 and 3 to see the effect of grading for stiffening substrates.

Figure 6 shows the effect of the nonhomogeneity parameter γa on the interfacial shear stress and the normal stress in the film for $\lambda=1/28$, which corresponds to an aluminum film on polyimide substrate. As the nonhomogeneity parameter increases, both the

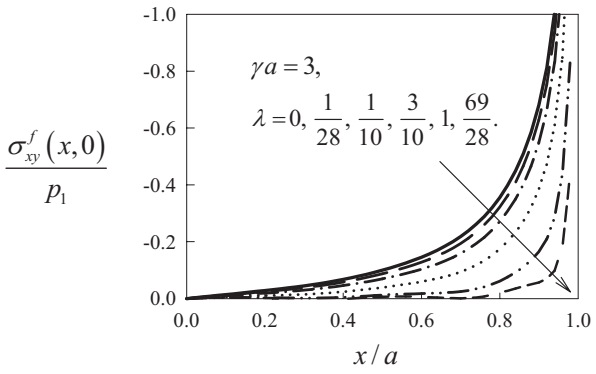

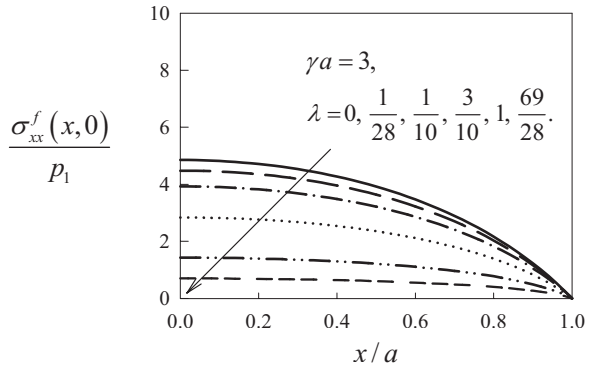

Fig. 8 Interfacial stress $\sigma^f_{xy}(x,0)$ and the axial normal stress in the film $\sigma^f_{xx}(x,0)$ for various values of the parameter λ for graded substrate, $\gamma a=3$, $l/h_f=32$

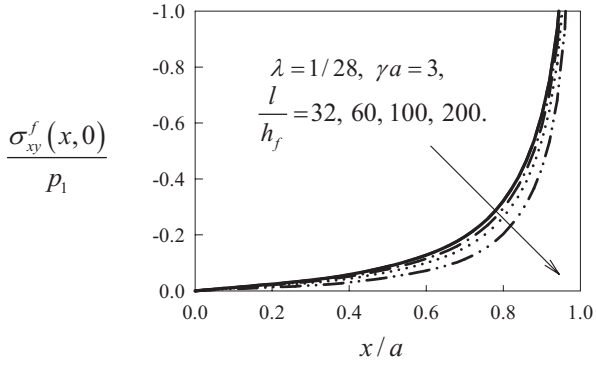

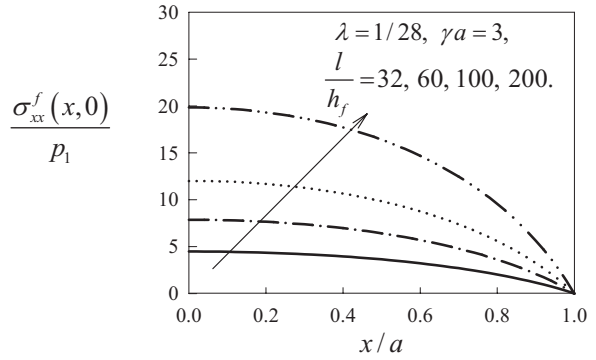

Fig. 9 Interfacial stress $\sigma^f_{xy}(x,0)$ and the normal stress in the film $\sigma^f_{xx}(x,0)$ for various values of the aspect ratio l/h_f for graded substrate, $\gamma a=3$, $\lambda=1/28$

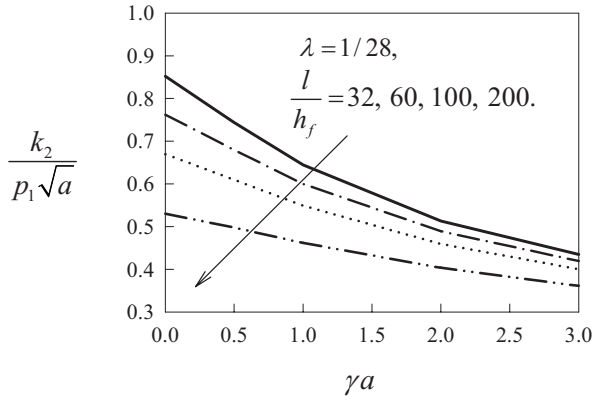

Fig. 10 Mode II stress intensity factor versus the nonhomogeneity parameter γa for various values of the aspect ratio l/h_f for graded substrate, $\lambda=1/28$

interfacial shear stress and the normal stress in the film decrease. This suggests that grading the material helps to lower the normal stress at the midsection where it is most likely to crack.

The effect of the nonhomogeneity parameter γa on the Mode II stress intensity factor is illustrated in Fig. 7. Grading the material properties helps to reduce the stress intensity factor for lower values of the parameter λ, thereby reducing the likelihood of edge debonding at the free edges. As in the homogeneous material case, as the substrate-to-film stiffness ratio parameter λ increases, the stress intensity factor decreases.

The effect of the substrate-to-film stiffness ratio parameter λ on the interfacial shear stress and the normal stress in the film can be seen in Fig. 8. Fixing the nonhomogeneity parameter at $\gamma a=3$ and the aspect ratio at $l/h_f=32$, the interfacial shear stress $\sigma_{xy}^f(x,0)$ and the normal stress in the film $\sigma_{xx}^f(x,0)$ are plotted along the interface of the graded substrate. It can be seen that as λ increases, both the interfacial shear stress and the normal stress in the film decrease.

The effect of the aspect ratio l/h_f on the stresses and the stress intensity factor was investigated next. Figure 9 shows the normal stress distribution in the film for various values of the aspect ratio l/h_f. It is observed that as the aspect ratio increases, the normal stress in the film $\sigma_{xx}^f(x,0)$ increases. Therefore, for a fixed film thickness, a longer film will be more likely to fail than a shorter one.

Finally, Fig. 10 illustrates the effect of the aspect ratio l/h_f on the stress intensity factors at the free edges of the film. It can be seen that as l/h_f increases, the Mode II stress intensity factor decreases. This demonstrates that a thinner film will be more unlikely to fail than a thicker one from the edge debonding perspective.

6 Some Concluding Remarks

Based on the analysis and the results presented in this study, one may make the following observations regarding the contact mechanics of thin films on graded media.

- Thin films, stiffeners, or cover plates bonded to graded substrates exhibit square-root singularity near the free edges and may cause edge debonding.
- The interfacial shear stress is symmetric (i.e., $\sigma_{xy}^f(t,0)=-\sigma_{xy}^f(-t,0)$) and self-equilibrating.
- The normal stress in the film is symmetric and a monotonically decreasing function of the axial coordinate x. It attains a maximum at the midsection of the film, which may lead to cracking at its midsection from the mechanics perspective.
- The stress intensity factor decreases as the aspect ratio l/h_f increases and as the substrate-to-film stiffness ratio λ increases.
- As the substrate-to-film stiffness ratio λ increases, grading the material properties of the substrate helps to decrease the film stresses and the stress intensity factors at the free edges for lower values of the parameter λ. However, as λ becomes larger, the effect of material property grading on the stress intensity factor is not visible.
- An increase in the nonhomogeneity parameter γa lowers the normal stresses at the midsection where it is most likely to crack.

Acknowledgment

This study was supported by the Scientific and Technical Research Council of Turkey (TUBITAK) under Research Grant No. MAG-107M053. The author is grateful to Dr. F. Erdogan and Dr. S. Dag for helpful discussions during the formulation phase of this work.

Appendix

Functions Appearing in the Integral Equations

$$k_{11}(t,x)=-\frac{4}{\kappa_s+1}\int_0^\infty \Phi_{11}(\alpha)\sin\alpha(t-x)d\alpha \tag{A1a}$$

$$k_{12}(t,x)=-\frac{4}{\kappa_s+1}\int_0^\infty \Phi_{12}(\alpha)\cos\alpha(t-x)d\alpha \tag{A1b}$$

$$k_{21}(t,x)=-\frac{4}{\kappa_s+1}\int_0^\infty \Phi_{21}(\alpha)\sin\alpha(t-x)d\alpha \tag{A1c}$$

$$k_{22}(t,x)=-\frac{4}{\kappa_s+1}\int_0^\infty \Phi_{22}(\alpha)\cos\alpha(t-x)d\alpha \tag{A1d}$$

$$\Phi_{11}(\alpha)=-\frac{\alpha(\kappa_s-1)}{\Delta_0}(\overline{Z_2}+Z_2)-\frac{\kappa_s+1}{4} \tag{A2a}$$

$$\Phi_{12}(\alpha)=\frac{i\alpha}{\Delta_0}(-\overline{Z_1}+Z_1)+\frac{\kappa_s-1}{4} \tag{A2b}$$

$$\Phi_{21}(\alpha)=-\frac{\alpha}{\Delta_0}(A_1\overline{Z_1}+\overline{A_1}Z_1)-\frac{\kappa_s+1}{4} \tag{A2c}$$

$$\Phi_{22}(\alpha)=-\frac{i\alpha(\kappa_s-1)}{\Delta_0}(A_1\overline{Z_2}-\overline{A_1}Z_2)-\frac{\kappa_s-1}{4} \tag{A2d}$$

$$Z_1=(3-\kappa_s)i\alpha A_1+(\kappa_s+1)n_1 \tag{A3a}$$

$$Z_2=n_1A_1+i\alpha \tag{A3b}$$

$$\Delta_0=-(Z_1\overline{Z_2}+Z_2\overline{Z_1}) \tag{A3c}$$

$$A_j(\alpha)=-\frac{(\kappa_s+1)(n_j^2+\gamma n_j)-(\kappa_s-1)\alpha^2}{i\alpha[2n_j+\gamma(3-\kappa_s)]},\quad j=1,\ldots,4 \tag{A4}$$

$$n_1=\frac{1}{2}(-\gamma+\sqrt{\gamma^2+4(\alpha^2+i|\alpha||\gamma|\delta)}) \tag{A5}$$

$$n_2=\frac{1}{2}(-\gamma-\sqrt{\gamma^2+4(\alpha^2+i|\alpha||\gamma|\delta)}) \tag{A6}$$

$$n_3=\frac{1}{2}(-\gamma+\sqrt{\gamma^2+4(\alpha^2-i|\alpha||\gamma|\delta)}) \tag{A7}$$

$$n_4=\frac{1}{2}(-\gamma-\sqrt{\gamma^2+4(\alpha^2-i|\alpha||\gamma|\delta)}) \tag{A8}$$

$$\delta^2=\frac{3-\kappa_s}{\kappa_s+1} \tag{A9}$$

Solution of the Problem for Homogeneous Materials

Inextensible Membrane. For homogeneous materials, the kernel $k_{21}(x,t)$ is zero and as $\mu_1\to\infty$, from Eq. (15), we have $\lambda=0$. Therefore, Eq. (23) reduces to

$$\frac{1}{\pi}\int_{-1}^{1}\sum_0^\infty a_n\frac{T_n(s)}{(s-r)\sqrt{1-s^2}}ds=1,\quad -1<r<1 \tag{A10}$$

Using the properties of Chebychev polynomials, we have

$$\sum_{1}^{\infty} a_n U_{n-1}(s) = 1 \tag{A11}$$

Expanding the right hand side of Eq. (A11) into Chebychev polynomials of the second kind,

$$\sum_{1}^{\infty} a_n U_{n-1}(s) = 1 = a_1 U_0(s) + a_2 U_1(s) + \cdots \tag{A12}$$

where

$$U_0(s) = 1, \quad U_1(s) = \frac{\sin 2\theta}{\sin \theta} = 2\cos\theta = 2s \tag{A13}$$

Therefore,

$$a_1 = 1, \quad a_2 = 0, \quad \cdots \tag{A14}$$

From Eq. (22),

$$\phi(s) = a_1 T_1(s) = T_1(s) \tag{A15}$$

where

$$T_1(s) = s \tag{A16}$$

Therefore, the interfacial shear stress and the stress intensity factor at $x=-a$ become

$$\sigma_{xy}^{f}(x) = -\frac{4\mu_s \varepsilon_0}{\kappa_s + 1} \frac{x/a}{\sqrt{1 - \left(\frac{x}{a}\right)^2}} \tag{A17}$$

$$k_2 = \lim_{x \to -a} \sqrt{2(x+a)}\, \sigma_{xy}^{s}(x,0) = p_1 \sqrt{a} \tag{A18}$$

where p_1 is given in Eq. (17*e*).

The normal stresses in the film can be found from

$$\sigma_{xx}^{f}(x,0) = \frac{1}{h(x)} \int_{-a}^{x} f(t)dt = \frac{4\mu_s \varepsilon_0}{\kappa_s + 1} \frac{a}{h_f} \sqrt{1 - (x/a)^2} \tag{A19}$$

Extensible Membrane. For homogeneous materials, the kernel $k_{21}(x,t)$ in the integral equation (23) is zero. In this case, the membrane is extensible, i.e., $\lambda \neq 0$. Therefore, Eq. (23) reduces to

$$\frac{1}{\pi} \int_{-1}^{1} \sum_{0}^{\infty} a_n \frac{T_n(s)}{(s-r)\sqrt{1-s^2}} ds - \frac{\lambda}{2} \frac{a}{H(r)} \int_{-1}^{r} \sum_{0}^{\infty} a_n \frac{T_n(s)}{\sqrt{1-s^2}} ds = 1, \quad -1 < r < 1 \tag{A20}$$

Using the properties of Chebychev polynomials (Eqs. (26) and (27)), we have

$$\sum_{1}^{\infty} a_n \left[U_{n-1}(r) + \frac{\lambda}{2n} \frac{a}{H(r)} U_{n-1}(r) \sqrt{1-r^2} \right] = 1 \tag{A21}$$

Therefore, the interfacial shear stress becomes

$$\sigma_{xy}^{f}(r) = -\frac{4\mu_2 \varepsilon_0}{\kappa_2 + 1} \sum_{1}^{N} a_n \frac{T_n(r)}{\sqrt{1-r^2}}, \quad -1 < r < 1 \tag{A22}$$

References

[1] Miyamoto, M., Kaysser, W. A., Rabin, B. H., Kawasaki, A., and Ford, R. G., eds., 1999, *Functionally Graded Materials: Design, Processing and Applications*, Kluwer Academic, Norwell, MA.

[2] Suresh, S., and Mortensen, A., 1998, *Fundamentals of Functionally Graded Materials*, IOM Communications, London.

[3] Booker, J. R., Balaam, N. P., and Davis, E. H., 1985, "The Behavior of an Elastic Nonhomogeneous Half Space. Part I: Line and Point Loads. Part II: Circular and Strip Footings," Int. J. Numer. Analyt. Meth. Geomech., **9**, pp. 353–381.

[4] Giannakopoulos, A., and Suresh, S., 1997, "Indentation of Solids With Gradients in Elastic Properties: Part I. Point Force Solution. Part II. Axisymmetric Indenters," Int. J. Solids Struct., **34**, pp. 2357–2428.

[5] Suresh, S., Giannakopoulos, A. E., and Alcala, J., 1997, "Spherical Indentation of Compositionally Graded Materials: Theory and Experiments," Acta Mater., **45**, pp. 1307–1321.

[6] Suresh, S., Olsson, M., Giannakopoulos, A. E., Padture, N. P., and Jitcharoen, J., 1999, "Engineering the Resistance to Sliding-Contact Damage Through Controlled Gradients in Elastic Properties at Contact Surfaces," Acta Mater., **47**, pp. 3915–3926.

[7] El-Borgi, S., Abdelmoula, R., and Keer, L., 2006, "A Receding Contact Plane Problem Between a Functionally Graded Layer and a Homogeneous Substrate," Int. J. Solids Struct., **43**, pp. 658–674.

[8] Ke, L.-L., and Wang, Y.-S., 2006, "Two-Dimensional Contact Mechanics of Functionally Graded Materials With Arbitrary Spatial Variations of Material Properties," Int. J. Solids Struct., **43**, pp. 5779–5798.

[9] Ke, L.-L., and Wang, Y.-S., 2007, "Two-Dimensional Sliding Frictional Contact of Functionally Graded Materials," Eur. J. Mech. A/Solids, **26**, pp. 171–188.

[10] Ke, L.-L., and Wang, Y.-S., 2007, "Fretting Contact With Finite Friction of a Functionally Graded Coating With Arbitrarily Varying Elastic Modulus. Part 1: Normal Loading. Part 2: Tangential Loading," J. Strain Anal. Eng. Des., **42**, pp. 293—312.

[11] Zhang, X. C., Xu, B. S., Wang, H. D., Wu, Y. X., and Jiang, Y., 2007, "Hertzian Contact Response of Single-Layer, Functionally Graded and Sandwich Coatings," Mater. Des., **28**, pp. 47—54.

[12] Watremetz, B., Baietto-Dubourg, M. C., and Lubrecht, A. A., 2007, "2D Thermo-Mechanical Contact Simulations in a Functionally Graded Material: A multigrid-Based Approach," Tribol. Int., **40**, pp. 754—762.

[13] Choi, H. C., and Paulino, G. H., 2008, "Thermoelastic Contact Mechanics for a Flat Punch Sliding Over a Graded Coating/Substrate System With Frictional Heat Generation," J. Mech. Phys. Solids, **56**(4), pp. 1673–1692.

[14] Dag, S., and Erdogan, F., 2002, "A Surface Crack in a Graded Medium Loaded by a Sliding Rigid Stamp," Eng. Fract. Mech., **69**, pp. 1729–1751.

[15] Guler, M. A., and Erdogan, F., 2004, "Contact Mechanics of Graded Coatings," Int. J. Solids Struct., **41**, pp. 3865–3889.

[16] Guler, M. A., and Erdogan, F., 2006, "Contact Mechanics of Two Deformable Elastic Solids With Graded Coatings," Mech. Mater., **38**, pp. 633–647.

[17] Guler, M. A., and Erdogan, F., 2007, "The Frictional Sliding Contact Problems of Rigid Parabolic and Cylindrical Stamps on Graded Coatings," Int. J. Mech. Sci., **49**(2), pp. 161–182.

[18] Freund, L. B., and Suresh, S., 2004, *Thin Film Materials; Stress, Defect Formation and Surface Evolution*, Cambridge University Press, Cambridge, UK.

[19] Akisanya, A. R., and Fleck, N. A., 1994, "The Edge Cracking and Decohesion of Thin Films," Int. J. Solids Struct., **31**(23), pp. 3175–3199.

[20] Yu, H. H., He, M. Y., and Hutchinson, J. W., 2001, "Edge Effects in Thin Film Delamination," Acta Mater., **49**, pp. 93–107.

[21] Erdogan, F., and Gupta, G. D., 1971, "The Problem of an Elastic Stiffener Bonded to a Half Plane," ASME J. Appl. Mech., **38**(4), pp. 937–941.

[22] Hein, V. L., and Erdogan, F., 1971, "Stress Singularities in a Two-Material Wedge," Int. J. Fract. Mech., **7**(3), pp. 317–330.

[23] Bogy, D. B., 1970, "On the Problem of Edge-Bonded Elastic Quarter-Planes Loaded at the Boundary," Int. J. Solids Struct., **6**, pp. 1287–1313.

[24] Erdogan, F., and Joseph, P. F., 1990, "Mechanical Modeling of Multilayered Films on an Elastic Substrate—Part I: Analysis," ASME J. Electron. Packag., **112**, pp. 309–316.

[25] Erdogan, F., and Joseph, P. F., 1990, "Mechanical Modeling of Multilayered Films on an Elastic Substrate—Part II: Results and Discussion," ASME J. Electron. Packag., **112**, pp. 317–326.

[26] Saif, M. T. A., Hui, C. Y., and Zehdner, A. T., 1993, "Interface Shear Stresses Induced by Non-Uniform Heating of a Film on a Substrate," Thin Solid Films, **224**, pp. 159–167.

[27] Tilscher, M., Munz, D., and Yang, Y. Y., 1995, "The Stress Intensity Factor in Bonded Quarter Planes After a Change in Temperature," J. Adhes., **49**, pp. 1–21.

[28] Akisanya, A. R., and Fleck, N. A., 1997, "Interfacial Cracking From the Freeedge of a Long Bi-Material Strip," Int. J. Solids Struct., **34**(13), pp. 1645–1665.

[29] Jiang, Z. Q., Huang, Y., and Chandra, A., 1997, "Thermal Stresses in Layered Electronic Assemblies," ASME J. Electron. Packag., **119**, pp. 127–132.

[30] Shield, T. W., and Kim, K. S., 1992, "Beam Theory Models for Thin Film Segments Cohesively Bonded to an Elastic Half Space," Int. J. Solids Struct., **29**(9), pp. 1085–1103.

[31] Alaca, B. E., Saif, M. T. A., and Sehitoglu, H., 2002, "On the Interface Debond at the Edge of a Thin Film on a Thick Substrate," Acta Mater., **50**, pp. 1197–1209.

[32] Takahashi, M., and Shibuya, Y., 2003, "Thermoelastic Analysis of Interfacial Stress and Stress Singularity Between a Thin Film and Its Substrate," J. Therm. Stresses, **26**(10), pp. 963—976.

[33] Guler, M. A., Erdogan, F., and Dag, S., 2008, "Modeling of Thin Films and Cover Plates Bonded to Graded Substrates," *Proceedings of the Multiscale and Functionally Graded Materials Conference 2006*, Honolulu, HI, G. H. Paulino, M.-J. Pindera, R. H. Dodds, Jr., F. A. Rochinha, E. V. Dave, and L. Chen, eds., American Institute of Physics, **978**, pp. 790–795.

[34] Erdogan, F., and Gupta, G. D., 1972, "On the Numerical Solution of Singular Integral Equations," Q. Appl. Math., **29**, pp. 525–534.

Delamination of Compressively Stressed Orthotropic Functionally Graded Material Coatings Under Thermal Loading

Bora Yıldırım[1]
Mechanical Engineering Department,
Hacettepe University,
06800 Ankara, Turkey
e-mail: boray@hacettepe.edu.tr

Suphi Yılmaz
Aselsan Inc.,
06172 Ankara, Turkey

Suat Kadıoğlu
Mechanical Engineering Department,
Middle East Technical University,
06531 Ankara, Turkey

The objective of this study is to investigate a particular type of crack problem in a layered structure consisting of a substrate, a bond coat, and an orthotropic functionally graded material coating. There is an internal crack in the orthotropic coating layer. It is parallel to the coating bond-coat interface and perpendicular to the material gradation of the coating. The position of the crack inside the coating is kept as a variable. Hence, the case of interface crack is also addressed. The top and bottom surfaces of the three layer structure are subjected to different temperatures and a two-dimensional steady-state temperature distribution develops. The case of compressively stressed coating is considered. Under this condition, buckling can occur, the crack can propagate, and the coating is prone to delamination. To predict the onset of delamination, one needs to know the fracture mechanics parameters, namely, Mode I and Mode II stress intensity factors and energy release rates. Hence, temperature distributions and fracture parameters are calculated by using finite element method and displacement correlation technique. Results of this study present the effects of boundary conditions, geometric parameters (crack length and crack position), and the type of gradation on fracture parameters.
[DOI: 10.1115/1.2936239]

Keywords: orthotropic FGM, buckling, displacement correlation technique, stress intensity factor, thermal barrier coating

1 Introduction

Since their inception about two decades ago, functionally graded materials (FGMs) have found themselves a broad area of applications. These materials have thermomechanical properties, which are varied continuously (graded) in a certain manner so that under severe working conditions (such as exposure to very high temperatures, corrosive environment, sliding contact, etc.) they can fulfill performance requirements, which cannot be met adequately by homogeneous materials or by layered structures consisting of homogeneous layers. The required properties include the capability to withstand high temperatures, high corrosion resistance, low heat conduction, high toughness and stiffness, and wear resistance. For example, by using a composite coating consisting of a ceramic layer on a metal substrate (the main structural component), the substrate can be protected from high temperature. However, using a ceramic coating on a metallic component means bonding dissimilar homogeneous materials, which causes problems such as poor interfacial bonding strength, low toughness, and high thermal stresses due to the mismatch of material properties. As a result, a tendency for cracking and debonding arises. Now, it is generally accepted that when used as thermal barrier coatings (TBCs) or interfacial zones, FGMs can alleviate these problems. The grading of the thermomechanical properties is accomplished by varying the composition of the coating (or the interfacial zone) in the thickness direction.

Fracture mechanics problems associated with FGMs have become very active fields of research. The literature on crack problems for FGMs is extensive (see, for example, Refs. [1,2]). Nonetheless, a particular fracture mechanics problem, which has received relatively less attention, is the delamination of compressively stressed FGM coatings. Compressive stresses can arise in the FGM coating due to the mechanical loads, temperature gradients, or due to a uniform temperature change since the coefficients of thermal expansion for the metal substrate and the FGM coating are different. In the presence of a crack (or a sufficiently weak zone) at the interface or within the coating parallel to the interface, these residual stresses can cause buckling along the crack face, which can lead to crack propagation, delamination of the coating, and ultimately spallation. The problem described above was considered by Bao and Cai [3]. They simplified the analysis by studying a two-layer (FGM coating and substrate) structure under plane strain. Materials were assumed to be linear elastic and isotropic. The use of a power law variation for thermomechanical properties of FGM was justified. They used the split beam approach supplemented with finite element calculations along with the solution of postbuckling problem for a wide beam to calculate the fracture parameters (energy release rates and phase angles) under uniform temperature change. This approach allows investigation of very long cracks compared to coating thickness. Their results indicate that functional gradation of the coating can significantly reduce the fracture driving force of the delamination crack in buckle-driven delamination cases.

Chiu and Erdogan also considered the buckling driven delamination problem under mechanical [4] and thermal [5] loadings by using analytical and finite element methods. Mechanical loading consisted of a uniform far field compressive strain, whereas thermal loading was a uniform temperature drop. The authors considered only interface cracks. The geometry investigated under mechanical loading was similar to that considered in Ref. [3] and the solution was obtained for plane strain. For the thermal loading case, more realistic structures consisting of a metallic substrate, bond coat, thermally grown oxide layer (TGO), and functionally

[1]Corresponding author.

Contributed by the Applied Mechanics Division for publication in the JOURNAL OF APPLIED MECHANICS. Manuscript received May 30, 2007; final manuscript received September 26, 2007; published online July 11, 2008. Review conducted by Marek-Jerzy Pindera.

graded (or homogeneous) coating were considered. Materials were assumed to be isotropic. The most important feature of both Refs. [4,5] is that the solutions to instability and postbuckling problems were obtained by using kinematically nonlinear continuum elasticity as well as structural mechanics (plate theory) approach. In Ref. [4], the influence of material nonhomogeneity, kinematic nonlinearity, and plate approximation on the critical instability load and on such fracture mechanics parameters as strain energy release rate, stress intensity factors (SIFs) and crack opening displacements was investigated. In Ref. [5], in addition to the above listed factors, the effect of substrate curvature and TGO layer was also addressed.

Sahin and Erdogan [6] also conducted a study where debonding of TBCs was considered. In this study, a three-layer structure (metallic substrate, bond coat, and functionally graded coating) with a crack at the interface of the FGM layer and bond coat was considered. Plane elasticity solution was obtained. Fracture parameters were calculated under specified crack surface tractions, for various material and geometric parameters. However, issues such as compressive stresses in the coating, instability, and postbuckling were not addressed.

In a recent article, El-Borgi et al. [7] considered the problem of an embedded crack in a functionally graded coating, bonded to a homogeneous substrate and subjected to compressive loading. The problem and the solution approach in this article are very similar to that in Ref. [4], and the difference is only due to the location of the crack (embedded versus interface). Hence, the main objective of this article was to study the influence of material nonhomogeneity on the buckling resistance of the graded layer for various crack positions and coating thicknesses.

In all the articles that have been reviewed so far, the materials were taken to be isotropic. It is, however, known that depending on the manufacturing processes, FGM coatings can also be orthotropic with the principal axes of orthotropy parallel and perpendicular to the interface (see, for example, Ref. [8]). In such cases, planes parallel to the interface can also become weak cleavage planes along which cracks can propagate. Interface crack problems for graded orthotropic coating-substrate structures have been considered by some authors.

Two recent examples of such studies are by Dag et al. [9] and Chen [10], respectively. In these articles, both the coating and the substrate were modeled as orthotropic materials. In Ref. [9], different types of mechanical loadings were considered, whereas in Ref. [10] thermal SIFs were calculated after solving the steady-state conduction problem. In both articles, analytical and numerical methods were employed to solve linear (thermo) elasticity problems. Hence, instability, postbuckling, and buckling driven delamination issues were not addressed.

The objective of the current study is to model a particular type of crack problem in a layered structure consisting of an isotropic substrate (nickel-based superalloy), an isotropic bond coat (NiCrAlZr), and an orthotropic FGM coating in order to investigate the effects of geometric parameters and the type of gradation on fracture parameters.

The crack is perpendicular to material gradation of the coating and its position is taken as a variable (see Fig. 1). Thermal loading arises from steady-state heat flow, which is implemented by specifying different temperatures at the top (coating) and bottom (substrate) surfaces. Lateral surfaces are insulated. A two-dimensional finite element model of an internal crack in the orthotropic layer or an interface crack is prepared using the ANSYS finite element software. In the calculation of Mode I and Mode II SIFs displacement correlation technique (DCT) is used. Having given a short review of relevant literature and the scope of this study, the rest of this article is organized as follows. In Sec. 2, a brief description of DCT is provided. In Sec. 3, some details of the finite element modeling are explained. Sample results from Ref. [9] are also provided for comparison with our results, thereby verifying the employed finite element procedures. Sec. 4 includes the original results of this study and their discussion, while Sec. 5 provides conclusions.

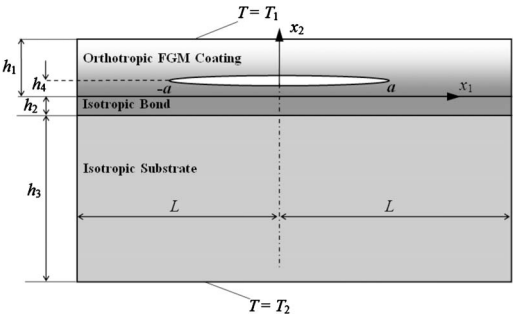

Fig. 1 The geometry of the embedded crack problem

2 Displacement Correlation Technique

There are several techniques used to determine SIFs through finite element calculations. For example, DCT, virtual crack extension, modified crack closure method and J-integral method can be cited. Of these methods, DCT is a direct approach through which SIFs are found by using the displacement values from the finite element solution. The other methods are referred to as energy approaches. Although energy approaches are more accurate, direct approaches, which are relatively simple have been widely employed in the SIF calculations.

In the two-dimensional thermal large deformation problem considered here, SIFs are determined by employing DCT. The displacement field of the coating-substrate system is found by using ANSYS finite element software. In DCT, one substitutes the displacement results from the finite element analysis into the asymptotic expressions at the crack tip. In the model of the crack region, the elements around the crack tip should be quadratic. For an accurate numerical solution of a fracture problem, it is advantageous to use elements, which directly model the $1/\sqrt{r}$ near tip elastic strain field singularity. The most convenient way of introducing this strain field singularity into a quadratic isoparametric element is by manipulation of the midside node positions. The desired strain singularity can be obtained by moving midside nodes to the quarter-point position off the crack tip node. The details on the formulation of these elements can be found in Ref. [11].

In this study, the crack is taken to be either embedded in the orthotropic FGM coating or on the interface. To see the application of DCT in orthotropic media and the comparison of results obtained through this method versus other methods, one can refer to Refs. [8,12].

2.1 Crack Tip Fields in Orthotropic FGMs. For a general anisotropic material, the stress-strain relationships are given as follows:

$$\begin{pmatrix} \varepsilon_1 \\ \varepsilon_2 \\ \varepsilon_3 \\ \varepsilon_4 \\ \varepsilon_5 \\ \varepsilon_6 \end{pmatrix} = \begin{pmatrix} C_{11} & C_{12} & C_{13} & C_{14} & C_{15} & C_{16} \\ & C_{22} & C_{23} & C_{24} & C_{25} & C_{26} \\ & & C_{33} & C_{34} & C_{35} & C_{36} \\ & & & C_{44} & C_{45} & C_{46} \\ & & & & C_{55} & C_{56} \\ & \text{sym} & & & & C_{66} \end{pmatrix} \begin{pmatrix} \sigma_1 \\ \sigma_2 \\ \sigma_3 \\ \sigma_4 \\ \sigma_5 \\ \sigma_6 \end{pmatrix} \tag{1}$$

where

$$\sigma_1 = \sigma_{11}, \quad \sigma_2 = \sigma_{22}, \quad \sigma_3 = \sigma_{33}, \quad \sigma_4 = \tau_{23}, \quad \sigma_5 = \tau_{13}, \quad \sigma_6 = \tau_{12} \tag{2}$$

$$\varepsilon_1 = \varepsilon_{11}, \quad \varepsilon_2 = \varepsilon_{22}, \quad \varepsilon_3 = \varepsilon_{33},$$

$$\varepsilon_4 = 2\varepsilon_{23}, \quad \varepsilon_5 = 2\varepsilon_{13}, \quad \varepsilon_6 = 2\varepsilon_{12} \tag{3}$$

For an orthotropic material, whose principal planes of orthotropy are orthogonal to x_1, x_2, x_3 coordinates, Eq. (1) reduces to [13]

$$\varepsilon_{11} = C_{11} \cdot \sigma_{11} + C_{12} \cdot \sigma_{22} + C_{13} \cdot \sigma_{33} \tag{4}$$

$$\varepsilon_{22} = C_{12} \cdot \sigma_{11} + C_{22} \cdot \sigma_{22} + C_{23} \cdot \sigma_{33} \tag{5}$$

$$\varepsilon_{33} = C_{13} \cdot \sigma_{11} + C_{23} \cdot \sigma_{22} + C_{33} \cdot \sigma_{33} \tag{6}$$

$$\gamma_{23} = C_{44} \cdot \tau_{23} \tag{7}$$

$$\gamma_{13} = C_{55} \cdot \tau_{13} \tag{8}$$

$$\gamma_{12} = C_{66} \cdot \tau_{12} \tag{9}$$

In order to calculate the SIFs, the crack tip fields in an orthotropic material are required. In the problem under consideration, the crack is assumed to be parallel to x_1. Necessary expressions are given in Ref. [12] and duplicated here (with some changes in the notation) for the convenience of the reader. Note that these equations are valid when the crack tip coordinates and material coordinates coincide.

$$K_{\mathrm{I}} = \frac{\sqrt{2\pi}}{4} \cdot \frac{1}{\sqrt{S_{22}} \cdot D_0} \cdot \frac{\Delta u_2}{\sqrt{r}} \tag{10}$$

$$K_{\mathrm{II}} = \frac{\sqrt{2\pi}}{4} \cdot \frac{1}{\sqrt{S_{11}} \cdot D_0} \cdot \frac{\Delta u_1}{\sqrt{r}} \tag{11}$$

$$K_{\mathrm{III}} = \frac{1}{4 \cdot \sqrt{S_{44} \cdot S_{55} - S_{45}}} \cdot \sqrt{\frac{2\pi}{r}} \cdot \Delta u_3 \tag{12}$$

where $\Delta u_i = u(r,\pi) - u(r,-\pi)$, $(i = 1,2,3)$ are the displacement jumps along the crack faces in the neighborhood of the crack tip [12], the term D_o is defined as

$$D_o = [2 \cdot \sqrt{S_{11} \cdot S_{22}} + 2S_{12} + S_{66}]^{1/2} \tag{13}$$

and S_{ij} terms are derived from compliance parameters for plane strain case

$$S_{ij} = C_{ij} - \frac{C_{i3} \cdot C_{3j}}{C_{33}} \tag{14}$$

2.2 Calculation of Mode I and Mode II Stress Intensity Factors. The crack opening model is given in Fig. 2. The nodes are located by their (r, θ) coordinates with respect to the crack tip. For the upper crack face $\theta > 0$ and for the lower crack face $\theta < 0$. In the calculation of K_I, displacements in the x_2-direction are used. Substituting the values of these displacements obtained from the finite element solution into Eq. (10) and taking $\theta = \pi$ for the upper and $\theta = -\pi$ for the lower side of the crack, one obtains

$$K_{\mathrm{I}} = \frac{\sqrt{2\pi}}{4} \cdot \frac{1}{\sqrt{S_{22}} \cdot D_o} \cdot \left(\lim_{r \to 0} \frac{U_2(r,\pi) - U_2(r,-\pi)}{\sqrt{r}} \right) \tag{15}$$

Assuming the part of Eq. (15) whose limit is being taken is linear in r, one can write

$$\frac{U_2(r,\pi) - U_2(r,-\pi)}{\sqrt{r}} = Ar + B \tag{16}$$

Then

$$r = R_2 \rightarrow \frac{U_2(R_2,\pi) - U_2(R_2,-\pi)}{\sqrt{R_2}} = \frac{U_{22} - U_{24}}{\sqrt{R_2}} = AR_2 + B \tag{17}$$

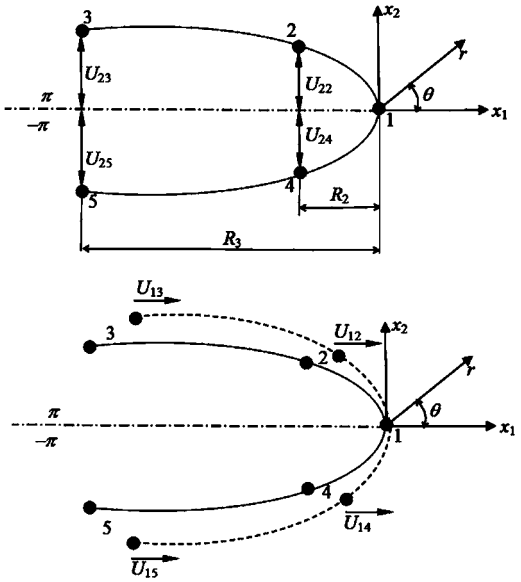

Fig. 2 Nodal displacements in x_2 and x_1 directions near the crack tip

$$r = R_3 \rightarrow \frac{U_2(R_3,\pi) - U_2(R_3,-\pi)}{\sqrt{R_3}} = \frac{U_{23} - U_{25}}{\sqrt{R_3}} = AR_3 + B \tag{18}$$

As r approaches zero, the left-hand side of Eq. (16) becomes equal to B. Then B can be calculated from Eqs. (17) and (18) as

$$B = \frac{(U_{22} - U_{24}) \cdot R_3^{3/2} - (U_{23} - U_{25}) \cdot R_2^{3/2}}{\sqrt{R_2 \cdot R_3} \cdot (R_3 - R_2)} \tag{19}$$

The elements at the crack tip are modeled such that $R_3 = 4R_2$. Using this relation and then combining Eqs. (15) and (19), K_I is written in terms of the nodal displacements.

$$K_{\mathrm{I}} = \frac{\sqrt{2\pi}}{24} \cdot \frac{1}{\sqrt{S_{22}} \cdot D_0} \cdot \left[\frac{8 \cdot (U_{22} - U_{24}) - (U_{23} - U_{25})}{\sqrt{R_2}} \right] \tag{20}$$

The derivation of K_{II} follows basically the same steps. Displacements in the x_1-direction are used. Following the same procedure, one obtains

$$K_{\mathrm{II}} = \frac{\sqrt{2 \cdot \pi}}{24} \cdot \frac{1}{\sqrt{S_{11}} \cdot D_o} \cdot \left[\frac{8 \cdot (U_{12} - U_{14}) - (U_{13} - U_{15})}{\sqrt{R_2}} \right] \tag{21}$$

Equations (20) and (21) are also valid for isotropic materials when appropriate values of compliances are used to calculate S_{11}, S_{22}, and D_0.

2.3 Calculation of Energy Release Rate. The strain energy release rate for cracks between dissimilar orthotropic materials is given as [14]

$$G = \frac{H_{11}\left(\frac{H_{22}}{H_{11}} K_{\mathrm{I}}^2 + K_{\mathrm{II}}^2 \right)}{4 \cosh^2 \pi\varepsilon} \tag{22}$$

For a crack at bimaterial interface between two dissimilar materials, ε is defined as

$$\varepsilon = \frac{1}{2\pi} \ln\left(\frac{1-\beta}{1+\beta} \right) \tag{23}$$

where

$$\beta = \frac{\lfloor \sqrt{S_{11}S_{22}} + S_{12} \rfloor_2 - \lfloor \sqrt{S_{11}S_{22}} + S_{12} \rfloor_1}{\sqrt{H_{11}H_{22}}} \tag{24}$$

H_{11} and H_{22} terms are given as

$$H_{11} = [2n\lambda^{1/4}\sqrt{S_{11}S_{22}}]_1 + [2n\lambda^{1/4}\sqrt{S_{11}S_{22}}]_2 \tag{25}$$

$$H_{22} = [2n\lambda^{-1/4}\sqrt{S_{11}S_{22}}]_1 + [2n\lambda^{-1/4}\sqrt{S_{11}S_{22}}]_2 \tag{26}$$

with n and λ given by

$$n = \sqrt{(1+\rho)/2} \tag{27}$$

$$\lambda = \frac{S_{11}}{S_{22}} \tag{28}$$

where

$$\rho = \frac{2S_{12} + S_{66}}{2\sqrt{S_{11}S_{22}}} \tag{29}$$

In our problem, at the interface of the FGM coating and the bond coat, material properties are assumed to be the same. Hence, both β and ε are equal to zero not only for a crack embedded in the FGM coating but for an interface crack as well. Then, energy release rate can be obtained from

$$G = \frac{H_{22}K_I^2 + H_{11}K_{II}^2}{4} \tag{30}$$

3 Finite Element Analysis of the Problem

In order to calculate the fracture parameters, the displacement field of the problem is obtained using the ANSYS finite element analysis software. For the problem under consideration, the loading is the temperature difference ΔT between the upper and lower surfaces of the layered structure. Because of the variation in the thermal expansion coefficients and the temperature gradient, compressive stresses develop in the FGM layer. In the presence of an internal or an interface crack, these stresses can cause a "buckled" shape along the upper crack face. When the vertical displacement of the midpoint of the upper crack surface is taken as the response of the structure to this loading, it is evident that the load versus displacement relationship is not linear.

The nonlinear response can take two distinct forms. For a perfect system (which corresponds to a FGM layer, which remains perfectly flat during loading), a typical buckling (bifurcation) problem is obtained. On the other hand, when there is an imperfection (i.e., initial curvature) the problem becomes a nonlinear large deformation problem. This type of behavior is discussed in Ref. [5]. Although the buckling load can be found with relative ease through a linear analysis, the determination of the postbuckled curve or the deflection curves of the imperfect systems requires a nonlinear analysis. Hence, in the solution of the problem, nonlinear analysis options of ANSYS are invoked.

The solution is obtained by employing a nonlinear static analysis with gradually increasing loads. Fracture mechanics parameters are calculated using nodal displacements near the crack tip. In order to calculate these parameters accurately, region around the crack tip must be modeled carefully. Six node triangular Plane 2 elements are used in the modeling (Fig. 3). Here, midside nodes are placed at the quarter points of the elements around the crack tip.

Since the object of this study is to investigate the effects of position and length of the crack, the same problem must be solved for different values of crack position and layer thicknesses. In order to reduce modeling time, Ansys Parametric Design Language (APDL) is used. APDL is a scripting language that one can use to automate common tasks and build a model in terms of parameters. In particular, the definition of graded orthotropic material properties can only be accomplished with APDL. The variation of the material properties such as conduction coefficient, Young's modulus, and Poisson's ratio is incorporated into the model by defining material properties at the centroid of each element. The calculations of Mode I and Mode II SIFs are done by using the appropriate nodal displacements in Eqs. (20) and (21) also with an APDL code. In the finite element models up to 100,000, elements are used depending on position and length of the crack. The use of more elements in the thickness direction while modeling the FGM layer improves the accuracy. The elements used near the crack tip are singular elements. The radius of singular elements is taken as $a/1000$ and 48 elements are used around the crack tip. A close-up view of the crack tip region is shown in Fig. 4.

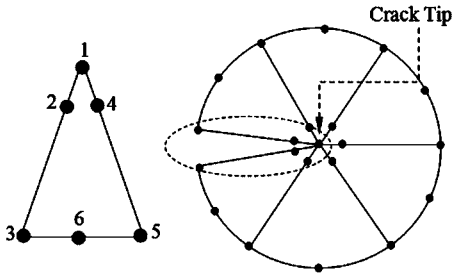

Fig. 3 Plane 2 elements and modeling of crack tip region

3.1 Verification of Finite Element Procedures. To make sure that the results of fracture analyses obtained from the models prepared in ANSYS are correct, a crack problem in the literature [9] is modeled. SIF values from this article are compared with our results calculated by ANSYS and DCT.

In Ref. [9], SIF values are obtained by both analytical and numerical (enriched finite elements) methods. An interface crack problem between a graded orthotropic coating and a homogeneous orthotropic substrate is solved, as discussed in Sec. 1. The crack length is $2a$. The thicknesses of the coating and the substrate are h_1 and h_2, respectively. Pressure is applied to the crack surfaces. Material property variation in the thickness direction is assumed to be exponential. For example, effective Young's modulus is given as $E(x_2)=E_0\exp(\beta x_2)$ where the origin is at the midpoint of the crack. Normalized SIFs are calculated. A comparison of results is given in Table 1. It is observed that the agreement is very good.

4 Results And Discussion

The results of interest in this study are fracture mechanics parameters (Mode I and Mode II SIFs and energy release rate). Geometric parameters, thermal boundary conditions, and material properties used in the calculations are as follows.

4.1 Geometric Parameters. The geometry of the orthotropic FGM coating bonded to an isotropic substrate containing a crack parallel to the interface is shown in Fig. 1. For an interface crack, $h_4=0$. For an embedded crack, $0 \leq h_4/h_1 \leq 1$, and h_4/h_1 is the

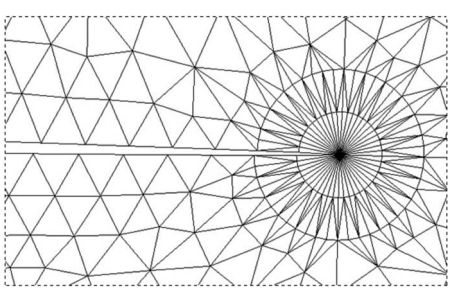

Fig. 4 Close-up view of the crack tip region

Table 1 Mixed mode SIFs for orthotropic interface crack problem, solution with 58073 elements, $h_1/a=1$, $h_2/a=10$

	Analytical Dag et al. [9]		Enriched finite elements Dag et al. [9]		DCT (ANSYS)		% error (DCT)	
βa	Kin	Kiin	Kin	Kiin	Kin	Kiin	Kin	Kiin
−2.00	1.885	−0.449	1.887	−0.449	1.888	−0.449	−0.13	−0.08
−1.00	1.631	−0.285	1.633	−0.285	1.633	−0.285	−0.11	0.13
−0.50	1.520	−0.214	1.522	−0.214	1.520	−0.214	−0.03	−0.10
0.00	1.418	−0.152	1.420	−0.151	1.418	−0.151	−0.01	0.35
0.50	1.326	−0.096	1.328	−0.096	1.326	−0.096	0.00	0.01
1.00	1.244	−0.047	1.246	−0.047	1.243	−0.047	0.04	−0.71
2.00	1.107	0.032	1.109	0.032	1.106	0.032	0.12	0.59

crack position variable. In both cases, a/h_1 is taken as the crack length variable. For sample results, the fixed dimensions are taken as

$$L = 8a, \quad h_1/h_2 = 2, \quad h_3/h_2 = 10 \tag{31}$$

4.2 Thermal Boundary Conditions. The whole structure is initially at the reference temperature T_0. Then the temperature of the upper surface of the coating ($x_2=h_1$) is specified as T_1, while the lower surface of the substrate ($x_2=-(h_2+h_3)$) is kept at $T_2=T_0$. For a given temperature difference ΔT between the top and the bottom surfaces, heat conduction occurs. The input temperatures are

$$T_0 = 293 \text{ K}, \quad T_1 = 1273 \text{ K}, \quad \Delta T_{\max} = T_1 - T_2 = 980 \text{ K} \tag{32}$$

The solution is done by nonlinear analysis with gradually increasing temperature differences between the top and bottom surfaces. In the finite element model, 250 time steps are defined and plots of SIFs and energy release rate are generated by using results calculated at each time step. Since the problem is symmetric about the x_2 axis, half of the problem is modeled. The x_2 axis is the symmetry axis and the lateral surface is taken as thermally insulated.

So far as the thermal boundary conditions on the crack surfaces are concerned, the two extreme cases are perfect conduction (where the temperature and the heat flux are continuous across the crack) and perfect insulation (where the heat flux is zero on both crack faces) [15]. In Ref. [15], it is further stated that actually neither one of these conditions were realistic and the actual temperature boundary conditions on the crack surfaces would depend on the crack opening displacement, the crack surface morphology, and the properties of the gas filling the gap created by the crack.

Yet, to the best of our knowledge, there are not any studies where an attempt has been made to model the heat transfer across the crack faces accurately. A brief literature survey of this topic reveals that either a simple partial insulation model (see, for example, Refs. [15–17]) is employed or more commonly the crack faces are assumed to be completely insulated (see, for example, Refs. [10,18–20]). In the former approach, it is assumed that the crack allows some heat flux which is only a certain percentage of the flux corresponding to the perfect conduction case. To adjust that percentage a parameter k^* (heat conductivity index) is introduced such that $0 \leqslant k^* \leqslant 1$. The limiting values $k^*=0$ and $k^*=1$ represent, respectively, the perfect insulation and perfect conduction along the crack surfaces. With an additional parameter, partial insulation model could produce more realistic results and reveal certain aspects of a problem, such as crack closure, which would not have been otherwise observed. Results in Refs. [15–17] indicate that crack closure is observed for some material types when a certain amount of heat flux across the crack faces is allowed. Hence partial insulation model appears to be most useful for cases where crack closure is involved.

On the other hand, adopting this model makes the problem somewhat more difficult and especially in finite element studies its implementation is not very simple and straightforward. The perfect insulation model is easier to implement in analytical and numerical studies. Judging by its widespread usage, it is probably more realistic compared to perfect conduction case. Furthermore, SIFs calculated for perfect insulation case are reported to be greater than those for partial insulation and perfect conduction cases in at least one study [16], so in similar problems this approach could give conservative results.

In this study, the emphasis is on large deformation behavior rather than crack closure and crack contact phenomena. Furthermore, there are already too many material and geometric parameters to be considered. To keep the number of runs at a reasonable level, some simplifiying assumptions must be made. Hence, a partial insulation model is not adopted but rather the crack faces are assumed to be thermally insulated.

4.3 Material Properties. Material properties used in the sample results are given below for orthotropic coating, bond coat, and isotropic substrate. The superscripts cr, bc, and s stands for the FGM, bond coat, and substrate. For the FGM coating [21],

$$E_i(x_2) = E^{\text{bc}} + (E_i^{\text{cr}} - E^{\text{bc}})(x_2/h_1)^{\gamma_i} \quad (i=1,2) \tag{33}$$

$$\nu_{2i}(x_2) = \nu^{\text{bc}} + (\nu_{2i}^{\text{cr}} - \nu^{\text{bc}})(x_2/h_1)^{\beta_{2i}} \quad (i=1,3) \tag{34}$$

$$\nu_{3i}(x_2) = \nu^{\text{bc}} + (\nu_{3i}^{\text{cr}} - \nu^{\text{bc}})(x_2/h_1)^{\beta_{3i}} \quad (i=1,2) \tag{35}$$

$$G_{12}(x_2) = G^{\text{bc}} + (G_{12}^{\text{cr}} - G^{\text{bc}})(x_2/h_1)^{\gamma_{12}} \tag{36}$$

$$\alpha_i(x_2) = \alpha^{\text{bc}} + (\alpha_i^{\text{cr}} - \alpha^{\text{bc}})(x_2/h_1)^{\delta_i} \quad (i=1,2,3) \tag{37}$$

$$k_i(x_2) = k^{\text{bc}} + (k_i^{\text{cr}} - k^{\text{bc}})(x_2/h_1)^{\omega_i} \quad (i=1,2) \tag{38}$$

Material property variations related to the position are given above and are assumed to be function of x_2. The exponents γ, β, δ, and ω are variables. By changing these variables, metal rich (MR) and ceramic rich (CR) compositions in FGM layer can be obtained. Values of these parameters are given in Table 2. The material properties for ceramic, bond coat, and the substrate are given in Table 3.

In the analyses, first steady-state temperature distribution between the top and bottom surfaces is obtained. Then the thermal solution is used as input for nonlinear mechanics problem. Results are presented in nondimensional form, by using nondimensional normalized SIFS, $\hat{K}_{\text{I}}=K_{\text{I}}/K_0$, $\hat{K}_{\text{II}}=K_{\text{II}}/K_0$, where $K_0=E^s\alpha^s T_0\sqrt{\pi h_3}$ and normalized energy release rate $\hat{G}=G/G_0$, where $G_0=(1-\nu_s^2)K_0^2/E^s$.

In this study, three sets of results are presented. In the first set,

Table 2 Constants of material variation in orthotropic FGM

Material	γ_1	γ_2	γ_{12}	β_{21}	β_{23}	β_{32}	β_{31}	δ_1	δ_2	δ_3	ω_1	ω_2
Metal rich (MR1)	2.5	2.5	2.5	2	2	2	2	1.5	1.5	1.5	1.5	1.5
Metal rich (MR2)	2.5	2.5	2.5	2.5	2.5	2.5	2.5	2.5	2.5	2.5	2.5	2.5
Ceramic rich (CR1)	0.4	0.4	0.4	0.5	0.5	0.5	0.5	0.6	0.6	0.6	0.6	0.6
Ceramic rich (CR2)	0.4	0.4	0.4	0.4	0.4	0.4	0.4	0.4	0.4	0.4	0.4	0.4

the effect of the mechanical boundary condition at the lateral surface on the fracture parameters is investigated for an interface crack. This boundary condition governs the overall deformation response of the structure. In the second set, an interface crack is considered again. The effects of material property variation and crack length on fracture parameters are addressed. In the third set, an embedded crack is considered and its location is varied.

4.4 Effect of Mechanical Boundary Conditions. The fracture parameters depend on the deformation of the coating-substrate structure. Subsequently, the deformation under the given thermal loading depends on the boundary conditions. Two cases are considered in this paper. In both cases, the top and bottom surfaces are taken to be stress free, and there is a crack at the interface. In the first case, the rotation of the lateral surfaces are prevented but the structure is allowed to expand. This is done by coupling the nodes in the x_1 direction at the free end. This boundary condition ensures that the layered structure remains flat during loading (Fig. 5). Consequently, a typical bifurcation problem arises. On the other hand, in the second case, the lateral sides are also taken to be stress free. Then, because of the temperature gradient and the variation of thermal expansion coefficients, the unrestrained structure bows as soon as the temperature changes (Fig. 6). This bowing serves as an imperfection, and no distinct bifurcation point is observed. As the temperature difference ΔT is increased, the crack opens up gradually but in a nonlinear fashion. These two different behaviors are observed in Fig. 7.

In the bifurcation problem, a very small transverse force is applied at the earlier load steps to provide a bias so that the FGM layer buckles upwards rather than toward the substrate. This concentrated crack-face load is applied upwards at the center of the upper crack face only up to a certain time step (corresponding to roughly $\Delta T/T_0=0.8$) and then it is removed. The minimum normalized magnitude of this force P, which is necessary to induce buckling in the correct direction (i.e., upwards) is found to be in the order of $P/(E^s\alpha^s T_0 h_1 a)=1.75\times10^{-7}$. Both the magnitude and the duration of application of the load to obtain buckling in the correct direction have been calculated in the APDL code by trial and error. These values depend on the material properties, magnitude of the thermal loads, and the geometric dimensions considered in the analysis.

If the duration of application and the magnitude of this force are not chosen to be sufficiently large, the coating buckles toward the substrate. In the numerical simulation, if no special precautions are taken, the coating just appears to penetrate into the substrate, which is of course physically impossible. Yet, the SIFS calculated for such a case have the same numerical value but the

Table 3 Material properties

Material property	Ceramic (cr)	Bond Coat (bc)	Substrate (s)
E_1 (GPa)	90.43	137.9	175.8
E_2 (GPa)	116.36	137.9	175.8
G_{12} (GPa)	38.21	54.29	70.32
ν_{21}	0.28	0.27	0.25
ν_{23}	0.27	0.27	0.25
ν_{32}	0.21	0.27	0.25
ν_{31}	0.14	0.27	0.25
α_1 (1/°C)	0.8×10^{-6}	15.16×10^{-6}	13.91×10^{-6}
α_2 (1/°C)	7.5×10^{-6}	15.16×10^{-6}	13.91×10^{-6}
α_3 (1/°C)	9.0×10^{-6}	15.16×10^{-6}	13.91×10^{-6}
k_1 (W/(mK))	21.25	25.0	7.0
k_2 (W/(mK))	29.82	25.0	7.0

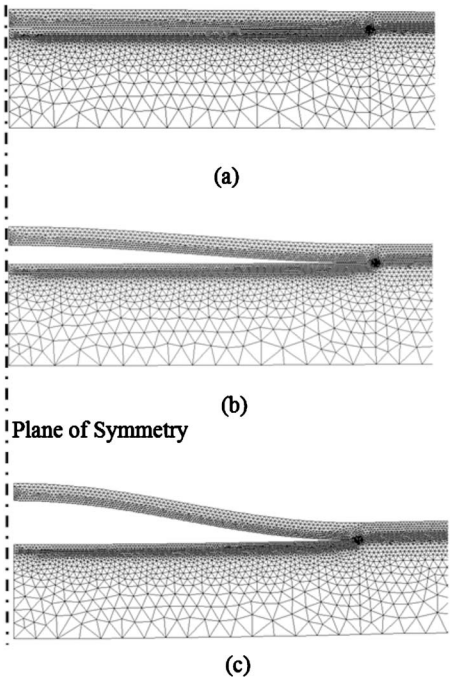

Fig. 5 Deformed mesh of the FGM, bond coat and substrate system (*a*) just before buckling, $\Delta T/T_0=0.8$; (*b*) just after buckling, $\Delta T/T_0=0.88$; (*c*) at maximum temperature difference, $\Delta T/T_0=3.34$ ($a/h_1=20$, MR1 material, true scale, lateral rotation is prevented)

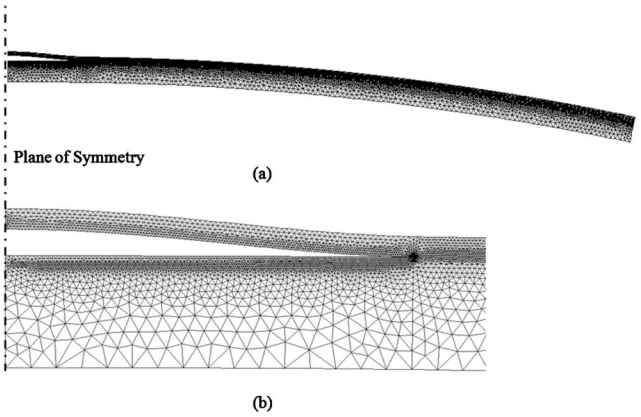

Fig. 6 Deformed shape of the FGM, bond coat and substrate system: (*a*) overall deformation response at maximum temperature difference, $\Delta T/T_0=3.34$; (*b*) close-up view of crack region ($a/h_1=20$ and MR1 material, true scale, lateral rotation is allowed)

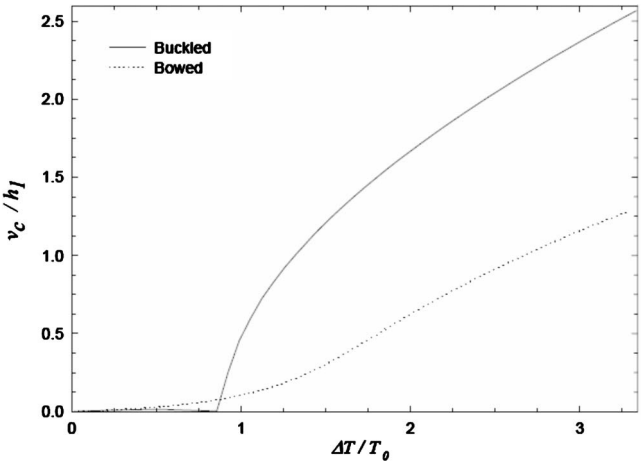

Fig. 7 Displacement of the midpoint of upper crack surface ($a/h_1=20$ and MR1 material)

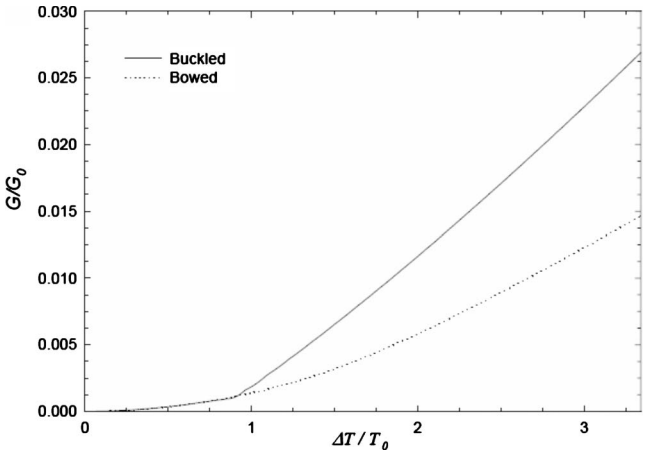

Fig. 9 Normalized strain energy release rates for buckling and bowing cases ($a/h_1=20$ and MR1 material)

opposite sign as the ones obtained from a simulation where the coating buckles upwards with the help of the small biasing force. On the other hand, one can of course model the crack faces with "contact elements," which prevents interpenetration of surfaces and run the simulation without P. Then, even when the coating buckles toward the substrate, the simulation can be continued to predict the subsequent loading-deformation behavior. In this case, partial or complete crack closure would occur and one should also consider the (nonlinear) contact problem. This more complicated problem is not addressed in the scope of this study.

The variations of fracture parameters for buckling and bowing cases are given in Figs. 8 and 9. It is interesting to note that even in the buckling problem, the SIFs and the energy release rate are nonzero prior to buckling due to the thermal stresses around the crack tip. Mode I SIF is nonzero in the bifurcation problem prior to buckling because of the applied crack-face load. This can be inferred from Fig. 7 where a small vertical displacement of mid-crack face (i.e., crack opening) due to this force can be seen at lower $\Delta T/T_0$ values. As one can observe from Fig. 8, the magnitude of resulting K_I is very small up to the bifurcation point for the buckling case. On the other hand, K_{II} is not influenced much neither by this load nor by the free-edge constraint. Magnitudes of K_{II} for buckling and bowing cases are very close to each other up to the bifurcation point. Results produced without applying the vertical point load also supports this conclusion. Since crack closure problem is not in the scope, these results are not presented in this article.

Before the onset of buckling, $K_{II}>0$ indicating that if the material were isotropic the crack would tend to deflect into the substrate, whereas after buckling $K_{II}<0$ indicating that the crack would tend to deflect toward the free surface. It is also observed that energy release rate for the buckling case is greater than that for the bowing case.

For the remaining results, the second type of boundary condition where all the sides are stress free is adopted and the effects of geometric parameters and material properties on fracture mechanics parameters are given for sample cases.

4.5 Interface Crack Problem. Figures 10 and 11 give the normalized Mode I and Mode II SIFs and energy release rate as functions of applied temperature difference, $\Delta T/T_0$, for four different material grading types. In these figures, crack length ratio is kept constant at $a/h_1=20$. For all coating types, it is observed that as $\Delta T/T_0$ increases so does K_I, whereas K_{II} reaches a maximum and starts to decrease. K_I and G curves for different ceramic and metal rich coatings appear to be grouped together and the differences between the MR and CR cases are not very large either. K_I and G values are higher and K_{II} values are lower for MR materials at relatively large temperature changes. At higher temperature differences ($\Delta T/T_0>1.5$), Mode I is dominant. In the next group of results, MR1 is chosen as the material parameter variation and the effect of crack length is investigated. Figures 12 and 13 show the variations of SFFs and energy release rate with respect to applied temperature difference for various values of a/h_1. K_I and G increase as temperature increases for both short and long cracks. However, it interesting to note that, for relatively short cracks, K_{II} increases with increasing temperature but for longer cracks, beyond a certain temperature it starts to decrease.

4.6 Embedded Crack Problem. The problem considered here is the change in the position of the crack in FGM coating and effect of this change on fracture mechanics parameters. Crack location is given by h_4/h_1. Other dimensions and thermal and mechanical boundary conditions are the same as interface crack case. Crack length is taken as $a/h_1=20$. MR1 profile is chosen as the material property variation. Five different crack positions are considered. These are $h_4/h_1=0.00$, 0.10, 0.25, 0.50, and 0.75. Figures 14 and 15 give normalized fracture mechanics parameters as functions of $\Delta T/T_0$ for various crack locations. It is observed that as h_4/h_1 approaches to zero, SIF and energy release rate values approach to those of the interface crack. As the crack gets closer to the free surface, the SFFs and energy release rates decrease.

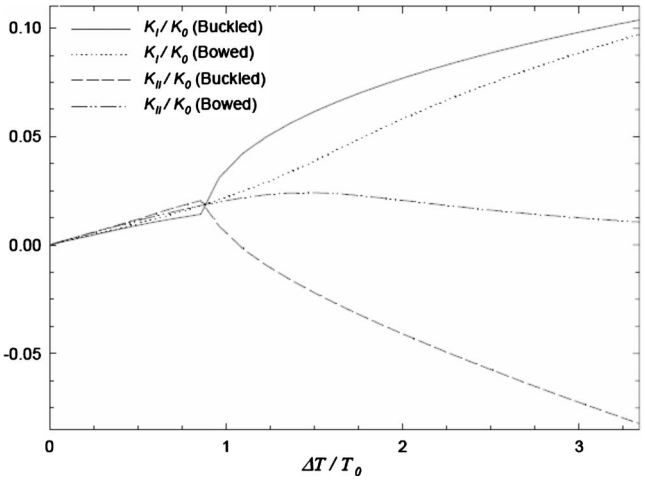

Fig. 8 Normalized SIFs, for buckling and bowing cases ($a/h_1=20$ and MR1 material)

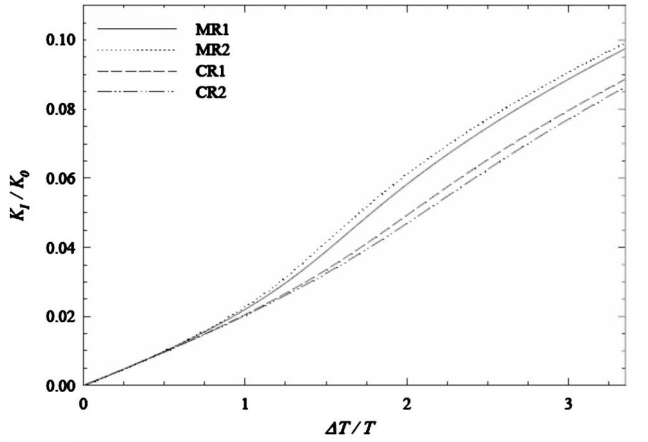

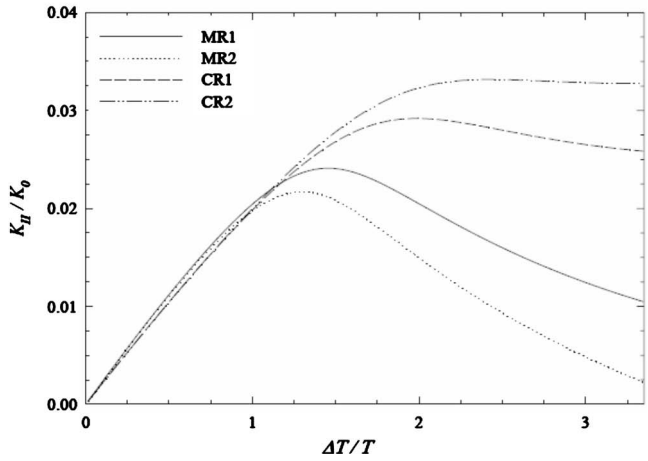

Fig. 10 Normalized Mode I and Mode II SIFs for crack at the bond coat-FGM interface, $a/h_1=20$

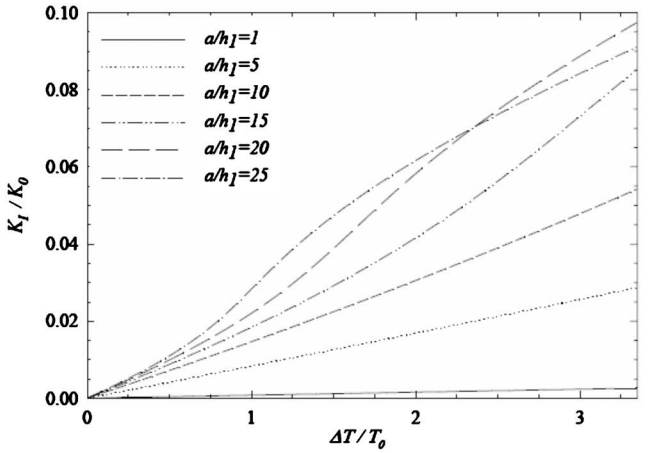

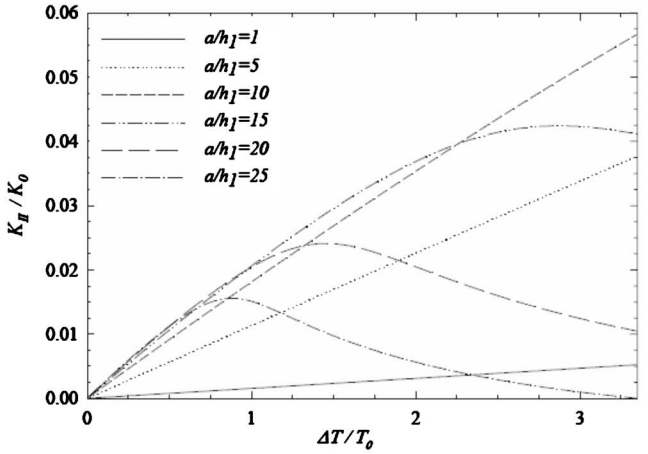

Fig. 12 Normalized Mode I and Mode II SIFs for crack at the bond coat-FGM interface, MR1 material properties for FGM

5 Conclusion

Implementation of the DCT in ANSYS is succesfully used to calculate SIFs and energy release rate for the buckling driven delamination problem of an orthotropic FGM coating-bond coat-substrate structure under thermal loading. Both interface and embedded crack problems are addressed. Case studies are performed by varying boundary conditions, geometric, and material parameters.

The effect of boundary conditions on the overall deformation response of the structure and the effect of this overall response on the fracture parameters is demonstrated. For an unrestrained structure no distinct buckling behavior is observed. If the structure is restrained such that buckling of the coating forming the upper

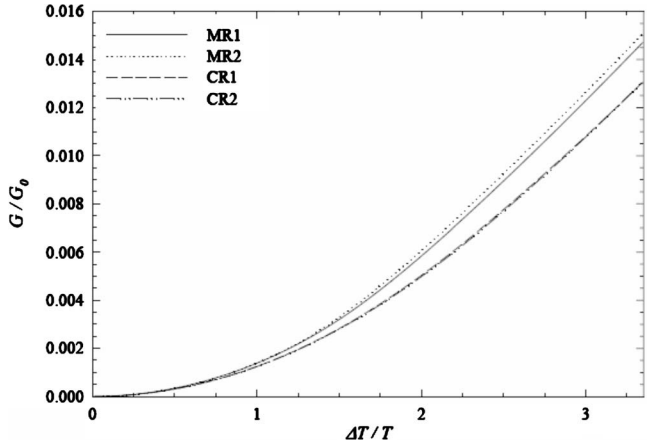

Fig. 11 Normalized energy release rate values for crack at the bond coat-FGM interface, $a/h_1=20$

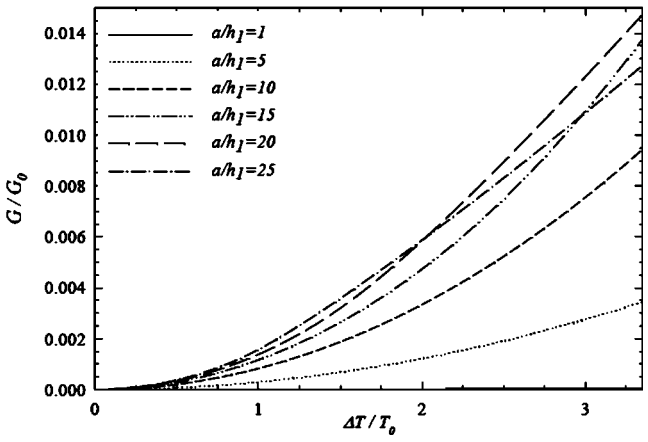

Fig. 13 Normalized energy release rate values for crack at the bond coat-FGM interface, MR1 material properties for FGM

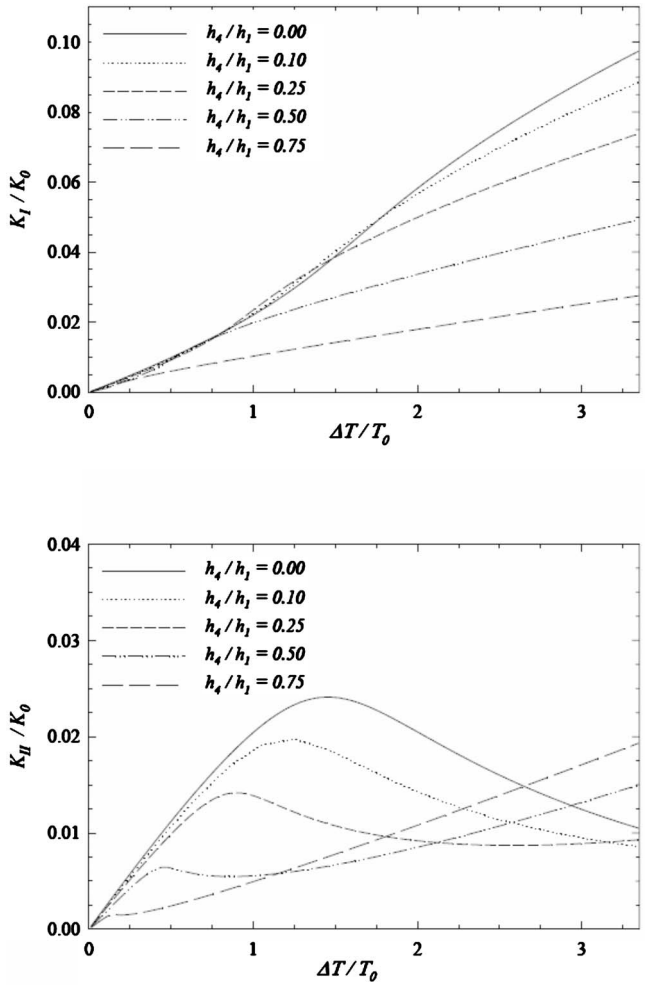

Fig. 14 Normalized Mode I and Mode II SIFs for changing crack heights, $a/h_1=20$ and MR1 material properties

crack face occurs, then higher normal crack opening displacements, Mode I SIFs, and energy release rates are observed.

In the absence of buckling, the whole structure bows and the crack opens. In this case, the fracture parameters are again nonlinear functions of applied temperature difference. For such a loading, it is found that as temperature difference increases, so does energy release rate for all material property profiles and crack lengths. It is also observed that for larger temperature differences and longer crack lengths Mode I becomes dominant.

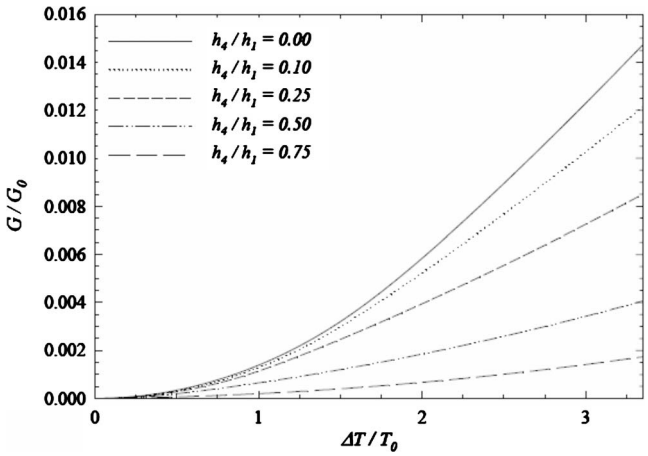

Fig. 15 Normalized energy release rate values for changing crack heights, $a/h_1=20$ and MR1 material properties

As far as the effect of different grading profiles on fracture parameters are concerned, the following observations are made for an interface crack between the bond coat and the functionally graded coating.

- A crack between the bond coat and a MR layer has somewhat greater K_I and G than a crack of the same size between the bond coat and a CR layer for the whole range of applied temperature differences considered in this study.
- A crack between the bond coat and a MR layer has slightly greater K_{II} than a crack of the same size between the bond coat and a CR layer only up to a certain applied temperature difference. Beyond that point, K_{II} for the crack between the bond coat and a CR layer becomes larger.
- K_{II} for an interface crack between the bond coat and a MR layer increases up to a certain applied temperature difference and then it starts to decrease rapidly. This temperature difference depends on the crack size. On the other hand, K_{II} for an interface crack between the bond coat and a CR layer also reaches a maximum but when the temperature difference is further increased, it decreases just slightly.

K_I versus $\Delta T/T_0$ and G versus $\Delta T/T_0$ curves for the different MR coatings considered in this study are rather closely packed. As far as K_{II} versus $\Delta T/T_0$ curves are concerned, a somewhat significant difference is observed only when $\Delta T/T_0$ is large. The same is true also for different CR coatings. From Table 2, one can observe that different metal (or ceramic) rich coatings have been assigned the same grading profile for Young's moduli and modulus of rigidity but different grading profiles for the other material properties. Consequently, among the many grading profile parameters, those governing Young's moduli (γ_1, γ_2) and modulus of rigidity (γ_{12}) seem to have the greatest influence on the fracture parameters. The other parameters (that govern the grading profiles of Poisson ratios, coefficients of thermal expansion and conductivities) seem to have a significant effect only on K_{II} for relatively large crack lengths at large temperature differences.

Finally, it is observed that the energy release rate of an interface crack is greater than that of an embedded crack of the same size.

Acknowledgment

The authors gratefully acknowledge the valuable contributions of Dr. Serkan Dag.

References

[1] Erdogan, F., 1995, "Fracture Mechanics of Functionally Graded Materials," Composites Eng., **5**, pp. 753–770.
[2] Noda, N., 1999, "Thermal Stresses in Functionally Graded Materials," J. Therm. Stresses, **22**, pp. 477–512.
[3] Bao, G., and Cai, H., 1997, "Delamination Cracking in Functionally Graded Coating/Metal Substrate System," Acta Mater., **45**, pp. 1055–1066.
[4] Chiu, T. C., and Erdogan, F., 2003, "Debonding of Graded Coatings Under In-Plane Compression," Int. J. Solids Struct., **40**, pp. 7155–7179.
[5] Erdogan, F., and Chiu, T. C., 2003, "Plane Strain and Axisymmetric Spallation of Graded Coatings Under Thermal Loading," J. Therm. Stresses, **26**, pp. 497–523.
[6] Sahin, A., and Erdogan, F., 2004, "On Debonding of Graded Thermal Barrier Coatings," Int. J. Fract., **129**, pp. 341–359.
[7] El-Borgi, S., Aloulou, W., and Zghal, A., 2006, "Buckling of a Functionally Graded Coating With an Embedded Crack Bonded to a Homogeneous Substrate," Int. J. Fract., **142**, pp. 137–150.
[8] Kim, J. H., and Paulino, G. H., 2002, "Mixed-Mode Fracture of Orthotropic Functionally Graded Materials Using Finite Elements and the Modified Crack Closure Method," Eng. Fract. Mech., **69**, pp. 1557–1586.
[9] Dag, S., Yıldırım, B., and Erdogan, F., 2004, "Interface Crack Problems in Graded Orthotropic Media: Analytical and Computational Approaches," Int. J. Fract., **130**, pp. 471–496.
[10] Chen, J., 2005, "Determination of Thermal Stress Intensity Factors for an Interface Crack in a Graded Orthotropic Coating-Substrate Structure," Int. J. Fract., **133**, pp. 303–328.
[11] Barsoum, R. S., 1976, "On the Use of Isoparametric Finite Elements in Linear

Fracture Mechanics," Int. J. Numer. Methods Eng., **10**, pp. 25–37.
[12] Banks-Sills, L., Hershkovitz, I., Wawrzynek, P. A., Eliasi, R., and Ingraffea, A. R., 2005, "Methods for Calculating Stress Intensity Factors in Anisotropic Materials, Part I—$z=0$ is a Symmetric Plane," Eng. Fract. Mech., **72**, pp. 2328–2358.
[13] Lekhnitskii, S. G., 1968, *Anisotropic Plates*, Gordon and Breach Science, New York.
[14] Kaya, A. C., and Nied, H. F., 1993, "Interface Fracture Analysis of Bonded Ceramic Layers Using Enriched Finite Elements," *Ceramic Coatings*, K. Kokini, ed., Proceedings of the ASME Winter Annual Meeting, New Orleans, LA, MD-Vol. 44, pp. 47–71.
[15] Lee, Y. D., and Erdogan, F., 1998, "Interface Cracking of FGM Coatings Under Steady-State Heat Flow," Eng. Fract. Mech., **59**, pp. 361–380.
[16] El-Borgi, S., Erdogan, F., and Ben Hatira, F., 2003, "Stress Intensity Factors for an Interface Crack Between a Functionally Graded Coating and a Homogeneous Substrate," Int. J. Fract., **123**, pp. 139–162.
[17] El-Borgi, S., Erdogan, F., and Hidri, L., 2004, "A Partially Insulated Embedded Crack in an Infinite Functionally Graded Medium Under Thermo-Mechanical Loading," Int. J. Eng. Sci., **42**, pp. 371–393.
[18] Itou, S., 2005, "Thermal Stresses Around a Crack in a Non-Homogeneous Diffusion Layer Between a Coating Plate and an Elastic Half-Plane," J. Therm. Stresses, **28**, pp. 1161–1178.
[19] Kaczynski, A., and Matysiak, S., 2003, "On the Three-Dimensional Problem of an Interface Crack Under Uniform Heat Flow in a Bimaterial Periodically-Layered Space," Int. J. Fract., **123**, pp. 127–138.
[20] Noda, N., and Jin, Z. H., 1993, "Thermal Stress Intensity Factors for a Crack in a Strip of a Functionally Gradient Material," Int. J. Solids Struct., **30**, pp. 1039–1056.
[21] Yılmaz, S., 2006, "Buckling Driven Delamination of Orthotropic Functionally Graded Materials," M.S. thesis, Middle East Technical University, Ankara.

Analysis of Interacting Cracks Using the Generalized Finite Element Method With Global-Local Enrichment Functions

Dae-Jin Kim

Carlos Armando Duarte[1]
e-mail: caduarte@uiuc.edu

Jeronymo Peixoto Pereira

Department of Civil and Environmental Engineering, Newmark Laboratory, University of Illinois at Urbana-Champaign, 205 North Mathews Avenue, Urbana, IL 61801

This paper presents an analysis of interacting cracks using a generalized finite element method (GFEM) enriched with so-called global-local functions. In this approach, solutions of local boundary value problems computed in a global-local analysis are used to enrich the global approximation space through the partition of unity framework used in the GFEM. This approach is related to the global-local procedure in the FEM, which is broadly used in industry to analyze fracture mechanics problems in complex three-dimensional geometries. In this paper, we compare the effectiveness of the global-local FEM with the GFEM with global-local enrichment functions. Numerical experiments demonstrate that the latter is much more robust than the former. In particular, the GFEM is less sensitive to the quality of boundary conditions applied to local problems than the global-local FEM. Stress intensity factors computed with the conventional global-local approach showed errors of up to one order of magnitude larger than in the case of the GFEM. The numerical experiments also demonstrate that the GFEM can account for interactions among cracks with different scale sizes, even when not all cracks are modeled in the global domain. [DOI: 10.1115/1.2936240]

1 Introduction

Three-dimensional interacting cracks appear in many practical engineering problems. Examples include corrosion-assisted cracks, multisite damage analysis of lap joints, and thermal fatigue cracks in cooling systems of nuclear power plants [1–4]. This class of problems is difficult to analyze due to the singularities at crack fronts and the complex stress distribution caused by the interaction of many cracks. The situation gets even more challenging when cracks with different scale sizes are involved, like in the case of macrocracks interacting with many microcracks. Small microcracks cannot be modeled by a global mesh designed to capture macrocracks. To handle this problem, the finite element method (FEM) requires extreme local refinements around the front of macrocracks and in regions where microcracks are located, leading to a high computational cost, especially in the three-dimensional case.

The global-local or submodeling procedure in the FEM [5–7] is an alternative to analyze interacting cracks. However, this approach is known to be sensitive to the quality of boundary conditions used in the local domains (submodels) [7]. Accurate local solutions require the use of sufficiently large local domains and, in some cases, modeling of interacting features, such as cracks, in the global problem. This leads to a large number of degrees of freedom in both global and local domains, and offsets some of the advantages of the procedure.

In this paper, we demonstrate that interacting cracks can be efficiently analyzed using the so-called generalized finite element method (GFEM) with global-local enrichment functions [8,9]. In this procedure, local solutions computed in a global-local analysis are used to enrich the global solution space through the partition of unity framework used in the GFEM. The local solution enrichments are hierarchical and used only at a few nodes in the coarse global mesh. As a result, the enriched global problem can be solved at a low computational cost [9]. We also show that interactions among several cracks with different scale sizes can be accurately captured using the GFEM with global-local enrichment functions. The quality of the numerical solutions is measured using analytical solutions derived by Civelek and Erdogan [10] for the problem of an infinite strip containing multiple cracks.

The outline of this paper is as follows. The global-local FEM is briefly reviewed in Sec. 2. The GFEM with global-local enrichment functions is summarized in Sec. 3. Numerical experiments comparing the global-local FEM and the GFEM with global-local enrichments are presented in Sec. 4. Section 5 draws the main conclusions from this investigation.

2 Global-Local Approach in the Finite Element Method

The global-local approach in the finite element method has a long history whose origin can be traced to the 1960s. It has also been called *zooming technique* or *submodeling* [5,6]. This technique has been extensively used in industry although it is rarely mentioned in academic textbooks [5]. More recently, this approach has begun to be incorporated into parallel processing algorithms [11].

As an example to illustrate the approach, let us consider a structural part with a planar crack surface shown in Fig. 1. The boundary conditions and geometric description of the crack surface are represented in Fig. 1(*a*). The global-local FEM procedure involves two steps [5,6]. First, the solution of the problem is computed on a coarse, global, quasiuniform mesh like that shown in Fig. 1(*a*). No mesh refinement around local features, such as crack surfaces, is usually performed. Next, small subdomains containing local features are extracted from the global domain and analyzed using

[1]Corresponding author.

Contributed by the Applied Mechanics Division of ASME for publication in the JOURNAL OF APPLIED MECHANICS. Manuscript received June 6, 2007; final manuscript received February 14, 2008; published online July 11, 2008. Review conducted by Marek-Jerzy Pindera.

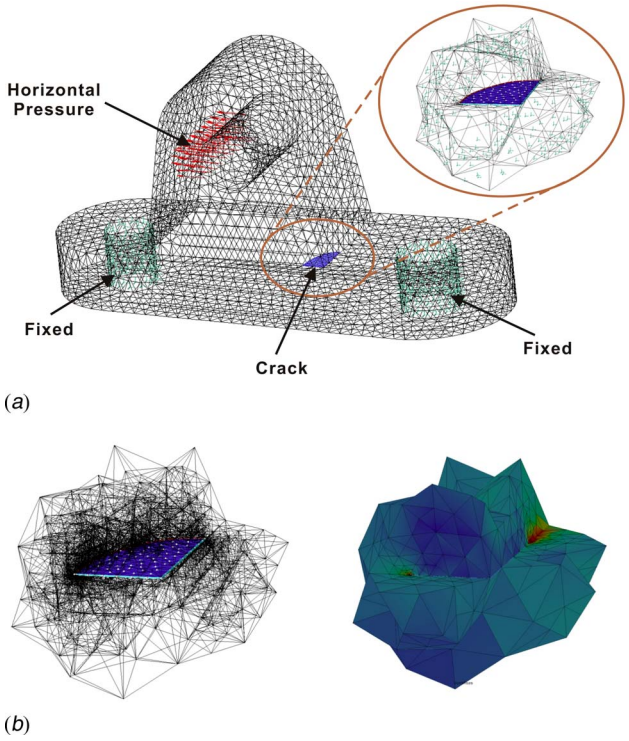

Fig. 1 Global-local analysis for a structural component with a planar crack surface. (*a*) Global analysis with a coarse mesh to provide boundary conditions for the extracted local domain. (*b*) Refined local problem and its solution.

the global solution as boundary conditions [5,6]. Local domains are typically analyzed using very refined meshes such as the one shown in Fig. 1(*b*). The use of the crude global solution as boundary conditions for local problems is a key point in the procedure. Either displacement (Dirichlet) or traction (Neumann) boundary conditions can be used [5].

The computational cost of factorizing a matrix grows faster than linearly with respect to problem size. Therefore, by solving the global problem on a coarse mesh, and local problems on fine meshes, instead of refining the global mesh, the global-local FEM can significantly reduce computational costs when applied to large practical engineering problems.

In the procedure described above, the crack was discretized in the (coarse) global mesh. This may be difficult when the geometry of the domain is complex, when the crack is small, or when the analysis of several crack locations and configurations is required. Therefore, in engineering applications of the global-local FEM, local features such as cracks are often not discretized in the global mesh and the global problem is solved as if there were no cracks in the domain. The cracks are modeled *only* in the local domains [5,7]. This significantly reduces mesh generation efforts and enables the use of a single global solution for the analysis of any configuration of cracks in the domain. However, as demonstrated later in Sec. 4.1.2, this approach may lead to large errors in the solution of the local problems.

An important issue for the global-local FEM is the size of local domains. The basic assumption of this approach is that the global solution is sufficiently accurate at the boundary of a local domain, or that the local domain is large enough such that a crude boundary condition does not affect the quality of the local solution. It is not always easy to comply with this assumption since local problems are modeled in the neighborhood of local features such as cracks and cutouts where the solution exhibits strong gradients or singularities. In addition, the well known pollution effect may cause the propagation of *discretization* errors over large distances

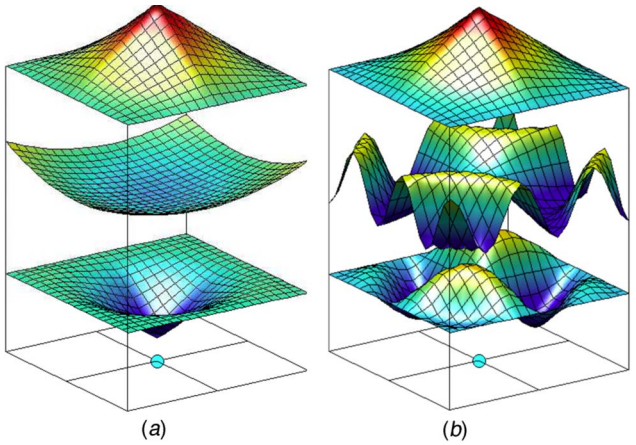

Fig. 2 Construction of a GFEM shape function using a polynomial (*a*) and a nonpolynomial enrichment (*b*). Here, φ_α are the functions at the top, the enrichment functions, $L_{\alpha i}$, are the functions in the middle, and the generalized FE shape functions, $\phi_{\alpha i}$, are the resulting bottom functions.

in a domain [12]. For crack problems, it is usually recommended that the size of a subdomain be at least 2.5 to 3 times larger than the length of the crack [7]. This may require, for example, the inclusion of more than one crack in a local domain leading to large local problems and to difficulties in generating appropriate meshes in the local domains.

3 Generalized Finite Element Method With Global-Local Enrichment Functions

This section describes the basic concepts of the GFEM and the construction of enrichment functions using a procedure similar to that employed in the global-local FEM. The main features of these so-called global-local enrichment functions are discussed. We also compare the global-local FEM with the GFEM enriched with global-local functions.

3.1 Generalized Finite Element Method. The construction of generalized finite element approximations is briefly reviewed in this section. Further details can be found in, for example, Refs. [13–17].

A shape function, $\phi_{\alpha i}$, in the GFEM is built from the product of a linear finite element shape function, φ_α, and an enrichment function, $L_{\alpha i}$,

$$\phi_{\alpha i}(\boldsymbol{x}) = \varphi_\alpha(\boldsymbol{x}) L_{\alpha i}(\boldsymbol{x}) \quad \text{(no summation on } \alpha) \tag{1}$$

where α is a node in the finite element mesh. Figure 2 illustrates the construction of GFEM shape functions. The linear finite element shape functions $\varphi_\alpha, \alpha = 1, \ldots, N$, in a finite element mesh with N nodes constitute a partition of unity, i.e., $\Sigma_{\alpha=1}^{N} \varphi_\alpha(\boldsymbol{x}) = 1$ for all $\boldsymbol{x}$ in a domain Ω covered by the finite element mesh. This is a key property used in partition of unity methods such as the GFEM. Linear combination of the GFEM shape functions $\phi_{\alpha i}, \alpha = 1, \ldots, N$, can represent *exactly* any enrighment function $L_{\alpha i}$

Several enrichment functions can be hierarchically added to any node α in a finite element mesh. Thus, if $m(\alpha)$ is the number of enrichment functions at node α, the GFEM approximation, u_{hp}, of a function u can be written as

$$u_{hp}(\boldsymbol{x}) = \sum_{\alpha=1}^{N} \sum_{i=1}^{m(\alpha)} a_{\alpha i} \phi_{\alpha i}(\boldsymbol{x}) = \sum_{\alpha=1}^{N} \sum_{i=1}^{m(\alpha)} a_{\alpha i} \varphi_\alpha(\boldsymbol{x}) L_{\alpha i}(\boldsymbol{x})$$

The main strength of the generalized FEM is its ability to use nonpolynomial enrichment functions, as illustrated in Fig. 2(*b*). Expansions of the elasticity solution in the neighborhood of a crack (Westergaard functions) can be taken as enrichment func-

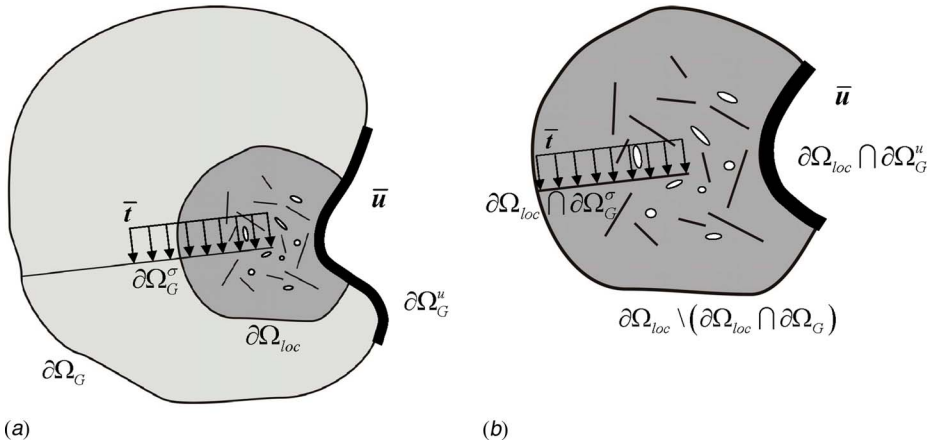

(*a*) (*b*)

Fig. 3 Notations for the GFEM with global-local enrichment functions. (*a*) A global domain containing one macrocrack and several microcracks. (*b*) A local domain extracted from the global domain in the neighborhood of the macrocrack front.

tions at nodes near a crack front [14,18–22]. Discontinuities in a displacement field can be approximated independently of the underlying finite element mesh if Heaviside functions are used as enrichment functions [21–25]. Custom-built enrichment functions that are solutions of local boundary value problems can be used as well [8,9,26]. These so-called global-local enrichment functions are described in detail in Sec. 3.2.

3.2 Global-Local Approach to Build Enrichment Functions. In this section, we review a global-local approach to build enrichment functions for the GFEM. Additional details can be found in Refs. [8,9]. We focus on three-dimensional linear elasticity problems. The formulation is, however, applicable to other classes of problems as well.

3.2.1 Formulation of Global Problem. Consider the domain $\bar{\Omega}_G = \Omega_G \cup \partial\Omega_G \subset \boldsymbol{R}^3$ illustrated in Fig. 3(*a*). The boundary is decomposed as $\partial\Omega_G = \partial\Omega^u_G \cup \partial\Omega^\sigma_G$ with $\partial\Omega^u_G \cap \partial\Omega^\sigma_G = \emptyset$.

The strong form of the equilibrium and constitutive equations is given by

$$\nabla \cdot \boldsymbol{\sigma} = \boldsymbol{0}, \quad \boldsymbol{\sigma} = \boldsymbol{C}:\boldsymbol{\varepsilon} \quad \text{in } \Omega_G \tag{2}$$

where $\boldsymbol{C}$ is Hooke's tensor. The following boundary conditions are prescribed on $\partial\Omega_G$:

$$\boldsymbol{u} = \bar{\boldsymbol{u}} \text{ on } \partial\Omega^u_G, \quad \boldsymbol{\sigma}\cdot\boldsymbol{n} = \bar{\boldsymbol{t}} \text{ on } \partial\Omega^\sigma_G \tag{3}$$

where $\boldsymbol{n}$ is the outward unit normal vector to $\partial\Omega^\sigma_G$, and $\bar{\boldsymbol{t}}$ and $\bar{\boldsymbol{u}}$ are prescribed tractions and displacements, respectively.

Let $\boldsymbol{u}^0_G$ denote a GFEM approximation of the solution $\boldsymbol{u}$ of problems (2) and (3). The approximation $\boldsymbol{u}^0_G$ is the solution of the following problem.

Find $\boldsymbol{u}^0_G \in \boldsymbol{X}^{hp}_G(\Omega_G) \subset H^1(\Omega_G)$ such that $\forall \boldsymbol{v}^0_G \in \boldsymbol{X}^{hp}_G(\Omega_G)$

$$\int_{\Omega_G} \boldsymbol{\sigma}(\boldsymbol{u}^0_G):\boldsymbol{\varepsilon}(\boldsymbol{v}^0_G)d\boldsymbol{x} + \eta\int_{\partial\Omega^u_G} \boldsymbol{u}^0_G\cdot\boldsymbol{v}^0_G d\boldsymbol{s} = \int_{\partial\Omega^\sigma_G} \bar{\boldsymbol{t}}\cdot\boldsymbol{v}^0_G d\boldsymbol{s} + \eta\int_{\partial\Omega^u_G} \bar{\boldsymbol{u}}\cdot\boldsymbol{v}^0_G d\boldsymbol{s} \tag{4}$$

where $\boldsymbol{X}^{hp}_G(\Omega_G)$ is a discretization of the Hilbert space $H^1(\Omega_G)$ built with GFEM shape functions, and η is a penalty parameter. Problem (4) leads to a system of linear equations for the unknown degrees of freedom of $\boldsymbol{u}^0_G$. The mesh used to solve problem (4) is typically a coarse quasiuniform mesh. This problem is analogous to the first step of the global-local FEM presented in Fig. 1(*a*) and denoted hereafter as *initial global problem*.

3.2.2 Local Problems. Let Ω_{loc} denote a subdomain of Ω_G, as shown in Fig. 3(*b*). This local domain may contain cracks, holes, inclusions, fibers, or other local features of interest.

The following local problem is solved on Ω_{loc} after the global solution $\boldsymbol{u}^0_G$ is computed as described above.

Find $\boldsymbol{u}_{\text{loc}} \in \boldsymbol{X}^{hp}_{\text{loc}}(\Omega_{\text{loc}}) \subset H^1(\Omega_{\text{loc}})$ such that $\forall \boldsymbol{v}_{\text{loc}} \in \boldsymbol{X}^{hp}_{\text{loc}}(\Omega_{\text{loc}})$

$$\int_{\Omega_{\text{loc}}} \boldsymbol{\sigma}(\boldsymbol{u}_{\text{loc}}):\boldsymbol{\varepsilon}(\boldsymbol{v}_{\text{loc}})d\boldsymbol{x} + \eta\int_{\partial\Omega_{\text{loc}}\setminus(\partial\Omega_{\text{loc}}\cap\partial\Omega^\sigma_G)} \boldsymbol{u}_{\text{loc}}\cdot\boldsymbol{v}_{\text{loc}} d\boldsymbol{s} = \eta\int_{\partial\Omega_{\text{loc}}\setminus(\partial\Omega_{\text{loc}}\cap\partial\Omega_G)} \boldsymbol{u}^0_G\cdot\boldsymbol{v}_{\text{loc}} d\boldsymbol{s} + \eta\int_{\partial\Omega_{\text{loc}}\cap\partial\Omega^u_G} \bar{\boldsymbol{u}}\cdot\boldsymbol{v}_{\text{loc}} d\boldsymbol{s} + \int_{\partial\Omega_{\text{loc}}\cap\partial\Omega^\sigma_G} \bar{\boldsymbol{t}}\cdot\boldsymbol{v}_{\text{loc}} d\boldsymbol{s} \tag{5}$$

where $\boldsymbol{X}^{hp}_{\text{loc}}(\Omega_{\text{loc}})$ is a discretization of $H^1(\Omega_{\text{loc}})$ using GFEM shape functions.

A key aspect of problem (5) is the use of the GFEM solution of the global problem, $\boldsymbol{u}^0_G$, as boundary condition on $\partial\Omega_{\text{loc}}\setminus(\partial\Omega_{\text{loc}}\cap\partial\Omega_G)$. Exact boundary conditions are prescribed on portions of $\partial\Omega_{\text{loc}}$ that intersect either $\partial\Omega^u_G$ or $\partial\Omega^\sigma_G$. This problem is analogous to the second step of the global-local FEM presented in Fig. 1(*b*) and denoted hereafter as *local problem*.

3.2.3 Global-Local Enrichment Functions. The error in the local solution $\boldsymbol{u}_{\text{loc}}$ depends not only on the discretization used in the local domain Ω_{loc}, but, more importantly, also on the quality of boundary conditions used on $\partial\Omega_{\text{loc}}\setminus(\partial\Omega_{\text{loc}}\cap\partial\Omega_G)$, i.e., $\boldsymbol{u}^0_G$. In the GFEM proposed in Refs. [8,9], this issue is addressed by going one step further in a global-local analysis; *the local solution $\boldsymbol{u}_{\text{loc}}$ is used as an enrichment function for the global problem.* The local solution is called a *global-local enrichment function* and is used to define the following vector-valued global shape function:

$$\boldsymbol{\phi}_\alpha = \varphi_\alpha \boldsymbol{u}_{\text{loc}} \tag{6}$$

where φ_α denotes a partition of unity function defined in the coarse *global* mesh used to solve the global problem presented in Sec. 3.2.1. This function is used at nodes $\boldsymbol{x}_\alpha$ of the global mesh whose support, ω_α, is contained in the local domain Ω_{loc}. In our implementation, we enrich each component of the displacement vector with the corresponding component of the local solution $\boldsymbol{u}_{\text{loc}}$. Thus, a global-local enrichment adds three degrees of freedom to a node when solving a three-dimensional elasticity problem. The global problem defined in Sec. 3.2.1 is then solved again

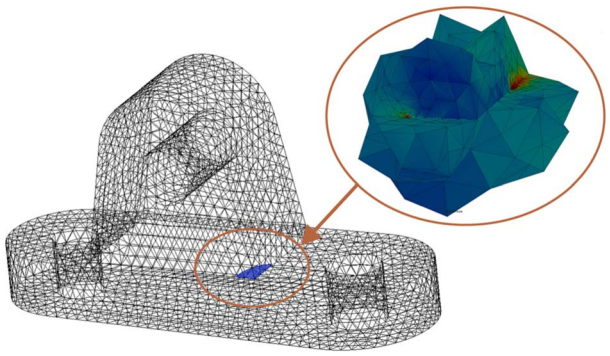

Fig. 4 Enrichment of the coarse global mesh with a local solution

using these global functions. The solution of this enriched global problem is denoted by $\boldsymbol{u}_G^E$. This problem is denoted hereafter as *enriched global problem*. In Ref. [9], we demonstrated how this problem can be efficiently solved using the solution of the initial global problem.

The GFEM with global-local enrichment functions can account for possible interactions of local (near crack, for example) and global (structural) behaviors. This procedure also addresses the loss of accuracy in the local solution caused by the crude boundary conditions used in the local domain. Roughly speaking, this can be explained by the fact that the global partition of unity φ_α, and therefore $\boldsymbol{\phi}_\alpha$, are zero at the boundary of local domain Ω_{loc}, where the accuracy of $\boldsymbol{u}_{\text{loc}}$ is more severely affected by the boundary conditions applied at $\partial\Omega_{\text{loc}}$. The enrichment of the global mesh with the local solution is illustrated in Fig. 4 using the same example introduced in Sec. 2. Hereafter, GFEM^{g-l} denotes the GFEM with global-local enrichment functions.

4 Numerical Experiments

In this section, we analyze the performance of the GFEM^{g-l} in the analysis of interacting cracks. We compare the quality of stress intensity factors (SIFs) extracted from the solution of the enriched global problem, $\boldsymbol{u}_G^E$, with those extracted from the local solution, $\boldsymbol{u}_{\text{loc}}$.

The local solution $\boldsymbol{u}_{\text{loc}}$ is computed using the GFEM described in Sec. 3.1. This enables us to solve the local problems using meshes that do not fit the crack surfaces in contrast with the FEM. Therefore, strictly speaking, $\boldsymbol{u}_{\text{loc}}$ is computed using a global-local GFEM and not a global-local FEM. However, these methods suffer from the same limitations, and it is reasonable to assume that the conclusions drawn here are also valid for the global-local FEM. Hereafter, the procedure used to compute $\boldsymbol{u}_{\text{loc}}$ is denoted by GL-FEM.

The numerical examples presented below include an analysis of interacting cracks, an inclined crack, and cracks with different scale sizes. The main focus of the numerical experiments is on how the quality of boundary conditions for the local problems affects that of the SIFs extracted from GFEM^{g-l} and GL-FEM solutions. The numerical experiments show that the GFEM^{g-l} is much less sensitive to the quality of local boundary conditions and provides more accurate SIFs than the GL-FEM.

4.1 Analysis of Two Interacting Macrocracks. An example with two interacting cracks in an infinite strip is considered in this section. The problem is illustrated in Fig. 5. The general plane elastic problem of an infinite strip containing multiple cracks perpendicular to its boundary was analysized by Civelek and Erdogan [10]. They showed that for the configuration shown in Fig. 5, the interaction between the cracks produces a nonzero Mode II SIF, K_{II}. This leads to the propagation of the cracks away from each other. This effect becomes more significant as the distance

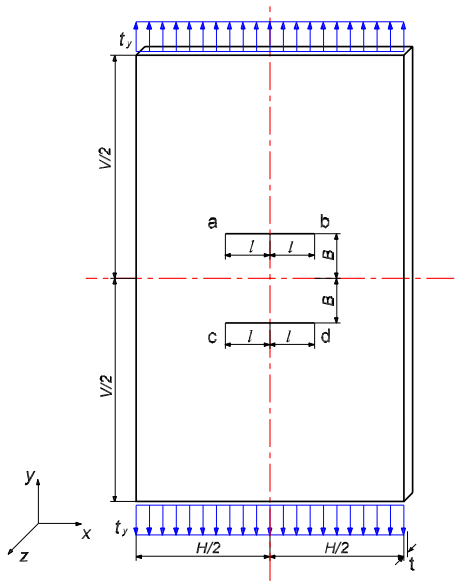

Fig. 5 Description of a problem with two interacting cracks in an infinite strip

between the cracks decreases [10]. In this section, we investigate how well the GFEM^{g-l} and the GL-FEM can capture the interaction between the two cracks as B/H goes to zero (cf. Fig. 5). The SIFs are extracted from $\boldsymbol{u}_G^E$ and $\boldsymbol{u}_{\text{loc}}$, respectively, as discussed above.

Three-dimensional tetrahedron elements are used in our computations. Poisson's ratio is set to zero in order to minimize three-dimensional effects in the computed solution. This enables us to use Civelek and Erdogan's solution presented in Ref. [10] as a reference. The other parameters assumed in our computations are as follows: Young's modulus $E=200{,}000$; in-plane dimensions $H=10.0$, $2l=4.0$, $V=200.0$; domain thickness $t=1.0$; and vertical traction $t_y=100.0$. Since the vertical dimension is 20 times larger than the horizontal dimension, we can assume that the solution on this finite domain is very close to the case of an infinite strip.

The SIFs are extracted using the cut-off function method [27–29] and normalized as in Ref. [10] using

$$k_{\text{I(II)}} = \frac{K_{\text{I(II)}}}{t_y\sqrt{\pi l}} \tag{7}$$

where $k_{\text{I(II)}}$ denotes the normalized Mode I (II) SIF, $K_{\text{I(II)}}$ denotes the original Mode I (II) SIF, t_y is the traction applied at $y = \pm V/2$, and $2l$ is the crack length.

4.1.1 Analysis With Cracks Discretized in the Global Domain. The discretizations shown in Fig. 6 are used in the analysis presented in this section. The global mesh is quite coarse, as shown in Fig. 6(*a*), and has only one layer of elements in the out-of-plane direction. Heaviside enrichment functions are used to represent the cracks. This enables the cracks to cut elements in the mesh, as described in Sec. 3.1.

Four local problems are created, one for each crack front as illustrated in Fig. 6(*a*). The local meshes are strongly refined in the neighborhood of the crack fronts. Westergaard functions are used in the elements intersecting the crack front. In the case of the GL-FEM, SIFs are extracted from solutions computed in these local domains.

The local solutions are used to enrich nodes in the global mesh, as illustred in Fig. 6(*c*). Only four nodes per crack front are enriched with these functions (two nodes at $z=0$ and two at $z=t$). As a result, the enriched global problem has almost the same number

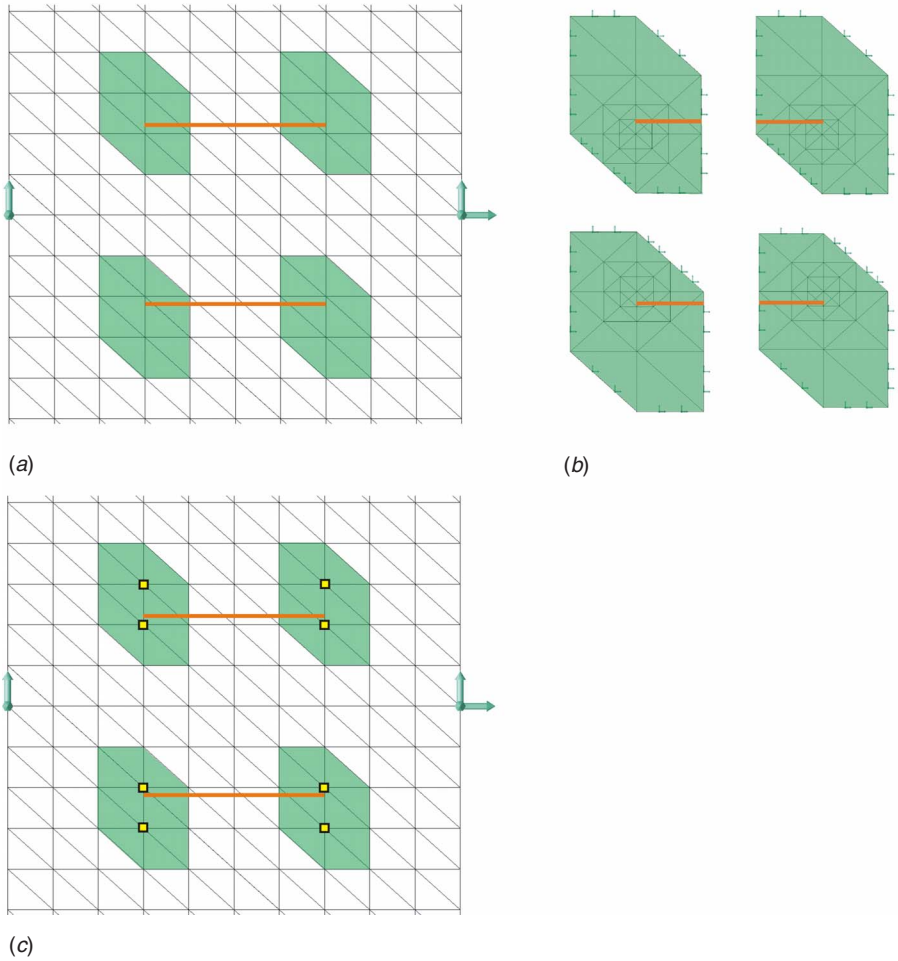

Fig. 6 Discretization of a problem with two interacting cracks using tetrahedral elements. Front view of the strip shown in Fig. 5 for the case $B/H=2$. Note that the cracks are discretized in the global domain and a three-dimensional discretization is used. (*a*) Discretization of cracks in the initial global problem. The shaded areas represent the local domains extracted from the coarse global mesh. (*b*) Graded meshes used in the discretization of local problems. (*c*) Enrichment of global discretization with local solutions. Global nodes enriched with local solutions are represented with squares.

of degrees of freedom as the initial global problem (cf. Table 1). In the case of the GFEM^{g-1}, SIFs are extracted from the solution computed in this enriched global problem.

The polynomial order of the shape functions used in the initial and enriched global problems is $p=1$, whereas cubic polynomial shape functions ($p=3$) are used in the local problems. It should be emphasized that the interacting cracks *are discretized* in the global domain. This is in contrast to the analysis presented in Sec. 4.1.2 where the cracks are not discretized in the global domain.

Table 1 lists the computed (normalized) Mode I and II SIFs (k_I and k_{II}) extracted from GL-FEM and GFEM^{g-1} solutions. The reference values from Civelek and Erdogan [10] are also listed. Figure 7 plots the data from the table. The results show that Mode I SIFs extracted from GFEM^{g-1} solutions are much more accurate than those from the GL-FEM solutions. For the case $B/H=0.2$, the relative error of k_I extracted from the GFEM^{g-1} solution is 5.08%, whereas the error is 24.5% in the case of the GL-FEM. The relative error in the computed k_I by GL-FEM is therefore almost five times larger than the one computed with the GFEM^{g-1}.

Table 1 Mode I and II SIFs for the problem shown in Fig. 5, and cracks are discretized in the global domain. Global problems are solved with linear shape functions. Abbreviations nDOFs, IG, L, and EG in the table represent the number of degrees of freedom, initial global, local, and enriched global problems, respectively.

				Normalized Mode I SIF			Normalized Mode II SIF		
B/H	nDOFs (IG)	nDOFs (L)	nDOFs (EG)	GL-FEM	GFEM^{g-1}	Ref.	GL-FEM	GFEM^{g-1}	Ref.
0.2	3438	18,018	3486	0.7360	0.9254	0.9749	−0.0273	−0.0777	−0.0656
0.3	3438	19,278	3486	0.7709	0.9758	1.0437	−0.0182	−0.0474	−0.0330
0.4	3438	17,328	3486	0.7893	1.0072	1.0839	−0.0104	−0.0410	−0.0155
1.0	3438	19,278	3486	0.7998	1.0445	1.1096			

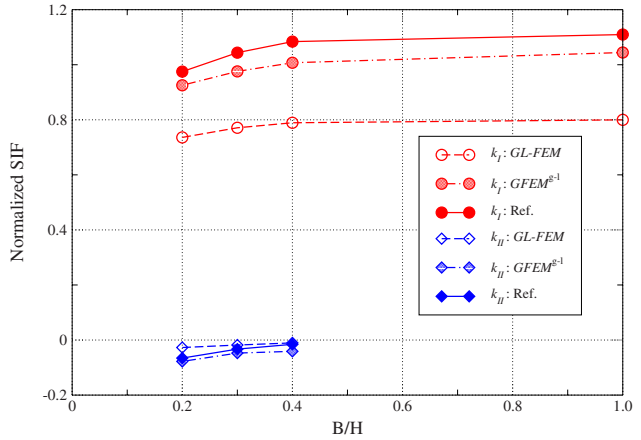

Fig. 7 Analysis with interacting cracks discretized in the global domain. Global problems are solved with linear shape functions. Ref. represents the reference SIF values obtained from Ref. [10].

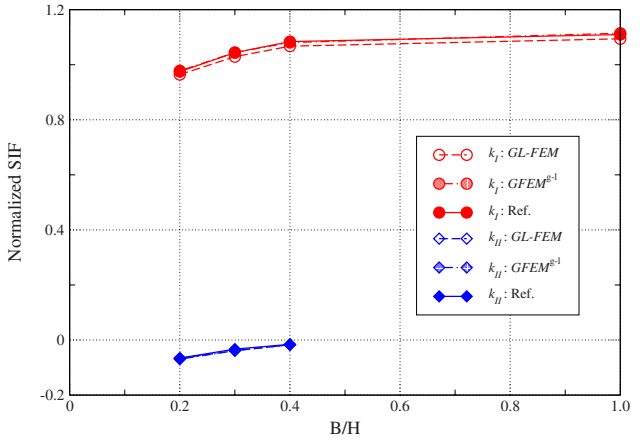

Fig. 9 Analysis with interacting cracks discretized in the global domain. Global problems are solved with cubic shape functions and Westergaard function enrichments. Global problems are solved with cubic shape functions

A similar trend is observed for other values of B/H. Mode II SIFs are also listed in Table 1 for reference. However, since for this problem k_{II} is much smaller than k_I, it cannot be computed as accurately as k_I using either the GL-FEM or the GFEM^{g-1}. Thus, we do not use k_{II} as a basis for comparison of performance of the methods. This comparison is done instead in Sec. 4.2.

As a subsequent analysis, we investigate the effect of the quality of boundary conditions used in local problems on the quality of the SIFs computed with the GL-FEM and GFEM^{g-1}. Two approaches are used to improve the quality of the boundary conditions. The global problem is solved with (i) cubic shape functions, and (ii) cubic shape functions and Westergaard function enrichments at nodes of the global mesh close to the crack fronts (four nodes per crack front). The Westergaard enrichments are subsequently replaced by the local solutions in the enriched global problem, as illustrated in Fig. 6(*c*). All other parameters are the same as in the $p=1$ case. The results for these two cases are presented in Figs. 8 and 9. Table 2 lists the results for Case (i). It is observed, as expected, that the SIFs in the GL-FEM greatly improve as more accurate boundary conditions are used in the local problems. However, they are still significantly less accurate than those computed with the GFEM^{g-1}. The relative error of k_I extracted from GFEM^{g-1} solutions is consistently below 0.5% whereas it is about 10% in the case of the GL-FEM.

The robustness of the GFEM^{g-1} demonstrated in this example is an important advantage over the GL-FEM since, in practice, it is generally not possible to quantify the quality of the boundary conditions.

4.1.2 Analysis With Cracks Not Discretized in the Global Domain. As discussed in Sec. 2, quite often in practical finite element simulations, local features such as cracks are not discretized in the global problem. In this section, we perform the same analysis as in Sec. 4.1.1 but the initial global problem is solved without any cracks in the domain. The problem shown in Fig. 5 is solved using this approach along with the discretizations shown in Fig. 10. Only two local problems are created in this case, and each local problem includes the entire crack, as illustrated in Fig. 10(*b*). The cracks are described only in the local problems using Heaviside and Westergaard enrichment functions. The refinement level at the crack fronts is the same as in Sec. 4.1.1. The local solutions are used to enrich nodes in the global mesh, as illustrated in Fig. 10(*c*). Twenty nodes per crack are enriched in this case. It should be emphasized that the interacting cracks *are not discretized* in the global domain in contrast with the example analyzed in Sec. 4.1.1.

The polynomial order of shape functions used in the initial and enriched global problems is set to $p=1$, whereas cubic polynomial shape functions ($p=3$) are used in the local problems. Table 3 lists the results for this case. Figure 11 plots the data from the table. The difference in quality of SIFs extracted from GFEM^{g-1} and GL-FEM is even more significant than in the previous section. For example, the relative error in Mode I SIF for $B/H=0.2$ computed by the GFEM^{g-1} is 4.05%, whereas in the case of the GL-FEM it is 52.64%. We can observe that the error in k_I computed with the GL-FEM is about twice as large as in the case reported in Table 1. In contrast, the error in the case of the GFEM^{g-1} is about the same as in Table 1, in spite of the fact that the cracks were not modeled in the initial global problem.

As in the analysis presented in Sec. 4.1.1, we investigate the effect of using cubic shape functions in the global problem. All other parameters are kept unchanged. The results for this choice of shape functions are presented in Fig. 12 and in Table 4. Westergaard enrichments are not used in the global domain since in this domain the cracks are not discretized. It can be observed from Fig. 12 and Table 4 that the Mode I SIFs computed with the GL-FEM do *not* improve in this case. This shows that if the cracks are not discretized in the global problem, the quality of boundary conditions used in the local problems may not improve even if higher order elements or finer meshes are used in the global prob-

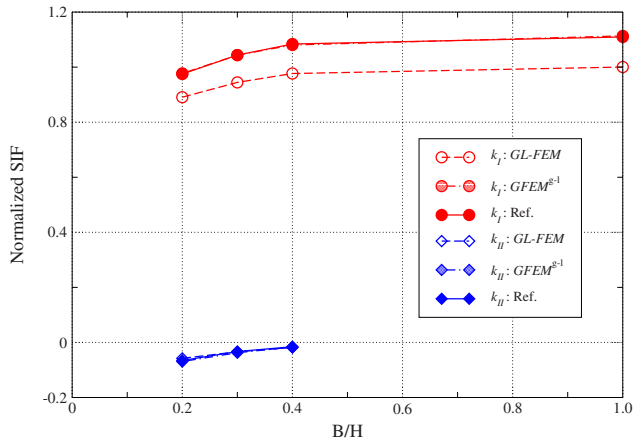

Fig. 8 Analysis with interacting cracks discretized in the global domain. Global problems are solved with cubic shape functions.

Table 2 Mode I and II SIFs for the problem shown in Fig. 5, and cracks are discretized in the global domain. Global problems are solved with cubic shape functions.

B/H	nDOFs (IG)	nDOFs (L)	nDOFs (EG)	Mode I SIF			Mode II SIF		
				GL-FEM	GFEM^{g-1}	Ref.	GL-FEM	GFEM^{g-1}	Ref.
0.2	34,380	18,018	34,428	0.8908	0.9771	0.9749	−0.0578	−0.0693	−0.0656
0.3	34,380	19,278	34,428	0.9446	1.0436	1.0437	−0.0338	−0.0375	−0.0330
0.4	34,380	17,328	34,428	0.9767	1.0803	1.0839	−0.0186	−0.0169	−0.0155
1.0	34,380	19,278	34,428	1.0005	1.1135	1.1096			

lem. The Mode I SIFs in the GFEM^{g-1} have an error of less than 1% while in the case of the GL-FEM the error is about five times larger than those reported in Table 2. This, again, shows that the GFEM^{g-1} is more robust and can provide more accurate solutions than the GL-FEM, even in such an extreme situation where no local features are represented in the global domain.

4.2 Analysis of an Inclined Crack. As a second example, we analyze the mixed-mode fracture problem shown in Fig. 13. In contrast with the problem analyzed in Sec. 4.1, here Mode I and II SIFs are of the same order of magnitude. Thus, they can be extracted with the same level of accuracy. We compare SIFs extracted from GL-FEM and GFEM^{g-1} solutions with reference values computed by Szabo and Babuška [27] using the p version of the FEM with $p=8$.

Three-dimensional tetrahedron elements are used in our computations as in Sec. 4.1. Poisson's ratio is set to zero to compare our results with the reference values computed assuming plane stress condition. The following parameters are also adopted in our simulation: Young's modulus $E=1.0$, in-plane dimensions $w=1.0$, domain thickness $t=1.0$, and vertical traction $t_y=1.0$.

The SIFs are extracted using the cut-off function method [27–29] and normalized using

$$k_{\mathrm{I(II)}} = \frac{K_{\mathrm{I(II)}}}{t_y\sqrt{2\pi w}} \tag{8}$$

where $k_{\mathrm{I(II)}}$ denotes the normalized Mode I (II) SIF.

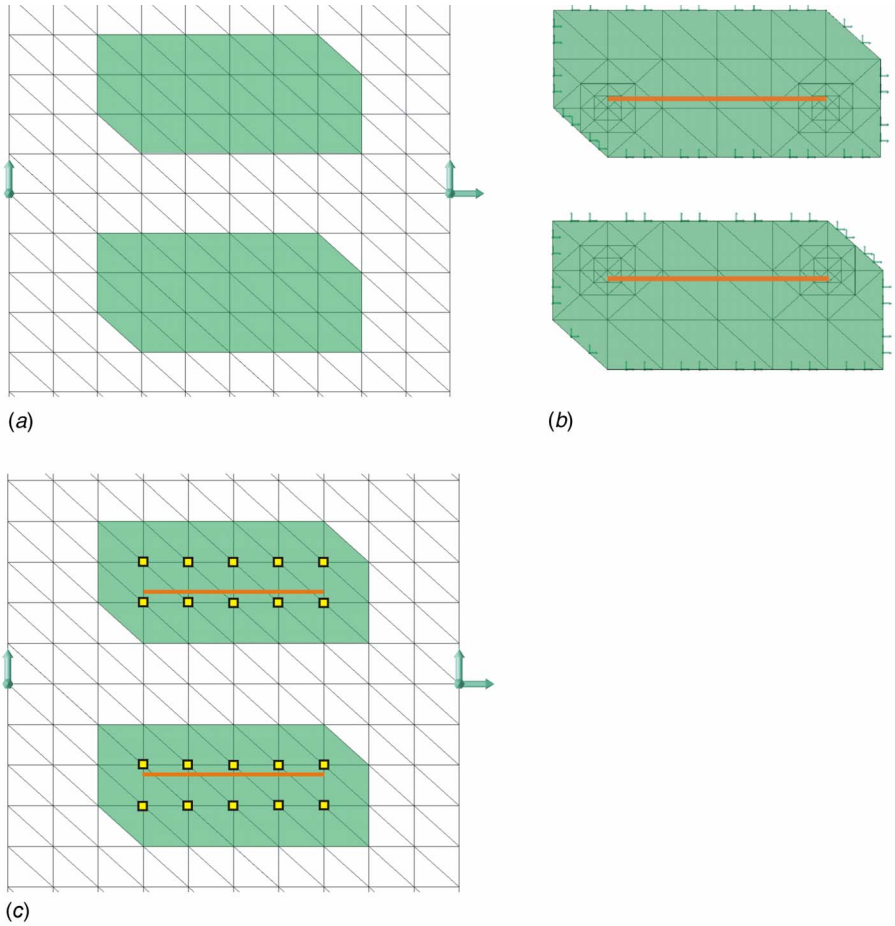

Fig. 10 Discretization of a problem with two interacting cracks. Front view for the case $B/H=2$. The cracks are not discretized in the global domain. (*a*) The shaded areas represent the local domains extracted from the coarse global mesh. (*b*) Graded meshes used in the discretization of local problems. (*c*) Enrichment of global discretization with local solutions. Global nodes enriched with local solutions are represented with squares.

Table 3 Mode I and II SIFs for the problem shown in Fig. 5. Cracks are not discretized in the global domain, and linear shape functions are used in the global domain.

B/H	nDOFs (IG)	nDOFs (L)	nDOFs (EG)	Normalized Mode I SIF			Normalized Mode II SIF		
				GL-FEM	GFEM^{g-1}	Ref.	GL-FEM	GFEM^{g-1}	Ref.
0.2	3366	36,708	3486	0.4617	0.9354	0.9749	−0.0270	−0.0906	−0.0656
0.3	3366	39,228	3486	0.4625	0.9834	1.0437	−0.0162	−0.0537	−0.0330
0.4	3366	35,328	3486	0.4630	0.9987	1.0839	−0.0043	−0.0103	−0.0155
1.0	3366	39,228	3486	0.4604	1.0425	1.1096			

The domain is discretized, as shown in Fig. 14. The global mesh is quite coarse, and only one layer of elements is used in the out-of-plane direction. The inclined crack is discretized only in the local domain, as in Sec. 4.1.2, and is modeled using Heaviside and Westergaard functions. The local mesh is refined around the crack front to obtain accurate solutions, as in the previous section. In the case of GFEM^{g-1}, the local solutions are used to enrich 18 nodes in the global mesh, as illustrated in Fig. 14(*b*). Quadratic shape functions are used in the global domain, and cubic shape functions in the local domain.

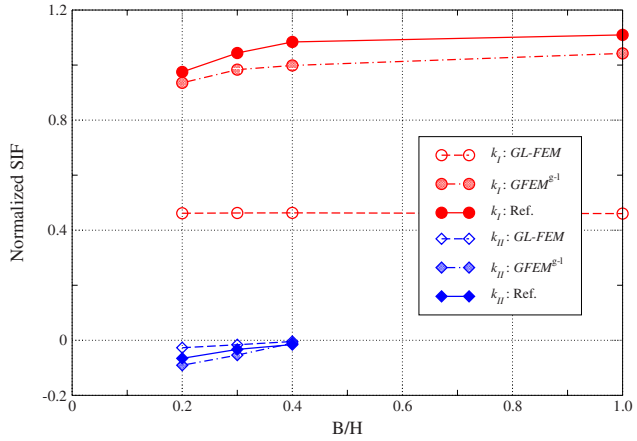

Fig. 11 Analysis with interacting cracks not discretized in the global domain. Global problems are solved with linear shape functions.

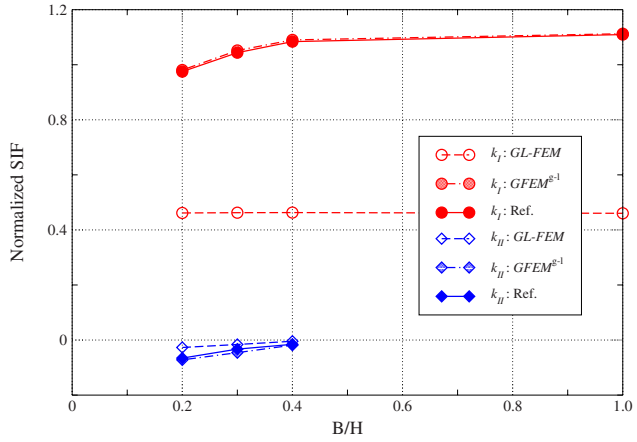

Fig. 12 Analysis with interacting cracks not discretized in the global domain. Global problems are solved with cubic shape functions.

Table 5 lists normalized Mode I and II SIFs extracted from GL-FEM and GFEM^{g-1} solutions. The reference values from Szabo and Babuška [27] are also listed. The relative error of k_I extracted from the GFEM^{g-1} solution is 2.65%, while it is 64.29% in the case of GL-FEM. Thus, k_I computed with the GL-FEM has an error almost 24 times larger than the one computed with GFEM^{g-1}. This same level of accuracy is achieved by GFEM^{g-1} in the case of k_{II}. The relative errors in Mode II SIF are 3.21% and 56.03% in the GFEM^{g-1} and GL-FEM, respectively. This result demonstrates that GFEM^{g-1} can deliver much higher level of accuracy in the extraction of both Mode I and II SIFs than GL-FEM even if the crack is not discretized in the global domain.

4.3 Multiple Site Damage Problem. A multiple site damage (MSD) example is analyzed in this section. MSD problems focus on the combined effect of multiple growing cracks where each individual crack can be harmless, but the combined effect of several cracks can be disastrous [30]. In this class of problems, cracks cannot be treated separately, and the interaction among them must be considered during the analysis. One example of MSD is the case of small fatigue cracks developing around regions with high stress concentration and manufacturing or material defects. The microcracks may grow and coalesce into a larger macrocrack which can lead to the failure of the structure [31]. The global-local FEM requires sufficiently large local domains in order to minimize the effect of the approximate boundary conditions. In the case of MSD problems, this will invariably lead to the inclusion of perhaps several microcracks in the local problems, offsetting some of the advantages of the method. In this section, we analyze the MSD problem shown in Fig. 15 using both the GL-FEM and the GFEM^{g-1}. This problem was originally proposed in Ref. [32]. We investigate the effect of the local domain size on the quality of the energy release rate extracted from GL-FEM and GFEM^{g-1} solutions.

In the example shown in Fig. 15, there are two small MSD cracks on the left and right sides of the main crack. The modeling

Table 4 Mode I and II SIFs for the problem shown in Fig. 5. Cracks are not discretized in the global domain and cubic shape functions are used in the global domain.

B/H	nDOFs (IG)	nDOFs (L)	nDOFs (EG)	Mode I SIF			Mode II SIF		
				GL-FEM	GFEM^{g-1}	Ref.	GL-FEM	GFEM^{g-1}	Ref.
0.2	33,660	36,708	33,780	0.4617	0.9807	0.9749	−0.0270	−0.0720	−0.0656
0.3	33,660	39,228	33,780	0.4625	1.0517	1.0437	−0.0162	−0.0459	−0.0330
0.4	33,660	35,328	33,780	0.4630	1.0902	1.0839	−0.0043	−0.0186	−0.0155
1.0	33,660	39,228	33,780	0.4604	1.1125	1.1096			

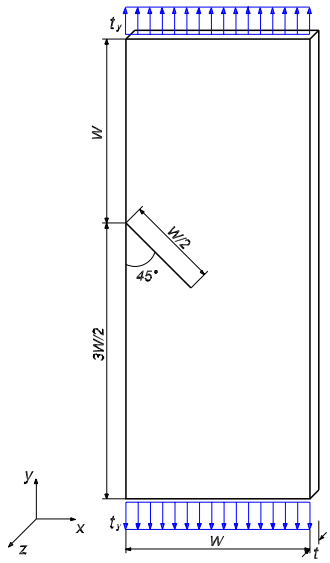

Fig. 13 Rectangular panel with a through-the-thickness inclined crack

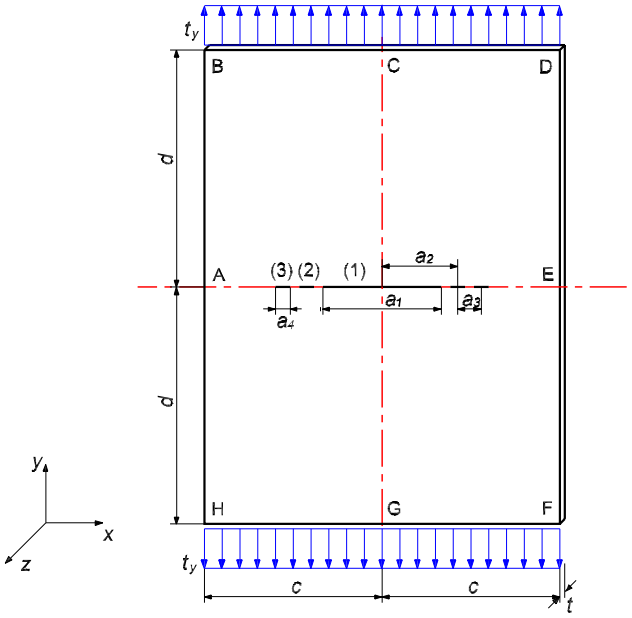

Fig. 15 Description of a MSD problem

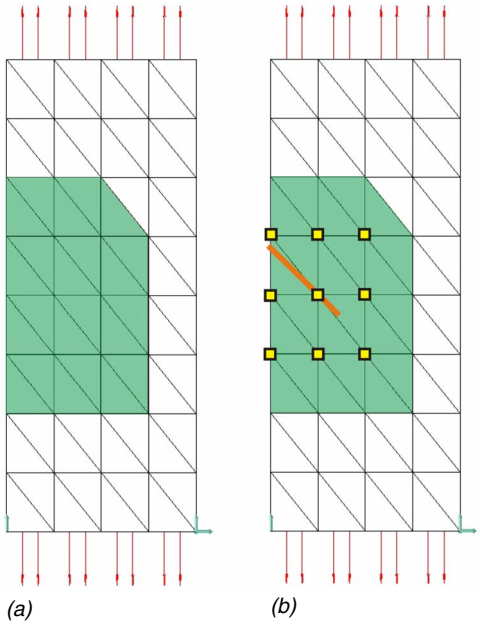

Fig. 14 Discretization of the problem with an inclined crack. The crack is *not* discretized in the global domain. (*a*) The shaded area represents the local domain extracted from the coarse global mesh. (*b*) Enrichment of global discretization with local solutions. Global nodes enriched with local solutions are represented with squares.

of the MSD cracks in the global domain would require extremely fine meshes leading to a large global problem. The following parameters are assumed in the simulations: Poisson's ratio $\nu=0.33$; Young's modulus $E=10{,}500$ ksi; in-plane dimensions $d=75.0$ in., $c=45.0$ in., $a_1=20.0$ in., $a_2=11.5$ in., $a_3=2.0$ in.; size of MSD cracks $a_4=1.0$ in.; domain thickness $t=1.0$ in.; and vertical traction $t_y=20.0$. We take advantage of symmetry in geometry and boundary conditions and model only the right half (CDEFG) of the domain.

The energy release rate ($\mathcal{G}$) is computed at the center of the front of the main crack, i.e., at $z=t/2$. Plane strain conditions are assumed at this location and the energy release rate is computed using the relation

$$\mathcal{G}=\frac{1-\nu^2}{E}K_{\mathrm{I}}^2+\frac{1-\nu^2}{E}K_{\mathrm{II}}^2+\frac{1+\nu}{E}K_{\mathrm{III}}^2 \tag{9}$$

where ν is Poisson's ratio and E is Young's modulus. The SIFs K_{I}, K_{II}, and K_{III} are extracted using the contour integral method [27–29,33,34]. The reference value for the $\mathcal{G}$ is taken as 2.5609. This value was computed using a very refined mesh and high order shape functions ($p=4$) with all cracks modeled in the global problem. This reference discretization has a total of 365,538 degrees of freedom. We checked the convergence of the computed reference value for $\mathcal{G}$ by solving the problem using a smaller model, with 311,742 degrees of freedom. The difference in the energy release rates between these two models was less than 0.01%.

The discretizations shown in Fig. 16 are used in the analysis presented below. Local domains of different sizes are used, as illustrated in Fig. 16(*a*). Only the main crack is discretized in the global problem. The neighborhood of the main crack front and the entire MSD cracks are modeled in the local domains (cf. Figs.

Table 5 Normalized Mode I and II SIFs for the problem shown in Fig. 13. Cracks are not discretized in the global domain.

nDOFs (IG)	nDOFs (L)	nDOFs (EG)	Mode I SIF			Mode II SIF		
			GL-FEM	GFEM^{g-1}	Ref.	GL-FEM	GFEM^{g-1}	Ref.
1080	21,240	1134	0.2147	0.5854	0.6013	−0.1280	−0.3003	−0.2910

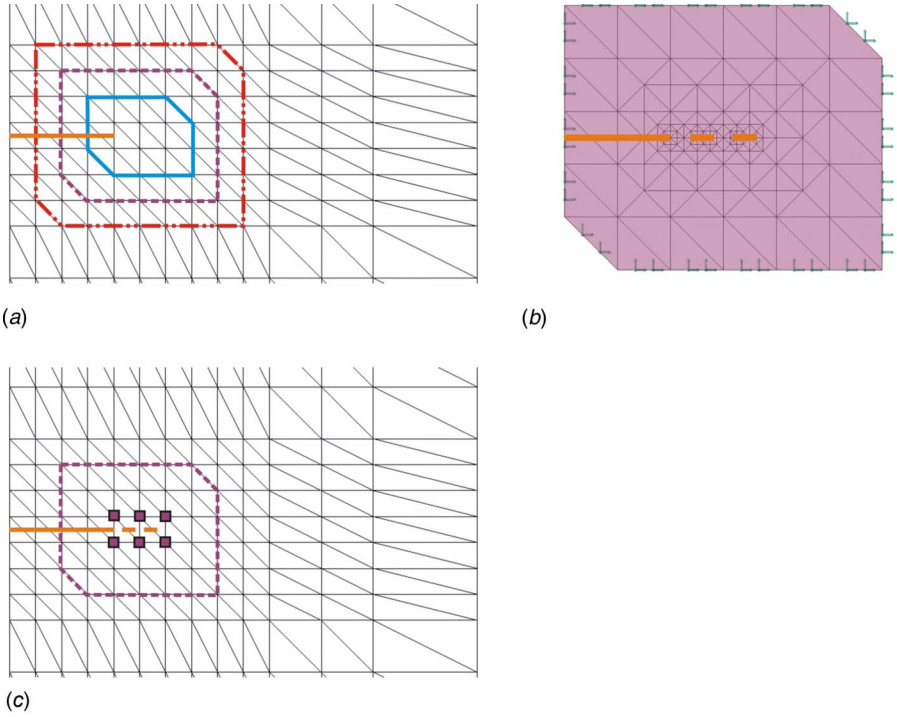

Fig. 16 Discretization of the MSD problem (front view). *Only the main crack is discretized in the global domain* while both the main and MSD cracks are discretized in the local domains. (*a*) Discretization of cracks in the initial global problem. Solid, dashed, and long dash-double dotted lines represent the boundaries of local domains with three different sizes used in this analysis. (*b*) Graded mesh used in the discretization of the local problem represented by a dashed line in (*a*). (*c*) Enrichment of global discretization with the local solution in (*b*). Global nodes enriched with the local solution are represented by squares.

16(*a*) and 16(*b*)). Not modeling the MSD cracks in the global domain considerably reduces the computational cost and also facilitates the creation of the macroscale discretization. In the case of the GFEM^{g-1}, the local solutions are used to enrich the global nodes illustrated in Fig. 16(*c*). The same set of 12 nodes is enriched, regardless of the size of local domain.

The local meshes are strongly refined in the neighborhood of the crack fronts. Singular Westergaard functions are used in local elements intersecting a crack front. Cubic shape functions are used in the initial and enriched global problems and in the local problems as well.

Table 6 lists the energy release rate ($\mathcal{G}$) extracted from GL-FEM and GFEM^{g-1} solutions for varying sizes of local domains. In the table, the three different sizes of local domains illustrated in Fig. 16(*a*) are denoted by "small," "middle," and "large." The results show that, for all sizes of local problems used, the energy release rate computed by the GFEM^{g-1} is more accurate than in the case of the GL-FEM. The relative error in $\mathcal{G}$ computed with the GL-FEM is about six times greater than the one by GFEM^{g-1} when the small local domain is used, and four times greater for the large local domain. This demonstrates, again, that the GFEM^{g-1} is more robust and accurate than the GL-FEM.

The deformed shape of the global domain before and after enrichment with the local solution is displayed in Fig. 17. The opening of the small MSD cracks can be clearly captured in the global domain after the enrichment with the local solution, as shown in Fig. 17(*b*), although they are represented only in the local problem.

5 Summary and Concluding Remarks

In this paper, we have compared the effectiveness of the global-local approach used in the FEM with the GFEM with global-local enrichment functions presented in Refs. [8,9]. Our focus is on problems involving interacting macrocracks as well as interactions among cracks with different scale sizes. The numerical experiments presented in this paper show that the GFEM^{g-1} is much

Table 6 Energy release rate ($\mathcal{G}$) extracted from GL-FEM and GFEM^{g-1} solutions for varying sizes of local domains. Rel. err. stands for relative error of extracted $\mathcal{G}$.

Size of local domain	nDOFs (IG)	nDOFs (L)	nDOFs (EG)	GL-FEM		GFEM^{g-1}	
				$\mathcal{G}$	Rel. err. (%)	$\mathcal{G}$	Rel. err. (%)
Small	17,280	40,662	17,316	1.9630	23.35	2.4706	3.53
Middle	17,280	42,294	17,316	2.1566	15.79	2.4828	3.05
Large	17,280	44,406	17,316	2.2783	11.04	2.4942	2.60
Ref.	365,538			2.5609		2.5609	

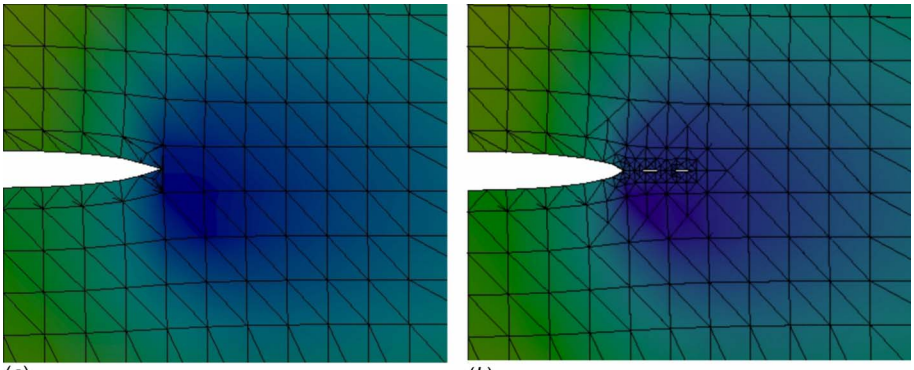

Fig. 17 Deformed shape of the global domain in the MSD problem before and after enrichment with a local solution. The elements of the local problem nested in the global mesh are visualized in (*b*). (*a*) Deformed shape of the global domain before enrichment with a local solution. (*b*) Deformed shape of the global domain after enrichment with a local solution.

more robust than the GL-FEM. Specifically, the following observations regarding the robustness of the methods can be made.

- The numerical examples presented in Sec. 4.1 show that the GFEM^{g-1} is less sensitive to the quality of boundary conditions applied to the local problems than the GL-FEM. Accurate SIFs could be extracted from GFEM^{g-1} solutions even when cracks were not modeled in the global problem. The SIFs extracted from GL-FEM solutions showed an error of up to one order of magnitude larger than in the case of the GFEM^{g-1}.
- When cracks were modeled in the initial global problems, the quality of SIFs extracted from GL-FEM solutions improved significantly with the accuracy of the initial global problem. However, increasing the polynomial order used in the initial global problem did *not* improve the performance of the GL-FEM much when cracks were not modeled in the global problem.
- Energy release rates extracted from GFEM^{g-1} solutions of a MSD problem consistently exhibited higher accuracy than in the case of the GL-FEM for all sizes of local domains considered in the numerical experiments.
- The GFEM^{g-1} can account for interactions among cracks with the same or different scale sizes, even when not all cracks are modeled in the initial global problem. This makes the GFEM^{g-1} an appealing method to analyze problems with phenomena spanning multiple spatial scales.

Our work in Ref. [9] also shows that the GFEM^{g-1} is computationally very efficient. The cost of the method when analyzing stationary cracks, like in this paper, is very close to the GL-FEM, since the cost of solving the enriched global problem is small when compared with the cost for the initial global problem [9]. The cost analysis presented in Ref. [9] was done on a single processor machine for the case of a single local problem defined per crack in the domain. Our ongoing research shows, however, that the method is also highly scalable and can be parallelized without difficulty. The robustness and computational efficiency of the GFEM^{g-1} makes it suited to the analysis of practical fracture mechanics engineering problems.

Acknowledgment

The partial support of this work by the National Center for Supercomputing Applications and the University of Illinois at Urbana-Champaign, under the auspices of the NCSA/UIUC Faculty Fellows Program, and by the National Science Foundation under Grant No. DMS-0611094 is gratefully acknowledged. This work is dedicated to Professor Fazil Erdogan for his seminal contributions to the analysis of fracture mechanics problems.

References

[1] Kayama, M., and Totsuka, N., 2002, "Influence of Interaction Between Multiple Cracks on Stress Corrosion Crack Propagation," Corros. Sci., **44**, pp. 2333–2352 (2002).
[2] Kayama, M., and Kitamura, T., 2004, "A Simulation on Growth of Multiple Small Cracks Under Stress Corrosion," Int. J. Fract., **130**, pp. 787–801.
[3] Kebir, H., Roelandt, J. M., and Chambon, L., 2006, "Dual Boundary Element Method Modelling of Aircraft Structural Joints With Multiple Site Damage," Eng. Fract. Mech., **73**, pp. 418–434.
[4] Seyedi, M., Taheri, S., and Hild, F., 2006, "Numerical Modeling of Crack Propagation and Shielding Effects in a Striping Network," Nucl. Eng. Des., **236**, pp. 954–964.
[5] Felippa, C. A., 2004, "Introduction to Finite Element Methods," Course Notes, Department of Aerospace Engineeing Sciences, University of Colorado at Boulder, available at http://www.colorado.edu/engineering/Aerospace/CAS/courses.d/IFEM.d/.
[6] Noor, A. K., 1986, "Global-Local Methodologies and Their Applications to Nonlinear Analysis," Finite Elem. Anal. Design, **2**, pp. 333–346.
[7] Diamantoudis, A. Th., and Labeas, G. N., 2005, "Stress Intensity Factors of Semi-Elliptical Surface Cracks in Pressure Vessels by Global-Local Finite Element Methodology," Eng. Fract. Mech., **72**, pp. 1299–1312.
[8] Duarte, C. A., Kim, D.-J., and Babuška, I., 2007, *Advances in Meshfree Techniques* (Computational Methods in Applied Sciences, Vol. 5), V. M. A. Leitão, C. J. S. Alves, and C. A. Duarte, eds., Springer, The Netherlands, pp. 1–26.
[9] Duarte, C. A., and Kim, D.-J., 2008, "Analysis and Applications of a Generalized Finite Element Method With Global-Local Enrichment Functions," Comput. Methods Appl. Mech. Eng., **197**(6–8), pp. 487–504.
[10] Civelek, M. B., and Erdogan, F., 1982, "Crack Problems for a Rectangular Plate and an Infinite Strip," Int. J. Fract., **19**, pp. 139–159.
[11] Sun, C. T., and Mao, K. M., 1988, "A Global-Local Finite Element Method Suitable for Parallel Computations," Comput. Struct., **29**, pp. 309–315.
[12] Babuška, I., and Strouboulis, T., 2001, *The Finite Element Method and its Reliability* (Numerical Mathematics and Scientific Computation) Oxford Science, New York.
[13] Babuška, I., and Melenk, J. M., 1997, "The Partition of Unity Finite Element Method," Int. J. Numer. Methods Eng., **40**, pp. 727–758.
[14] Duarte, C. A., Babuška, I., and Oden, J. T., 2000, "Generalized Finite Element Methods for Three Dimensional Structural Mechanics Problems," Comput. Struct., **77**, pp. 215–232.
[15] Oden, J. T., Duarte, C. A., and Zienkiewicz, O. C., 1998, "A New Cloud-Based *hp* Finite Element Method," Comput. Methods Appl. Mech. Eng., **153**, pp. 117–126.
[16] Strouboulis, T., Copps, K., and Babuška, I., 2001, "The Generalized Finite Element Method," Comput. Methods Appl. Mech. Eng., **190**, pp. 4081–4193.
[17] Duarte, C. A., Kim, D.-J., and Quaresma, D. M., 2006, "Arbitrarily Smooth Generalized Finite Element Approximations," Comput. Methods Appl. Mech. Eng., **196**, pp. 33–56.
[18] Oden, J. T., and Duarte, C. A., 1997, *Recent Developments in Computational and Applied Mechanics*, B. D. Reddy, ed., International Center for Numerical Methods in Engineering (CIMNE), Barcelona, Spain, pp. 302–321.
[19] Oden, J. T., and Duarte, C. A. M., 1996, *The Mathematics of Finite Elements and Applications—Highlights 1996*, J. R. Whiteman, ed., Wiley, New York, Chap. 2, pp. 35–54.
[20] Duarte, C. A., Hamzeh, O. N., Liszka, T. J., and Tworzydlo, W. W., 2001, "A Generalized Finite Element Method for the Simulation of Three-Dimensional Dynamic Crack Propagation," Comput. Methods Appl. Mech. Eng., **190**, pp. 2227–2262.
[21] Moes, N., Dolbow, J., and Belytschko, T., 1999, "A Finite Element Method for Crack Growth Without Remeshing," Int. J. Numer. Methods Eng., **46**, pp. 131–150.

[22] Sukumar, N., Moes, N., Moran, B., and Belytschko, T., 2000, "Extended Finite Element Method for Three-Dimensional Crack Modelling," Int. J. Numer. Methods Eng., **48**(11), pp. 1549–1570.
[23] Wells, G. N., and Sluys, L. J., 2001, "A New Method for Modeling Cohesive Cracks Using Finite Elements," Int. J. Numer. Methods Eng., **50**, pp. 2667–2682.
[24] Simone, A., 2004, "Partition of Unity-Based Discontinuous Elements for Interface Phenomena," Int. J. Math. Model., **20**, pp. 465–478.
[25] Duarte, C. A., Reno, L. G., and Simone, A., 2007, "A High-Order Generalized FEM for Through-The-Thickness Branched Cracks," Int. J. Numer. Methods Eng., **72**(3), pp. 325–351.
[26] Strouboulis, T., Zhang, L., and Babuška, I., 2003, "Generalized Finite Element Method Using Mesh-Based Handbooks: Application to Problems in Domains With Many Voids," Comput. Methods Appl. Mech. Eng., **192**, pp. 3109–3161.
[27] Szabo, B. A., and Babuška, I., 1988, "Computation of the Amplitude of Stress Singular Terms for Cracks and Reentrant Corners," *Fracture Mechanics: Nineteenth Symposium*, T. A. Cruse, ed., American Society for Testing and Materials, Philadelphia, pp. 101–124, ASTM STP, 969.
[28] Pereira, J. P., and Duarte, C. A., 2005, "Extraction of Stress Intensity Factors From Generalized Finite Element Solutions," Eng. Anal. Boundary Elem., **29**, pp. 397–413.
[29] Pereira, J. P., and Duarte, C. A., 2004, "Computation of Stress Intensity Factors for Pressurized Cracks Using the Generalized Finite Element Method and Superconvergent Extraction Techniques," *XXV Iberian Latin-American Congress on Computational Methods in Engineering*, Recife, PE, Brazil, Nov., P. R. M. Lyra, S. M. B. A. da Silva, F. S. Magnani, L. J. do, N. Guimaraes, L. M. da Costa, and E. Parente, Jr., eds.
[30] Babuška, I., and Andersson, B., 2005, "The Splitting Method as a Tool for Multiple Damage Analysis," SIAM J. Sci. Comput. (USA), **26**, pp. 1114–1145.
[31] Yohannes, A., Cartwright, D. J., and Collins, R. A., 1996, "Application of a Discontinuous Strip Yield Model to Multiple Site Damage in Stiffened Sheets," *The 1996 Forth International Conference on Computer-Aided Assessment and Control*, Fukuoka, Japan, pp. 565–572.
[32] Wang, L., Brust, F. W., and Atluri, S. N., 1997, "The Elastic-Plastic Finite Element Alternating Method (EPFEAM) and the Prediction of Fracture Under WFD Conditions in Aircraft Structures," Comput. Mech., **19**, pp. 356–369.
[33] Stern, M., Becker, E. B., and Dunham, R. S., 1976, "A Contour Integral Computation of Mixed-Mode Stress Intensity Factors," Int. J. Fract., **12**, pp. 359–368.
[34] Pereira, J. P., and Duarte, C. A., 2006, "The Contour Integral Method for Loaded Cracks," Int. J. Math. Model., **22**(5), pp. 421–432.

J. E. Ortiz
Group of Elasticity and Strength of Materials,
University of Seville,
Camino de los Descubrimientos s/n,
41092 Sevilla, Spain

W. A. Shelton
Computer Science and Mathematics Division,
Oak Ridge National Laboratory,
Oak Ridge, TN 37831-6367

V. Mantič

R. Criado

Group of Elasticity and Strength of Materials,
University of Seville,
Camino de los Descubrimientos s/n,
41092 Sevilla, Spain

L. J. Gray
Computer Science and Mathematics Division,
Oak Ridge National Laboratory,
Oak Ridge, TN 37831-6367;
Group of Elasticity and Strength of Materials,
University of Seville,
Camino de los Descubrimientos s/n,
41092 Sevilla, Spain

F. París
Group of Elasticity and Strength of Materials,
University of Seville,
Camino de los Descubrimientos s/n,
41092 Sevilla, Spain

A Parallel Domain Decomposition BEM Algorithm for Three-Dimensional Exponentially Graded Elasticity

A parallel domain decomposition boundary integral algorithm for three-dimensional exponentially graded elasticity has been developed. As this subdomain algorithm allows the grading direction to vary in the structure, geometries arising from practical functionally graded material applications can be handled. Moreover, the boundary integral algorithm scales well with the number of processors, also helping to alleviate the high computational cost of evaluating the Green's functions. For axisymmetric plane strain states in a radially graded material, the numerical results for cylindrical geometries are in excellent agreement with the analytical solution deduced herein. [DOI: 10.1115/1.2936232]

Keywords: functionally graded material, radially graded material, boundary integral equation, domain decomposition, distributed computing

1 Introduction

This article is a continuation of previous work aimed at the development of effective boundary integral equation (BIE) methods for the computational analysis of exponentially graded materials (the commonly used acronym FGM for general *functional* grading [1,2] will be employed herein for this subclass). In these solids, the Poisson ratio ν is assumed constant, while the Lamé moduli, μ and λ, vary with position $\mathbf{x}=(x_1,x_2,x_3)$ as

$$\mu(\mathbf{x}) = \mu_0 e^{2\boldsymbol{\beta}\cdot\mathbf{x}}, \quad \lambda(\mathbf{x}) = \lambda_0 e^{2\boldsymbol{\beta}\cdot\mathbf{x}} \tag{1.1}$$

where the constant vector $\boldsymbol{\beta}=(\beta_1,\beta_2,\beta_3)$ specifies the grading direction and $\lambda(\mathbf{x})/\mu(\mathbf{x})=\lambda_0/\mu_0=2\nu/(1-2\nu)$. Equation (1.1) gives the exponential grading for the Young elastic modulus $E(\mathbf{x})=E_0 e^{2\boldsymbol{\beta}\cdot\mathbf{x}}$, with $E_0=2(1+\nu)\mu_0$.

It should be noted that sophisticated finite element methods for FGMs exist, with special graded finite elements developed by Paulino and co-workers [3–6], Naghdabadi and Kordkheili [7], and Santare and co-workers [8,9]. However, boundary element methods (BEMs) can be advantageous for various types of problems in FGMs (e.g., contact, flaw detection, and fracture problems, a topic dominated by the work of Erdogan and co-workers [10–12]), and thus the development of a BEM/FGM capability is worth pursuing. Moreover, considering the important work of Erdogan and co-workers on singular integral equations [13–15], this is certainly an appropriate topic for this special issue.

1.1 3D BEM for Exponentially Graded Elasticity. A boundary integral formulation requires a fundamental solution, for example, the Kelvin solution for homogeneous isotropic elasticity [16–18]. The fundamental solution $\boldsymbol{\mathcal{U}}(\mathbf{x},\mathbf{y})$ for an exponentially graded isotropic elastic material has been obtained in Refs. [19,20] for two and three dimensions. In three dimensions, it can be written as

$$\boldsymbol{\mathcal{U}}(\mathbf{x},\mathbf{y}) = \exp\{-\boldsymbol{\beta}\cdot(\mathbf{x}+\mathbf{y})\}\{\boldsymbol{\mathcal{U}}^0(\mathbf{x}-\mathbf{y}) + \boldsymbol{\mathcal{U}}^g(\mathbf{x}-\mathbf{y})\} \tag{1.2}$$

where $\mathcal{U}_{j\ell}(\mathbf{x},\mathbf{y})$ $(j,\ell=1,2,3)$ represents the displacement in the j direction at point $\mathbf{x}$ due to a unit point force acting in the ℓ-direction at point $\mathbf{y}$ in the graded material, and $\boldsymbol{\mathcal{U}}^0$ is the weakly singular Kelvin fundamental solution for a homogeneous isotropic material defined by λ_0 and μ_0 [16–18]. The so-called grading term

$$\boldsymbol{\mathcal{U}}^g(\mathbf{x}-\mathbf{y}) = -\frac{1}{4\pi\mu_0 r}(1-e^{-\beta r})\boldsymbol{\mathcal{I}} + \boldsymbol{\mathcal{A}}(\mathbf{x}-\mathbf{y}) \tag{1.3}$$

is bounded for $r\to 0$, $r=\|\mathbf{r}\|$, where $\mathbf{r}=\mathbf{x}-\mathbf{y}$, and vanishes for $\beta=\|\boldsymbol{\beta}\|=0$. $\boldsymbol{\mathcal{I}}$ is the identity matrix. $\boldsymbol{\mathcal{A}}$ is expressed through a sum of five single and double integrals, whose quite complicated ex-

Contributed by the Applied Mechanics Division of ASME for publication in the JOURNAL OF APPLIED MECHANICS. Manuscript received June 15, 2007; final manuscript received March 14, 2008; published online July 11, 2008. Review conducted by Marek-Jerzy Pindera.

pressions include integrals of the modified first kind Bessel functions and hyperbolic functions (see Ref. [20] for details). The correctness and ability to implement the above formulas for $\mathcal{U}$ (also termed the Green's function or displacement kernel) was established in Ref. [21].

The derivation and numerical treatment of the expression for the corresponding traction kernel $\mathcal{T}(\mathbf{x},\mathbf{y})$, associated with the unit normal vector $\mathbf{n}(\mathbf{x})$, were detailed in Ref. [22],

$$\mathcal{T}(\mathbf{x},\mathbf{y}) = \exp(\boldsymbol{\beta}\cdot(\mathbf{x}-\mathbf{y}))(\mathcal{T}^0(\mathbf{x},\mathbf{y}) + \mathcal{T}^g(\mathbf{x},\mathbf{y})) \tag{1.4}$$

with $\mathcal{T}^0(\mathbf{x},\mathbf{y})$ representing the well-known strongly singular fundamental solution in tractions for a homogeneous material (with parameters μ_0 and λ_0) [16–18] and $\mathcal{T}^g(\mathbf{x},\mathbf{y})$ being the weakly singular grading term defined as

$$\mathcal{T}^g_{i\ell}(\mathbf{x},\mathbf{y}) = \left[\mu_0\left(\frac{\partial \mathcal{U}^g_{i\ell}}{\partial x_j} + \frac{\partial \mathcal{U}^g_{j\ell}}{\partial x_i} - \beta_i(\mathcal{U}^0_{j\ell} + \mathcal{U}^g_{j\ell}) - \beta_j(\mathcal{U}^0_{i\ell} + \mathcal{U}^g_{i\ell})\right) + \lambda_0\left(\frac{\partial \mathcal{U}^g_{k\ell}}{\partial x_k} - \beta_k(\mathcal{U}^0_{k\ell} + \mathcal{U}^g_{k\ell})\right)\delta_{ij}\right] n_j(\mathbf{x}) \tag{1.5}$$

With the appropriate Green's function kernels, the BIE for an exponentially graded elastic domain $\Omega \subset \mathbb{R}^3$ with a constant vector $\boldsymbol{\beta}$ takes the same form as that for homogeneous elasticity [16–18],

$$\mathcal{C}_{i\ell}(\mathbf{y})u_i(\mathbf{y}) + \int_\Gamma [\mathcal{T}_{i\ell}(\mathbf{x},\mathbf{y})u_i(\mathbf{x}) - \mathcal{U}_{i\ell}(\mathbf{x},\mathbf{y})\tau_i(\mathbf{x})]d\Gamma(\mathbf{x}) = 0 \tag{1.6}$$

where a bounded domain boundary $\Gamma = \partial\Omega$ is assumed and $\mathbf{y} \in \Gamma$. $\mathcal{C}(\mathbf{y})$ is the symmetric coefficient tensor of the free term, whose value coincides with its value for a homogeneous isotropic material defined by the Poisson ratio ν [22,23],

$$\mathcal{C}(\mathbf{y}) = \lim_{\varepsilon\to 0_+}\int_{S_\varepsilon(\mathbf{y})\cap\Omega} \mathcal{T}(\mathbf{x},\mathbf{y})dS(\mathbf{x}) = \lim_{\varepsilon\to 0_+}\int_{S_\varepsilon(\mathbf{y})\cap\Omega} \mathcal{T}^0(\mathbf{x},\mathbf{y})dS(\mathbf{x}) \tag{1.7}$$

with $S_\varepsilon(\mathbf{y})$ being a spherical surface of radius ε centered at $\mathbf{y}$ and oriented by the unit normal vectors pointing to the center.

The numerical solution of this equation only requires approximation of Γ and of the boundary displacements and tractions, $\mathbf{u}(\mathbf{x})$ and $\boldsymbol{\tau}(\mathbf{x})$, leading to the following form of the system of linear equations:

$$\mathcal{H}\mathbf{u} = \mathcal{G}\mathbf{t} \tag{1.8}$$

where the matrices $\mathcal{H}$ and $\mathcal{G}$ contain integrals of the kernel functions $\mathcal{T}(\mathbf{x},\mathbf{y})$ and $\mathcal{U}(\mathbf{x},\mathbf{y})$, respectively, and the vectors $\mathbf{u}$ and $\mathbf{t}$, respectively, collect the nodal values of boundary displacements and tractions. Applying the boundary conditions and collecting all unknowns by moving columns results in a system of linear equations $Ax=b$ that can be solved. Notice that in Eq. (1.6), the grading is exactly captured by the Green's functions, and it is not necessary to employ a refined mesh to accurately track the exponential variation in the Lamé moduli.

1.2 Motivation and Description of the Present Work. There are several serious issues in utilizing Eq. (1.6). First, previous numerical work has only considered simple situations wherein the grading direction $\boldsymbol{\beta}$ is constant throughout the material. While this sufficed for testing the kernel expressions, practical applications will necessarily involve complicated geometries wherein the grading direction varies over the structure. This situation can be handled by decomposing the domain Ω into subdomains having (approximately) a constant value of $\boldsymbol{\beta}$ and by applying Eq. (1.6), and then Eq. (1.8), to each subdomain (for the literature on domain decomposition with boundary elements, see Refs. [16–18,24,25]). A primary objective of this work is the development of this domain decomposition FGM algorithm.

Although this approach introduces new internal surfaces (interfaces between subdomains) and new unknowns (displacements and tractions associated with these interfaces), the computational cost can, depending on the geometry, actually be less than it would be when working with the entire boundary Γ. The system of linear equations for each subdomain will involve significantly less integrations than the corresponding system of linear equations for a direct implementation of Eq. (1.6). For a FGM analysis, domain decomposition is particularly attractive because the kernel function evaluations are quite expensive: The complicated expressions for $\mathcal{U}(\mathbf{x},\mathbf{y})$ and $\mathcal{T}(\mathbf{x},\mathbf{y})$, presented in Eqs. (1.2)–(1.5), require the numerical computation of one- and two-dimensional integrals. Thus, the tradeoff between the computational cost of introducing new surfaces and that of reducing the total number of integrations swings heavily in favor of reduced number of quadratures. Moreover, FGM applications will often involve thin films, and in this case the (created) interior surfaces will be small, and domain decomposition is especially advantageous.

Nevertheless, the high cost of Green's function evaluation means that any solution of Eq. (1.6) will be quite slow. Without significant improvements in the kernel evaluation algorithms, a multiprocessor implementation is therefore essential for obtaining reasonable run times. Fortunately, as boundary integral computations are a collection of independent integrations, they generally scale very well, and this will be seen in the results reported below.

Parallel domain decomposition implementations for the classical BEM, aimed at solving large-scale, linear and nonlinear, steady-state, and time dependent problems, have been previously reported by several authors [26–29]. They are based on efficient iterative domain decomposition algorithms (e.g., the alternative Schwarz methods and the Uzawa method) that satisfy the coupling conditions between subdomains while avoiding the high storage and computing time requirements associated with solving the large, nonsymmetric global system via a serial direct solver. Nevertheless, at this point, the evaluation of Green's functions in Eqs. (1.2)–(1.5) is so expensive that it would take a very large problem for the cost of the solver to be an issue. Therefore, in the initial algorithm applied in this work (see Sec. 2), an iterative algorithm has not been employed; instead, the global linear system is assembled and solved directly. In fact, as will be seen in Sec. 3, the solver time for the problems considered was only a very small fraction of the time used in the generation and assembly of the BEM matrices.

To validate the parallel domain decomposition algorithm, simulations have been carried out for the radially graded hollow cylinders studied in the work of Zhang and Hasebe [30]. Considering the distributions of tractions applied to the inner and outer boundaries of the cylinder, an analytical solution is obtained in Ref. [30] by decomposing the cylinder into M homogeneous cylindrical layers. The elastic constants in the layers are chosen to approximate the exponential grading. The solution for this piecewise constant representation of $\mu(\mathbf{x})$ and $\lambda(\mathbf{x})$ then approaches that for the continuous grading as $M\to\infty$. Herein, for the case of constant internal and external pressures, a new fully explicit form for this analytic solution is derived in Appendix A. The agreement of the computational results with the formulas in Ref. [30] and with this new expression gives confidence that both the numerical analysis and the analytic expressions are correct.

2 BEM Algorithm

2.1 Domain Decomposition. For domain decomposition, the domain Ω is first subdivided into n subdomains Ω_s $(s=1,\ldots,n)$ with boundaries $\Gamma_s=\partial\Omega_s$, defining the interfaces $\Gamma_{ss'}=\Gamma_s\cap\Gamma_{s'}$ between subdomains Ω_s and $\Omega_{s'}$ $(s\neq s')$. In the present case, this partitioning is chosen with an eye toward effectively approximating a smooth variation in the functional grading direction $\boldsymbol{\beta}(\mathbf{x})$ present in the problem by a piecewise constant approximation

defining a constant $\boldsymbol{\beta}^s$ inside each Ω_s.

As is standard practice in the BEM [16–18], the boundary Γ_s of a homogeneous elastic subdomain Ω_s is represented as a union of elements, and this boundary partition permits a piecewise parametric approximation of the geometry and field variables. In this work, standard nine-noded quadratic quadrilateral elements are used for the boundary approximation, whereas nine-noded discontinuous quadratic quadrilateral elements are used for interpolating the displacement and traction components. In most instances, the use of continuous boundary elements is more efficient than the use of discontinuous elements; however, for a domain decomposition algorithm employing collocation, the equations generated at the nodes of a continuous element do not suffice in treating interface corners and cross points where several subdomains meet. Consequently, suitable additional collocation equations are required. Thus, discontinuous elements lead to a simpler implementation of the continuity conditions across the interfaces, always generating an equal number of unknowns and equations [24,25]. Nevertheless, the ultimate goal of this work is to develop a multidomain Galerkin formulation, as presented in Refs. [31–33].

The BIE in Eq. (1.6) is then implemented for each subdomain boundary Γ_s, together with constraint equations across the interfaces $\Gamma_{ss'}$ that replace the missing boundary conditions. Although the details of a domain decomposition algorithm can vary (e.g., direct versus iterative solver and continuous versus discontinuous elements), the basic procedures in the BEM are standard and have been presented in the literature (see Refs. [16–18,24,25] and references therein). The goal of discussion herein is to briefly illustrate the general technique using the simple case of two subdomains ($n=2$). The extension to multiple divisions is relatively straightforward.

Separating the added internal boundary (interface) variables from those for the original external boundary, the systems of linear equations (Eq. (1.8)) for the two subdomains ($s=1,2$) can be written in the form

$$[\mathcal{H}^s_{\text{int}} \quad \mathcal{H}^s_{\text{ext}}]\begin{bmatrix}\mathbf{u}^s_{\text{int}}\\ \mathbf{u}^s_{\text{ext}}\end{bmatrix} = [\mathcal{G}^s_{\text{int}} \quad \mathcal{G}^s_{\text{ext}}]\begin{bmatrix}\mathbf{t}^s_{\text{int}}\\ \mathbf{t}^s_{\text{ext}}\end{bmatrix} \tag{2.1}$$

where the column vectors $\mathbf{u}^s$ and $\mathbf{t}^s$ contain the nodal values of the approximated displacements and tractions on Γ_s, and the subscripts int and ext, respectively, indicate the interface part and the remainder external part of Γ_s.

In most domain decomposition methods, the compatibility and equilibrium conditions for displacements and tractions on the interface are imposed pointwise, i.e., for $\mathbf{x} \in \Gamma_{12}$

$$\mathbf{u}^1_{\text{int}}(\mathbf{x}) - \mathbf{u}^2_{\text{int}}(\mathbf{x}) = \mathbf{0}$$

$$\boldsymbol{\tau}^1_{\text{int}}(\mathbf{x}) + \boldsymbol{\tau}^2_{\text{int}}(\mathbf{x}) = \mathbf{0} \tag{2.2}$$

with displacement and traction vectors being given in a global reference system. Herein, these equations are instead enforced in a weak sense, the primary motivation being to allow (in the future) nonmatching discretizations of internal interfaces, as in Ref. [34]. Equation (2.2) therefore takes the form

$$\int_{\Gamma_{12}} \phi(\mathbf{x})(\mathbf{u}^1_{\text{int}}(\mathbf{x}) - \mathbf{u}^2_{\text{int}}(\mathbf{x}))d\Gamma(\mathbf{x}) = \mathbf{0}$$

$$\int_{\Gamma_{12}} \phi(\mathbf{x})(\boldsymbol{\tau}^1_{\text{int}}(\mathbf{x}) + \boldsymbol{\tau}^2_{\text{int}}(\mathbf{x}))d\Gamma(\mathbf{x}) = \mathbf{0} \tag{2.3}$$

where the weight function $\phi(\mathbf{x})$ stands for any of the shape functions defined by the boundary elements on one or the other side of the interface Γ_{12}; thus, a series of equations that represent the weak coupling conditions is generated. Incorporating these equations with Eq. (2.1) results in the global system

$$\begin{bmatrix}\mathcal{H}^1_{\text{int}} & \mathcal{H}^1_{\text{ext}} & \mathbf{0} & \mathbf{0}\\ \mathbf{0} & \mathbf{0} & \mathcal{H}^2_{\text{int}} & \mathcal{H}^2_{\text{ext}}\\ \mathcal{M}^1_{\text{int}} & \mathbf{0} & \mathcal{M}^2_{\text{int}} & \mathbf{0}\\ \mathbf{0} & \mathbf{0} & \mathbf{0} & \mathbf{0}\end{bmatrix}\begin{bmatrix}\mathbf{u}^1_{\text{int}}\\ \mathbf{u}^1_{\text{ext}}\\ \mathbf{u}^2_{\text{int}}\\ \mathbf{u}^2_{\text{ext}}\end{bmatrix} = \begin{bmatrix}\mathcal{G}^1_{\text{int}} & \mathcal{G}^1_{\text{ext}} & \mathbf{0} & \mathbf{0}\\ \mathbf{0} & \mathbf{0} & \mathcal{G}^2_{\text{int}} & \mathcal{G}^2_{\text{ext}}\\ \mathbf{0} & \mathbf{0} & \mathbf{0} & \mathbf{0}\\ \mathcal{N}^1_{\text{int}} & \mathbf{0} & \mathcal{N}^2_{\text{int}} & \mathbf{0}\end{bmatrix}\begin{bmatrix}\mathbf{t}^1_{\text{int}}\\ \mathbf{t}^1_{\text{ext}}\\ \mathbf{t}^2_{\text{int}}\\ \mathbf{t}^2_{\text{ext}}\end{bmatrix} \tag{2.4}$$

where the "mass" matrices $\mathcal{M}$ and $\mathcal{N}$, respectively, represent the discrete form of the compatibility and equilibrium conditions across the interface in Eq. (2.3). As for a single domain problem, collecting all unknowns on the left hand side by moving columns and applying the boundary conditions on the right-hand side results in the standard form of the system of linear equations $Ax=b$. As noted above, the global BEM matrix A is, for simplicity in this preliminary implementation, explicitly constructed and solved via a direct method. For large-scale computations, it is clearly essential to exploit the zero blocks in matrix A, and this will be incorporated in the future.

2.2 Parallel Implementation. The parallel implementation is a single program multiple data (SPMD) algorithm utilizing a simple *host/node* model (host is the manager processor and node is a worker processor), and the Message Passing Interface (MPI) library handles communication between processors. The host/node format results in a calculation, described in Appendix B, that is highly load balanced. Each node calls a procedure determining how many and which boundary elements this node will integrate. When the node completes its task, it sends the results to the host. Since the integrations over a boundary element are independent of other boundary element integrations, the tasks performed by different nodes are independent. Therefore, in the course of constructing the boundary integral matrices, there is no communication between nodes, only with the host. Once the host has collected all the BEM integration results from the nodes and has applied the boundary conditions, the matrix and the right-hand side vector are completely set up and the host solves the BEM system of equations.

This parallel algorithm leads to very good load balancing. For instance, if the time necessary to integrate over a boundary element is roughly the same for all elements, the load balancing is close to optimal when the total number of elements is a multiple of the number of processors; if this is not the case, at most, mod (boundary elements, *nodes*) processors will have one additional element to integrate. This results in a highly parallel algorithm (the ratio of the communication costs to computation being small) that is almost perfectly load balanced.

All calculations were run on the Oak Ridge Institutional Cluster, which consists of 526 dual core 3.4 GHz Intel Xeon processors, for a total of 1052 CPUs with a peak performance of 7.154 Tflops. Each dual core has 4 Gbytes of random access memory (RAM).

As noted above, this initial parallel domain decomposition implementation can be improved. First, the iterative methods successfully employed for the classical BEM [26–29] can be incorporated. Second, the sparsity of the global BEM matrix can be exploited by incorporating parallel sparse linear algebra techniques [35,36]. This will include both direct and iterative methods. The advantage of an iterative approach is that the major computational cost per iteration is a matrix-vector product, which is highly parallel, resulting in a highly scalable approach. A direct sparse method relies on the factorization of the global BEM matrix (i.e., *LU* decomposition), which is inherently serial. However, by taking advantage of the sparse representation, the memory

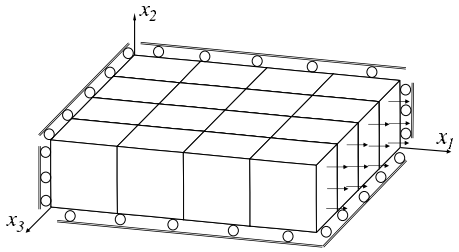

Fig. 1 Domain decomposition mesh and boundary conditions for the graded parallelepiped

costs should scale linearly with increasing matrix size, and combining this with preconditioned iterative methods will also result in a highly scalable algorithm.

3 Computational Results

As a first check of the parallel domain decomposition code, the performance of the algorithm on a simpler, $\boldsymbol{\beta}$ constant, problem will be examined. The results for the cylinder problem mentioned in the Introduction, will then be discussed.

3.1 Parallelepiped: $\boldsymbol{\beta}$ Constant. Let the rectangular elastic domain Ω, defined by $0<x_2<\ell$, $0<x_1, x_3<4\ell$, be graded in the x_3 direction, $\boldsymbol{\beta}=(0,0,\log(2)/(4\ell))$, and set the Poisson ratio to be $\nu=0.3$. If the face $x_1=4\ell$ is subjected to a constant normal displacement,

$$\mathbf{u}(4\ell,x_2,x_3)=(\sigma_0 4\ell/E_0,0,0) \tag{3.1}$$

the faces $x_2=\ell$ and $x_3=4\ell$ are traction free, and the symmetry boundary conditions are prescribed at the other faces. Then, an exact solution exists [21], the displacements being given by

$$\mathbf{u}(\mathbf{x})=(\sigma_0 x_1/E_0,-\nu\sigma_0 x_2/E_0,-\nu\sigma_0 x_3/E_0) \tag{3.2}$$

In addition, the stress component $\sigma_{11}(\mathbf{x})=\sigma_0\exp(2\beta x_3)$ and the remaining stresses vanish, $\sigma_{ij}=0$ for $(i,j)\neq(1,1)$.

Figure 1 shows the above boundary conditions and the partition of the parallelepiped into $n=16$ subdomains Ω_s, each one being a cube of side ℓ discretized by six boundary elements.

Figures 2 and 3 plot, respectively, the displacement components $u_1(x_1)E_0/\ell\sigma_0$ and $u_3(x_3)E_0/\ell\sigma_0$ versus the exact solution, and Fig. 4 plots the corresponding results for the nonzero component of the stress tensor $\sigma_{11}(x_3)/\sigma_0$. In all cases, the accuracy for this simple problem is excellent.

Regarding parallel efficiency, Fig. 5 is a plot of the total computation time (in minutes) versus the number of processors. The computation time used by the serial direct solver to solve the global BEM system on the host, included in the total computation time in Fig. 5, was 7s, representing only a small fraction of the total computation time. When the number of processors is small compared to the number of boundary elements (96) and boundary nodes (864), the algorithm scales, as expected, very well. However, a large number of processors (>30) applied to this relatively small problem is ineffective, as each node's communication time with the host begins to be significant compared to its computation time.

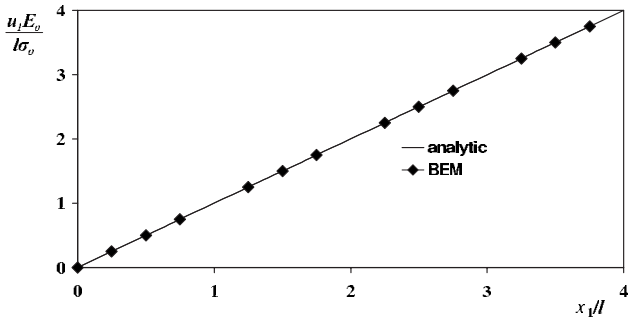

Fig. 2 The $u_1E_0/\ell\sigma_0$ displacement component for the graded parallelepiped

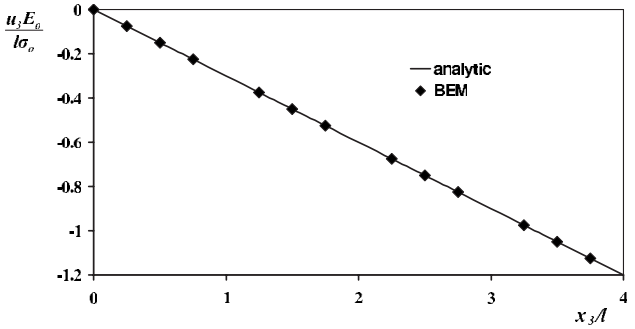

Fig. 3 The $u_3E_0/\ell\sigma_0$ displacement component for the graded parallelepiped

3.2 Cylinder. Following Zhang and Hasebe [30], we consider a hollow cylinder, inner radius r_0, and outer radius r_e, with grading in the radial direction,

$$\mu(\mathbf{x})=\mu(r)=\mu_0 e^{2\beta r},\quad \lambda(\mathbf{x})=\lambda(r)=\lambda_0 e^{2\beta r},\quad E(\mathbf{x})=E(r)=E_0 e^{2\beta r} \tag{3.3}$$

where μ_0, λ_0, E_0, and β are constants. (Note that the grading β in this equation conforms to the notation in Ref. [20] and differs, by the factor of 2, from that employed in Ref. [30].) The Poisson ration is $\nu=0.3$.

The boundary conditions are zero traction on the outer ring $r=r_e$, while on $r=r_0$ the constant internal pressure $p>0$ is pre-

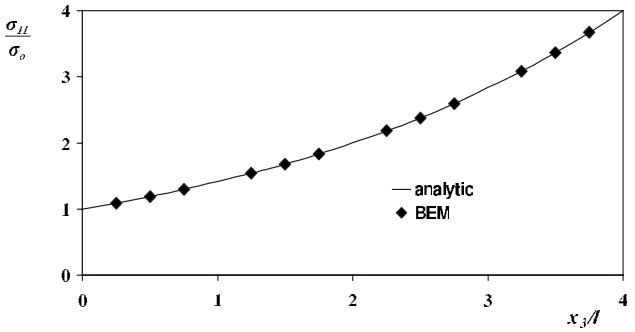

Fig. 4 The normal stress σ_{11}/σ_0 for the graded parallelepiped

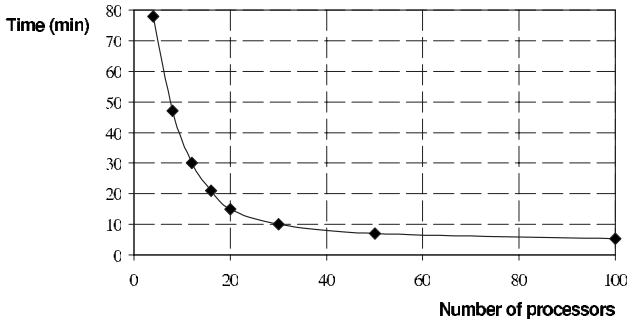

Fig. 5 Computation time versus number of processors for the graded parallelepiped

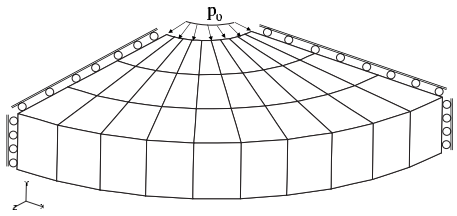

Fig. 6 Domain decomposition for the very thick hollow cylinder

scribed. This will allow modeling a one-quarter section of the cylinder defining the elastic domain Ω, as shown in Fig. 6, with symmetry boundary conditions applied on the surfaces $\theta=0$ and $\theta=\pi/2$.

The domain decomposition of the quarter cylinder Ω employed in the calculations, with $r_0=1$ and $r_e=5$ (this very thick cylinder was considered in Ref. [30]), is shown in Fig. 6. An analogous domain decomposition was also employed for a thinner cylinder with $r_0=1$ and $r_e=2$. These are relatively coarse decompositions as there are only $n=10$ subdomains (polar segments) Ω_s, each one being discretized by three boundary elements in the radial direction. The (constant) grading direction for each subdomain Ω_s is approximated by the vector $\boldsymbol{\beta}^s$ in the radial direction associated with the midpoint in θ. For $\beta=0.75$, one of the cases considered in Ref. [30], the change in elastic stiffness is extremely large for the very thick cylinder, i.e., $E(r_e)/E(r_0)\doteq 403.4$, whereas it is moderate for the less thick cylinder, $E(r_e)/E(r_0)\doteq 4.5$. Accurate results are nevertheless obtained with the crude discretization used in both cases, a consequence of the exponential grading being handled exactly within the Green's function.

Considering first the very thick cylinder, Figs. 7 and 8, respectively, show the BEM results for $u_rE(r_0)/r_0p$ and $\sigma_\theta(r)/p$ for $\beta=0.75$, and as in Ref. [30], the homogeneous case, $\beta=0$, is included for comparison. These graphs agree very well with the new analytic solutions in displacements and stresses introduced in Appendix A (Eqs. (A5)–(A10)), with the stress solution shown in Ref. [30] for the radially graded material, and with the classic analytical solution [37] for the homogeneous material. Consider the percentages of the normalized errors defined as

$$\mathrm{err}(u_r)=\left|\frac{u_r^{\mathrm{num}}-u_r^{\mathrm{an}}}{\max\limits_{r_0\le r\le r_e} u_r^{\mathrm{an}}}\right|\times 100 \text{ and } \mathrm{err}(\sigma_\theta)=\left|\frac{\sigma_\theta^{\mathrm{num}}-\sigma_\theta^{\mathrm{an}}}{\max\limits_{r_0\le r\le r_e} \sigma_\theta^{\mathrm{an}}}\right|\times 100 \tag{3.4}$$

where "num" and "an" refer to numerical and analytical values, respectively. Then, evaluating these errors for the radial displacements at nodes in the radial direction of the homogeneous and graded cylinders, respectively, it is obtained that $0.5\% < \mathrm{err}(u_r^{\mathrm{hom}}) < 2.7\%$ and $0.4\% < \mathrm{err}(u_r^{\mathrm{grad}}) < 2.9\%$. Thus, the numerical solutions match equally well the analytical ones in both cases. Notice that the differences between the numerical and analytical solutions are more visible in Fig. 7 in the homogeneous case due to higher absolute values of these displacements. When looking at the hoop stresses, $0.007\% < \mathrm{err}(\sigma_\theta^{\mathrm{hom}}) < 0.4\%$ and $0.6\% < \mathrm{err}(\sigma_\theta^{\mathrm{grad}}) < 9.9\%$. Thus, these errors are significantly higher in the graded cylinder possibly due to a steeper gradient in the stress solution, in this case approximated by a very coarse mesh, together with a very large change in the Young modulus.

Considering now the moderately thick cylinder, the displacement and stress solutions shown in Figs. 9 and 10 for $\beta=\pm 0.75$ agree excellently with the new analytic solutions in displacements and stresses found in Eqs. (A5)–(A10). In fact, the normalized errors, defined by Eq. (3.4) with superscripts $\pm$ referring to $\beta=\pm 0.75$, computed for this moderately thick graded cylinder—$0.2\% < \mathrm{err}(u_r^{+}) < 0.6\%$ and $0.7\% < \mathrm{err}(u_r^{-}) < 1.3\%$ in

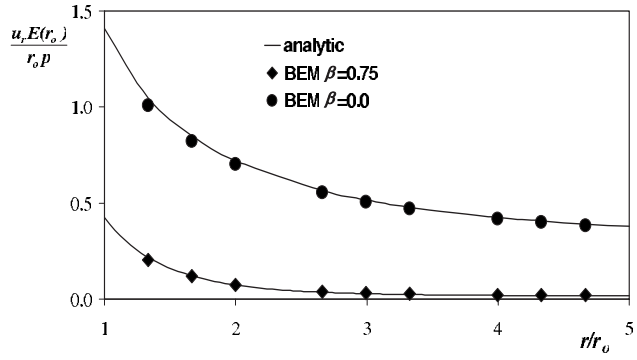

Fig. 7 Computed values of $u_rE(r_0)/r_0p$ for $\beta=0.75$ and $\beta=0$ in the very thick hollow cylinder

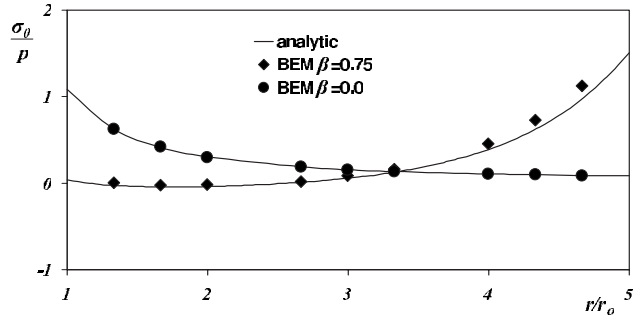

Fig. 8 Computed values of σ_θ/p for $\beta=0.75$ and $\beta=0$ in the very thick hollow cylinder

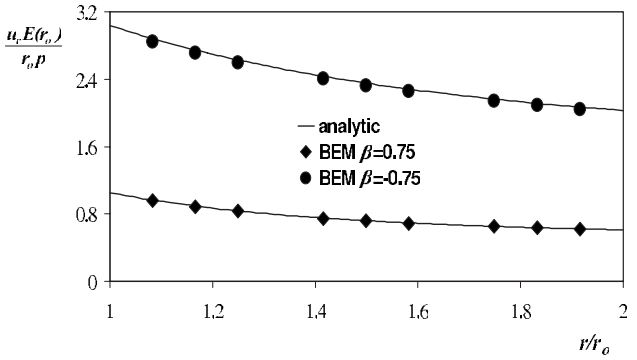

Fig. 9 Computed values of $u_rE(r_0)/r_0p$ for $\beta=\pm 0.75$ in the thick hollow cylinder

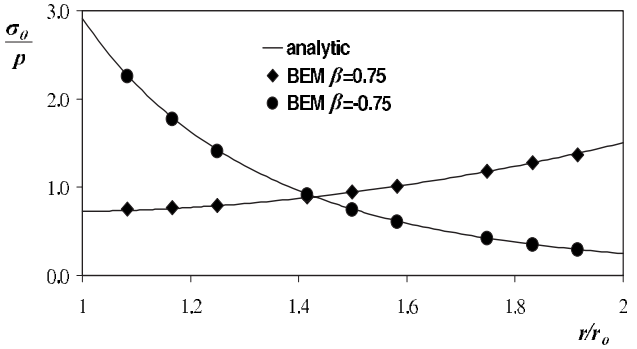

Fig. 10 Computed values of σ_θ/p for $\beta=\pm 0.75$ in the thick hollow cylinder

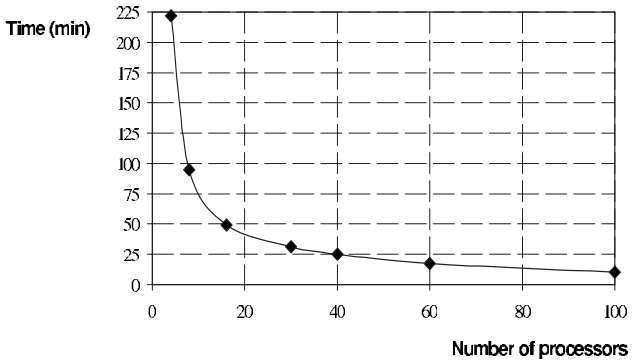

Fig. 11 Computation time versus number of processors for the very thick hollow cylinder

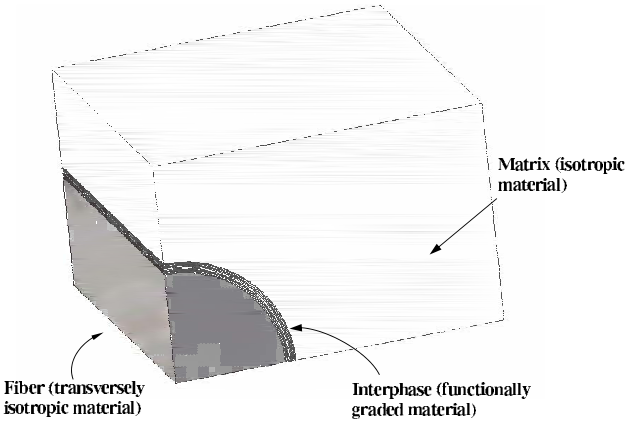

Fig. 12 Geometry of a transversally isotropic carbon fiber embedded in an isotropic epoxy matrix with a radially graded interphase

the radial displacements and $0.01\% < \mathrm{err}(\sigma_\theta^+) < 1.3\%$ and $0.08\% < \mathrm{err}(\sigma_\theta^-) < 0.7\%$ in the hoop stresses—are somewhat smaller when compared with their values for the very thick graded cylinder. This can be understood as a consequence of using the same number of boundary elements in the radial direction for both very and moderately thick graded cylinders with the same modulus of the grading exponent β.

Regarding parallel efficiency, from Fig. 11, where the total computation time is shown, it is seen that the algorithm scales better for the cylinder than for the parallelepiped due to a larger number of boundary elements in the present more complex BEM model. In fact, the ratio of the computation time required for the maximum number of processors used in both examples is about $t_{\mathrm{cyl}}/t_{\mathrm{par}} \doteq 1.9$, whereas the ratio of integration collocation points/boundary elements required is $(10\times9\times14\times14)/(16\times9\times6\times6) \doteq 3.4$. The computation time used by the serial solver to solve the global BEM system on the host, included in the total computation time in Fig. 11, was 17s, again representing only a small fraction of the total computation time.

Even with the complexity of the fundamental solutions, the fully quadratic elements (9 nodes) are presumed to behave as with other boundary integral analyses, *e.g.*, the expected convergence rate in both displacements and tractions should be $\mathcal{O}(h^3)$, h the characteristic size of the mesh. Although it would certainly be desirable to test this experimentally by running a sequence of finer meshes, the computational cost of evaluating the kernel functions makes this somewhat impractical at this point. However, new techniques for evaluating the Green's function quantities are currently being developed, and these methods will hopefully permit the necessary convergence testing to be carried out.

4 Conclusion

Based on the successful comparisons with the series expansion representations in Ref. [30] and with the new fully explicit solution deduced herein, it can be concluded that the boundary integral algorithm is capable of producing accurate FGM solutions when the grading direction $\boldsymbol{\beta}$ is not constant. Utilizing domain decomposition to handle the varying $\boldsymbol{\beta}$ and parallel computing to overcome the high cost of Green's function evaluation, reasonable computation times are obtained. Even with large variation in the elastic moduli, accurate solutions have been obtained with reasonably coarse grids, and as expected, the algorithm scales very well with the number of processors. It should therefore be possible to tackle applications involving complex geometries. To address large-scale calculations, the algorithm will be modified to incorporate either an iterative domain decomposition algorithm or a sparse matrix storage format and a parallel sparse solver, as discussed in Sec. 2.2.

A specific problem in fiber composite materials that partially motivated this work is shown in Fig. 12. The manufacturing process creates a thin layer between the fiber and polymer matrix that can be modeled as radially graded. The effects of this interphase on the properties of the composite have been studied experimentally [38] and computationally [39–41]. Modeling the composite at this microscopic level will necessarily require a large-scale calculation.

Acknowledgment

This work was supported by the Spanish Ministry of Education and Science through Projects TRA2005-06764 and TRA2006-08077, by the Junta de Andalucía through the Projects of Excellence TEP1207 and TEP2045, and by the Office of Advanced Scientific Computing Research, U.S. Department of Energy under Contract No. DE-AC05-00OR22725 with UT-Battelle, LLC. Part of this research was performed during the stay of J.E.O. at Oak Ridge National Laboratory, which was funded by the Junta de Andalucía and Oak Ridge National Laboratory.

The submitted manuscript has been authored by a contractor of the U. S. Government under Contract DE-AC05-00OR22725. Accordingly the U. S. Government retains a non-exclusive, royalty free license to publish or reproduce the published form of this contribution, or allow others to do so, for U. S. Government purposes.

Appendix A: Axisymmetric Plane Strain Solution for Radially and Exponentially Graded Material

Let $\sigma_{ij}(r)$, $\varepsilon_{ij}(r)$, and $u_i(r)$ $(i,j=r,\theta)$ represent an axisymmetric plane strain state in a radially and exponentially graded material defined in polar coordinates (r,θ) by Eq. (3.3). Then, the constitutive law is written as

$$\sigma_r(r) = (2\mu(r) + \lambda(r))\varepsilon_r(r) + \lambda(r)\varepsilon_\theta(r),$$

$$\sigma_\theta(r) = (2\mu(r) + \lambda(r))\varepsilon_\theta(r) + \lambda(r)\varepsilon_r(r) \tag{A1}$$

with $\sigma_{r\theta}=\varepsilon_{r\theta}=0$. After substituting standard relations between strains and displacements given in polar coordinates [37] into Eq. (A1), the equilibrium equation (with vanishing body forces) in the radial direction,

$$\sigma_{r,r}(r) + r^{-1}(\sigma_r(r) - \sigma_\theta(r)) = 0 \tag{A2}$$

reduces to the second order ordinary differential equation in displacements

$$\frac{d^2u_r}{dr^2}(r) + (r^{-1} + 2\beta)\frac{du_r}{dr}(r) - r^{-1}(r^{-1} - 2\beta\nu')u_r(r) = 0 \tag{A3}$$

where

$$\nu' = \frac{\nu}{1-\nu} \tag{A4}$$

Notice that the equilibrium equation in the angular direction is fulfilled due to the axial-symmetry assumption.

It can be verified that Eq. (A3) is a particular case of the general confluent (hypergeometric) equation, as defined in Abramowitz and Stegun [42] whose (formal) general solution can be written as

$$u_r(r) = re^{-2\beta r}(c_1 M(2-\nu',3,2\beta r) + c_2 U(2-\nu',3,2\beta r)) \tag{A5}$$

where $M(a,b,z)$ (a,b,z being in general complex numbers) is the Kummer confluent hypergeometric function (denoted also as ${}_1F_1(a,b,z)$ or $\Phi(a,b,z)$), $U(a,b,z)$ is the confluent hypergeometric function of the second kind (denoted also as $\Psi(a,b,z)$), and c_1 and c_2 are constants to be determined from the boundary conditions of an axially symmetric plane-strain problem. For exact definitions and properties of these hypergeometric functions, see Ref. [42].

Whereas $M(a,b,z)$ is well defined for any complex z, $U(a,b,z)$ has, in general, a branch cut along the negative real axis in the complex z-plane. Thus, the case of $\beta<0$ requires special attention when evaluating $U(2-\nu',3,2\beta r)$ in Eq. (A5). The application of the analytic continuation of $U(a,b,z)$ given in Ref. [42] and the fact that in the present case $b=3$ is an odd number lead to a well defined form of the general solution of Eq. (A3) for $\beta<0$,

$$u_r(r) = r(c_1 M(1+\nu',3,-2\beta r) + c_2 U(1+\nu',3,-2\beta r)) \tag{A6}$$

where the Kummer transformation [42] for $M(a,b,z)$ has been used as well.

Differentiating the general solutions in displacements, Eqs. (A5) and (A6), and applying the graded constitutive law in Eq. (A1) gives the corresponding solutions in stresses,

$$\begin{aligned}\sigma_r(r) = (2\mu_0+\lambda_0)\{&c_1[(1+\nu'-2\beta r)M(2-\nu',3,2\beta r) \\ &+ 2\beta r(2-\nu')M(3-\nu',4,2\beta r)/3] + c_2[(1+\nu'-2\beta r) \\ &\times U(2-\nu',3,2\beta r) - 2\beta r(2-\nu')U(3-\nu',4,2\beta r)]\}\end{aligned} \tag{A7}$$

$$\begin{aligned}\sigma_\theta(r) = (2\mu_0+\lambda_0)(1+\nu')\{&c_1[(1-2\beta\nu r)M(2-\nu',3,2\beta r) \\ &+ 2\beta\nu r(2-\nu')M(3-\nu',4,2\beta r)/3] + c_2[(1-2\beta\nu r) \\ &\times U(2-\nu',3,2\beta r) - 2\beta\nu r(2-\nu')U(3-\nu',4,2\beta r)]\}\end{aligned} \tag{A8}$$

for $\beta>0$, and

$$\begin{aligned}\sigma_r(r) = (2\mu(r)+\lambda(r))(1+\nu')\{&c_1[M(1+\nu',3,-2\beta r) \\ &- 2\beta r M(2+\nu',4,-2\beta r)/3] + c_2[U(1+\nu',3,-2\beta r) \\ &+ 2\beta r U(2+\nu',4,-2\beta r)]\}\end{aligned} \tag{A9}$$

$$\begin{aligned}\sigma_\theta(r) = (2\mu(r)+\lambda(r))(1+\nu')\{&c_1[M(1+\nu',3,-2\beta r) \\ &+ 2\beta\nu' r M(2+\nu',4,-2\beta r)/3] + c_2[U(1+\nu',3,-2\beta r) \\ &+ 2\beta\nu' r U(2+\nu',4,-2\beta r)]\}\end{aligned} \tag{A10}$$

for $\beta<0$.

The advantage of the present solution in comparison with the analytic solution in Ref. [30] (which, however, is not restricted to the present axially symmetric case) is that it provides not only stresses but also displacements in an explicit form in terms of the well-known hypergeometric functions instead of infinite series for the Airy stress function with recursively defined coefficients provided in Ref. [30].

Appendix B: Brief Description of the Parallel BEM Program

```
! myproc:      Number of a processor (myproc=0 identifies the
!              host)
! nproc:       Total number of processors
! nel:         Total number of elements
! mynumsubd:   Number of subdomains treated by the processor
!              myproc
! mysubd:      List of the subdomains treated by the processor
!              myproc
! mynumelm:    List of the total numbers of elements from the
!              subdomains defined by mysubd which
!              are integrated by the processor myrproc
! myelm:       Lists of the global numbers of elements from the
!              subdomains defined by mysubd
!              which are integrated by the processor myrproc

program BEM
! MPI initialization
call mpi_init(ierr)
! Get the processor number myproc
call mpi_comm_rank(mpi_comm_world, myproc, ierr)
! Get the total number of processors nproc
call mpi_comm_size(mpi_comm_world, nproc, ierr)
! All the processors read the BEM model
if (myproc.ne.0) then
! Definition of the subdomains, total number of elements from a
! subdomain and which elements from a subdomain the
! processor myrproc will integrate
  call
procdiv(IN:myproc,nproc;OUT:mynumsubd,mysubd,mynumelm,
     myelm)
do is=1,mynumsubd
       s=mysubd(is)
     do ie=1,mynumelm(is)
       e=myelm(ie,is)
!      Integration over the element e in the subdomain s
       call mpi_send(…)
!     Columns of the matrices H and G corresponding to the
! element e sent to the host
     enddo
  enddo
endif
if(myproc.eq.0) then
  do ie=1,nel
       call mpi_recv(…)
!     Columns of the matrices H and G corresponding to an
! element received by the host
     enddo
endif
if (myproc.eq.0) then
!     Application of the boundary conditions
!     Assembly of the matrix A and the right-hand side vector b
!     Solution of the global BEM system of equations Ax=b
endif
!     MPI Exit
call mpi_finalize(ierr)
end program
```

References

[1] Miyamoto, Y., Kaysser, W. A., Rabin, B. H., Kawasaki, A., and Ford, R. G., 1999, *Functionally Graded Materials: Design, Processing and Applications*, Kluwer Academic, Dordrecht.

[2] Suresh, S., and Mortensen, A., 1998, *Fundamentals of Functionally Graded Materials*, The Institute of Materials, IOM Communications Ltd., London.

[3] Kim, J.-H., and Paulino, G. H., 2002, "Finite Element Evaluation of Mixed-Mode Stress Intensity Factors in Functionally Graded Materials," Int. J. Numer. Methods Eng., **53**, pp. 1903–1935.

[4] Kim, J.-H., and Paulino, G. H., 2002, "Mixed-Mode Fracture of Orthotropic

Functionally Graded Materials Using the Finite Element Method," Eng. Fract. Mech., **69**, pp. 1769–1790.
[5] Kim, J.-H., and Paulino, G. H., 2002, "Isoparametric Graded Finite Elements for Nonhomogeneous Isotropic and Orthotropic Materials," ASME J. Appl. Mech., **69**, pp. 502–514.
[6] Silva, E. C. N., Carbonari, R. C., and Paulino, G. H., 2007, "On Graded Elements for Multiphysics Applications," Smart Mater. Struct., **16**, pp. 2408–2428.
[7] Naghdabadi, R., and Kordkheili, S. A. H., 2005, "A Finite Element Formulation for Analysis of Functionally Graded Plates and Shells," Arch. Appl. Mech., **74**, pp. 375–386.
[8] Anlas, G., Santare, M. H., and Lambros, J., 2000, "Numerical Calculation of Stress Intensity Factors in Functionally Graded Materials," Int. J. Fract., **104**, pp. 131–143.
[9] Santare, M. H., and Lambros, J., 2000, "Use of Graded Finite Elements to Model the Behavior of Nonhomogeneous Materials," ASME J. Appl. Mech., **67**, pp. 819–822.
[10] Erdogan, F., 1995, "Fracture Mechanics of Functionally Graded Materials," Composites Eng., **5**, pp. 753–770.
[11] Konda, N., and Erdogan, F., 1994, "The Mixed Mode Crack Problem in a Nonhomogeneous Elastic Medium," Eng. Fract. Mech., **47**, pp. 533–545.
[12] Lee, Y. D., and Erdogan, F., 1994, "Residual/Thermal Stresses in FGM and Laminated Thermal Barrier Coatings," Int. J. Fract., **69**, pp. 145–165.
[13] Erdogan, F., and Bahar, L. Y., 1964, "On the Solution of Simultaneous Dual Integral Equations," J. Soc. Ind. Appl. Math., **12** pp. 666–675.
[14] Kaya, A. C., and Erdogan, F., 1987, "On the Solution of Integral Equations With a Generalized Cauchy Kernel," Q. Appl. Math., **45**, pp. 455–469.
[15] Kaya, A. C., and Erdogan, F., 1987, "On the Solution of Integral Equations With Strongly Singular Kernels," Q. Appl. Math., **45**, pp. 105–122.
[16] París, F., and Cañas, J., 1997, *Boundary Element Method: Fundamentals and Applications*, Oxford University Press, Oxford.
[17] Bonnet, M., 1998, *Boundary Integral Equation Methods for Solids and Fluids*, Wiley, England.
[18] Aliabadi, M. H., 2002, *The Boundary Element Method*, Vol. II, Wiley, Chichester.
[19] Chan, Y.-S., Gray, L. J., Kaplan, T., and Paulino, G. H., 2004, "Green's Function for a Two-Dimensional Exponentially Graded Elastic Medium," Proc. R. Soc. London, Ser. A, **460**, pp. 1689–1706.
[20] Martin, P. A., Richardson, J. D., Gray, L. J., and Berger, J., 2002, "On Green's Function for a Three-Dimensional Exponentially-Graded Elastic Solid," Proc. R. Soc. London, Ser. A, **458**, pp. 1931–1948.
[21] Criado, R., Gray, L. J., Mantič, V., and París, F., 2008, "Green's Function Evaluation for Three Dimensional Exponentially Graded Elasticity," Int. J. Numer. Methods Eng., **74**, pp. 1560–1591.
[22] Criado, R., Ortiz, J. E., Mantič, V., Gray, L. J., and París, F., 2007, "Boundary Element Analysis of Three-Dimensional Exponentially Graded Isotropic Elastic Solids," Comput. Model. Eng. Sci., **22**, pp. 151–164.
[23] Mantič, V., 1993, "A New Formula for the C-Matrix in the Somigliana Identity," J. Elast., **33**, pp. 191–201.
[24] Araújo, F. C., Silva, K. I., and Telles, J. C. F., 2006, "Generic Domain Decomposition and Iterative Solvers for 3-D BEM Problems," Int. J. Numer. Methods Eng., **68**, pp. 448–472.
[25] Araújo, F. C., Silva, K. I., and Telles, J. C. F., 2007, "Application of a Generic Domain-Decomposition Strategy to Solve Shell-Like Problems Through 3D BE Models," Commun. Numer. Methods Eng., **23**, pp. 771–785.
[26] Kamiya, N., Iwase, H., and Kite, E., 1996, "Parallel Implementation of Boundary Element Method With Domain Decomposition," Eng. Anal. Boundary Elem., **18**, pp. 209–216.
[27] Kamiya, N., Iwase, H., and Kite, E., 1996, "Performance Evaluation of Parallel Boundary Element Analysis by Domain Decomposition Method," Eng. Anal. Boundary Elem., **18**, pp. 217–222.
[28] Divo, E., Kassab, A. J., and Rodriguez, F., 2003, "Parallel Domain Decomposition Approach for Large-Scale Three-Dimensional Boundary-Element Models in Linear and Nonlinear Heat Conduction," Numer. Heat Transfer, Part B, **44**, pp. 417–437.
[29] Ingber, M. S., Schmidt, C. C., Tanski, J. A., and Phillips, J., 2003, "Boundary-Element Analysis of 3-D Diffusion Problems Using a Parallel Domain Decomposition Method," Numer. Heat Transfer, Part B, **44**, pp. 145–164.
[30] Zhang, X., and Hasebe, N., 1999, "Elasticity Solution for a Radially Nonhomogeneous Hollow Circular Cylinder," ASME J. Appl. Mech., **66**, pp. 598–606.
[31] Maier, G., Diligenti, M., and Carini, A., 1991, "A Variational Approach to Boundary Element Elastodynamic Analysis and Extension to Multidomain Problems," Comput. Methods Appl. Mech. Eng., **92**, pp. 193–213.
[32] Hölzer, S. M., 1992, "The Symmetric Galerkin BEM for Plane Elasticity: Scope and Applications," *Numerical Methods in Engineering*, C. Hirsch, ed., Elsevier, New York.
[33] Gray, L. J., and Paulino, G. H., 1997, "Symmetric Galerkin Boundary Integral Formulation for Interface and Multi-Zone Problems," Int. J. Numer. Methods Eng., **40**, pp. 3085–3101.
[34] Blázquez, A., París, F., and Mantič, V., 1998, "BEM Solution of Two Dimensional Contact Problems by Weak Application of Contact Conditions With Non-Conforming Discretizations," Int. J. Solids Struct., **35**, pp. 3259–3278.
[35] Li, X. S., 2005, "An Overview of SuperLU: Algorithms, Implementation, and User Interface," ACM Trans. Math. Softw., **31**, pp. 302–325.
[36] Saad, Y., 2003, *Iterative Methods for Sparse Linear Systems*, 2nd ed., SIAM, Philadelphia.
[37] Barber, J. R., 1992, *Elasticity*, Kluwer Academic, Dordrecht.
[38] Wacker, G., Bledzki, A. K., and Chate, A., 1998, "Effect of Interphase on the Transverse Young's Modulus of Glass/Epoxy Composites," Composites, Part A, **29A**, pp. 619–626.
[39] Jasiuk, I., and Kouider, M. W., 1993, "The Effect of an Inhomogeneous Interphase on the Elastic Constants of Transversely Isotropic Composites," Mech. Mater., **15**, pp. 53–63.
[40] Liu, Y., and Xu, N., 2000, "Modeling of Interphase Cracks in Fiber-Reinforced Composites With the Presence of Interphases Using the Boundary Element Method," Mech. Mater., **32**, pp. 769–783.
[41] Luo, J. F., Liu, Y., and Berger, E. J., 2000, "Interfacial Stress Analysis for Multi-Coating Systems Using an Advanced Boundary Element Method," Comput. Mech., **24**, pp. 448–455.
[42] Abramowitz, M., and Stegun, I. A., 1972, *Handbook of Mathematical Functions With Formulas, Graphs and Mathematical Tables*, Dover, New York.

Fracture Mechanics of Periodic Multilayers With Different Microstructural Scales and Moduli Contrast

Linfeng Chen
Gilsanz, Murray & Steficek LLP,
Structural Engineers,
New York, NY 10001

Marek-Jerzy Pindera
Civil Engineering Department,
University of Virginia,
Charlottesville, VA 22904

In a recent investigation of microstructural effects in finite periodic multilayers, we have shown that under Mode I loading, the crack-opening displacement approaches that of the same crack in an equivalent homogenized material as the microstructure comprised of alternating stiff and soft layers becomes increasingly finer. In contrast, Mode I stress intensity factor asymptotically converges to values that depend on the stiffness of the cracked layer. Preliminary calculation of Mode I strain energy release rate as a function of the microstructural refinement suggested that this may be a better fracture mechanics parameter for assessing fracture toughness of periodic layered media. Herein, we extend the above investigation by considering both Mode I and II loading to study the effect of layer modulus ratio on fracture mechanics parameters as a function of microstructural refinement. The previously introduced concept of partial homogenization of the microstructure sufficiently far from the crack is also pursued in order to gauge its efficiency in correctly capturing fracture mechanics parameters with a minimum of computational effort. The fracture mechanics parameters are shown to be influenced by the local microstructure to an extent that depends on the layer modulus mismatch. An accurate calculation of these parameters requires the retention of several layers adjacent to the affected cracked layer whose number depends on the modulus mismatch and loading mode. [DOI: 10.1115/1.2936236]

1 Introduction

Stress analysis of heterogeneous materials is typically conducted at the so-called macroscopic scale upon replacing the actual microstructure with averaged or *effective* elastic moduli. The replacement scheme depends on whether the microstructure is statistically homogeneous or periodic (Drago and Pindera [1]). For periodic microstructures characterized by replicated (or repeating) unit cells (RUCs), the homogenization technique has been developed for the calculation of effective moduli (see Sanchez-Palencia [2], Suquet [3], and Hornung [4]. This approach enables a systematic analysis of heterogeneous materials in the limit as the microstructural scale becomes vanishingly small relative to the overall structural dimensions and, thus, replaceable by equivalent homogenized moduli (Fig. 1). Real microstructures, however, typically consist of phases or inclusions that are finite relative to either the structural scale or the imposed stress gradient. High stress gradients occur in the vicinity of material or geometric discontinuities, i.e., geometric or material boundaries, or concentrated loads. In such regions, homogenization breaks down since the calculation of effective moduli is based on the concept of periodicity under uniform far-field boundary conditions. These regions are of technological importance due to the initiation of localized failures, e.g., crack or delamination initiation, or plastic localization, and cannot be reliably analyzed based solely on effective moduli. These issues were discussed by Pagano and Rybicki [5], Hollister and Kikuchi [6], and Pindera et al. [7] in the context of unidirectional composites with large-diameter fibers, and porous and functionally graded materials, respectively. More recent results were reported by Pagano and Yuan [8], Wang and Yan [9], and Lipton [10], who addressed issues related to the reconstruction of local fields in periodic and nonperiodic composites from homogenization-based analyses.

The above investigations were purely numerical due to the type of reinforcement in the investigated composites. Most recent studies of microstructural effects in periodic lamellar materials were conducted by Chen et al. [11] and Pindera and Chen [12] in the context of contact and crack problems, respectively, using exact elasticity approaches developed by Pindera and Lane [13] and Chen and Pindera [14,15]. Lamellar composites play an important role in existing and emerging technologies, including nanotechnology applications. The solution of Chen and Pindera [14] enabled an accurate determination of stress intensity factors and crack-opening displacements in periodic multilayers with single and multiple cracks based either on the actual or homogenized microstructures, leading to firm conclusions regarding the applicability of homogenization-based approaches applied to periodically layered structures in the presence of very large stress gradients induced by technologically important delaminations. In particular, Pindera and Chen [12] investigated the effect of microstructural refinement in periodic multilayers on the crack intensity factors and crack-opening displacements under Mode I loading. This study demonstrated that while the crack-opening displacement approaches that of the same crack in an equivalent homogenized material as the microstructure becomes increasingly finer, the stress intensity factor asymptotically converges to values that depend on the stiffness of the layer containing the crack. A preliminary calculation of the strain energy release rate as a function of the microstructural refinement suggested that this may be a better fracture mechanics parameter for periodic layered media.

Herein, we extend the above investigation into microstructural effects in periodic multilayers comprised of alternating soft and stiff layers. In particular, we include the effect of a stiff/soft layer modulus contrast to investigate the stress intensity factors and strain energy release rates as a function of microstructural refinement under both Mode I and II loadings. The previously intro-

Contributed by the Applied Mechanics Division of ASME for publication in the JOURNAL OF APPLIED MECHANICS. Manuscript received June 20, 2007; final manuscript received September 30, 2007; published online July 11, 2008. Review conducted by Robert M. McMeeking.

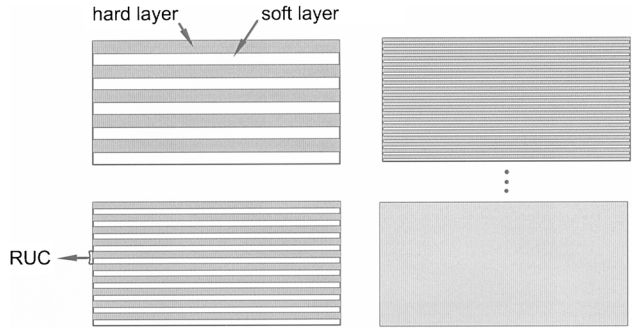

Fig. 1 Periodic multilayers with increasingly finer microstructural scales, constructed with RUCs containing the same proportion of the individual layers (after Hornung [4])

duced concept of partial homogenization of the microstructure sufficiently far from the crack is also pursued in order to gauge its efficiency in correctly capturing both fracture mechanics parameters with a minimum of computational effort.

The paper is organized as follows. In Sec 2, we specialize the exact elasticity solution developed for finite layered media in the analysis plane containing arbitrarily distributed horizontal cracks for the present analysis, which is used to derive expressions for the strain energy release rates (and the crack-opening displacement and stress intensity factors) presented in Sec. 3. In Sec. 4, we investigate the effect of layer refinement on fracture mechanics parameters for a single crack centrally embedded in a periodic multilayer composed of alternating hard and soft plies under uniform Mode I and II tractions applied to the crack faces for different layer moduli ratios, and we compare their asymptotic values with those of the fully homogenized configurations. Then, the convergence behavior of the fracture mechanics parameters to those in a fully discrete multilayered configuration is established for different levels of partial homogenization where different numbers of layers directly adjacent to the crack are retained and the remaining layers homogenized. As in our previous investigation, partial homogenization is carried out using the exact model developed by Postma [16]. A discussion of the obtained results and comparison with previous related results is provided in Sec. 5. Our ultimate aim is to identify which set of parameters is most appropriate in the fracture mechanics analysis of periodically layered media and how microstructure, layer modulus contrast, and homogenization-based analysis influence these parameters.

2 Analytical Solution

The exact elasticity solution developed by Chen and Pindera [14,15], employed to investigate microstructural effects in periodic layered media, applies to a finite-height, finite-length multilayer of dimensions H and L in the x-z plane that extends to infinity in the out-of-plane direction. The total number of layers is n, the kth layer thickness is h_k, the layers may be (transversely) isotropic, orthotropic, or monoclinic, and the number of cracks along any interface is arbitrary, as is the number of interfaces containing cracks. Herein, we specialize this solution to periodic multilayers in plane strain state, comprised of isotropic or orthotropic layers that contain a single crack lying in the interval $c_\alpha < x < d_\alpha$ along the cracked interface α.

The solution for the displacement field within each layer is obtained in the local coordinate system, with the origin centered vertically halfway at each layer's left end. For horizontally pinned end constraints considered herein, the vertical and horizontal displacement components, $w(x,z)$ and $u(x,z)$, are represented by half-range cosine and sine Fourier series, respectively, as follows:

$$\mathbf{U}(x,z) = \bar{\mathbf{U}}^0(z) + \sum_{m=1}^{\infty} \boldsymbol{\zeta}^m(x)\bar{\mathbf{U}}^m(z) \tag{1}$$

where $\mathbf{U}(x,z)=[w(x,z),u(x,z)]^T$, $\bar{\mathbf{U}}^m(z)=[\bar{w}_m(z),\bar{u}_m(z)]^T$, $\bar{\mathbf{U}}^0(z)=[\bar{w}_0(z),0]^T$, and $\boldsymbol{\zeta}^m(x)=\mathrm{diag}[\cos(m\pi x/L),\sin(m\pi x/L)]$. The solutions for the displacement harmonics $\bar{w}_m(z)$, $\bar{u}_m(z)$ have been obtained from Navier's equations for isotropic and orthotropic layers in the x-z plane by Chen and Pindera [14].

The problem is then reformulated in terms of the local stiffness matrix for each harmonic, which relates traction harmonics on the top and bottom faces of the kth layer, $\bar{\mathbf{T}}_k^{m+}, \bar{\mathbf{T}}_k^{m-}$, to the corresponding displacement harmonics, $\bar{\mathbf{U}}_k^{m+}, \bar{\mathbf{U}}_k^{m-}$ (see Bufler [17] and Pindera [18]). Symbolically, the local stiffness matrix has the form

$$\begin{bmatrix} \bar{\mathbf{T}}_k^{m+} \\ \bar{\mathbf{T}}_k^{m-} \end{bmatrix} = \begin{bmatrix} \mathbf{K}_{11}^{m,k} & \mathbf{K}_{12}^{m,k} \\ \mathbf{K}_{21}^{m,k} & \mathbf{K}_{22}^{m,k} \end{bmatrix} \begin{bmatrix} \bar{\mathbf{U}}_k^{m+} \\ \bar{\mathbf{U}}_k^{m-} \end{bmatrix} \tag{2}$$

where the elements of the local stiffness submatrices $\mathbf{K}_{11}^{m,k},\ldots,\mathbf{K}_{22}^{m,k}$ have been obtained in closed form in terms of the harmonic number m, layer elastic moduli, and geometry.

Subsequently, a crack-opening displacement vector in the harmonic domain along the cracked interface is introduced to account for the resulting displacement discontinuity due to the applied loading (either tractions applied externally and/or directly to the crack faces). The interfacial displacement harmonics $\bar{\mathbf{U}}_{\alpha-1}^{m-}$ and $\bar{\mathbf{U}}_{\alpha}^{m+}$ on the bottom face of the $(\alpha-1)$th layer and top face of the αth layer, respectively, are represented in terms of the common interfacial displacement vector $\bar{\mathbf{U}}_\alpha^m$ and the displacement discontinuity vector $\bar{\mathbf{U}}_\alpha^{m*}$ along the cracked interface α,

$$\bar{\mathbf{U}}_{\alpha-1}^{m-} = \bar{\mathbf{U}}_\alpha^m + [\mathbf{K}^{*\alpha}]^{-1}\mathbf{K}_{11}^{*\alpha}\bar{\mathbf{U}}_\alpha^{m*}$$

$$\bar{\mathbf{U}}_{\alpha}^{m+} = \bar{\mathbf{U}}_\alpha^m - [\mathbf{K}^{*\alpha}]^{-1}\mathbf{K}_{22}^{*\alpha-1}\bar{\mathbf{U}}_\alpha^{m*} \tag{3}$$

where $[\mathbf{K}^{*,\alpha}]^{-1}=[\mathbf{K}_{22}^{*,\alpha-1}+\mathbf{K}_{11}^{*,\alpha}]^{-1}$, $\mathbf{K}_{22}^{*,\alpha-1}, \mathbf{K}_{11}^{*\alpha}$ are asymptotic local stiffness submatrices as $m\to\infty$.

Application of interfacial traction and displacement continuity, and boundary conditions, assembles the local stiffness matrices into the global stiffness matrix for the response of the entire structure. The resulting global system of equations has the form

$$\begin{bmatrix} \mathbf{K}_{11}^1 & \mathbf{K}_{12}^1 & \mathbf{0} & \cdots & \cdots & \mathbf{0} \\ \mathbf{K}_{21}^1 & \mathbf{K}_{22}^1+\mathbf{K}_{11}^2 & \mathbf{K}_{12}^2 & \cdots & \cdots & \mathbf{0} \\ \mathbf{0} & \mathbf{K}_{21}^2 & \mathbf{K}_{22}^2+\mathbf{K}_{11}^3 & \cdots & \cdots & \mathbf{0} \\ \vdots & \vdots & \vdots & \cdots & \cdots & \cdots \\ \vdots & \vdots & \vdots & \cdots & \cdots & \cdots \\ \vdots & \vdots & \vdots & \cdots & \cdots & \cdots \\ \mathbf{0} & \mathbf{0} & \mathbf{0} & \cdots & \mathbf{K}_{21}^n & \mathbf{K}_{22}^n \end{bmatrix}^m \begin{bmatrix} \bar{\mathbf{U}}_1 \\ \bar{\mathbf{U}}_2 \\ \vdots \\ \vdots \\ \vdots \\ \bar{\mathbf{U}}_n \\ \bar{\mathbf{U}}_{n+1} \end{bmatrix}^m$$

$$= \begin{bmatrix} \bar{\mathbf{T}}_1^+ \\ \mathbf{0} \\ \vdots \\ \vdots \\ \vdots \\ \mathbf{0} \\ \bar{\mathbf{T}}_n^- \end{bmatrix}^m - \begin{bmatrix} \vdots \\ \mathbf{0} \\ \mathbf{L}_{(\alpha-1)\alpha} \\ \mathbf{L}_{\alpha\alpha} \\ \mathbf{L}_{(\alpha+1)\alpha} \\ \mathbf{0} \\ \cdot \end{bmatrix}^m \bar{\mathbf{U}}_\alpha^{m*} \tag{4}$$

where $\mathbf{L}_{(\alpha-1)\alpha}^m$, $\mathbf{L}_{\alpha\alpha}^m$, and $\mathbf{L}_{(\alpha+1)\alpha}^m$ are given by

$$\mathbf{L}_{(\alpha-1)\alpha}^m = \mathbf{K}_{12}^{m,\alpha-1}[\mathbf{K}^{*,\alpha}]^{-1}\mathbf{K}_{11}^{*,\alpha}$$

$$\mathbf{L}^m_{\alpha\alpha} = \mathbf{K}^{m,\alpha-1}_{22}[\mathbf{K}^{*,\alpha}]^{-1}\mathbf{K}^{*,\alpha}_{11} - \mathbf{K}^{m,\alpha}_{11}[\mathbf{K}^{*,\alpha}]^{-1}\mathbf{K}^{*,\alpha-1}_{22}$$

$$\mathbf{L}^m_{(\alpha+1)\alpha} = -\mathbf{K}^{m,\alpha}_{21}[\mathbf{K}^{*,\alpha}]^{-1}\mathbf{K}^{*,\alpha-1}_{22} \tag{5}$$

The additional equations for the determination of the unknown crack-opening displacement are obtained by specifying traction conditions on the crack faces. First, we define the displacement discontinuity density vector $\mathbf{\Theta}_\alpha(x)=[\theta_z(x),\theta_x(x)]^T_\alpha$ as follows:

$$\mathbf{U}^-_{\alpha-1}(x) - \mathbf{U}^+_\alpha(x) = \mathbf{U}^*_\alpha(x) = \begin{cases} \displaystyle\int_{c_\alpha}^{x} \mathbf{\Theta}_\alpha(x')dx', & c_\alpha \leqslant x \leqslant d_\alpha \\ 0 & \text{otherwise} \end{cases} \tag{6}$$

with the constraint $\mathbf{U}^*_\alpha(d_\alpha)=0$, and we consider a horizontal crack between layers of the same elastic moduli to avoid complications associated with the oscillatory crack-tip behavior in the case of dissimilar adjacent plies (Ting [19]). The corresponding Fourier series representation of $\mathbf{U}^*_\alpha(x)$ is then given by $\mathbf{U}^*_\alpha(x) = \Sigma^\infty_{m=1}\boldsymbol{\zeta}^m\bar{\mathbf{U}}^{m*}_\alpha$, where $\bar{\mathbf{U}}^{m*}_\alpha$ is obtained in the form

$$\bar{\mathbf{U}}^{m*}_\alpha = \frac{2}{m\pi}\int_{c_\alpha}^{d_\alpha} \hat{\boldsymbol{\zeta}}^m \mathbf{\Theta}_\alpha(x')dx' \tag{7}$$

with $\hat{\boldsymbol{\zeta}}^m = \text{diag}[-\sin(m\pi x/L), \cos(m\pi x/L)]$.

The mth harmonic of the traction vector on the top surface of the αth ply is then obtained from the local stiffness matrix expression (Eq. (2) with $k=\alpha$) in the form

$$\bar{\mathbf{T}}^{m+}_\alpha = \mathbf{K}^{m,\alpha}_{11}\bar{\mathbf{U}}^{m+}_\alpha + \mathbf{K}^{m,\alpha}_{12}\bar{\mathbf{U}}^{m-}_\alpha \tag{8}$$

Substituting for $\bar{\mathbf{U}}^{m+}_\alpha$ and $\bar{\mathbf{U}}^{m-}_\alpha$ using Eq. (3) and separating the singular contributions, i.e., contributions that do not vanish as $m \to \infty$, the following expression for the mth harmonic of the traction vector along the cracked αth interface is obtained:

$$\begin{aligned}\bar{\mathbf{T}}^{m+}_\alpha = {} & \mathbf{K}^{m,\alpha}_{11}\bar{\mathbf{U}}^{m}_\alpha + \mathbf{K}^{m,\alpha}_{12}\bar{\mathbf{U}}^{m}_{\alpha+1} - \mathbf{K}^{*,\alpha}_{11}[\mathbf{K}^{*,\alpha}]^{-1}\mathbf{K}^{*,\alpha-1}_{22}\bar{\mathbf{U}}^{m*}_\alpha \\ & - \bar{\mathbf{K}}^{m,\alpha}_{11}[\mathbf{K}^{*,\alpha}]^{-1}\mathbf{K}^{*,\alpha-1}_{22}\bar{\mathbf{U}}^{m*}_\alpha\end{aligned} \tag{9}$$

where $\bar{\mathbf{K}}^{m,\alpha}_{11} = \mathbf{K}^{m,\alpha}_{11} - \mathbf{K}^{*,\alpha}_{11}$, so that $\bar{\mathbf{K}}^{m,\alpha}_{11} \to \mathbf{0}$ as $m \to \infty$. The above equation can be expressed solely in terms of the mth harmonics of the displacement discontinuity functions along the cracked interface and external loading by solving Eq. (4) for the common interfacial displacements $\bar{\mathbf{U}}^m_\alpha$ and $\bar{\mathbf{U}}^m_{\alpha+1}$. Summing up the traction vector harmonics and using Eqs. (6) and (7), we obtain an expression for the traction vector $\mathbf{T}^+_\alpha(x)$ on the bottom crack face of the αth interface in terms of the unknown displacement discontinuity density vector Θ_α. Using certain identities and manipulations (Chen and Pindera [14]) this expression is then reduced to the following singular integral equation valid in the interval $c_\alpha < x < d_\alpha$:

$$\begin{aligned}\mathbf{T}^+_\alpha(x) = {} & \frac{1}{\pi}\int_{c_\alpha}^{d_\alpha} \bar{\mathbf{B}}^*_\alpha \frac{\mathbf{\Theta}_\alpha(x')}{x'-x}dx' + \frac{1}{\pi}\int_{c_\alpha}^{d_\alpha} \bar{\mathbf{K}}_{\alpha\alpha}(x,x')\mathbf{\Theta}_\alpha(x')dx' \\ & + \mathbf{F}_\alpha(x)\end{aligned} \tag{10}$$

where $\bar{\mathbf{K}}_{\alpha\alpha}(x,x')$ are regular Fredholm kernels obtained from the solution of Eq. (4), $\mathbf{F}_\alpha(x)$ is the specified external load vector, and $\bar{\mathbf{B}}^*_\alpha$ is a constant square matrix, which has the form

$$\bar{\mathbf{B}}^*_\alpha = \begin{bmatrix} B^{*\alpha}_{11} & 0 \\ 0 & B^{*\alpha}_{22} \end{bmatrix} \tag{11}$$

with $B^{*\alpha}_{ij}$'s given in terms of the asymptotic values of the elements of the local stiffness matrices of adjacent layers, namely, $\mathbf{B}^*_\alpha = \mathbf{K}^{*,\alpha}_{11}[\mathbf{K}^{*,\alpha}]^{-1}\mathbf{K}^{*,\alpha-1}_{22}$.

The unknown crack-opening density functions for the normalized crack in the interval $|t_\alpha| \leqslant 1$ along the αth interface are approximated by a series of Chebyshev polynomials $T_j(t_\alpha)$ of the first kind, with the associated influence coefficients $\mathbf{C}_{j(\alpha)}$ multiplied by the weight function $\boldsymbol{\omega}_\alpha(t_\alpha) = (1-t_\alpha)^{-1/2}(1+t_\alpha)^{-1/2}$,

$$\mathbf{\Theta}_\alpha(t_\alpha) = \frac{(d_\alpha - c_\alpha)}{2}(1-t_\alpha)^{-1/2}(1+t_\alpha)^{-1/2}\sum_{j=0}^{N_j}\frac{(2j)!}{2^{2j}(j!)^2}\mathbf{C}_{j(\alpha)}T_j(t_\alpha) \tag{12}$$

Using a collocation technique developed by Erdogan and coworkers [20–22] based on a Chebyshev polynomial orthogonality identity, the singular integral equation for the traction vector $\mathbf{T}^+_\alpha(x)$ is reduced to a system of algebraic equations in the unknown influence coefficients,

$$\frac{\pi}{2}\theta^{(1/2,1/2)}_j\mathbf{C}_{(j+1)(\alpha)} + \sum_{k=0}^{N_j}\frac{(d_\alpha - c_\alpha)}{2}\mathbf{D}_{jk(\alpha\alpha)}\mathbf{C}_{k(\alpha)} = \mathbf{G}^{\text{I}}_{j(\alpha)} + \mathbf{G}^{\text{II}}_{j(\alpha)} \tag{13}$$

for each $j=0,1,2,\ldots,N_j$, where

$$\theta^{(1/2,1/2)}_j = \frac{2\Gamma\left(j+\frac{3}{2}\right)\Gamma\left(j+\frac{3}{2}\right)}{j!(j+1)\Gamma(j+2)} \tag{14}$$

The constant matrices and vectors $\mathbf{D}^{(pq)}_{jk(\alpha\beta)}$, $\mathbf{G}^{\text{I}(p)}_{j(\alpha)}$, and $\mathbf{G}^{\text{II}(p)}_{j(\alpha)}$ are given below,

$$\begin{aligned}\mathbf{D}_{jk(\alpha\alpha)} = {} & \frac{(2j)!}{2^{2j}(j!)^2}\frac{(2k)!}{2^{2k}(k!)^2}\int_{-1}^{+1}\left[\int_{-1}^{+1}\mathbf{h}_{\alpha\alpha}(t_\alpha,\tau_\alpha)T_j(t_\alpha)\hat{\boldsymbol{\omega}}_\alpha(t_\alpha)dt_\alpha\right] \\ & \times T_k(\tau_\alpha)\boldsymbol{\omega}_\alpha(\tau_\alpha)d\tau_\alpha \\ \mathbf{G}^{\text{I}}_{j(\alpha)} = {} & -\frac{(2j)!}{2^{2j}(j!)^2}\int_{-1}^{+1}\bar{\mathbf{B}}^{*-1}_\alpha\mathbf{F}_\alpha(t_\alpha)T_j(t_\alpha)\hat{\boldsymbol{\omega}}_\alpha(t_\alpha)dt_\alpha \\ \mathbf{G}^{\text{II}(p)}_{j(\alpha)} = {} & \frac{(2j)!}{2^{2j}(j!)^2}\int_{-1}^{+1}\bar{\mathbf{B}}^{*-1}_\alpha\mathbf{T}^+_\alpha(t_\alpha)T_j(t_\alpha)\hat{\boldsymbol{\omega}}_\alpha(t_\alpha)dt_\alpha\end{aligned} \tag{15}$$

where $\hat{\boldsymbol{\omega}}_\alpha(t_\alpha) = (1-t_\alpha)^{1/2}(1+t_\alpha)^{1/2}$ and $\mathbf{h}_{\alpha\alpha}(x,x') = \bar{\mathbf{B}}^{*-1}_\alpha\bar{\mathbf{K}}_{\alpha\alpha}(x,x')$.

The above results are exact in the limit as $m \to \infty$ and $N_j \to \infty$ but nonetheless require numerical implementation. As discussed by Chen and Pindera [15], the solution's accuracy depends on an accurate representation of the crack-opening displacements using a sufficient number of Chebyshev polynomials N_j and an accurate calculation of the single and double integrals in Eqs. (15). These calculations involve the use of a sufficient number of harmonics in the Fourier series representation of the displacement field. The guidelines for ensuring convergent and accurate results have been provided by Chen and Pindera [15] as a function of the layer and crack dimensions, crack location, and spacing. The results presented in this paper have been generated following these guidelines to ensure their accuracy and convergence.

3 Energy Release Rates and Stress Intensity Factors

The strain energy release rate caused by an infinitesimal crack extension along the αth interface under self-similar crack growth is calculated by evaluating the integral,

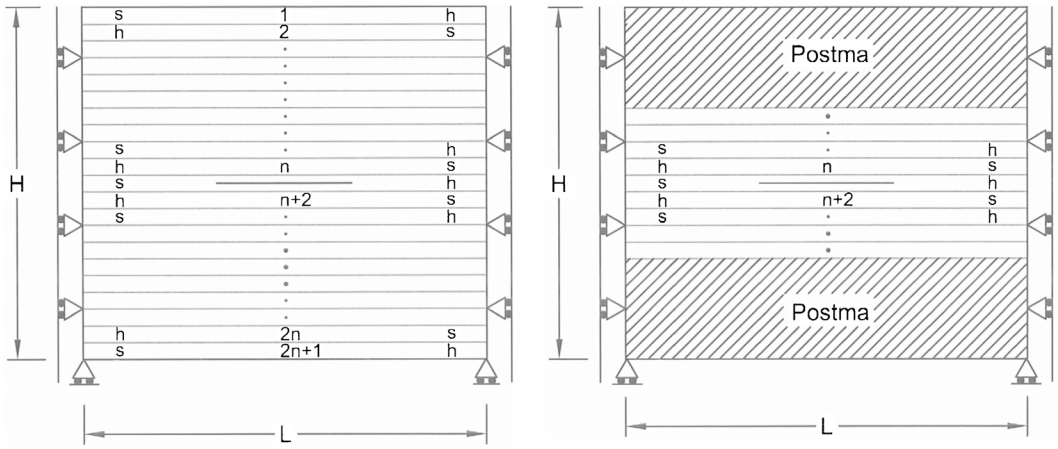

Fig. 2 Geometry of the (2*n*+1)-layered structure with alternating soft and hard layers weakened by a single centrally positioned crack subjected to tractions applied to the crack faces: (*a*) fully discrete and (*b*) partially homogenized microstructures

$$\frac{\partial U_\alpha}{\partial a} = \lim_{\delta \to 0} \frac{1}{\delta} \frac{1}{2} \int_{\pm 1}^{\pm 1 \pm \delta'} \frac{(d_\alpha - c_\alpha)}{2} \mathbf{T}_\alpha^+(t_\alpha) \circ \mathbf{U}_\alpha^*(t'_\alpha) dt_\alpha \tag{16}$$

where the symbol $\circ$ denotes dot product operation, $\pm$ denotes the right or left tip of the crack, $t'_\alpha = t_\alpha - 2\delta/(d_\alpha - c_\alpha)$, and $\delta' = 2\delta/(d_\alpha - c_\alpha)$. In the above expression, it is sufficient to consider only the limiting values of the traction $\mathbf{T}_\alpha^+(t_\alpha)$ and crack-opening displacement $\mathbf{U}_\alpha^*(t_\alpha)$ in the neighborhood of $t_\alpha = \pm 1$. In the vicinity of the right crack tip, the crack-opening displacement integral given by Eqs. (6) and (12) is governed by the dominant part of the kernel, yielding

$$\mathbf{U}_\alpha^*(t_\alpha) = \frac{(d_\alpha - c_\alpha)}{2} (1 - t_\alpha)^{1/2} \frac{2}{\sqrt{2}} \sum_{j=0}^{N_j} \frac{(2j)!}{2^{2j}(j!)^2} \mathbf{C}_{j(\alpha)} \tag{17}$$

Similarly, using a result from the complex variable theory, the asymptotic behavior of the traction vector in the vicinity of the right crack tip for $|t_\alpha| > 1$ becomes

$$\mathbf{T}_\alpha^+(t_\alpha) = -(t_\alpha - 1)^{-1/2} \bar{\mathbf{B}}_\alpha^* \frac{1}{\sqrt{2}} \sum_{j=0}^{N_j} \frac{(2j)!}{2^{2j}(j!)^2} \mathbf{C}_{j(\alpha)} \tag{18}$$

Using the asymptotic expressions for the crack-tip tractions and displacements in the integral for the strain energy release rate and separating the individual contributions, we obtain the following integrals for the energy release rates due to the opening and sliding modes in the *x*-*z* plane:

$$\frac{\partial U_{\mathrm{I}\alpha}}{\partial a} = \lim_{\delta \to 0} \frac{1}{\delta} \frac{(d_\alpha - c_\alpha)^2}{4\pi} B_{11}^{*\alpha} (A_\alpha)^2 \int_1^{1+\delta'} (t_\alpha - 1)^{-1/2} (1 - t'_\alpha)^{1/2} dt_\alpha \tag{19}$$

$$\frac{\partial U_{\mathrm{II}\alpha}}{\partial a} = \lim_{\delta \to 0} \frac{1}{\delta} \frac{(d_\alpha - c_\alpha)^2}{4\pi} B_{22}^{*\alpha} (B_\alpha)^2 \int_1^{1+\delta'} (t_\alpha - 1)^{-1/2} (1 - t'_\alpha)^{1/2} dt_\alpha \tag{20}$$

which reduce to

$$\frac{\partial U_{\mathrm{I}\alpha}}{\partial a} = \frac{1}{4} (d_\alpha - c_\alpha) B_{11}^{*\alpha} (A_\alpha)^2, \quad \frac{\partial U_{\mathrm{II}\alpha}}{\partial a} = \frac{1}{4} (d_\alpha - c_\alpha) B_{22}^{*\alpha} (B_\alpha)^2 \tag{21}$$

with similar expressions at the left crack tip.

The stress intensity factors are obtained by multiplying the asymptotic expressions for crack-tip tractions by $(t_\alpha - 1)^{1/2}$ and then taking the limit of these equations as $t \to 1$, which yields

$$K_{\mathrm{I}\alpha} = B_{11}^{*\alpha} A_\alpha, \quad K_{\mathrm{II}\alpha} = B_{22}^{*\alpha} B_\alpha \tag{22}$$

where $[A_\alpha, B_\alpha]^T = -1/\sqrt{2} \Sigma_{j=0}^{N_j} (2j)!/[2^{2j}(j!)^2] \mathbf{C}_{j(\alpha)}$ and $B_{ij}^{*\alpha}$ are elements of $\bar{\mathbf{B}}_\alpha^*$. The expressions for the left crack tip are similar.

4 Crack Embedded in a Periodic Multilayer

Using the outlined solution, we investigate the effect of microstructure on fracture mechanics parameters of a single crack situated in the middle of a $(2n+1)$-layered structure that is horizontally pinned at the left and right vertical boundaries, while the top and bottom surfaces are traction free (Fig. 2(*a*)). Specifically, we focus on the stress intensity factors, crack-opening displacements, and strain energy release rates for different microstructural refinements and different layer elastic moduli contrast under loading by unit normal and shear tractions applied separately to the crack faces. The multilayer is comprised of soft and hard layers alternating symmetrically with respect to the central layer containing the crack. The stiffness of the middle layer (hard or soft) determines the alternating sequence of the remaining layers. The hard and soft layers have the same thickness, and the overall thickness H of the entire periodic multilayer and the crack length $2a$ are fixed so that $H/2a = 10$. The layer length L is chosen to produce the ratio $L/2a = 10$ to eliminate interaction with the boundaries.

Microstructural refinement is accomplished by increasing the number of the $2n+1$ layers while preserving the overall multilayer dimensions and crack length. The coarsest miscrostructure, $2n+1=5$, produces central layer thickness that is twice the crack length, while the finest microstructure, $2n+1=201$, makes the crack length slightly more than 20 times longer than the layer thickness. In our previous investigation (Pindera and Chen [12]), we employed layers with a large Young's moduli contrast of $E_h/E_s = 20$, which was representative of glass or aluminum and epoxy. Herein, we employ a wide range of ratios, $E_h/E_s = 20, 10, 2$, in a parametric study, which further supports our observation of the significant microstructural effects in multilayers that can potentially have a great impact on fracture mechanics calculations. The stiffest and softest layers have the same properties as those used previously, while the two additional sets of elastic moduli that produce the above ratios have been adjusted with the stiffest layer as the reference (Table 1). Thus, decreasing

Table 1 Elastic properties of the hard and soft layers

Material	E (msi)	G (msi)	ν
Soft (epoxy)	0.50	0.188	0.33
Intermediate 1	1.0	0.376	0.33
Intermediate 2	5.0	1.879	0.33
Hard (aluminum)	10.0	3.759	0.33

modulus contrast corresponds to increasing Young's modulus of the soft layer and, thus, decreasing extent of anisotropy. The homogenized elastic properties of the multilayers with the three moduli ratios given in Table 2 were generated by applying the Postma homogenization scheme described in the Appendix to the alternating sequence of hard and soft layers with the same material and geometric parameters as those of the investigated configurations.

The numerical results were generated using 10 Chebyshev polynomials for the crack-opening displacement when the number of layers was less than 41, and 20 polynomials for larger layer numbers up to 201. The number of harmonics for the employed $L/2a$ ratio was 50 and 2000 for 5 and 201 layers, respectively (smaller $L/2a$ ratios require substantially more harmonics), in order to ensure converged results (Chen and Pindera [15]).

We mention that the investigated configurations circumvent the problem of Mode I and II couplings under a Mode I–type loading when the crack is situated between two isotropic layers with dissimilar moduli and the concomitant issues associated with the vanishing of Mode II crack-opening displacement in the fully homogenized microstructure. Further, Mode I and II crack-opening displacements become uncoupled when the crack lies in the plane of structural symmetry, as is the case here, and normal or shear loading is applied separately to the crack faces. Coupling between Mode I and II crack-opening displacements occurs when the crack is situated near the top surface. This case was investigated previously under external normal displacement and traction boundary conditions in the context of partial homogenization (Pindera and Chen [12]). In the present context, partial homogenization under normal tractions applied to the crack faces produces acceptably accurate results with just a few retained layers below the top cracked layer for a multilayer with a large number of alternating layers. Under shear tractions applied to the crack faces, however, crack tip closure occurs at one of the crack tips, requiring either application of a normal traction of sufficient magnitude to eliminate compressive stress at the affected crack tip or modification of the present solution to admit crack closure. Therefore, microstructural effects in multilayers with subsurface cracks under Mode II loading will be investigated elsewhere.

4.1 Effect of Microstructural Refinement. We start by investigating the effect of layer refinement on the stress intensity factors, energy release rates and crack-opening displacement in the described multilayers. Figure 3 presents Mode I stress intensity factor K_I and the corresponding strain energy release rate $\partial U_I/\partial a = G_I$ for a crack subjected to normal traction as a function of the layer refinement $(2n+1)$ for the two cases when the middle layer is soft and hard. Both quantities have been normalized by the corresponding quantities generated for the fully homogenized configurations, which are given in Table 3. The fracture mechanics parameters for the homogenized multilayers with effective orthotropic elastic moduli listed in Table 2 are virtually the same as those for an infinite orthotropic medium with a single crack using the results of Sih et al. [23], as summarized by Hutchinson and Suo [24]. For comparison, fracture mechanics parameters for homogeneous isotropic plates of the same dimensions based on the elastic moduli in Table 1 are provided in Table 4, illustrating that the known relationship between the strain energy release rates, stress intensity factors, and elastic moduli is satisfied exactly. Both sets of results given in Tables 3 and 4 indicate that

Table 2 Homogenized elastic properties of the periodically layered structure, with the *x-y* or 1-2 plane of isotropy, based on the Postma model ($E^*_{11} = E^*_{22}$, etc)

E_h/E_s	E^*_{11} (Msi)	E^*_{33} (Msi)	G^*_{12} (Msi)	G^*_{13} (Msi)	ν^*_{12}	ν^*_{13}
2=10/5	7.5	6.916	2.820	2.506	0.33	0.33
10=10/1	5.50	2.324	2.068	0.684	0.33	0.33
20=10/0.5	5.25	1.298	1.974	0.358	0.33	0.33

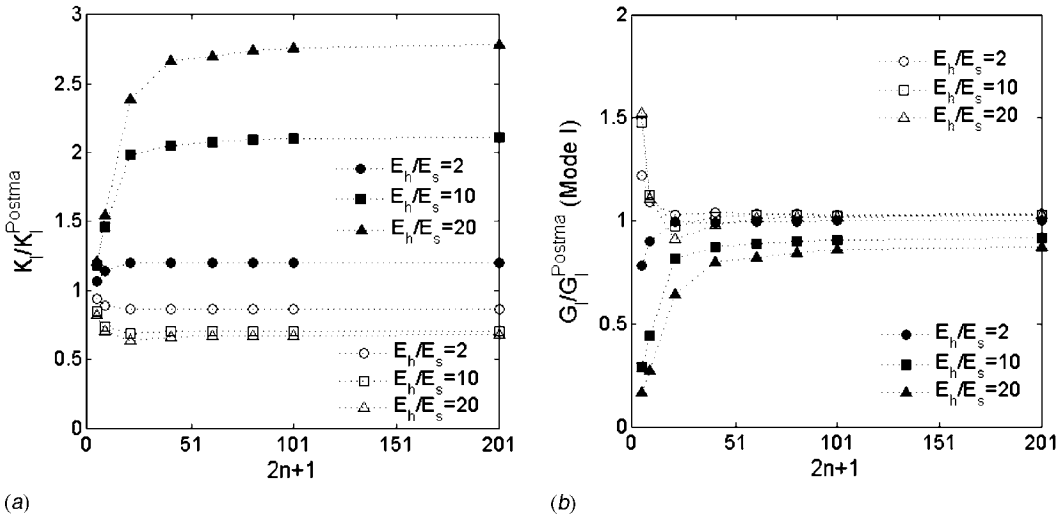

Fig. 3 (*a*) Normalized Mode I stress intensity factors K_I/K_I^{Postma} and (*b*) normalized Mode I strain energy release rate G_I/G_I^{Postma} of the crack embedded in a hard (filled symbols) and soft (open symbols) layer as a function of the layer refinement $2n+1$ for the elastic moduli ratios $E_h/E_s = 20, 10, 2$

Table 3 Stress intensity factors and strain energy release rates for a central crack under internal normal and shear tractions of magnitude 1 psi in the Postma-homogenized equivalent medium comprised of layers with different moduli ratios

E_h/E_s	$K_{\mathrm{I}}^{\mathrm{Postma}}$	$K_{\mathrm{II}}^{\mathrm{Postma}}$	$G_{\mathrm{I}}^{\mathrm{Postma}}$ $(\times 10^{-7})$	$G_{\mathrm{II}}^{\mathrm{Postma}}$ $(\times 10^{-7})$
2=10/5	1.008903	1.005766	1.337082	1.269971
10=10/1	1.009146	1.002019	4.398934	2.724713
20=10/0.5	1.009147	1.000601	8.056702	3.768926

there is very little influence of the investigated configurations' boundaries on the fracture mechanics parameters and that material orthotropy has a large influence on the strain energy release rates.

As previously observed for multilayers with the modulus contrast ratio $E_h/E_s=20$ subjected to external loading, stress intensity factors of the presently investigated layered configurations depart from the stress intensity factor of fully homogenized configurations with increasing layer refinement and reach asymptotic values for large numbers of alternating layer pairs that differ substantially from their homogenized counterparts (Fig. 3(*a*)). Specifically, K_{I} of crack embedded in a soft layer is always lower than $K_{\mathrm{I}}^{\mathrm{Postma}}$ of crack in Postma-homogenized solid, whereas K_{I} of crack embedded in a hard layer is always higher. The differences for this large modulus contrast are significant, and the asymptotic ratios $K_{\mathrm{I}}/K_{\mathrm{I}}^{\mathrm{Postma}}$ are below 0.7 and over 2.5, respectively. These differences decrease with decreasing layer modulus contrast. Nonetheless, even for the smallest modulus contrast ratio $E_h/E_s=2$, the homogenization-based analysis underestimates K_{I} of crack in hard layer by about 20% and overestimates it by 10% when the crack is embedded in a soft layer. With proper interpretation, the asymptotic behavior of stress intensity factors may have been anticipated based on the work of Wang et al. [25] dealing with fracture mechanics of thin adhesive bonds discussed in Sec. 5.

The corresponding Mode I strain energy release rates $\partial U_{\mathrm{I}}/\partial a = G_{\mathrm{I}}$ for cracks situated in hard and soft layers, normalized by the energy release rates calculated for Postma-homogenized configuration, $G_{\mathrm{I}}^{\mathrm{Postma}}$, as a function of the layer refinement are presented in Fig. 3(*b*) for the three elastic moduli contrast ratios. In contrast to stress intensity factors, energy release rates of the layered configurations tend to converge to their homogenized counterparts with increasing microstructural refinement. The asymptotic convergence occurs from above and below for cracks embedded in soft and hard layers, respectively. It is much more rapid for cracks embedded in soft than hard layers. For cracks embedded in soft layers, the effect of the moduli contrast ratio becomes small beyond $2n+1=51$, and the asymptotic energy release rates are just slightly greater than those of Postma-homogenized configurations as the microstructure becomes very fine. We note that in this case, the mismatch between the Young's modulus of the soft layer and the homogenized configurations in the direction of loading is relatively small (see Tables 1 and 2). In contrast, when the crack is embedded in a hard layer with the concomitant larger Young's modulus mismatch in the direction of loading, the difference between asymptotic energy release rates of actual multilayers and those of homogenized configurations persists even when the microstructure becomes very fine for the two largest moduli ratios.

Table 4 Stress intensity factors and strain energy release rates for a central crack under internal normal and shear tractions of magnitude 1 psi in finite homogeneous plates with different isotropic elastic moduli

E	K_{I}	K_{II}	G_{I} $(\times 10^{-7})$	G_{II} $(\times 10^{-7})$
10	1.008871	1.006365	0.9069799	0.9024795
5	1.008867	1.006234	1.813945	1.804489
0.5	1.008867	1.006234	18.13945	18.04489

In order to explain similar trends in stress intensity factors and energy release rates as those observed in Fig. 3 for multilayers with the modulus ratio $E_h/E_s=20$ subjected to external loading, crack-opening displacements were examined as a function of layer refinement by Pindera and Chen [12]. Specifically, cracks embedded in soft layers initially experienced larger crack-opening displacements than cracks in hard layers for coarsely layered configurations under the same vertical displacement applied to the multilayer's top surface. As the layer refinement increased, crack-opening displacements asymptotically converged to that of Postma-homogenized solid but in a different manner. For crack embedded in a hard layer, the crack-opening displacement became larger and monotonically tended toward the Postma model with increasing number of alternating layers. The convergence for the finest microstructure with $2n+1=201$ layers, however, was not completely attained. In contrast, the crack-opening displacement in a soft layer decreased substantially during the initial microstructural refinement stage but quickly rebounded to the Postma model with further refinement, producing complete convergence for the $2n+1=201$ layer microstructure. Herein, we demonstrate the effect of E_h/E_s on the crack-opening displacement under internal normal loading in Fig. 4 for the finest microstructure containing $2n+1=201$ layers. For a crack embedded in a hard layer (Fig. 4(*a*)), difference in the crack-opening displacements of the actual and homogenized microstructures is also observed in the present case for the largest E_h/E_s ratio. This difference vanishes with decreasing moduli contrast ratio, and the crack-opening displacements in the actual multilayers with $E_h/E_s=10,2$ are indistinguishable from their counterparts in the corresponding homogenized microstructures. In contrast, no differences in the crack-opening displacements in the actual and homogenized microstructures are observed for all three E_h/E_s ratios when the crack is embedded in a soft layer (Fig. 4(*b*)). In this case, the contrast between the elastic moduli of the cracked layer and the surrounding periodic medium is smaller (see Tables 1 and 2).

The corresponding results for stress intensity factors and energy release rates under pure shear loading applied to crack faces are shown in Fig. 5. Mode II stress intensity factor K_{II} and the corresponding strain energy release rate G_{II} exhibit qualitatively similar asymptotic behaviors with increasing microstructural refinement as under pure normal loading, with some notable differences. The asymptotic behavior of K_{II} tends to be slower in both instances when the crack is embedded in hard and soft layers for all three moduli contrast ratios (Fig. 5(*a*)). Further, the normalized values of K_{II} for cracks embedded in hard layers are smaller relative to those of K_{I} for the two largest E_h/E_s ratios; i.e., the deviations from the Postma model are smaller for the same modulus contrast ratio, while the opposite is true for cracks embedded in soft layers. Decreasing the modulus contrast decreases the deviation from Postma-homogenized results, as was also the case under pure normal loading. Nonetheless, even for the smallest modulus contrast ratio, the deviations from Postma model are on the order of 15% for the finest microstructure comprised of $2n+1=201$.

Similarly, the asymptotic behavior of G_{II} with increasing microstructural refinement is also more gradual relative to that observed for G_{I} (Fig. 5(*b*)). In this case, however, the initial values of G_{II} are substantially higher than those for G_{I} when the crack is embedded in soft layers. The differences between homogenized and actual strain energy release rates substantially decrease with decreasing modulus contrast and become small when $E_h/E_s=2$ for sufficiently refined microstructures. However, even for the finest microstructure, the deviations from the Postma model remain greater than the corresponding deviations under normal traction loading.

The differences in the asymptotic behavior of G_{II} for the two cases of cracks embedded in soft and hard layers are reflected in the corresponding differences observed in the crack sliding displacements for the finest microstructure shown in Fig. 6. First, it is

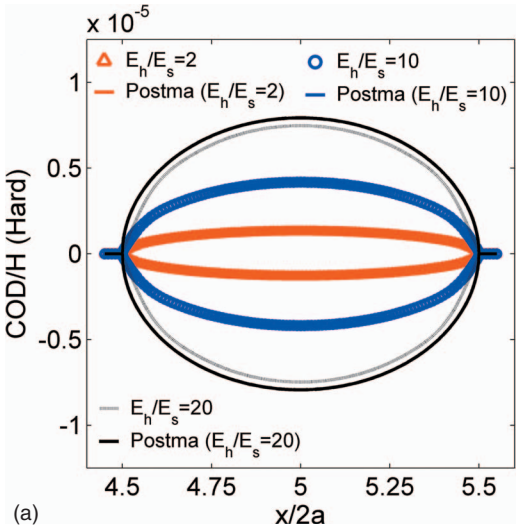

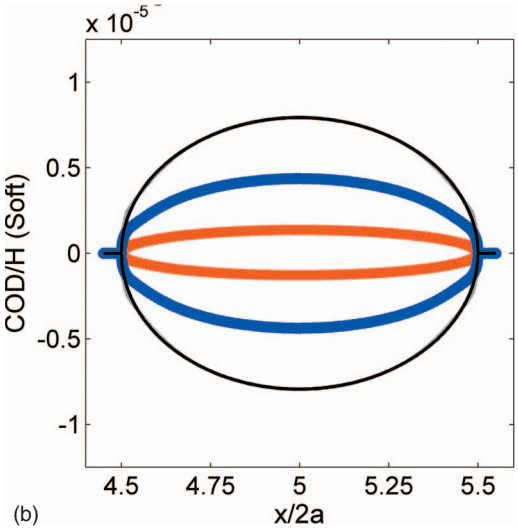

Fig. 4 Comparison of the crack-opening displacements under Mode I loading in the actual $2n+1=201$ and homogenized multilayers with the elastic moduli layer ratios $E_h/E_s=20,10,2$: (*a*) crack in hard layer and (*b*) crack in soft layer

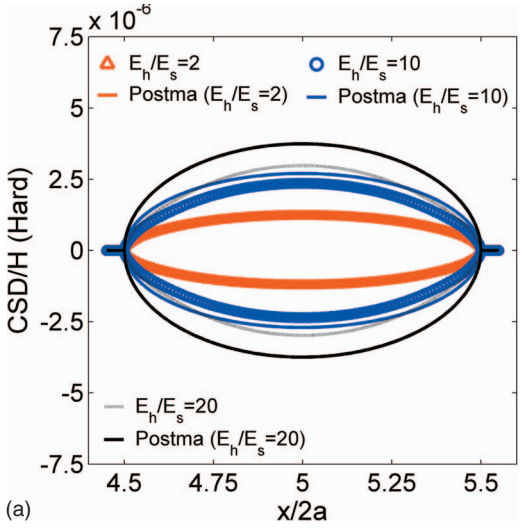

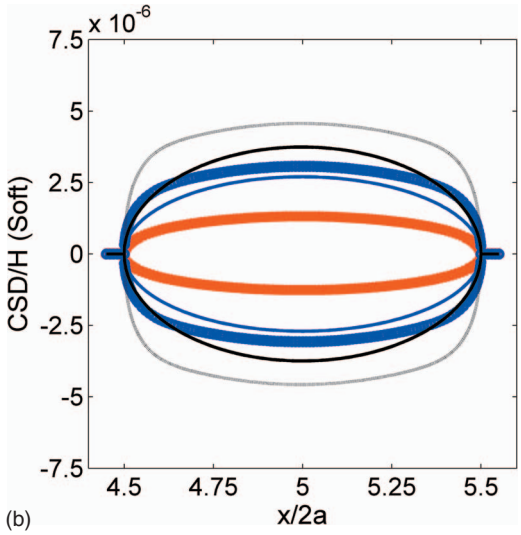

Fig. 6 Comparison of the crack-opening displacements under Mode II loading in the actual $2n+1=201$ and homogenized multilayers with the elastic moduli layer ratios $E_h/E_s=20,10,2$: (*a*) crack in hard layer and (*b*) crack in soft layer

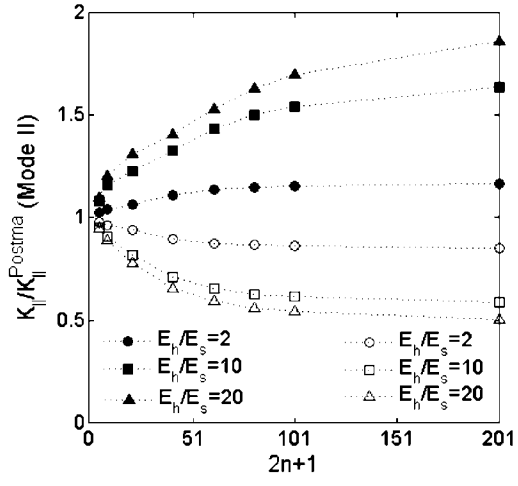

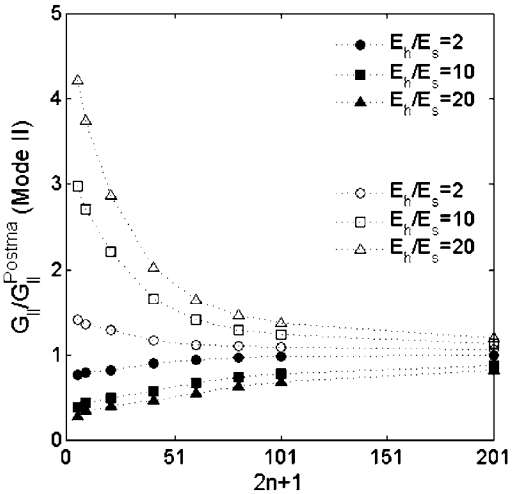

Fig. 5 (*a*) Normalized Mode II stress intensity factor K_{II}/K_{II}^{Postma} and (*b*) normalized Mode II strain energy release rate G_{II}/G_{II}^{Postma} of the crack embedded in hard (filled symbols) and soft (open symbols) layers as a function of the layer refinement $2n+1$ for the elastic moduli ratios $E_h/E_s=20,10,2$

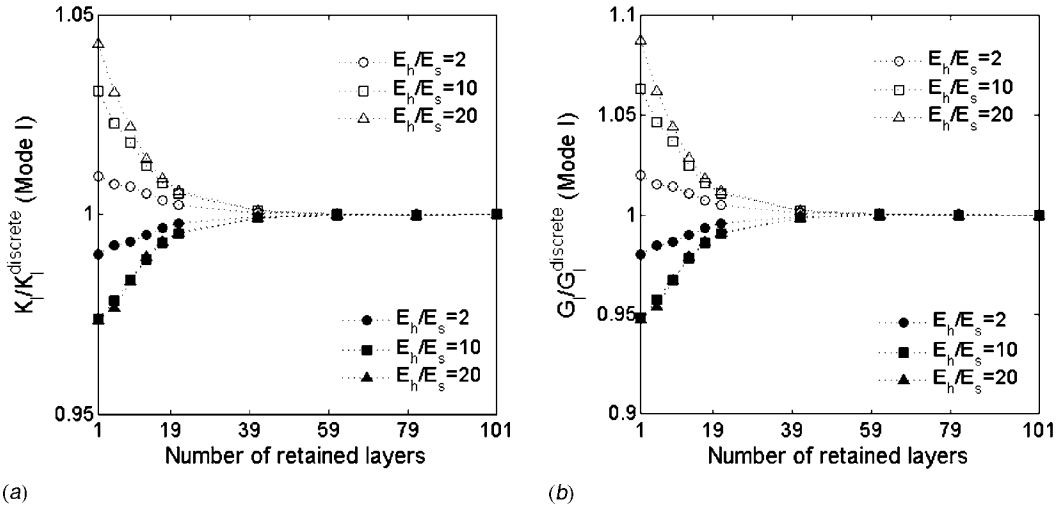

Fig. 7 (*a*) **Normalized Mode I stress intensity factor $K_I/K_I^{discrete}$ and** (*b*) **normalized Mode I strain energy release rate $G_I/G_I^{discrete}$ of the crack embedded in a hard (filled symbols) and soft (open symbols) layer as a function of the number of retained layers for the elastic moduli ratios E_h/E_s=20,10,2 and a multilayer with 101 discrete layers**

only for the lowest moduli contrast ratio $E_h/E_s=2$ that the crack sliding displacements in the actual microstructures converge to those in the homogenized multilayers in both instances of cracks embedded in soft and hard layers. For the remaining ratios, differences in the crack sliding displacements relative to the homogenized configurations are observed for both crack locations. These differences depend on, and decrease with, the moduli contrast ratio. For a crack embedded in hard layer, the crack sliding displacement is smaller than that in the homogenized medium since the shear modulus of the layer is greater than the pertinent effective shear modulus (G_{13}^*) (see Tables 1 and 2). The opposite behavior is observed for cracks embedded in soft layers whose shear moduli are now smaller than those of the corresponding homogenized media. In this case, the crack sliding displacement shapes depart substantially from those of cracks in the homogenized media.

4.2 Effect of Partial Homogenization. The efficiency with which fracture mechanics parameters are accurately calculated in multilayers can be increased by retaining the actual layered microstructure in the vicinity of the layer where the crack is embedded while homogenizing the rest (Fig. 2(*b*)). Such partial replacement scheme is called partial homogenization and has been successfully employed in the context of contact problem on multilayers, as discussed in the Introduction. We demonstrate the efficacy of this device by comparing Mode I and II stress intensity factors and the corresponding energy release rates in partially homogenized 101-layer configurations with those of fully discrete configurations as a function of the retained layer pairs adjacent to the middle cracked layer for the three modulus contrast ratios.

Figure 7 illustrates that partial homogenization substantially reduces the discrepancy between Mode I stress intensity factors and energy release rates of fully homogenized and actual microstructures even when only one hard or soft layer containing the crack is retained, with the remaining microstructure homogenized. For the largest modulus contrast, the discrepancy is less than 5% and 3% for cracks embedded in soft and hard layers, respectively, which is further reduced to approximately 1% when the modulus ratio decreases to 2. When the number of retained layers is 40, the discrepancy practically vanishes for all three modulus ratios, and for 60 layers the difference is graphically indistinguishable. The differences between strain energy release rates of fully and partially homogenized microstructures are initially greater for low numbers of retained layers but quickly disappear at about the same rate as the differences in the stress intensity factors. They also depend on the modulus contrast, with higher contrasts producing greater differences.

Figure 8 illustrates the corresponding normalized Mode II stress intensity factors and energy release rates. For just one retained layer, the differences are substantially greater in both cases relative to the differences under Mode I loading. However, these differences disappear much more rapidly with increasing number of retained layers than under Mode I loading, demonstrating greater effectiveness of partial homogenization.

5 Discussion

An examination of the stress intensity factors and energy release rates in homogeneous isotropic, homogenized orthotropic, and actual multilayered media listed in Tables 3–5, and limiting crack shapes in Figs. 4 and 6, suggests the reason for the trends observed in the stress intensity factors and energy release rates with increasing microstructural refinement. First, for the coarsest multilayer with $2n+1=5$, the layer containing the crack is twice as thick as the crack length, and thus interaction with the adjacent layers is very weak. This results in stress intensity factors that are nearly those of an infinite isotropic matrix, or homogenized orthotropic microstructure, regardless of the middle layer's elastic moduli. The accompanying crack-opening or sliding displacements are also not significantly affected by the adjacent layers in this case (as previously demonstrated by Pindera and Chen [12] for Mode I externally applied loading and $E_h/E_s=20$) and depend on the middle layer's elastic moduli, as do the strain energy release rates, which vary inversely with the layer's Young modulus. With increasing microstructural refinement, the interaction of the crack with adjacent layers becomes important and clearly depends on the contrast of the elastic moduli of the layer containing the crack and the adjacent layers. For the finest multilayers with $2n+1=201$, the layer thickness is slightly more than 20 times smaller than the crack length. Therefore, the stress intensity factors must deviate from those of cracks in homogeneous isotropic or homogenized media with increasing microstructural refinement. The results presented here illustrate that they converge to different values that depend on the layer stiffness. In contrast, crack-opening or sliding displacements approach those of the

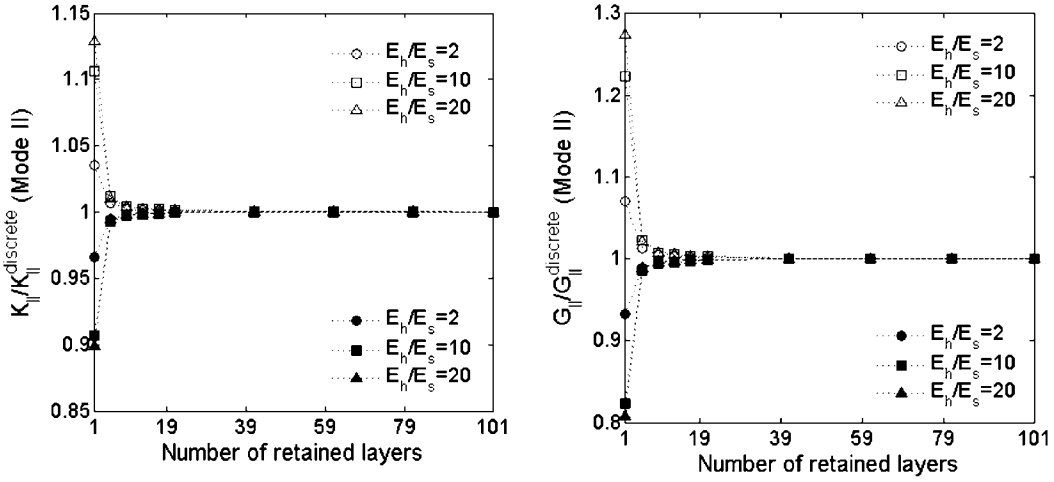

Fig. 8 (*a*) **Normalized Mode II stress intensity factor $K_{II}/K_{II}^{discrete}$ and** (*b*) **normalized Mode II strain energy release rate $G_{II}/G_{II}^{discrete}$ of the crack embedded in hard (filled symbols) and soft (open symbols) layers as a function of the number of retained layers for the elastic moduli ratios $E_h/E_s=20,10,2$ and a multilayer with 101 discrete layers**

equivalent homogenized orthotropic media with increasingly greater constraint of the adjacent layers concomitant with increasing microstructural refinement.

Pindera and Chen [12] explained the differences in the asymptotic behavior of K_I with microstructural refinement for a centrally embedded crack in a periodic multilayer with the moduli contrast ratio $E_h/E_s=20$ subjected to external vertical displacement loading in the following way:

> The different asymptotic behavior is due to the difference in the stiffness of the actual layer in which the crack is embedded and the fictitious stiffness of the Postma-homogenized solid. The crack-opening displacement vector is represented by a product of Chebyshev polynomials and the associated weight function. In contrast, stress intensity factors depend on both the layer stiffness around the crack through the elements of $\bar{B}_\alpha^*$ and the coefficients $C_{j(\alpha)}^{(p)}$. Therefore, although the shapes of cracks embedded in hard and soft layers of very finely layered configurations approach the crack shape in Postma-homogenized solid, the use of different material stiffnesses in the expressions for the stress intensity factors, which depend on the actual location (or material) of the embedded crack, produces different values for the stress intensity factors. That is, for the same crack-opening displacement, the stiffer (softer) the material the bigger (smaller) the stress intensity factor K_I.

The present results provide convincing evidence that the moduli contrast ratio plays a critical role in the asymptotic behavior of the stress intensity factors under both Mode I and II loadings applied directly to the crack faces; thus, they provide additional support for the original hypothesis.

Pindera and Chen [12] also suggested that given the convergence of crack-opening displacement to that of homogenized multilayer with increasing microstructural refinement, a comparison of the strain energy release rates for cracks in fully discrete and homogenized multilayers may be a more effective way of bridging the differences that result from the two distinct analysis approaches. The present results indicate that convergence of the strain energy release rates depends on the loading mode, the layer moduli contrast, and the elastic moduli of the layer containing the crack. The importance of the actual local microstructural details decreases with decreasing moduli contrast, but it does matter even for very fine microstructures when this contrast is large.

As mentioned earlier, the limiting behavior of the stress intensity factors may have been anticipated based on the work of Wang et al. [25] dealing with fracture mechanics of thin adhesive films between isotropic media with the same elastic moduli. As discussed by Hutchinson and Suo [24], the relationship between the apparent or effective stress intensity factor K_I of a crack in a thin adhesive film under Mode I loading and the stress intensity factor K_I^∞ of a crack embedded in the surrounding medium without the adhesive film (that is, ignoring the adhesive film's presence) is given by

$$\frac{K_I}{K_I^\infty}=\sqrt{\frac{1-\alpha}{1+\alpha}}$$

where

$$\alpha=\frac{\bar{E}_1-\bar{E}_2}{\bar{E}_1+\bar{E}_2}$$

with $\bar{E}_1=E_1/(1-\nu_i^2)$, $i=1,2$, for plane strain. The subscripts 1, 2, refer to adjacent isotropic half planes and thin adhesive films, respectively. Adapting the above formula to our situation by choosing the Young's modulus E_{33}^* in the direction of normal loading as E_1 (see Table 2), we obtain the following asymptotic values for the ratio K_I/K_I^∞ for different E_h/E_s ratios,

$$\text{Crack in soft layer: } E_h/E_s=20,10,2 \rightarrow \frac{K_I}{K_I^\infty}=0.621,0.656,0.850$$

Table 5 Stress intensity factors and strain energy release rates for a central crack under internal normal and shear tractions of magnitude 1 psi in multilayers with different layer moduli ratios comprised of $2n+1=201$ plies

E_h/E_s	K_I	K_{II}	G_I ($\times10^{-7}$)	G_{II} ($\times10^{-7}$)
2=10/5 (hard)	1.213253	1.174954	1.311684	1.230178
2=10/5 (soft)	0.8725883	0.8576713	1.356986	1.310986
10=10/1 (hard)	2.127076	1.639872	4.031739	2.396330
10=10/1 (soft)	0.7141212	0.5884896	4.544334	3.086058
20=10/0.5 (hard)	2.813711	1.862577	7.054811	3.091399
20=10/0.5 (soft)	0.6828595	0.5033149	8.310346	4.514775

$$\text{Crack in hard layer: } E_h/E_s = 20,10,2 \rightarrow \frac{K_I}{K_I^{\infty}} = 2.776, 2.074, 1.202$$

These asymptotic ratios can be compared with the limiting ratios K_I/K_I^{Postma} in Fig. 3(*a*) for the finest microstructure $2n+1=201$ given below,

$$\text{Crack in soft layer: } E_h/E_s = 20,10,2 \rightarrow \frac{K_I}{K_I^{\infty}} = 0.677, 0.708, 0.865$$

$$\text{Crack in hard layer: } E_h/E_s = 20,10,2 \rightarrow \frac{K_I}{K_I^{\infty}} = 2.788, 2.108, 1.202$$

A surprisingly good agreement is observed between the exact results and the back-of-the-envelope type, or first order, calculations based on the assumption that the entire periodically layered microstructure adjacent to the middle layer can be replaced by an equivalent homogenized medium with the proper selection of the orthotropic modulus commensurate with the crack deformation mode. The differences in the two sets of results are due to the orthotropy and the manner of the replacement scheme as observed in the partial homogenization results provided in Fig. 7(*a*). In particular, retaining more layers adjacent to the cracked layer will eliminate the differences between exact and first order homogenized analyses, albeit at a more computational expense requiring a truly multilayer solution capability.

We end this discussion by pointing out that the results presented herein, which demonstrate the limitations of the widely employed homogenized-based approach in the analysis of heterogeneous materials, must be interpreted taking into account the stability of crack growth in multilayered media. In particular, the strain energy release rates have been generated assuming self-similar crack extension. Hutchinson and Suo [24] discussed these issues, pointing out that self-similar crack growth is stable in compliant adhesive layers but unstable in hard layers, leading to crack deflection toward the layer interface. The present approach can be extended to investigate fracture mechanics parameters of multilayers in the presence of interfacial crack propagation using the general solution for cracks in arbitrary multilayered media developed by Chen and Pindera [14].

6 Conclusions

The fracture parameters of periodic multilayers differ substantially from those of equivalent homogenized media. The stress intensity factors of a crack in an actual multilayer exhibit significant departures from the corresponding values in the homogenized medium, the extent of which depends on the layer modulus contrast, microstructural refinement, and loading mode. For large moduli contrasts, the differences are very substantial, becoming smaller with decreasing modulus mismatch. In contrast, the crack-opening displacements tend to those in the homogenized media with sufficient microstructural refinement in a manner that depends on the modulus contrast and the stiffness of the layer containing the crack. This explains the asymptotic convergence of the strain energy release rates of cracks in actual multilayers with those of cracks in the equivalent homogenized media. However, the convergence tends to be slow under Mode I loading for large moduli contrasts and for cracks embedded in stiff layers. Under Mode II loading, the convergence rate is about the same for cracks situated in both soft and hard layers for sufficiently refined microstructures.

Therefore, the actual microstructure immediately adjacent to the crack does matter and must be taken into account when calculating fracture mechanics parameters of cracks situated far from the boundaries of periodic multilayers comprised of isotropic layers under Mode I and II loadings. The efficiency of calculating the stress intensity factors and energy release rates can be significantly enhanced by using a partial homogenization scheme wherein the actual microstructure in the immediate vicinity of the crack is retained, with the far-field periodic material replaced by the equivalent homogenized medium. Our results indicate that Mode II fracture mechanics parameters converge faster with such partial homogenization, i.e., with a smaller number of layers retained in the crack's immediate vicinity, than Mode I parameters. This sets the stage and guidelines for applying partial homogenization to structures comprised of a very large number of layers wherein the full microstructural details cannot be readily taken into account in the course of obtaining a solution for the local fields and fracture parameters associated with particular noninteracting cracks.

Acknowledgment

The authors thank the Civil Engineering Department at the University of Virginia and the Engineered Materials Concepts, LLC for providing partial support.

Appendix

Postma [16] developed an exact solution to determine the overall transversely isotropic properties of periodically layered structures consisting of alternating layers with different material properties, with the direction of anisotropy orthogonal to the plane of alternating layers. The homogenized elastic stiffness matrix elements C_{ij}^* of the layered medium are given in terms of Lame's constants λ_i and μ_i of the individual isotropic layers $i=1,2$ and their thicknesses h_i in the form

$$C_{11}^* = \frac{1}{D}\{(h_1+h_2)^2(\lambda_1+2\mu_1)(\lambda_2+2\mu_2) + 4h_1h_2(\mu_1-\mu_2)[(\lambda_1+\mu_1)-(\lambda_2+\mu_2)]\}$$

$$C_{12}^* = \frac{1}{D}\{(h_1+h_2)^2\lambda_1\lambda_2 + 2(\lambda_1h_1+\lambda_2h_2)(\mu_2h_1+\mu_1h_2)\}$$

$$C_{13}^* = \frac{1}{D}\{(h_1+h_2)[\lambda_1h_1(\lambda_2+2\mu_2)+\lambda_2h_2(\lambda_1+2\mu_1)]\}$$

$$C_{33}^* = \frac{1}{D}\{(h_1+h_2)^2(\lambda_1+2\mu_1)(\lambda_2+2\mu_2)\}$$

$$C_{44}^* = (h_1+h_2)\mu_1\mu_2/(h_1\mu_2+h_2\mu_1)$$

$$C_{66}^* = (\mu_1h_1+\mu_2h_2)/(h_1+h_2) \tag{23}$$

where $D=(h_1+h_2)(h_1(\lambda_2+2\mu_2)+h_2(\lambda_1+2\mu_1))$, $\lambda_i=\upsilon_iE_i/((1+\upsilon_i)\times(1-2\upsilon_i))$, $\mu_i=E_i/2(1+\upsilon_i)$, and $C_{11}^*=C_{22}^*$, $C_{44}^*=C_{55}^*$, and $C_{66}^*=(C_{11}^*-C_{12}^*)/2$. These relations among the stiffness matrix elements indicate that the laminated medium is transversely isotropic with the $x-y$ (or $1-2$) plane of isotropy. The knowledge of the elastic stiffness matrix elements C_{ij}^* allows one to calculate the homogenized engineering constants using standard formulas, i.e., $E_{11}^*=E_{22}^*=1/S_{11}^*$, $E_{33}^*=1/S_{33}^*$, $G_{13}^*=G_{23}^*=C_{44}^*$, $G_{12}^*=C_{66}^*$, $\upsilon_{13}^*=\upsilon_{23}^*=-E_{11}^*/S_{31}^*$, and $\upsilon_{12}^*=-E_{11}^*/S_{21}^*$, where the compliance matrix elements S_{ij}^* are obtained from the inverse of the elastic stiffness matrix $\mathbf{C}^*$ or $[\mathbf{C}^*]^{-1}=\mathbf{S}^*$.

References

[1] Drago, A. S., and Pindera, M.-J., 2007, "Micro-Macromechanical Analysis of Heterogeneous Materials: Macroscopically Homogeneous Vs Periodic Microstructures," Compos. Sci. Technol., **67**(6), pp. 1243–1263.

[2] Sanchez-Palencia, E., 1980, *Non-Inhomogeneous Media and Vibration Theory*, Lecture Notes in Physics Vol. 127, Springer-Verlag, Berlin.

[3] Suquet, P. M., 1987, *Elements of Homogenization for Inelastic Solid Mechanics*, Lecture Notes in Physics Vol. 272, Springer-Verlag, Berlin, pp. 193–278.

[4] 1997, *Homogenization and Porous Media*, U. Hornung, ed., Springer, Berlin.

[5] Pagano, N. J., and Rybicki, E. F., 1974, "On the Significance of the Effective Modulus Solutions for Fibrous Composites," J. Compos. Mater., **8**, pp. 214–228.

[6] Hollister, S. J., and Kikuchi, N., 1992, "A Comparison of Homogenization and Standard Mechanics Analyses for Periodic Porous Composites," Comput. Mech., **10**, pp. 73–95.
[7] Pindera, M.-J., Aboudi, J., and Arnold, S. M., 1995, "Limitations of the Uncoupled, RVE-Based Micromechanical Approach in the Analysis of Functionally Graded Composites," Mech. Mater., **20**(1), pp. 77–94.
[8] Pagano, N. J., and Yuan, F. G., 2000, "The Significance of Effective Modulus Theory (Homogenization) in Composite Laminate Mechanics," Compos. Sci. Technol., **60**, pp. 2471–2488.
[9] Wang, A. S. D., and Yan, K. C., 2005, "On Modeling Matrix Failure Modes," Composites, Part A, **36**, pp. 1335–1346.
[10] Lipton, R. P., 2003, "Assessment of the Local Stress State Through Macroscopic Variables," Philos. Trans. R. Soc. London, Ser. A, **361**, pp. 921–946.
[11] Chen, L., Urquhart, E. E., and Pindera, M.-J., 2005. "Microstructural Effects in Multilayers With Large Moduli Contrast Loaded by Flat Punch," AIAA J., **43**(5), pp. 962–973.
[12] Pindera, M.-J., and Chen, L., 2007, "Microstructural Effects in Finite Multilayers With Aligned Cracks," Eng. Fract. Mech., **74**(11), pp. 1697–1718.
[13] Pindera, M.-J., and Lane, M. S., 1993, "Frictionless Contact of Layered Half Planes. Part I: Analysis," ASME J. Appl. Mech., **60**(3), pp. 633–639.
[14] Chen, L., and Pindera, M.-J., 2007, "Plane Analysis of Finite Multilayered Media With Multiple Aligned Cracks. Part I: Theory," ASME J. Appl. Mech., **74**(1), pp. 128–143.
[15] Chen, L., and Pindera, M.-J., 2007, "Plane Analysis of Finite Multilayered Media With Multiple Aligned Cracks. Part II: Numerical Results," ASME J. Appl. Mech., **74**(1), pp. 144–160.
[16] Postma, G. W., 1955, "Wave Propagation in a Stratified Medium," Geophysics, **20**(4), pp. 780–806.
[17] Bufler, H., 1971, "Theory of Elasticity of a Multilayered Medium," J. Elast., **1**, pp. 125–143.
[18] Pindera, M.-J., 1991, "Local/Global Stiffness Matrix Formulation for Composite Materials and Structures," Composites Eng., **1**(2), pp. 69–83.
[19] Ting, T. C. T., 1996, *Anisotropic Elasticity (Theory and Applications)*, Oxford University Press, Oxford.
[20] Erdogan, F., and Gupta, G. D., 1971, "The Stress Analysis of Multi-Layered Composites With a Flaw," Int. J. Solids Struct., **7**, pp. 39–61.
[21] Erdogan, F., and Gupta, G. D., 1971, "Layered Composites With an Interface Flaw," Int. J. Solids Struct., **7**, pp. 1089–1107.
[22] Erdogan, F., Gupta, G. D., and Cook, T. S., 1973, "Numerical Solution of Singular Integral Equations," *Methods of Analysis and Solutions of Crack Problems*, G. C. Sih, ed., Noordhoff, Leyden, Netherlands, pp. 368–425.
[23] Sih, G. C., Paris, P. C., and Irwin, G. R., 1965, "On Cracks in Rectilinearly Anisotropic Bodies," Int. J. Fract. Mech., **1**, pp. 189–203.
[24] Hutchinson, J. W., and Suo, Z., 1992, "Mixed Mode Cracking in Layered Media," Adv. Appl. Mech., **29**, pp. 63–191.
[25] Wang, S. S., Mandell, J. F., and McGarry, F. J., 1978, "An Analysis of the Crack Tip Stress Field in DCB Adhesive Fracture Specimens," Int. J. Fract., **14**, pp. 39–58.

Crack Initiation in Functionally Graded Materials Under Mixed Mode Loading: Experiments and Simulations

Alpay Oral
Department of Mechanical Engineering,
Bogazici University,
34342 Bebek,
Istanbul, Turkey

John Lambros
Department of Aerospace Engineering,
University of Illinois, Urbana-Champaign,
Urbana, IL 61801

Gunay Anlas
Department of Mechanical Engineering,
Bogazici University,
34342 Bebek,
Istanbul, Turkey

In this work, quasistatic crack initiation under mixed mode loading in planar (two-dimensional plane stress) functionally graded materials (FGMs) is studied. The goal of this work is to directly compare experiments and simulations so as to evaluate the applicability of the maximum tangential stress (MTS) criterion in predicting crack kinking in FGMs. Initially, crack initiation in the homogeneous material, which forms the basis of our FGM—polyethylene—is studied. The (generalized) maximum tangential stress is applied through the use of finite elements to determine crack initiation angles in the same graded configurations studied experimentally. Computational results of fracture parameters (stress intensity factors and T-stress), and crack initiation angles are compared to experimental results and good agreement is obtained. It is seen that the MTS criterion is applicable to FGM crack initiation prediction if the inherent material gradient length scale is larger than the fracture process zone. [DOI: 10.1115/1.2936238]

Keywords: FGM, crack initiation angle, mixed mode fracture, digital image correlation

1 Introduction

As applied loading is seldom controlled in practice, it is common for a mixed mode stress field to develop in the vicinity of a notch or crack tip in a material. In general, this will involve all three modes of crack deformation: Modes I, II, and III, although the out-of-plane Mode III has received far less attention than the two in-plane Modes I and II. In homogeneous materials, crack growth is usually observed to occur under Mode I conditions, but crack initiation is dependent on the details of Modes I and II mix. Several criteria exist for predicting when a crack in a homogeneous material will initiate under mixed mode loading conditions. The two most common are the maximum tangential stress (MTS) criterion, $(\sigma_{\theta\theta})_{\max}$ [1], and the maximum strain energy release rate criterion, $G_{\max}$ [2]. Both have shown good agreement with experiments for quasibrittle homogeneous materials.

For the case of functionally graded materials (FGMs), the situation is further affected by the fact that near-tip mixity can arise by virtue of the property variation in the material even when far field loading is symmetric. Compared to homogeneous materials, mixed mode crack initiation in FGMs has received far less scrutiny. Most efforts are purely numerical and typically use finite element analyses (FEAs) to evaluate the validity of the above mentioned crack initiation criteria for FGMs. Becker et al. [3] found that, in contrast to homogeneous materials, for kink angles that maximize the energy release rate the Mode II stress intensity factor (SIF) K_{II} is not necessarily zero. This result was also confirmed experimentally in the work of Abanto-Bueno and Lambros [4]. Kim and Paulino [5], using a generalized MTS criterion that also includes the T-stress, found that positive T-stress values increase the crack initiation angle, and vice versa, when compared to the homogeneous case. In addition, they observed a significant influence of the FGMs' intrinsic degree of nonhomogeneity on the magnitude and sign of the T-stress.

Experimental studies on the mixed mode quasistatic loading of FGMs are very limited in number. Rousseau and Tippur [6] investigated the fracture behavior of FGMs with cracks perpendicular to the elastic gradient and found that the crack kinked toward the more compliant region, and both the MTS and the vanishing K_{II} criteria [7] could also be applied to predict the kinking angle in their FGMs. More recently, Abanto-Bueno and Lambros [4] performed an investigation of crack initiation and growth in FGMs that possessed near-tip mixity generated by either applied loading or material gradient, or both factors combined. They also found that for their FGMs the MTS criterion predicted kink angles well, although continued crack growth under mixed mode was possible with nonzero K_{II}.

To date, however, there has been no attempt to combine the existing experimental and numerical studies in order to evaluate the validity of possible fracture criteria for more general situations. This is the goal of the present work. Our approach is to combine the experimental results of Abanto-Bueno and Lambros [4] with detailed numerical simulations of the precise material geometry and loading used in the experiments. In this fashion, a direct comparison between numerics and experiments can be made, thus providing a much better understanding of mixed mode crack initiation in FGMs.

2 Experiments

The experimental results used in this study are taken from those obtained by Abanto-Bueno and Lambros [4]. Details of the experimental methodology are described in that work and will not be repeated in the interest of brevity. Only the results relevant to the current work will be described here. The testing protocol of Abanto-Bueno and Lambros [4] included mixed mode fracture experiments on the base homogeneous material, polyethylene, used for manufacturing the FGMs. Subsequently, mixed mode fracture experiments were conducted on FGMs with near-tip mixity generated through either applied load/geometry asymmetry, or a material property gradient inclined to the crack tip, or both.

The graded FGM samples were manufactured using selective ultraviolet (UV) light irradiation on a photodegradable polyethylene carbon monoxide copolymer. Typically, a thin sheet (thickness

Contributed by the Applied Mechanics Division of ASME for publication in the JOURNAL OF APPLIED MECHANICS. Manuscript received June 29, 2007; final manuscript received December 31, 2007; published online July 11, 2008. Review conducted by Marek-Jerzy Pindera.

of 0.406 mm) of in-plane dimensions 300×150 mm^2 was irradiated for times varying from 5 h to 300 h. After irradiation, the sheet was cut in half parallel to the irradiation direction, and two samples of 150×150 mm^2 were obtained. One of these was then cut perpendicularly to the irradiation direction into 15 strips of 10 mm width, which were used in uniaxial tension tests to measure elastic and failure property variation as a function of position on the sample. The remaining 150×150 mm^2 sample from the original sheet was then used for a single edge notch fracture experiment. Therefore, the variation of local material properties such as elastic modulus, failure stress, and failure strain was measured independently of the fracture experiments, but originating from exactly the same manufacturing process. By measuring local properties in this fashion for every experiment material, variability issues were circumvented.

Figure 1 shows the elastic modulus variation for three FGM cases: Case I, Fig. 1(*a*), which possesses a symmetric geometry, but the material property gradient is perpendicular to the crack line; Case II, Fig. 1(*b*), in which mixity is introduced by an asymmetry in both geometry and material property gradient; and Case III, Fig. 1(*c*), in which the material property gradient is parallel to the crack line, but the loading is not.

Fracture experiments were conducted in which detailed near-tip full-field experimental data were obtained throughout crack initiation and growth. In the present work, we will only concentrate on the crack initiation results and compare them to companion numerical simulations. Both components of the in-plane crack tip displacement field were measured experimentally using the digital image correlation (DIC) technique [8]. The theoretical asymptotic near-tip opening displacement field, denoted here as u_y, for a homogeneous isotropic linearly elastic material subjected to in-plane mixed mode loading is given by

$$u_y = \frac{K_I}{2\mu}\left(\frac{r}{2\pi}\right)^{1/2} \sin\frac{\theta}{2}\left(\frac{3-\nu}{1+\nu} - \cos\theta\right) - \frac{T\nu}{2\mu(1+\nu)} r \sin\theta + \frac{K_{II}}{4\mu}\left(\frac{r}{2\pi}\right)^{1/2}\left(\frac{5\nu-3}{1+\nu}\cos\frac{\theta}{2} - \cos\frac{3\theta}{2}\right) + A_1 r\cos\theta + u_{0y} \tag{1}$$

where A_1 and u_{0y} represent rigid body rotation and translation, respectively, ν is Poisson's ratio and μ is the shear modulus of the material, and r and θ are polar coordinates centered at the crack tip. Three terms associated with the crack tip field itself are shown in Eq. (1)—those corresponding to the mixed mode SIFs K_I and K_{II}, and the T-stress. The T-stress term represents a stress component parallel to the crack line and is highly dependent on specimen configuration and loading. For the case of a FGM, the properties used in Eq. (1) are those measured at the crack tip, and are denoted as ν_{tip} and μ_{tip}.

All three values of K_I, K_{II}, and T, as well as the constants for rigid body motion A_1 and u_{0y}, are obtained simultaneously by performing a least squares fit of experimental DIC values to Eq. (1). It is important to note that in purely K-dominant field the T-stress term in Eq. (1) would be negligible. Abanto-Bueno and Lambros [4] found that for the configurations used here, the K-dominant field often times did not represent the experimentally measured displacement fields well, and the T-stress had to be included to get a good comparison. The importance of T-stress in this configuration can be judged by the experimental results shown in Tables 1 and 3. Depending on the specimen geometry and gradient, the T-stress ranged from −0.069 MPa to over −4.2 MPa. The importance of the T-stress should be judged not only with respect to the singular term (i.e., amount of stress biaxiality), but also with respect to the yield stress of the material. The biaxiality ratio, defined here for a mixed mode situation as $\beta = T\sqrt{(\pi a)}/\sqrt{(K_I^2 + K_{II}^2)}$, is a relative measure of T-stress compared to the singular field. Values of experimentally obtained biaxiality for each case are shown in Tables 1 and 3. In addition, for

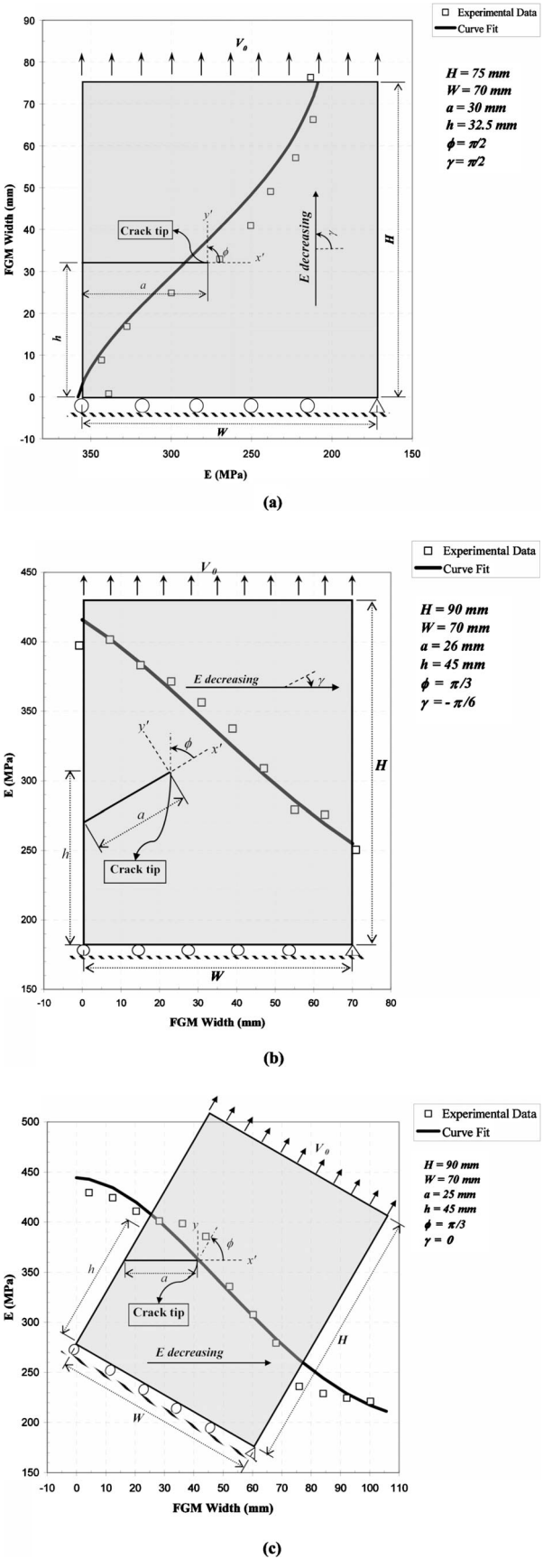

Fig. 1 Geometry, loading, and elastic modulus variation for three FGM specimens used in Ref. [4]: (*a*) Case I, symmetric loading and nonsymmetric property gradient; (*b*) Case II, nonsymmetric loading and property gradient; and (*c*) Case III, symmetric gradient and nonsymmetric loading

Table 1 Experimental and numerical results for K_I, K_{II}, and T-stress, for homogeneous edge cracked specimen

	K_I (MPa m$^{0.5}$)	K_{II} (MPa m$^{0.5}$)	T (MPa)	Biaxiality β
Expt. results	0.903	0.245	−0.784	−0.270
Num. results	0.793	0.212	−0.992	

the polyethylene used here, the yield stress varies between 8 MPa and 12 MPa [4]. Therefore, a value of −4.272 MPa T-stress is very significant, whereas a value of −0.069 MPa corresponds to an almost K-dominant situation. Thus, the presence of T-stress can significantly affect the values of K_I and K_{II} in many cases, and has therefore been included in Eq. (1).

Figure 2 shows the final cracked geometry in each of the three FGM cases after loading. Crack kinking is evident in each case. However, the crack initiation angle was measured after each experiment using an optical microscope to zoom into the crack tip.

3 Numerical Simulations

Finite element simulations were conducted using MSC.Marc® 2005r3 [9]. An example of a mesh used in the simulations is shown in Fig. 3(*a*). The entire plate used in the fracture experiments in Ref. [4] is discretized with between 3300 and 3600 four node quadratic plane stress elements. Since for each specimen, whether homogeneous or FGM, the dimensions and geometry tested in Ref. [4] are somewhat different, each case was discretized separately. Note, therefore, that in some cases the crack would be horizontal, unlike what is shown in Fig. 3(*a*). However, to allow for comparison between all cases, the near-tip discretization was kept the same, and consisted of a focused mesh centered at the crack tip out to a radius of $r/a=0.2$, where r is the radial coordinate (defined in Fig. 3(*c*)) and a is the crack length for each specimen. The focused portion of the mesh consisted of 36 elements along the tangential direction, and 14 elements along the radial direction, with a total of 504 elements as shown in Fig. 3(*b*). The remainder of each specimen outside of this region was automeshed by the software package used, thus accounting for the irregular mesh shape outside the focused region, and for the dif-

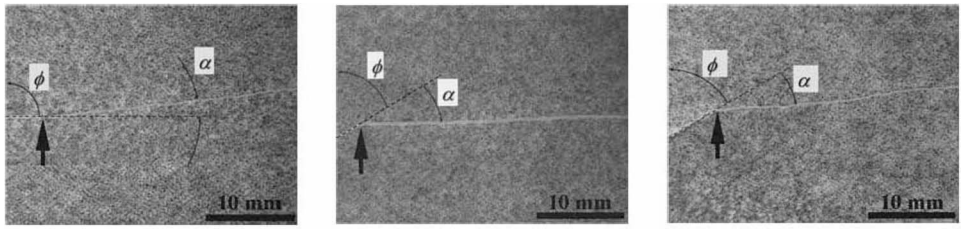

Fig. 2 Photograph of the final crack path for (*a*) Case I, (*b*) Case II, and (*c*) Case III from the experiments of Abanto-Bueno and Lambros [4]

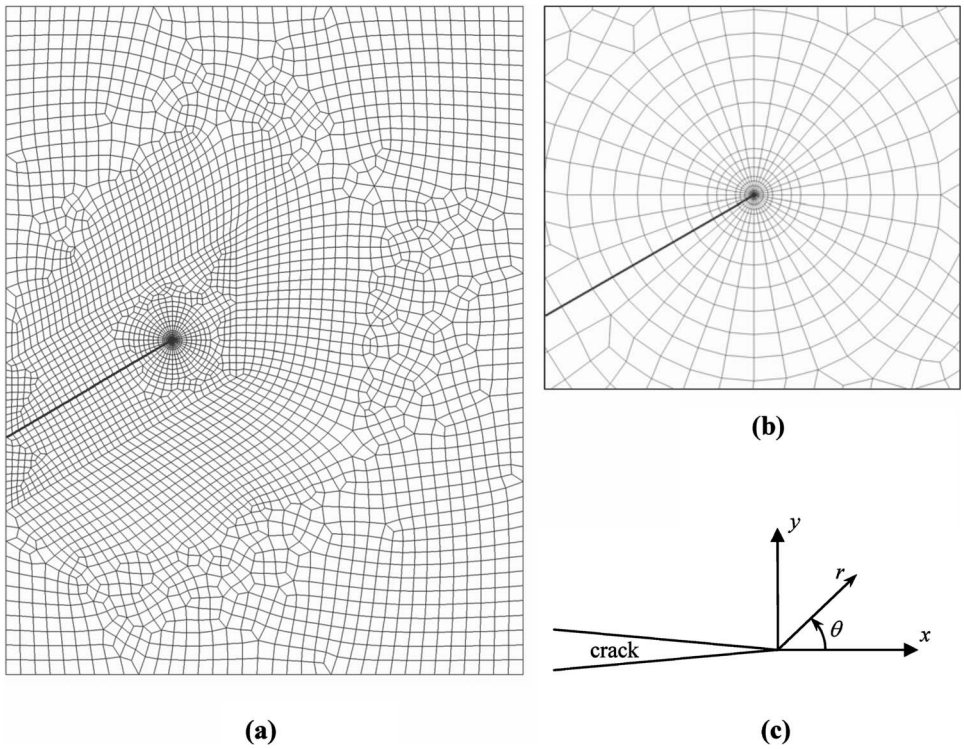

Fig. 3 Typical finite element mesh used for (*a*) complete model and (*b*) near crack tip. (*c*) Shows the local coordinate system at the crack tip. All quantities must be rotated into this coordinate system.

Table 2 Experimental and numerical results for crack initiation angle for homogeneous edge cracked specimen

Expt.	Crack initiation angles, α (deg)				
	FE—Using $(\sigma_{\theta\theta})_{max}$		Using GMTS, Eq. (4)		Using MTS, Eq. (4), $r_c=0$
	−31.5	for $r/a=0.01$	−24.1	for $r_c/a=0.01$	
-28 ± 1.5	−30.8	for $r/a=0.02$	−23.1	for $r_c/a=0.02$	−26.7
	−30.1	for $r/a=0.05$	−21.3	for $r_c/a=0.05$	
	−29.7	for $r/a=0.1$	−19.6	for $r_c/a=0.1$	

ference in the total number of elements in each case.

The specimen dimensions used in each case were those reported in Ref. [4]. The specimen thickness, common to all homogeneous and FGM samples, was 0.406 mm. Loading was applied as a fixed vertical displacement boundary condition along the upper edge of the specimen because the experiments of Abanto-Bueno and Lambros [4] were conducted under displacement control. Since the focus of this work is to study mixed mode crack initiation, and assuming a quasistatic loading process, the value of the displacement applied in the simulations was exactly that recorded in each experiment *at the precise instant of crack initiation*. In addition to the applied displacement along the upper edge, the vertical displacement was set to 0 at the lower edge, matching the experimental setup, and the horizontal displacement was set to 0 at the lower right hand corner in order to eliminate rigid body motion (Fig. 3(*a*)). Material properties used were also those measured experimentally. More details on the allocation of material properties in the FGM case are given below. In both the homogeneous and graded cases, the material was assumed to behave in a linear elastic fashion. The material used in Ref. [4] was UV light irradiated polyethylene, which after irradiation failed by crazing while showing very little shear yielding. The linear elastic assumption therefore should be applicable, and was, in fact, also made in the data analysis of Abanto-Bueno and Lambros [4].

Abanto-Bueno and Lambros [4] used the full-field method of DIC to measure the displacement field in an area surrounding the crack tip. They then extracted fracture quantities K_I, K_{II}, and T as described in the previous section. In the present work, the simulations provide full-field stress and displacement fields, which must then be processed to provide K_I, K_{II}, and T. K_I and K_{II} can reasonably be obtained from FEA; but, there are few reliable methods of obtaining T-stress from the full-field stress field. One methodology involving the difference of $\sigma_{xx}-\sigma_{yy}$ near the crack tip is presented in Ref. [10]. This method was attempted, but yielded unclear results usually producing a large variation of the constant T-stress around the crack tip. A more robust method using an interaction integral approach is presented in Ref. [5]. However, this technique is computationally more involved and was not available for FGMs in the software package used. Therefore, since the FEA simulations produce full-field displacement data similar to the DIC experiments, it was decided to use the same procedure as in the experiments, i.e., the least squares fitting of u_y in Eq. (1) to the full-field displacement, to extract values of K_I, K_{II}, and T. These values are somewhat sensitive to the area around the crack tip selected for the fitting process, but through an iterative scheme it is possible to obtain convergent values of the three quantities that fit the displacement field around the crack tip extremely well. More details about this issue are given in Sec. 5.

4 Results

4.1 Homogeneous Material. The base homogeneous material studied is a 0.406 mm thick polyethylene cocarbon monoxide sheet irradiated for 50 h under UV light. Its elastic properties were measured in Ref. [4] as Young's modulus $E=280$ MPa and Poisson's ratio $\nu=0.45$. Mixed mode loading in the homogeneous case was generated by inclining the crack in an otherwise symmetrically loaded single edge cracked plate, as shown in Fig. 4.

Using the procedure outlined in the previous section, values of K_I, K_{II}, and T were extracted from the finite element simulations corresponding to the experimentally recorded instant of crack initiation. Table 1 shows a comparison of these values with the corresponding experimental results given in Ref. [4]. The results agree reasonably well, especially for quantities K_{II} and T, which are usually more difficult to obtain.

The MTS criterion states that a crack will grow perpendicular to the direction of MTS, $\sigma_{\theta\theta}$ [1,11]. The FEA results provide as an output $\sigma_{\theta\theta}$, whose maximum for a given r is easy to establish. The stress results are rotated into a coordinate frame shown in Fig. 3(*c*), and the angle at which the maximum $\sigma_{\theta\theta}$ occurs is recorded. This can vary as a function of r, as shown in Table 2. The comparison with the experimentally measured kink angle value of -28 deg $\pm$ 1.5 deg is good especially for $r/a=0.1$.

The MTS criterion can also be cast in terms of SIFS by computing the angle for which $\sigma_{\theta\theta}$ predicted by the asymptotic field is maximum. Using only the singular term in the asymptotic expansion for stresses produces a unique kink angle independent of r. However, in the configuration used in the experiments of Abanto-Bueno and Lambros [4], large values of T-stress were measured compared to K_I and K_{II} (e.g., Table 1). Therefore, the effect of T-stress may need to be taken into account in determining the crack kinking angle using the so-called generalized maximum tangential stress (GMTS) criterion [11]. The asymptotic equation for $\sigma_{\theta\theta}$ to second order is [11]

$$\sigma_{\theta\theta}=\frac{1}{\sqrt{2\pi r}}\cos\frac{\theta}{2}\left[K_I\cos^2\frac{\theta}{2}-\frac{3}{2}K_{II}\sin\theta\right]+T\sin^2\theta \quad (2)$$

Using the GMTS criterion, the crack initiation angle α can then be obtained along the direction of MTS, from

$$\frac{\partial\sigma_{\theta\theta}}{\partial\theta}=0\Rightarrow\theta=\alpha \quad (3)$$

Substituting Eq. (2) into Eq. (3) yields

$$K_I\sin\alpha+K_{II}(3\cos\alpha-1)-\frac{16}{3}T\sqrt{2\pi r_c}\sin\frac{\alpha}{2}\cos\alpha=0 \quad (4)$$

where r_c is a length scale, considered a material property, at which the tangential stress must reach a critical value. If r_c is 0, Eq. (4) reduces to the MTS criterion result. Since r_c is external to the theory, it can only be obtained by comparison with experiments. This is usually done by conducting experiments over a range of mode mixity and finding a single value of r_c with which the predictions of Eq. (4) agree with experiments in Ref. [12]. Unfortunately, in the present work, we have experimental results for a single mode mixity; therefore, we cannot directly determine a value for r_c.[1] Therefore, in Table 2, we present the predictions of the MTS criterion along with the GMTS theory using the values

[1]Note that although it is feasible to obtain different mode mixities for the homogeneous case, it is virtually impossible for the FGM case, which would require testing of FGMs with exactly the same material property variation, but different loading conditions.

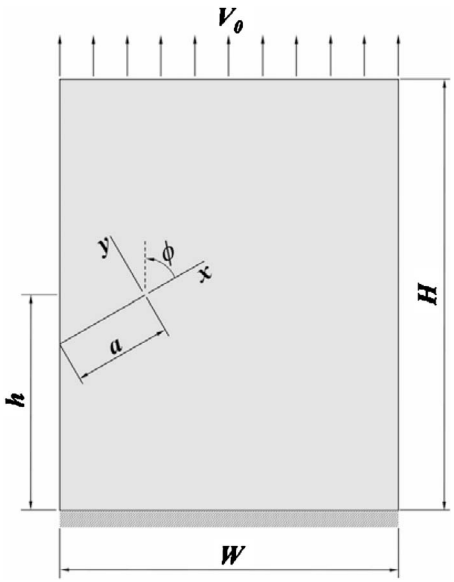

Fig. 4 Edge cracked specimen geometry for homogeneous material (V_0 is the applied displacement), H=90 mm, W=70 mm, h=45 mm, a=33 mm, and $\phi=\pi/3$

of K_I, K_{II}, and T obtained in the FEA (Table 1) and various values of r_c. The results are again in good agreement with the experiments, with the MTS result being closest to the experimental one.

4.2 Graded Material. The loading geometry and elastic modulus distribution for the three FGM cases are shown in Fig. 1. In all three cases, Poisson's ratio ν was taken as constant at 0.45. The three FGMs have been designed such that the local mode mixity is generated by a host of different methods. In Case I, mode mixity is a result solely of material gradient orientation. In Case II, it is a result of both loading and material gradient asymmetry. Finally, in Case III, the crack is parallel to the material gradient and asymmetry is introduced only from a loading asymmetry.

The finite element simulation procedure for the FGM specimens is similar to that used for the homogeneous material. The loading applied in the simulations is again the displacement measured at crack initiation. The main difference is the allocation of varying elastic properties to the discretization shown in Fig. 1. One option is to assign material properties at Gauss quadrature points in each element [13,14]. A second option, employed in the present work, is to provide an elastic modulus variation by assuming temperature dependent modulus and providing the material with an initial temperature distribution to match the elastic modulus variation desired.

Results for the fracture parameters K_I, K_{II}, and T-stress, presented in Table 3, are obtained following the procedure used for the homogenous case, with the exception of μ_{tip} and ν_{tip} used in the least squares fitting process of Eq. (1). Crack initiation angles are also obtained by identifying the radial direction along which the tangential stress $\sigma_{\theta\theta}$ is maximum. Figure 5 shows the variation

Table 3 Experimental and numerical results for K_I, K_{II}, and T-stress for the FGM edge cracked specimens

	Case	K_I (MPa m$^{0.5}$)	K_{II} (MPa m$^{0.5}$)	T (MPa)	Biaxiality β
Expt. results	I	0.554	0.039	−4.272	−2.361
Num. results		0.551	−0.022	−2.149	
Expt. results	II	0.755	0.179	−0.069	−0.025
Num. results		0.722	0.204	−0.673	
Expt. results	III	0.969	0.224	−0.930	−0.262
Num. results		0.878	0.230	−0.870	

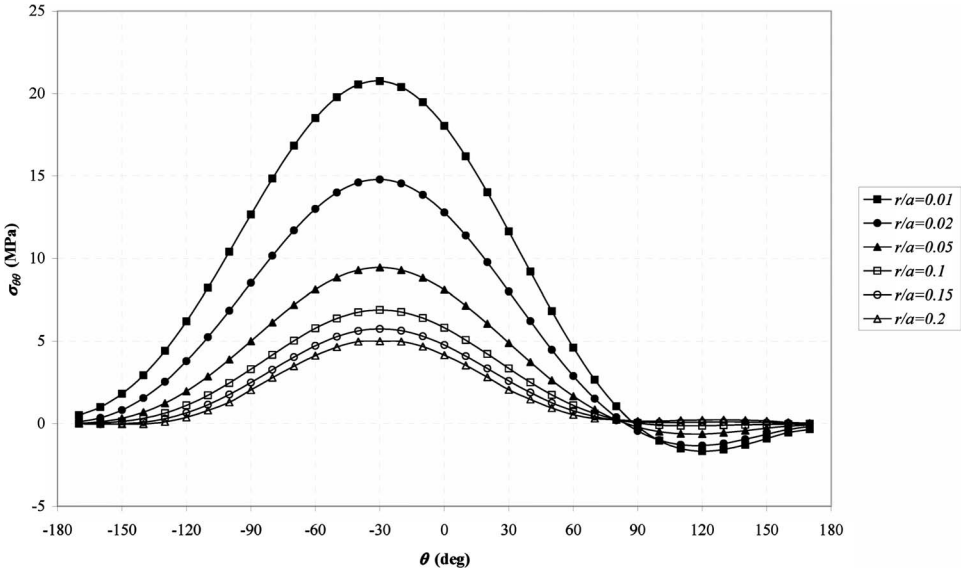

Fig. 5 Variation of $\sigma_{\theta\theta}$ with angle around the crack tip for specific radial directions obtained numerically for the FGM in Case II

Table 4 Experimental and numerical results for crack initiation angles for the FGM edge cracked specimens

	Crack initiation angles, α (deg)				
	Expt.	FE—using $(\sigma_{\theta\theta})_{max}$		Using GMTS, Eq. (4)	Using MTS, Eq. (4), $r_c=0$
Case I	0 ± 1.5	2.3 for $r/a=0.01$		3.1 for $r_c/a=0.01$	4.6
		2.0 for $r/a=0.02$		2.8 for $r_c/a=0.02$	
		1.2 for $r/a=0.05$		2.3 for $r_c/a=0.05$	
		0.5 for $r/a=0.1$		1.9 for $r_c/a=0.1$	
Case II	-28 ± 1.5	-31.3 for $r/a=0.01$		-26.0 for $r_c/a=0.01$	-27.8
		-30.7 for $r/a=0.02$		-25.3 for $r_c/a=0.02$	
		-30.1 for $r/a=0.05$		-24.0 for $r_c/a=0.05$	
		-29.8 for $r/a=0.1$		-22.6 for $r_c/a=0.1$	
Case III	-19 ± 1.5 (Crack growth size smaller than initial craze)	-30.2 for $r/a=0.01$		-24.4 for $r_c/a=0.01$	-26.3
		-29.7 for $r/a=0.02$		-23.7 for $r_c/a=0.02$	
		-29.3 for $r/a=0.05$		-22.4 for $r_c/a=0.05$	
	-26 ± 1.5 (Crack growth size larger than initial craze)	-29.3 for $r/a=0.1$		-21.0 for $r_c/a=0.1$	

of tangential stress with angle around the tip for different radial distances for the FGM of Case II. For the discretization used here, the maximum is clearly identifiable. As in the homogeneous case, there is a small radial dependence of the location of maximum $\sigma_{\theta\theta}$ away from the tip, likely a result of the relatively large T-stress present in this configuration. The experimentally measured and numerically predicted crack initiation angles are given in Table 4, along with the predictions of the MTS and GMTS models.

5 Discussion

In Tables 1 and 3, K_I, K_{II}, and T-stresses are computed from both the numerical and experimental results using a least squares fit to Eq. (1). In general, K_I, K_{II}, and T-stresses are in reasonably good agreement between experiments and numerical analysis, although there are some important deviations. As discussed earlier, T-stress is a difficult quantity to extract both numerically and experimentally. Therefore, the largest discrepancies appear there. The configurations used in the experimental study produce a large T-stress variation, which is also affected by the property gradient direction. The experimental values of T-stress obtained at crack initiation range from -4.272 MPa to -0.069 MPa depending on geometry and gradient, but are always negative.

All the results, especially the T-stress, are affected by the region where the least squares minimization is applied. Experimentally measured displacements are fitted to the asymptotic displacement equation by excluding a rectangular region around the crack tip where the digital image correlation cannot be performed. In the numerical case, however, data as close to the crack tip as is desired can be included in the fit—especially given the fact that the simulations are purely elastic whereas in the experiments failure occurs by crazing. We conducted a series of least square fits to the FEA data including points increasingly closer to the crack tip. The results in Table 3 are obtained when using the FEA displacement field down to the fifth ring of elements around the tip ($r/a=0.02$). A negative value of K_{II} is obtained in Case I, in contrast to the positive value measured experimentally. The value of K_{II} is relatively small in Case I, but the sign affects the direction of crack kinking. Although at initiation in the experiment the crack appears to grow straight, it does kink in a positive direction of about 7 deg $\pm$ 1.5 deg after about 2 mm of crack growth (see Fig. 2(a)). The *positive* value of K_{II} obtained experimentally incorrectly predicts a small *negative* kink angle [4]. The numerical results obtained here, when fitted to displacement data very near the crack tip, provide a *negative* K_{II}, which correctly predicts the *positive* sign of subsequent crack kinking. Care must therefore be taken in extracting fracture parameters solely from experiments, especially regarding the sign of K_{II} when it is small.

The GMTS criterion was used either directly form the FEA or through use of the asymptotic equation (4) to predict crack initiation angle, α. Except for Case III, predicted crack initiation angles are generally in good agreement with the experimentally measured ones. In Case III, -19 deg is quoted in Ref. [4] for kink angle. However, this value was obtained right after crack kinking, for extremely small crack kink length, as seen in Fig. 6. Although strictly speaking this is the appropriate scale to determine the kink angle, the crack extension in Fig. 6 is comparable to the craze length, and therefore is clearly not elastic. The details of the stress field associated with the mixed mode craze dominate the crack deflection in Fig. 6. It is therefore unreasonable to expect a good comparison with a purely elastic simulation. If one allows the crack to grow to a size much larger than the initial craze, as seen in Fig. 2(c), an angle of -26 deg is found for the kinking angle, which compares much better with elastic FEA results. This discrepancy between near- and far-field kink angles is not as prevalent in Cases I and II because in Case I the angles involved (and the value of K_{II}) are small, and in Case II right after the crack

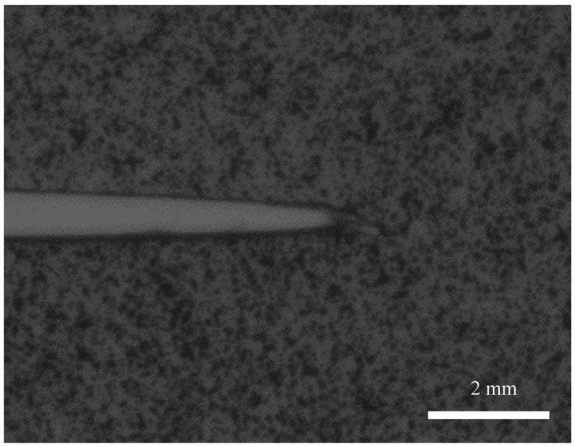

Fig. 6 Close-up photograph showing initial crack kinking for Case III FGM

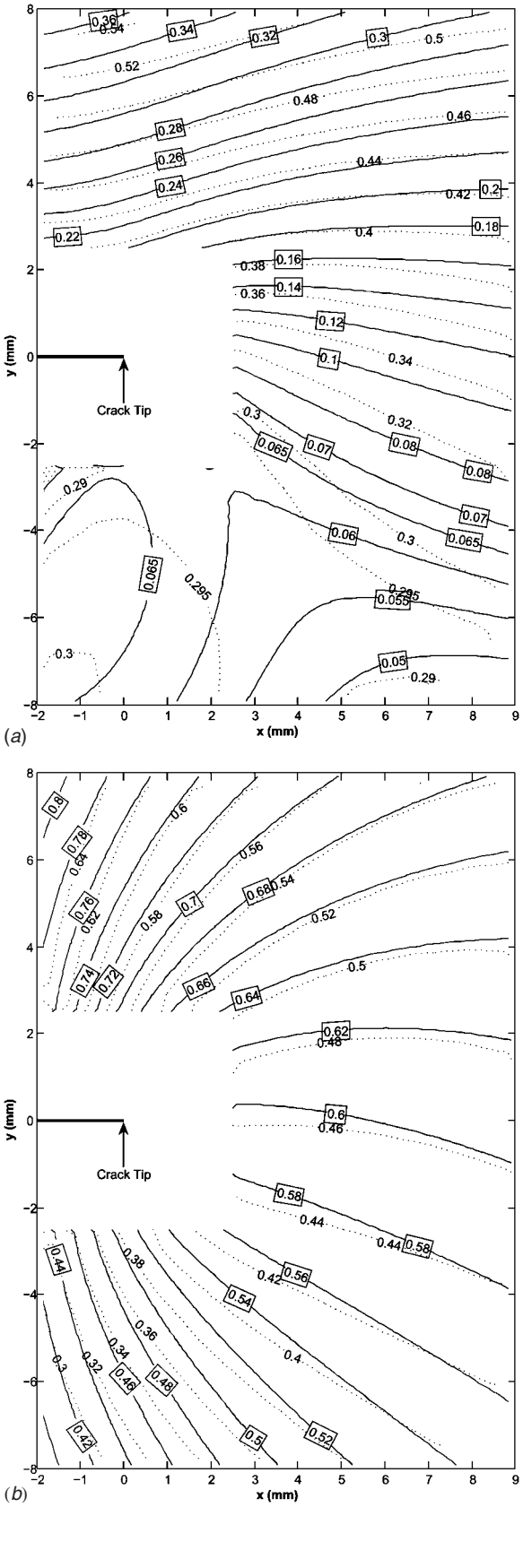

Fig. 7 Contours of (*a*) u_x and (*b*) u_y for Case III (solid lines and values in boxes are experimental results, and dashed lines, and values without boxes are numerical results)

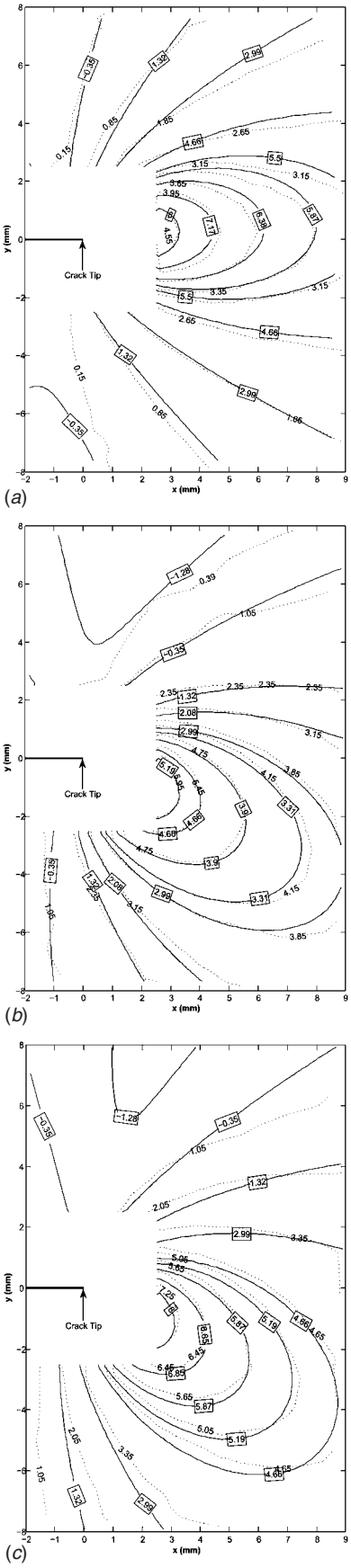

Fig. 8 Contours of $\sigma_{\theta\theta}$ for (*a*) Case I, (*b*) Case II, and (*c*) Case III (solid lines and values in boxes are experimental results, and dashed lines and values without boxes are numerical results)

kinks it becomes Mode I, by virtue of the geometry and material gradient. However, in Case III, continued mode mixity is seen at the crack tip as the crack grows.

The full-field nature of both the DIC experimental measurements and the FEA numerical results also allow for a comparison of displacement and stress fields around the crack tip. The two in-plane displacement components are the fundamental measurement made by DIC. Figure 7 shows contour plots comparing the experimentally measured and numerically predicted displacement field at the time of crack initiation for Case III. Although the values are somewhat different, especially for u_x, the fields are very similar. In the work of Abanto-Bueno and Lambros [4], stresses were also derived by using the DIC displacement measurements to calculate strain and then, knowing the local material properties, calculate stress by taking into account the material nonhomogeneity. Figure 8 shows a comparison of $\sigma_{\theta\theta}$ contours obtained numerically and experimentally for Cases I–III. The values of stress at the same contour level for Cases I and II differ substantially. Agreement is far better for Case III. The discrepancy is likely a result of the fact that stresses are not directly measured by DIC, but have to be calculated through a multistep process involving differentiation and interpolation by combining the displacement data and local material properties. As such, the stresses are particularly susceptible to property discretization errors, both on the FEA side and on the experimental side. However, the good agreement in Case III is encouraging. In addition, the shape of the contour lines in all three cases is very similar. As a result, the MTS direction, which predicts the crack initiation angle, is the same for each case.

6 Conclusions

Quasistatic crack initiation in FGMs subjected to mixed mode loading was studied in this work. The goal of the study was to directly compare as closely as possible experiments and simulations in order to evaluate the applicability of the GMTS criterion in predicting crack kinking in FGMs. The MTS criterion was seen to predict the kinking response in homogeneous polyethylene well. For the FGM case, fracture parameters of SIFs and *T*-stress were compared to experimental results and good agreement was obtained. However, it was found that to correctly predict the sign of K_{II} care needs to be taken in the process in which K_{II} is extracted when a least squares fitting approach is employed. This has significant implications for many optical experimental techniques used in fracture mechanics, which limit the amount of data accessible in the crack tip region. Using the GMTS criterion, either directly from the finite elements or from the fracture parameters extracted from FEA, provided reasonably good values for the experimentally measured kink angles for crack extensions larger than the craze length. Therefore, we can conclude that the MTS criterion is applicable to FGM crack initiation prediction if the inherent material gradient length scale is larger than the fracture process zone.

Acknowledgment

This study was supported by the National Science Foundation (NSF) through Grant No. NSF-INT-0322271. G.A. and A.O. acknowledge partial support of the State Planning Agency (DPT) through Grant No. DPT 01 K 120270.

References

[1] Erdogan, F., and Sih, G. C., 1963, "On the Crack Extension in Plates Under Plane Loading and Transverse Shear," ASME J. Basic Eng., **85**(4), pp. 519–525.
[2] Cotterell, B., 1965, "On the Brittle Fracture Paths," Int. J. Fract. Mech., **1**(2), pp. 96–103.
[3] Becker, T. L., Cannon, R. M., and Ritchie, R. O., 2001, "Finite Crack Kinking and T-Stresses in Functionally Graded Materials," Int. J. Solids Struct., **38**,(32–33), pp. 5545–5563.
[4] Abanto-Bueno, J., and Lambros, J., 2006, "An Experimental Study of Mixed Mode Crack Initiation and Growth in Functionally Graded Materials," Exp. Mech., **46**(2), pp. 179–196.
[5] Kim, J.-H., and Paulino, G. H., 2003, "T-Stress, Mixed-Mode Stress Intensity Factors, and Crack Initiation Angles in Functionally Graded Materials: A Unified Approach Using the Interaction Integral Method," Comput. Methods Appl. Mech. Eng., **112**(11–12), pp. 1463–1494.
[6] Rousseau, C.-E., and Tippur, H. V., 2000, "Compositionally Graded Materials With Cracks Normal to the Elastic Gradient," Acta Mater., **48**(16), pp. 4021–4033.
[7] He, M.-Y., and Hutchinson, J. W., 1989, "Kinking of a Crack Out of an Interface," ASME J. Appl. Mech., **56**, pp. 270–278.
[8] Peters, W. H., and Ranson, W. F., 1982, "Digital Imaging Techniques in Experimental Stress Analysis," Opt. Eng. (Bellingham), **21**(3), pp. 427–431.
[9] MSC.MARC®, User Documentation, version 2005r3, MSC.Software Corporation, 2 MacArthur Place, Santa Ana, CA 92707.
[10] Ayatollahi, M. R., Pavier, M. J., and Smith, D. J., 1998, "Determination of *T*-Stress From Finite Element Analysis for Mode I and Mixed Mode I/II Loading," Int. J. Fract., **91**(3), pp. 283–298.
[11] Williams, J. G., and Ewing, P. D., 1972, "Fracture Under Complex Stress—Angled Crack Problem," Int. J. Fract., **8**(4), pp. 441–446.
[12] Chen, C. S., Wawrzynek, P. A., and Ingraffea, A. R., 1999, "Crack Growth Simulation and Residual Strength Prediction in Airplane Fuselages," NASA/CR-1999-209115.
[13] Santare, M. H., and Lambros, J., 2000, "Use of Graded Finite Elements to Model the Behavior of Nonhomogeneous Materials," ASME J. Appl. Mech., **67**(4), pp. 819–822.
[14] Kim, J.-H., and Paulino, G. H., 2002, "Isoparametric Graded Finite Elements for Nonhomogeneous Isotropic and Orthotropic Materials," ASME J. Appl. Mech., **69**(4), pp. 502–514.

On the Singularities in Fracture and Contact Mechanics

Fazil Erdogan

Murat Ozturk

Department of Mechanical Engineering and Mechanics,
Lehigh University,
Bethlehem, PA 18015

Generally, the mixed boundary value problems in fracture and contact mechanics may be formulated in terms of integral equations. Through a careful asymptotic analysis of the kernels and by separating nonintegrable singular parts, the unique features of the unknown functions can then be recovered. In mechanics and potential theory, a characteristic feature of these singular kernels is the Cauchy singularity. In the absence of other nonintegrable kernels, Cauchy kernel would give a square-root or conventional singularity. On the other hand, if the kernels contain, in addition to a Cauchy singularity, other nonintegrable singular terms, the application of the complex function theory would show that the solution has a non-square-root or unconventional singularity. In this article, some typical examples from crack and contact mechanics demonstrating unique applications of such integral equations will be described. After some remarks on three-dimensional singularities, the key examples considered will include the generalized Cauchy kernels, membrane and sliding contact mechanics, coupled crack-contact problems, and crack and contact problems in graded materials. [DOI: 10.1115/1.2936241]

1 Introduction

Many of the problems in fracture and contact mechanics may be formulated as mixed boundary value problems which, in turn, may be reduced to integral equations of the general form [1–5]

$$A(x)\phi(x) + \int_a^b \left[\frac{B(x,t)}{t-x} + k_s(x,t) + k_f(x,t) \right] \phi(t)dt = f(x), \quad a < x < b \tag{1}$$

where $\phi(x)$ is the unknown function and $f(x)$ is the free term or the input function. The known functions $A(x)$, $B(x,t)$, $k_s(x,t)$ and $k_f(x,t)$ define the physical problem. The limits a and b are known finite constants. $k_f(x,t)$ is continuous in $a \leqslant (x,t) \leqslant b$ or discontinuous in such a way that the double integral $\int_a^b \int_a^b |k_f^2(x,t)| dxdt$ is finite (e.g., $k_f(x,t) = \log|x-t|$). $k_f(x,t)$ is then called a *Fredholm* kernel [6]. If $B(x,t)$ is a differentiable function of x and t, $B(x,t)/(t-x)$ is said to be a *Cauchy* kernel. With $k_s(x,t) = 0$, for any combination of $A(x)$, $B(x,t)$, and $k_f(x,t)$, the treatment of Eq. (1) is rather straightforward. In this study, however, our main interest is in $k_s(x,t)$.

The advantage of formulating the fracture and contact problems in mechanics of materials and generally the mixed boundary value problems in potential theory in terms of integral equations is that by examining asymptotic behavior of the kernels, by separating their singular parts, and by using the complex function theory, it is possible to determine the exact nature of the singularity and the correct form of the asymptotic distribution of the unknown functions at and near the singular points. This procedure also leads to determination of the fundamental function of the problem or the weight function of the unknown $\phi(x)$. Thus, by using the properties of the associated orthogonal polynomials, it is possible to develop highly effective methods to solve the main problem and, in particular, to determine directly such physically important quantities as stress (or flux) intensity factors, strain energy release rates, and crack opening displacements.

In examining the possible contribution of $k_s(x,t)$ to the nature of the singularities of $\phi(x)$ at $x=a$ and $x=b$, one may note that (a) $k_s(x,t)$ must be singular at one or both end points, (b) the singularity must not be as strong as the Cauchy singularity so that it cannot be lumped with the Cauchy kernel $B(x,t)/(t-x)$, (c) it must not be weak enough to be square integrable so that it cannot be lumped with the Fredholm kernel $k_f(x,t)$, and (d) the singularity of $k_s(x,t)$ must be strong enough to contribute to the singular behavior of the unknown function $\phi(x)$. As typical examples for sufficiently strong dominant terms in $k_s(x,t)$ one may mention $k_s(x,t) = A_1(t)\delta(x-t)$ which is not square integrable where $A_1(t)$ is continuous in the interval $[a,b]$ and adds to $A(x)$ if $A(x) \neq 0$ or changes the integral equation from first kind to the second kind if $A(x) = 0$, thereby changing the singular nature of $\phi(x)$ drastically. As a second example we mention $k_s(x,t) = 1/(x+t)$. Thus, for $a > 0$, k_s behaves as a Fredholm kernel; and for $a = 0$, k_s becomes unbounded (as $1/t$); for $x = 0$ and $t \to 0$ and changes the power of the singularity of the unknown function $\phi(x)$ (see Sec. 3 of this article.)

It may easily be shown that if the dominant kernel of the integral equation (1) has only a Cauchy kernel (that is, if $A(x) = 0$ and $k_s = 0$), the function $\phi(x)$ would have a conventional or square-root singularity. On the other hand, if $k_s(x,t) \neq 0$ then $\phi(x)$ would have an unconventional or non-square-root singularity. Generally, the problems with unconventional singularities are mathematically difficult to analyze and physically difficult to interpret. In this article, after making some remarks on three-dimensional crack problems, a number of key examples in fracture and contact mechanics with non-square-root singularities are considered. It is shown that the common feature of these mixed boundary value problems is certain types of singular kernels in addition to the standard Cauchy singularity. The main interest in this article is in studying the influence of such nonintegrable singular kernels $k_s(x,t)$ on the singularities of the related weight functions and, consequently, of the solution. Note that the integral equation given by Eq. (1) may be generalized to system of equations replacing the functions $A(x)$, $B(x,t)$, $k_f(x,t)f(x)$, and $\phi(x)$ by appropriate (square and column) matrices [4,7]. It should also be pointed out that one of the important techniques for solving the mixed boundary value problems in mechanics is the boundary integral equations (BIEs). However, up to now, the applications of BIEs have been restricted to problems with standard square-root singularities. For some applications and extensive references, see Refs. [8,9].

Contributed by the Applied Mechanics Division of ASME for publication in the JOURNAL OF APPLIED MECHANICS. Manuscript received August 31, 2007; final manuscript received January 10, 2008; published online July 11, 2008. Review conducted by Marek-Jerzy Pindera.

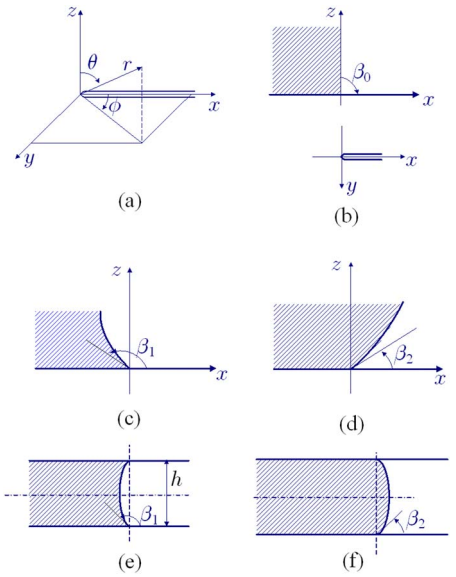

Fig. 1 (***a***) **and** (***b***) **the initial crack geometry,** (***c***) **the qualitative crack geometry after some subcritical crack growth under Mode I conditions,** (***d***) **the qualitative crack geometry after some subcritical crack growth under Mode II/Mode III dominated loading conditions,** (***e***) **thumbnail, and** (***f***) **reverse thumbnail crack fronts in a plate with constant thickness**

2 Some Remarks on Three-Dimensional Singularities

The integral equations given by Eq. (1) generally describe two-dimensional mixed boundary value problems in mechanics. However, largely due to the effect of the geometry of the medium, free surfaces or other constraints and the material properties, in most cases these-problems are seldom two dimensional. There are only a few "exact" solutions of the three-dimensional crack and stamp problems (see Refs. [10,11] for survey). The existing exact solutions are primarily based on and take advantage of the symmetry in loading, and crack and stamp geometry. The following may be mentioned as some examples: planar circular cracks under uniform tension [12,13], under arbitrary loading [10,14], and planar elliptic cracks under uniform tension [15] and uniform shear [10]. From the standpoint of non-square-root singularities considered in this article, such problems with planar smooth boundaries are not very interesting. Three-dimensional singularity problems being somewhat more interesting have been the studies by Keer and Parihar on the planar wedge-shaped crack, stamp, and inclusion problems [16,17].

Among the three-dimensional singularity problems that have been studied in the past few decades, perhaps the most important one has been a plane crack intersecting a stress-free plane boundary [18–20]. The problem is of quite considerable practical interest since many of the crack propagation problems such as surface and through cracks locally involve this basic crack geometry. The problem has also a wide range of applications and is theoretically difficult to investigate. The crack problem considered by Benthem is shown in Fig. 1 [18,19]. The problem is formulated in spherical coordinates r, θ, ϕ as follows:

$$x = r \sin\theta \cos\phi, \quad y = r \sin\theta \sin\phi, \quad z = r \cos\phi \tag{2}$$

in the half space $z>0$ and the crack occupies the quarter plane $y=0, x>0, z>0$. The boundary $z=0$ and the crack surfaces are traction-free. The solution is sought in the form

$$\sigma_{ij} = r^{\lambda} f_{ij}(\lambda, \theta, \phi), \quad (i,j) = (x,y,z) \tag{3}$$

The boundedness of the strain energy in a finite region near $r=0$ requires that the acceptable roots of the transcendental equation for λ are $\lambda > -\frac{3}{2}$. Introducing Bousinesq's basic solution of Papkovich–Neuber equations and by using a separation of variable technique, Benthem reduced the problem to an eigenvalue problem and determined the leading acceptable eigenvalues (i.e., $-1<\lambda<0$) as a function of the Poisson's ratio ν. Technically the problem is one of a system of infinite number of equations ("degrees of freedom"), which is solved and the convergence of the solution is verified by using a technique similar to the method of reduction [21].

Table 1 Singularities for Mode I and Modes II and III loading conditions for a crack intersecting a stress-free plane boundary perpendicularly as functions of Poisson's ratio ν

ν	Mode I	Modes II and III
0.0	−0.5	−0.5
0.15	−0.4836	−0.5668
0.3	−0.4523	−0.6073
0.4	−0.4132	−0.6286
0.5	−0.3318	−0.6462

In a subsequent article [19], Benthem used a method of finite differences to verify the Mode I results obtained in Ref. [18] and to determine the results for Modes II and III loading conditions. Table 1 shows the leading acceptable eigenvalues (i.e., the singularities) for Mode I and Modes II and III as a function of Poisson's ratio ν. In the elasticity solution of the three-dimensional crack problems, even though Mode I is separable, Modes II and III are always coupled. Consequently, for the same crack geometry, the Mode I singularity can be different from that of Modes II and III, but singularities for Modes II and III must be the same. Furthermore, even though Mode I singularity is a monotonically decreasing function of ν, the coupled singularity of Modes II and III is an increasing function of ν.

The crack problem shown in Fig. 1 and studied by Benthem [18,19] was also considered by Bazant and Estenssoro [20]. In Ref. [20], a variational principle was used to formulate the problem, which was then reduced to a nonlinear eigenvalue problem in λ by applying a finite element method. The numerical results seem to agree with that found in Refs. [18,19] and given in Table 1. The solution was extended to cracks whose plane is no longer perpendicular to the y-axis (the angle γ in Ref. [20]) and the angle of intersection of which with the stress-free surface $z=0$ is no longer 90 deg (the angle β in Ref. [20].) These angles of inclination of the crack plane (γ) and the front edge (β) were calculated by using an energy flux argument. The importance of this study lies in the fact that it provides us with the tool needed to describe and quantitatively monitor the subcritical crack growth process. First, it should be made clear that in homogeneous, isotropic materials physically there is no such thing as pure Mode II or Mode III crack growth. The solutions given by Refs. [18–20] are best suitable to study the Mode I fracture. Thus, initially, it may be assumed that the crack inclination angle γ and the crack front inclination angle β are $\pi/2$ (Figs. 1(*a*) and 1(*b*)).

Then, the medium is subjected to subcritical constant amplitude Mode I loading (Fig. 1(*c*)). Since the crack growth rate at the surface ($z=0$) is trailing that of in the interior and since the stress intensity factor at the corner $z=x=0$ increases with increasing angle β_1, the crack growth rate at the surface $z=0$ increases and some kind of equilibrium is reached resulting in the conventional thumbnail crack front often observed experimentally (Fig. 1(*e*)). If it were physically possible to grow the crack subcritically in a self-similar manner under Mode II/III loading, one would observe the reverse thumbnail crack front shown in Fig. 1(*f*) (see Ref. [22] for some additional qualitative remarks). Note that in Figs. 1(*e*) and 1(*f*) the crack grows from right to left.

More complicated crack and contact problems involve layered materials, corner singularities, graded coatings, surface cracks, nonlinear materials, dynamic loading, thermal stresses, etc. The

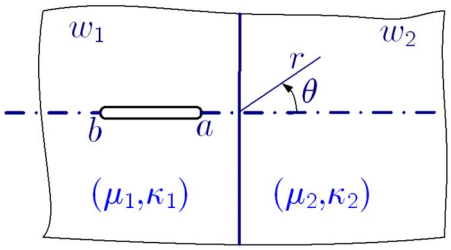

Fig. 2 Crack perpendicular to a bimaterial interface

mathematics to treat these problems has not yet been developed. Consequently, few solutions that exist are obtained by using mostly the finite element methods. Aside from the important application given in Ref. [20], the application of enriched finite elements to solve three-dimensional crack problems appears to be quite promising [23–25]. (See also Ref. [26] for the application of enriched quarter point elements in conjunction with BIEs to two-dimensional crack problems.)

3 Generalized Cauchy Kernels

In an article titled "On a Class of Singular Integral Equations" published in 1966, Bueckner introduced the following integral equation [27]:

$$\frac{1}{\pi}\int_0^1 \frac{v(t)dt}{t-x} + \sum_{k=1}^{n} a_k \int_0^1 \frac{t^{k-1}v(t)dt}{(t+x)^k} = g(x), \quad 0<x<1 \tag{4}$$

where $a_1, a_2, \cdot, a_n$ are real valued constant coefficients and $v(x)$ and $g(x)$ are real valued functions. Note that Eq. (4) is a special case of Eq. (1) with $A(x)=0, k_f(x,t)=0, a=0$ and $b=1$. The remaining kernels $k_s(x,t)$ become unbounded as $t\to 0$ for $x=0$ and, hence, together with $(t-x)^{-1}$ constitute a *generalized Cauchy kernel*. Bueckner further remarked that for $a_2=a_3=\cdots=a_n=0$, Eq. (4) is the well known airfoil equation and for $n=3$ it appears in connection with a boundary value problem in elasticity. He then proceeded to state that in this first part he will deal with the case of $n=1$, namely,

$$\frac{1}{\pi}\int_0^1 \frac{v(t)dt}{t-x} + \frac{\gamma}{\pi}\int_0^1 \frac{v(t)dt}{t+x} = g(x), \quad 0<x<1 \tag{5}$$

Even though Bueckner did not relate his investigation to any problem in mechanics, it is well known from potential theory, materials science, and elasticity that the integral equation as stated by Eq. (5) has many applications in the study of cracks and flux barriers intersecting bimaterial interfaces.

Referring to Fig. 2, in the terminology of antiplane shear problem in elasticity, the problem may be expressed as [28]

$$\frac{1}{\pi}\int_a^b \left(\frac{1}{t-r} + \frac{\lambda}{t+r}\right) f(t)dt = \frac{2}{\mu_1} q(r), \quad a<r<b \tag{6}$$

$$\lambda = \frac{\mu_1 - \mu_2}{\mu_1 + \mu_2} \tag{7}$$

$$f(r) = \frac{\partial}{\partial r}[w_1(r,\pi+0) - w_1(r,\pi-0)] = -2\frac{\partial}{\partial r} w_1(r,\pi-0) \tag{8}$$

$$\int_a^b f(t)dt = 0 \tag{9}$$

$$q(r) = \sigma_{1\theta z}(r,\pi) \tag{10}$$

where μ_1 and μ_2 are the shear moduli of Materials 1 and 2, respectively, w_1 and w_2 are the z-components of the displacements, and $q(r)$ is the loading. For $a>0$, $\lambda/(t+x)$ is bounded and by normalizing the interval (a,b) and the unknown function $f(t)$ as

$$t = \frac{b-a}{2}s + \frac{b+a}{2}, \quad f(t) = F(s), \quad a<t<b, \quad -1<s<1 \tag{11}$$

and by observing that the fundamental function of the integral equation is $(1-s^2)^{-1/2}$ and the associated orthogonal polynomial is the Chebyshev polynomial $T_n(s)$, the solution may be obtained as follows:

$$F(s) = (1-s^2)^{-1/2}\sum_{n=0}^{\infty} A_n T_n(s) \tag{12}$$

For a given $q(r)$, by using the properties of $T_n(s)$ Eq. (12) may be reduced to a linear infinite system of algebraic equations, and $F(s)$ can then be obtained by using the method of reduction [21].

For the more interesting case of $a=0, t=(b/2)(1+s), f(t)=F(s)$, the fundamental function of the integral equation is found to be $(1-s)^{-\alpha}(1+s)^{-\beta}$, and by using the function theoretic method (see the Appendix), the characteristic equations are obtained as

$$\cot(\pi\alpha) = 0, \quad \alpha = \tfrac{1}{2} \tag{13}$$

$$\cos(\pi\beta) + \lambda = 0 \tag{14}$$

The orthogonal polynomial associated with the weight function $(1-s)^{-1/2}(1+s)^{-\beta}$ is the Jacobi polynomial $P_n^{(-1/2,-\beta)}(s)$ and the solution of Eq. (6) may be expressed as

$$F(s) = (1-s)^{-1/2}(1-s)^{-\beta}\sum_{n=0}^{\infty} B_n P_n^{(-1/2,-\beta)}(s) \tag{15}$$

The unknown coefficients $B_n, (n=0,1,\ldots)$ are then obtained by using the properties of the Jacobi polynomials [5]. For uniform loading $q(r)=q_0$, Bueckner obtained the closed form solution of Eq. (6) as follows:

$$\psi(u) = \frac{q_0}{\mu_1}\frac{1}{\sin(\pi\beta/2)}\left[\left(\frac{u}{1+\sqrt{1-u^2}}\right)^{\beta}\left(\frac{\beta}{\sqrt{1-u^2}}+1\right) + \left(\frac{u}{1+\sqrt{1-u^2}}\right)^{-\beta}\left(\frac{\beta}{\sqrt{1-u^2}}-1\right)\right], \quad \psi(u) = f(r), \quad u = r/b \tag{16}$$

Going now back to the more general integral equation (4) introduced by Bueckner, it can be shown that for $n=3$ Eq. (4) indeed corresponds to the formulation of the plane strain crack problem shown in Fig. 2. By using polar coordinates and Mellin transform, the mixed boundary value problem described in Fig. 2 may be expressed as follows [29,30]:

$$\frac{1+\kappa_1}{2\mu_1}p(r) = \frac{1}{\pi}\int_a^b \frac{f(t)dt}{t-r} + \frac{1}{\pi}\int_a^b k_s(r,t)f(t)dt, \quad a<r<b \tag{17}$$

where μ_1 and κ_1, are the elastic constants of the half plane 1,

$$f(r) = -2\frac{\partial}{\partial r}u_{1\theta}(r,\pi-0), \quad a<r<b \tag{18}$$

$$p(r) = -\sigma_{1\theta\theta}(r,\pi-0), \quad a<r<b \tag{19}$$

and the singular kernel k_s is given by

$$k_s(r,t) = \frac{1}{2(1+m\kappa_1)(m+\kappa_2)}\left\{\frac{A}{t+r} + B\left[\frac{12r}{(t+r)^2} - \frac{8r^2}{(t+r)^3}\right]\right\} \tag{20}$$

$$A = (1 + m\kappa_1)(m + \kappa_2) - m(1 + \kappa_1)(1 + m\kappa_1) - 3(1 - m)(m + \kappa_2)$$

$$B = (1 - m)(m + \kappa_2)$$

$$m = \frac{\mu_2}{\mu_1} \tag{21}$$

For $a > 0$, $k_s(r,t)$ is bounded and the solution of Eq. (17) may be obtained in a straightforward manner (see Eqs. (6) and (12)). However, for $a=0$, $k_s(r,t)$ becomes unbounded at the end point $r=0$ and contributes to the singular behavior of the solution. Again, by expressing the solution of Eq. (17) in the form

$$f(t) = \frac{g(t)}{t^{\omega}(b-t)^{\eta}} \tag{22}$$

and by using the function-theoretic method (see the Appendix), the characteristic equations to determine the singularities ω and η may be obtained as follows:

$$\cot(\pi\eta) = 0, \quad \eta = \tfrac{1}{2} \tag{23}$$

$$2\alpha\cos[\pi(1-\omega)] - \beta(1-\omega)^2 - \gamma = 0 \tag{24}$$

where real valued coefficients α, β, and γ are given in terms of the elastic constants $m=\mu_2/\mu_1$, κ_1, and κ_2 [29,30] and may also be expressed in terms of Dundurs' coefficients. The solution of Eq. (17) is obtained by introducing the following normalized quantities:

$$r = \frac{b}{2}(v+1), \quad t = \frac{b}{2}(u+1), \quad f(t) = F(u), \quad g(t) = G(u)$$

$$\frac{1+\kappa_1}{2\mu_1}p(r) = P(v), \quad k_s(r,t) = K(v,u) \tag{25}$$

and by expressing the unknown function $F(u)$ as

$$F(u) = (1-u)^{-\eta}(1+u)^{-\omega}\sum_{n=0}^{\infty} C_n P_n^{(-\eta,-\omega)}(u) \tag{26}$$

where C_0, C_1,... are unknown coefficients which are determined using the orthogonality properties of Jacobi polynomials $P_n^{(-\eta,-\omega)}(u)$.

The characteristic equation (24) would show that if $\mu_1 > \mu_2$ the singularity ω is greater than 1/2 and if $\mu_1 < \mu_2$ ω is less than 1/2 (Fig. 2). An important special case of the problem described in Fig. 2 is the edge crack problem for a semi-infinite medium, which is often used as a benchmark for surface crack solutions. The problem is formulated by substituting $m=0$ in Eq. (20) giving

$$k_s(r,t) = -\frac{1}{t+r} + \frac{6r}{(t+r)^2} - \frac{4r^2}{(t+r)^3} \tag{27}$$

By using the function-theoretic method from Eqs. (17), (22), and (27), it may be shown that

$$\eta = \tfrac{1}{2}, \quad \omega = 0 \tag{28}$$

and the solution may be expressed as

$$F(u) = (1-u)^{-1/2}\sum_{n=0}^{\infty} C_n P_n^{(-\eta,0)}(u) \tag{29}$$

At the crack tip $r=b$, the Mode I stress intensity factor $k_1(b)$ is defined by and calculated from

$$k_1(b) = \lim_{r\to b}\sqrt{2(r-b)}\sigma_{1\theta\theta}(r,\pi) = -\frac{2\mu_1}{1+\kappa_1}\lim_{r\to b}\sqrt{2(b-r)}f(r) \tag{30}$$

For a uniform crack surface pressure p_0, Table 2 shows the Mode I stress intensity factor normalized with respect to $p_0\sqrt{b}$ [31]. The results given in Table 2 are obtained by truncating the infinite series (29) at $n=N$.

Table 2 Normalized Mode I stress intensity factor for an edge crack in a half plane under uniform tension p_0

N	$k_1(b)/p_0\sqrt{b}$
10	1.121518230454
15	1.121522319145
20	1.121522334904
25	1.121522287226
30	1.121522267425
35	1.121522259954
45	1.121522255943

The solution of the edge crack problem was also given by Koiter in closed form [32,11] in terms of an infinite integral as follows:

$$\frac{k_1(b)}{p_0\sqrt{b}} = \frac{\sqrt{2(B+1)}}{A\sqrt{\pi}} \tag{31}$$

where B is an arbitrary constant greater than 1, the result is independent of the choice of B, and A is given by

$$\log A = -\frac{1}{\pi}\int_0^{\infty}\frac{1}{1+\alpha^2}\log\left(\frac{\alpha\sin(\pi\alpha)}{\sqrt{B^2+\alpha^2}[\cosh(\pi\alpha) - 2\alpha^2 - 1]}\right)d\alpha \tag{32}$$

The numerical results show that [9]

$$\frac{k_1(b)}{p_0\sqrt{b}} = 1.121\,522\,26 \tag{33}$$

where there may be an error only in the last digit. Table 2 indicates that in an example with only one length parameter b, which is normalized out, the accuracy of the method and convergence are extremely good.

4 On the Singularities in Contact Mechanics

Generally, the contact problems in mechanics can be studied in two broad categories. In both cases, the substrate is a two-dimensional continuum, which may consist of single or multiple layers. In the first group of problems (also known as cover plates, thin films, reinforcements, and stiffeners), the thickness of the contacting medium is very small in comparison with its in-plane dimensions. Consequently, it may be approximated by a "membrane" or a "plate" [31] and the contact condition is usually perfect adhesion or bonding through a shear layer. In the membrane case, the normal component of the contact stress is assumed to be negligible. The second group of contact problems is known as "stamp" or "punch" problems in which the contacting medium may be a rigid or elastic solid with known profile. In this case, too, the problem is simplified by assuming the contact to be either frictionless (i.e., with zero interface shear) or with constant friction (i.e., the sliding contact.) In this section, we will describe some sample problems in contact mechanics with unconventional singularities.

4.1 Membrane Stiffener With Variable Thickness. Dielectric or metallic thin film overlays on elastic substrates are known to involve severe stress concentrations, which may lead to cracking of the film and the substrate, debonding of the film, generation or pileup of dislocations, and the motion of interstitials in the substrates. In microelectronics the thicknesses of the films and the substrate are generally of the order of microns and millimeters, respectively. Thus, from the standpoint of studying the stress concentrations near the film edges assuming the film to be a membrane and the substrate to be a semi-infinite elastic continuum is

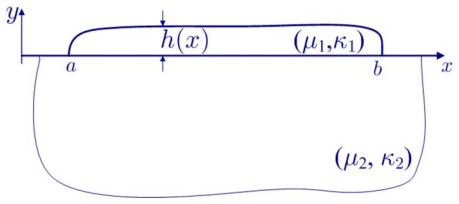

Fig. 3 Contact problem for a membrane stiffener with variable thickness

fairly realistic.

The related contact problem under consideration is described in Fig. 3. Let the contacting medium be a stiffener with variable thickness $h(x)$ and elastic constants μ_1 and κ_1. The substrate is assumed to be a semi-infinite solid with elastic constants μ_2 and κ_2. The problem is one of plane elasticity.

From the equilibrium of the stiffener, we obtain

$$\int_a^x \phi(t)dt = h(x)\sigma_{1xx} = \frac{8\mu_1}{1+\kappa_1}\frac{\partial u_1(x,0)}{\partial x} \tag{34}$$

where $\phi(t)=\sigma_{2xy}(t,0)$, $a<t<b$, is the interface shear stress. Similarly, by observing that $\sigma_{2yy}(x,0)=0$, $-\infty<x<\infty$, from the elasticity solution for the half plane (Medium 2) it may be shown that

$$\frac{\partial u_2(x,0)}{\partial x} = \frac{1+\kappa_2}{4\mu_2}\frac{1}{\pi}\int_a^b \frac{\phi(t)}{t-x}dt + p(x), \quad a<x<b \tag{35}$$

where $p(x)$ is the sum of all external loads (as expressed by ε_{2xx}) acting on the substrate such as uniform strain ε_0 in x-direction, thermal strain $\alpha_2 T$, and other local applied loads. From the strain compatibility $\varepsilon_{1xx}(x,0)=\varepsilon_{2xx}(x,0)$ at $y=0$, it now follows that

$$\frac{1}{\pi}\int_a^b \frac{\phi(t)}{t-x}dt - \frac{\lambda}{h(x)}\int_a^x \phi(t)dt = -\frac{4\mu_2}{1+\kappa_2}p(x), \quad a<x<b \tag{36}$$

$$\lambda = \frac{\mu_2(1+\kappa_1)}{2\mu_1(1+\kappa_2)} \tag{37}$$

$$\int_a^b \phi(t)dt = 0 \tag{38}$$

From Eq. (36), it is clear that for $h(x)=h_0=$const. the equation is an ordinary singular integral equation with a simple Cauchy kernel and may be treated in a straightforward manner. It is, however, the behavior of $h(x)$ near the end points that may influence the singularity of the unknown function $\phi(x)$. To examine the question, let us assume that near the end point $x=a$ $h(x)$ has the following behavior:

$$h(x) = A(x-a)^\gamma, \quad \gamma \geq 0 \tag{39}$$

where A is a positive real constant. The sketch given in Fig. 4 shows the behavior of $h(x)$ for various values of γ. These four thickness profiles show nearly all physically possible cases. Thus,

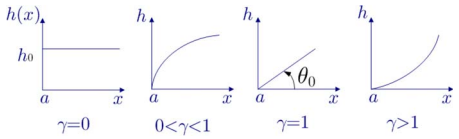

Fig. 4 The sketch of end point behavior of the stiffener with thickness $h(x)=A(x-a)^\gamma$

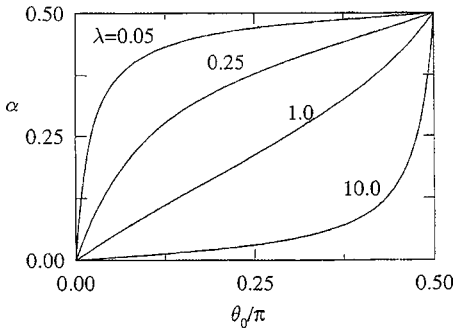

Fig. 5 Variation of the singularity α with the system parameters λ and θ_0 (see Eq. (44))

we may now proceed with the singularity analysis. Expressing the unknown function $\phi(x)$ as

$$\phi(x) = \frac{g(x)}{(x-a)^\alpha(b-x)^\beta}, \quad 0<\Re(\alpha,\beta)<1 \tag{40}$$

and referring to the Appendix, from Eq. (36) it follows that

$$\frac{g(a)}{(b-a)^\beta}\frac{\cot(\pi\alpha)}{(x-a)^\alpha} + G_1(x) - \frac{g(a)}{(b-a)^\beta}\frac{\lambda}{A(1-\alpha)}\frac{(x-a)^{1-\gamma}}{(x-a)^\alpha} = -\frac{4\mu_2}{1+\kappa_2}p(x) \tag{41}$$

where near and at $x=a$ $G_1(x)$ is a bounded function. Multiplying both sides of Eq. (41) by $(x-a)^\alpha$ and letting $x\to a$ for $0\leq\gamma<1$ Eq. (41) would reduce to

$$\cot(\pi\alpha) = 0, \quad \alpha = \tfrac{1}{2} \tag{42}$$

Similarly, for $\gamma>1$, from Eq. (41) we obtain

$$\cot(\pi\alpha) = \infty, \quad \alpha = 0 \tag{43}$$

Finally, for $\gamma=1$ (see Fig. 4), we observe that since $A=h'(a)=\tan\theta_0$, Eq. (41) becomes

$$\cot(\pi\alpha) - \frac{\lambda}{1-\alpha}\cot\theta_0 = 0, \quad 0<\alpha<\frac{1}{2} \tag{44}$$

Note that λ is the stiffness ratio ($\approx\mu_2/\mu_1$), for $\mu_1\to\infty$, $\alpha\to 1/2$ and for $\mu_2\to\infty$, $\alpha\to 0$. Similar analysis gives the singularity β at the end point b. Referring to Eq. (40), the solution is obtained, after some normalizations, by expanding the bounded unknown $g(x)$ into a series of orthogonal polynomials $P_n^{(-\beta,-\alpha)}(x)$. Figure 5 shows the variation of the singularity α at $x=a$ with the two system parameters λ and θ_0 (see Eq. (44)).

4.2 Some Simple Examples for Sliding Contact. Consider an elastic medium $y<0$, $-\infty<x<\infty$ with the elastic constants μ and κ, acted upon by a rigid flat stamp $-a<x<a$, $y=0$. Let the applied load be the stamp displacement $v(x,0)=-v_0$. The stamp is pressed to the elastic medium by a pair of resultant forces $P_y=-P$, $P_x=-Q$, $Q=\eta P$ where η is the coefficient of friction. The primary unknown function is the contact pressure $p(x)=-\sigma_{yy}(x,0)$. The problem is formulated in terms of a singular integral equation of the second kind and the solution is obtained as follows [33]:

$$\frac{p(x)}{P/2a} = \frac{2\sin(\pi\alpha)}{\pi}(1-x/a)^\alpha(1+x/a)^\beta \tag{45}$$

$$\frac{\sigma_{xx}(x,0)}{P/2a} = \frac{2\sin(\pi\alpha)}{\pi}\begin{cases}(1-x/a)^{\alpha}(1+x/a)^{\beta}+\dfrac{2\eta}{\pi}L(x), & -a<x<a\\ \dfrac{2\eta}{\pi}L(x), & |x|>a\end{cases} \tag{46}$$

$$L(x)=\frac{\pi}{\sin(\pi\alpha)}\begin{cases}(1-x/a)^{\alpha}(1+x/a)^{\beta}, & -\infty<x<-a\\ (1-x/a)^{\alpha}(1+x/a)^{\beta}\cos(\pi\alpha), & -a<x<a\\ (x/a-1)^{\alpha}(1+x/a)^{\beta}, & a<x<\infty\end{cases} \tag{47}$$

$$\alpha=-1+\theta/\pi,\quad \beta=-\theta/\pi,\quad \theta=\arctan\left|\frac{\kappa+1}{\eta(\kappa-1)}\right| \tag{48}$$

$$\sigma_{xy}(x,0)=\eta\sigma_{yy}(x,0),\quad \sigma_{yy}(x,0)=-p(x) \tag{49}$$

Similarly, if we consider a rigid wedge-shaped stamp $x=0$, $y=mx$, the stamp displacement $v(x,0)=-v_0+mx$ and the resultant force $P_y=-P$ and $P_x=-Q$, $Q=\eta P$ acting on the stamp, the closed form solution of the contact problem may be obtained as follows [33]:

$$\frac{p(x)}{m\mu}=\frac{4}{1+\kappa}\sin(\pi\alpha)\left(\frac{b-x}{x}\right)^{\alpha} \tag{50}$$

$$\frac{\sigma_{xx}(x,0)}{m\mu}=-\frac{4\sin(\pi\alpha)}{\kappa+1}\begin{cases}\left(\dfrac{b-x}{x}\right)^{\alpha}+\dfrac{2\eta}{\pi}L(x), & 0<x<b\\ \dfrac{2\eta}{\pi}L(x), & x<0, x>b\end{cases} \tag{51}$$

$$L(x)=\frac{\pi}{\sin(\pi\alpha)}\begin{cases}-\left(\dfrac{b-x}{x}\right)^{\alpha}-1, & x<0\\ \left(\dfrac{b-x}{x}\right)^{\alpha}\cos(\pi\alpha)-1, & 0<x<b\\ \left(\dfrac{x-b}{x}\right)^{\alpha}, & x>b\end{cases} \tag{52}$$

$$\alpha=\theta/\pi,\quad \beta=-\theta/\pi,\quad \theta=\arctan\left|\frac{\kappa+1}{\eta(\kappa-1)}\right| \tag{53}$$

where $0<x<b$ is the contact area and the load P and the contact area b are related by

$$\frac{P}{m\mu}=\frac{4\pi\alpha}{1+\kappa}b \tag{54}$$

Note that in the contact problems with friction, α and β are not conventional or square-root singularities. From the standpoint of fracture initiation on the surface $y=0$, the significance of the contact problems with friction is that, even though the stresses on the surface are generally compressive, the in-plane stress component $\sigma_{xx}(x,0)$ (e.g., Eqs. (46) and (51)) has a tensile peak, which increases with the increasing coefficient of friction.

4.3 On Coupling of Singularities. Consider the frictionless contact problem shown in Fig. 6 where a rigid stamp is pressed to an elastic wedge of angle $\theta_0(2\pi-\theta_0<\theta<2\pi)$. The problem is formulated in polar coordinates r, θ, solved by using the Mellin transform and is reduced to a singular integral equation of the following standard form (see Ref. [34] for details):

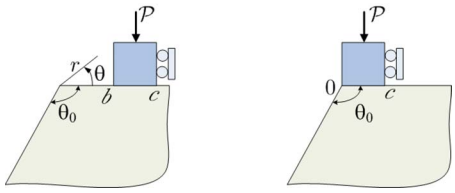

Fig. 6 Coupling of singularities in an elastic wedge and a rigid stamp

$$\frac{4\mu}{1+\kappa}g(r)=\frac{1}{\pi}\int_b^c\left[\frac{1}{t-r}+k_s(r,t)+k_f(r,t)\right]f(t)dt,\quad b<r<c \tag{55}$$

where

$$f(r)=\sigma_{\theta\theta}(r,0),\quad b<r<c \tag{56}$$

$$g(r)=\frac{\partial}{\partial r}u_{\theta}(r,0),\quad b<r<c \tag{57}$$

$k_f(r,t)$ is bounded and $k_s(r,t)$ is a generalized Cauchy kernel in the sense that for $b=0$ it becomes unbounded as $r\to 0$ and $t\to 0$.

In the general case of $0<b<c<\infty$ (Fig. 6(*a*)), there are three singular points, which are uncoupled and are located at (0,0), $(b,0)$ and $(c,0)$. The characteristic equations giving the singularities at these three points are

$$\sigma_{\theta\theta}(r,0)\sim r^{-\lambda};\quad (\lambda-1)^2(1-\cos 2\theta_0)-\{1-\cos[2(\lambda-1)\theta_0]\}=0,\quad 0<\Re(\lambda)<1 \tag{58}$$

$$\sigma_{\phi\phi}(\rho_1,\phi_1)\sim \rho_1^{-\lambda_1};\quad \cot\pi\lambda_1=0,\quad \lambda_1=\tfrac{1}{2} \tag{59}$$

$$\sigma_{\phi\phi}(\rho_2,\phi_2)\sim \rho_2^{-\lambda_2};\quad \cot\pi\lambda_2=0,\quad \lambda_2=\tfrac{1}{2} \tag{60}$$

where λ, λ_1, and λ_2 are singularities at (0,0), $(b,0)$, and $(c,0)$, respectively, and (r,θ), (ρ_1,ϕ_1), and (ρ_2,ϕ_2) are the local polar coordinates.

In the important special case of $b=0$, the two singular points at (0,0) and $(b,0)$ coincide and as expected, the power of the combined singularity becomes greater than λ and λ_1 (Fig. 6(*b*)). To determine this singularity in the integral equation (55), we let $b=0$ and assume the solution $f(t)$ to be of the form

$$f(t)=F(t)t^{\beta}(c-t)^{\alpha},\quad -1<\Re(\alpha,\beta)\le 0 \tag{61}$$

where $F(t)$ is a bounded unknown function. Thus, substituting from Eq. (61) into Eq. (55) and using the complex function theory, the characteristic equations giving the singularities at the point c and zero may be obtained as follows:

$$\cot\pi\alpha=0,\quad \alpha=\tfrac{1}{2} \tag{62}$$

$$(1+\beta)\sin 2\theta_0+\sin[2(1+\beta)\theta_0]=0 \tag{63}$$

In the case of $b=0$ (Fig. 6(*b*)), it can be shown that the singularity β is that of a symmetrically loaded wedge of angle $2\theta_0$. Also, from Eqs. (62) and (63), it may be seen that α and β are real, $\alpha=1/2$, $\beta=0$ for $0<\theta_0\le\pi/2$, and $-1<\beta<0$ for $\pi/2<\theta_0\le 2\pi$. In particular, $\beta=0$, $-1/2$, $-2/3$, $-3/4$ for $\theta_0=\pi/2$, π, $3\pi/2$, 2π, respectively.

5 Singularities in Graded Materials

Graded materials (also known as functionally graded materials (FGMs)) are multiphase composites with continuously varying thermomechanical properties. From the standpoint of fracture mechanics, the distinct problem areas involving graded materials are the investigation of singularities near a crack tip embedded in a nonhomogeneous medium with smoothly varying properties, the

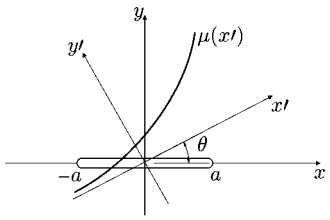

Fig. 7 Notation for a plane crack in a nonhomogeneous medium

same problem for a graded medium containing "kink lines," and the basic surface crack problem. Similarly, the distinct problems in contact mechanics are the investigation of the effect of material nonhomogeneity coefficients, the geometry of the cover plates or stamps, and the coefficient of friction on the singularities of contact stresses. In this section, these questions will be described very briefly and some simple problems will be discussed.

5.1 Crack Problems in Graded Materials. To examine the influence of the material nonhomogeneity on the asymptotic stress state near the crack tips, we first consider the plane elasticity problem described in Fig. 7. It is assumed that Poisson's ratio is constant and the shear modulus is approximated by

$$\mu(x,y) = \mu_0 e^{(\beta x+\gamma y)} \tag{64}$$

where μ_0, β, and γ are known constants. The problem was solved for arbitrary loading conditions [35] and it was shown that near the crack tip $x=a$ the stresses have the following asymptotic behavior:

$$\sigma_{ij}(r,\theta) = \frac{e^{r\phi_1(\theta)}}{\sqrt{2r}}[k_1 f_{1ij}(\theta) + k_2 f_{2ij}(\theta)], \quad (i,j) = (r,\theta) \tag{65}$$

$$\sigma_{iz}(r,\theta) = e^{r\phi_2(\theta)}\frac{k_3}{\sqrt{2r}} f_{3i}(\theta), \quad i = (r,\theta) \tag{66}$$

The known functions ϕ_1 and ϕ_2 are associated with the in-plane and antiplane loading problems, respectively, for a crack tip embedded in a nonhomogeneous medium with smoothly varying material properties. k_1, k_2, and k_3 are the stress intensity factors and the functions f_{1ij}, f_{2ij}, and f_{3i} are identical to those found for the homogeneous materials [36,37].

Referring to Fig. 8, we consider the crack problems in piecewise homogeneous (Figs. 8(*a*) and 8(*c*)) and piecewise nonhomogeneous (Figs. 8(*b*) and 8(*d*)) materials.

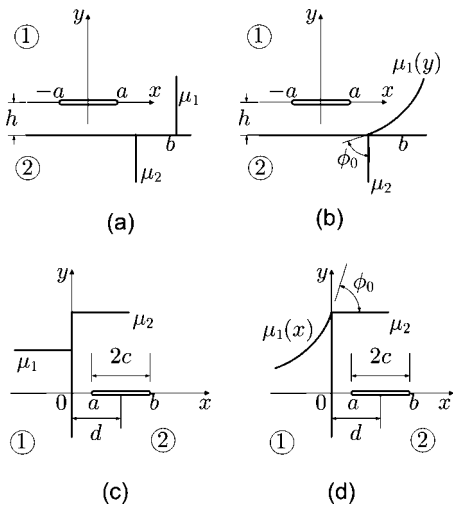

Fig. 8 Geometry and notation for a plane crack

For the mixed-mode problems, Figs. 8(*a*) and 8(*b*), the integral equations may be expressed as [36]

$$\frac{1}{\pi}\int_{-a}^{a}\sum_{1}^{2}\left[\frac{\delta_{ij}}{t-x} + k_{ij}^{s}(x,t) + k_{ij}^{f}(x,t)\right] f_j(t)dt = \frac{1+\kappa_1}{4\mu_i(0)} p_i(x),$$
$$|x| < a, \quad i = 1,2 \tag{67}$$

where

$$\begin{Bmatrix} f_1(x) \\ f_2(x) \end{Bmatrix} = \begin{Bmatrix} \frac{\partial}{\partial x}(v^+ - v^-) \\ \frac{\partial}{\partial x}(u^+ - u^-) \end{Bmatrix}, \quad \begin{Bmatrix} p_1(x) \\ p_2(x) \end{Bmatrix} = \begin{Bmatrix} \sigma_{yy}(x,0) \\ \sigma_{xy}(x,0) \end{Bmatrix}, \quad |x| < a \tag{68}$$

$k_{ij}^{s}(x,t)$ and $k_{ij}^{f}(x,t)$ are known functions, which depend on h and material parameters. k_{ij}^{s} are generally associated with the infinite medium and become unbounded for $h=0$, and k_{ij}^{f} represent the details of the geometry and are bounded for all values of h. For $h>0$, all kernels k_{ij}^{s} as well as k_{ij}^{f} are bounded, the problem is one of embedded crack, $1/(t-x)$ is the only dominant kernel, and consequently the solution has the standard square-root singularity [35,36]. For $h\to 0$, $k_{ij}^{s}(x,t)$ contain generalized Cauchy kernels giving

$$k_{11}^{s}(x,t) \sim k_{22}^{s}(x,t) \sim \frac{t-x}{h^2+(t-x)^2} \to \frac{1}{t-x} \tag{69}$$

$$k_{12}^{s}(x,t) \sim -k_{21}^{s}(x,t) \sim \frac{1}{\pi}\frac{2h}{4h^2+(t-x)^2} \to \delta(t-x) \tag{70}$$

Thus, in the limiting case of the interface crack ($h=0$), Eq. (67) becomes a system of coupled singular integral equations of the second kind and its solution may be obtained in closed form [4,5]. In the case of piecewise nonhomogeneous materials (Fig. 8(*b*)), for $h=0$ the crack is located along the interface, which is a material property kink line. The asymptotic analysis of the kernels k_{ij}^{s} shows that [37]

$$k_{11}^{s}(x,t) = k_{22}^{s}(x,t) = -\frac{\pi\gamma}{8}\frac{|t-x|}{t-x} \tag{71}$$

$$k_{12}^{s}(x,t) = k_{21}^{s}(x,t) = \frac{\gamma}{4}\log|t-x|, \quad \gamma = \tan\phi_0 \tag{72}$$

The important consequence of Eqs. (71) and (72) is that, aside from the Cauchy kernels, since all kernels in the related integral equations are square integrable, the solution would have the standard square-root singularity.

Note that the Mode I problem for piecewise homogenous materials was considered in Sec. 3 of this article (see Fig. 2 and Eqs. (17)–(26)). Again, for $a>0$, Cauchy kernel is the only dominant kernel and the solution has the square-root singularity. For $a=0$, the singularity is greater than $1/2$ if $\mu_2>\mu_1$ and less than $1/2$ if $\mu_2<\mu_1$ (Fig. 8(*c*)). On the other hand, if we "smooth" the material properties by eliminating the discontinuity and replacing it by a "kink" (Fig. 8(*d*)), it can be shown that for $a=0$ the leading term in $k^{s}(x,t)$ becomes [38]

$$k_s(x,t) = \frac{d_1 t}{t+x} + \frac{d_2 x}{t+x} + \frac{d_3 tx}{(t+x)^2} + d_4\log(t+x) \tag{73}$$

where d_1, d_2, d_3 and d_4 are known bimaterial constants. Observing that the remaining terms in k_s and k_f in the related integral equation are square integrable, $(t-x)^{-1}$ would be the only dominant kernel and the solution would again have the standard square-root singularity. It can also be shown that [38] in the general case of the crack terminating at the interface at an arbitrary angle, in

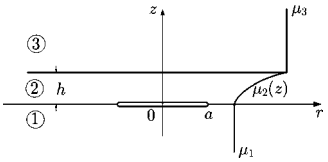

Fig. 9 Geometry of the problem for a penny-shaped crack

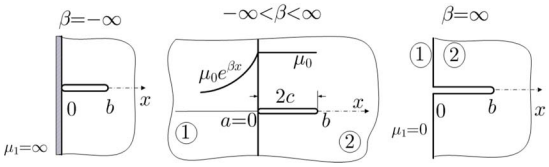

Fig. 11 Geometry of the crack terminating at the interface

addition to the square-root singularity the angular distribution of the stresses at the crack tip would remain identical to that found for the homogeneous materials (see Eqs. (65) and (66)). It is seen that the absence of material property discontinuities in graded materials eliminates the anomalous behavior of crack tip stress and displacement oscillations associated with interface cracks (Fig. 8(*a*), $h=0$) and the non-square-root singularity associated with cracks intersecting bimaterial interfaces (Fig. 8(*c*), $a=0$). The important consequence of this result is that one may now apply the fracture theories based on the energy balance concept by calculating the stress intensity factors and the energy release rate from the standard formulas. For example, after solving the problem Modes I, II, and III, stress intensity factors and strain energy release rates at the crack tip $x=a$, $y=0$ may be obtained as follows (Figs. 2, 7, and 8):

$$k_1(a) = \lim_{x\to a} \sqrt{2(x-a)}\sigma_{yy}(x,0)$$

$$k_2(a) = \lim_{x\to a} \sqrt{2(x-a)}\sigma_{xy}(x,0)$$

$$k_3(a) = \lim_{x\to a} \sqrt{2(x-a)}\sigma_{xz}(x,0) \tag{74}$$

$$\mathcal{G}_{\mathrm{I}}(a) = \frac{\pi(1+\kappa)}{8\mu(a,0)}k_1^2(a)$$

$$\mathcal{G}_{\mathrm{II}}(a) = \frac{\pi(1+\kappa)}{8\mu(a,0)}k_2^2(a)$$

$$\mathcal{G}_{\mathrm{III}}(a) = \frac{\pi}{2\mu(a,0)}k_3^2(a) \tag{75}$$

Some results for the axisymmetric interface crack problem described in Fig. 9 are shown in Fig. 10 [36,39].

The homogeneous dissimilar Materials 1 and 3 are bonded through a nonhomogeneous interfacial Zone 2 of thickness h. κ is assumed to be constant throughout the medium and μ is given by

$$\mu_2(z) = \mu_1 e^{\alpha z}, \quad \alpha = \frac{1}{h}\log\left(\frac{\mu_3}{\mu_1}\right) \tag{76}$$

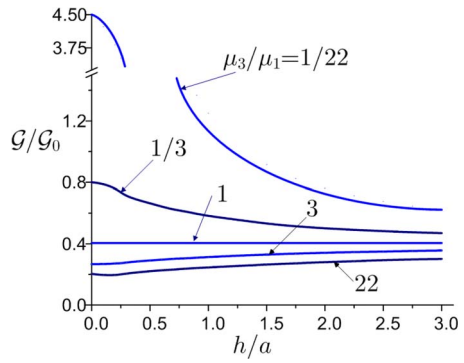

Fig. 10 Normalized strain energy release rates for a penny-shaped crack in graded interfacial zone (Fig. 9)

Figure 10 shows the normalized strain energy release rate $\mathcal{G}/\mathcal{G}_0$ for various values of μ_3/μ_1, $\mathcal{G}=\mathcal{G}_{\mathrm{I}}+\mathcal{G}_{\mathrm{II}}$ (see Eq. (75)), $\mu(a,0)=\mu_1$ (calculated at the crack tip), $\mathcal{G}_0=\pi(1+\kappa_1)p_0 a/8\mu_1$ is the corresponding plane strain value in a uniformly loaded homogeneous medium, and both $\mathcal{G}$ and $\mathcal{G}_0$ are calculated for unit crack length along the crack front. For fixed μ_1 and μ_3, $\mathcal{G}$ is a function of the dimensionless length parameter h/a. For each μ_3/μ_1, $\mathcal{G}_{13}=\lim_{h\to 0}\mathcal{G}(h)$ is obtained independently from the corresponding penny-shaped interface crack problem as follows [36,39]:

$$\mathcal{G}_{13} = \frac{1+\kappa}{c\mu_1}\frac{\pi}{4}(k_1^2+k_2^2), \quad c=(1+\kappa)\left\{\frac{\mu_3}{\mu_1+\mu_3\kappa}+\frac{\mu_3}{\mu_3+\mu_1\kappa}\right\} \tag{77a}$$

$$k_1+ik_2 = 2p_0\left(\frac{a}{\pi}\right)^{1/2}\frac{\Gamma(2+i\omega)}{\Gamma\left(\frac{1}{2}+i\omega\right)}, \quad \omega=\frac{1}{2\pi}\log\left(\frac{\mu_3+\mu_1\kappa}{\mu_1+\mu_3\kappa}\right) \tag{77b}$$

where Γ is the Gamma function.

The values of $\mathcal{G}_{13}$ obtained from Eqs. (77*a*) and (77*b*) and as the limit of $\mathcal{G}(h)$ for $h\to 0$ are shown in Fig. 10 and seem to be consistent. Similarly, as $h\to\infty$, the problem described in Fig. 9 reduces to a simple penny-shaped crack problem for an infinite homogeneous medium and has the value

$$\lim_{h\to\infty}\mathcal{G}(h) = \frac{4}{\pi^2}\mathcal{G}_0 \tag{78}$$

This trend, too, may be observed in Fig. 10. Note that $\mathcal{G}(h)>\mathcal{G}(\infty)$ if $\mu_3<\mu_1$ and $\mathcal{G}(h)<\mathcal{G}(\infty)$ if $\mu_3>\mu_1$.

An example showing the results for the plane strain problem in bonded homogenous and nonhomogeneous materials is described in Figs. 11 and 8(*d*). The results are given only for the more interesting case of a crack terminating at the interface, that is, for $a=0$. The material nonhomogeneity parameter β for Medium 1 is given by $\mu_1(x)=\mu_0\exp(\beta x)$ (Fig. 11). Note that at both ends of the crack, $x=0$ and $x=b$, the problem has square-root singularities, and the half crack length $c=b/2=d$ is the only length parameter and is used for normalizing the results. The normalized Mode I stress intensity factors $k(a)=k_1(a)/\sigma_0\sqrt{c}$ and $k(b)=k_1(b)/\sigma_0\sqrt{c}$ calculated, respectively, at the crack tips $x=0$ and $x=b$ are presented in Fig. 12 as functions of the dimensionless variable βc for $-\infty<\beta c<\infty$. The external load σ_0 is the crack surface traction, $-\sigma_{yy}(x,0)$. From $\mu_1(x)=\mu_0\exp(\beta x)$, it may be seen that the limiting cases of $\beta=-\infty$ and $\beta=\infty$ correspond to an elastic half plane $x>0$ containing a crack along $0<x<2c$ with rigid and stress-free boundaries, respectively.

For $\beta=0$, $\mu_1=\mu_2=\mu_0$ and $k_1(a)=k_1(b)=\sigma_0\sqrt{c}$. If $\beta>0$, the half plane $x>0$ is stiffer than the half plane $x<0$ and consequently $k(a)$ and $k(b)$ are greater than $\sigma_0\sqrt{c}$. Opposite observation may be made for $\beta<0$. In the limiting case of $\beta\to\infty$, we have the homogeneous half plane $x>0$ with an edge crack and the stress inten-

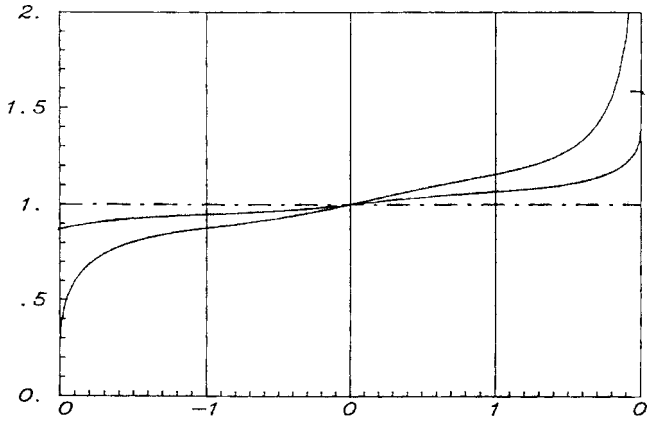

Fig. 12 Normalized stress intensity factors for a plane crack in a homogeneous medium bonded to a nonhomogeneous half space, Fig. 8(*d*), $a=0$, $\mu_1(x)=\mu_0\exp(\beta x)$, $d=c=b/2$, $k(a)=k_1(a)/\sigma_0\sqrt{c}$, $\nu=0.3$, $k(b)=k_1(b)/\sigma_0\sqrt{c}$, $\sigma_0=-\sigma_{yy}(x,0)$, and $0<x<b$

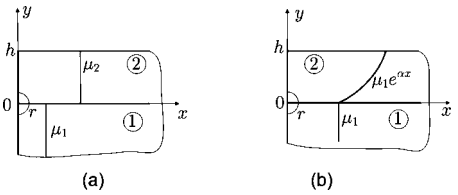

Fig. 13 Semi-infinite homogeneous (*a*) and graded (*b*) coating bonded to a homogeneous quarter plane

sity factors $k(a)\to\infty$ and $k(b)\to 1.5861\sigma_0\sqrt{c}$ (or the standard $k(b)=1.1215\sigma_0\sqrt{b}$).[1] Similarly, as $\beta\to-\infty$, $k(a)\to 0$, and $k(b)$ approaches the known finite limit $k_1(b)\to 0.8710\sigma_0\sqrt{c}$.

Figure 13 describes a possible edge debonding problem in layered materials, specifically piecewise homogeneous (Fig. 13(*a*)) or nonhomogeneous coatings (Fig. 13(*b*)) debonding from a homogeneous substrate.

Figure 13(*a*) shows the well known problem of bonded wedges near the apex ($x=0,y=0$). Near this singular point, the stress state is known to have the form [30]

$$\sigma_{ij}(r,\theta)\sim\frac{1}{r^{\alpha}}F_{ij}(\theta),\quad (i,j)=(r,\theta),\quad 0<\alpha<1/2 \tag{79}$$

If we now remove the material property discontinuity replacing the interface by a kink line, the asymptotic analysis shows that at the singular point the stress state becomes bounded [40] and the likelihood of the initiation of debonding fracture would be highly diminished.

5.2 Contact Problems in Graded Materials. From the standpoint of analysis, contact problems in graded materials have no unique features. In formulating these problems, the components in the material system, which are homogeneous elastic continua, may be replaced, for physical reasons, by nonhomogeneous or graded materials. In contact mechanics involving thin films or cover plates, similar to the case of homogeneous substrates in graded substrates, the critical variables that determine the singularity α are (Fig. 4, Eqs. (40) and (44)) the contact angle θ_0 and the stiffness parameter λ, i.e.,

$$\cot(\pi\alpha)-\frac{\lambda}{1-\alpha}\cot\theta_0=0,\quad \lambda=\frac{\mu_2(0)}{2\mu_1}\frac{1+\kappa_1}{1+\kappa_2(0)} \tag{80}$$

where $\mu_2(y)$ and $\kappa_2(y)$ are the elastic constants of the substrate. Note that the singularity α is dependent on the contact angle θ_0 and stiffness parameter λ only and λ is defined by the elastic constants calculated at the interface $y=0$ (Fig. 3). The material property grading and the geometry of the medium would simply complicate the derivation and the evaluation of the kernels.

In sliding contact problems of rigid stamps pressed upon a graded medium, the general problem may be formulated in terms of an integral equation of the following form [3]:

$$\omega\eta p(x)+\frac{1}{\pi}\int_{-a}^{b}\left[-\frac{1}{t-x}+k(x,t)\right]p(t)dt=f(x),\quad -a<x<b \tag{81}$$

where

$$f(x)=\lambda_0\frac{\partial}{\partial x}v(x,0),\quad \lambda_0=\frac{4\mu(0)}{\kappa(0)+1},\quad \omega=\frac{\kappa(0)-1}{\kappa(0)+1},\quad -a<x<b \tag{82a}$$

$$p(x)=-\sigma_{yy}(x,0),\quad \eta p(x)=-\sigma_{xy}(x,0),\quad -a<x<b \tag{82b}$$

η is the coefficient of friction, Eq. (81) is the contact condition, $p(x)$ is the contact stress, $\mu(y)$ and $\kappa(y)$ are the elasticity coefficients of the substrate, $v(x,y)$ is the y-component of the displacement, and $v(x,0)$ is the known stamp profile giving the input function. If we now introduce the normalizing quantities,

$$x=\frac{(b+a)}{2}r+\frac{(b-a)}{2},\quad t=\frac{(b+a)}{2}s+\frac{(b-a)}{2},\quad -a<(x,t)<b,\quad -1<(r,s)<1 \tag{83}$$

The integral equation (81) becomes

$$\omega\eta\phi(r)-\frac{1}{\pi}\int_{-1}^{1}\frac{\phi(s)}{s-r}ds+\frac{1}{\pi}\int_{-1}^{1}K(r,s)\phi(s)ds=F(r),\quad -1<r<1 \tag{84}$$

The first two terms in Eq. (84) constitute the dominant part of the singular integral equation. By using the complex function theory [4] (see also the Appendix), from the dominant part of the integral equation, the weight function of $\phi(r)$ is found to be

$$w(s)=(1-s)^{\alpha}(1+s)^{\beta},\quad -1<s<1 \tag{85}$$

$$\alpha=\frac{\theta}{\pi}+N_0,\quad \beta=-\frac{\theta}{\pi}+M_0,\quad \theta=\arctan\left(\frac{1}{\omega\eta}\right),\quad -1<\Re(\alpha,\beta)<1,\quad 0<\theta<\frac{\pi}{2} \tag{86}$$

where N_0 and M_0 are arbitrary (positive, zero, or negative) integers and are determined from the physics of the problem. To make the solution given by Eq. (84) single valued, the following two additional conditions are needed: (a) the consistency condition of the integral equation [4] and (b) the resultant force equilibrium condition given by

$$\int_{-a}^{b}p(x)dx=P \tag{87}$$

Figure 14 shows all simplified but typical stamp geometries. In the stamp described in Fig. 14(*a*), it is seen that $a=b$, the contact area is known, and the stress state is unbounded at both ends of the contact region. Consequently, $N_0=-1$, $M_0=0$, $\alpha=-1+\theta/\pi$,

[1]This may not be very clear from Fig. 12. However, by expressing $k(b)$ as a function of the crack tip location $x=a$, it can be shown that $\lim_{a\to 0}d/da k(b)=\infty$ and, as expected the function $k(b)$, at $x=a=0$, is ill defined.

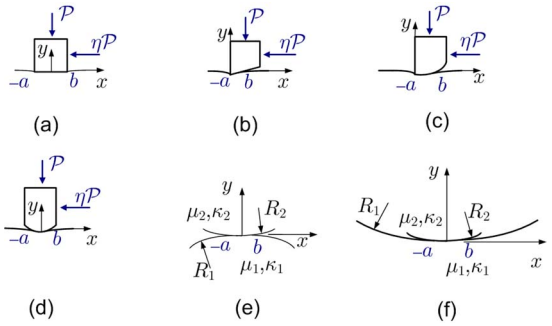

Fig. 14 Typical stamp geometries pressed upon a graded substrate

$\beta=-\theta/\pi$.

Similarly, in the stamp shown in Figs. 14(*b*) and 14(*c*), $a=0$, b is unknown, the stress is unbounded at $x=0$ and bounded at $x=b$; hence, $N_0=M_0=0$, $\alpha=\theta/\pi$, and $\beta=-\theta/\pi$. In Fig. 14(*d*), both a and b are unknown, the stress state at both ends of the contact region is bounded, $N_0=0$, $M_0=1$, $\alpha=\theta/\pi$, and $\beta=1-\theta/\pi$. All unknowns shown in Fig. 14 are determined by using the additional conditions.

In two contacting graded deformable solids the local geometry that may often be encountered in practice is shown in Figs. 14(*e*) and 14(*f*), and the integral equation of the problem may be expressed as [41]

$$\eta A p(x) - \frac{1}{\pi}\int_{-a}^{b}\frac{p(t)}{t-x}dt - \frac{1}{D\lambda_1\pi}\int_{-a}^{b}k_1(x,t)p(t)dt + \frac{1}{D\lambda_2\pi}\int_{-a}^{b}k_2(x,t)p(t)dt = \frac{x}{RD}, \quad -a<x<b \tag{88}$$

where

$$\lambda_1=\frac{4\mu_1}{\kappa_1+1}, \quad \lambda_2=\frac{4\mu_2}{\kappa_2+1}, \quad \Gamma=\frac{\mu_1}{\mu_2}, \quad \frac{1}{R}=\frac{1}{R_1}+\frac{1}{R_2}$$

$$A=\frac{(\kappa_1-1)-(\kappa_2-1)\Gamma}{(\kappa_1+1)+(\kappa_2+1)\Gamma}, \quad D=\frac{(\kappa_1+1)+(\kappa_2-1)\Gamma}{4\mu_1}$$

$$\frac{\partial}{\partial x}v_1(x,0)=\frac{x}{R_2}, \quad \frac{\partial}{\partial x}v_2(x,0)=-\frac{x}{R_1} \tag{89}$$

After normalizing the interval $(-a,b)$ and introducing $\phi(r)=2RDp(x)$, the weight function of $\phi(r)$ is obtained to be

$$w(r)=(1-r)^{\alpha}(1+r)^{\beta}, \quad -1<\Re(\alpha,\beta)<1, \quad -1<r<1 \tag{90}$$

$$\alpha=\frac{\theta}{\pi}+N_0, \quad \beta=-\frac{\theta}{\pi}+M_0, \quad \theta=\arctan\left(\frac{1}{\eta A}\right), \quad 0<\theta<\frac{\pi}{2} \tag{91}$$

Since the contact is smooth at both $-a$ and b, α and β must be positive. From Eqs. (90) and (91), it then follows that

$$\alpha=\frac{\theta}{\pi}, \quad \beta=1-\frac{\theta}{\pi} \tag{92}$$

After obtaining $w(r)$, the solution of the contact problems described in Figs. 14(*a*)–14(*f*) may be expressed as follows:

$$\phi(s)=\sum_{0}^{\infty}c_n w(s)P_n^{(\alpha,\beta)}(s), \quad -1<s<1 \tag{93}$$

Again, it must be emphasized that the dimensionless parameters η, κ_1, κ_2, and Γ (see Eqs. (88) and (89)) that appear in the dominant part of the integral equation (88) and, hence, influence the determination of the singularities α and β are evaluated on the contacting surface $y=0$, $-a<x<b$.

In the formulation of mixed boundary value problems in mechanics, the dominant kernels leading to unconventional singularities are $1/(t-x)$, $\delta(t-x)$ and $t^{k-1}/(t+x)^k$, $k=1,2,\ldots,n$. The problem can also be formulated in terms of "strong singularities" (or "hypersingularities"), which have certain advantages in solving the crack problems in plates and shells [42,43]. Some extensive and useful results for the evaluation of related singular integrals are given in Refs. [44,11,45,46].

In the subcritical crack growth processes in homogeneous or graded materials due to mixed-mode conditions at the crack tip, the crack path is usually curved. Assuming that the stress intensity factors at the crack tip and the crack propagation parameters of the material under basic Mode I loading condition are known, the path of the propagating crack can be (approximately) determined incrementally by using an appropriate crack growth model. In such a model, the so-called "maximum stress theory" or "maximum strain energy release rate theory" may be used as the local crack growth criterion (see Ref. [47] for the description of the proposed criterion). The details of the model and its application to the fatigue crack propagation of a surface crack in plates are described in Ref. [22]. Similarly, the creep crack growth in glasses and ceramics under residual stresses is studied in Ref. [48].

6 Concluding Remarks

Theoretical methods and exact solutions involving stress singularities are essential in dealing with the mixed boundary value problems in mechanics for two main reasons. First, they provide the correct form of singularities and asymptotic results that may be needed to analyze and interpret the experimental results and to improve the accuracy of purely numerical solutions. Secondly, they provide exact solutions for relatively simple geometries and idealized material behavior that could be used as benchmarks for numerical and approximate procedures. However, in practical applications the geometry of the medium is seldom simple and realistic material models seldom lead to analytically tractable formulations. The mathematics dealing with these mostly three-dimensional mixed boundary value problems has not yet been developed.[2] It is, therefore, necessary to develop purely numerical and hybrid methods that can accommodate complicated geometries and realistic material models. The finite element model, particularly enriched special elements, appears to be especially well suited for this purpose.

In solving the mixed boundary value problems in order to determine the correct singularities, a careful asymptotic analysis of the kernels is necessary. In particular, to investigate the existence of unconventional singularities, it is important to separate the dominant part of the kernel, which includes the delta function.

Regarding the crack tip singularities in graded materials at the crack tip as long as the material properties are continuous with continuous or discontinuous derivatives, the stress state has a square-root singularity and the angular distribution of stresses around the crack tip is identical to that in homogeneous materials. Thus, by eliminating the discontinuities in material property distributions, the mathematical anomalies concerning the crack tip stress oscillations for the interface cracks and the non-square-root

[2]Some of the techniques to be developed for dealing with three-dimensional mixed boundary value problems may include a 3D theory equivalent to the conventional two-dimensional complex function theory and two-dimensional singular integral equations.

singularities for the cracks intersecting the interfaces are also eliminated. In practice, the importance of this result lies in the fact that in graded materials one can now use the crack tip finite element modeling developed for homogeneous materials and apply the methods of energy balance theories of conventional fracture mechanics.

In sliding contact problems, the stress concentration at the trailing end of the contact region is greater than that at the leading end. Despite the fact that contact stresses are predominantly compressive, a tensile peak develops at the trailing end of the contact region. As indicated by experiments, this in-plane tensile stress may cause crack initiation on the surface of the substrate.

In sliding contact problems with rigid stamps, the singularities depend only on the coefficient of friction and Poisson's ratio of the substrate at the contacting surface and are independent of the material property coefficients and the shear modulus. In contact problems for two deformable elastic solids, the singularities depend on the coefficient of friction and the values of Poisson's ratios ν_1, and ν_2 and the stiffness ratio μ_1/μ_2 at the contacting surfaces, and are independent of material property coefficients.

Acknowledgment

The authors would like to thank Professor Marek-Jerzy Pindera and Professor Glaucio Paulino for their support in preparing this article.

Appendix: The Complex Function Theory

To demonstrate the application of the complex function theory, we consider the following singular integral equation with the generalized Cauchy kernel:

$$\gamma f(x) + \frac{1}{\pi}\int_a^b \frac{f(t)}{t-x}dt + \frac{1}{\pi}\int_a^b \sum_0^n c_k(x-a)^k \frac{d^k}{dx^k}(t-z_1)^{-1}f(t)dt = \phi(x), \quad a<x<b \tag{A1}$$

$$z_1 = a + (x-a)e^{i\theta_1}, \quad a<x<b \tag{A2}$$

where γ, a, b, c_k, $(k=0,1,\ldots,n)$, and θ_1 are real valued known constants, $f(x)$ is the unknown, and $\phi(x)$ is a known bounded function. The most general class of solution of Eq. (A1) may be expressed as [4]

$$f(t) = g(t)(b-t)^{\alpha}(t-a)^{\beta} = g(t)e^{-\pi i\alpha}(t-b)^{\alpha}(t-a)^{\beta} \tag{A3}$$

where $g(t)$ is Hölder-continuous in $a \leqslant t \leqslant b$, nonzero at $z=a$ and $z=b$, and

$$-1 < \Re(\alpha,\beta) < 1 \tag{A4}$$

We now introduce the following sectionally holomorphic function:

$$F(z) = \frac{1}{\pi}\int_a^b \frac{f(t)}{t-z}dt = \frac{e^{-\pi i\alpha}}{\pi}\int_a^b (t-b)^{\alpha}(t-a)^{\beta}g(t)\frac{dt}{t-z} \tag{A5}$$

Referring to Ref. [4], the singular behavior of $F(z)$ near the end points may be obtained as

$$F(z) = -g(a)(b-a)^{\alpha}\frac{e^{-\pi i\beta}}{\sin(\pi\beta)}(z-a)^{\beta} + g(b)(b-a)^{\beta}\frac{1}{\sin(\pi\alpha)}(z-b)^{\alpha} + F_0(z) \tag{A6}$$

where $F_0(z)$ is bounded everywhere except possibly at the ends a and b near which it may have a singularity weaker than that of $F(z)$. By using the Plemelj formula,

$$\frac{1}{2}[F^+(x) + F^-(x)] = \frac{1}{\pi}\int_a^b \frac{f(t)}{t-x}dt \tag{A7}$$

we obtain

$$\frac{1}{\pi}\int_a^b \frac{f(t)}{t-x}dt = -g(a)(b-a)^{\alpha}\cot(\pi\beta)(x-a)^{\beta} + g(b)(b-a)^{\beta}\cot(\pi\alpha)(b-x)^{\alpha} + F_1(x), \quad a<x<b \tag{A8}$$

where the behavior of $F_1(x)$ near the end points is the same as that of F_0.

Observing that $F(z)$ is holomorphic everywhere outside the cut $a<x<b$, we have

$$\frac{1}{\pi}\int_a^b \frac{f(t)}{t-z_1}dt = F(z_1) \tag{A9}$$

Substituting now $z=z_1=a+(x-a)e^{i\theta_1}$, near the end point $x=a$ from Eq. (A6), we obtain

$$F(z_1) = -g(a)(b-a)^{\alpha}\frac{e^{-\pi i\beta}}{\sin(\pi\beta)}e^{i\beta\theta_1}(x-a)^{\beta} + F_2(x), \quad a<x<b \tag{A10}$$

where $F_2(x)$ represents all remaining terms bounded near and at $x=a$. Since $F(z)$ is holomorphic at $z=z_1$, a typical term in the summation (A1) may be expressed as

$$\frac{1}{\pi}\int_a^b f(t)(x-a)^k\frac{d^k}{dx^k}(t-z_1)^{-1}dt = (x-a)^k\frac{d^k}{dx^k}F(z_1) = -g(a)(b-a)^{\alpha}\frac{e^{-\pi i\beta}}{\sin(\pi\beta)}e^{i\beta\theta_1}\beta(\beta-1)\cdots(\beta-k+1)(x-a)^{\beta} + (x-a)^k\frac{d^k}{dx^k}F_2(x), \quad a<x<b \tag{A11}$$

By substituting from Eqs. (A8), (A10), and (A11) into Eq. (A1), it follows that

$$-g(a)(b-a)^{\alpha}\cot(\pi\beta)(x-a)^{\beta} + g(b)(b-a)^{\beta}\cot(\pi\alpha)(b-x)^{\alpha} + F_1(x) - c_0 g(a)(b-a)^{\alpha}\frac{e^{-\pi i\beta}}{\sin(\pi\beta)}e^{i\beta\theta_1}(x-a)^{\beta} + F_2(x) + \sum_1^n c_k\left[-g(a)(b-a)^{\alpha}\frac{e^{-\pi i\beta}}{\sin(\pi\beta)}e^{i\beta\theta_1}\beta(\beta-1)\cdots(\beta-k+1)(x-a)^{\beta} + (x-a)^k\frac{d^k}{dx^k}F_2(x)\right] + \gamma g(a)(b-a)^{\alpha}(x-a)^{\beta} + F_3(x) = \phi(x), \quad a<x<b \tag{A12}$$

where $F_3(x)$ represents the bounded part of $\gamma f(x)$ at $x=a$. Observing that $g(a)\neq 0$, $g(b)\neq 0$, $-1<\mathbb{R}(\alpha,\beta)<0$, and

$$\lim_{x\to a}(x-a)^{-\beta}[\phi(x),F_1(x),(x-a)^kF_2(x),F_3(x)]=0,\quad k=0,1,\ldots,n \tag{A13}$$

$$\lim_{x\to a}(b-x)^{-\alpha}[\phi(x),F_1(x),(x-a)^kF_2(x),F_3(x)]=0,\quad k=0,1,\ldots,n \tag{A14}$$

from Eq. (A12) by multiplying both sides first by $(x-a)^{-\beta}$ and letting $x\to a$ and then by $(b-x)^{-\alpha}$ and letting $x\to b$ the following characteristic equations for α and β are obtained:

$$\cot(\pi\alpha)=0,\quad \alpha=-1/2 \tag{A15}$$

$$\cos(\pi\beta)+e^{i\beta}(\theta_1-\pi)\left[c_0+\sum_1^n c_k\beta(\beta-1)(\beta-2)(\beta-k+1)\right]+\gamma\sin(\pi\beta)=0 \tag{A16}$$

References

[1] Sneddon, I. N., 1966, *Mixed Boundary Value Problems in Potential Theory*, North-Holland, Amsterdam.
[2] Gakhov, F. D., 1966, *Boundary Value Problems*, Pergamon, Oxford.
[3] Muskhelishvili, N. I., 1953, *Some Basic Problems of the Mathematical Theory of Elasticity*, P. Noordroff Ltd., Groningen, Holland.
[4] Muskhelishvili, N. I., 1953, *Singular Integral Equations*, P. Noordroff Ltd., Groningen, Holland.
[5] Erdogan, F., 1978, "Mixed Boundary Value Problems in Mechanics," Mechanics Today, **4**, pp. 1–86.
[6] Mikhlin, S. G., 1964, *Integral Equations*, Pergamon, Oxford.
[7] Erdogan, F., 1969, "Approximate Solutions of Systems of Singular Integral Equations," SIAM J. Appl. Math., **17**, pp. 1041–1059.
[8] Gray, L. J., and Paulino, G. H., 1998, "Crack Tip Interpolation, Revisited," SIAM J. Appl. Math., **58**, pp. 428–455.
[9] Sutradhar, A., and Paulino, G. H., 2004, "Symmetric Galerkin Boundary Element Computation of T-Stress and Stress Intensity Factors for Mixed-Mode Cracks by the Interaction Integral Method," Eng. Anal. Boundary Elem., **28**, pp. 1335–1350.
[10] Kassir, M. K., and Sih, G. C., 1975, *Three-Dimensional Crack Problems*, Noordhoff, Leyden.
[11] Kaya, A. C., 1984, "Applications of Integral Equations With Strong Singularities in Fracture Mechanics," Ph.D. dissertation, Lehigh University, Bethlehem, PA.
[12] Sneddon, I. N., 1946, "The Distribution of Stress in the Neighborhood of a Crack in an Elastic Solid," Proc. R. Soc. London, Ser. A, **187**, pp. 229–260.
[13] Sack, R. A., 1946, "Extension of Griffith's Theory to Rupture in Three Dimensions," Proc. Phys. Soc. London, **58**, pp. 729–736.
[14] Smith, F. W., Kobayashi, A. S., and Emery, A. F., 1967, "Stress Intensity Factor for Penny-Shaped Crack—Part I: Infinite Solid," ASME J. Appl. Mech., **89**, pp. 947–952.
[15] Green, A. E., and Sneddon, I. N., 1950, "The Distribution of Stress in the Neighborhood of a Flat Elliptical Crack in an elastic Solid," Proc. Cambridge Philos. Soc., **46**, pp. 159–163.
[16] Keer, L. M., and Parihar, K. S., 1978, "Singularity at the Corner of a Wedge-Shaped Punch or Crack," SIAM J. Appl. Math., **34**, pp. 297–302, for pyramidal notches, see also Q. Appl. Math., 1977, pp. 401–405.
[17] Parihar, K. S., and Keer, L. M., 1978, "Stress Singularity at the Corner of Wedge-Shaped Crack or Inclusion," ASME J. Appl. Mech., **45**, pp. 791–796.
[18] Benthem, J. P., 1977, "State of Stress at the Vertex of a Quarter Infinite Crack in a Half Space," Int. J. Solids Struct., **13**, pp. 479–492.
[19] Benthem, J. P., 1980, "The Quarter-Infinite Crack in a Half Space; Alternative and Additional Solutions," Int. J. Solids Struct., **16**, pp. 119–130.
[20] Bažvant, Z. P., and Estenssoro, L. F., 1979, "Surface Singularity and Crack Propagation," Int. J. Solids Struct., **15**, pp. 405–426.
[21] Kantorovich, L. V., and Krylov, V. I., 1958, *Approximate Methods of Higher Analysis*, Interscience, New York.
[22] Joseph, P. F., and Erdogan, F., 1989, "Surface Crack Problems in Plates," Int. J. Fract., **41**, pp. 105–131.
[23] Ayhan, A. O., Kaya, A. C., and Nied, H. F., 2006, "Analysis of Three-Dimensional Interface Cracks Using Enriched Finite Elements," Int. J. Fract., **142**, pp. 255–276.
[24] Ayhan, A. O., and Nied, H. F., 2002, "Stress Intensity Factors for Three-Dimensional Surface Cracks Using Enriched Finite Elements," Int. J. Numer. Methods Eng., **54**, pp. 899–921.
[25] Xu, A. Q., and Nied, H. F., 2000, "Finite Element Analysis of Stress Singularities in Attached Flip-Chip Packages," ASME J. Electron. Packag., **122**, pp. 301–305.
[26] Gray, L. J., Phan, A.-V., Paulino, G. H., and Kaplan, T., 2003, "Improved Quarter-Point Crack Tip Element," Eng. Fract. Mech., **70**, pp. 269–283.
[27] Bueckner, H. F., 1966, "On a Class of Singular Integral Equations," J. Math. Anal. Appl., **14**, pp. 392–426.
[28] Erdogan, F., and Cook, T. S., 1974, "Antiplane Shear Crack Terminating at and Going Through a Bimaterial Interface," Int. J. Fract., **10**, pp. 227–240.
[29] Cook, T. S., and Erdogan, F., 1972, "Stresses in Bonded Materials With a Crack Perpendicular to the Interface," Int. J. Eng. Sci., **10**, pp. 667–697.
[30] Erdogan, F., and Biricikoglu, V., 1973, "Two Bonded Half Planes With a Crack Going Through the Interface," Int. J. Eng. Sci., **11**, pp. 745–766.
[31] Mahajan, R., and Erdogan, F., 1993, "The Crack Problem for an Orthotropic Half-Plane Stiffened by Elastic Films," Int. J. Eng. Sci., **31**, pp. 403–424.
[32] Koiter, W. T., 1965, "Discussion of Rectangular Tensile Sheet With Symmetrical Edge Cracks," ASME J. Appl. Mech., **87**, p. 237.
[33] Guler, M. A., and Erdogan, F., 2004, "Contact Mechanics of Graded Coatings," Int. J. Solids Struct., **41**, pp. 3865–3889.
[34] Erdogan, F., and Gupta, G. D., 1976, "Contact and Crack Problems for an Elastic Wedge," Int. J. Eng. Sci., **14**, pp. 153–164.
[35] Konda, N., and Erdogan, F., 1994, "The Mixed-Mode Crack Problem in a Nonhomogeneous Elastic Medium," Eng. Fract. Mech., **47**, pp. 533–545.
[36] Erdogan, F., 1997, "Damage Mechanics of Interfaces," *Damage and Failure of Interfaces*, H.-P. Rossmanith, ed., A. A. Balkema, Rotterdam, pp. 3–36.
[37] Delale, F., and Erdogan, F., 1988, "Interface Crack in a Nonhomogeneous Medium," Int. J. Eng. Sci., **28**, pp. 609–614.
[38] Erdogan, F., Kaya, A. C., and Joseph, P. F., 1991, "The Crack Problem in Bonded Nonhomogeneous Materials," ASME J. Appl. Mech., **58**, pp. 410–418.
[39] Ozturk, M., and Erdogan, F., 1996, "Axisymmetric Crack Problem in Bonded Materials With a Graded Interfacial Region," Int. J. Solids Struct., **33**, pp. 193–219.
[40] Kasmalkar, M., 2000, "The Surface Crack Problem for a Functionally Graded Coating Bonded to a Homogeneous Layer," Ph.D. dissertation, Lehigh University, Bethlehem, PA.
[41] Guler, M. A., 2001, "Contact Mechanics of FGM Coatings," Ph.D. dissertation, Lehigh University, Bethlehem, PA.
[42] Joseph, P. F., and Erdogan, F., 1988, "A Surface Crack in Shells Under Mixed Mode Loading Conditions," ASME J. Appl. Mech., **55**, pp. 795–804.
[43] Joseph, P. F., and Erdogan, F., 1991, "Surface Crack in a Plate Under Antisymmetric Loading Conditions," Int. J. Solids Struct., **27**, pp. 725–750.
[44] Chan, Y.-S., Fannjiang, A. C., and Paulino, G. H., 2003, "Integral Equations With Hypersingular Kernels-Theory and Applications to Fracture Mechanics," Int. J. Eng. Sci., **41**, pp. 683–720.
[45] Kaya, A. C., and Erdogan, F., 1987, "On the Solution of Integral Equations With Strongly Singular Kernels," Q. Appl. Math., **45**, pp. 105–122.
[46] Kaya, A. C., and Erdogan, F., 1987, "On the Solution of Integral Equations With a Generalized Cauchy Kernel," Q. Appl. Math., **45**, pp. 455–469.
[47] Erdogan, F., and Sih, G. C., 1963, "On the Crack Extension in Plates Under Plane Loading and Transverse Shear," ASME J. Basic Eng., **85**, pp. 519–526.
[48] Erdogan, F., 1989, "Slow Crack Growth in Glasses and Ceramics Under Residual Stresses," ASME J. Electron. Packag., **111**, pp. 61–67.

A Generalized Interaction Integral Method for the Evaluation of the *T*-Stress in Orthotropic Functionally Graded Materials Under Thermal Loading

Jeong-Ho Kim[1]
Department of Civil and Environmental Engineering,
University of Connecticut,
261 Glenbrook Road,
U-2037,
Storrs, CT 06269
e-mail: jhkim@engr.uconn.edu

Amit KC
GM2 Associates Inc.,
730 Hebron Avenue,
Glastonbury, CT 06033

The interaction integral method that is equipped with the nonequilibrium formulation is generalized to evaluate the nonsingular T-stress as well as mixed-mode stress intensity factors in orthotropic functionally graded materials under thermomechanical loads. This paper addresses both Mode-I and mixed-mode fracture problems and considers various types of orthotropic material gradation. The orthotropic thermomechanical material properties are graded spatially and integrated into the element stiffness matrix using the direct Gaussian formulation. The types of orthotropic material gradation considered include exponential, power-law, and hyperbolic-tangent functions, and the numerical formulation is generalized for any type of smooth material gradation. The T-stress and mixed-mode stress intensity factors are evaluated by means of the interaction integral method developed in conjunction with the finite element method. The accuracy of numerical results is assessed by means of thermomechanically equivalent problems.
[DOI: 10.1115/1.2936234]

Keywords: functionally graded material (FGM), thermal fracture, stress intensity factor (SIF), T-stress, interaction integral, finite element method (FEM)

1 Introduction

The asymptotic stress field around the crack tip in an orthotropic material is given by [1]

$$\sigma_{ij}(r,\theta) = \frac{K_{\mathrm{I}}}{\sqrt{2\pi r}} f_{ij}^{\mathrm{I}}(\theta,\mu_1,\mu_2) + \frac{K_{\mathrm{II}}}{\sqrt{2\pi r}} f_{ij}^{\mathrm{II}}(\theta,\mu_1,\mu_2) + T\delta_{1i}\delta_{1j} \quad \text{as } r \to 0 \tag{1}$$

where σ_{ij} denotes the stress tensor, K_{I} and K_{II} are the Mode-I and Mode-II stress intensity factors (SIFs), respectively, T is the nonsingular stress, and μ_1 and μ_2 are defined in the Appendix. The nonsingular T-stress [2] influences crack initiation angle and crack growth under mixed-mode loading [3–5]. This stress also has influence on crack path stability for mode-I loading with a small imperfection [6]. The T-stress also affects crack-tip constraint and toughness under plane strain conditions [7]. Larsson and Carlson [8] found that the T-stress affects the size and shape of the plastic zone. Betegón and Hancock [9] investigated two-parameter-based (J-T) elastic-plastic crack-tip fields. Du and Hancock [10] investigated the effect of T-stress on crack-tip fields in elastic perfectly plastic materials. Later O'Dowd and Shih [11] proposed the J-Q theory that provides a framework for quantifying the evolution of constraint from small-scale yielding to large-scale yielding conditions. They found a one-to-one correspondence between Q and T for the case when the load and the geometry affect Q only through T. O'Dowd and Shih [12] showed that the J-Q theory allows fracture toughness to be measured and used in engineering applications. The above investigations on the T-stress were performed for homogeneous materials.

After their introduction, functionally graded materials (FGMs) have been extensively investigated in evaluating fracture parameters by means of analytical and numerical approaches, e.g., Erdogan and his co-workers [13–21]. In addition to SIFs for singular stress fields, the nonsingular T-stress has also been investigated for FGMs. Becker et al. [22] calculated the T-stress using the difference of the normal stresses along $\theta=0$, i.e., $(\sigma_{xx}-\sigma_{yy})$. Kim and Paulino [23] used the interaction integral method to evaluate the T-stress and investigated the effect of T-stress on the crack initiation angle. Dag [24] recently used the J_k-integral [25,26] to evaluate the T-stress in FGMs under thermal loads, but the formulation for the T-stress works for only mixed-mode cases, i.e., $K_{\mathrm{II}} \neq 0$. These investigations on the T-stress, however, have been performed for isotropic FGMs.

The nature of processing techniques of some FGMs, however, may lead to loss of isotropy. For example, both functionally graded thermal barrier coatings that are processed by a plasma spray technique [27] and functionally graded solid oxide fuel cells fabricated by a screen printing technique [28] may have a lamellar structure where flattened splats and relatively weak splat boundaries create an oriented material with higher stiffness and weak cleavage planes parallel to the boundary. Furthermore, FGMs manufactured by the electron beam physical vapor deposition technique may have a columnar structure [29], which leads to a higher stiffness in the thickness direction and weaker fracture planes perpendicular to the boundary. Thus, such materials would be considered to be orthotropic with two preferential material directions that are perpendicular to each other. Kim and Paulino [30,31] investigated the T-stress for cracks arbitrarily oriented in orthotropic FGMs. These studies, however, are performed for FGMs under mechanical loads. Thus this paper will focus on the

[1]Corresponding author.

Contributed by the Applied Mechanics Division of ASME for publication in the JOURNAL OF APPLIED MECHANICS. Manuscript received June 5, 2007; final manuscript received December 28, 2007; published online July 22, 2008. Review conducted by Marek-Jerzy Pindera.

evaluation of the T-stress in orthotropic FGMs under thermal loads using a generalized energy conservation integral, so-called the interaction integral, explained below.

Several numerical methods have been used to evaluate the elastic T-stress. Leevers and Radon [32] used a variational formulation to evaluate T-stress. Cardew et al. [33] and Kfouri [34] used the path-independent J-integral in conjunction with the interaction integral to calculate T-stress in Mode-I crack problems. Sladek et al. [35] used the Betti–Rayleigh reciprocal theorem for evaluating T-stress in mixed-mode loadings. Ayatollahi et al. [36] used direct approaches, which consist of both the stress method and the displacement method. For the stress method [37], they used

$$T = \lim_{r\to 0} \sigma_{xx,\theta=\pi \text{ or } -\pi} \quad \text{for the Mode-I case}$$

$$= \lim_{r\to 0} \tfrac{1}{2}(\sigma_{xx,\theta=-\pi} + \sigma_{xx,\theta=\pi}) \quad \text{for the mixed-mode case} \tag{2}$$

For the displacement method, they used

$$T = \lim_{r\to 0} E^* \left(\frac{du_x}{dx}\right)_{\theta=\pi \text{ or } -\pi} \quad \text{for the Mode-I case}$$

$$= \lim_{r\to 0} \frac{E^*}{2}\left(\frac{du_x}{dx}_{\theta=-\pi} + \frac{du_x}{dx}_{\theta=\pi}\right) \quad \text{for the mixed-mode case} \tag{3}$$

These direct methods using field quantities along the crack faces are more accurate than using those along other angular directions. These methods, however, require substantial mesh discretization for orthotropic homogeneous and graded materials, which is one of the reasons for developing the energy-based conservation interaction integral. In addition, although the stress method can be applied to FGMs with sufficient mesh discretization, the displacement method of the current form cannot be used for FGMs and needs modification for FGMs considering varying material properties. Recently Chen et al. [38] investigated the T-stress under Mode-I loading by means of both the Betti–Rayleigh reciprocal theorem and the path-independent J-integral using the p-version finite element method (FEM).

The interaction integral method is an accurate and robust scheme for evaluating mixed-mode SIFs in isotropic FGMs under mechanical [39,40] and thermal [41–43] loads. The method has also been used to evaluate the T-stress in isotropic FGMs under mechanical [23,44,31] and thermal [43] loads. The method has been extended to evaluate mixed-mode SIFs in orthotropic FGMs under mechanical [45,31] and thermal [46] loads, and the T-stress in orthotropic FGMs under mechanical loads [30,31]. Recently, Sladek et al. [47] used a meshless method and the interaction integral method to evaluate the T-stress in orthotropic FGMs. They considered Mode-I plane-stress fracture problems assuming constant thermal conductivity, shear modulus, and Poisson's ratio. Comprehensive study on the T-stress in orthotropic FGMs under thermal loads considering material gradation (e.g., thermal conductivity), plane-strain (as well as plane-stress) conditions, and mixed-mode fracture problems has not been done anywhere in literature. Thus this paper focuses on the evaluation of the T-stress for mixed-mode fracture in orthotropic FGMs under thermal loads using the interaction integral method in conjunction with the FEM that is generalized for thermomechanical loads. The interaction integral method is formulated on the basis of conservation laws, which lead to the establishment of a conservation integral for two admissible states of elastic solid, actual and auxiliary fields. Based on the assumption that the graded orthotropic material is locally homogeneous near the crack tip, with continuous, differentiable, and bounded material properties, this paper establishes the relationship between the asymptotically defined interaction integral (M-integral) and the T-stress and mixed-mode SIFs, converts the M-integral to an equivalent domain integral (EDI) using auxiliary fields, and calculates such parameters using a finite domain.

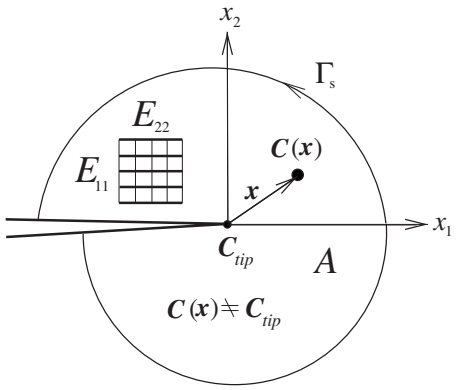

Fig. 1 A crack in an orthotropic FGM. Notice that $\boldsymbol{C}(\boldsymbol{x}) \neq \boldsymbol{C}_{\text{tip}}$ for $\boldsymbol{x} \neq \boldsymbol{0}$. The area A denotes a representative region around the crack tip.

This paper is organized as follows. Section 2 presents the auxiliary fields selected for evaluating mixed-mode SIFs and the T-stress and M-integral formulation. Sections 3 and 4 explain the relationship of mixed-mode SIFs and the T-stress, respectively, to the M-integral. Section 5 presents numerical examples to examine the accuracy and performance of the interaction integral in evaluating the T-stress for orthotropic FGMs under thermal loads. Finally, Sec. 6 provides some discussions and Sec. 7 concludes this work.

2 Generalized Interaction Integral

2.1 Auxiliary Fields. The interaction integral makes use of auxiliary (secondary) fields, such as displacements ($\boldsymbol{u}^{\text{aux}}$), strains ($\boldsymbol{\varepsilon}^{\text{aux}}$), and stresses ($\boldsymbol{\sigma}^{\text{aux}}$). The auxiliary fields have to be suitably defined in order to evaluate mixed-mode SIFs and the T-stress. In this paper we adopt displacement and strain fields for a homogeneous material under mechanical loads and construct new auxiliary stress fields based on the nonequilibrium formulation using $\boldsymbol{\sigma}^{\text{aux}} = \boldsymbol{C}_{ijkl}(\boldsymbol{x})\ \boldsymbol{\varepsilon}^{\text{aux}}$, where $\boldsymbol{C}_{ijkl}(\boldsymbol{x})$ is the constitutive tensor of FGM (see Fig. 1). The auxiliary displacement and strain fields adopted for SIFs and the T-stress are described below.

For mixed-mode SIFs, the auxiliary displacement, strain, and stress fields are selected from the crack-tip asymptotic fields (i.e., $O(r^{1/2})$ for the displacements and $O(r^{-1/2})$ for the strains and stresses) with the material properties sampled at the crack-tip location (e.g., Ref. [25]). Figure 1 shows a crack in an orthotropic FGM under two-dimensional fields in local Cartesian coordinates originating at the crack tip. The auxiliary displacement and strain fields are given by [1]

$$\boldsymbol{u}^{\text{aux}} = K_{\text{I}}^{\text{aux}} \boldsymbol{f}^{\text{I}}(r^{1/2}, \theta, \boldsymbol{a}^{\text{tip}}) + K_{\text{II}}^{\text{aux}} \boldsymbol{f}^{\text{II}}(r^{1/2}, \theta, \boldsymbol{a}^{\text{tip}}) \tag{4}$$

$$\boldsymbol{\varepsilon}^{\text{aux}} = (\text{sym}\ \nabla)\boldsymbol{u}^{\text{aux}} \tag{5}$$

where $K_{\text{I}}^{\text{aux}}$ and $K_{\text{II}}^{\text{aux}}$ are the auxiliary Mode-I and Mode-II SIFs, respectively, and $\boldsymbol{a}^{\text{tip}}$ denotes the contracted notation of the compliance tensor $\boldsymbol{S}$ evaluated at the crack tip and are given in the Appendix. The representative functions $\boldsymbol{f}(r^{1/2}, \theta, \boldsymbol{a}^{\text{tip}})$ are given in other references, e.g., Refs. [1,31].

For the T-stress, the auxiliary displacement and strain fields are selected from those due to a point force in the local Cartesian coordinate (i.e., x_1) applied to the tip of a semi-infinite crack in an infinite homogeneous orthotropic body, as shown in Fig. 2. The auxiliary displacements and strains are given by [48,49]

$$\boldsymbol{u}^{\text{aux}} = \boldsymbol{t}^{u}(\ln r, \theta, f, \boldsymbol{a}^{\text{tip}}) \tag{6}$$

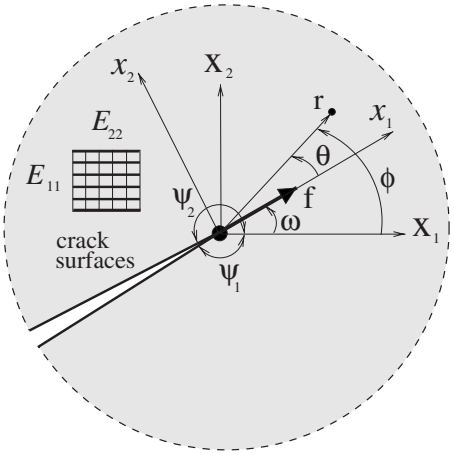

Fig. 2 A point force applied at the crack tip in the direction parallel to the crack surface in a homogeneous orthotropic body where material orthotropy directions are aligned with the global coordinates

$$\boldsymbol{\varepsilon}^{\text{aux}} = (\text{sym}\ \nabla)\boldsymbol{u}^{\text{aux}} \tag{7}$$

where f is the point force applied to the crack tip. The representative functions $\boldsymbol{t}^u(\ln r, \theta, f, \boldsymbol{a}^{\text{tip}})$ are given in other references, e.g., Refs. [48,31]. For orthotropic materials, the auxiliary fields may be determined by either the Stroh or Lekhnitskii formalism [30]. This papers utilizes the Lekhnitskii formalism.

2.2 *M*-Integral Formulation. The standard J-integral is given by [50]

$$J = \lim_{\Gamma_s \to 0} \int_{\Gamma_s} (\mathcal{W}\delta_{1j} - \sigma_{ij}u^t_{i,1})n_j d\Gamma \tag{8}$$

where n_j is the outward normal vector to the contour Γ_s, as shown in Fig. 1, and u^t_i is the total displacement. The parameter $\mathcal{W}$ is the strain energy density given by

$$\mathcal{W} = \tfrac{1}{2}\sigma_{ij}\varepsilon^m_{ij} = \tfrac{1}{2}\sigma_{ij}(\varepsilon^t_{ij} - \alpha_{ij}\Delta\theta\delta_{ij}) \tag{9}$$

where ε^m_{ij} denotes the mechanical part of the strain, ε^t_{ij} the total strain, $\alpha_{ij} = \alpha_{ij}(\boldsymbol{x})$ ($\alpha_{ij} = 0$ for $i \neq j$) thermal expansion coefficients that vary with spatial coordinates, $\Delta\theta = \theta - \theta_0$ with the initial temperature θ_0, and δ_{ij} the Kronecker delta. The EDI form of the J-integral is obtained as

$$J = \int_A (\sigma_{ij}u^t_{i,1} - \mathcal{W}\delta_{1j})q_{,j}dA + \int_A (\sigma_{ij}u^t_{i,1} - \mathcal{W}\delta_{1j})_{,j}qdA \tag{10}$$

where q is a weight function for which the plateau function is used [51,31]. Following the standard approach, the resulting interaction integral (M) for thermal loading becomes

$$M = M_{\text{local}} = \int_A \{\sigma_{ij}u^{\text{aux}}_{i,1} + \sigma^{\text{aux}}_{ij}u^t_{i,1} - \sigma_{ik}\varepsilon^{\text{aux}}_{ik}\delta_{1j}\}q_{,j}dA + \int_A \{\underline{\sigma^{\text{aux}}_{ij,j}u^t_{i,1}} - C_{ijkl,1}\varepsilon^m_{kl}\varepsilon^{\text{aux}}_{ij} + \sigma^{\text{aux}}_{ij}(\alpha_{ij,1}(\Delta\theta) + \alpha_{ij}(\Delta\theta)_{,1})\delta_{ij}\}qdA \tag{11}$$

where the underlined term is a nonequilibrium term that appears due to nonequilibrium of the auxiliary stress fields. The interaction integral for the pure mechanical loading is given by

$$M_{\text{local}} = \int_A \{\sigma_{ij}u^{\text{aux}}_{i,1} + \sigma^{\text{aux}}_{ij}u_{i,1} - \sigma_{ik}\varepsilon^{\text{aux}}_{ik}\delta_{1j}\}q_{,j}dA + \int_A \{\underline{\sigma^{\text{aux}}_{ij,j}u_{i,1}} - C_{ijkl,1}\varepsilon^m_{kl}\varepsilon^{\text{aux}}_{ij}\}qdA \tag{12}$$

For numerical computation by means of the FEM, the M-integral is evaluated first in global coordinates ($(M_m)_{\text{global}}$) $\times (m = 1, 2)$ and then transformed to local coordinates (M_{local}). The M-integral in Eq. (11) is numerically evaluated using

$$(M_m)_{\text{global}} = \sum_{\text{Elem}} \sum_{\text{Gauss}} [\{\sigma_{ij}u^{\text{aux}}_{i,m} + \sigma^{\text{aux}}_{ij}u^t_{i,m} - \sigma_{ik}\varepsilon^{\text{aux}}_{ik}\delta_{mj}\}q_{,j} + \{\sigma^{\text{aux}}_{ij,j}u^t_{i,m} - C_{ijkl,m}\varepsilon^m_{kl}\varepsilon^{\text{aux}}_{ij} + \sigma^{\text{aux}}_{ij}((\alpha_{ij})_{,m}\Delta\theta + \alpha_{ij}(\Delta\theta)_{,m})\delta_{ij}\}q]\det(\boldsymbol{J})w_{gp} \tag{13}$$

where the outer summation loops all the elements within the domain and the inner summation loops all Gauss points with corresponding weights w_{gp} at each element, and $\det(\mathbf{J})$ is the determinant of the standard Jacobian matrix relating (X_1, X_2) with (ξ, η) [52].

3 Evaluation of Stress Intensity Factors

The energy release rates $\mathcal{G}_{\text{I}}$ and $\mathcal{G}_{\text{II}}$ are related to mixed-mode SIFs for plane stress as follows:

$$\mathcal{G}_{\text{I}} = -\frac{K_{\text{I}}}{2}a^{\text{tip}}_{22}\,\text{Im}\left[\frac{K_{\text{I}}(\mu^{\text{tip}}_1 + \mu^{\text{tip}}_2) + K_{\text{II}}}{\mu^{\text{tip}}_1\mu^{\text{tip}}_2}\right]$$

$$\mathcal{G}_{\text{II}} = \frac{K_{\text{II}}}{2}a^{\text{tip}}_{11}\,\text{Im}[K_{\text{II}}(\mu^{\text{tip}}_1 + \mu^{\text{tip}}_2) + K_{\text{I}}(\mu^{\text{tip}}_1\mu^{\text{tip}}_2)] \tag{14}$$

where Im denotes the imaginary part of the complex function. For plane strain, a^{tip}_{ij} is replaced by b^{tip}_{ij}. Thus

$$J_{\text{local}} = \mathcal{G} = \mathcal{G}_{\text{I}} + \mathcal{G}_{\text{II}} = c_{11}K^2_{\text{I}} + c_{12}K_{\text{I}}K_{\text{II}} + c_{22}K^2_{\text{II}} \tag{15}$$

where, for plane stress,

$$c_{11} = -\frac{a^{\text{tip}}_{22}}{2}\,\text{Im}\left(\frac{\mu^{\text{tip}}_1 + \mu^{\text{tip}}_2}{\mu^{\text{tip}}_1\mu^{\text{tip}}_2}\right)$$

$$c_{12} = -\frac{a^{\text{tip}}_{22}}{2}\,\text{Im}\left(\frac{1}{\mu^{\text{tip}}_1\mu^{\text{tip}}_2}\right) + \frac{a^{\text{tip}}_{11}}{2}\,\text{Im}(\mu^{\text{tip}}_1\mu^{\text{tip}}_2)$$

$$c_{22} = \frac{a^{\text{tip}}_{11}}{2}\,\text{Im}(\mu^{\text{tip}}_1 + \mu^{\text{tip}}_2) \tag{16}$$

and, for plane strain a^{tip}_{ij} is replaced by b^{tip}_{ij} (see the Appendix). For two admissible fields, which are the actual $(\boldsymbol{u}, \boldsymbol{\varepsilon}, \boldsymbol{\sigma})$ and auxiliary $(\boldsymbol{u}^{\text{aux}}, \boldsymbol{\varepsilon}^{\text{aux}}, \boldsymbol{\sigma}^{\text{aux}})$ fields, one obtains M_{local} as [53]

$$M_{\text{local}} = 2c_{11}K_{\text{I}}K^{\text{aux}}_{\text{I}} + c_{12}(K_{\text{I}}K^{\text{aux}}_{\text{II}} + K^{\text{aux}}_{\text{I}}K_{\text{II}}) + 2c_{22}K_{\text{II}}K^{\text{aux}}_{\text{II}} \tag{17}$$

The Mode-I and Mode-II SIFs are evaluated by solving the following linear algebraic equations:

$$M^{(1)}_{\text{local}} = 2c_{11}K_{\text{I}} + c_{12}K_{\text{II}} \quad (K^{\text{aux}}_{\text{I}} = 1.0, K^{\text{aux}}_{\text{II}} = 0.0) \tag{18}$$

$$M^{(2)}_{\text{local}} = c_{12}K_{\text{I}} + 2c_{22}K_{\text{II}} \quad (K^{\text{aux}}_{\text{I}} = 0.0, K^{\text{aux}}_{\text{II}} = 1.0) \tag{19}$$

The relationships of Eqs. (18) and (19) are the same as those for homogeneous orthotropic materials [53] except that, for FGMs, the material properties are evaluated at the crack-tip location.

4 Evaluation of the *T*-Stress

The T-stress is evaluated from the interaction integral with no contributions of both singular (i.e., $O(r^{-1/2})$) and higher-order (i.e., $O(r^{1/2})$ and higher) terms in the crack-tip asymptotic fields. The M-integral in the form of a line integral is given by

$$M_{\text{local}} = \lim_{\Gamma_s \to 0} \int_{\Gamma_s} \{\sigma_{ik}\varepsilon^{\text{aux}}_{ik}\delta_{1j} - \sigma_{ij}u^{\text{aux}}_{i,1} - \sigma^{\text{aux}}_{ij}u^t_{i,1}\}n_j d\Gamma \tag{20}$$

Considering only the nonsingular stress parallel to the crack direction, i.e.,

$$\sigma_{ij} = T\delta_{1i}\delta_{1j} \tag{21}$$

one obtains

$$u^t_{i,1} = \varepsilon^t_{11}\delta_{i1} = (a^{\text{tip}}_{11}\sigma_{11} + (\alpha_{11})_{\text{tip}}\Delta\theta_{\text{tip}})\delta_{i1} \tag{22}$$

for plane stress and obtains that

$$u^t_{i,1} = \varepsilon^t_{11}\delta_{i1} = [b^{\text{tip}}_{11}\sigma_{11} + \{(\nu_{31})_{\text{tip}}(\alpha_{33})_{\text{tip}} + (\alpha_{11})_{\text{tip}}\}\Delta\theta_{\text{tip}}]\delta_{i1} \tag{23}$$

for plane strain. For plane stress, substituting Eqs. (21) and (22) into Eq. (20), one obtains

$$M_{\text{local}} = -\lim_{\Gamma_s\to 0}\int_{\Gamma_s}\sigma^{\text{aux}}_{ij}n_j u^t_{i,1}d\Gamma = -(a^{\text{tip}}_{11}\sigma_{11} + (\alpha_{11})_{\text{tip}}\Delta\theta_{\text{tip}})\lim_{\Gamma_s\to 0}\int_{\Gamma_s}\sigma^{\text{aux}}_{ij}n_j d\Gamma \tag{24}$$

Because the force f is in equilibrium (see Fig. 2)

$$f = -\lim_{\Gamma_s\to 0}\int_{\Gamma_s}\sigma^{\text{aux}}_{ij}n_j d\Gamma \tag{25}$$

Thus the following relationship is obtained:

$$T = \frac{M_{\text{local}}}{fa^{\text{tip}}_{11}} - \frac{(\alpha_{11})_{\text{tip}}\Delta\theta_{\text{tip}}}{a^{\text{tip}}_{11}} \tag{26}$$

for plane stress, where a^{tip}_{11} is a material parameter at the crack-tip location. For plane strain,

$$T = \frac{M_{\text{local}}}{fb^{\text{tip}}_{11}} - \frac{\{(\nu_{31})_{\text{tip}}(\alpha_{33})_{\text{tip}} + (\alpha_{11})_{\text{tip}}\}\Delta\theta_{\text{tip}}}{b^{\text{tip}}_{11}} \tag{27}$$

5 Numerical Examples

The performance of the interaction integral in evaluating the T-stress in orthotropic FGMs under thermal loads is examined in the following examples:

(1) strip with an edge crack
(2) plate with an inclined center crack
(3) thermal barrier coating (TBC) with an edge crack

All the examples are analyzed using the FEM code FGM-FRANC2D.[2] The code incorporates the gradation of thermomechanical material properties at the size scale of the element. The specific graded elements used here are based on the *direct Gaussian formulation* [56]. Isoparametric graded elements are used to discretize the geometry of all the above examples. Singular quarter-point six-node triangles (T6qp) are used for crack-tip elements, eight-node serendipity elements (Q8) are used for a circular region around crack-tip elements and over most of the mesh, and regular six-node triangles (T6) are used in the transition zone between regions of Q8 elements.

The present work addresses one-way coupling of thermomechanical analyses by which the field quantities such as displacements, strains, and stresses are affected by temperature and not vice versa. The temperature distribution is obtained solving the steady-state diffusion equation for orthotropic FGMs:

$$\frac{\partial}{\partial X_1}\left(\kappa_{11}\frac{\partial\theta}{\partial X_1}\right) + \frac{\partial}{\partial X_2}\left(\kappa_{22}\frac{\partial\theta}{\partial X_2}\right) = 0 \quad \text{with } \kappa_{11} = \kappa_{11}(X_1) \quad \text{and } \kappa_{22} = \kappa_{22}(X_1) \tag{28}$$

In this paper, heat flux is assumed to be directed along the horizontal axis (i.e., X_1). In Examples 1 and 3 with Mode-I crack problems, the crack is assumed to be insulated. In Example 2 with a mixed-mode crack problem, it is assumed that the temperature field is not affected by the existence of the crack and identical to that for the uncracked plate. The temperature fields in Example 3 are calculated using the Runge–Kutta method, which solves the one-dimensional diffusion equation (i.e., second-order ordinary differential equations).

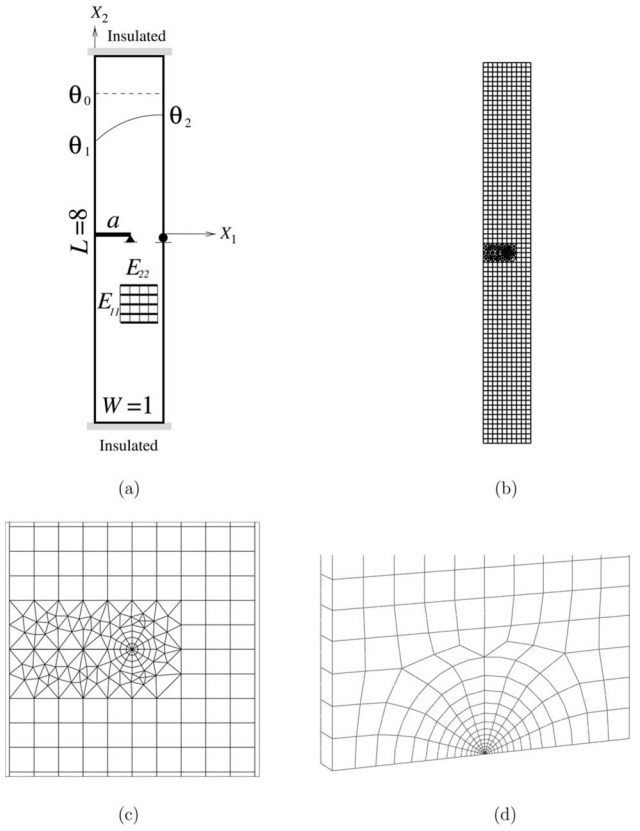

Fig. 3 Example 1: (*a*) An exponentially graded orthotropic strip with an edge crack under thermal loads, (*b*) complete finite element mesh, (*c*) mesh detail showing 12 sectors (S12) and 4 rings (R4) around the crack tip employed in the 2D analysis, and (*d*) mesh detail showing 10 sectors (S10) and 14 rings (R14) around the crack tip employed in the 3D analysis

5.1 Strip With an Edge Crack. Erdogan and Wu [16] solved the present thermal fracture problem with isotropic FGMs, and this example will provide partial verification of the M-integral formulation for the T-stress and SIFs in orthotropic FGMs. Figure 3(*a*) shows an edge crack of length a in an orthotropic exponentially graded plate subjected to steady-state thermal loads. Figure 3(*b*) shows the complete mesh configuration. Figure 3(*c*) shows the 2D mesh detail showing 12 sectors (S12) and 4 rings (R4) of elements around the crack tip. Figure 3(*d*) shows the 3D mesh detail showing 10 sectors (S10) and 14 rings (R14) of 20-node brick elements around the crack tip. Due to lack of verification examples, the 3D fracture analysis with identical boundary conditions is performed to verify the 2D T-stress solutions for the isotropic FGM case using the 3D formulation of the interaction integral (see the paper by Walters et al. [41]) and constraining out-of-plane displacements. The displacement boundary condition is prescribed such that $u_2=0$ at the crack-tip node and $u_1=u_2=0$ for the node at the coordinates $X_1=W$ and $X_2=0$. The 2D mesh discretization consists of 907 Q8, 47 T6, and 12 T6qp elements, with a total of 966 elements and 2937 nodes, and the 3D mesh discretization consists of 10 15-node quarter-point wedge elements and 528 20-node brick elements, with a total of 538 elements and

[2]The FEM code FGM-FRANC2D is upgraded based on I-FRANC2D [31] at the University of Illinois at Urbana-Champaign and also FRANC2D [54,55] at Cornell University.

Table 1 Example 1: The normalized Mode-I SIF in isotropic and orthotropic FGMs under thermal loads. The normalizing factor $K_0=[(E_{22}^L\alpha_{22}^L\theta_0)/(1-\nu_{12})]\sqrt{\pi a}$ for the orthotropic FGMs, and $K_0=[(E^L\alpha^L\theta_0)/(1-\nu)]\sqrt{\pi a}$ for the isotropic FGMs. Case 1: $E^R/E^L=5$, $\alpha^R/\alpha^L=2$; Case 2: $E^R/E^L=10$, $\alpha^R/\alpha^L=2$, $\kappa^R/\kappa^L=10$ (see Fig. 3).

			K_I/K_0					
			Present					
Case	Load	Analysis type	Ortho	Iso	Erdogan and Wu [16]	Walters et al.[41]	Yildirim et al.[58]	Yildirim [42]
1	$\theta_1=0.5\theta_0$	$pl-\varepsilon$	0.1610	0.0128	0.0125	0.0127	0.0124	0.0128
	$\theta_2=0.5\theta_0$	$pl-\sigma$	0.1589	0.0090	—	—	—	0.0090
	$\theta_1=0.05\theta_0$	$pl-\varepsilon$	0.3064	0.0244	0.0245	0.0241	0.0238	—
	$\theta_2=0.05\theta_0$	$pl-\sigma$	0.3040	0.0173	—	—	—	—
2	$\theta_1=0.2\theta_0$	$pl-\varepsilon$	0.2869	0.0334	0.0335	0.0335	0.0331	0.034
	$\theta_2=0.5\theta_0$	$pl-\sigma$	0.2850	0.0235	—	—	—	0.024
	$\theta_1=0.05\theta_0$	$pl-\varepsilon$	0.3007	0.0406	0.0410	0.0409	0.0404	—
	$\theta_2=0.5\theta_0$	$pl-\sigma$	0.2986	0.0288	—	—	—	—

4054 nodes.

Young's moduli, shear modulus, and thermal expansion (α_{ii}) and thermal conductivity (κ_{ii}) coefficients are exponential functions of X_1, while Poisson's ratios are constant. In this example, constant Poisson's ratios are used because they have negligible effect on fracture behavior of FGMs under pure Mode-I conditions and some mixed-mode conditions (see Ref. [57] for more information).

Below are the data used for finite element analysis (FEA).

In plane strain and plane stress,

$$a=0.5,\quad W=1,\quad L=8$$

$$\theta_1=\theta(X_1=0)\text{ and }\theta_2=\theta(X_1=W),\quad \theta_0=10^\circ\text{C}$$

In isotropic case,

$$E(X_1)=E^Le^{\beta X_1}\text{ and }\alpha(X_1)=\alpha^Le^{\gamma X_1}$$

$$E^L=E(X_1=0)=1.0\text{ and }E^R=E(X_1=W)=5\text{ or }10$$

$$\nu(X_1)=\nu=0.3$$

$$\alpha^L=\alpha(X_1=0)=0.01\ (^\circ\text{C}^{-1})\text{ and }\alpha^R=\alpha(X_1=W)=0.02\ (^\circ\text{C}^{-1})$$

In orthotropic case:

$$E_{11}(X_1)=E_{11}^Le^{\beta_{11}X_1},\quad E_{22}(X_1)=E_{22}^Le^{\beta_{22}X_1},$$

$$E_{33}(X_1)=E_{33}^Le^{\beta_{33}X_1},\quad G_{12}(X_1)=G_{12}^Le^{\beta_{12}X_1}$$

$$\beta_{11}=\beta_{22}=\beta_{33}=\beta_{12}=\beta$$

$$E_{11}^L=2.0\text{ and }E_{11}^R=10\text{ or }20,\quad E_{22}^L=1.0\text{ and }E_{22}^R=5.0\text{ or }10$$

$$E_{33}^L=0.5\text{ and }E_{22}^R=2.5\text{ or }5.0,\ G_{12}^L=0.3\text{ and }G_{12}^R=1.5\text{ or }3.0$$

$$\nu_{12}(X_1)=\nu_{12}=0.3,\quad \nu_{13}(X_1)=\nu_{13}=0.2,\quad \nu_{23}(X_1)=\nu_{23}=0.15$$

$$\alpha_{11}(X_1)=\alpha_{11}^Le^{\gamma_{11}X_1},\quad \alpha_{22}(X_1)=\alpha_{22}^Le^{\gamma_{22}X_1},\quad \alpha_{33}(X_1)=\alpha_{33}^Le^{\gamma_{33}X_1}$$

$$\gamma_{11}=\gamma_{22}=\gamma_{33}=\gamma$$

$$\alpha_{11}^L=0.02(^\circ\text{C}^{-1})\text{ and }\alpha_{11}^R=0.04(^\circ\text{C}^{-1})$$

$$\alpha_{22}^L=0.01(^\circ\text{C}^{-1})\text{ and }\alpha_{22}^R=0.02(^\circ\text{C}^{-1})$$

$$\alpha_{33}^L=0.015(^\circ\text{C}^{-1})\text{ and }\alpha_{33}^R=0.03(^\circ\text{C}^{-1})$$

Table 1 presents FEM results for the normalized Mode-I SIF in isotropic and orthotropic FGMs under various thermal loads in comparison with, for the isotropic case, the solutions provided by Erdogan and Wu [16], Walters et al. [41], Yildirim et al. [58], and Yildirim [42]. The FEM results for the isotropic FGM case show good agreement with the reference results. Case 1 considers constant thermal conductivity coefficients (κ or κ_{ii}) and constant temperature fields in the entire region, and Case 2 considers such varying coefficients as

$$\kappa(X_1)=\kappa^Le^{\delta X_1}\quad\text{where }\delta=\frac{1}{W}\ln\left(\frac{\kappa^R}{\kappa^L}\right),\quad \kappa^L=1\text{ and }\kappa^R=10$$

for the isotropic case and

$$\kappa_{11}(X_1)=\kappa_{11}^Le^{\delta_{11}X_1}\text{ where }\delta_{11}=\frac{1}{W}\ln\left(\frac{\kappa_{11}^R}{\kappa_{11}^L}\right),\ \kappa_{11}^L=1\text{ and }\kappa_{11}^R=10$$

$$\kappa_{22}(X_1)=\kappa_{22}^Le^{\delta_{22}X_1}\text{ where }\delta_{22}=\frac{1}{W}\ln\left(\frac{\kappa_{22}^R}{\kappa_{22}^L}\right),\ \kappa_{22}^L=5\text{ and }\kappa_{22}^R=50$$

for the orthotropic case. For both cases, the same temperature fields are obtained for the one-dimensional thermal diffusion along the horizontal axis. Note that the magnitudes of the normalized Mode-I SIF in the given orthotropic FGMs are much larger than those for isotropic FGMs, and the orthotropy affects SIFs significantly. Table 2 presents the FEM results for the T-stress in isotropic (both 2D and 3D analyses) and orthotropic FGMs. The T-stress results from 2D and 3D analyses are in good agreement for isotropic FGMs. Note that the T-stress is positive for the isotropic FGM case but is negative for the orthotropic FGM case. Note also that the absolute magnitudes of the T-stress in the orthotropic FGMs are much larger than those for isotropic FGMs. Also larger absolute values for SIFs and the T-stress are obtained for the plane-strain case than for the plane-stress case.

No reference solutions for the T-stress and SIFs are available for orthotropic FGMs. The 2D FEM solutions provided here, however, are obtained performing orthotropic FEA and using the M-integral formulation with the orthotropic auxiliary fields and are the same as those obtained using the isotropic FEA and the M-integral formulation with isotropic auxiliary fields. The stress method for the T-stress seems to work for the isotropic FGM case but not for the orthotropic FGM case with the given mesh discretization. The stress method also showed strong mesh dependence for the orthotropic case, and thus this simple nondomain integral technique is not used in this paper.

5.2 Plate With an Inclined Center Crack. This example is specially designed to verify the interaction integral method equipped with thermal effects for mixed-mode crack problems based on the equivalence of thermal and mechanical loads. For the sake of maintaining equivalence, it is strictly assumed that the

Table 2 Example 1: The *T*-stress in isotropic (2D and 3D) and orthotropic (2D) FGMs under thermal loads (see Fig. 3)

Case	Material variation	Load	Analysis type	T (ortho)	T (2D-iso)	T (3D-iso)
1	$E^R/E^L=5$	$\theta_1=\theta_2=0.5\theta_0$	$pl-\varepsilon$	−0.1597	0.0067	0.0060
	$\alpha^R/\alpha^L=2$		$pl-\sigma$	−0.1499	0.0046	—
		$\theta_1=\theta_2=0.05\theta_0$	$pl-\varepsilon$	−0.3031	0.0126	0.0115
			$pl-\sigma$	−0.2846	0.0090	—
2	$E^R/E^L=10$	$\theta_1=0.2\theta_0$	$pl-\varepsilon$	−0.2733	0.0183	0.0174
	$\alpha^R/\alpha^L=2$	$\theta_2=0.5\theta_0$	$pl-\sigma$	−0.2573	0.0128	—
		$\theta_1=0.05\theta_0$	$pl-\varepsilon$	−0.2810	0.0228	0.0218
		$\theta_2=0.5\theta_0$	$pl-\sigma$	−0.2648	0.0160	—

temperature field is not affected by the existence of the crack and heat flux is directed along the horizontal direction. Thus temperature varies in the horizontal direction. This example is employed to verify the *T*-stress solutions in a weak sense due to the lack of reference *T*-stress solutions in orthotropic homogeneous and graded materials under thermal loads.

Figures 4(*a*) and 4(*b*) show an inclined center crack of length $2a$ located with a geometric angle $\bar{\theta}$ (counterclockwise) in an orthotropic FGM plate subjected to thermal and equivalent fixed-grip loadings, respectively; Fig. 4(*c*) depicts the complete finite element mesh; and Fig. 4(*d*) shows four contours enclosing four corresponding domains that are used for EDI computation of the *M*-integral and the mesh detail using 12 sectors (S12) and 4 rings (R4) of elements around the crack tips. The mesh discretization consists of 1641 Q8, 94 T6, and 24 T6qp elements, with a total of 1759 elements and 5336 nodes. The two equivalent loadings result in a uniform mechanical strain $\varepsilon_{22}^m(X_1,X_2)=\bar{\varepsilon}$ in an uncracked plate, which corresponds to $\sigma_{22}(X_1,10)=\bar{\varepsilon}E^0e^{\beta X_1}$ for isotropic FGMs and $\sigma_{22}(X_1,10)=\bar{\varepsilon}E_{22}^0e^{\beta X_1}$ for orthotropic FGMs (see Figs. 4(*a*) and 4(*b*)). Young's moduli, shear modulus, and thermal expansion coefficients ($\alpha_{ii}(i=1,2)$) are exponential functions of X_1, while Poisson's ratio is assumed to be constant. Below are the data used for FEA.

In plane stress, nonhomogeneity parameter: $\beta a=0.5$,

$$a/W=0.1, \quad L/W=1.0, \quad \bar{\theta}=0-90 \text{ deg}$$

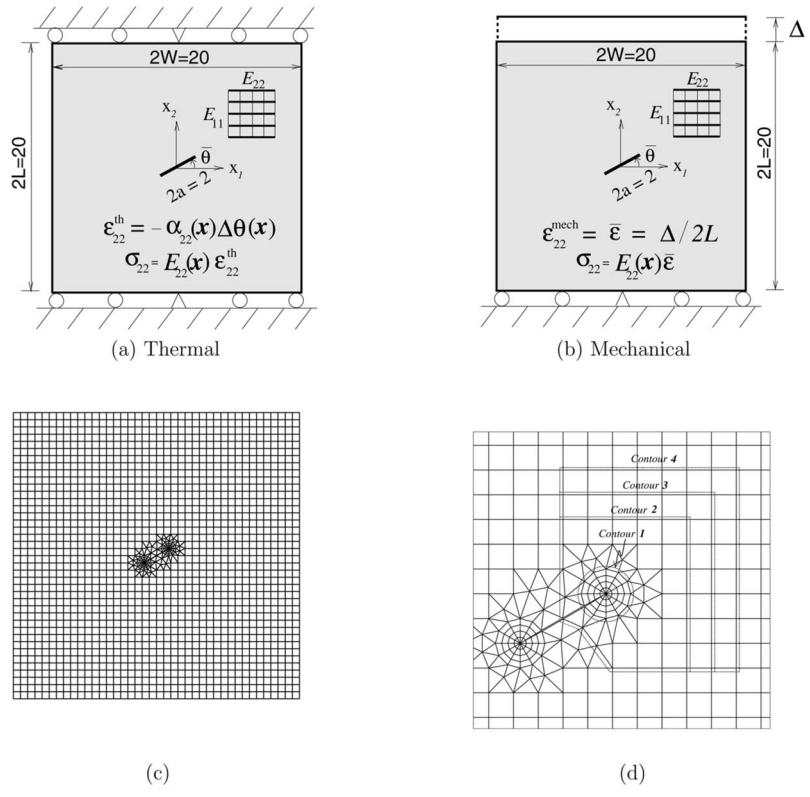

Fig. 4 Example 2: (*a*) An orthotropic FGM plate with an inclined crack with geometric angle $\bar{\theta}$ subjected to thermal loads, (*b*) mechanically equivalent fixed-grip loading, (*c*) typical finite element mesh, and (*d*) mesh detail using 12 sectors (S12) and 4 rings (R4) around the crack tips and four contour surrounding four domains used for interaction integrals ($\bar{\theta}$=30 deg counterclockwise)

Table 3 Example 2: Normalized mixed-mode SIFs in *orthotropic* FGMs for $\beta a=0.5$ ($K_0=\bar{\varepsilon}E_{22}^0\sqrt{\pi a}$) (see Fig. 4). The difference of each SIF value lies in the order of between $O(10^{-3})$ and $O(10^{-4})$.

Method	$\bar{\theta}$	K_I^+/K_0	K_{II}^+/K_0	K_I^-/K_0	K_{II}^-/K_0
M-integral (thermal)	0 deg	1.4279	0.0000	0.6663	0.0000
	18 deg	1.3224	0.2158	0.5992	0.2436
	36 deg	1.0194	0.4085	0.4164	0.4151
	54 deg	0.5997	0.4479	0.1803	0.4383
	72 deg	0.2157	0.2903	0.0061	0.2820
	90 deg	0.0000	0.0000	0.0000	0.0000
M-integral (mechanical)	0 deg	1.4279	0.0000	0.6663	0.0000
	18 deg	1.3224	0.2176	0.5997	0.2436
	36 deg	1.0177	0.4097	0.4150	0.4160
	54 deg	0.6008	0.4477	0.1814	0.4379
	72 deg	0.2154	0.2906	0.0056	0.2822
	90 deg	0.0000	0.0000	0.0000	0.0000

$$(\varepsilon_{11})_{\text{th}}=(\varepsilon_{22})_{\text{th}}=-\alpha(X_1)\Delta\theta(X_1)=1.0$$

$$\text{with } \alpha=\alpha_{11}=\alpha_{22},\quad (\varepsilon_{22})_{\text{mech}}=\bar{\varepsilon}=\Delta/(2L)=1.0$$

In isotropic case,

$$E(X_1)=E^0e^{\beta X_1},\quad \alpha(X_1)=\alpha^0e^{\delta X_1},\quad \nu(X_1)=\nu,$$

$$E^0=1.0,\quad \nu=0.3$$

In orthotropic case,

$$E_{11}(X_1)=E_{11}^0e^{\beta X_1},\quad E_{22}(X_1)=E_{22}^0e^{\beta X_1}$$

$$G_{12}(X_1)=G_{12}^0e^{\beta X_1},\quad \nu_{12}(X_1)=\nu_{12}^0$$

$$\alpha_{11}(X_1)=\alpha_{11}^0e^{\delta_1 X_1},\quad \alpha_{22}(X_1)=\alpha_{22}^0e^{\delta_2 X_1}$$

$$E_{11}^0=10^4,\quad E_{22}^0=10^3,\quad G_{12}^0=1216,\quad \nu_{12}^0=0.3 \qquad (29)$$

Table 3 provides the present FEM results for normalized mixed-mode SIFs in orthotropic FGMs subjected to thermal loading in comparison with those obtained for equivalent mechanical-loading. All FEM results in the table are converged solutions using Contours 2–4 that surround the corresponding integration domains (see Fig. 4(*d*)). The FEM results for SIFs are in good agreement within the order of between $O(10^{-3})$ and $O(10^{-4})$. Table 4 compares the FEM results for the normalized T-stress in orthotropic FGMs subjected to the thermal loading with those for the equivalent-mechanical loading. Comparing the two equivalent systems, we observe that, for the homogeneous case with $\beta a=0.0$, the average difference was 2.9%, and for the FGM case with $\beta a=0.5$, the average difference was 3.2%. These calculations considered all the given geometric angles except for 30 deg, which involves reference solutions of very small (or zero) magnitude. Table 5 compares the FEM results for normalized T-stress obtained (using the orthotropic M-integral formulation) for the isotropic FGMs under thermal loading with those reported by Paulino and Dong [59] who used the singular integral equation method and with those for the equivalent-mechanical loading. The present FEM results obtained by degenerating the orthotropic M-integral formulation to isotropic counterpart are in good agreement with those by Paulino and Dong [60]. Comparing the two equivalent systems, we observe that, for the homogeneous case with $\beta a=0.0$, the average difference was 1.2%, and for the FGM case with $\beta a=0.5$, the average difference was 1.4%. These calculations considered all the given geometric angles except for 45 deg, which involves reference solutions of very small (or zero)

Table 4 Example 2: Normalized *T*-stress in *orthotropic* FGMs for $\beta a=0.5$ ($\sigma_0=\bar{\varepsilon}E_{22}^0$) (see Fig. 4). The average difference was 2.9% for the homogeneous case and was 3.2% for the FGM case. These calculations considered all the given geometric angles except for 30 deg which involves reference solutions of small magnitude.

		M-integral (thermal)		M-integral (mechanical)	
βa	$\bar{\theta}$	$T(+a)/\sigma_0$	$T(-a)/\sigma_0$	$T(+a)/\sigma_0$	$T(-a)/\sigma_0$
$\beta a=0.0$	0 deg	−2.972	−2.972	−3.122	−3.122
	15 deg	−1.746	−1.746	−1.633	−1.633
	30 deg	0.0084	0.0084	0.0300	0.0300
	45 deg	0.707	0.707	0.714	0.714
	60 deg	0.950	0.950	0.933	0.933
	75 deg	1.001	1.001	0.987	0.987
	90 deg	1.002	1.002	0.996	0.996
$\beta a=0.5$	0 deg	−2.532	−2.643	−2.812	−2.724
	15 deg	−1.236	−1.343	−1.412	−1.403
	30 deg	0.212	0.094	0.158	0.079
	45 deg	0.819	0.713	0.784	0.700
	60 deg	0.983	0.915	0.971	0.909
	75 deg	1.010	0.977	1.003	0.973
	90 deg	1.001	1.001	0.996	0.996

Table 5 Example 2: Normalized *T*-stress in *isotropic* FGMs under thermal loads in comparison with available reference solutions considering equivalent-mechanical loads for $\beta a=0.5$ ($\sigma_0=\bar{\varepsilon}E^0$). The domains surrounded by Contours 2–4 have been used (see Fig. 4(*d*)) and the path-independent FEM results are obtained (see Fig. 4).

		M-integral (thermal)		Paulino and Dong [59]		*M*-integral (mechanical) [44]	
βa	$\bar{\theta}$	$T(+a)/\sigma_0$	$T(-a)/\sigma_0$	$T(+a)/\sigma_0$	$T(-a)/\sigma_0$	$T(+a)/\sigma_0$	$T(-a)/\sigma_0$
$\beta a=0.5$	0 deg	−0.879	−0.854	−0.867	−0.876	−0.896	−0.858
	15 deg	−0.757	−0.743	−0.748	−0.763	−0.773	−0.747
	30 deg	−0.418	−0.431	−0.420	−0.444	−0.434	−0.436
	45 deg	0.049	0.016	0.039	0.010	0.036	0.011
	60 deg	0.525	0.490	0.513	0.490	0.513	0.484
	75 deg	0.878	0.857	0.870	0.858	0.868	0.850
	90 deg	1.003	1.003	1.000	1.000	0.994	0.994

magnitude. Note that the FEM results for the *T*-stress considering thermal loads, however, are not exactly identical but very similar to those for equivalent-mechanical loads. Given the same discretization, we observe that the *T*-stress is more sensitive to the present domain-independent *M*-integral for such two equivalent loads than SIFs. Note also that material orthotropy increases the average differences for the *T*-stress.

More discussion is provided here on the equivalence of the *T*-stress results for thermal and mechanical loading cases. For the sake of simplicity, first consider the homogeneous case ($\beta a=0.0$) in which case the first integral in Eq. (11) is the complete domain *M*-integral and the second integral vanishes. The only difference between thermal and mechanical load cases in this domain *M*-integral is $u^t_{1,1}$ knowing that the auxiliary fields and σ_{ij} and $u^t_{2,1}$ are the same for both cases (compare the first integrals in Eq. (11) and (12)). For the thermal loading case along with the plane-stress case,

$$u^t_{1,1}=\varepsilon^t_{11}=\varepsilon^m_{11}+\alpha_{11}\Delta\theta$$

$$u^t_{2,1}=u_{2,1}=\varepsilon^m_{21} \tag{30}$$

For the FGM case, the same analogy can be applied and the complete *M*-integral is given in Eq. (11). For the present example, thermal strains $\varepsilon^{\text{th}}_{ij}$ are considered constant (e.g., $\varepsilon^{\text{th}}_{11}=\varepsilon^{\text{th}}_{22}=1.0$ and $\varepsilon^{\text{th}}_{12}=0$). Thus its derivative ($\varepsilon^{\text{th}}_{ij,1}=\alpha_{ij,1}(\Delta\theta)+\alpha_{ij}(\Delta\theta)_{,1}$) is zero meaning that the third term in the second integral of Eq. (11) vanishes. Again the only difference between thermal and mechanical load cases in this domain *M*-integral is $u^t_{1,1}$ (compare Eq. (11) with Eq. (12)). For both homogeneous and FGM cases, the difference of $u^t_{1,1}$ in the domain *M*-integral is taken into account in the derivation of *T*-stress (see Eq. (22)) and it results in the additional term (i.e., $(\alpha_{11})_{\text{tip}}\Delta\theta_{\text{tip}}/a^{\text{tip}}_{11}$) in Eq. (26). Thus we can conclude that the *M*-integral for the thermal loading case is identical to that for the equivalent-mechanical loading case. The difference of $u^t_{1,1}$ is also true for the *M*-integral for SIFs because the actual fields are the same for SIFs and *T*-stress for the given mesh discretization. Regardless of the continuum-based theoretical equivalence and the self-consistent *M*-integral formulation for orthotropic FGMs, we observe more difference in the *T*-stress than in SIFs in this specific example. We may conclude that such difference in the *T*-stress results is due to the characteristics of the selected auxiliary fields interacting with the actual fields in the given finite mesh discretization.

The present *M*-integral used in this verification example can deal with any kinds of smooth material gradation, crack orientation, and thermal gradients. First, although we consider a continuum function (e.g., exponential) in this example, material derivatives ($C_{ijkl,m}$, $\alpha_{ij,m}$) are calculated using shape function derivatives in the FEM and so the present *M*-integral is generalized for any kinds of smooth material gradation. Second, this example considers a crack that is inclined with respect to the loading and the two orthotropic axes. The present *M*-integral is formulated for general mixed-mode crack problems as long as the realistic temperature fields involving a crack are provided as an input. Finally, although constant thermal strains are considered, exponential gradations for thermal expansion coefficients (see Eq. (29)) and temperature are used for the sake of generality as follows:

$$\varepsilon^{\text{th}}_{ii}=\alpha_{ii}(X)\Delta\theta(X_1)=1.0$$

$$\alpha_{ii}(X_1)=\alpha^0_{ii}e^{\delta_1 X_1}\ \text{and}\ \Delta\theta(X_1)=\frac{1}{\alpha^0_{ii}}e^{-\delta_i X_1} \tag{31}$$

and these varying properties are incorporated into finite elements.

5.3 Thermal Barrier Coating With an Edge Crack. TBCs are subjected to surface cracking due to thermally induced residual stresses, and in this case they may contain periodic multiple surface cracks perpendicular to the coating surface, which is considered in this example. Figure 5(*a*) shows an orthotropic functionally graded TBC deposited on the isotropic bond coat and isotropic metallic substrate [42]. The isotropic metallic substrate is made of a nickel-based superalloy. The orthotropic FGM coating is 100% orthotropic zirconia-yttria at $X_1=0$ and 100% isotropic nickel-chromium-aluminum-zirconium (NiCrAlY) bond coat at $X_1=W_1$. The hyperbolic-tangent function is used to simulate potential interfacial diffusion using the steep gradation between the bond coat and the substrate. The orthotropic FGM coating is considered to contain a periodic crack of length *a* with the interval *b*. Due to periodicity, only one crack is modeled. Figure 5(*b*) shows the complete mesh configuration. Figure 5(*c*) shows the mesh detail using 16 sectors (S16) and 4 rings (R4) of elements around the crack tip. The representative mesh discretization consists of 800 Q8, 212 T6, and 16 T6qp elements, with a total of 1028 elements and 2975 nodes. The TBC system is assumed to be initially at a uniform temperature of θ_0 and is subjected to a temperature change due to one-dimensional (along the horizontal axis) steady-state diffusion involving temperature boundary conditions. Below are the data used for FEA.

For plane strain

$$a=0.1-0.9,\quad b=2,\quad W_1=1.0,\quad W_2=0.5,\quad W_3=5.0$$

$$\theta_1=\theta(X_1=0)=0.2\theta_0\ \text{and}\ \theta_3=\theta(X_1=6.5)=0.5\theta_0$$

$$\text{with}\ \theta_0=1000\,^\circ\text{C}$$

For the orthotropic FMG coating region,

$$E_{11}(X_1)=E^c_{11}+(E_{bc}-E^c_{11})X_1^2,\quad E_{22}(X_1)=E^c_{22}+(E_{bc}-E^c_{22})X_1^2$$

$$E_{33}(X_1)=E^c_{33}+(E_{bc}-E^c_{33})X_1^2,\quad G_{12}(X_1)=G^c_{12}+(G_{bc}-G^c_{12})X_1^2$$

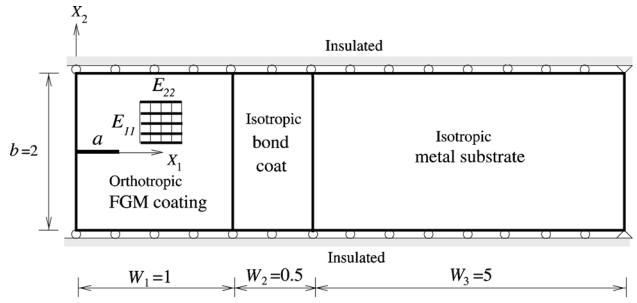

(*a*)

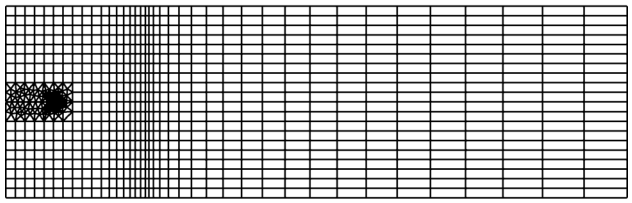

(*b*)

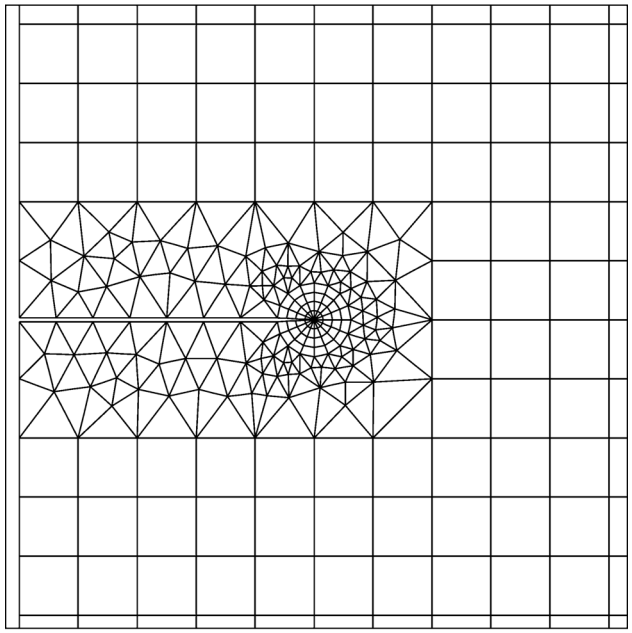

(*c*)

Fig. 5 Example 3: (*a*) A crack in an orthotropic functionally graded TBC, (*b*) complete finite element mesh, and (*c*) mesh detail using 16 sectors (S16) and 4 rings (R4) around the crack tip

$$\nu_{ij}(X_1) = \nu_{ij}^c + (\nu_{bc} - \nu_{ij}^c)X_1 \quad \text{(i.e., } \nu_{12}, \nu_{13}, \nu_{23})$$

$$\alpha_{ii}(X_1) = \alpha_{ii}^c + (\alpha_{bc} - \alpha_{ii}^c)X_1 \quad (i = 1,2,3)$$

$$\kappa_{ii}(X_1) = \kappa_{ii}^c + (\kappa_{bc} - \kappa_{ii}^c)X_1^2 \quad (i = 1,2,3)$$

$$E_{11}^c = 27.6 \text{ GPa},\ E_{22}^c = 120 \text{ GPa},\ E_{33}^c = 50 \text{ GPa},\ G_{12}^c = 34 \text{ GPa}$$

$$\nu_{12}^c = 0.25, \quad \nu_{13}^c = 0.2, \quad \nu_{23}^c = 0.15$$

$$\alpha_{11}^c = 10.01 \times 10^{-6}, \quad \alpha_{22}^c = 15 \times 10^{-6}, \quad \alpha_{33}^c = 12 \times 10^{-6}\ (^\circ\text{C}^{-1})$$

$$\kappa_{11}^c = 1, \quad \kappa_{22}^c = 5, \quad \kappa_{33}^c = 3 \text{ W/m K}$$

$$E_{bc} = 137.9 \text{ GPa}, \quad \nu_{bc} = 0.27, \quad \alpha_{bc} = 15.16 \times 10^{-6}$$

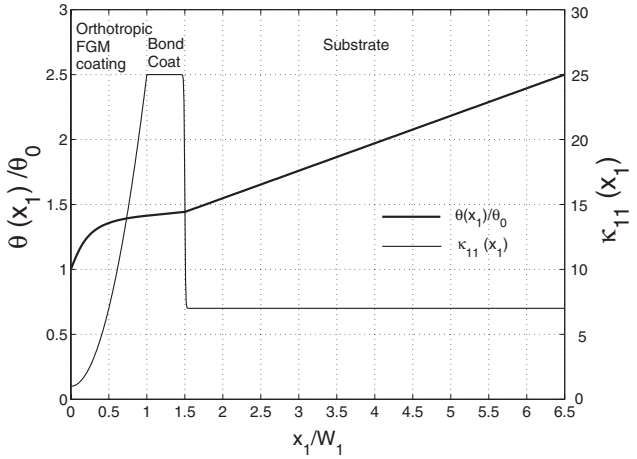

Fig. 6 Example 3: Variations of the thermal conductivity coefficient ($\kappa_{11}(X_1)$) and the resulting normalized temperature field ($\theta(X_1)/\theta_0$)

$$\kappa_{bc} = 25 \text{ W/m K}$$

For the isotropic region including the bond coat and the substrate,

$$P(X_1) = \frac{P_s + P_{bc}}{2} + \frac{P_s - P_{bc}}{2}\tanh(\beta X_1) \text{ with } \beta = 100$$

$$\text{and } P = E,\ \nu,\ \alpha, \text{ and } \kappa$$

$$E_s = 175.8 \text{ GPa}, \quad \nu_s = 0.25, \quad \alpha_s = 13.91 \times 10^{-6}, \quad \kappa_s = 7 \text{ W/m K}$$

Figure 6 illustrates the variation of coefficient of thermal conductivity ($\kappa_{11}(X_1)$) of graded TBCs and the resulting (normalized) temperature field obtained by the Runge–Kutta method. By defining temperature boundary conditions at both ends of the TBC system, one obtains the temperature profile. The artificial steep gradation of thermal conductivity at the interfacial region between bond coat and substrate is considered to simulate potential interfacial diffusion, and it also makes the derivative of the temperature field continuous in the entire region of TBC including the point $X_1 = 1.5$.

For a crack under Mode-I conditions, the T-stress can be best characterized by a nondimensional parameter. Thus by normalizing the T-stress by $K_I(\pi a)^{-1/2}$, one obtains the (stress) biaxiality ratio ($B = T\sqrt{\pi a}/K_I$) [32], where a is the crack length. As expected, the biaxiality ratio does depend on the geometry and loading type, but not on the load magnitude, and, for FGMs, it also depends on material gradients [26].

Table 6 presents the Mode-I SIF, the T-stress, and the biaxiality ratio for various a/W ratios in orthotropic TBCs. As a/W increases, the Mode-I SIF increases as expected. The T-stress in-

Table 6 Example 3: The Mode-I SIF, *T*-stress, and the biaxiality ratio for various *a/W* ratios in an orthotropic functionally graded TBC (see Fig. 5)

a/W	K_I	T	$B = T\sqrt{\pi a}/K_I$
0.1	982.9	−295.7	−0.1686
0.2	1252	−264.2	−0.1673
0.3	1367	−243.7	−0.1731
0.4	1423	−252.7	−0.1991
0.5	1452	−285.3	−0.2463
0.6	1461	−311.1	−0.2923
0.7	1525	−350.9	−0.3412
0.8	1600	−479.3	−0.4749
0.9	1718	−601.9	−0.5891

creases as the ratio a/W changes from 0.1 to 0.3 and decreases after 0.3. The biaxiality ratio increases as the ratio a/W increases from 0.2 to 0.9. The T-stress values are negative for all the a/W ratios considered. The present example considers a graded TBC under steady-state thermal stresses; however, a graded TBC is also subjected to transient thermal stresses [42]. The present M-integral can be used for transient thermal fracture problems by applying the temperature fields corresponding to each discrete time when initial effects are negligible. The true transient fracture analysis for orthotropic FGMs is beyond the scope of this paper.

6 Discussion

This paper presents a generalized interaction integral method to evaluate the T-stress and SIFs in orthotropic FGMs under steady-state thermal loads. Numerical examples presented in this paper demonstrate the accuracy and performance of the T-stress and mixed-mode SIFs obtained by the M-integral. The present formulation is capable of dealing with any kinds of crack orientation and smooth material gradations by using shape function derivatives. The present study demonstrates the following characteristics.

- The FEM results for the T-stress and mixed-mode SIFs agree well with the available reference results. For the verification of the T-stress and mixed-mode SIFs for thermal loads, two equivalent-mechanical and thermal systems are considered and well compared in Example 2. A generalized M-integral formulation for mixed-mode fracture establishes a self-consistent relationship between mechanical and thermal fracture problems.
- In general, for the same mesh discretization, the accuracy of SIFs is higher than that for the T-stress, and the accuracy in an orthotropic FGMs is lower than that for isotropic FGMs. We observe more difference in the T-stress than in SIFs in Example 2. We may conclude that such difference in the T-stress results is due to the characteristics of the selected auxiliary fields interacting with the actual fields in the given finite mesh discretization.
- The domain independence of the M-integral has been observed for both SIFs and the T-stress. However, the T-stress is more dependent on the domain than SIFs are. This may be due to the nature of the auxiliary fields used for the T-stress.
- Both material orthotropy and material gradation affect the magnitudes and signs of the T-stress and SIFs; however, it does not affect the crack-tip singularity.
- The M-integral is a domain-independent conservation integral and thus is more reliable than any direct approaches, which show strong mesh dependence, especially for nonisotropic materials.

7 Concluding Remarks

In this paper, the nonsingular T-stress as well as mixed-mode SIFs in orthotropic FGMs under steady-state thermal loads are evaluated by means of a generalized interaction integral in conjunction with FEAs. The nonequilibrium formulation is used and the corresponding auxiliary fields are tailored for orthotropic FGMs. Various numerical examples are presented to verify the accuracy and performance of the present method. The FEM results for the T-stress and SIFs showed very good agreement with the reference results.

We observed that both material orthotropy and material gradation significantly affect the magnitude and sign of the T-stress and SIFs. As such, these two factors affect crack initiation angle in linear-elastic fracture and also change crack-tip constraint in elastic-plastic fracture; however, they do not affect the crack-tip singularity. It must be noted that material gradation (i.e., thermal conductivity for steady-state thermal diffusion) in a FGM, in the case of involving the same boundary conditions as those for a homogeneous material, influences the temperature fields, which are different from those for a homogeneous material. The present study will provide basic framework for fracture analysis of potential processing-specific nonisotropic FGMs such as TBCs and solid oxide fuel cells. The potential extension of this work includes the evaluation of the T-stress and mixed-mode SIFs in 3D isotropic and orthotropic FGMs under transient thermal loading.

Acknowledgment

The author gratefully acknowledges the support from the National Science Foundation (NSF) under the Faculty Early Career Development (CAREER) Grant No. CMS-0546225 (Material Design and Surface Engineering Program, Program Director: Dr. Clark V. Cooper). The start-up support of the University of Connecticut is also acknowledged. Useful suggestions made by Dr. Mathew C. Walters regarding the numerical evaluation of the T-stress using the stress method are appreciated. Invaluable comments and suggestions by anonymous reviewers are also appreciated.

Appendix: Parameters for Anisotropic Elasticity

The presentation below follows Lekhnitskii's framework [49]. The generalized Hooke's law for stress-strain relationship is given by

$$\varepsilon_i = a_{ij}\sigma_j, \quad a_{ij} = a_{ji} \quad (i,j = 1,2,\ldots,6) \tag{A1}$$

where the compliance coefficients, a_{ij}, are contracted notations of the compliance tensor S_{ijkl}. For plane stress, the a_{ij} components of interest are

$$a_{ij} \quad (i,j = 1,2,6) \tag{A2}$$

and for plane strain, the a_{ij} components are exchanged with b_{ij} as follows:

$$b_{ij} = a_{ij} - \frac{a_{i3}a_{j3}}{a_{33}} \quad (i,j = 1,2,6) \tag{A3}$$

The parameters α_k and β_k are the real and imaginary parts of $\mu_k = \alpha_k + i\beta_k$, which can be determined from the following characteristic equation [49]:

$$a_{11}\mu^4 - 2a_{16}\mu^3 + (2a_{12} + a_{66})\mu^2 - 2a_{26}\mu + a_{22} = 0 \tag{A4}$$

where the roots μ_k are always complex or purely imaginary in conjugate pairs as $\mu_1, \bar{\mu}_1; \mu_2, \bar{\mu}_2$.

References

[1] Sih, G. C., Paris, P. C., and Irwin, G. R., 1965, "On Cracks in Rectilinearly Anisotropic Bodies," Int. J. Fract. Mech., **1**(2), pp. 189–203.
[2] Williams, M. L., 1957, "On the Stress Distribution at the Base of a Stationary Crack," ASME J. Appl. Mech., **24**(1), pp. 109–114.
[3] Williams, J. G., and Ewing, P. D., 1972, "Fracture Under Complex Stress-the Angled Crack Problem," Int. J. Fract., **8**(4), pp. 441–446.
[4] Ueda, Y., Ikeda, K., Yao, T., and Aoki, M., 1983, "Characteristics of Brittle Failure Under General Combined Modes Including Those Under Bi-axial Tensile Loads," Eng. Fract. Mech., **18**(6), pp. 1131–1158.
[5] Smith, D. J., Ayatollahi, M. R., and Pavier, M. J., 2001, "The Role of T-Stress in Brittle Fracture for Linear Elastic Materials Under Mixed-Mode Loading," Fatigue Fract. Eng. Mater. Struct., **24**(2), pp. 137–150.
[6] Cotterell, B., and Rice, J. R., 1980, "Slightly Curved or Kinked Cracks," Int. J. Fract., **16**(2), pp. 155–169.
[7] O' Dowd, N. P., Shih, C. F., and Dodds, R. H., Jr., 1995, "The Role of Geometry and Crack Growth on Constraint and Implications for Ductile/Brittle Fracture," *Constraint Effects in Fracture Theory and Applications*, ASTM STP 1244 Vol. 2, American Society for Testing and Materials, Philadelphia, PA, pp. 134–159.
[8] Larsson, S. G., and Carlson, A. J., 1973, "Influence of Non-Singular Stress Terms and Specimen Geometry on Small-Scale Yielding at Crack Tips in Elastic-Plastic Materials," J. Mech. Phys. Solids, **21**(4), pp. 263–277.
[9] Betegón, C., and Hancock, J. W., 1991, "Two-Parameter Characterization of Elastic-Plastic Crack-Tip Fields," ASME J. Appl. Mech., **58**(1), pp. 104–110.
[10] Du, Z.-Z., and Hancock, J. W., 1991, "The Effect of Non-Singular Stresses on Crack-Tip Constraint," J. Mech. Phys. Solids, **39**(3), pp. 555–567.
[11] O'Dowd, N. P., and Shih, C. F., 1991, "Family of Crack-Tip Fields Characterized by a Triaxiality Parameter-I. Structure of Fields," J. Mech. Phys. Solids, **39**(8), pp. 989–1015.

[12] O'Dowd, N. P., and Shih, C. F., 1992, "Family of Crack-Tip Fields Characterized by a Triaxiality Parameter-II. Fracture Applications," J. Mech. Phys. Solids, **40**(5), pp. 939–963.
[13] Delale, F., and Erdogan, F., 1983, "The Crack Problem for a Nonhomogeneous Plane," ASME J. Appl. Mech., **50**(3), pp. 609–614.
[14] Erdogan, F., 1995, "Fracture Mechanics of Functionally Graded Materials," Composites Eng., **5**(7), pp. 753–770.
[15] Lee, Y.-D., and Erdogan, F., 1995, "Residual/Thermal Stresses in FGM and Laminated Thermal Barrier Coatings," Int. J. Fract., **69**(2), pp. 145–165.
[16] Erdogan, F., and Wu, B. H., 1996, "Crack Problems in FGM Layers Under Thermal Stresses," J. Therm. Stresses, **19**(3), pp. 237–265.
[17] Erdogan, F., and Wu, B. H., 1997, "The Surface Crack Problem for a Plate With Functionally Graded Properties," ASME J. Appl. Mech., **64**(3), pp. 449–456.
[18] El-Borgi, S., Erdogan, F., and Hatira, F. B., 2003, "Stress Intensity Factors for an Interface Crack Between a Functionally Graded Coating and a Homogeneous Substrate," Int. J. Fract., **123**, pp. 139–162.
[19] Erdogan, F., and Chiu, T. C., 2003, "Plane Strain and Axisymmetric Spallation of Graded Coatings Under Thermal Loading," J. Therm. Stresses, **26**(6), pp. 497–523.
[20] El-Borgi, S., Erdogan, F., and Hidri, L., 2004, "A Partially Insulated Embedded Crack in an Infinite Functionally Graded Medium Under Thermo-Mechanical Loading," Int. J. Eng. Sci., **42**, pp. 371–393.
[21] Yildirim, B., and Erdogan, F., 2004, "Edge Crack Problems in Homogeneous and Functionally Graded Material Thermal Barrier Coatings Under Uniform Thermal Loading," J. Therm. Stresses, **27**(4), pp. 311–329.
[22] Becker, Jr., T. L., Cannon, R. M., and Ritchie, R. O., 2001, "Finite Crack Kinking and T-Stresses in Functionally Graded Materials," Int. J. Solids Struct., **38**(32–33), pp. 5545–5563.
[23] Kim, J.-H., and Paulino, G. H., 2003, "T-Stress, Mixed-Mode Stress Intensity Factors, and Crack Initiation Angles in Functionally Graded Materials: A Unified Approach Using the Interaction Integral Method," Comput. Methods Appl. Mech. Eng., **192**(11–12), pp. 1463–1494.
[24] Dag, S., 2007, "Mixed-Mode Fracture Analysis of Functionally Graded Materials Under Thermal Stresses: A New Approach Using JK-Integral," J. Therm. Stresses, **30**, pp. 269–296.
[25] Eischen, J. W., 1987, "Fracture of Non-Homogeneous Materials," Int. J. Fract., **34**(1), pp. 3–22.
[26] Kim, J.-H., and Paulino, G. H., 2002, "Finite Element Evaluation of Mixed-Mode Stress Intensity Factors in Functionally Graded Materials," Int. J. Numer. Methods Eng., **53**(8), pp. 1903–1935.
[27] Sampath, S., Herman, H., Shimoda, N., and Saito, T., 1995, "Thermal Spray Processing of FGMs," MRS Bull., **20**(1), pp. 27–31.
[28] Hart, N. T., Brandon, N. P., Day, M. J., and Shemilt, J. E., 2001, "Functionally Graded Cathodes for Solid Oxide Fuel Cells," J. Mater. Sci., **36**, pp. 1077–1085.
[29] Kaysser, W. A., and Ilschner, B., 1995, "FGM Research Activities in Europe," MRS Bull., **20**(1), pp. 22–26.
[30] Kim, J.-H., and Paulino, G. H., 2004, "T-Stress in Orthotropic Functionally Graded Materials: Lekhnitskii and Stroh Formalisms," Int. J. Fract., **126**(4), pp. 345–389.
[31] Kim, J.-H., and Paulino, G. H., 2005, "Consistent Formulations of the Interaction Integral Method for Fracture of Functionally Graded Materials," ASME J. Appl. Mech., **72**, pp. 351–364.
[32] Leevers, P. S., and Radon, J. C. D., 1982, "Inherent Stress Biaxiality in Various Fracture Specimen," Int. J. Fract., **19**(4), pp. 311–325.
[33] Cardew, G. E., Goldthorpe, M. R., Howard, I. C., and Kfouri, A. P., 1985, "On the Elastic T-Term," *Fundamentals of Deformation and Fracture: Eshelby Memorial Symposium*.
[34] Kfouri, A. P., 1986, "Some Evaluations of the Elastic T-Term Using Eshelby's Method," Int. J. Fract., **30**(4), pp. 301–315.
[35] Sladek, J., Sladek, V., and Fedelinski, P., 1997, "Contour Integrals for Mixed-Mode Crack Analysis: Effect of Nonsingular Terms," Theor. Appl. Fract. Mech., **27**(2), pp. 115–127.
[36] Ayatollahi, M. R., Pavier, M. J., and Smith, D. J., 1998, "Determination of T-Stress From Finite Element Analysis for Mode I and Mixed Mode I/II Loading," Int. J. Fract., **91**, pp. 283–298.
[37] Walters, M. C., 2007, private Communication.
[38] Chen, C. S., Krause, R., Pettit, R. G., Banks-Sills, L., and Ingraffea, A. R., 2001, "Numerical Assessment of T-Stress Computation Using a *p*-Version Finite Element Method," Int. J. Fract., **107**(2), pp. 177–199.
[39] Dolbow, J., and Gosz, M., 2002, "On the Computation of Mixed-Mode Stress Intensity Factors in Functionally Graded Materials," Int. J. Solids Struct., **39**(9), pp. 2557–2574.
[40] Rao, B. N., and Rahman, S., 2003, "Mesh-Free Analysis of Cracks in Isotropic Functionally Graded Materials," Eng. Fract. Mech., **70**(1), pp. 1–27.
[41] Walters, M. C., Paulino, G. H., and Dodds, R. H., Jr., 2004, "Stress Intensity Factors for Surface Cracks in Functionally Graded Materials Under Mode I Thermomechanical Loading," Int. J. Solids Struct., **41**, pp. 1081–1118.
[42] Yildirim, B., 2006, "An Equivalent Domain Integral Method for Fracture Analysis of Functionally Graded Materials Under Thermal Stresses," J. Therm. Stresses, **29**, pp. 371–397.
[43] Amit, K. C., and Kim, J.-H., 2008, "Interaction Integrals for Thermal Fracture of Functionally Graded Materials," Eng. Fract. Mech., **75**, pp. 2542–2565.
[44] Paulino, G. H., and Kim, J.-H., 2004, "A New Approach to Compute T-Stress in Functionally Graded Materials Using the Interaction Integral Method," Eng. Fract. Mech., **71**(13–14), pp. 1907–1950.
[45] Kim, J.-H., and Paulino, G. H., 2002, "Mixed-Mode Fracture of Orthotropic Functionally Graded Materials Using Finite Elements and the Modified Crack Closure Method," Eng. Fract. Mech., **69**(14–16), pp. 1557–1586.
[46] Dag, S., 2006, "Thermal Fracture Analysis of Orthotropic Functionally Graded Materials," Eng. Fract. Mech., **73**, pp. 2802–2828.
[47] Sladek, J., Sladek, V., Zhang, Ch., and Tan, C. L., 2006, "Evaluation of Fracture Parameters for Crack Problems in FGM by a Meshless Method," J. Theor Appl. Mech., **44**, pp. 603–636.
[48] Ting, C. T. C., 1996, *Anisotropic Elasticity: Theory and Applications*, Oxford University Press, Oxford.
[49] Lekhnitskii, S. G., 1968, *Anisotropic Plates*, Gordon and Breach Science, New York.
[50] Rice, J. R., 1968, "A Path-Independent Integral and the Approximate Analysis of Strain Concentration by Notches and Cracks," ASME J. Appl. Mech., **35**(2), pp. 379–386.
[51] Anderson, T. L., 1995, *Fracture Mechanics: Fundamentals and Applications*, CRC, Boca Raton, FL.
[52] Cook, R. D., Malkus, D. S., Plesha, M. E., and Witt, R. J., 2001, *Concepts and Applications of Finite Element Analysis*, 4th ed., Wiley, New York.
[53] Wang, S. S., Corten, H. T., and Yau, J. F., 1980, "Mixed-Mode Crack Analysis of Rectilinear Anisotropic Solids Using Conservation Laws of Elasticity," Int. J. Fract., **16**(3), pp. 247–259.
[54] Wawrzynek, P. A., 1987, "Interactive Finite Element Analysis of Fracture Processes: An Integrated Approach," M.S. thesis, Cornell University, Ithaca, NY.
[55] Wawrzynek, P. A., and Ingraffea, A. R., 1991, "Discrete Modeling of Crack Propagation: Theoretical Aspects and Implementation Issues in Two and Three Dimensions," School of Civil Engineering and Environmental Engineering, Cornell University, Report No. 91-5.
[56] Kim, J.-H., and Paulino, G. H., 2002, "Isoparametric Graded Finite Elements for Nonhomogeneous Isotropic and Orthotropic Materials," ASME J. Appl. Mech., **69**(4), pp. 502–514.
[57] Paulino, G. H., and Kim, J.-H., 2004, "On the Poisson's Ratio Effect on Mixed-Mode Stress Intensity Factors and T-stress in Functionally Graded Materials," Int. J. Comput. Eng. Sci., **5**(4), pp. 833–861.
[58] Yildirim, B., Dag, S., and Erdogan, F., 2005, "Three Dimensional Fracture Analysis of FGM Coatings Under Thermomechanical Loading," Int. J. Fract., **132**, pp. 369–395.
[59] Paulino, G. H., and Dong, Z., "A Novel Application of the Singular Integral Equation Approach to Evaluate T-Stress in Functionally Graded Materials," unpublished.
[60] Konda, N., and Erdogan, F., 1994, "The Mixed Mode Crack Problem in a Nonhomogeneous Elastic Medium," Eng. Fract. Mech., **47**(4), pp. 533–545.

H. M. Yin

G. H. Paulino[1]
e-mail: paulino@uiuc.edu

W. G. Buttlar

Department of Civil and Environmental Engineering,
Newmark Laboratory,
University of Illinois at Urbana-Champaign,
205 North Mathews Avenue,
Urbana, IL 61801

L. Z. Sun
Department of Civil and Environmental Engineering,
University of California,
4139 Engineering Gateway,
Irvine, CA 92697

Effective Thermal Conductivity of Functionally Graded Particulate Nanocomposites With Interfacial Thermal Resistance

By means of a fundamental solution for a single inhomogeneity embedded in a functionally graded material matrix, a self-consistent model is proposed to investigate the effective thermal conductivity distribution in a functionally graded particulate nanocomposite. The "Kapitza thermal resistance" along the interface between a particle and the matrix is simulated with a perfect interface but a lower thermal conductivity of the particle. The results indicate that the effective thermal conductivity distribution greatly depends on Kapitza thermal resistance, particle size, and degree of material gradient.
[DOI: 10.1115/1.2936893]

Keywords: functionally graded nanocomposites, effective thermal conductivity, self-consistent method, Kapitza thermal resistance, heat conduction

1 Introduction

Functionally graded materials (FGMs) are characterized by spatially varied microstructures of constituent phases and gradual variation of effective material properties. This class of materials has received considerable attention from researchers and engineers because of their unique and attractive thermomechanical properties [1–8]. Especially noteworthy in the area of mechanics of FGMs is the contribution of Erdogan and co-workers—see, for example, Refs. [1,4]. With miniaturization of microelectronic elements and coating components, FGMs with embedded nanoparticles (nano-FGMs) can be utilized in very small, lightweight components, while retaining the excellent physical properties of nanomaterials [9,10]. For instance, Zhang et al. [11] proposed to use nano-FGMs to construct a coupling solar energy generator system maximally utilizing both photo- and thermoelectric energies. However, with the decrease of particle size in an FGM, the surface-to-volume ratio of particles increases, such that the interface between a particle and the surrounding matrix produces a considerable effect on the effective material behavior, especially in the case of nano-FGMs.

In 1941, Kapitza [12] presented measurements indicating the existence of a temperature discontinuity near the interface between helium and a solid in the presence of a heat flux. A similar phenomenon was also found across the interface between two solids, which has been termed the "Kapitza thermal resistance" [13]. In randomly dispersed particulate nanocomposites, the Kapitza thermal resistance greatly decreases the effective thermal conductivity with increasing particle size [14–16]. Some analytical and numerical models have been developed to predict the effective thermal conductivity of nanocomposites considering the Kapitza thermal resistance [17–20]. However, for nano-FGMs, these models do not consider the graded microstructure, and thus, a novel model is needed for the accurate design and evaluation of nano-FGMs. This is the emphasis of the present paper.

Yin et al. [8] developed an analytical solution for the heat flux field for the case of a single particle embedded in an FGM matrix. In that solution, a perfect interface is assumed to exist between particles and the matrix, i.e., with temperature continuity across the interface. Therefore, the interfacial thermal resistance is not considered. This work addresses the effect of the Kapitza thermal resistance on the effective thermal properties of nano-FGMs. A particle with the Kapitza thermal resistance is simulated by a particle with a perfect interface, that is, one having a continuous temperature field across the interface, but modeled with a different thermal conductivity to accommodate the so-called Kapitza effect. Although the local heat flow in the particle with a perfect interface is different from that which would exist in one exhibiting Kapitza thermal resistance, the thermal conductivity of the particle is properly chosen to make the average heat flux of the particle equivalent for the two cases. Using the solution for an equivalent particle embedded in a graded matrix, a self-consistent formulation is developed to derive the average heat flux field of the particle phase. Then, the temperature gradient can be obtained in the gradation direction. From the relation between the effective flux and temperature gradient in the gradation direction, the effective thermal conductivity distribution is obtained.

If the gradient of the volume fraction distribution is zero, the FGM is reduced to a composite containing uniformly dispersed particles. Moreover, by disregarding the Kapitza thermal resistance, the proposed model recovers the conventional self-consistent model for uniform composites [21–23]. Mathematically, effective thermal conductivity is a quantity exactly analogous to effective electric conductivity, dielectric permittivity, magnetic permeability, and water permeability in a linear static state, and thus the solution presented herein can be applied to predict these other effective physical properties of graded materials.

The remainder of this paper is organized as follows. Section 2 presents a self-consistent formulation to determine the effective thermal conductivity distribution for an FGM containing nanoparticles and a continuous matrix. To address the effect of the interface between nanoparticles and the matrix, Sec. 3 proposes a scheme to replace particles with the Kapitza interfacial thermal resistance by an equivalent particle with a perfect interface but a lower thermal conductivity. Section 4 introduces the solution for a single inhomogeneity embedded in an FGM matrix under uniform heat flux field in the gradation direction. Using this solution in the self-consistent formulation, we can analytically obtain effective

[1]Corresponding author.
Contributed by the Applied Mechanics Division of ASME for publication in the JOURNAL OF APPLIED MECHANICS. Manuscript received September 24, 2007; final manuscript received April 17, 2008; published online July 24, 2008. Review conducted by Robert M. McMeeking.

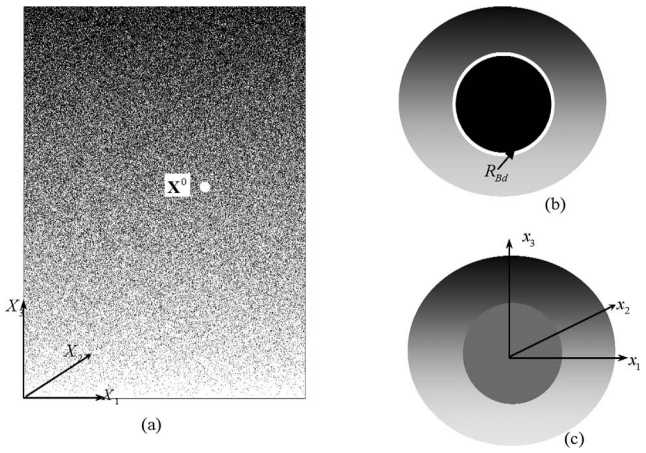

Fig. 1 Illustration of a self-consistent model for FGMs: (*a*) FGM containing nanoparticles (black) dispersed in Phase *B* matrix (white), (*b*) Phase *A* particle embedded in the FGM itself with an interfacial thermal resistance, and (*c*) equivalent particle embedded in the FGM with a perfect interface and a lower thermal conductivity

thermal conductivity distribution in the FGM. Section 5 illustrates typical results obtained with the new solution and demonstrates the capability of the proposed model using parametric analyses and comparison with available experimental data.

2 Self-Consistent Formulation

Consider an FGM containing Phase A nanoparticles embedded in a Phase B matrix as shown in Fig. 1(a), where the global coordinate system $X_1-X_2-X_3$ has its origin at the bottom left side of the displayed FGM. The effective thermal conductivity can be tested through the relation between the average heat flux and temperature gradient. A uniform heat flux load q^∞ is applied in the gradation direction. For any material point $\mathbf{X}^0$, because the material is homogeneous at each X_1-X_2 layer under steady conditions and without the presence of heat sources, the average heat flux should be equal to q^∞. At the microscopic scale, both the average heat flux and temperature gradient consist of the two portions from Phases A and B [17]:

$$\langle q_i\rangle^D(X_3^0) = q^\infty \delta_{i3} = \phi(X_3^0)\langle q_i\rangle^A(X_3^0) + [1-\phi(X_3^0)]\langle q_i\rangle^B(X_3^0) \quad (1)$$

and

$$\langle H_i\rangle^D(X_3^0) = \phi(X_3^0)[\langle H_i\rangle^A(X_3^0) + J_i(X_3^0)] + [1-\phi(X_3^0)][\langle H_i\rangle^B(X_3^0)] \quad (2)$$

where the angle brackets with superscripts D, A, and B denote the volume averages over the whole material point, Phase A, and Phase B, respectively; q_i and H_i represent the heat flux and temperature gradient, respectively, and ϕ is the volume fraction of Phase A. Notice that because the normal component of the heat flux across the interface between the particle and matrix is continuous, the average heat flux only includes two terms from the two material phases; whereas due to a temperature discontinuity existing across the interface, an additional term J_i is introduced to represent the contribution of the temperature jump across the interface, shown schematically in Fig. 1(b) as a white ring. Although shown schematically with finite thickness, the actual interface thickness is infinitesimally small.

The temperature jump is proportional to the normal heat flux across the interface q^n as follows:

$$\Delta T = -R_{Bd} q^n \quad (3)$$

where R_{Bd} denotes the interfacial thermal resistance [14], i.e., the Kapitza thermal resistance. To solve the average heat flux field in particle Phase A, the self-consistent method [21,22] is used as outlined below.

- For a given point $\mathbf{X}^0$ in the global FGM system as seen in Fig. 1(a), we build up a local coordinate system with a particle centered at the origin as seen in Fig. 1(c). The thermal conductivity of the graded matrix is assumed to be the same as the FGM itself at the global system.
- Because the particle is in contact with the continuous matrix Phase B, a constant interfacial thermal resistance exists along the interface between the particle and the matrix as seen in Fig. 1(b).
- To solve for the particle's average field, the particle with interfacial thermal resistance is replaced with an equivalent particle with a perfect thermal interface as seen in Fig. 1(c). Therefore, the particle's average heat flux field is obtained from the solution for one particle embedded in an unbounded graded matrix under uniform heat flux at far field.

Through the above procedure, Eq. (2) becomes

$$\langle H_i\rangle^D(X_3^0) = \phi(X_3^0)[\overline{\langle H_i\rangle}^A(X_3^0)] + [1-\phi(X_3^0)][\langle H_i\rangle^B(X_3^0)] \quad (4)$$

where the superscript $\overline{\langle H_i\rangle}$ denotes the presence of a temperature gradient over the equivalent particle. Because the relation between $\langle q_i\rangle^B(X_3^0)$ and $\langle H_i\rangle^B(X_3^0)$ satisfies the Fourier law, if $\langle q_i\rangle^A(X_3^0)$ and $\overline{\langle H_i\rangle}^A(X_3^0)$ can be solved, one can find the relation between overall average heat flux and temperature gradient at point $\mathbf{X}^0$. Because $\mathbf{X}^0$ is arbitrary and can move to any point in the global coordinate system, we can obtain the effective thermal conductivity distribution. Section 3 presents the relation between $\langle q_i\rangle^A(X_3^0)$ and $\overline{\langle H_i\rangle}^A(X_3^0)$, and then Sec. 4 provides the relation between $\langle q_i\rangle^A(X_3^0)$ and the applied test loading q^∞.

3 Equivalent Particle to Simulate the "Kapitza Thermal Resistance"

Although the heat flux field for a particle Ω embedded in an FGM with Kapitza thermal resistance (Fig. 1(b)) is fairly complex, we can treat the particle as a homogeneous particle with a perfect interface as long as the average heat flux and temperature gradient in the new particle are equal to those in the original particle with interfacial thermal resistance. For a stable heat flow in the original particle, observed from the outside surface, the average heat flux field can be written as

$$\langle q_i\rangle_\Omega = \frac{1}{V^\Omega}\left[\int_\Omega q_i(\mathbf{x})d\mathbf{x} + \int_{\partial\Omega} x_i \Delta q_j(\mathbf{x}) n_j dS\right] \quad (5)$$

where Δq_j denotes the difference of heat flux field cross the interface, and n_j the outward unit normal vector. Based on the continuity of heat flow, we have $\Delta q_j(\mathbf{x})n_j = 0$ across the interface. Therefore, Eq. (5) is reduced to

$$\langle q_i\rangle_\Omega = \frac{1}{V^\Omega}\int_\Omega q_i(\mathbf{x})d\mathbf{x} \quad (6)$$

Considering the temperature discontinuity, we can write the average temperature gradient observed from the outside surface as

$$\langle H_i\rangle_\Omega = \frac{1}{V^\Omega}\left[\int_\Omega H_i(\mathbf{x})d\mathbf{x} + \int_{\partial\Omega} \Delta T(\mathbf{x}) n_i dS\right] \quad (7)$$

Substituting Eq. (3) into the second term on the right hand side of Eq. (7) provides

$$\int_{\partial\Omega} \Delta T(\mathbf{x}) n_i dS = -\int_{\partial\Omega} R_{Bd}(q_j(\mathbf{x})n_j)n_i dS \quad (8)$$

Because $q_{j,j}(\mathbf{x}) = 0$ and $\int_\Omega n_{i,j}(\mathbf{x})d\mathbf{x} = (4/3)\pi a^2 \delta_{ij}$ with a being the radius of the particle, the above equation can be rewritten as

$$\int_{\partial\Omega} \Delta T(\mathbf{x}) n_i dS = -\frac{4}{3}\pi a^2 R_{Bd} \langle q_i \rangle_\Omega \tag{9}$$

Substituting Eq. (9) into Eq. (7) and using the Fourier law with Eq. (6), we can rewrite Eq. (7) as

$$\langle H_i \rangle_\Omega = -\left(\frac{1}{k^A} + \frac{R_{Bd}}{a}\right)\langle q_i \rangle_\Omega \tag{10}$$

where k^A denotes the thermal conductivity of the Phase A particle. Therefore, regardless of how complex the local heat flux field is in the particle domain, from an observation point outside the particle, the particle with the Kapitza thermal resistance in Fig. 1(*b*) is equivalent to a new particle with a perfect interface in Fig. 1(*c*) but with a lower thermal conductivity, namely, $\tilde{k}^A$, or,

$$\tilde{k}^A = k^A/(1 + R_{Bd}k^A/a) \tag{11}$$

Therefore, by using Eq. (11) and the Fourier law for Phase B, Eq. (4) can be further rewritten as

$$\langle H_i \rangle^D(X_3^0) = -\phi(X_3^0)\frac{\langle q_i \rangle^A(X_3^0)}{\tilde{k}^A} - [1 - \phi(X_3^0)]\frac{\langle q_i \rangle^B(X_3^0)}{k^B} \tag{12}$$

Combining Eqs. (1) and (12), we can obtain the relation between average heat flux and average temperature gradient if the relation between the particle's average heat flux $\langle q_i \rangle^A(X_3^0)$ and the applied heat flux q^∞ is provided.

4 Single Inhomogeneity in a Functionally Graded Material

A single particle embedded in a homogeneous matrix is a fundamental problem in materials modeling. Eshelby [24,25] derived the elastic solution for an ellipsoidal inclusion embedded in an unbounded matrix with a uniform, far-field loading. Hatta and Taya [26] extended Eshelby's method to heat conduction problems. Yin et al. [8] investigated the heat flux field for a single particle embedded in an FGM matrix.

Consider an unbounded FGM domain with heat conductivity, $k(x_3)$, containing a single spherical inhomogeneity Ω (see Fig. 2) with heat conductivity k^A, radius a, with its center located at the origin. A uniform heat flux field q^∞ is applied in the x_3 direction in the far field. Because the FGM is homogeneous in the x_1-x_2 plane, if the particle did not exist, then the heat flux field would be uniform. However, a disturbance in the heat flux field q_i' will be induced by the presence of the particle. Then, the local heat flux field can be denoted by two parts:

$$q_i(\mathbf{x}) = q^\infty \delta_{i3} + q_i'(\mathbf{x}) \tag{13}$$

The variation of the FGM properties is assumed to be continuous and differentiable in the gradation direction, so that the thermal conductivity distribution can be written as

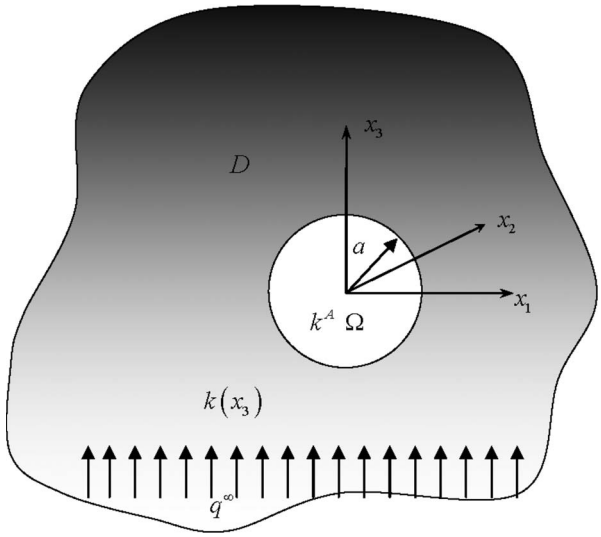

Fig. 2 A single spherical inhomogeneity in an FGM matrix subjected to a uniform heat flux field

$$k(x_3) = k^0(1 + \alpha x_3)^2 + O(x_3^2) \tag{14}$$

where the material variation parameter α is defined as

$$\alpha = 0.5k'(0)/k^0 \tag{15}$$

in which k^0 and $k'(0)$ are the thermal conductivity and its first derivative at the origin, respectively. The higher order terms $O(x_3^2)$ in Eq. (14) will be disregarded for the convenience of derivation. It is noted that accuracy of approximation in Eq. (14) also depends on the magnitude of the material gradient. Yin et al. [8] found that, when $\alpha a << 1$, which is satisfied for many FGMs, Eq. (14) provides a high degree of accuracy.

Using Eshelby's equivalent inclusion method, a linearly distributed prescribed heat flux field is introduced in the particle to represent the material mismatch between the particle and the surrounding graded material. The Green's function technique is employed to derive the disturbed heat flux field in Eq. (13). Finally, the heat flux field in both the particle and the graded material can be explicitly written as follows [8]:

$$q_i(\mathbf{x}) = q^\infty \delta_{i3} + q^*(\mathbf{x})\delta_{3i} - k^0(1 + \alpha x_3)U_{,i}(\mathbf{x}) + k^0\alpha\delta_{i3}U(\mathbf{x}) \tag{16}$$

where

$$q^*(\mathbf{x}) = \begin{cases} 0, & \mathbf{x} \notin \Omega \\ q^0 + \tilde{q}x_3, & \mathbf{x} \in \Omega \end{cases} \tag{17}$$

$$U(\mathbf{x}) = \begin{cases} \dfrac{1}{15k^0}[5\rho a q^0(\rho n_3 - 5\alpha a) - \rho^3 a^2(1 - 3n_3^2)(\tilde{q} - \alpha q^0) - \alpha\rho^2 a^3 n_3(\tilde{q} - 2\alpha q^0)], & \mathbf{x} \notin \Omega \\ \dfrac{1}{30k^0}[q^0(10x_3 - 5\alpha(3a^2 - |\mathbf{x}|^2)) - (\tilde{q} - \alpha q^0)(5a^2 - 3|\mathbf{x}|^2 - 6x_3^2) - \alpha(\tilde{q} - 2\alpha q^0)(5a^2 - 3|\mathbf{x}|^2)x_3], & \mathbf{x} \in \Omega \end{cases} \tag{18}$$

$$U_{,i}(\mathbf{x}) = \begin{cases} \dfrac{1}{15k^0}[5q^0\rho^2(\rho(\delta_{i3} - 3n_3n_i) + \alpha a n_i) + 3(\tilde{q} - \alpha q^0)\rho^4 a(2\delta_{i3}n_3 + n_i - 5n_3^2 n_i) - \alpha(\tilde{q} - 2\alpha q^0)\rho^3 a^2(\delta_{i3} - 3n_3 n_i)], & \mathbf{x} \notin \Omega \\ \dfrac{1}{30k^0}(10q^0(\delta_{i3} + \alpha x_i) + 6(\tilde{q} - \alpha q^0)(2\delta_{i3}x_3 + x_i) - \alpha(\tilde{q} - 2\alpha q^0)[(5a^2 - 3|\mathbf{x}|^2)\delta_{i3} - 6x_3 x_i]), & \mathbf{x} \in \Omega \end{cases} \tag{19}$$

in which $\mathbf{n}=\mathbf{x}/|\mathbf{x}|$, and $\rho=a/|\mathbf{x}|$, $\alpha=0.5k'(0)/k^0$, and q^0 and $\tilde{q}$ are written as

$$q^0=\frac{k^A-k^0}{3k^A-2(1-a^2\alpha^2)(k^A-k^0)}3q^\infty$$

$$\tilde{q}=\frac{2(k^A-k^0)^2-15k^0k^A}{(3k^A+2k^0)[3k^A-2(1-a^2\alpha^2)(k^A-k^0)]}2\alpha q^\infty \tag{20}$$

Taking a volume average of the heat flux field on the particle domain provides the particle's average heat flux as

$$\langle q_i\rangle_\Omega=\frac{3k^A}{3k^A-2(1-a^2\alpha^2)[k^A-k^0]}q^\infty\delta_{i3} \tag{21}$$

In Fig. 1(*c*), the equivalent particle with thermal conductivity $\tilde{k}^A$ is embedded in the FGM with effective thermal conductivity distribution $\bar{k}(X_3)$, which is yet unknown. Using the above equation, we can write the particle's average heat flux as

$$\langle q_i\rangle^A(X_3^0)=\frac{3\tilde{k}^A}{3\tilde{k}^A-2[1-a^2\alpha^2(X_3^0)][\tilde{k}^A-k(X_3^0)]}q^\infty\delta_{i3} \tag{22}$$

Using Eqs. (1), (12), and (22), we can derive the relation between the average heat flux and temperature gradient as

$$\langle q_3\rangle^D(X_3^0)=-k^B\left[1-\phi(X_3^0)\frac{3(\tilde{k}^A-k^B)}{3\tilde{k}^A-2[1-a^2\bar{\alpha}^2(X_3^0)][\tilde{k}^A-\bar{k}(X_3^0)]}\right]^{-1}\times\langle H_3\rangle^D(X_3^0) \tag{23}$$

Considering the arbitrariness of choosing $\mathbf{X}^0$, we can obtain the effective thermal conductivity at any location as

$$\bar{k}(X_3)=k^B\left[1-\phi(X_3)\frac{3(\tilde{k}^A-k^B)}{3\tilde{k}^A-2[1-a^2\bar{\alpha}^2(X_3)][\tilde{k}^A-\bar{k}(X_3)]}\right]^{-1} \tag{24}$$

Notice that the above expression is implicit because the right hand side includes $\bar{k}(X_3)$ itself and $\bar{\alpha}$ is still unknown as

$$\bar{\alpha}(X_3)=\frac{1}{2\bar{k}(X_3)}\frac{d\bar{k}(X_3)}{dX_3} \tag{25}$$

We solve Eq. (24) using a recursive method, in which a boundary condition is typically implied as

$$\bar{k}(0)=k^B \tag{26}$$

because the volume fraction of the particle Phase *A* is zero. For instances where the particle volume fraction does not start from 0%, the modified boundary condition of $\bar{k}(0)$ can be still obtained with the aid of the uniform composite model as seen in Eq. (27).

5 Results and Discussion

For a functionally graded particulate nanocomposite, if the volume fraction of nanoparticles continuously varies in the gradation direction, the effective thermal conductivity distribution can be predicted by Eq. (24) with Eqs. (11), (25), and (26). If the material gradation is zero, the nano-FGM is reduced into a uniformly dispersed nanocomposite, so in Eq. (24) $\bar{\alpha}(X_3)=0$ and the effective thermal conductivity can be rewritten as

$$\bar{k}=k^B\left(1-3\phi\frac{\tilde{k}^A-k^B}{\tilde{k}^A+2\bar{k}}\right)^{-1} \tag{27}$$

The above equation can be ultimately simplified into a quadratic equation with two roots. The correct root places $\bar{k}$ between $\tilde{k}^A$ and k^B.

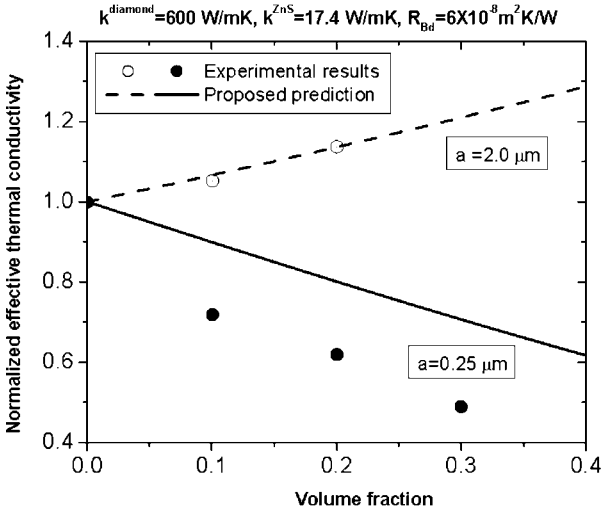

Fig. 3 Effective thermal conductivity versus volume fraction for diamond/ZnS composites

Notice that although this work studies the particle size in nanometers, nanoparticles are still much larger than molecular or atomic scales, so they can be treated as continuous bodies. If the particle's size is fairly large, the effect of the Kapitza thermal resistance can be disregarded, by setting $\tilde{k}^A=k^A$. In this case, the effective thermal conductivity in Eq. (24) can be rewritten as

$$\bar{k}(X_3)=k^B\left[1-\phi(X_3)\frac{3(k^A-k^B)}{3k^A-2[1-a^2\bar{\alpha}^2(X_3)][k^A-\bar{k}(X_3)]}\right]^{-1} \tag{28}$$

Notice that because $\bar{\alpha}(X_3)$ is related to the volume fraction distribution in its neighborhood, the effective thermal conductivity at a material point not only depends on the volume fraction at the point as shown in Eq. (28), but also depends on the global volume fraction distribution.

Disregarding both the Kapitza thermal resistance and material gradation, the proposed model recovers the conventional self-consistent model as

$$\bar{k}=k^B\left(1-3\phi\frac{k^A-k^B}{k^A+2\bar{k}}\right)^{-1} \tag{29}$$

To demonstrate the capability of the proposed model, we first compare it with available experiments. Every et al. [14] tested the effective thermal conductivity for diamond/ZnS composites with two radii, i.e., $a=250$ nm and 2.0 μm. The other material constants are $k^{\text{diamond}}=600$ W/m K, $k^{\text{ZnS}}=17.4$ W/m K, and $R_{Bd}=6\times10^{-8}$ m^2 K/W. In Fig. 3, for the case of $a=2.0$ μm, the effective thermal conductivity increases with the volume fraction of the diamond particles due to the reinforcement of the particles with much higher thermal conductivity; whereas for the case of $a=250$ nm, the effective thermal conductivity decreases because the interfacial thermal resistance plays a dominant role at this size. The present model predicts the tendency of the experimental data well, although some difference is found for the case of $a=250$ nm due to the irregular particle shape and nonuniform size of particles.

Figure 4 shows the effect of particle size on the effective thermal conductivity distribution in FGMs with linear volume fraction distribution. Here the thickness of the FGMs is set as $H=1$ mm. Four particle sizes are illustrated. For $a=10$ μm, the effective thermal conductivity increases with the volume fraction due to the high thermal conductivity of particles, whereas for $a=10$ nm and 100 nm, the effective thermal conductivity decreases with the vol-

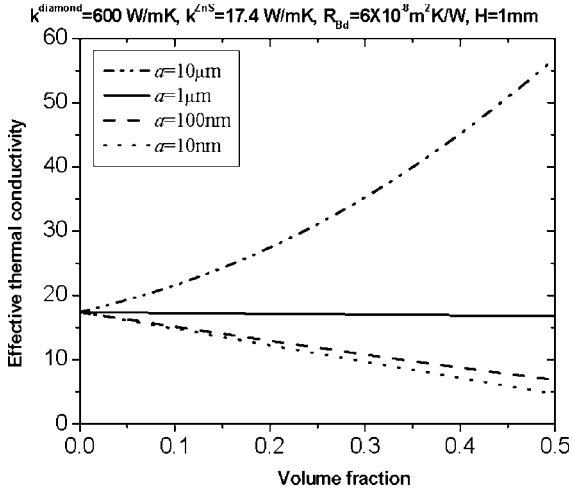

Fig. 4 Predicted effective thermal conductivity versus volume fraction for diamond/ZnS FGMs with different particle sizes

ume fraction due to the Kapitza thermal resistance of nanoparticles. When $a=1$ μm, the change of thermal conductivity of particles with the volume fraction is quite small because the equivalent thermal conductivity of particles at this size, $\tilde{k}^A = 16.2$ W/m K, is fairly close to the thermal conductivity of the matrix, $\tilde{k}^{\mathrm{ZnS}} = 17.4$ W/m K. Therefore, the particle size has a dramatic effect on the effective thermal conductivity distribution in FGMs.

To investigate the effect of the Kapitza thermal resistance, Fig. 5 illustrates the effective thermal conductivity distribution of FGMs containing carbon (C) particles and silicon carbide (SiC) matrix assuming different Kapitza thermal resistances. The material constants used are $k^C = 135$ W/m K and $k^{\mathrm{SiC}} = 9.5$ W/m K. The volume fraction of carbon particles with radius $a=1$ μm varies linearly from 0% to 50% in the gradation direction. The thickness of the FGM is set as $H=1$ mm. With an increase of the Kapitza thermal resistance, the effective thermal resistance decreases considerably. Although the carbon particles have a much higher thermal conductivity than the silicon carbide matrix, the

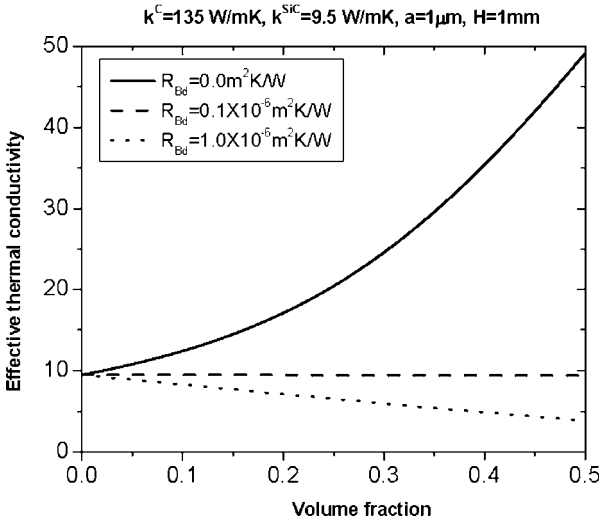

Fig. 5 Predicted effective thermal conductivity versus volume fraction for C/SiC FGMs with different "Kapitza thermal resistances"

particles may not result in an increased effective thermal conductivity if the particle size is fairly low and the Kapitza thermal resistance is considerably high.

Based on the work presented herein, the effective thermal conductivity at a material point in nano-FGMs not only depends on the thermal properties and volume fraction of each phase, which is predicted by conventional composite models, but also considerably depends on the particle size, the Kapitza thermal resistance of the interface, and the material gradient.

6 Conclusions

This work investigates the effective thermal conductivity distribution in nano-FGMs. The "Kapitza thermal resistance" of a nanoparticle is simulated by an equivalent particle with a lower thermal conductivity. A novel self-consistent formulation is developed to derive the average heat flux field of the particle phase based on the analytical solution for a single particle embedded in an FGM matrix. From the relation between the effective flux and temperature gradient in the gradation direction, the effective thermal conductivity distribution is derived.

If the Kapitza thermal resistance is disregarded, the proposed model can also predict the effective thermal conductivity for traditional FGMs. Because effective thermal conductivity is mathematically analogous to effective electric conductivity, dielectric permittivity, magnetic permeability, and water permeability in a linear static state, the solutions developed herein can be extended to obtain these other effective physical properties in graded materials.

If the gradient of the volume fraction distribution is zero, the nano-FGMs are reduced to composites containing uniformly dispersed nanoparticles. An explicit solution of the effective thermal conductivity is provided. Disregarding the interfacial thermal resistance, the proposed model recovers the conventional self-consistent model.

Acknowledgment

This work was sponsored by Federal Highway Administration–National Pooled Fund Study 776, whose support is gratefully acknowledged.

References

[1] Erdogan, F., Wu, B. H., 1996, "Crack Problems in FGM Layers Under Thermal Stresses," J. Therm. Stresses, **19**(3), pp. 237–265.
[2] Miyamoto, Y., Kaysser, W. A., Rabin, B. H., Kawasaki, A., and Ford, R. G., 1999, *Functionally Graded Materials: Design, Processing and Applications*, Kluwer, Dordrecht.
[3] Paulino, G. H., Jin, Z. H., and Dodds, R. H., 2003, "Failure of Functionally Graded Materials," *Comprehensive Structural Integrity*, Vol. 2, Elsevier Science, Amsterdam, pp. 607–644.
[4] Yildirim, B., and Erdogan, F., 2004, "Edge Crack Problems in Homogenous and Functionally Graded Material Thermal Barrier Coatings Under Uniform Thermal Loading," J. Therm. Stresses, **27**(4), pp. 311–329.
[5] Yin, H. M., Sun, L. Z., and Paulino, G. H., 2004, "Micromechanics-Based Elastic Modeling for Functionally Graded Materials With Particle Interactions," Acta Mater., **52**, pp. 3535–3543.
[6] Yin, H. M., Paulino, G. H., Buttlar, W. G., and Sun, L. Z., 2005, "Effective Thermal Conductivity of Functionally Graded Particulate Composites," J. Appl. Phys., **98**, p. 063704.
[7] Yin, H. M., Paulino, G. H., Buttlar, W. G., and Sun, L. Z., 2007, "Micromechanics-Based Thermoelastic Model for Functionally Graded Particulate Materials With Particle Interactions," J. Mech. Phys. Solids, **55**, pp. 132–160.
[8] Yin, H. M., Paulino, G. H., Buttlar, W. G., and Sun, L. Z., 2008, "Heat Flux Field for One Spherical Inhomogeneity Embedded in a Functionally Graded Material Matrix," Int. J. Heat Mass Transfer, **51**(11-12), pp. 3018–3024.
[9] Pompea, W., Worch, H., Epple, M., Friess, W., Gelinsky, M., Greil, P., Hempele, U., Scharnweber, D., and Schulte, K., 2003, "Functionally Graded Materials for Biomedical Applications," Mater. Sci. Eng., A, **362**, pp. 40–60.
[10] Songa, H. S., Hyuna, S. H., Moona, J., and Song, R. H., 2005, "Electrochemical and Microstructural Characterization of Polymeric Resin-Derived Multilayered Composite Cathode for SOFC," J. Power Sources, **145**, pp. 272–277.
[11] Zhang, Q. J., Tang, X. F., Zhai, P. C., Niino, M., and Endo, C., 2005, "Recent Development in Nano and Graded Thermoelectric Materials," Mater. Sci. Forum, **492–493**, pp. 135–140.
[12] Kapitza, P. L., 1941, "The Study of Heat Transfer in Helium II," J. Phys.

(USSR), **4**, pp. 181–210.
[13] Swartz, E. T., and Pohl, R. O., 1989, "Thermal-Boundary Resistance," Rev. Mod. Phys., **61**, pp. 605–668.
[14] Every, A. G., Tzou, Y., Hasselman, D. P. H., and Raj, R., 1992, "The Effect of Particle Size on the Thermal Conductivity of ZnS/diamond Composites," Acta Metall. Mater., **40**, pp. 123–129.
[15] Yang, H.-S., Bai, G.-R., Thompson, L. J., and Eastman, J. A., 2002, "Interfacial Thermal Resistance in Nanocrystalline Yttria-Stabilized Zirconia," Acta Mater., **50**, pp. 2309–2317.
[16] Cahill, D. G., Ford, W. K., Goodson, K. E., Mahan, G. D., Majumdar, A., Maris, H. J., Merlin, R., and Phillpot, S. R., 2003, "Nanoscale Thermal Transport," J. Appl. Phys., **93**, pp. 793–818.
[17] Benveniste, Y., 1987, "Effective Thermal Conductivity of Composites With a Thermal Contact Resistance Between the Constituents: Nondilute Case," J. Appl. Phys., **61**, pp. 2840–2843.
[18] Hasselman, D. P. H. and Johnson, L. F., 1987, "Effective Thermal-Conductivity of Composites With Interfacial Thermal Barrier Resistance," J. Compos. Mater., **21**, pp. 508–515.
[19] Nan, C. W., Birringer, R., Clarke, D. R., and Gleiter, H., 1997, "Effective Thermal Conductivity of Particulate Composites With Interfacial Thermal Resistance," J. Appl. Phys., **81**, pp. 6692–6699.
[20] Duong, H. M., Papavassiliou, D. V., Lee, L. L., and Mullen, K. J., 2005, "Random Walks in Nanotube Composites: Improved Algorithms and the Role of Thermal Boundary Resistance," Appl. Phys. Lett., **87**, p. 013101.
[21] Budiansky, B., 1965, "On the Elastic Moduli of Some Heterogeneous Materials," J. Mech. Phys. Solids, **13**, pp. 223–227.
[22] Hill, R., 1965, "A Self-Consistent Mechanics of Composite Materials," J. Mech. Phys. Solids, **13**, 213–222.
[23] Reiter, T., and Dvorak, G. J., 1998, "Micromechanical Models for Graded Composite Materials: II. Thermomechanical Loading," J. Mech. Phys. Solids, **46**, pp. 1655–1673.
[24] Eshelby, J. D., 1957, "The Determination of the Elastic Field of an Ellipsoidal Inclusion, and Related Problems," Proc. R. Soc. London, Ser. A, **241**, pp. 376–396.
[25] Eshelby, J. D., 1959, "The Elastic Field Outside an Ellipsoidal Inclusion," Proc. R. Soc. London, Ser. A, **252**, pp. 561–569.
[26] Hatta, H., and Taya, M., 1986, "Equivalent Inclusion Method for Steady State Heat Conduction in Composites," Int. J. Eng. Sci., **24**(7), pp. 1159–1172.

Uniform Stresses Inside an Elliptical Inhomogeneity With an Imperfect Interface in Plane Elasticity

X. Wang[1]
e-mail: xuwang_sun@hotmail.com

E. Pan

Department of Civil Engineering,
and Department of Applied Mathematics,
University of Akron,
Akron, OH 44325-3905

L. J. Sudak
Department of Mechanical and Manufacturing Engineering,
University of Calgary,
Calgary, AB, T2N-1N4, Canada

We consider an elliptical inhomogeneity embedded in an infinite isotropic elastic matrix subjected to in-plane deformations under the assumption of remote uniform loading. The inhomogeneity-matrix interface is assumed to be imperfect, which is simulated by the spring-layer model with vanishing thickness. Its behavior is based on the assumption that tractions are continuous but displacements are discontinuous across the interface. We further assume that the same degree of imperfection on the interface is realized in both the normal and tangential directions. We find a form of interface function, which leads to uniform stress field within the elliptical inhomogeneity. The explicit expressions for the uniform stress field within the elliptical inhomogeneity are derived. The obtained results are verified by comparison with existing solutions. The condition under which the internal stress field is not only uniform but also hydrostatic is also presented. [DOI: 10.1115/1.2913045]

Keywords: elliptical inhomogeneity, imperfect interface, uniform stress, in-plane deformation

1 Introduction

Micromechanical analysis for elastic inhomogeneities with an imperfect interface has received much attention in literature (see, for example, Refs. [1–3]). Here, the widely used springlike model of the imperfect interface is based on the assumption that tractions are continuous but displacements are discontinuous across the interface. More precisely, the jumps in displacement components are proportional, in terms of the "spring-factor-type" interface functions (or interface parameters), to the respective interface traction components.

Some interesting phenomena have been observed for inhomogeneities with an imperfect interface. Hashin [1] examined a spherical inhomogeneity imperfectly bonded to an infinite matrix, and he found that the stress field inside the spherical inhomogeneity is intrinsically *nonuniform* under a remote uniform stress field. Gao [2] and Shen et al. [4] drew similar conclusions for the two-dimensional circular and elliptical inclusions under plane deformations. In sharp contrast to the above results, Ru and Schiavone [3] found that the stress field inside the inclusion is still *uniform* under remote uniform antiplane shear stresses when the inhomogeneity is circular and the interface is homogeneously imperfect. Antipov and Schiavone [5] developed a novel method to identify the shape of the inhomogeneity and the form of the corresponding interface function, which leads to a uniform interior stress field under antiplane shear deformation. It shall be mentioned that the practical significance of uniform stress field inside the inhomogeneity lies in the fact that a uniform stress distribution is optimal in the sense that it eliminates stress peaks within the inhomogeneity, which usually dominate the mechanical failure of the inhomogeneity [5–7].

This research is motivated by the interesting results in Refs. [5–7] for uniform stress field inside an elastic inhomogeneity with an imperfect interface or with an interphase layer. In this investigation, we confine our attention to the special kind of imperfect interface in which the same degree of imperfection is realized in both the normal and tangential directions along the interface [8,9]. In Sec. 2, we present the basic boundary value problem describing the in-plane deformation of an elastic elliptical inhomogeneity with an inhomogeneously imperfect interface. Here, the circumferentially inhomogeneous interface can reflect the more realistic scenario in which the damage varies along the interface [3,10]. In Sec. 3, we derive the explicit expressions for the uniform stress field inside the elliptical inhomogeneity with an inhomogeneously imperfect interface. In Sec. 4, we discuss several special cases to verify and to illustrate the obtained solution. It is verified that our result can reduce to that for a circular inhomogeneity with a homogeneously imperfect interface [8–10] and can also reduce to that for an elliptical inhomogeneity with perfect bonding conditions [11,12]. We also present the condition under which the internal stress field is not only uniform but also hydrostatic.

2 Basic Formulation

Consider a domain in R^2, infinite in extent, containing a single internal elastic inhomogeneity, with elastic properties different from those of the surrounding matrix. The linearly elastic materials occupying the inhomogeneity and the matrix are assumed to be homogeneous and isotropic with associated shear moduli μ_1 and μ_2, respectively. We represent the matrix by the domain $S_2: x^2/a^2+y^2/b^2 \geq 1$ and assume that the inhomogeneity occupies the elliptical region $S_1: x^2/a^2+y^2/b^2 \leq 1$. The ellipse Γ, whose semimajor and semiminor axes are, respectively, a and b, will denote the inhomogeneity-matrix interface. In what follows, the subscripts 1 and 2 (or the superscripts (1) and (2)) refer to the regions S_1 and S_2, respectively. At infinity, the matrix is subject to in-plane remote uniform stresses σ_{xx}^{∞}, σ_{xy}^{∞}, and σ_{yy}^{∞}. Without losing generality, it is further assumed that the rigid-body rotation at infinity is zero, i.e., $\varepsilon^{\infty}=0$.

For plane deformation, the stresses can be expressed in terms of the two Muskhelishvili's complex potentials $\phi(\zeta)$ and $\psi(\zeta)$ as (Muskhelishvili [13])

[1]Corresponding author.

Contributed by the Applied Mechanics Division of ASME for publication in the JOURNAL OF APPLIED MECHANICS. Manuscript received October 23, 2007; final manuscript received January 6, 2008; published online June 20, 2008. Review conducted by Anthony Waas.

$$\sigma_{xx}+\sigma_{yy}=4\,\mathrm{Re}\left[\frac{\phi'(\zeta)}{\omega'(\zeta)}\right]$$
$$\sigma_{yy}-\sigma_{xx}+2i\sigma_{xy}=2\frac{\overline{m(\zeta)}\left\{\dfrac{\phi'(\zeta)}{\omega'(\zeta)}\right\}'+\psi'(\zeta)}{\omega'(\zeta)} \tag{1}$$
$$\sigma_{rr}+\sigma_{\theta\theta}=\sigma_{xx}+\sigma_{yy}$$
$$\sigma_{\theta\theta}-\sigma_{rr}+2i\sigma_{r\theta}=\frac{\zeta^2\omega'(\zeta)}{|\zeta|^2\overline{\omega'(\zeta)}}(\sigma_{yy}-\sigma_{xx}+2i\sigma_{xy})$$

The resultant force and displacements can be expressed in terms of $\phi(\zeta)$ and $\psi(\zeta)$ as

$$F_x+iF_y=(-i)\left[\phi(\zeta)+\frac{\omega(\zeta)}{\overline{\omega'(\zeta)}}\overline{\phi'(\zeta)}+\overline{\psi(\zeta)}\right] \tag{2}$$

$$2\mu(u_r+iu_\theta)=\frac{|\zeta\omega'(\zeta)|}{\zeta\omega'(\zeta)}\left[\kappa\phi(\zeta)-\frac{\omega(\zeta)}{\overline{\omega'(\zeta)}}\overline{\phi'(\zeta)}-\overline{\psi(\zeta)}\right] \tag{3}$$

where $\kappa=3-4\nu$ for plan strain (assumed henceforth in this research) and $\kappa=(3-\nu)/(1+\nu)$ for plane stress; μ and ν are the shear modulus and Poisson's ratio, respectively; u_r and u_θ are the normal and tangential displacement components in the curvilinear coordinate system expressed by the conformal mapping function $\omega(\zeta)$.

Here, we adopt the following conformal mapping function $\omega(\zeta)$, which maps the region S_2 (in the z-plane) onto the region $\sigma=\{|\zeta|\geq 1\}$ (in the ζ-plane):

$$\omega(\zeta)=d\left(\zeta+\frac{m}{\zeta}\right) \tag{4}$$

where

$$d=\frac{a+b}{2},\quad 0\leq m=\frac{a-b}{a+b}<1$$

It is assumed that the elliptical inhomogeneity is imperfectly bonded to the matrix along Γ by the spring-layer-type interface. The interface conditions are then given by

$$\sigma_{rr}^{(1)}+i\sigma_{r\theta}^{(1)}=\sigma_{rr}^{(2)}+i\sigma_{r\theta}^{(2)}=\beta(x,y)[(u_r^{(2)}+iu_\theta^{(2)})-(u_r^{(1)}+iu_\theta^{(1)})]\quad\text{on }\Gamma \tag{5}$$

where $\beta(x,y)$, which is non-negative, is the imperfect interface parameter. Equation (5) demonstrates that the same degree of imperfection is realized in both the normal and tangential directions [8,9]. When $\beta(x,y)\to+\infty$, the interface is perfect; while if $\beta(x,y)\to 0$, the interface becomes traction-free. Extending the results obtained by Antipov and Schiavone [5] for antiplane shear deformation, here, $\beta(x,y)$ is chosen to be

$$\beta(x,y)=\frac{2\mu_2}{\lambda|\omega'(\zeta)|}=\frac{2\mu_2}{\lambda b\sqrt{1+b^*\sin^2\theta}},\quad(\zeta=e^{i\theta}) \tag{6}$$

where λ ($\lambda>0$) is a dimensionless *constant* parameter and $b^*=(a^2-b^2)/b^2=4md^2/b^2$.

3 Uniform Stress Field Within the Elliptical Inhomogeneity

To simplify the expression for the boundary value problem, we introduce the following analytical continuation:

$$\phi_2(\zeta)=-\frac{\omega(\zeta)}{\bar{\omega}'(1/\zeta)}\overline{\phi_2'}(1/\zeta)-\bar{\psi}_2(1/\zeta),\quad|\zeta|<1 \tag{7}$$

Meanwhile, the two complex potentials $\phi_1(\zeta)$ and $\psi_1(\zeta)$ for the elliptical inhomogeneity must be assumed to take the following forms so as to ensure the uniform stress field within the elliptical inhomogeneity:

$$\phi_1(\zeta)=Ad\left(\zeta+\frac{m}{\zeta}\right),\quad\psi_1(\zeta)=Bd\left(\zeta+\frac{m}{\zeta}\right) \tag{8}$$

where A and B are two unknown complex constants to be determined.

In view of Eqs. (2), (3), and (6)–(8), the boundary condition (5) can be finally rewritten in terms of $\phi_2(\zeta)$ as

$$\begin{aligned}\phi_2^-(\zeta)-\phi_2^+(\zeta)&=d(A+\bar{A}+\bar{B}m)\zeta+d(Am+\bar{A}m+\bar{B})\zeta^{-1}\\ \kappa_2\phi_2^-(\zeta)+\phi_2^+(\zeta)&=d\left[A\left(\frac{\kappa_1\mu_2}{\mu_1}+\lambda\right)-\bar{A}\left(\frac{\mu_2}{\mu_1}-\lambda\right)-\bar{B}m\left(\frac{\mu_2}{\mu_1}-\lambda\right)\right]\zeta,\quad(|\zeta|=1)\\ &\quad+d\left[Am\left(\frac{\kappa_1\mu_2}{\mu_1}-\lambda\right)-\bar{A}m\left(\frac{\mu_2}{\mu_1}+\lambda\right)-\bar{B}\left(\frac{\mu_2}{\mu_1}+\lambda\right)\right]\zeta^{-1}\end{aligned} \tag{9}$$

where the superscripts "+" and "−" denote the limit values from the inner and outer sides of the circle $|\zeta|=1$.

Applying Liouville's theorem, we arrive at two expressions of $\phi_2(\zeta)$ as follows:

$$\begin{aligned}\phi_2(\zeta)&=d(Am+\bar{A}m+\bar{B}+\Gamma_2)\zeta^{-1}+d\Gamma_1\zeta,\quad(|\zeta|>1)\\ \phi_2(\zeta)&=d\Gamma_2\zeta^{-1}-d(A+\bar{A}+\bar{B}m-\Gamma_1)\zeta,\quad(|\zeta|<1)\end{aligned} \tag{10a}$$

$$\begin{aligned}\phi_2(\zeta)&=\frac{d}{\kappa_2}\left[Am\left(\frac{\kappa_1\mu_2}{\mu_1}-\lambda\right)-\bar{A}m\left(\frac{\mu_2}{\mu_1}+\lambda\right)-\bar{B}\left(\frac{\mu_2}{\mu_1}+\lambda\right)-\Gamma_2\right]\zeta^{-1}+d\Gamma_1\zeta,\quad(|\zeta|>1)\\ \phi_2(\zeta)&=d\Gamma_2\zeta^{-1}+d\left[A\left(\frac{\kappa_1\mu_2}{\mu_1}+\lambda\right)-\bar{A}\left(\frac{\mu_2}{\mu_1}-\lambda\right)-\bar{B}m\left(\frac{\mu_2}{\mu_1}-\lambda\right)-\kappa_2\Gamma_1\right]\zeta,\quad(|\zeta|<1)\end{aligned} \tag{10b}$$

where Γ_1 and Γ_2 are related to the remote loads σ_{xx}^∞, σ_{xy}^∞, and σ_{yy}^∞ through the following:

$$\Gamma_1=\frac{\sigma_{xx}^\infty+\sigma_{yy}^\infty}{4},\quad\Gamma_2=\frac{(2-m)\sigma_{xx}^\infty-(2+m)\sigma_{yy}^\infty}{4}+i\sigma_{xy}^\infty \tag{11}$$

In view of the fact that the two expressions of $\phi_2(\zeta)$ must be compatible, we can then uniquely determine the two unknowns A and B as

$$A=\frac{(1+\kappa_2)\left[(\sigma_{xx}^{\infty}+\sigma_{yy}^{\infty})\left(\kappa_2-m^2+(1+m^2)\frac{\mu_2}{\mu_1}+(1-m^2)\lambda\right)+2m(\sigma_{xx}^{\infty}-\sigma_{yy}^{\infty})\left(1-\frac{\mu_2}{\mu_1}+\lambda\right)\right]}{4\left(2+\frac{(\kappa_1-1)\mu_2}{\mu_1}+2\lambda\right)\left(\kappa_2+\frac{\mu_2}{\mu_1}+\lambda\right)-4m^2\left(2\kappa_2+\frac{(1-\kappa_1)\mu_2}{\mu_1}+2\lambda\right)\left(1-\frac{\mu_2}{\mu_1}+\lambda\right)}$$

$$+i\frac{m(1+\kappa_2)\left(1-\frac{\mu_2}{\mu_1}+\lambda\right)\sigma_{xy}^{\infty}}{(1+\kappa_1)\frac{\mu_2}{\mu_1}\left[\kappa_2+m^2+(1-m^2)\frac{\mu_2}{\mu_1}+\lambda(1+m^2)\right]}$$

$$B=\frac{(1+\kappa_2)\left[m(\sigma_{xx}^{\infty}+\sigma_{yy}^{\infty})\left((\kappa_2-1)+(1-\kappa_1)\frac{\mu_2}{\mu_1}\right)+(\sigma_{xx}^{\infty}-\sigma_{yy}^{\infty})\left(2+(\kappa_1-1)\frac{\mu_2}{\mu_1}+2\lambda\right)\right]}{2m^2\left(2\kappa_2+\frac{(1-\kappa_1)\mu_2}{\mu_1}+2\lambda\right)\left(1-\frac{\mu_2}{\mu_1}+\lambda\right)-2\left(2+\frac{(\kappa_1-1)\mu_2}{\mu_1}+2\lambda\right)\left(\kappa_2+\frac{\mu_2}{\mu_1}+\lambda\right)}$$

$$+i\frac{(1+\kappa_2)\sigma_{xy}^{\infty}}{\kappa_2+m^2+(1-m^2)\frac{\mu_2}{\mu_1}+\lambda(1+m^2)} \tag{12}$$

Now that the uniform stresses within the elliptical inhomogeneity can be explicitly given by

$$\sigma_{xx}=\frac{(1+\kappa_2)\left[\begin{array}{l}(\sigma_{xx}^{\infty}+\sigma_{yy}^{\infty})\left(\kappa_2-m^2+m(\kappa_2-1)+(1-m^2)\lambda+(1+m^2+m-m\kappa_1)\frac{\mu_2}{\mu_1}\right)\\+(\sigma_{xx}^{\infty}-\sigma_{yy}^{\infty})\left(2(1+m)(1+\lambda)+(\kappa_1-1-2m)\frac{\mu_2}{\mu_1}\right)\end{array}\right]}{2\left(2+\frac{(\kappa_1-1)\mu_2}{\mu_1}+2\lambda\right)\left(\kappa_2+\frac{\mu_2}{\mu_1}+\lambda\right)-2m^2\left(2\kappa_2+\frac{(1-\kappa_1)\mu_2}{\mu_1}+2\lambda\right)\left(1-\frac{\mu_2}{\mu_1}+\lambda\right)} \tag{13a}$$

$$\sigma_{yy}=\frac{(1+\kappa_2)\left[\begin{array}{l}(\sigma_{xx}^{\infty}+\sigma_{yy}^{\infty})\left(\kappa_2-m^2-m(\kappa_2-1)+(1-m^2)\lambda+(1+m^2-m+m\kappa_1)\frac{\mu_2}{\mu_1}\right)\\+(\sigma_{xx}^{\infty}-\sigma_{yy}^{\infty})\left(2(m-1)(1+\lambda)-(\kappa_1-1+2m)\frac{\mu_2}{\mu_1}\right)\end{array}\right]}{2\left(2+\frac{(\kappa_1-1)\mu_2}{\mu_1}+2\lambda\right)\left(\kappa_2+\frac{\mu_2}{\mu_1}+\lambda\right)-2m^2\left(2\kappa_2+\frac{(1-\kappa_1)\mu_2}{\mu_1}+2\lambda\right)\left(1-\frac{\mu_2}{\mu_1}+\lambda\right)} \tag{13b}$$

$$\sigma_{xy}=\frac{(1+\kappa_2)\sigma_{xy}^{\infty}}{\kappa_2+m^2+(1-m^2)\frac{\mu_2}{\mu_1}+\lambda(1+m^2)} \tag{13c}$$

and the rigid-body rotation ε of the elliptical inhomogeneity is given by

$$\varepsilon=\frac{1}{2}\left(\frac{\partial u_y}{\partial x}-\frac{\partial u_x}{\partial y}\right)=\frac{m\kappa_1(1+\kappa_2)\left(1-\frac{\mu_2}{\mu_1}+\lambda\right)\sigma_{xy}^{\infty}}{2\mu_2(1+\kappa_1)\left[\kappa_2+m^2+(1-m^2)\frac{\mu_2}{\mu_1}+\lambda(1+m^2)\right]} \tag{14}$$

which is a monotonic function of λ. Consequently, if $\sigma_{xy}^{\infty}>0$, we then obtain the following inequality for ε:

$$\frac{m\kappa_1(1+\kappa_2)\left(1-\frac{\mu_2}{\mu_1}\right)\sigma_{xy}^{\infty}}{2\mu_2(1+\kappa_1)\left[\kappa_2+m^2+(1-m^2)\frac{\mu_2}{\mu_1}\right]}\leq\varepsilon\leq\frac{m\kappa_1(1+\kappa_2)\sigma_{xy}^{\infty}}{2\mu_2(1+\kappa_1)(1+m^2)} \tag{15}$$

Furthermore, $\psi_2(\zeta)$ defined within the unbounded matrix can be determined from Eqs. (7) and (10*a*) as follows:

$$\psi_2(\zeta)=-d\bar{\Gamma}_2\zeta+\frac{d(A+\bar{A}+Bm-\Gamma_1)}{\zeta}-\frac{d(m\zeta^2+1)[\Gamma_1\zeta^2-(Am+\bar{A}m+\bar{B}+\Gamma_2)]}{\zeta(\zeta^2-m)},\quad|\zeta|>1 \tag{16}$$

Now that the two complex potentials $\phi_2(\zeta)$ and $\psi_2(\zeta)$, ($|\zeta|$

>1) defined in the unbounded matrix have been completely determined, it is not difficult to derive the stress and displacement fields in the unbounded matrix by using Eqs. (1) and (3).

4 Discussions

In this section, we will discuss several special cases to verify and to illustrate the obtained solution.

4.1 Circular Inhomogeneity With an Imperfect Interface. For a circular inclusion ($a=b$), we have $m=0$, then it follows from Eqs. (4) and (6) that $\beta(x,y)=2\mu_2/\lambda a$, which means that the imperfection must be circumferentially homogeneous along the circular interface so as to get uniform internal stress field. Furthermore, it follows from Eqs. (13*a*) and (13*b*) that

$$\sigma_{xx}=\frac{(1+\kappa_2)\left[(\sigma_{xx}^{\infty}+\sigma_{yy}^{\infty})\left(\kappa_2+\lambda+\frac{\mu_2}{\mu_1}\right)+(\sigma_{xx}^{\infty}-\sigma_{yy}^{\infty})\left(2(1+\lambda)+(\kappa_1-1)\frac{\mu_2}{\mu_1}\right)\right]}{2\left(2+\frac{(\kappa_1-1)\mu_2}{\mu_1}+2\lambda\right)\left(\kappa_2+\frac{\mu_2}{\mu_1}+\lambda\right)} \tag{17a}$$

$$\sigma_{yy}=\frac{(1+\kappa_2)\left[(\sigma_{xx}^{\infty}+\sigma_{yy}^{\infty})\left(\kappa_2+\lambda+\frac{\mu_2}{\mu_1}\right)+(\sigma_{yy}^{\infty}-\sigma_{xx}^{\infty})\left(2(1+\lambda)+(\kappa_1-1)\frac{\mu_2}{\mu_1}\right)\right]}{2\left(2+\frac{(\kappa_1-1)\mu_2}{\mu_1}+2\lambda\right)\left(\kappa_2+\frac{\mu_2}{\mu_1}+\lambda\right)} \tag{17b}$$

$$\sigma_{xy}=\frac{(1+\kappa_2)\sigma_{xy}^{\infty}}{\kappa_2+\frac{\mu_2}{\mu_1}+\lambda} \tag{17c}$$

which are just the results obtained in Refs. [8–10]. In addition, it is found from Eq. (14) that the rigid-body rotation ε of the imperfectly bonded circular inhomogeneity is always zero. It is added that the stress field within a circular inhomogeneity is nonuniform for a homogeneously imperfect interface on which the degree of imperfection in the normal direction and that in the tangential direction are not equal [2,10].

4.2 Elliptical Inhomogeneity With a Perfect Interface. When $\lambda=0$ for a perfect interface, we have carefully checked that Eqs. (13*a*) and (13*b*) for this case will just reduce to that derived by Hardiman [11] and Sendeckyj [12] for an elliptical inhomogeneity with a perfect interface.

4.3 Materials Comprising the Matrix and the Inhomogeneity are Identical ($\mu_1=\mu_2=\mu$, $\kappa_1=\kappa_2=\kappa$). In this case, it follows from Eq. (13*a*) that the stress component σ_{xx} is uniformly distributed within the inhomogeneity as

$$\sigma_{xx}=\frac{(1+\kappa)[\sigma_{xx}^{\infty}(2+2\kappa+3\lambda+2\lambda m-\lambda m^2)-\lambda\sigma_{yy}^{\infty}(1+m)^2]}{2(1+\kappa+2\lambda)(1+\kappa+\lambda-\lambda m^2)} \tag{18}$$

Some interesting phenomena can be observed from the above internal stress expression. For example, if $\sigma_{xx}^{\infty}=0$ while $\sigma_{yy}^{\infty}>0$ (i.e., the matrix is subjected to uniaxial tension along the y-direction), then the internal stress σ_{xx} is given by

$$\sigma_{xx}=-\frac{\lambda\sigma_{yy}^{\infty}(1+\kappa)(1+m)^2}{2(1+\kappa+2\lambda)(1+\kappa+\lambda-\lambda m^2)}\leq 0 \tag{19}$$

which means that σ_{xx} is compressive. It is found from the above expression that $\sigma_{xx}=0$ when the interface is perfect ($\lambda=0$) or when the interface is completely debonded ($\lambda=\infty$). Particularly, when the dimensionless imperfect parameter λ attains the following value:

$$\lambda=\frac{1+\kappa}{\sqrt{2(1-m^2)}} \tag{20}$$

the internal compressive stress component σ_{xx} will get its maximum magnitude of

$$|\sigma_{xx}|_{\max}=\frac{(1+m)^2\sigma_{yy}^{\infty}}{2[\sqrt{2}+\sqrt{1-m^2}]^2} \tag{21}$$

We have checked that the above phenomenon is also valid for the more general case in which the elastic properties of the elliptical inhomogeneity and those of the surrounding matrix are distinct, i.e., $\mu_1\neq\mu_2$, $\kappa_1\neq\kappa_2$.

4.4 Condition for Internal Uniform Hydrostatic Stresses. Here, the uniform hydrostatic stress state within the elliptical inhomogeneity is especially preferred because it achieves both uniform normal stress and vanishing tangential stress along the entire interface [7]. It is observed from Eqs. (1) and (12) that the uniform stresses within the elliptical inhomogeneity is also hydrostatic when $B=0$, i.e.,

$$\frac{\sigma_{yy}^{\infty}-\sigma_{xx}^{\infty}}{\sigma_{xx}^{\infty}+\sigma_{yy}^{\infty}}=\frac{m[\mu_1(\kappa_2-1)-\mu_2(\kappa_1-1)]}{2\mu_1(1+\lambda)+\mu_2(\kappa_1-1)},\quad \sigma_{xy}^{\infty}=0 \tag{22}$$

Hence, it follows from Eqs. (12) and (22) that

$$\sigma_{rr}=\sigma_{\theta\theta}=\frac{\mu_1(1+\kappa_2)(\sigma_{xx}^{\infty}+\sigma_{yy}^{\infty})}{2[2\mu_1(1+\lambda)+\mu_2(\kappa_1-1)]} \tag{23}$$

within the elliptical inhomogeneity.

When $\lambda=0$, Eq. (22) reduces to the condition of uniform hydrostatic stress state within a perfectly bonded elliptical inhomogeneity (Ref. [7], Eq. 4.1). It is also observed from Eq. (22) that the two remote principal stresses must have the same sign to ensure the existence of uniform hydrostatic stresses within the imperfectly bonded elliptical inhomogeneity.

5 Conclusions

In this research, we find that uniform stress field can still be retained for an elliptical inhomogeneity with an inhomogeneously

imperfect interface under remote uniform in-plane stresses. The conditions for the uniform stress state within the elliptical inhomogeneity are as follows: (i) the same degree of imperfection is realized in both the normal and tangential directions along the interface; and (ii) the imperfect interface parameter $\beta(x,y)$ is inversely proportional to $|\omega'(\zeta)|$, $(\zeta=e^{i\theta})$ in which $z=\omega(\zeta)$ maps the elliptical interface in the z-plane onto a unit circle in the ζ-plane. Finally, it shall be mentioned that the conclusion for the uniform stress field also holds when uniform eigenstrains are imposed on the elliptical inhomogeneity.

Acknowledgment

The reviewers' comments and suggestions are highly appreciated. This work is supported in part by AFOSR FA9550-06-1-0317.

References

[1] Hashin, Z., 1991, "The Spherical Inhomogeneity With Imperfect Interface," ASME J. Appl. Mech., **58**, pp. 444–449.
[2] Gao, J., 1995, "A Circular Inhomogeneity With Imperfect Interface," ASME J. Appl. Mech., **62**, pp. 860–866.
[3] Ru, C. Q., and Schiavone, P., 1997, "A Circular Inclusion With Circumferentially Inhomogeneous Interface in Antiplane Shear," Proc. R. Soc. London, Ser. A **453**, pp. 2551–2572.
[4] Shen, H., Schiavone, P., Ru, C. Q., and Mioduchowski, A., 2001, "Stress Analysis of an Elliptic Inclusion With Imperfect Interface in Plane Elasticity," J. Elast., **62**, pp. 25–46.
[5] Antipov, Y. A., and Schiavone, P., 2003, "On the Uniformity of Stresses Inside an Inhomogeneity of Arbitrary Shape," IMA J. Appl. Math., **68**, pp. 299–311.
[6] Ru, C. Q., Schiavone, P., and Mioduchowski, A., 1999, "Uniformity of the Stresses Within a Three-Phase Elliptical Inclusion in Anti-Plane Shear," J. Elast., **52**, pp. 121–128.
[7] Ru, C. Q., 1999, "Three-Phase Elliptical Inclusions With Internal Uniform Hydrostatic Stresses," J. Mech. Phys. Solids, **47**, pp. 259–273.
[8] Sudak, L. J., Ru, C. Q., Schiavone, P., and Mioduchowski, A., 1999, "A Circular Inclusion With Inhomogeneously Imperfect Interface in Plane Elasticity," J. Elast., **55**, pp. 19–41.
[9] Wang, X., Zhang, J. Q., and Guo, X. M., 2005, "Two Circular Inclusions With Inhomogeneously Imperfect Interfaces in Plane Elasticity," Int. J. Solids Struct., **42**, pp. 2601–2623.
[10] Ru, C. Q., 1998, "A Circular Inclusion With Circumferentially Inhomogeneous Sliding Interface in Plane Elastostatics," ASME J. Appl. Mech., **65**, pp. 30–38.
[11] Hardiman, N. J., 1954, "Elliptic Elastic Inclusion in an Infinite Elastic Plate," Q. J. Mech. Appl. Math., **7**(2), pp. 226–230.
[12] Sendeckyj, G. P., 1970, "Elastic Inclusion Problems in Plane Elastostatics," Int. J. Solids Struct., **6**, pp. 1535–1543.
[13] Muskhelishvili, N. I., 1953, *Some Basic Problems of the Mathematical Theory of Elasticity*, Noordhoff, Groningen.

Direct Evaluation of Pressure Distribution of Frictionless Axisymmetric Indentation Problems

Guanghui Fu
LC Dental,
43713 Boscell Road,
Fremont, CA 94538
e-mail: guanghuifu@yahoo.com

The pressure distribution between a rigid frictionless axisymmetric punch and an elastic half-space can be evaluated if the punch shape can be expressed by a polynomial function. However, there is a lack of investigation on how to calculate the pressure distribution when the punch shape cannot be expressed by a polynomial formula. This paper shows that with the help of a mathematical software, the pressure distribution can be evaluated directly from its corresponding analytical solutions. Using this technique, we evaluate the pressure distributions of a cosine punch and a hyperbolic cosine punch, and compare the results with Hertz's solution. [DOI: 10.1115/1.2913000]

1 Introduction

Contact pressure distribution between two surfaces has always been of great interest to engineers. Perhaps, the most widely used equation for bearing application is Hertz's solution. Boussinesq solution for flat-ended punch finds its application in the safety evaluation of foundations in civil engineering. Recently, researchers used Love and Sneddon solution for conical punch to explain nanoindentation experimental data (e.g., Fu and Fischer-Cripps [1]). For the better understanding of fretting fatigue, Ciavarella investigated the pressure distribution for indenters with rounded corners [2].

When a rigid axisymmetric punch indents normally into an elastic half-space, there are two possibilities: one is that the entire punch surface contacts with the half-space; the other is that only part of the punch contacts with the half-space. Following the terminology by Gladwell [3], the first contact is called complete or bonded, and the second one is termed incomplete or unbonded. In the second case, the contact pressure will drop to zero at the boundary of the contact area. In this paper, we will consider incomplete contact.

The axisymmetric solutions for a punch whose shape is flat ended, conical, or parabolic have been known for years. Hertz derived the solution for parabolic punches in 1881 when he investigated the pattern of interference fringes between glass lenses (see Ref. [4]). Later, he tried to extend it to a hardness definition [5]. Hertz's solution is only valid when the contact is incomplete. Bousinessq obtained the pressure distribution for a flat-ended punch in 1885, and found the square root singularity at the punch edge (see Ref. [4]). To solve the conical punch problem, Love [6] used potential theory and Sneddon [7] used integral transform method to get the same result. They found that there exists a logarithmetric singularity at the conical tip, and their solutions are also for incomplete contact. Fu and Chandra [8] found the general solution for polynomial punches. The existing flat-ended, conical, and parabolic punch solutions are special cases of the general solution.

There is a lack of investigation on how to evaluate the pressure distribution when the punch shape cannot be expressed by a polynomial formula. When this happens, the punch is modeled as either a sphere or a cone depending on the bluntness or the sharpness of its tip. Instead of such an approximation, this paper shows that if the punch shape can be expressed by elementary functions, the pressure distribution can be evaluated directly by using its corresponding analytical solutions with the help of a mathematical software. The contact between a rigid cosine punch and an elastic half-space and the contact between a rigid hyperbolic cosine punch and an elastic half-space are investigated. The pressure distributions of these two punches, which may be modeled approximately as spherical punches, are compared with Hertz's solution.

2 Problem Formulation in the Theory of Linear Elasticity

We consider a rigid smooth frictionless axisymmetric punch with its axis of revolution as the z-axis. It indents normally into the plane $z=0$ of an elastic half-space $z \geq 0$ (Fig. 1). The problem is considered in the linear theory of elasticity and the half-space is assumed to be isotropic and homogeneous. The contact region between the punch and the half-space is simply connected. The following equations give the relevant displacement and stresses for the half-space. The vertical component of the displacement is denoted by u_z, and the stress components have two subscripts corresponding to the appropriate coordinates. E and ν are Young's modulus and Poisson's ratio of the half-space.

The boundary conditions for the half-space at $z=0$ are

$$\tau_{zr} = \tau_{z\theta} = 0 \quad (0 \leq r < \infty) \tag{1}$$

$$\sigma_{zz} = 0 \quad (r > a) \tag{2}$$

$$u_z = h + f(r) \quad (0 \leq r \leq a) \tag{3}$$

where a is the radius of the contact area and h is the depth of the indentation ($h \geq 0$). Equation (1) describes the frictionless contact condition (zero shear stresses and discontinuity of tangential displacements at the punch–half-space interface). The second term at the right hand side of Eq. (3) describes the shape of the punch. $f(0)=0$, if $f'(0) \neq 0$; the punch will have a sharp tip at its apex.

Under incomplete contact conditions, we have the interface pressure [2]

$$p(r) = \frac{E}{\pi(1-\nu^2)} \int_r^a \frac{g(t)}{\sqrt{t^2 - r^2}} dt \quad (0 \leq r \leq a) \tag{4}$$

where

$$g(r) = -\frac{d}{dr}\left(r \int_0^r \frac{f'(t)}{\sqrt{r^2 - t^2}} dt \right) \quad (0 \leq r \leq a) \tag{5}$$

If the punch shape can be expressed by elementary functions, the pressure distribution in Eqs. (4) and (5) can be evaluated directly with the aid of a mathematical software.

3 Cosine Punch and Hyperbolic Cosine Punch

Wavy rough surface may be modeled as a cosine function [4]. Each asperity is approximated as a spherical punch so that Hertz's solution can be used. For now, we do not know how good is Hertz's approximation. In this section, we will also consider hyperbolic cosine punch and compare its pressure distribution with Hertz's solution.

We consider a cosine punch described by the following formula:

$$f(r) = A(\cos r - 1) \quad (0 \leq r \leq a, A > 0) \tag{6}$$

where A is a constant.

The hyperbolic cosine punch is defined as

Contributed by the Applied Mechanics Division of ASME for publication in the JOURNAL OF APPLIED MECHANICS. Manuscript received September 12, 2007; final manuscript received November 3, 2007; published online July 17, 2008. Review conducted by Yonggang Huang.

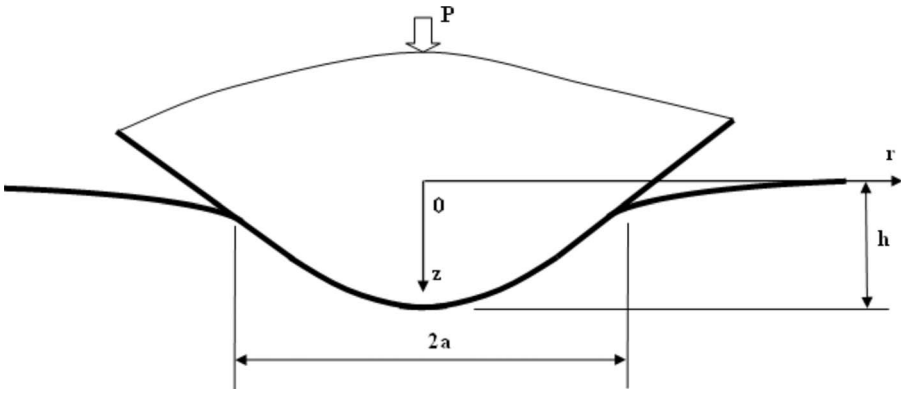

Fig. 1 Indentation of an elastic half-space with a rigid frictionless punch

$$f(r) = B(\cosh r - 1) \quad (0 \leq r \leq a, B > 0) \tag{7}$$

where B is a constant.

After derivation, we put function $f'(r)$ directly into Eqs. (4) and (5). The pressure distributions can be plotted directly with the mathematical software MATHCAD [9]. Note that functions, defined in Eqs. (4) and (5), can be put into the MATHCAD without any simplification. They can be treated just like regular functions.

Figure 2 is the comparison plot of three contacts: Hertz's contact, cosine punch–half-space contact, and hyperbolic cosine punch–half-space contact. To make the comparison simple, we normalize the contact radius and the pressure. Compared to Hertz's solution, the normalized pressure for cosine punch contact is lower while it is higher for the hyperbolic cosine punch contact. Figure 2 is generated directly from the software. Other mathematical software, such as MATHEMATICA, may also be used for the simulation.

The plots for the depth of the indentation versus the radius of the contact area and the total load versus the radius of the contact area can be generated in a similar manner by using their corresponding analytical solutions. Compared to the pressure evaluation, their calculation is much easier.

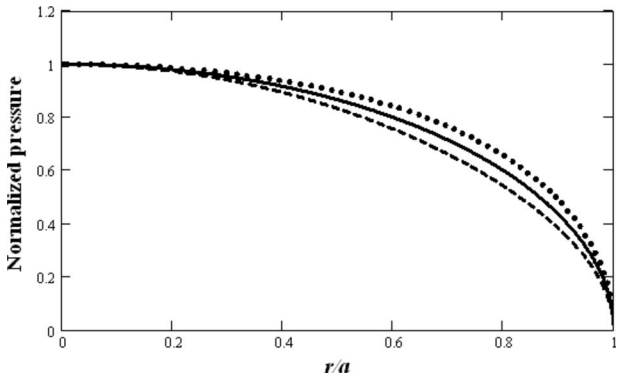

Fig. 2 Contact pressure distributions: the solid line is for the Hertzian contact, the dashed line is for the cosine punch–half-space contact, and the dotted line is for the hyperbolic cosine punch–half-space contact

Interestingly, it will be very difficult or impossible to carry out this direct evaluation technique if we use the pressure distribution in the format given by Green [10].

In the simulation, we only consider two simple elementary functions; however, the presented technique may be used in more complicated cases. The elementary function and its first order derivative need to be continuous in order to use Eqs. (4) and (5). The defined punch shape also needs to be convex so that the contact area is simply connected.

In this paper, we use one elementary function to describe the entire punch surface shape. It may not be necessary. The punch shape may be defined locally in a piecewise fashion by local shape functions. Those shape functions and their first order derivatives need to be continuous for the entire punch surface in order to use the analytical solution presented in this paper. The piecewisely defined punch problem has been considered by Ciavarella. He obtained the pressure distribution for a flat-ended punch with rounded corners, and a cone with a rounded tip [2]. We only consider the frictionless contact in this paper. The same tool may be used in the evaluation of friction contact problems.

References

[1] Fu, G., and Fischer-Cripps, A. C., 2005, "On Sneddon's Boundary Conditions Used in the Analysis of Nanoindentation Data," J. Mater. Sci., **40**, pp. 1789–1791.
[2] Ciavarella, M., 1999, "Indentation by Nominally Flat or Conical Indenters With Rounded Corners," Int. J. Solids Struct., **36**, pp. 4149–4181.
[3] Gladwell, G. M. L., 1980, *Contact Problems in the Classical Theory of Elasticity*, Sijthoff & Noordhoof, Alphen aan den Rijn, The Netherland.
[4] Johnson, K. L., 1985, *Contact Mechanics*, Cambridge University Press, Cambridge, UK, Chap. 4.
[5] Hertz, H., 1896, *Miscellaneous Papers by Heinrich Hertz*, MacMillan & Co., London, UK, pp. 146–183.
[6] Love, A. E. H., 1939, "Boussinesq's Problem for a Rigid Cone," Q. J. Math., **10**, pp. 161–175.
[7] Sneddon, I. N., 1948, "Boussinesq's Problem for a Rigid Cone," Proc. Cambridge Philos. Soc., **44**, pp. 492–507.
[8] Fu, G., and Chandra, A., 2002, "Normal Indentation of Elastic Half-Space With a Rigid Frictionless Axisymmetric Punch," ASME J. Appl. Mech., **69**, pp. 142–147.
[9] MATHCAD 2001I, 2001, *Mathcad User's Guide With Reference Manual*, MathSoft Engineering & Education, Inc., Cambridge, MA.
[10] Green, A. E., and Zerna, W., 1954, *Theoretical Elasticity*, Oxford University Press, London, pp. 175–176.

On a Mass Conservation Criterion in Micro-to-Macro Transitions

İ. Temizer

P. Wriggers

Institute of Mechanics and Computational Mechanics,
Leibniz University of Hannover,
Appelstrasse 9a,
30167 Hannover, Germany

1 Introduction

In order to characterize the macroscopic behavior of a microscopically heterogeneous material, a homogenization methodology is typically employed where a micromechanical sample is identified and tested. See Refs. [1–4] for details and extensive references. This micromechanical testing (*micro-to-macro transition*) procedure for solids at finite deformations is governed by certain criteria. The fundamental criterion to be satisfied is a micro-macro work balance in the incremental form[1]

$$\langle \boldsymbol{P} \cdot \mathrm{d}\boldsymbol{F} \rangle_{\mathcal{V}_0} = \bar{\boldsymbol{P}} \cdot \mathrm{d}\bar{\boldsymbol{F}} \tag{1}$$

that will be referred to as the *work criterion*. Here, the macroscopic first Piola–Kirchhoff stress tensor $\bar{\boldsymbol{P}}$ and the macroscopic deformation gradient $\bar{\boldsymbol{F}}$ are the fundamental macroscopic kinetical and kinematical measures that are used to construct all remaining measures via the usual continuum mechanics relationships and they are defined in terms of the volume average of their microscopic counterparts using the reference configuration $\mathcal{V}_0$ of the following sample:[2]

$$\bar{\boldsymbol{F}} = \langle \boldsymbol{F} \rangle_{\mathcal{V}_0}, \quad \bar{\boldsymbol{P}} = \langle \boldsymbol{P} \rangle_{\mathcal{V}_0} \tag{2}$$

Originally proposed by [5] for the infinitesimal deformation regime and later extended to the finite deformation regime in Ref. [6], the work criterion states that the rate of work done at the microscale should be equal to the rate of work that is measured by using the proposed macroscopic measures. It is well known that this criterion is not satisfied for arbitrary boundary conditions (BCs) applied to the sample. Among BCs that satisfy this criterion, of practical interest are as follows.

1. Uniform traction (UT) BCs: $\boldsymbol{p} = \boldsymbol{\mathcal{P}}\boldsymbol{N}$ so that $\langle \boldsymbol{P} \rangle_{\mathcal{V}_0} = \boldsymbol{\mathcal{P}}$.
2. Linear deformation (LD) BCs: $\boldsymbol{x} = \boldsymbol{\mathcal{F}}\boldsymbol{X}$ so that $\langle \boldsymbol{F} \rangle_{\mathcal{V}_0} = \boldsymbol{\mathcal{F}}$.
3. Periodic (PR) BCs: $\boldsymbol{x}^+ - \boldsymbol{x}^- = \boldsymbol{\mathcal{F}}(\boldsymbol{X}^+ - \boldsymbol{X}^-)$ (periodicity of deformation) and $\boldsymbol{p}^- = -\boldsymbol{p}^+$ (antiperiodicity of tractions) so that $\langle \boldsymbol{F} \rangle_{\mathcal{V}_0} = \boldsymbol{\mathcal{F}}$.

Here, $^{\pm}$ denotes points assigned to each other on opposing sides of the micromechanical sample such that $\partial\mathcal{V}_0^+ \cup \partial\mathcal{V}_0^- = \partial\mathcal{V}_0$ and $\partial\mathcal{V}_0^+ \cap \partial\mathcal{V}_0^- = \emptyset$, $\boldsymbol{x}$ and $\boldsymbol{X}$ are the position vectors in the current and reference configurations, respectively, and $\boldsymbol{p} = \boldsymbol{P}\boldsymbol{N}$ is the traction in the reference configuration with $\boldsymbol{N}$ as the outward unit normal to $\mathcal{V}_0$. Standard prerequisites to show that these BCs satisfy the work criterion are that the material is perfectly bonded and that the material testing procedure is conducted in the absence of body forces and accelerations. These BCs may be enforced by prescribing $\langle \boldsymbol{F} \rangle_{\mathcal{V}_0} = \boldsymbol{\mathcal{F}}$ ($\boldsymbol{\mathcal{F}}$-*controlled*) or by prescribing $\langle \boldsymbol{P} \rangle_{\mathcal{V}_0} = \boldsymbol{\mathcal{P}}$ ($\boldsymbol{\mathcal{P}}$-*controlled*), and therefore there are six possibilities for these three types of BCs. In this work, the discussion is concerned with the four practically important cases, namely, (1) $\boldsymbol{\mathcal{F}}$-LD-BCs, (2) $\boldsymbol{\mathcal{P}}$-UT-BCs, (3) $\boldsymbol{\mathcal{F}}$-PR-BCs, and (4) $\boldsymbol{\mathcal{F}}$-UT-BCs, the latter two being relatively nonstandard. Enforcing $\boldsymbol{\mathcal{P}}$-UT-BCs follows simply by specifying tractions on the surface and is straightforward. Methods of enforcing the remaining types of BCs are discussed in the Appendix.

In addition to the work criterion, consistent with the admittance of a macroscale continuum in the classical sense and using the macroscale continuum definition for the Cauchy stress in terms of the fundamental measures as ($\bar{J} = \det(\bar{\boldsymbol{F}})$)

$$\bar{\boldsymbol{T}} = \bar{J}^{-1}\bar{\boldsymbol{P}}\bar{\boldsymbol{F}}^T \tag{3}$$

an additional criterion that should be satisfied is

$$\bar{\boldsymbol{T}} = \bar{\boldsymbol{T}}^T \tag{4}$$

which corresponds to the conservation of the angular momentum at a macroscale continuum point. This is referred to as the *angular momentum criterion* and it is also well known that the BCs listed above automatically satisfy this observation [6].[3]

2 Micro-Macro Mass Balance

In this work, a third criterion that governs the micro-to-macro transition procedure is pointed out. Enforcing a micro-macro mass balance individually for the deformed ($\mathcal{V}$) and undeformed ($\mathcal{V}_0$) configurations of the micromechanical sample, see Fig. 1, yields the following identifications for the macroscopic densities:

$$m = \bar{\rho}|\mathcal{V}| = \int_{\mathcal{V}} \rho \mathrm{d}v \Rightarrow \bar{\rho} = \langle \rho \rangle_{\mathcal{V}},$$

$$m_0 = \bar{\rho}_0|\mathcal{V}_0| = \int_{\mathcal{V}_0} \rho_0 \mathrm{d}V \Rightarrow \bar{\rho}_0 = \langle \rho_0 \rangle_{\mathcal{V}_0} \tag{5}$$

One may directly express a relationship among these densities by using the fact that the mass of the material in the deformed and undeformed configurations must be equal,

$$m = m_0 \Rightarrow \bar{\rho}|\mathcal{V}| = \bar{\rho}_0|\mathcal{V}_0| \tag{6}$$

Using the kinematical identity $|\mathcal{V}| = \langle J \rangle_{\mathcal{V}_0}|\mathcal{V}_0|$ with this relationship, one immediately obtains

$$\bar{\rho}\langle J \rangle_{\mathcal{V}_0} = \bar{\rho}_0 \tag{7}$$

Finally, combining this result with the fact that $\bar{\rho}\bar{J} = \bar{\rho}_0$ with $\bar{J} = \det(\bar{\boldsymbol{F}}) = \det(\langle \boldsymbol{F} \rangle_{\mathcal{V}_0})$ must hold on the macroscale continuum yields a consistency condition for the homogenization process

$$\bar{\rho}\langle J \rangle_{\mathcal{V}_0} = \bar{\rho}_0 = \bar{\rho}\bar{J} \Rightarrow \bar{J} = \langle J \rangle_{\mathcal{V}_0} \Rightarrow \det(\langle \boldsymbol{F} \rangle_{\mathcal{V}_0}) = \langle \det(\boldsymbol{F}) \rangle_{\mathcal{V}_0} \tag{8}$$

Note that this result need not hold for arbitrary BCs. As a consequence, one may not define *both* $\bar{\rho}$ and $\bar{\rho}_0$ as in Eq. (5) for arbitrary BCs. *Defining either one, the relationship* $\bar{\rho}\bar{J} = \bar{\rho}_0$ *provides the other*. On the other hand, if this result is viewed as a restriction, then the BCs must be chosen such that $\det(\langle \boldsymbol{F} \rangle_{\mathcal{V}_0}) = \langle \det(\boldsymbol{F}) \rangle_{\mathcal{V}_0}$ is satisfied and one may state the following criterion that governs a *kinematical consistency* among the micro-macro mass balance equations:

---

[1] $\langle \mathcal{Q} \rangle_{\Psi} \overset{\text{def}}{=} 1/|\Psi| \int_{\Psi} \mathcal{Q} \mathrm{d}\Psi$ denotes the volume average of the quantity $\mathcal{Q}$ with respect to the domain Ψ.

[2] The notation ($\bullet$) will be used to denote the macroscopic counterpart of a microscopic quantity ($\bullet$).

Contributed by the Applied Mechanics Division of ASME for publication in the JOURNAL OF APPLIED MECHANICS. Manuscript received September 27, 2007; final manuscript received January 10, 2008; published online July 17, 2008. Review conducted by Robert M. McMeeking.

[3] In this reference, only UT-BCs and LD-BCs are considered. However, it is a straightforward task to extend the same line of discussion to PR-BCs.

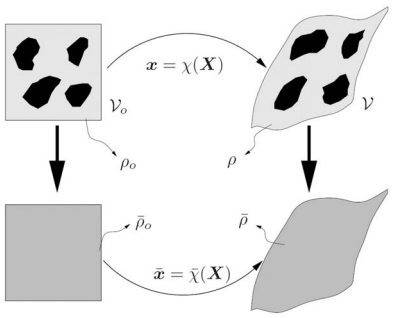

Fig. 1 The original and the homogenized micromechanical problems

$$\textit{Micro-macro mass criterion}: \det(\langle \boldsymbol{F} \rangle_{\mathcal{V}_0}) = \langle \det(\boldsymbol{F}) \rangle_{\mathcal{V}_0} \tag{9}$$

For $\boldsymbol{\mathcal{F}}$-controlled BCs, this constraint reads $\det(\boldsymbol{\mathcal{F}}) = \langle J \rangle_{\mathcal{V}_0}$. One observes the following.

- For $\boldsymbol{\mathcal{F}}$-LD-BCs, one may project the BCs on $\partial\mathcal{V}_0$ into $\mathcal{V}_0$ to obtain a kinematically admissible[4] deformation field (KA-DF) $\boldsymbol{x} = \boldsymbol{\mathcal{F}}\boldsymbol{X}$ in $\mathcal{V}_0$. For this KA-DF, $\boldsymbol{F} = \boldsymbol{\mathcal{F}}$ for all $\boldsymbol{x} \in \mathcal{V}_0$ and therefore the mass criterion is trivially satisfied.
- For $\boldsymbol{\mathcal{F}}$-PR-BCs, one may project the BCs on $\partial\mathcal{V}_0^-$ into $\mathcal{V}_0$ to obtain a KA-DF $\boldsymbol{x} = \boldsymbol{x}^- + \boldsymbol{\mathcal{F}}(\boldsymbol{X} - \boldsymbol{X}^-)$ in $\mathcal{V}_0$. For this KA-DF, $\boldsymbol{F} = \boldsymbol{\mathcal{F}}$ for all $\boldsymbol{x} \in \mathcal{V}_0$ and therefore the mass criterion is again trivially satisfied.

Now recall that $\langle J \rangle_{\mathcal{V}_0}$ appears in the change of the volume of the tested sample via $|\mathcal{V}| = \langle J \rangle_{\mathcal{V}_0} |\mathcal{V}_0|$. However, the change in the volume of the sample is only prescribed by the motion of its boundaries. In other words, for given BCs, any KA-DF will give the same $\langle J \rangle_{\mathcal{V}_0}$, whether or not the deformation field is the solution to the problem. Accordingly, one concludes that LD-BCs and PR-BCs satisfy the mass criterion.[5] Whether the micromechanical test is $\boldsymbol{\mathcal{F}}$-or $\boldsymbol{\mathcal{P}}$-controlled is insignificant since for $\boldsymbol{\mathcal{P}}$-controlled tests the deformation on $\partial\mathcal{V}_0$ is of the same type as $\boldsymbol{\mathcal{F}}$-controlled tests with $\boldsymbol{\mathcal{F}}$ not as a given but rather chosen such that $\langle \boldsymbol{\mathcal{P}} \rangle_{\mathcal{V}_0} = \boldsymbol{\mathcal{P}}$.

The foregoing argument cannot, however, be extended to UT-BCs since a KA-DF for which the mass criterion is satisfied cannot be built in general. In this case, one may drop the requirement of the satisfaction of the mass criterion and employ $\bar{\rho} \overset{\text{def}}{=} \det(\boldsymbol{\mathcal{F}})\overline{\rho_0} \neq \langle \rho \rangle_{\mathcal{V}}$. Note that there is no need to know $\bar{\rho}$ if the boundary value problem is formulated in the reference configuration. On the other hand, if there is a need to compute this quantity without an inconsistency when UT-BCs are employed, one may show that if the test sample is successively enlarged then the inconsistency $\det(\boldsymbol{\mathcal{F}}) - \langle J \rangle_{\mathcal{V}_0} \neq 0$ diminishes and in the limit it is eliminated. For this purpose, a two-dimensional particulate microstructure is considered in periodic and random settings as depicted in Fig. 2 and analyzed using the finite element method. The constituents of the microstructure are modeled as hyperelastic materials of a modified Kirchhoff–St.Venant type [8], for which the strain energy function takes the form

$$\mathcal{W} = \kappa_1 (\ln(J))^2/2 + \kappa_2 (\mathrm{tr}(\boldsymbol{E}))^2/2 + \mu \boldsymbol{E}' \cdot \boldsymbol{E}' \tag{10}$$

where $\kappa_1 + \kappa_2 = \kappa$ with κ and μ as the bulk and shear moduli from linear elasticity, respectively, and $\boldsymbol{E}'$ is the deviatoric part of the Lagrangian strain tensor $\boldsymbol{E}$. In particular, it is assumed that $\kappa_1 = \kappa_2 = \kappa/2$. The bulk and shear moduli of the matrix are set to 4 and 1, respectively, with the particles being ten times stiffer with respect to both moduli. For a sample macroscopic deformation, the variation of the inconsistency error

$$e = \frac{\langle J \rangle_{\mathcal{V}_0} - \det(\boldsymbol{\mathcal{F}})}{\det(\boldsymbol{\mathcal{F}})} \times 100 \tag{11}$$

is monitored in Fig. 3 as a measure of the violation of the mass criterion. It is observed that for both periodic and random arrangements of the microstructure, the mass criterion is violated for UT-BCs, which were enforced in a $\boldsymbol{\mathcal{F}}$-controlled fashion (see Appendix) in order to be able to compare it with the same input $\boldsymbol{\mathcal{F}}$ for all microstructures.[6] The violation seems to be negligible in magnitude for this example ($|e| < 1$). However, its magnitude may depend on the particular problem at hand. For the present case, the violation decreases monotonically to zero for periodic microstructures with increasing sample size. For the random case, the degree of violation depends on the particular realization for a given microstructure. However, similar to classical homogenization observations, the amount of scatter decreases with increasing sample size. Since *ensemble averaging* (equivalent to arithmetic averaging in the present case) is typically employed to extract a statistical measure from an ensemble of realization responses [9], the ensemble averaged violation $\langle\langle e \rangle\rangle$ is also plotted for the random case. It is observed that $\langle\langle e \rangle\rangle$ approaches to zero with increasing sample size. The implication is that one may safely use the relationship $\langle J \rangle_{\mathcal{V}_0} = \det(\boldsymbol{\mathcal{F}})$ with UT-BCs for sufficiently large sample sizes, i.e., the mass criterion will be satisfied. This result is not prohibitive since for homogenization one already has to employ a relatively large sample that qualifies as a representative volume element (RVE).

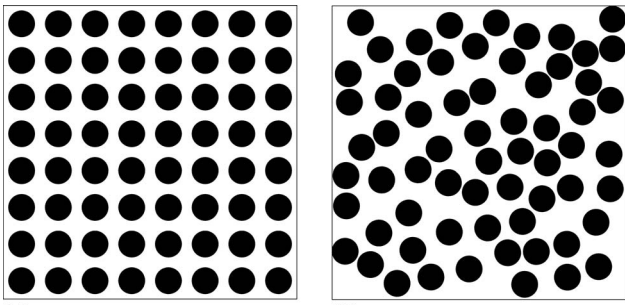

Fig. 2 The periodic (LEFT) and a random realization (RIGHT) of a micromechanical sample size with 64 particles. The volume fraction of the disklike particles in the reference configuration is set to 0.4

3 Conclusion

In this work, a micro-to-macro transition criterion based on a conservation of mass principle has been suggested in addition to the existing work and angular momentum criteria. Interpreting this mass criterion as a restriction on the applicable types of BCs, it was shown using $\boldsymbol{\mathcal{F}}$-controlled experiments that LD-BCs and PR-BCs automatically satisfy this criterion while for UT-BCs it is violated for small sample sizes. Accordingly, for sufficiently large samples, one may use UT-BCs with a negligible violation of the mentioned criterion.

As an application of the investigated criterion, this diminishing behavior of the violation may be used to characterize a numerical

[4]The enforcement procedure for the BCs employs tractions only (see Appendix). Here, kinematic admissibility is used in the sense that the proposed displacements match the solution displacements on the boundary.

[5]In Ref. [7], the fact that $\det(\boldsymbol{\mathcal{F}}) = \langle J \rangle_{\mathcal{V}_0}$ for $\boldsymbol{\mathcal{F}}$-LD-BCs has been used to derive a key identity.

[6]If the tests are $\boldsymbol{\mathcal{P}}$-controlled, then $\langle \boldsymbol{F} \rangle_{\mathcal{V}_0}$ is different for each realization of the random case and for each sample size and therefore it would not make sense to compare the results.

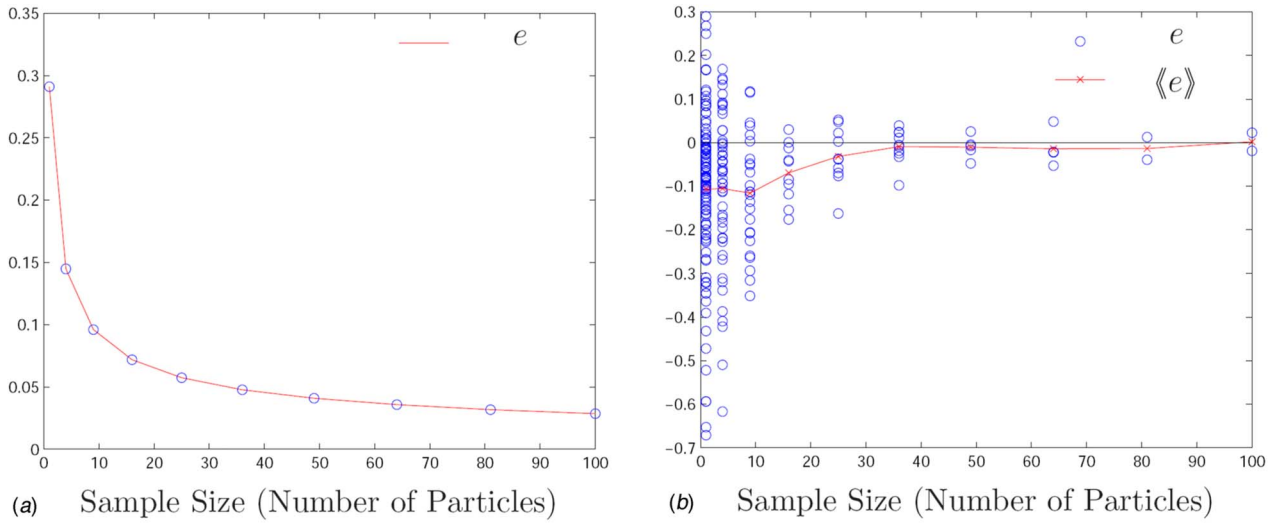

Fig. 3 The inconsistency associated with the micro-macro mass balance is plotted for periodic (LEFT) and random (RIGHT) samples employing $\mathcal{F}$-UT-BCs on a particulate hyperlastic microstructure depicted in Fig. 2. $\mathcal{F}$ has components $\mathcal{F}_{11}=\mathcal{F}_{22}=1.2$ and $\mathcal{F}_{12}=\mathcal{F}_{21}=0.4$.

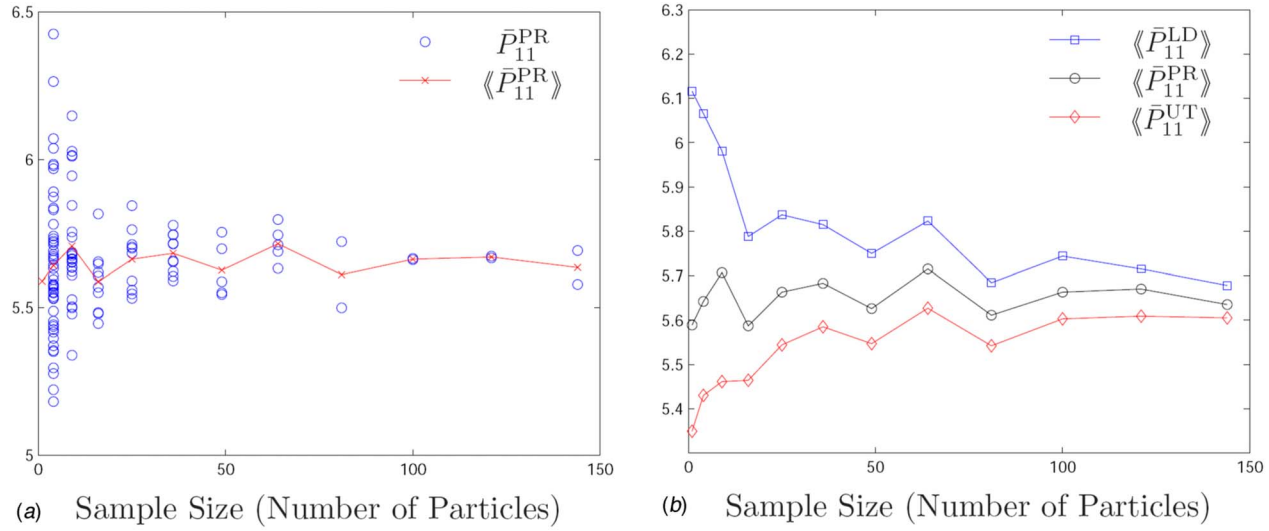

Fig. 4 The variation of the stress component $\bar{P}_{11}$ and its ensemble average (arithmetic mean) is monitored for $\mathcal{F}$-LD/PR/UT-BCs for the random microstructure that was considered in Fig. 3

RVE size for random microstructures.[7] In such a numerical RVE size determination scheme, one would subject increasingly larger samples to $\mathcal{F}$-UT-BCs until the scatter in the sample responses (in this case the violation) for a given sample size is minimal and the ensemble average of the responses saturate. See Ref. [9] for similar schemes. It may be observed from Fig. 3 that such a numerical RVE size would contain at least 50 particles for the prescribed deformation. However, more often than not, the primary macroscopic variable of concern in solid mechanics is the stress. Figure 4 shows the variation of the stress component $\bar{P}_{11}$ for various types of BCs applied to the same microstructural problem that was analyzed earlier. Monitoring, for example, only $\mathcal{F}$-PR-BCs, it is observed that an associated numerical RVE size should contain at least 100 particles for a response that is relatively independent of the sample size and realization. This is verified by comparing ensemble averaged stress components $\langle\langle \bar{P}_{11} \rangle\rangle$ for the three types of BCs and observing that the responses from different types of BCs continue to approach each other with higher sample sizes, in the limit ideally capturing the response of an infinitely sized sample. Therefore, while the mass criterion may also be employed to determine a numerical RVE size, this RVE size would be based on purely kinematical measures and therefore may not reflect the RVE size that would be obtained via the monitoring of kinetical measures such as stress.

Appendix: Enforcing Deformation Controlled Boundary Conditions

In order to employ $\mathcal{F}$-controlled BCs, constraint formulations may be used. In Ref. [10], the Lagrange multiplier method has been employed to enforce these BCs in the context of the small deformation regime. Here, recalling the averaging theorems

[7]For periodic microstructures, one simply takes a unit cell and subjects it to PR-BCs.

$$\langle \boldsymbol{F} \rangle_{\mathcal{V}_0} = \frac{1}{|\mathcal{V}_0|} \int_{\partial \mathcal{V}_0} \boldsymbol{x} \otimes \boldsymbol{N} \mathrm{d}A, \quad \langle \boldsymbol{P} \rangle_{\mathcal{V}_0} = \frac{1}{|\mathcal{V}_0|} \int_{\partial \mathcal{V}_0} \boldsymbol{p} \otimes \boldsymbol{X} \mathrm{d}A \tag{A1}$$

which are valid whenever the prerequisites mentioned earlier for the work criterion hold, the penalty method is suggested to construct the following constraint potentials C for the finite deformation regime such that $\langle \boldsymbol{F} \rangle_{\mathcal{V}_0} = \boldsymbol{\mathcal{F}}$ is enforced when the variation δC of the constraint is added to the variational form

$$\delta U \overset{\text{def}}{=} \int_{\mathcal{V}_0} \delta \boldsymbol{F} \cdot \boldsymbol{P} \mathrm{d}V \tag{A2}$$

of the material testing problem in order to solve $\delta V \overset{\text{def}}{=} \delta U + \delta C = 0$ ($\mathcal{K}$: penalty parameter):[8]

1. $\boldsymbol{\mathcal{F}}$-LD-BCs:

$$C = \frac{1}{2} \int_{\partial \mathcal{V}_0} \mathcal{K} [\boldsymbol{\mathcal{F}} \boldsymbol{X} - \boldsymbol{x}] \cdot [\boldsymbol{\mathcal{F}} \boldsymbol{X} - \boldsymbol{x}] \mathrm{d}A \tag{A3}$$

   which induces $\boldsymbol{p} = \mathcal{K}(\boldsymbol{\mathcal{F}} \boldsymbol{X} - \boldsymbol{x})$ as the traction applied on the boundary to enforce LD-BCs.
2. $\boldsymbol{\mathcal{F}}$-PR-BCs:

$$C = \frac{1}{2} \int_{\partial \mathcal{V}_0^+} \mathcal{K} [\boldsymbol{\mathcal{F}} (\boldsymbol{X}^+ - \boldsymbol{X}^-) - (\boldsymbol{x}^+ - \boldsymbol{x}^-)] \cdot [\boldsymbol{\mathcal{F}} (\boldsymbol{X}^+ - \boldsymbol{X}^-) - (\boldsymbol{x}^+ - \boldsymbol{x}^-)] \mathrm{d}A \tag{A4}$$

   which induces $\boldsymbol{p}^+ = \mathcal{K}[\boldsymbol{\mathcal{F}} (\boldsymbol{X}^+ - \boldsymbol{X}^-) - (\boldsymbol{x}^+ - \boldsymbol{x}^-)]$ and $\boldsymbol{p}^- = -\mathcal{K}[\boldsymbol{\mathcal{F}} (\boldsymbol{X}^+ - \boldsymbol{X}^-) - (\boldsymbol{x}^+ - \boldsymbol{x}^-)]$ as antiperiodic tractions applied on the boundary to enforce PR-BCs.
3. $\boldsymbol{\mathcal{F}}$-UT-BCs:

$$C = \frac{\mathcal{K}}{2} \left(\boldsymbol{\mathcal{F}} - \frac{1}{|\mathcal{V}_0|} \int_{\partial \mathcal{V}_0} \boldsymbol{x} \otimes \boldsymbol{N} \mathrm{d}A \right) \left(\boldsymbol{\mathcal{F}} - \frac{1}{|\mathcal{V}_0|} \int_{\partial \mathcal{V}_0} \boldsymbol{x} \otimes \boldsymbol{N} \mathrm{d}A \right) \tag{A5}$$

which induces $\boldsymbol{p} = \boldsymbol{\mathcal{P}} \boldsymbol{N}$ as the traction applied on the boundary to enforce UT-BCs, with $\boldsymbol{\mathcal{P}}$ not as a given but rather defined by $\boldsymbol{\mathcal{P}} = \mathcal{K} / |\mathcal{V}_0| (\boldsymbol{\mathcal{F}} - 1 / |\mathcal{V}_0| \int_{\partial \mathcal{V}_0} \boldsymbol{x} \otimes \boldsymbol{N} \mathrm{d}A)$.

Note that the induced tractions may easily be concluded by comparing the weak formulation $\delta V = 0$ with a pure traction BC problem of the form

$$\delta U - \int_{\partial \mathcal{V}_0} \boldsymbol{p} \cdot \delta \boldsymbol{x} \mathrm{d}A = 0 \tag{A6}$$

[8] For $\boldsymbol{\mathcal{F}}$-PR-BCs and $\boldsymbol{\mathcal{F}}$-UT-BCs, translational degrees of freedom should additionally be constrained to avoid rigid body motion.

References

[1] Nemat-Nasser, S., and Hori, M., 1999, *Micromechanics, Overall Properties of Heterogeneous Materials*, 2nd ed. North-Holland, Amsterdam.
[2] Torquato, S., 2002, *Random Heterogeneous Materials: Microstructure and Macroscopic Properties*, Springer, Berlin.
[3] Zohdi, T. I., and Wriggers, P., 2005, *Introduction to Computational Micromechanics*, Springer, Berlin.
[4] Nemat-Nasser, S., 2004, *Plasticity: A Treatise on Finite Deformation of Heterogeneous Inelastic Materials*, Cambridge University Press, Cambridge, Chap. 8.
[5] Hill, R., 1963, "Elastic Properties of Reinforced Solids: Some Theoretical Principles," J. Mech. Phys. Solids, **11**, pp. 357–372.
[6] Hill, R., 1972, "On Constitutive Macro-Variables for Heterogeneous Solids at Finite Strain," Proc. R. Soc. London, Ser. A, **326**(1565), pp. 131–147.
[7] Zohdi, T., 2003, "On the Compaction of Cohesive Hyperelastic Granules," Proc. R. Soc. London, Ser. A, **459**, pp. 1395–1401.
[8] Holzapfel, G. A., 2001, *Nonlinear Solid Mechanics: A Continuum Approach for Engineering*, Wiley, Chichester.
[9] Temizer, İ., and Zohdi, T. I., 2007, "A Numerical Method for Homogenization in Non-Linear Elasticity," Comput. Mech., **40**, pp. 281–298.
[10] Miehe, C., and Koch, A., 2002, "Computational Micro-to-Macro Transitions of Discretized Microstructures Undergoing Small Strains," Arch. Appl. Mech., **72**, pp. 300–317.